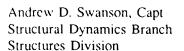
WL-TR-91-3013

AD-A235 843

PROCEEDINGS OF THE FOURTH NASA/DOD CONTROL/STRUCTURES INTERACTION TECHNOLOGY CONFERENCE



January 1991

Final Report for Period 5 - 7 November 1990

Approved for Public Release; Distribution is Unlimited



APIGHT LABORATO

FLIGHT DYNAMICS LABORATORY
WRIGHT LABORATORY
AIR FORCE SYSTEMS COMMAND
WRIGHT-PATTERSON AIR FORCE BASE, OHIO 45433-6553

91-00468

NOTICE

WHEN GOVERNMENT DRAWINGS, SPECIFICATIONS, OR OTHER DATA ARE USED FOR ANY PURPOSE OTHER THAN IN CONNECTION WITH A DEFINITELY GOVERNMENT-RELATED PROCUREMENT, THE UNITED STATES GOVERNMENT INCURS NO RESPONSIBILITY OR ANY OBLIGATION WHATSOEVER. THE FACT THAT THE GOVERNMENT MAY HAVE FORMULATED OR IN ANY WAY SUPPLIED THE SAID DRAWINGS, SPECIFICATIONS, OR OTHER DATA, IS NOT TO BE REGARDED BY IMPLICATION, OR OTHERWISE IN ANY MANNER CONSTRUED, AS LICENSING THE HOLDER, OR ANY OTHER PERSON OR CORPORATION; OR AS CONVEYING ANY RIGHTS OR PERMISSION TO MANUFACTURE, USE, OR SELL ANY PATENTED INVENTION THAT MAY IN ANY WAY BE RELATED THERETO.

THIS REPORT HAS BEEN REVIEWED BY THE OFFICE OF PUBLIC AFFAIRS (ASD/CPA) AND IS RELEASABLE TO THE NATIONAL TECHNICAL INFORMATION SERVICE (NTIS). AT NTIS. IT WILL BE AVAILABLE TO THE GENERAL PUBLIC, INCLUDING FOREIGN NATIONS.

THIS TECHNICAL REPORT HAS BEEN REVIEWED AND IS APPROVED FOR PUBLICATION.

ANDREW D. SWANSON, Captain, USAF

Space Systems Project Leader Vibration Group

STEPHEN R. WHITEHOUSE, Major, USAF

Chief, Vibration Group

Structural Dynamics Branch

FOR THE COMMANDER

JEROME PEARSON, Chief Structural Dynamics Branch

Structures Division

IF YOUR ADDRESS HAS CHANGED, IF YOU WISH TO BE REMOVED FROM OUR MAILING LIST, OR IF THE ADDRESSEE IS NO LONGER EMPLOYED BY YOUR ORGANIZATION PLEASE NOTIFY WL/FIBG, WRIGHT-PATTERSON AFB, OH 45433-6553 TO HELP US MAINTAIN A CURRENT MAILING LIST.

COPIES OF THIS REPORT SHOULD NOT BE RETURNED UNLESS RETURN IS REQUIRED BY SECURITY CONSIDERATIONS, CONTRACTUAL OBLIGATIONS, OR NOTICE ON A SPECIFIC DOCUMENT.

REPORT DOCUMENTATION PAGE

Form Approved
OMB No. 0704-0188

Public reporting burden for this collection of information is estimated to average 1 hour per response, including the time for reviewing instructions, searching existing data sources, gathering and maintaining the data needed, and completing and reviewing the collection of information. Send comments regarding this burden estimate or any other aspect of this collection of information, including suggestions for reducing this burden. To Washington Headquarters Services, Directorate for Information Department and Reports, 1215 Jefferson Davis Highway, Suite 1204, Arlington, VA 22202-4302, and to the Office of Management and Budger, Paperwork Reduction Project (0704-0188), Washington, DA 22503.

| | | Budger, Paperwork Reduction Project (0704-01 | |
|--|--|---|---|
| 1. AGENCY USE ONLY (Leave blan | nk) 2. REPORT DATE 15 January 1991 | 3. REPORT TYPE AND DATES Final, 5-7 Novemb | |
| Proceedings of the Fourth NASA/DoD Control/Structures | | | DING NUMBERS 1F 24010432 |
| 6. AUTHOR(S) | | | |
| Compiled by Captain An | idrew D Swanson | | |
| 7. PERFORMING ORGANIZATION N | AME(S) AND ADDRESS(ES) | | ORMING ORGANIZATION ORT NUMBER |
| 9. SPONSORING/MONITORING AG WL/FIBGC (Capt Andrew | SENCY NAME(S) AND ADDRESS(ES Swanson) (513-255-523 | | NSORING / MONITORING NCY REPORT NUMBER |
| Flight Dynamics Laboratory Wright-Patterson AFB OH 45433-6553 | | | -TR-91-3013 |
| 11. SUPPLEMENTARY NOTES | | | |
| 12a. DISTRIBUTION / AVAILABILITY | STATEMENT | 12b. Dis | STRIBUTION CODE |
| Approved for public re | | s unlimited. | |
| 13. ABSTRACT (Maximum 200 word | is) | | |
| the NASA Langley Resea (I) O'erview, (2) Post (5) Integrated Dosign, | etures Interaction Technic conference was cosponented to Conference The Conference (3) Control Systems | hnology Conference, Or onsored by the Wright erence consisted of se ems Development, (4) S | lando, Florida, Laboratory and even sessions: ensors and Actuators, eriments. |
| 14. SUBJECT TERMS Active control, large space structures, passive damping | | | 15. NUMBER OF PAGES 966 |
| control/structures interaction, vibration control | | | 16. PRICE CODE |
| 17. SECURITY CLASSIFICATION OF REPORT UNCLASSIFIED | 18. SECURITY CLASSIFICATION OF THIS PAGE UNCLASSIFIED | 19. SECURITY CLASSIFICATION OF ABSTRACT UNCLASSIFIED | 20. LIMITATION OF ABSTRACT UL |

GENERAL INSTRUCTIONS FOR COMPLETING SF 298

The Report Documentation Page (RDP) is used in announcing and cataloging reports. It is important that this information be consistent with the rest of the report, particularly the cover and title page. Instructions for filling in each block of the form follow. It is important to stay within the lines to meet optical scanning requirements.

- Block 1. Agency Use Only (Leave blank).
- **Block 2.** Report Date. Full publication date including day, month, and year, if available (e.g. 1 Jan 88). Must cite at least the year.
- Block 3. Type of Report and Dates Covered. State whether report is interim, final, etc. If applicable, enter inclusive report dates (e.g. 10 Jun 87 30 Jun 88).
- Block 4. <u>Title and Subtitle</u>. A title is taken from the part of the report that provides the most meaningful and complete information. When a report is prepared in more than one volume, repeat the primary title, add volume number, and include subtitle for the specific volume. On classified documents enter the title classification in parentheses.
- Block 5. Funding Numbers. To include contract and grant numbers; may include program element number(s), project number(s), task number(s), and work unit number(s). Use the following labels:

C - Contract PR - Project
G - Grant TA - Task
PE - Program WU - Work Unit
Element Accession No.

Block 6. <u>Author(s)</u>. Name(s) of person(s) responsible for writing the report, performing the research, or credited with the content of the report. If editor or compiler, this should follow the name(s).

- **Block 7.** <u>Performing Organization Name(s) and Address(es)</u>. Self-explanatory.
- **Block 8.** <u>Performing Organization Report</u>
 <u>Number.</u> Enter the unique alphanumeric report number(s) assigned by the organization performing the report.
- Block 9. Sponsoring/Monitoring Agency Name(s) and Address(es). Self-explanatory.
- Block 10. <u>Sponsoring/Monitoring Agency</u> <u>Report Number</u>. (If known)

Block 11. Supplementary Notes. Enter information not included elsewhere such as: Prepared in cooperation with...; Trans. of...; To be published in.... When a report is revised, include a statement whether the new report supersedes or supplements the older report.

Block 12a. <u>Distribution/Availability Statement</u>. Denotes public availability or limitations. Cite any availability to the public. Enter additional limitations or special markings in all capitals (e.g. NOFORN, REL, ITAR).

DOD - See DoDD 5230.24, "Distribution Statements on Technical Documents."

DOE - See authorities.

NASA - See Handbook NHB 2200.2.

NTIS - Leave blank.

Block 12b. Distribution Code.

DOD - Leave blank.

 DOE - Enter DOE distribution categories from the Standard Distribution for Unclassified Scientific and Technical Reports.

NASA - Leave blank. NTIS - Leave blank.

- **Block 13.** <u>Abstract.</u> Include a brief (*Maximum 200 words*) factual summary of the most significant information contained in the report.
- **Block 14.** <u>Subject Terms</u>. Keywords or phrases identifying major subjects in the report.
- **Block 15.** <u>Number of Pages</u>. Enter the total number of pages.
- **Block 16.** <u>Price Code</u>. Enter appropriate price code (NTIS only).
- Blocks 17. 19. Security Classifications. Self-explanatory. Enter U.S. Security Classification in accordance with U.S. Security Regulations (i.e., UNCLASSIFIED). If form contains classified information, stamp classification on the top and bottom of the page.

Block 20. <u>Limitation of Abstract</u>. This block must be completed to assign a limitation to the abstract. Enter either UL (unlimited) or SAR (same as report). An entry in this block is necessary if the abstract is to be limited. If blank, the abstract is assumed to be unlimited.

PREFACE

The Department of Defense and the National Aeronautics and Space Administration are cooperating in the development of a validated technology base in the areas of control/structures interaction, deployment dynamics, and system performance for large, flexible spacecraft. The development of these technologies is essential for the successful operation of new classes of spacecraft whose missions require unprecedented performance, reliability, and low cost. To fulfill these goals, the Air Force Wright Laboratory and the NASA Langley Research Center have agreed to sponsor alternately a series of annual control/structures interaction technology conferences.

This publication is a compilation of the unclassified papers presented at the Fourth NASA/DOD Control/Structures Interaction Technology Conference, held in Orlando, Florida, on 5-7 November 1990, sponsored by the Wright Laboratory. The proceedings were produced from the original manuscripts provided by the individual authors as camera-ready copy. Special thanks are due to the authors for their care in preparing the manuscripts.

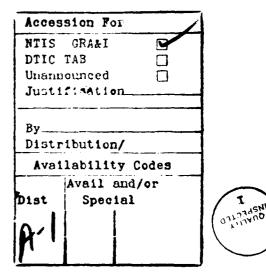


TABLE OF CONTENTS

SESSION I - OVERVIEW

| NASA CSI TECHNOLOGY PROGRAM FOCUS MISSION AND BENEFIT STUDIES |
|--|
| SESSION II - POSTERS |
| EIGENSENSITIVITY IN INTEGRATED DESIGN |
| THE D-STRUT TM : A VISCOUS PASSIVE DAMPER FOR USE IN PRECISION TRUSS STRUCTURES |
| AN INTEGRATED STRUCTURE/OPTICS/CONTROL MODELING AND ANALYSIS SOFTWARE BREADBOARD |
| 2ND GENERATION ACTIVE MEMBER |
| THE MIT SERC INTERFEROMETER CSI TESTBED |
| MODEL REFINEMENT/DAMAGE DETECTION USING MEASURED TEST DATA 87 D. C. Zimmerman and M. Kaouk, University of Florida |
| JPL CSI PHASE B TESTBED |
| FAILURE DETECTION, IDENTIFICATION, AND CONTROL SYSTEM RECONFIGURATION (FDI&R) USING THE SEQUENTIAL PROBABILITY RATIO TEST (SPRT) |
| SESSION III - CONTROL SYSTEMS DEVELOPMENT |
| ROBUST LQG/LTR CONTROL DESIGN SYNTHESIS OF DISCRETE-TIME SYSTEMS WITH LARGE SPACE STRUCTURAL CONTROL APPLICATION |

| STATION FREEDOM ASSEMBLY COMPLETE CONFIGURATION |
|--|
| H _∞ CONTROL DESIGN FOR THE ASCIE SEGMENTED OPTICS TEST BED: ANALYSIS, SYNTHESIS AND EXPERIMENT |
| ASTREX CONTROLLER DESIGN: OVC AND OCC APPROACH |
| USING INPUT COMMAND SHAPING TO SUPPRESS MULTIPLE MODE VIBRATION IN FLEXIBLE STRUCTURES |
| EVALUATION OF SYSTEM IDENTIFICATION WITH CONTROL LAW UPDATE FOR THE CONTROLS, ASTROPHYSICS, AND STRUCTURES EXPERIMENT IN SPACE |
| SURPRISES IN OPEN SECTION SMART STRUCTURES |
| SESSION IV - SENSORS AND ACTUATORS |
| OPTIMAL ACTIVE MEMBER AND PASSIVE DAMPER PLACEMENT AND TUNING |
| MODAL DOMAIN OPTICAL FIBER SENSORS FOR VIBRATION SENSING IN LARGE FLEXIBLE TRUSS STRUCTURES |
| ELECTRO-OPTICAL FIGURE SENSOR FOR LARGE FLEXIBLE ANTENNAS 295 C. W. Gillard and L. L. Ames, Lockheed Missiles & Space Co. |
| A VELOCITY COMMAND STEPPER MOTOR FOR CSI APPLICATIONS |

| OPTICS FOR CONTROL/STRUCTURES/OPTICS INTEGRATION |
|--|
| SELECTION OF SENSORS AND ACTUATORS WITH APPLICATIONS TO THE ASTREX FACILITY |
| SESSION V - INTEGRATED DESIGN |
| ANALYTICAL AND EXPERIMENTAL ISSUES IN THE DESIGN OF INTELLIGENT STRUCTURES |
| INTEGRATED CONTROLS-STRUCTURES DESIGN FOR A CLASS OF FLEXIBLE SPACECRAFT |
| AN OPTIMIZATION METHOD FOR CONTROLLED SPACE STRUCTURES WITH VARIABLE ACTUATOR MASS |
| INFLUENCE OF UTILITY LINES AND THERMAL BLANKETS ON THE DYNAMICS AND CONTROL OF SATELLITES WITH PRECISION POINTING REQUIREMENTS |
| EXPERIENCES IN INTEGRATED CONTROL/STRUCTURE/OPTICS DESIGN OPTIMIZATION |
| COMBINED CONTROL/STRUCTURE/OPTICS OPTIMIZATION: ANALYSIS AND MATHEMATICAL METHODS |
| OPTIMAL SIMULTANEOUS CONTROL AND STRUCTURE DESIGN WITH DISCRETE STRUCTURAL PARAMETERS |

SESSION VI - GROUND EXPERIMENTS

| 12 METER TRUSS ACTIVE CONTROL EXPERIMENT |
|--|
| PACOSS: THE FINAL CHAPTER |
| STATUS OF THE DSMT RESEARCH PROGRAM |
| EXPERIMENTAL DEMONSTRATION OF VIBRATION CONTROL FOR FLEXIBLE STRUCTURES |
| THE LaRC CSI PHASE-0 EVOLUTIONARY MODEL TESTBED: DESIGN AND EXPERIMENTAL RESULTS |
| JPL CSI PHASE-0 EXPERIMENT RESULTS AND REAL TIME CONTROL COMPUTER |
| THE MULTI-LOOP CONTROL/STRUCTURE INTERACTION EFFECT: EXPERIMENTAL VERIFICATION USING THE ASCIE TEST BED 629 J-N Aubrun and K. R. Lorell, Lockheed Palo Alto Research Laboratory |
| SESSION VII - FLIGHT EXPERIMENTS |
| THE MODE FAMILY OF ON-ORBIT EXPERIMENTS: THE MIDDECK ACTIVE CONTROL EXPERIMENT (MACE) |
| SPACE STATION FREEDOM: DYNAMIC INSTRUMENTATION FOR A LARGE SPACE STRUCTURE |

| 12 METER TRUSS ZERO-G FLIGHT TEST | 694 |
|---|-----|
| SHUTTLE REMOTE MANIPULATOR SYSTEM (RMS)-BASED CONTROLS- | |
| STRUCTURES INTERACTION FLIGHT EXPERIMENT | 721 |
| M. E. Demeo, Charles Stark Draper Laboratory; A. Fontana, NASA Langley Research | |
| Center; E. M. Bains, NASA Johnson Space Center | |
| ACTIVE DAMPING APPLICATION TO THE SHUTTLE RMS | 742 |
| M. G. Gilbert, NASA Langley Research Center | |

NASA CSI TECHNOLOGY PROGRAM

FOCUS MISSION

AND

BENEFIT STUDIES

William L. Grantham Langley Research Center Hampton, Virginia

Robert A. Laskin Jet Propulsion Laboratory Pasadena, California

ABSTRACT

This paper addresses two questions: 1) which future missions need Controls-Structures Interaction (CSI) technology for implementing large spacecraft in-orbit? 2) what specific benefits are to be derived if the technology is available? The answers to these questions have been used to help formulate and direct the CSI technology development program being jointly pursued at Langley Research Center (LaRC), Jet Propulsion Laboratory (JPL), and Marshall Space Flight Center (MSFC). Many future NASA missions have common CSI technology needs which can best be developed in a broad-based, but focused, technology program to provide the greatest benefit to the largest number of users.

Three CSI benefit studies have been completed to date as part of an ongoing assessment process and have addressed missions requiring large antennas, missions requiring large optical systems, and missions requiring the use of closed-loop controlled, flexible, remote manipulator arms for in-space assembly.

The CSI benefits study results for the Mission-To-Planet-Earth show that significantly larger antennas (80 meters) can be used if CSI technology is available as compared to much smaller (20 meters) antennas if it isn't. Likewise, the science benefits study for the precipitation mapper on Mission-To-Planet-Earth geostationary platform shows it is possible to meet science requirements of maximum measurable rain rate and resolution cell size using CSI technology to suppress antenna beam jitter whereas, without that control ability, the science requirements simply can not be met.

The CSI benefits study for the optical Focus Mission Interferometer (FMI), although for a specific interferometer configuration, has relevance to a broad class of future optical missions that offer much promise in astronomy. The study shows that long baseline (~30 meters) optical interferometers are possible only with the use of CSI technology that must provide three orders of magnitude spacecraft vibration response reduction in order to satisfy the nanometer dimensional stability requirement.

Results from the Remote Manipulator System (RMS) benefit study, assuming use of CSI technology, show a decrease in the amount of RMS settling time by a factor of five, which significantly speeds up the Space Station Freedom assembly.

OUTLINE

An outline is given below for the subjects to be covered. The first part of the paper is concerned with identification of missions that have common CSI technology needs so that progress in those technology areas would be of greatest benefit to all. The second part of the paper deals with benefits that could be realized by specific programs if an advanced CSI technology is developed and applied to their spacecraft design.

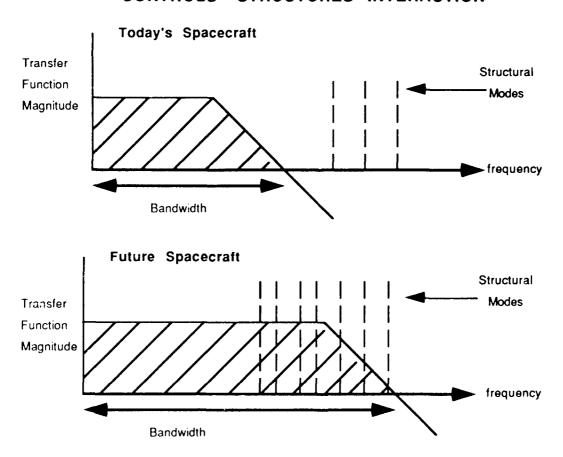
SUBJECTS

- CSI Technology Needs/Mission Categories
- Focus Mission Selections
- CSI Benefit Study Results
 - * Large Space Antennas
 - * Large Optical Systems
 - * Flexible Manipulators
- Current Benefit Studies
- Summary

CONTROLS-STRUCTURES INTERACTION

Spacecraft design is accomplished conventionally by estimating sizes and masses of spacecraft components and designing a structure sufficiently stiff to maintain the structure shape during operations; the control system is then designed to orient, guide and/or move the spacecraft to obtain the required performance. This approach attempts to separate the lowest structural frequency and the control bandwidth, as shown below, so that the structure and control system do not interact. Future spacecraft are expected to get larger and more flexible with structural frequencies decreasing, in many cases, below 1 Hz with closely packed modes. Performance demands on the control system are expected to become more stringent and drive the control bandwidth to higher values into the same spectral region as the structural modes (see bottom of this chart). The goal of the CSI program is to develop technology to the point that the control bandwidth and structural modes can coexist in the same spectral space without adverse interaction or loss of system performance.

CONTROLS- STRUCTURES INTERACTION



CSI PROGRAM CHARTER

The CSI program long term goals are unusually specific for a technology development program. This has the advantage of helping target several specific future programs that could benefit from the new CSI technology, and it allows one to be definitive about what those benefits might be. Focusing the technology development in the direction of selected future missions also involves greater interaction between the technology developer and the technology user so that each is more sensitive to the needs of the other.

CSI PROGRAM CHARTER

- The overall objective of the CSI program is to develop and validate the technology needed to design, verify, and operate spacecraft in which the structure and control interact beneficially to meet the requirements of 21st-century NASA missions.
 - Dynamic response amplitude reductions of 50 percent.
 - Several orders of magnitude improvement in pointing.
 - Predict on-orbit performance within 10 percent.
 - Unified controls-structures model, analysis and design.
 - Verify flight system performance by analysis/ground test.

DEVELOPMENT OF THE TECHNOLOGY ROADMAP

The CSI technology needs were developed using information from a number of available visionary documents and technology workshops. These documents define long range NASA mission options that can be accomplished if the appropriate technology is developed. Many of the future programs have common technology needs which can best be addressed in a broad-based CSI technology program providing the greatest benefit to the largest number of users. The major documents and information sources used in this study are listed below.

General geometrical features of future spacecraft given in these reference documents have been incorporated into the analytical models and ground tests of the CSI program. For example, four model classes were selected in order to represent different levels of sophistication for the design and analysis problems typical of future large space platforms and antenna systems. Likewise, the ground test articles to be used for model validation will evolve to represent the more complex features of spacecraft of the 21st century.

INFORMATION SOURCES

PUBLICATIONS

- * "Leadership and America's Future in Space." Dr. Sally Ride August '87.
- * "Space Technology to Meet Future Needs." Aeronautics & Space Engineering Board. '87.
- * "Earth System Science--a Closer View." Earth System Sciences Committee. NAC '88.
- * "Pioneering the Space Frontier." National Committee on Space. Dr. T. Paine, '86.
- "Space Science in the 21st Century." Space Science Board. NRC, NAS, '88.
- * "Space-Based Remote Sensing of the Earth. A Report to the Congress."1987.

• WORKSHOPS (9)

- * Technology for Earth Science Geo-Plat.--Sep 21 and 22, 1989.
- * IN-STEP. Dec 6-9, 1989.
- * Beamed Power. Feb 2---Mar 3, 1989.
- Global Change Technology Initiative (GCTI)
 - * # 1--JPL Mar 1989
 - * # 2--LaRC April 1989
 - * # 3--GSFC May 1989
- Workshop on Technologies for Space Optical Interferometry, April 1989 & 1990
- * Workshop on the Next Generation Space Telescope, September 1989.

FOCUS MISSION SELECTION CRITERIA

Several focus missions have been selected and their spacecraft features incorporated into the analytical and ground test models. The criteria for selecting the focus missions are listed below. The model features are discussed in papers by Maghami, et al.; Belvin, et al.; and Fanson, et al. at this conference, and Laskin at the 1989 CSI Conference.

FOCUS MISSIONS SHOULD HAVE------

- Maturity in mission concept and need
- Many CSI features common to other future missions
- High priority in terms of national need
- Challenging CSI features relative to current technology

MISSION CATEGORIES

Future missions with a potential for benefiting from CSI technology have been divided into four main categories listed here. Lead center responsibility for each category is shown in parentheses. Specific features of each mission concept can be found in the reference literature. Many of the spacecraft (S/C) geometric features taken from these mission categories have been included in the analytical models and ground test articles selected by LaRC, JPL, and MSFC as focus mission characteristics. The details related to this selection are given later for the work at LaRC and JPL.

The astrophysics systems category being addressed by Marshall Space Flight Center (MSFC) includes missions such as the X-Ray pinhole occulter flight experiment. That flight experiment will provide science as well as serve as a CSI technology experiment on Space Shuttle then later on Space Station Freedom. MSFC is developing the ground test facilities and definition studies for technology flight experiments in this area.

Plans are currently being made to address CSI issues associated with specific features of Space Station Freedom listed on the chart below.

MISSION CATEGORIES

- LARGE SPACE ANTENNAS (LaRC)
- LARGE OPTICAL SYSTEMS (JPL)
- ASTROPHYSICS SYSTEMS (MSFC)
- SPACE STATION SYSTEMS
 - Flexible RMS
 - * Attached Payloads
 - * Microgravity Facilities

LARGE SPACE ANTENNA FUTURE TECHNOLOGY NEEDS

Many missions need antennas larger than the 9-meter ATS-6 flown in 1973. CSI technology will be required to maintain their precise shape and beam pointing stability. This is because larger antennas will be very flexible and more subject to distortion, and because they must work at shorter wavelengths requiring much higher quality control on antenna figure than ever before.

The six specific programs listed here must use Large Space Antennas (LSA) in order to meet the mission requirements. The antenna diameters needed by each mission shown in parentheses are taken from white papers and workshops. In some cases, the large antennas must be attached to a large platform with many other sensors having disturbance generating scanning mirrors, etc. This, of course, makes the CSI design even more challenging and the potential of CSI technology benefits still greater.

The first focus mission selected by LaRC for a detailed look at technology needs and related CSI benefits (assuming successful development of CSI technology) is the Mission-To-Planet-Earth Geostationary Platform (Geoplat). Specific elements of this program are discussed in the next series of charts as they relate to CSI technology needs.

LARGE SPACE ANTENNA RELATED MISSIONS

- MISSION-TO-PLANET-EARTH
 - ' leo
 - * Geo (4.4 m --->200 m)
- DMSP BLOCK-6 (6 m)
- FAA AIRCRAFT SURVEILLANCE / COMM (20 m)
- RADIO ASTRONOMY-----VLBI (20 m)
- COMMUNICATION SATELLITES (15 --> 55 m)
- IN-SPACE POWER TRANSFER (1000 m)

MISSION-TO-PLANET-EARTH

The centerpiece of the U.S. contribution to the international Mission-To-Planet-Earth Program is the Earth Observing System (EOS) polar orbiter with later plans to add five geostationary spacecraft. New-start for the low Earth orbiter EOS-A is expected in FY 91 and does not require new technology to meet its measurement requirements. The geostationary orbiting spacecraft (5), however, require very large scanning microwave radiometer antennas for making precipitation maps of the Earth every 30 minutes, and have very stringent infrared and visible band sensor pointing requirements. Both of these require technology development to be met. New-start of the geostationary spacecraft part of this program is not expected until FY '95.

A Geoplat Phase-A study by MSFC includes a small antenna (4.4 meters) for precipitation mapping because current technology will not allow anything larger that will fit within the vehicle launch envelope. This size, however, is more than a factor of 10 too small to meet the science requirements of the Geoplat mission as will be shown later in this report.

Larger antennas for Geoplat (20 meters) have been considered in a Goddard Space Flight Center (GSFC) study which assumes assembly in orbit, but the serious question of antenna beam jitter for the larger antennas remains. Studies have been conducted at LaRC specifically regarding the three-dimensional dynamics of a large S/C such as Geoplat that show prohibitively large pointing jitter for the antennas unless CSI technology is employed (Wahls, et. al.; Turner, et. al). Details of this study are discussed later in this paper.

The specific CSI features of interest for Mission-To-Planet-Earth geostationary spacecraft are the large platform used to mount multiple sensors (>15), many of which cause significant disturbances due to scanning mirrors, etc., the flexible articulating antennas, and the sensor pointing requirements that exceed current state of the art.

CSI FEATURES OF MISSION-TO-PLANET-EARTH

- Large Multi-Sensor Platform
- Flexible Articulating Attachments
- Pointing/Control Requirements Exceed State of the Art

PURPOSE OF BENEFIT STUDY

The purpose of the Large Space Antenna (LSA) benefit study is to define the specific advantages of developing a new integrated control/structures design and analysis capability for future missions requiring large space antennas. The advantages will be expressed in terms of traditional design parameters.

The traditional design approach to avoid interaction between the structure and control system is to stiffen the structure (costly in mass, inertia, and fuel consumption) and/or slow down the control system response (costly in performance capability).

The LSA study results, reported herein, define antenna performance improvement benefits (pointing jitter improvement) which would result if control/structures systems could be designed to operate in the same bandwidth as the closely spaced structural modes and in an environment of many spacecraft disturbances. Another CSI benefit quantified in this study is the science benefit of being able to use larger antennas with the microwave and millimeter wave precipitation mapping sensors.

For some missions, the CSI technology is enabling and, thus, the mission simply cannot be done without the new technology.

BENEFIT STUDY

• Purpose: Define specific advantages of CSI technology for future missions requiring large space structures.

• Approach: Select a NASA focus mission and define differences in the spacecraft performance capability using both the conventional and CSI approach.

ANTENNA PERFORMANCE IMPROVEMENT WITH CSI TECHNOLOGY

In order to provide the needed precipitation maps of the Earth every 30 minutes for Mission-To-Planet-Earth, precision pointing and beam scanning are necessary for the large microwave radiometer antennas shown on each end of the geostationary platform. Since this beam scanning will most likely be accomplished mechanically by moving some parts of the antenna, this and other spacecraft disturbances will cause feed-mast flexure and antenna distortion resulting in beam pointing jitter. Jitter up to 10 percent of the resolution cell size is allowed without seriously degrading the quality of the precipitation map developed by the beam raster scan. As the graph shows for the 20 GHz microwave antenna, beam jitter requirement becomes more stringent as LSA diameter increases since beam width varies inversely with antenna diameter. The 15-meter antenna jitter results were scaled to other antenna diameters using scaling laws presented in the reference publication of Photon Research Associates (Turner, et. al).

The two performance curves indicate expected pointing capability with and without the use of Control-Structures Interaction technology for the LaRC/Ford Aerospace model. Without CSI technology, the beam jitter is acceptable only for antennas below 20 meters in diameter. In contrast to that limit, antennas up to 80 meters in diameter could be used while still meeting a 10 percent pointing jitter requirement if CSI technology is employed.

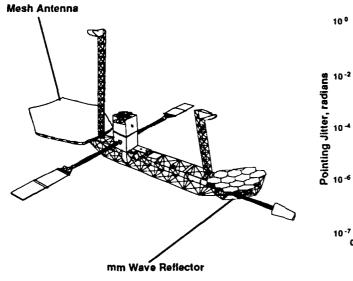
The technology benefit, for this example case study, is that significantly larger antennas can be used with improved performance for future missions if CSI technology can be developed to provide the two orders of magnitude active control and increased passive damping from 0.5 percent to 5 percent as assumed here. This is a design goal of the CSI program. Currently demonstrated active control for ground-based experiments provides only about one order of magnitude in pointing improvement.

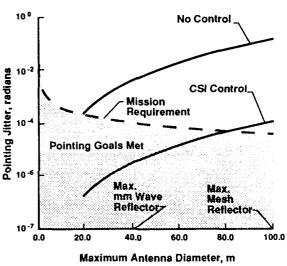
Once developed, the CSI technology will enable a number of important missions, such as the Mission-To-Planet-Earth, and assure improved performance capability for similar large space antenna missions such as Quasat (Very Long Baseline Interferometer), advanced communication systems, and aircraft surveillance systems.

CSI PERFORMANCE IMPROVEMENT

"Mission to Planet Earth" Platform

Pointing Performance





CONVERSION OF ANTENNA PERFORMANCE IMPROVEMENT INTO SCIENCE BENEFITS

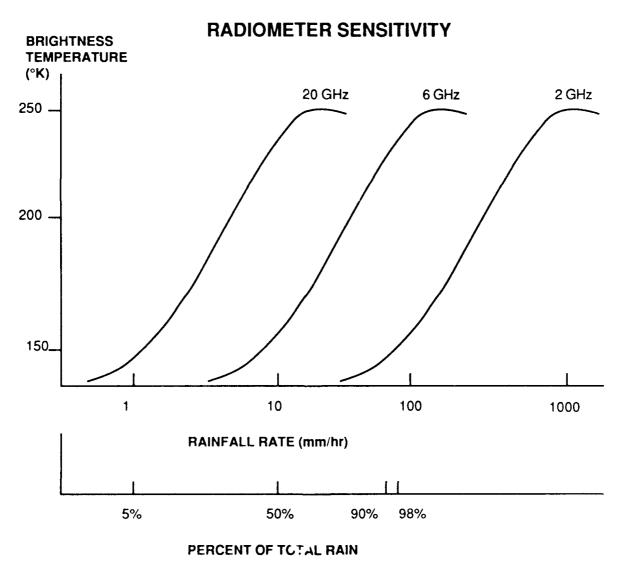
In order to translate the antenna performance improvements into specific science benefits for the microwave precipitation mapper, one must utilize the relations shown below. Resolution cell size is an important sensor feature since measurement errors will result if the rain cell is smaller than the resolution cell. The resolution cell size is proportional to the ratio of spacecraft altitude to the product of electromagnetic frequency (f) and antenna diameter (D). If it were not for the fact that choice of frequency also determines the maximum measurable rain rate, the antenna diameter could be kept small by using ultra high frequencies (millimeter wavelength band). The microwave radiometer sensitivity to different rain rates is shown on the next chart.

CONVERSION OF LARGE SPACE ANTENNA BENEFITS INTO SCIENCE BENEFITS FOR GEOPLAT

| SCIENCE PARAMETERS | ANTENNA PARAMETERS |
|----------------------|---|
| Resolution Cell Size | ∝ (Altitude) / (f x D) |
| Rain Fall Rate | Max. Meas. Rain Rate ∝ 1 / f ² |

MICROWAVE RADIOMETER SENSITIVITY

The 1/f² dependence is depicted on this graph and shows that a 20 GHz radiometer frequency is limited to measuring rain rates below approximately 10 mm/hr. This limit was demonstrated by the 1973 Electrically Scanning Microwave Radiometer (ESMR) in low Earth-orbit (Rao, et. al.). As can be seen from the lower abscissa scale, 50 percent of the rain that falls is at a rate above 10 mm/hr. This percentage is based on rain statistics derived from the tropics (Chiu). In order to measure the higher rain rates, a lower microwave frequency must be used. Six GHz is shown as an example. For a required resolution cell size of 20 km and a geostationary orbit altitude of 35,000 km., the antenna diameter must be about 80 meters for 6 GHz.



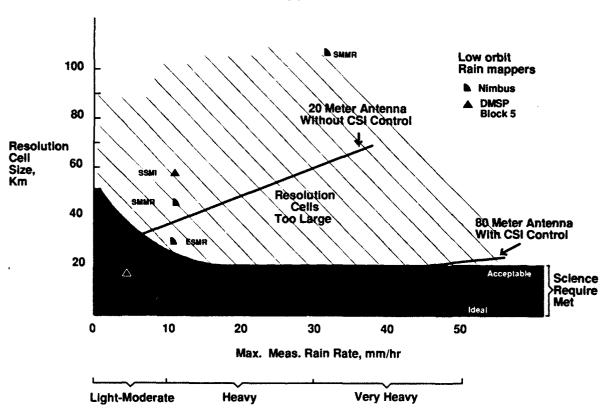
CSJ TECHNOLOGY SCIENCE BENEFITS

Although it is clear that CSI technology allows larger microwave and millimeter wave antennas for remote sensing, the key question is: how does that improve science for the Mission-To-Planet-Earth Program? The answer is, in two ways. First, the use of larger antennas allows superior spatial resolution to better match the correlation length of rain cells (typically 10 km or less); whereas, measurements with small antennas incur serious errors if their large footprints are only partially filled by rain cells. Second, CSI technology allows rain rate measurements over the full dynamic range by using both millimeter and microwave frequencies rather than being restricted to light rain measurements (<10 mm/hr.) with small millimeter wave antennas. Only through the additional use of the lower frequency microwaves with large jitter-controlled antennas can the moderate and heavy rain rates be measured, thus, providing a comprehensive data set.

This science benefits chart shows specifically how CSI technology improves resolution and rain rate measurements as an example case study. Without beam jitter control, the precipitation measurements would be restricted to the region on the left of the 20-meter antenna diameter curve labeled "Without CSI Control", which severely limits the maximum measurable rain rate and the resolution cell size. In contrast to that limit, the use of CSI control with an 80-meter antenna provides data that are almost completely within the science measurement requirements zone.

For comparison, the capability of several previous and current low Earth orbit satellite radiometers are shown which have been used to provide rain maps of the Earth. It is clear that large antennas will have to be used for GeoPlat and that CSI technology will be needed to meet the science requirements. There is currently underway a considerable effort to develop millimeter wave radiometry to infer the high rain rates. If successful, this measurement method would, when combined with CSI technology, allow resolution cell sizes to approach ideal science values (1 km) rather than be limited to the 20 km "acceptable" values possible at 6 GHz.

CSI Technology Science Benefits



LARGE OPTICAL SYSTEM MISSIONS

Future space-based large optical systems can be divided into two broad categories: 1) interferometers, where an array of "small" collecting apertures are used to synthesize the performance of a single large aperture; 2) filled aperture telescopes, which are essentially large conventional telescopes that typically incorporate segmented primary mirrors due to the difficulty (and inherent weight) of fabricating very large monolithic mirrors. Representative future missions from each of these classes are given in the accompanying chart.

LARGE OPTICAL SYSTEM RELATED MISSIONS

- · Optical Interferometers
 - Cosmic (100 m)
 - OSI (Orbiting Stellar Interferometer--20 m)
 - Points (Precision Optical Interferometer in Space--2 m)
 - Moon-Based Interferometer (10 km)
- · Filled Aperture Telescopes
 - Advanced Space Telescope (16 m)
 - Moon-Based Telescope/Segmented Reflector (20 m)
 - Large Deployable Reflector (20 m)

CSI FEATURES OF LARGE OPTICAL SYSTEMS

Key features of many of the future optical missions described on the previous chart have been selected for the optical focus mission. Those features are listed below.

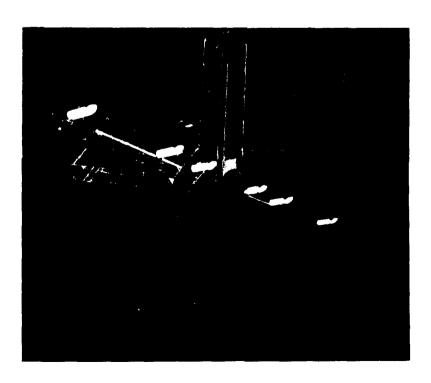
CSI FEATURES OF LARGE OPTICAL SYSTEMS

- Flexible Support Structure
- Multiple Articulating Optical Elements
- Pointing/Positioning Requirements Exceeding State of the Art
- Launch Weight/Packaging Difficulty too Great Using Conventional "Stiff" Structure Design

LARGE OPTICAL SYSTEMS FOCUS MISSION SELECTION

The Focus Mission Interferometer (FMI) is the Large Optical System (LOS) reference mission chosen by JPL to drive its CSI technology development. The FMI does an excellent job of embodying the CSI features of Large Optical Systems:

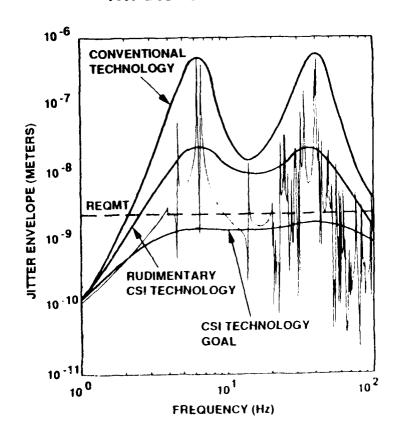
- i) The optical elements are situated on a flexible support structure whose fundamental frequency is in the neighborhood of 4 Hz. Optical element control loops will have bandwidths as high as 100 Hz.
- ii) Many (twenty four) separate optical elements need to be articulated, either in translation or rotation, via closed loop control.
- iii) The requirements for optical element positioning (2.5 nanometers) and pointing (40 nanoradians) both exceed current state-of-the-art capability. The positioning requirement is the more stressing of the two.
- iv) Attempts to reach the required performance goals by simply stiffening the structure are impractical from launch weight and cost considerations. This will be illustrated in this paper.



CSI PERFORMANCE IMPROVEMENT (FMI)

The optical performance of the FMI relative to the 2.5 nanometers differential pathlength positioning requirement has been analyzed in some detail and is summarized in the chart below. This graph shows the pathlength response envelope to the disturbance forces generated by a Hubble Space Telescope-class reaction wheel (RW) operating in the 0 - 10 rps range. The "conventional technology" envelope corresponds to the application of optical positioning control only with no attempt to control the structure. "Rudimentary CSI technology" includes the addition of active and/or passive structural vibration dampers. When these devices were added to the simulation, modal damping ratios were increased from 0.1 percent (assumed for an undamped structure) to a range from 1 percent to 10 percent. The resulting performance improvement of over an order of magnitude still leaves us about a factor of 10 short of the performance goal. It is this additional order of magnitude improvement that we are challenged to achieve with the more sophisticated approaches to structural control and vibration isolation that are currently under development in the CSI Program.

PATHLENGTH JITTER ENVELOPE DUE TO RW DISTURBANCE



, 1

PERFORMANCE IMPROVEMENT VIA STRUCTURAL STIFFENING

From a conceptual standpoint, an alternative approach to using CSI technology to improve FMI performance is to stiffen the structure to the point where the requirements can be met through the use of conventional technology alone. Since the FMI trusswork was originally designed according to standards that put a premium on stiffness-to-weight ratio (e.g., graphite epoxy is the assumed material), it is doubtful that much additional stiffness can be gained within accepted structural design practice.

However, for the sake of comparison with the performance available using CSI technology, we have attempted to use "rule-of-thumb" structural scaling laws to arrive at an FMI capable of meeting the optical positioning requirements using conventional (structural stiffening) technology only. Since the FMI is comprised of four somewhat slender truss "arms", it was decided to use scaling laws based on a generic beam of cross-section t x t and length L. If L is considered a given, which it would be for a particular interferometer baseline, then we can write the following relations:

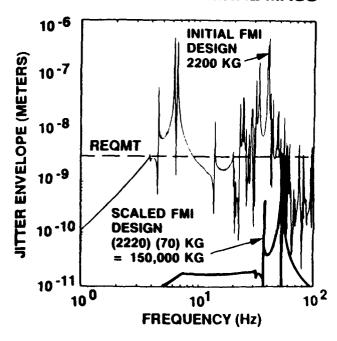
$$f \propto (k/w) = 0.5$$
 $w \propto t^2$
 $k \propto t^4 \propto w^2$

where f is beam bending frequency, k is beam bending stiffness, and w is the weight of the beam. Thus we can express frequency as a function of weight for beam-like systems:

$$f \propto w 0.5$$

Using this rule allows us to estimate the effect that increased FMI mass has on the reaction wheel disturbance to pathlength response transfer function. Increasing the mass will cause the frequencies to go up according to the above scaling rule and will simultaneously cause the entire transfer function response plot to move down with the 1/w rigid body response. When mapped onto the "jitter envelope" plot introduced in the previous chart, it is seen that a mass increase of 70 times is required for the FMI requirements to be met in this fashion. It is recognized that the scaling law breaks down before such a mass increase is approached. But the point is made that it is impractical to achieve acceptable FMI performance via conventional structural stiffening.

FMI AT 70 TIMES NOMINAL MASS



- LARGER MASS SUPPRESSES RESPONSE
- HIGHER STIFFNESS RAISES FREQUENCIES

BENEFITS OF CSI TECHNOLOGY TO SPACE STATION ASSEMBLY BY FLEXIBLE ROBOTIC MANIPULATOR SYSTEMS

Based on experiences from many previous Shuttle flights, the oscillations of the RMS/payload system has been found to add time to payload deployment, retrieval and maneuvering. For example, the crew must wait for the oscillations to damp sufficiently to determine the results of the last input. This insures that the next input is not phased so as to enhance the oscillation. A robotic system with a CSI controller might significantly reduce settling time during Freedom assembly and later for Moon and Mars vehicles assembly.

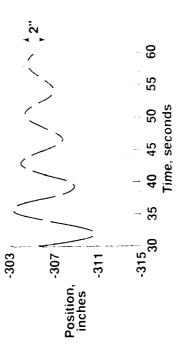
To quantify the CSI advantages, a benefits study was conducted by McDonnell Douglas for a CSI controller applied to the flexible Space Shuttle RMS for the assembly of Space Station Freedom (Lamb, et. al). The CSI case was compared with assembly times using the present Space Shuttle RMS . The comparison was for baseline assembly sequence #20/13. The number designation indicates 20 flights are required to accomplish assembly complete (for the first 13 flights Freedom is unmanned). This was the most detailed assembly sequence defined at the time the study began. There were 101 items in the 20 flights and RMS settling time was estimated as a function of the payloads for 8 different weight classes. In the study it was found that 65 percent of the RMS settling times--without CSI technology-are predominantly related to payloads in two weight classes (3000 lbs \pm 2000 lbs. and 7500 lbs \pm 2500 lbs).

A typical RMS time response is shown at the top right of the figure. For this study, settling time was defined as the amount of time required for the oscillations at the tip of the RMS to reduce to 2 inches. The RMS settling time without the CSI controller was computed for each of the 20 missions relative to the total RMS activity time (see bottom left graph). Following that, the potential settling time reductions for a CSI controller with different assumed damping factor improvements was calculated as is shown on the right hand bottom inset. Significant time savings can be realized with even modest CSI improvement in arm damping.

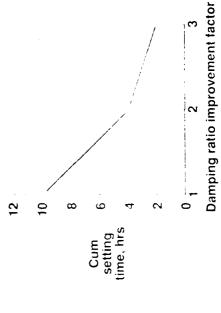
POTENTIAL SPACE STATION ASSEMBLY BENEFITS DUE TO CSI (Timeline)



Draper RMS Simulator response Payload 3500 lbs



Potential CSI benefits





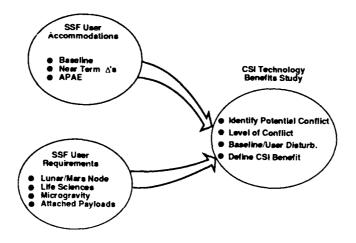
RMS settling time, 2"



CURRENT BENEFIT STUDIES UNDERWAY

Having completed the three benefit studies presented in this report, the next focus mission and benefit study has been initiated to determine if CSI technology could improve user accommodations on Evolutionary Space Station Freedom. Early studies have already shown that some baseline activities on Freedom such as crew treadmill and RMS activities are most likely to require schedule work-arounds to avoid conflicts with user requirements of microgravity and precision pointing. In the benefits study, user requirements and related disturbances will be defined and used as input to a Finite Element Model of Freedom (Extended Operating Capability -XOC Configuration) developed at LaRC (ref. 10). The study will determine the extent of improvement possible using CSI technology.

CSI Technology Benefits Study for SSF Transportation Node



INTERDISCIPLINARY COMMUNICATIONS NEEDED

In order to take advantage of interdisciplinary derived improvements, the CSI technologist must have a good understanding of what specific types of environmental improvements the microgravity researcher needs to provide design countermeasures. Just as in the Geoplat case where the physics of the precipitation measurement played an important part in choice of electromagnetic frequency (and thus antenna diameter), it is important that the physics of preferred microgravity environment be understood in order to design countermeasures to improve it. This chart shows an example of the degree of concern the researcher has with different types of environmental disturbance imposed for several types of material processing (Naumann, Feuerbacher, et. al).

ENVIRONMENTAL EFFECTS ON MATERIAL PROCESSING

| Type Envir. Exp. Example | Contained Solidification | Quasi- Containerless Solidification | Containerless Experiments | Fluid Experiments |
|--------------------------------------|-----------------------------|---|------------------------------|----------------------|
| Low-Level Steady Accelerations | Possibly Serious | Possibly Serious | Unimportant | Possibly Serious |
| Crew Soar | Relatively | Possibly | Possibly | Relatively |
| | Unimportant | Serious | Serious | Unimportant |
| RCS Firing | Possibly | Possibly | Relatively | Possibly |
| | Serious | Serious | Unimportant | Serious |
| Rotation- | Should be | Should be | Unimportant | Should be |
| Induced Flows | Avoided | Avoided | | Avoided |

SUMMARY

Several future mission categories have been identified that need Controls-Structures Interaction (CSI) technology for implementing large spacecraft in-orbit. Three specific focus missions selected in this study have been used to help formulate and direct the CSI technology development program being pursued at LaRC, JPL, and MSFC.

Three CSI benefit studies have been completed to date as part of an ongoing assessment process and have addressed missions requiring large antennas, missions requiring large optical systems, and settle time reduction using flexible remote manipulator arms.

The CSI benefits study results for the Mission-To-Planet-Earth show that Large Space Antenna performance can be improved significantly with larger antennas (80 meters) if CSI technology is available as compared to a much smaller (20 meters) antenna limit, if it isn't. Likewise, the science benefits study for the precipitation mapper on Mission-To-Planet-Earth geostationary platform shows it is possible to measure rain rates with needed resolution cell size using CSI technology to suppress antenna beam jitter, whereas, without it, the science requirements simply cannot be met.

The CSI benefits study for the Focus Mission Interferometer, although for a specific interferometer configuration, has relevance to a broad class of future missions that offer much promise in astronomy. The study shows that long baseline interferometers are possible only with the use of CSI technology that can provide vibration response reduction of a factor of 1000.

Results from the benefit study assuming use of CSI technology to speed up Freedom assembly shows a decrease of 5 in the amount of settling time for the Shuttle RMS if the damping factor is improved by a factor of 3. Damping factor improvements in this range are considered achievable with current CSI technology.

SUMMARY

- Multi-Sensor Platform / Large Space Antenna Focus Mission Selected for Analytical and Ground Test Models
 - Larger Antennas Possible
 - Precipitation Mapper Enabled
- Large Optical Interferometer Mission Selected for JPL Focus Possible Only With CSI Technology
- Flex RMS Operations with CSI Technology Will Reduce Space Station Freedom Assembly Time
- Space Station Freedom User Accommodation Improvements Anticipated

REFERENCES

- Maghami, Peiman G.; Joshi, Suresh M.; Walz, Joseph E.; and Armstrong, Ernest S.: Integrated Controls-Structures Design Methodology Development for a Class of Flexible Spacecraft. Presented at Third Air Force/NASA Symposium on Recent Advances in Multidisciplinary Analysis and Optimization, San Francisco, California, September 24-26, 1990.
- Belvin, W. K.; Horta, L. G.; and Elliott, K. B.: The LaRC CSI Phase-0 Evolutionary Model Testbed Design and Experimental Results. Presented at Fourth Annual NASA/DOD Conference on Control/Structures Interaction Technology, Orlando, Florida, November 5-7, 1990.
- 3) Fanson, J.; Briggs, H. C.; et al.: JPL Phase-0 CSI Experiment Results and Real Time Control Computer. Presented at Fourth Annual NASA/DOD Conference on Control/Structures Interaction Technology, Orlando, Florida, November 5-7, 1990.
- 4) Laskin, R. A.: A Spaceborne Optical Interferometer: The JPL CSI Mission Focus. NASA/DOD Controls-Structures Interaction Technology 1989, Compiled by Jerry R. Newsom, NASA Conference Publication 3041, January 29 February 2, 1989, pp. 1-15.
- 5) Wahls, Deborah M.; Farmer, Jeffery T.; and Sleight, David W.: On-Orbit Structural Dynamic Performance of a 15-Meter Microwave Radiometer Antenna. TP-3041, 1990.
- 6) Photon Research Associates, Cambridge Research Division: Control-Structure-Interaction (CSI) Technologies and Trends for Future NASA Missions. Submitted to Lawrence Livermore National Laboratory Contract No. B063679, August 1990.
- 7) Rao, M. S. V.; Abbott III, W. V.; and Theon, J. S.: Satellite-Derived Global Oceanic Rainfall Atlas (1973 and 1974). NASA SP-410, 1976.
- 8) Chiu, L. S.: Estimating Areal Rainfall from Rain Area. Int. Symp. on Tropical Precipitation Measurements, Tokyo, Japan, Oct. 28-30, 1987.
- 9) Lamb, B. A.; and Nowlan, D. R.: Benefits of Control-Structure Interaction (CSI) Technology to Space Station Assembly by Flexible Robotic Systems (RS). Aircraft and Spacecraft Guidance and Control Technology, Informal Final Report, CRAD NAS1-18763, November 1989.

- 10) Space Station Freedom Evolution Reference Configuration Document. 1990.
- 11) Naumann, Robert J.: Susceptibility of Materials Processing Experiments to Low-Level Accelerations. Spacecraft Dynamics as Related to Laboratory Experiments in Space, Edited by G. H. Fichtl, B. N. Antar, and F. G. Collins, NASA Conference Publication 2199, May 1-2, 1979, pp. 63-68.
- 12) Feuerbacher, B.; Hamacher, H.; and Jilg, R.: Compatibility of Mi rogravity Experiments with Spacecraft Disturbances. A. Flugwiss. Weltraumforsch. 12 (1988) 145-151.

EIGENSENSITIVITY IN INTEGRATED DESIGN

Sean P. Kenny
NASA Langley Research Center, Hampton, Va.

Gene J. Hou
Old Dominion University, Norfolk, Va.

W. Keith Belvin
NASA Langley Research Center, Hampton, Va.

ABSTRACT

An approximate structural eigenvalue/vector analysis technique which uses eigensensitivities in a truncated Taylor series expression is presented. It is shown that this technique can provide the computational efficiency urgently needed for large-scale, control-structure optimization problems.

INTRODUCTION

Applications of eigensensitivity analysis to interdisciplinary design has recently emerged as a fruitful area of engineering research. The simultaneous control-structure optimization of large flexible space structures (integrated design) is a specific application of interdisciplinary design techniques. This problem has been addressed from a variety of perspectives. Belvin and Park [1] proposed a structural tailoring procedure to increase the system performance and simultaneously decrease the control effort. Knot, et al. [2] presented a structural modification technique for increasing the active modal damping factor of the structure. These techniques are different in form and objective; however, all require intensive computations. Most of such computations involve repetitive structural eigensolutions.

RESEARCH OBJECTIVE

The objective of this paper is to present an application of eigensensitivity analysis to the control-structure integrated design process. An emphasis is on the applications of eigensensitivity analysis and approximate analysis for computational efficiency improvement of the overall design optimization process. For a detailed development of both eigenvalue and eigenvector sensitivity equations as well as a complete description of the eigensolution approximation technique used in this work see Kenny [3].

RESEARCH OBJECTIVES

Develop computationally efficient methods of calculating $\lambda(bs,bc)$, X(bs,bc), and

$$\frac{\partial \lambda}{\partial (bs,bc)}$$
, $\frac{\partial X}{\partial (bs,bc)}$

THE STRUCTURAL EIGENVALUE PROBLEM

$$M\ddot{x} + Kx = 0$$
 \Longrightarrow $(K-\lambda_i M) X_i = 0$
EIGENVALUE/VECTOR DERIVATIVES

$$\begin{split} \frac{\partial \lambda_{i}}{\partial b_{j}} &= X_{i}^{T} (\frac{\partial K}{\partial b_{j}} - \lambda_{i} \frac{\partial M}{\partial b_{j}}) X_{i} \\ (K - \lambda_{i} M) \frac{\partial X_{i}}{\partial b_{i}} &= \frac{\partial \lambda_{i}}{\partial b_{i}} M X_{i} - (\frac{\partial K}{\partial b_{i}} - \lambda_{i} \frac{\partial M}{\partial b_{i}}) X_{i} \end{split}$$

STRUCTURAL EIGENSOLUTION APPROXIMATION

A Taylor series approximation to nonlinear functions will be the technique used in this work. A function which has derivatives of all orders on an open interval containing the point b^0 can be represented by the Taylor series expansion about the point b^0 as

$$F(b) = F(b^0) + \frac{\partial F(b^0)}{\partial b} \Delta b + \frac{1}{2!} \frac{\partial^2 F(b^0)}{\partial b^2} \Delta b^2 + \dots + \frac{1}{n!} \frac{\partial^n F(b^0)}{\partial b^n} \Delta b^n$$

where F(b) is the value of the function evaluated in the neighborhood of b^0 , and $\Delta b = b \cdot b^0$. Assuming the function is relatively well-behaved in the neighborhood of b^0 , the above representation can be truncated to any desired level of accuracy. The nature of the function and the available information dictate what terms are retained and in turn the allowable magnitude of the perturbation, Δb . In most engineering applications, information regarding higher order derivatives of eigenvalues/vectors is very limited and in some cases nonexistent. Therefore, linear theory is generally used in approximate analysis.

STRUCTURAL EIGENSOLUTION APPROXIMATION

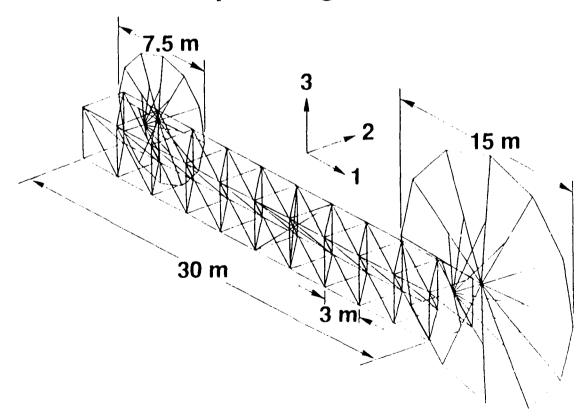
$$\lambda_i(b_s, b_c) \approx \lambda_i(b_s^o, b_c^o) + \sum_{j=1}^{\text{ndev}} \frac{\partial \lambda_i}{\partial (b_s^o, b_c^o)_j} \Delta(b_s^o, b_c^o)_j$$

$$X_i(b_s,b_c) \approx X_i(b_s^o,b_c^o) + \sum_{j=1}^{\text{ndev}} \frac{\partial X_i}{\partial (b_s^o,b_c^o)_j} \Delta(b_s^o,b_c^o)_j$$

EARTH POINTING SATELLITE

An Earth Pointing Satellite (EPS) structure will be used as an example to demonstrate the applications of approximate analysis in an integrated design environment. This model, shown below, has three main components: the main truss (bus), the antenna supports, and the two antennas (15 and 7.5 meters). The finite element model consists of 97 nodes and 249 Euler beam elements. Each node has six degrees of freedom, three translational and three rotational. for a total of 582 degrees of freedom. The model has been divided into 11 structural design variables. The truss section has been divided into three subsections, each containing three design variables for a total of nine truss structural design variables. In each of the three subsections, the longerons. battens, and diagonals are considered as independent design variables. antenna supports make up the remaining two structural design variables. structural variables are the radial dimensions of the tube members. A structural design variable linking has been chosen such that the inner radius of the tube members remains proportional to the outer radius.

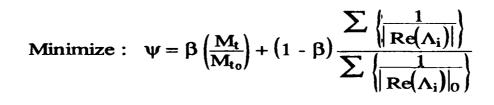
Earth pointing satellite



OPTIMIZATION PROBLEM

The control-structure optimization problem considered in this study is a multi-objective cost function with a single constraint. The cost function is composed of the total mass of the structure including the actuator masses, along with a performance measure based on the real parts of the closed-loop eigenvalues. A constraint is placed on the RMS pointing error of the center of the 15-meter antenna of the EPS.

OPTIMIZATION PROBLEM



ADS Optimization
Module

Cost & Constraint
Punctions

Exact
Pigensolution

Exact
Pigensolution

Condient
Calc.

Conce per iter.)

Eigensensitivity
Analysis
(once per iter.)

Structural
Pigensolution
Approximation

M_t - total mass.

 Λ_i - ith closed-loop eigenvalue.

β - design trade off parameter. Subscript 0 - initial values.

CONTROL-STRUCTURE INTERACTION

The control design is a proportional-plus-derivative controller with three control moment gyros located near the structure's center of gravity. Colocated sensors and actuators are employed. Twelve control design variables directly specify elements in the Cholesky-factored feedback gain matrices.

The technique used herein for relating the actuator mass to the feedback control law is based upon a linear combination of the infinity norms of the feedback gain matrices. The actuator mass equation used in this study is shown below. The parameter γ is based upon an empirical relationship between actuator torque and mass per unit torque; θ_{max} and θ_{max} are constants based upon worst case attitude and attitude rate, respectively. $|G_p|_{\infty}$ and $|G_r|_{\infty}$ are the largest row sum of G_p and G_r , respectively.

CONTROL-STRUCTURE INTERACTION

Control Law:
$$u = G_r y_r + G_p y_p$$

Where G_r and G_p are the rate gain and position gain feedback matrices.

Actuator Mass Equation

$$M_{act} = \gamma \left(|G_p|_{\infty} \theta_{max} + |G_r|_{\infty} \theta_{max} \right)$$

EVALUATION STUDIES

The objective of this section is to demonstrate the efficiency of undamped structural eigenvalue and eigenvector approximate analysis in an integrated design environment. Numerical results will be presented that compare effects of various levels of eigensolution approximations. A total of four separate cases will be considered. They are outlined as follows

- Case 1. Pure finite difference with no eigensolution approximations.
- Case 2. 2% allowable design variable perturbation with actuator mass derivatives included.
- Case 3. 8% allowable design variable perturbation with actuator mass derivatives included.
- Case 4. 2% allowable design variable perturbation without actuator mass derivatives included.

EVALUATION STUDIES:



Nominal (Case 1)



2% "Linear" Design Δ with Actuator Mass (Case 2)



8% "Linear" Design Δ with Actuator Mass (Case 3)



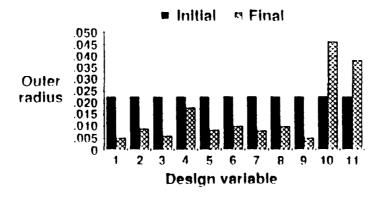
2% "Linear" Design Δ w/o Actuator Mass (Case 4)

OPTIMAL DESIGN

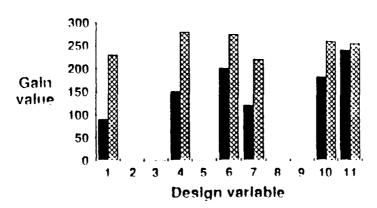
Two different assumptions within the approximate analysis loop will be considered. In Cases 2 and 3, the approximated undamped structural eigenvalues and eigenvectors are assumed to be functions of all design variables, structural plus control. However, Case 4 assumes that the approximated undamped structural eigenvalues and eigenvectors are functions of only the structural design variables. It should be noted that the effects of the actuator masses are neglected only when eigensolutions are approximated. If design variable perturbations are larger than the allowable limits, exact eigensolutions are obtained which include the effects of the actuator masses.

The following control-structure optimization results are obtained using the Automatic Design Synthesis (ADS) software package [4]. The solutions were computed using an interior penalty function method with a BFGS (Broyden-Fletcher-Goldfarb-Shanno) method [5] for the unconstrained subproblem. Additionally, the trade off parameter, β , in the objective function was arbitrarily set to a value of 0.15 for all solution schemes.

Structural design variables



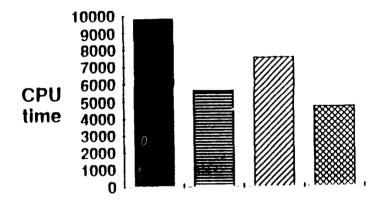
Control design variables



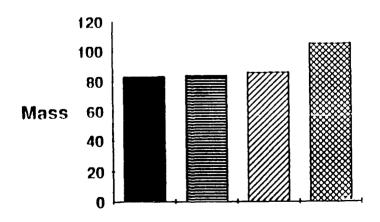
ALGORITHM PERFORMANCE COMPARISON

The bar charts below present a performance comparison of the various approximation schemes. These charts show that the allowable design variable perturbation of Cases 2 and 4 produced the best results. Furthermore, in terms of computational efficiency, the method neglecting the effects of the actuator masses (Case 4) outperformed the method that included actuator mass effects (Case 2). However, Case 4 suffers adverse effects from partially uncoupling the actuator masses from the solution process. The resulting optimal actuator masses are approximately 20 percent higher than those obtained in Cases 1 and 2. Although the actuator masses represent only a small fraction of the total objective, it is suggested that their effects remain within the solution process in an effort to obtain a truly optimal integrated design.

Algorithm performance comparison



Optimal actuator mass



CONCLUDING REMARKS

The Earth Pointing Satellite was used as an example to demonstrate the computational efficiency of eigenvalue/vector sensitivity analysis as applied to a control-structure integrated design problem. In this design study, various levels of allowable design variable perturbation were investigated. The results for a 2 percent design variable perturbation with and without the effects of the actuator mass show a 42 and 52 percent reduction in CPU time, respectively. However, since it results in a larger actuator mass, the method neglecting the effects of the actuator mass is not recommended.

REFERENCES

- 1. Belvin, W. K.; and Park, K. C.: Structural Tailoring and Feedback Control Synthesis: An Interdisciplinary Approach. Proceedings of the 29th Structures, Dynamics, and Materials Conference, AIAA Paper No. 88-2206, May, 1988, also to be published in the AIAA Journal of Guidance Control and Dynamics, 1990.
- 2. Knot, N. S., et al.: Optimal Structural Modifications to Enhance the Optimal Active Vibration Control of Large Flexible Structures. 26th Structures, Dynamics, and Materials Conference, Orlando, FL, April 15-17, 1985.
- 3. Kenny, S. P.: Eigensensitivity Analysis for Space Structures with Applications in Design Optimization. Master's Thesis, Old Dominion University, May 1990.
- 4. Vanderplaats, G. N.: ADS- A FORTRAN Program for Automated Design Synthesis, Version 1.10. NASA Contractor Report 177985, September 1985.
- 5. Vanderplaats, G. N.: <u>Numerical Optimization Techniques for Engineering Design with Applications</u>. McGraw-Hill Book Co., 1984.

The D-StrutTM: A Viscous Passive Damper for Use in Precision Truss Structures

Fourth NASA/DOD CSI Technology Conference Orlando, FL, Nov. 5-7, 1990

Jet Propulsion Laboratory California Institute of Technology 4800 Oak Grove Drive Pasadena, CA 91109 Honeywell Satellite Systems Division P. O. Box 52199 Phoenix, AZ 85072-2199

Eric Anderson (MIT): (617)253-8207

Bob Laskin: (818)354-5086 Mike O'Neal: (818)354-2875 Porter Davis: (602)561-3483 Steve Ginter: (602)561-3244

Int a duction

A viscous damping technique which offers high damping for spacecraft truss structures has been under development for several years (Ref. [1-3]). The technique, now known as the D-Strut, employs a small, mechanical viscous damper configured in an inner-outer tube strut configuration. The D-Strut serves as a basic element in a truss structure, replacing the nominal type strut. The viscous damping concept, employed in more compliant isolation systems, has been qualified for at least three space applications and is currently flying in the Hubble Space Telescope, where the function is to isolate disturbances emanating from the attitude control reaction wheel assembly (Ref. [4-5]).

The United States Air Force and the Jet Propulsion Laboratory (JPL) have investigated the use of D-Struts in high specific stiffness truss structures. Results from the tests carried out at JPL to characterize the D-Strut at submicron displacement levels are presented, along with data illustrating the effect of placing a single D-Strut in the JPL Precision Truss Phase 0 testbed. With considerable development heritage, the viscous D-Strut now provides an attractive means for attaining significant damping levels in space structures. The D-Strut is basically simple in design and construction, is easy to model, and is readily incorporated into the overall structure design and analysis process.

This document provides a brief overview of the D-Strut. The document describes the current D-Strut configuration, presents analytical models and D-Strut damping performance, summarizes experiments conducted with the D-Strut at JPL, and provides a glimpse of future plans.

D-StrutTM Configuration

The D-Struts designed and built to date, as illustrated in Figure 1, employ three basic elements: a small viscous damper, an inner tube, and an outer tube. The damper is placed in series with the inner tube and the damper/inner tube is placed in parallel with the outer tube. An axial displacement across the strut produces a displacement across the damper. Under an axial displacement, the damper forces fluid through a small diameter orifice, thereby causing a shear in the fluid. The fluid shear is actually proportional to the displacement rate across the damper and thus, a true viscous damping force is obtained (i.e. a force proportional to velocity).

The compliances of the damper, the inner tube, and the outer tube are key to the damping performance of the D-Strut. The damper is the most compliant element and the inner tube is the least compliant element. The outer tube provides the basic static stiffness of the strut and is pertinent to applications where the strut is a critical load bearing element in the structure. Otherwise, the outer tube is not necessary and can be eliminated with a resulting improvement in damping performance.

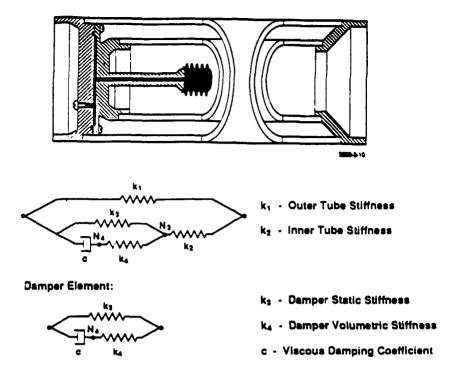


Figure 1. An Inner-Outer Tube D-Strut

The damper element basically consists of two compliant metal cavities connected by a small diameter orifice of a certain length. The damper cavities are hermetically sealed to avoid outgassing and fluid loss. The damper is mechanically simple, has no moving parts or wear mechanisms, and is completely tolerant of space vacuum and radiation.

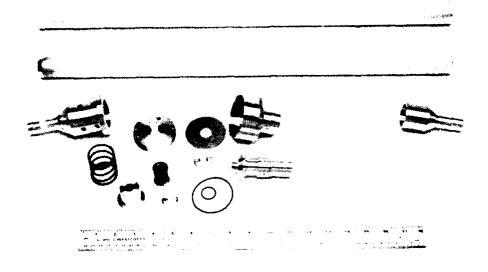
To achieve maximum performance, the damper element should approximate an ideal dashpot. This is accomplished in practice by making the damper stiffness ratio k_3/k_4 small. If the damper is replaced by an ideal dashpot, then the D-Strut damping performance is established by the stiffness ratio of the inner to outer tube, k_2/k_1 .

A diaphragm damper is actually illustrated in Figure 1. Extensive design and testing of the diaphragm damper was accomplished on the PACOSS program (Ref. [3]). In the diaphragm damper the flexing of a metal diaphragm is the mechanism which forces fluid through the small orifice. The assembly parts of a diaphragm D-Strut are pictured in Figure 2.

D-StruiTM Model

A D-Strut is readily modeled by five physical lumped parameters as indicated by Figure 1. Considerable insight to the damping performance is gained by regarding the D-Strut as a mechanical impedance. Mechanical impedance is somewhat analogous to electrical impedance and relates, in the frequency domain, the axial force f to the axial displacement x across the strut:

$$z(s)\equiv\frac{f(s)}{x(s)},$$



11-22600-2C

Figure 2. Diaphragm D-Strut Assembly Parts

with s denoting the Laplace transform variable. For no damping, the impedance reduces to a standard stiffness. The mechanical impedance is a good characterization of the D-Strut behavior as long as the mass lumped at the internal nodes labeled N_3 and N_4 in Figure 1 is negligible. This is typically a very good approximation over the frequency range of interest.

The impedance of a D-Strut is a function of three parameters and has a classic lead-lag network characteristic

$$z(s) = k_s \frac{\omega_p}{\omega_z} \frac{s + \omega_z}{s + \omega_p},$$

with

$$k_{s} = \frac{k_{1}k_{2} + k_{1}k_{3} + k_{2}k_{3}}{k_{2} + k_{3}}$$

$$\omega_{z} = \frac{k_{4}}{c} \frac{k_{1}k_{2} + k_{1}k_{3} + k_{2}k_{3}}{k_{1}k_{2} + k_{1}k_{3} + k_{1}k_{4} + k_{2}k_{3} + k_{2}k_{4}}$$

$$\omega_{p} = \frac{k_{4}}{c} \frac{k_{2} + k_{3}}{k_{2} + k_{3} + k_{4}}.$$

Because the impedance depends only on three parameters, an equivalent three parameter physical model of the D-Strut can be obtained as indicated in Figure 3. The equivalent model impedance is

$$z(s) = k_A \frac{\omega_B}{\omega_A} \frac{s + \omega_A}{s + \omega_B},$$

with

$$\omega_A = \frac{1}{c_A} \frac{k_A k_B}{k_A + k_B}$$

$$\omega_B = \frac{k_B}{c_A}.$$

Of course, the parameters $\{k_A, k_B, c_A\}$ depend on $\{k_1, \ldots, k_4, c\}$ in a rather complicated way. The equivalent model indicates that perhaps only three parameters, two stiffness values and a dashpot coefficient, are needed to model the D-Strut in overall structure design and analysis. D-Strut testing verifies that this is indeed the case.

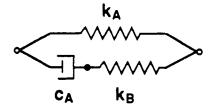


Figure 3. Equivalent D-Strut Model

D-StrutTM Performance

The D-Strut damping performance is easily understood under the condition of sinusoidal displacements and forces. If a sinusoidal displacement

$$x(t) = X \sin \omega t$$

is prescribed across the D-Strut, then the resulting force developed in the strut is also sinusoidal

$$f(t) = XA(\omega)\sin(\omega t + \phi(\omega))$$

where $A(\omega)$ and $\phi(\omega)$ are the amplitude and phase angle of the impedance at the frequency ω :

$$z(j\omega) = A(\omega)e^{j\phi(\omega)}$$
.

Defining the parameter α as

$$\alpha \equiv \sqrt{\frac{\omega_B}{\omega_A}} = \sqrt{1 + \frac{k_B}{k_A}},$$

the amplitude and phase of the impedance are given by

$$A(\omega) = k_A \alpha^2 \frac{\sqrt{1 + (\omega/\omega_A)^2}}{\sqrt{\alpha^4 + (\omega/\omega_A)^2}}$$
$$\tan \phi(\omega) = \frac{(\alpha^2 - 1)(\omega/\omega_A)}{\alpha^2 + (\omega/\omega_A)^2}.$$

A typical impedance characteristic is illustrated in Figure 4.

The energy dissipated per cycle due to the damping is determined by $\phi(\omega)$. In fact, using the classical definition of damping loss factor

$$\eta(\omega) \equiv \frac{1}{2\pi} \frac{\text{energy dissipated / cycle}}{\text{max energy stored / cycle}},$$

then $\eta(\omega) = \tan \phi(\omega)$. It is easy to demonstrate that the maximum loss factor is given by

$$\eta^{\bullet} \equiv \max_{\omega} \eta(\omega) = \frac{1}{2} \frac{\alpha^2 - 1}{\alpha}$$

and that η^* occurs at $\omega^* = \sqrt{\omega_B \omega_A} = \alpha \omega_A$. Thus, the maximum loss factor is determined only by the stiffness of the damper and tubes, not by the damping coefficient c. Since ω_A is determined by the damping coefficient, c is used to set the frequency at which the maximum loss factor occurs.

A D-Strut using a diaphragm damper, as constructed for the PACOSS program, achieves a typical value of $\alpha=1.3$, which corresponds to a maximum loss factor of $\eta^*=0.3$. For PACOSS, the frequency at which the maximum loss factor occurs is $\omega^*=5$ Hz.

One factor which establishes the D-Strut performance is the ratio of the damper's static to volumetric stiffness k_3/k_4 . The volumetric stiffness is actually due to the fluid bulk modulus and the change in cavity volume due to stretching of the metal. Metal stretching due to fluid pressure reduces the forcing action on the fluid with a resultant loss in damping. An achievable stiffness ratio for a typical diaphragm damper is approximately $k_3/k_4 = 0.05$. A significant factor which prevents a smaller ratio for the diaphragm damper is the difficulty increasing the volumetric stiffness.

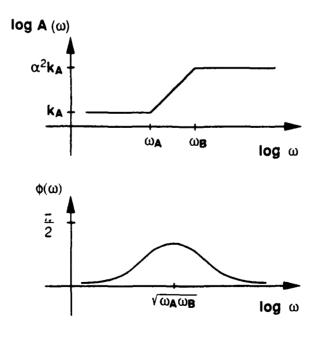


Figure 4. D-Strut Impedance Characteristic

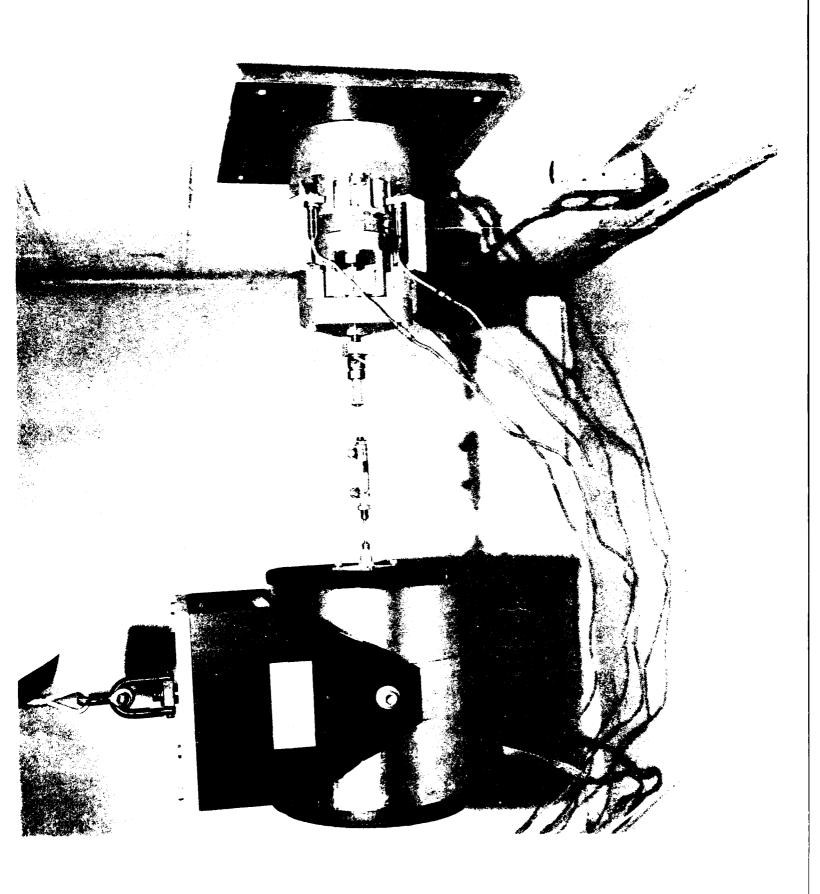


Figure 5. Microdynamics Test Apparatus

This limiting factor of the diaphragm damper has lead to the development of an improved damper with a greater volumetric stiffness. The improved damper is able to achieve a significantly smaller ratio of static to volumetric stiffness. Preliminary testing of several prototype designs has indicated a ratio of $k_3/k_4=0.025$, which is half the ratio for a diaphragm damper. If the improved damper is used in place of a diaphragm damper to construct a typical D-Strut, all other parameters being equal, then the maximum loss factor would increase to $\eta^*=0.5$, representing a 67% improvement in the damping performance. Parametric optimization indicates that, depending on additional constraints, even further improvements are possible.

Microdynamic Testing at JPL

The CSI program at JPL is concerned with developing the hardware and methodologies necessary for observatories such as a space-based optical interferometer (Ref. [6]), which require structures controlled to within a few nanometers in order gather useful scientific data. Passive damping augmentation is a significant part of a control approach which includes vibration isolation and active structural control.

The Honeywell D-Strut was experimentally characterized at submicron displacement levels for use in CSI truss testbeds at JPL (Ref. [7]). The test apparatus (Fig. 5) included three linear variable differential transformers (LVDTs) as displacement sensors and a load cell as a force sensor. The input was supplied by a 100 lb. shaker. All experiments were carried out at room temperature.

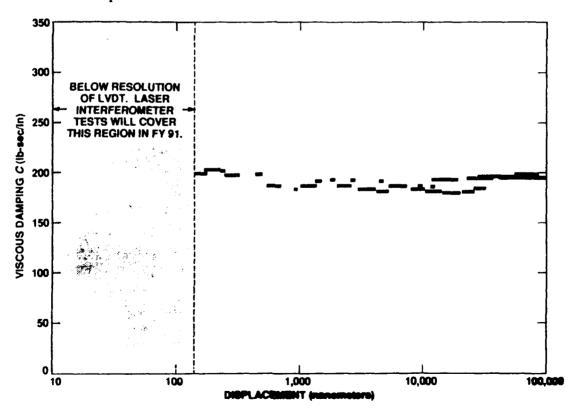


Figure 6. Viscous Damping as a Function of Displacement

JPL CSI ACTIVE STRUCTURE CLOSEUP OF ACTIVE BAYS

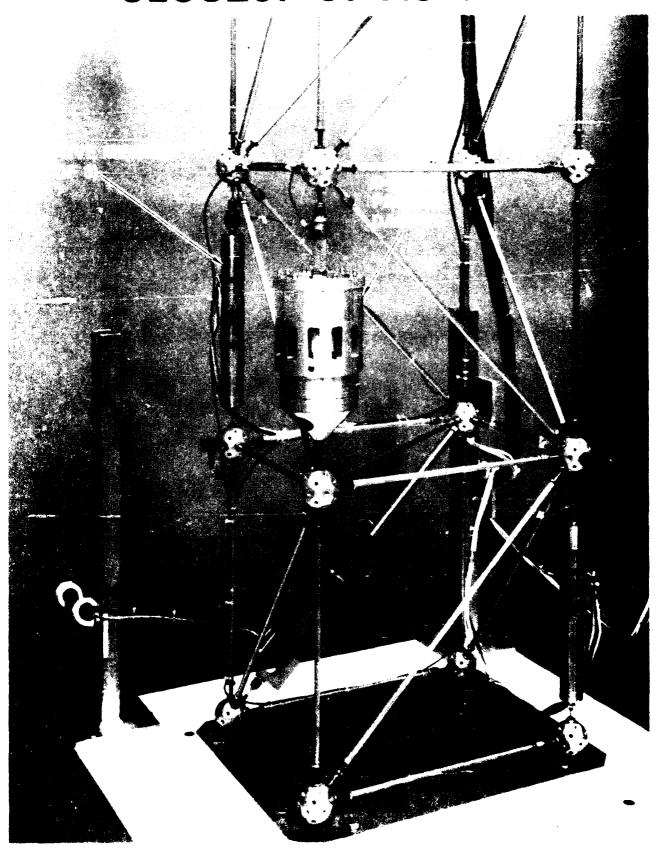


Figure 7.

The damping coefficient was determined by performing curve fit analysis on force-to-displacement transfer functions in the frequency domain from 5 to 15 Hz. The D-Strut behaves in a linear fashion (Fig. 6) over the displacement range where the LVDTs are valid (135-100,000 nanometers). The mean value for the damping coefficient was determined to be 190.1 lb-sec/in (33,292 N-sec/m) with a standard deviation of 6.7 lb-sec/in (1173 N-sec/m). Further experimentation, using laser interferometry to measure displacement, will extend the data into the nanometer regime.

D-Strut in the JPL Precision Truss

A single D-Strut was incorporated into the JPL Precision Truss (Ref. [8]) experiment in order to measure its effectiveness in adding damping to a complex structure (Fig. 7). Several possible locations were selected based on high strain energy content in the modes of interest. The stiffness of the D-Strut was adjustable. One set of experiments was run with the damper stiffness equal to the stiffness of the surrounding struts, and another with the damper strut only 2.5% as stiff.

The damper was added to an existing NASTRAN model of the structure, with the damping coefficient set to the value determined from the microdynamic testing.

The results (Fig. 8) show that appreciable damping can be added to a structure using only a single strut and the total system damping can be predicted fairly accurately.

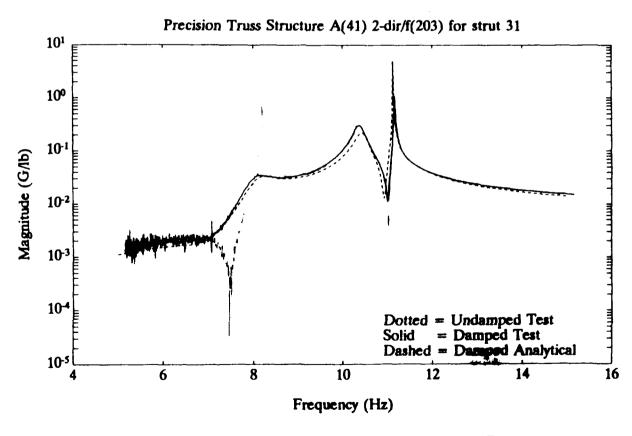


Figure 8. Effect of D-Strut in JPL Precision Truss

Future Plans

Future plans for the D-Strut involve further improvements in the damper element of the strut with completely new designs under consideration. With the damper performance more closely approximating the behavior of an ideal dashpot, the next factor affecting the performance of an inner-outer tube D-Strut is ratio of the inner to outer tube stiffness k_2/k_1 .

D-Struts fabricated to date have used the same material, aluminum, for the inner and outer tubes. Since the damper length is small compared to the overall strut length, the lengths of the two tubes are approximately equal. Thus, using the same material for both tubes, the only way to increase the stiffness ratio k_2/k_1 is to either decrease the outer tube cross sectional area or increase the inner tube cross sectional area. Decreasing the outer tube area quickly leads to buckling problems while increasing the inner tube area quickly leads to a considerable weight penalty.

An obvious alternative is to use different materials for the inner and outer tubes. For example, an aluminum outer tube with a metal matrix composite inner tube would give a factor of 2 improvement in the ratio k_2/k_1 , due solely to the difference in the modulus of elasticity. The use of different materials for the inner and outer tubes is an important aspect under investigation.

Of course, for a non-load bearing strut the outer tube may be eliminated providing a significant improvement in damping. Other factors then become important. To date, no D-Struts have be designed and fabricated without an outer tube. There are applications where this will be an important consideration.

The incorporation of the D-Strut in the JPL Precision Truss contributed significantly to the ability to perform effective closed-loop control on that structure (Ref. [9]). Several units of the modified D-Strutwill be available for use in the JPL Phase B testbed.

References

- Wilson, J. F., "Very High Damping in Large Space Structures", ASME Vibrations Conference, Boston, MA, 1987.
- Davis, L. P. and Wilson, J. F., "New Structure Design Criteria Offer Improved Pointing and Lower Weight", 59th Shock and Vibration Symposium, Albuquerque, NM, October 1988.
- ³ Cunningham, D. C., "Final Technical Report PACOSS D-Strut Development", Prepared for Martin Marietta, Honeywell Satellite Systems Operation, Glendale, AZ, August 1990.

- Roddeb, J. J., Dougherty, H. J., Reschke, L. F., Hasha, M. D., and Davis, L. P., "Line of Sight Performance Improvement with Reaction Wheel Isolation", AAS Guidance and Control Conference, Keystone, CO, February 1986.
- Davis, L. P., Wilson, J. F., and Jewell, R. E., Workshop on Structural Dynamics and Control Interaction of Flexible Structures, NASA Marshall Space Flight Center, Huntsville, AL, April 1986.
- 6 Laskin, R. and San Martin, M., "A Spaceborn Imaging Interferometer The JPL CSI Mission Focus", Third NASA/DOD CSI Technology Conference, San Diego, CA, Jan. 29-Feb. 2, 1989.
- Anderson, E. H. and Trubert, M., "Experimental Investigation of a Passive Damper for Use in Precision Truss Structures", JPL D-7653, August, 1990.
- Fanson, J. L., Blackwood, G. H., and Chu, C. C., "Active-member Control of Precision Structures, Proceedings, 30th AIAA SDM Conference, Mobile, AL, pp. 1480-1494, 1989.
- Fanson, J. L. and Briggs, H. C., et al., "JPL Phase-0 CSI Experiment Results and Real Time Control Computer", Fourth NASA/DOD CSI Technology Conference, Orlando, FL, Nov. 5-Nov. 7, 1990.

An Integrated Structure/Optics/Control Modeling and Analysis Software Breadboard

Hugh C. Briggs

Jet Propulsion Laboratory
California Institute of Technology
Pasadena, California

4th NASA/DOD Control/Structures
Interaction Technology Conference
Orlando, Florida
November 5-7, 1990

An Integrated Structure/Optics/Control Modeling and Analysis Software Breadboard

This poster session paper describes an integrated modeling and analysis capability developed at JPL under the Control/Structures Interaction Program for analysis of flexible optical spacecraft. The objective of the development was to build a proof-of-concept capability quickly to explore issues and design features and to generate requirements for the JPL CSI Conceptual Design Tool. 1 The paper summarizes the capabilities and illustrates their application through an example. The JPL Control/Structure Interaction Program is developing new analytical methods for designing micro-precision spacecraft with controlled structures. One of these, the Conceptual Design Tool, will illustrate innovative new approaches to the integration of multi-disciplinary analysis and design methods. The Tool will be used to demonstrate homogeneity of presentation, uniform data representation across analytical methods, and integrated systems modeling. The Tool differs from current "integrated systems" that support design teams most notably in its support for the new CSI multi-disciplinary engineer.

The Design Tool will utilize a 3-dimensional solid model of the spacecraft-under-design as the central data organization configuration layout, will store and retrieve data from a hierarchical, object oriented data structure that supports assemblies of components with associated data and algorithms. In addition to managing numerical model data, the Tool will assist the designer in metaphor. Various analytical methods, such as finite element structural analysis, control system analysis and mechanical organizing, stating and tracking system requirements. The software breadboard was developed to demonstrate homogeneity of presentation and uniform data representation for controls, structures and optics analysis methods. This was accomplished by utilizing the finite element modeling paradigm for both structures and optics and implementing the breadboard in Pro-Matlab which is an existing general purpose analysis program. As a result, the model viewing functions can be applied to both structural models and optical models alike. Pro-Matlab enabled the quick development of the breadboard because all the necessary supporting matrix algebra, data storage and programming functions

The research described in this paper was performed as part of the Control Structure Interaction Program at the Jet Propulsion Laboratory, California Institute of Technology, under contract with the National Aeronautics and Space Administra-

the Proceedings of the Third Air Force/NASA Symposium on Recent Advances in Multidisciplinary Analysis and The Conceptual Design Tool is described in "Control/Structure Interaction Conceptual Design Tool" by H.C. Briggs in Optimization, San Francisco, CA, September 24-26, 1990.

Structural Dynamics Modeling

structural dynamics equations can be stated simply in terms of the system matrices and nodal degrees of freedom as shown. The vector of forces, {F}, might describe external forces acting on the system such as disturbances, vibrations of on-board equipment, gravity, and forces caused by a control system. For spacecraft, the latter might be inertially reacting, such as a thruster which results in a single entry in {F}, or internally reacting, such as an active structural member which results in equal and opposite The first chart begins a description of the equations used to model dynamics of controlled optical structures. 2 entries in {F}.

The structural dynamics equations are assembled in an easily automated procedure. The nodal degrees of freedom are numbered in a simple counting process and used as indices into the system matrices in the subsequent system assembly. The element the element connectivity list. In a typical implementation, the complete matrices for an element are computed and components associated with unmodeled or missing degrees of freedom are simply discarded during system assembly. This occurs, for example, matrices, such as stiffness and mass, are computed element by element and inserted into the system matrices by the assembly process. The proper location in the system matrices is obtained from the degree of freedom numbers associated with the nodes in when 3-D truss elements are used in the analysis of a planar truss. These practices have been used in the implementation of the optical analysis to be presented in a subsequent section.

ä

For more discussion, see "Integrated Control/Structure/Optics Dynamic Performance Modeling of a Segmented Reflector Telescope" by H.C. Briggs, D.C. Redding, and C.C. Ih, in the Proceedings of the Twenty-First Annual Pittsburgh Conference on Modeling and Simulation, Pittsburgh, PA, May 3-4, 1990.

Structural Dynamics Modeling

Typical Structural Dynamics Equations in Terms of the Physical Degrees of Freedom which are Nodal Displacements {d}

$$[M]^*\{\ddot{d}\} + [D]^*\{\dot{d}\} + [K]^*\{\dot{d}\} = \{F\}$$

The Forces {F} include

Disturbances

Equipment Vibrations

Gravity

Control System Forces - Internally & Externally Reacting

Implementation Features Might Include

Many Element Types Such As Truss, Beam, Plate

Local Nodal Coordinate Systems

Programming Language

Typical Operations Include

Model Reduction, e.g. Guyan Reduction

Calculating System Modes

Simulating System Dynamic Response to Forces

Modeling of Controlled Structures

as the plant) which utilizes first order differential equations. The next chart illustrates this and shows how the structural dynamics provided by the controller are in {u}. In certain situations, the states themselves may be directly measured, but as is common in control law will be implemented in a controller that coexists with the structure, taking measurements {y} and computing commands Methods for analysis of controlled systems are typically based upon a description of the system to be controlled (known equations can be cast into this form. The degrees of freedom of the plant are described by a state vector, {x}, and the forces controlled structures, the sensed variables, {y}, are not the states but can be related to the states by an algebraic equation. The {u}. As stated, these are assumed to be continuous systems but the realities of discrete systems can be readily handled. Ultimately, a discrete controller will be used to control a continuous structure but these details will not be addressed here. When the plant is modeled by finite elements, the structural dynamic equations can be cast into the first order form used n control analysis by identifying the structural displacements and velocities as the states of the plant. If a modal model reduction has been applied, the states are the modal amplitudes and velocities. Then the finite element equations are shown in first order form in the chart. Here, the forces have been explicitly partitioned into external forces {F} and controller generated forces {u}. The matrix [B] is typically filled with 1 at locations i, j when inertial control force j is applied to degree of freedom i. When an internally reacting control actuator k, such as an active member, connects degree of freedoms i and j, [B] contains +1 at location i,k and -1 at location j,k.

Modeling of Controlled Structures

Most Methods Describe the Plant Degrees of Freedom via a State Vector $\{x\}$ and First Order Differential Equations

$$\{\dot{x}\}=[A]^*\{x\}+[B]^*\{u\}$$

External Forces are $\{u\}$ and Typically Represent Control Forces. Sensed Variables $\{y\}$ Are

$${y} = [C]^* {x}$$

For Plants Modelled by Finite Elements, Let

$$\begin{cases} x \\ d \end{cases} = \begin{cases} d \\ d \end{cases}$$

The Equations of Motion Become

$$\{\dot{x}\} = \begin{bmatrix} 0 & I \\ M^{-1}K & M^{-1}D \end{bmatrix} * \{x\} + \begin{bmatrix} 0 \\ M^{-1} \end{bmatrix} * [B] * \{u\} + \begin{bmatrix} 0 \\ M^{-1} \end{bmatrix} * \{F\}$$

Modeling of Controlled Structures (Cont'd)

described by differential equations containing the closed-loop system matrix {A_{cl}}. In addition to the sensed values used in the controls, other observations that describe the system performance might also be constructed from the states. These might include optical beam positions, motions of mirror attachment points, or even the spacecraft line of sight. System simulations will require both [C'] and [C] to compute the closed loop system dynamics and the system performance measures. The new optics methods Typical linear control laws compute controller commands based upon constant gains which leads to a closed loop system presented in the next section can be used to compute these matrices for optical systems.

Modeling of Controlled Structures

Typical Linear Control Laws Compute Forces via

$$\{u\} = -[G]^* \{y\}$$

Which Leads To

$$\{\dot{x}\} = [A_{cl}]^* \{x\} + \begin{bmatrix} 0 \\ M^{-1} \end{bmatrix}^* \{F\}$$

where

$$[A_{cl}] = \begin{bmatrix} A & -\begin{bmatrix} 0 \\ M^{-l} \end{bmatrix} *B*G*C \end{bmatrix}$$

Other Observations Might Be Constructed From

$${z} = [C'] * {x}$$

Modeling of Controlled Optics

alignment and phase. Deviations from the nominal geometry due to spacecraft dynamics and control or other causes can move the Spacecraft imaging systems typically collect light via a sequence of optical elements that compress and guide the beam to one or more detectors. Performance of these instruments depends on the optical elements maintaining their nominal figure, instrument line of sight, distort the image, lower the signal-to-noise ratio, reduce the crispness of interference fringes, or lower the available energy at the detector.

cases to trace a single ray past each element to the focal plane. 3 If the motions are sufficiently small, the linear ray-trace equations presented in Ref. 3 can be applied. In cases where more fidelity is desired, perhaps to simulate the change in the wavefront due to deforming optical elements, a full grid of rays can be traced. Beyond this, the rays can be traced using the nonlinear large-motion equations of Ref. 3. Optical performance metrics of many kinds can be computed from the states of the These effects can be modelled by tracing the optical system, from the input aperture to the focal plane or other reference surface. To capture the (first-order) effects of spacecraft motions on the instrument line of sight, it suffices in many rays at an appropriately chosen reference surface. The simplest optical model capable of representing the line of sight and phasing of a large segmented telescope will be described in the following sections. The ray through the centroid of each segment represents the nominal ray geometry and is propagated through the secondary to the focal plane. The small-motion equations of Ref. 3 are used to define matrices that describe the deviation of each ray from nominal. The matrices capture the effects of translation and tilt of each optical element on the position, direction and path length of each ray. The nominal geometry of the optical system is described much as the finite elements of the structural model. Points in 3-space are provided for locations of elements and rays connect elements into segments of the beam train. The optical elements are assembled based upon the ray connectivities and describe the relationships between the output elements and the ray degrees of of various types and have individual transformation matrices that describe their effects on the rays. The system matrices are

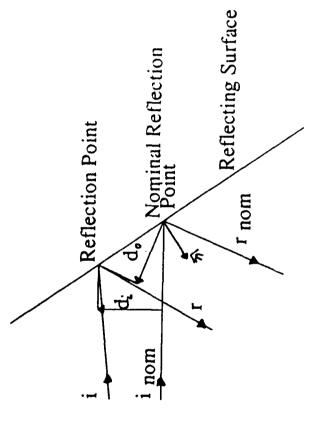
The degrees of freedom are associated with each ray at its intersection with an optical element. The small deviations of the ray from its nominal are described by displacements, directions, and phase delays at the nominal optical element intersection point. The element matrix relates these to the element output displacements and directions. Ray elements have a matrix that transforms the degrees of freedom from the output of one element to the input of the next.

See "Optical Modeling for Dynamics and Control Analysis" by D.C. Redding and W. Breckinridge in Proceedings of the AIAA 1990 Guidance and Control Conference, Paper 90-3383, Portland, OR, August 20-22, 1990.

Modeling of Controlled Optics

Approach:

Trace Nominal Rays Through Structure
Allocate Degrees of Freedom for Small Perturbations in Ray
Compute Sensitivity Matrices for Motion of Optical Elements



Reflection Geometry

Modeling of Controlled Optics (Cont'd)

entire spacecraft. The system transformation matrices depict the transfer of this misaligned input ray through the beam train and produce the errors or offsets at the detector. Other disturbances to the beam train might arise from displacement or rotation of optical elements themselves. This might occur due to vibration of the element support structure or rotation of beam steering The rays might deviate from the nominal configuration for several reasons that are of interest in the design of controlled optical systems. For example, the incident rays might have a small directional component caused by rotation of the elements by control system actuators.

temperature-related distortions of the element. This leads to a wide variety of elements whose transformation matrices account Thus, the transformation matrices for each element must account not only for input deviations, but also for displacement and rotation of the element itself. This leads to a natural dissection of the causes of the deviations into several sets. Input errors have already been mentioned. In addition, the motion of the elements has displacement and rotation components. Other events that are significant to the element transformation can be included, such as imperfections in the element or for optical properties, support motions, control system actuation and other error sources.

To illustrate the optical modeling technique, the transformation matrix for a general optical element will be presented in this section. Although several elements are derived in Ref. 3, the telescope example in the last section uses only conic elements. The equations for the element are summarized in this chart to illustrate their similarity to finite elements.

parameters such as principal axis direction, focal length and eccentricity. The input ray describes the deviations in terms of an input offset d_i, an input orientation i, and a path length differential dL_i. The departing ray is described by the offset d_o, direction r, and path length differential dL₀. With these degrees of freedom, the element transformation matrix [te] is as shown. See Ref. 3 The optical element is described by the coordinates of the intersection point of the nominal ray and a list of optical for detailed descriptions of the partials contained in the matrix.

element on its up-beam end to the input degrees of freedom on its down-beam end. Although it is possible to include distortions The ray connects optical elements and its transformation matrix transfers the output degrees of freedom from the and attenuations due to media transmission effects, the perfect ray simply maintains the beam orientation and increases the offset in proportion to its length. Let L be the length of the ray computed from the coordinates of its end points. The ray transformation matrix [tr] is then defined as shown for a ray with up beam element j and down-beam element k.

Modeling of Controlled Optics

Optical Elements Relate Ray Perturbations in to an Element to Ray Perturbations out of an Element

$$\begin{pmatrix} d_o \\ r \\ dL_o \end{pmatrix} = [t_e]^* \begin{cases} d_i \\ i \\ dL_i \end{pmatrix}$$

where

$$\begin{bmatrix} dd_o & dd_o \\ dd_i & di \\ dd_i & di \end{bmatrix} \begin{bmatrix} da_o \\ dd_i & di \\ dd_i & di \end{bmatrix}$$

Rays Propogate the Ray State from the Output of One Element to the Input of Another $\begin{cases} d_i \\ i \\ dL_i \end{cases} = \begin{bmatrix} I_3 & L*I_3 & 0 \\ 0_3 & I_3 & 0 \\ 0 & 0 & 1 \end{bmatrix} * \begin{cases} d_o \\ r \\ dL_o \end{cases}$

Modeling of Controlled Optics (Cont'd)

three elements, numbered i-1, i, and i+1, that are connected by rays. The ray offsets and orientations are related by a transformation matrix [t] which is the product of the ray transformation matrix, [tr] and the element transformation matrix, [te]. If the values of the internal degrees of freedom are not required in the solution, they can be condensed out. Consider The equation in the chart shows the result of compacting out all internal degrees from the input element 0 to the output detector With the individual element transformation matrices, the system matrix can be assembled much as finite element matrices are assembled. The internal optical degrees of freedom are collected and numbered to correspond to rows and columns of the system transfer matrix. In addition, the control inputs that cause displacement and rotation of the elements are collected and numbered. The ray system inputs and outputs form other sets. Based upon this partitioning, the system matrix can be written as shown in the last equation.

degrees of freedom, are returned. For system simulations, the optical performance can be computed at each time step, given only To compute the optical system outputs, the input ray deviations and the control element motions are collected and passed along with the transformation matrix [t] to a sweep routine. The resulting output vector, and optionally the internal the current values of the control element motions.

Modeling of Controlled Optics

The Optics Transfer Matrices can be Compacted to Eliminate all Intermediate Optical Degrees of Freedom

$${d_o \brace r}^n = [t]^n * \cdots * [t]^{2*} [t]^{1*} {d_o \brace r}$$

The Entire Optical Model Transfer Matrix is

This Constant Matrix is [C'] and Multiplies a Vector of Input Ray Perturbations and Control Motions of Optical Elements to Produce the Motion of the Rays in the Detector.

Telescope Models and Disturbance Excitation

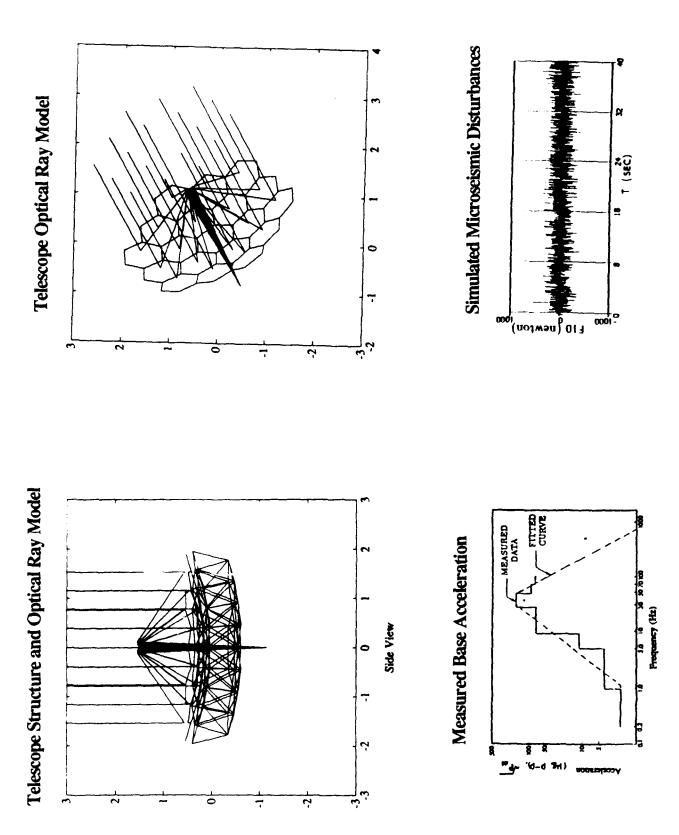
few slides. The model of the structure, the panels and the panel supports is described in "3D Dynamic Modeling and Simulation of a Precision Segmented Reflector Telescope" by C. C. Ih, H. C. Briggs, and S. J. Wang. The optical model and the simulation results As another example of this new capability, analysis results from a segmented telescope design are presented in the next are described in the companion paper "Integrated Control/Structure/Optics Dynamic Performance Modeling of a Segmented Reflector Telescope" by H. C. Briggs, D. C. Redding, and C. C. Ih. Both papers can be found in the Proceedings of the Twenty First Annual Pittsburgh Conference on Modeling and Simulation, 3-4 May, 1990.

inner ring are positioned by three linear actuators with lateral restraining flexures while the outer ring panels are simply attached to The telescope model is shown in the facing slide and contains the typical elements of a controlled optic structure. The primary reflector is supported by a truss paneled by 18 curved hexagonal reflector segments. Each of the six segments of the the truss. The panels are assumed rigid and are modeled by stiff elements. The structural model of the secondary mirror is a concentrated mass supported by a tripod of truss elements. The structural dynamic model contains 300 degrees of freedom which are reduced to 102 vertical displacements for subsequent analysis. The optical model consists of a segment principal ray that enters parallel to the telescope axis. The primary segments are represented by conic optical elements that reflect the rays to an output detector behind the primary. The output of the optical model is the pair of ray displacements, for each of the six rays of the inner panel ring, in the plane of the detector.

mirrors due to truss dynamics and the action of the control system. Specifically, the six active primary segments have piston and two tilt freedoms and the secondary elements have three translation freedoms to be associated with the structural motion of the Optical degrees of freedom have been included in the model to represent the motion of the primary and secondary secondary mirror. For this telescope, the primary segment freedoms represert control inputs while the secondary reflector freedoms represent the coupling induced by structurally supported optical elements.

To illustrate the use of the optics model in the system dynamic simulation, a seismic disturbance has been applied to the base of the truss to analyse expected conditions in the technology validation laboratory. In this analysis, no control system is present and the inner ring panels bounce freely on their soft support fixtures. The spectral content of the seismic acceleration is shown in the chart along with a typical time history of the input force.

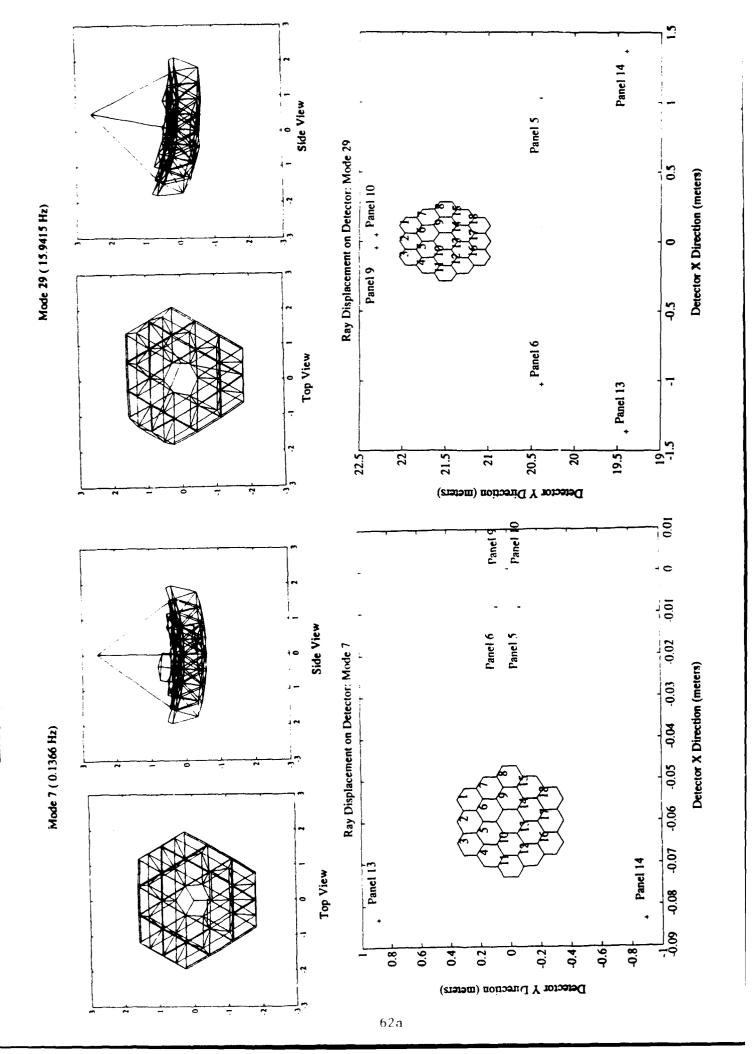
Telescope Models and Disturbance Excitation



Effect of Structural Modes on Panel Chief Rays

The time domain simulation utilized a reduced order model with 23 dominant modes out of 102. These consisted of 18 modes are shown in the facing chart. On the left is one of the 18 panel modes in which panels 13 and 14 show a strong asymetric panel modes ranging from 0.1366 Hz to 0.1718 Hz, and 5 truss modes with frequencies from 15.8 Hz to 74.3 Hz. Two typical motion. The right figure show a truss bending mode. Since no damping data for the demonstration test article were available, a modal damping ratio of 5% was assumed for all modes. Tests of the panel suspension controller have demonstrated a capability to damp the panels at this level, although no data for the truss is available. The simulation was executed in ACSL and the results transferred to Pro-Matlab for this analysis. The modal cost in terms of the optical performance can be measured by the ray displacements resulting from a given mode shape. That is, [C]*[\Phi] provides the x and y displacements of each segment principal ray in the plane of the detector for mode i. The bottom half of the facing chart shows these displacements for the panel mode and the truss mode.

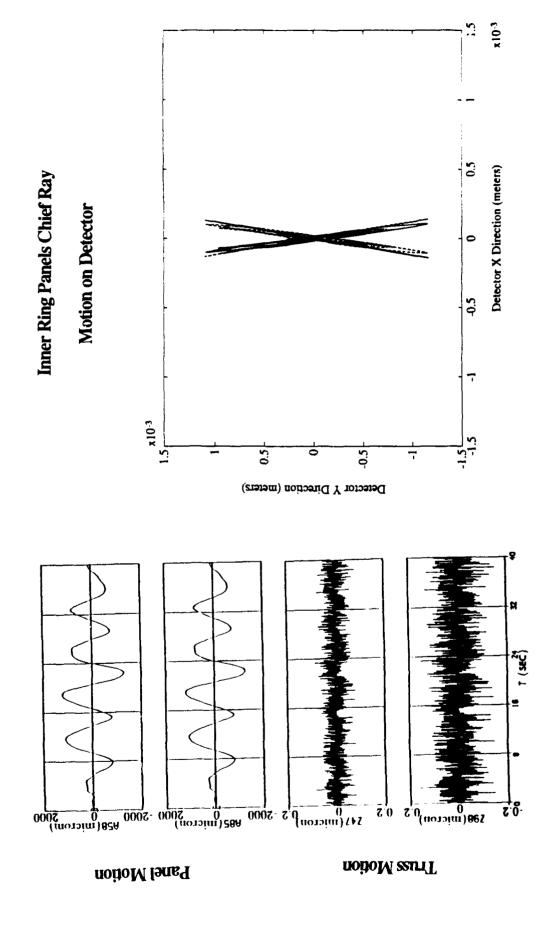
Effect of Structural Modes on Panel Chief Rays



Open Loop Time Response

response of the panel passive support system at approximately 0.1 Hz. The excitation contained a small spectral energy below 1 Hz The time histories from the simulation are shown in this chart along with motion of the rays in the detector. The left plots show typical panel motions caused by the base accelerations with no panel control system. The motion is dominated by which is its design function. The lower plots show the motion of a typical truss node and clearly shows the spectral content of which is exciting the panel support mode. The panel support system effectively eliminates all disturbances above this frequency the disturbance.

The right plot show the traces of the six inner panel rays in the detector plane. These show the basically sinusoidal motion of the panel responses on the left.



CONTROL/STRUCTURES/OPTICS CAPABILITIES IN PRO-MATLAB

FINITE ELEMENT STRUCTURAL DYNAMICS

- Model 3D Trusses and Frames
- Rod. Beam & Concentrated Mass Elements
 - Local Nodal Coordinate Systems

CONTROLS SYSTEM DESIGN AND ANALYSIS

- All Standard Matlab Capabilities
- All Tool Boxes, e.g. Robust Control
- First Order Plants from Finite Element Models Using Physical Coordinates or Modal Models

CONTROLLED OPTICS MODELING

- Linear Geometric Ray Trace Optics from COMP
- 3D Conic Reflector Elements
- All Internal Perturbation DOF Available
- Observation Matrix [C] Computed via Compaction

3D GRAPHIC MODEL VIEWING

- Wire Frame Based On Standard Matlab Plotting
 - Full Transformation Features
 Rotations, Translations, Scaling
- Perspective, Isometric ViewsRed-Blue Stereo Pair Images
- Multiple Views Per Page Using Matlab Subplot
 - View All Structure and Optical Elements
 - Deformed and Undeformed Models

SUMMARY OF CAPABILITIES

APPLICATIONS TO DATE

- CSI Focus Mission Interferometer Structural Geometry Only
- CSI Phase B Test Bed Structure and Optical Delay Line Dynamic Model
 - PSR 3D Dynamic Model Structure and Geometric Optics
- Heavy Structural Damping 2D Truss with Complex Modes
 - Eldred Tubbs' "Optical Trusses"
- Multiple Objective Optimization of Controlled Structures

PROBLEM SIZES

- Modal Analysis of ~200 DOF Models Takes ~40 mins on Sun 3/60
 - 3D Views of FMI Draw in ~3 secs
- Reduced Order 30 Mode Model Time Simulation in ~10 secs
 - Bottom Line: Interactive Nature of Matlab is Preserved

ADVANTAGES

- Homogeneous Integration of Structures and Optics
 - All Features of Matlab Preserved and Available
- Finite Element and Optic Modules Available in Source
- 3D Interactive Graphics of Structures & Optics Significantly Reduces Modeling Time

DESIREMENTS

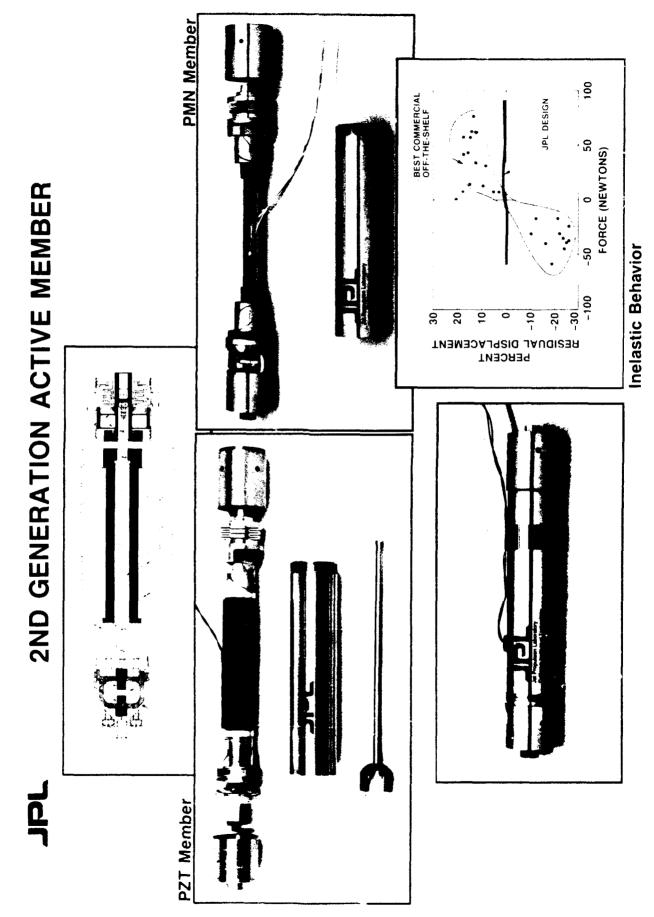
- Sparse Matrix Storage
- Direct 3D Plotting with Surfaces

2ND GENERATION ACTIVE MEMBER

E. H. Anderson Massachusetts Institute of Technology

J. Fanson and D. Moore Jet Propulsion Laboratory

M. A. Ealey Litton ITEK Optical Systems



2nd Generation Active Member

The Jet Propulsion Laboratory has embarked on a program to develop the technology to achieve submicron evel dimensional stability on large complex optical class spacecraft. One key technology is active structures which incorporate active members that exert control forces internal to the structure and thereby improve the structure's dimensional stability. A second generation active member has been design and tested that eliminates stiction and backlash by utilizing flexures and preload springs that are machined from monolithic blocks of metal. Cross-blade flexures are used on either side of the linear motor element to prevent the motor from experiencing bending moments or shear forces. A parallel motion flexure is used to guide the moving stem and transfer applied bending moments and shear forces to the outer housing. A motion transfer rod runs down the centerline to enable the change in the member's length to be measured. The motion is measured with a differential eddy-current proximity sensor to a resolution of a few nanometers. The member was designed such that it could be disassembled and the linear motor interchanged. Two members with piezoelectric (PZT) motors were assembled and tested giving performance that was within one percent of each other for all properties. The device has a stroke of about 65 micrometers, and a small signal bandwidth of several hundred hertz. The active member can also be used statically. The actuator is rated to 100 lb tension or compression; higher loads can be achieved by resizing of the preload spring. An electrostrictive (PMN) motor developed by Itek Optical Systems was also tested, and showed essentially no hysteresis or creep, effects which are common to piezoelectric actuators. Currently, a magnetostrictive motor is being designed that can be fitted into the active member for testing. Test results show that the inelastic behavior of the new design is a factor of ten superior to the best available commercial design. Care has been taken in the mechanical design to enable this actuator to eventually be flight

Reference:

Anderson, E. H., D. M. Moore, J. L. Fanson, and M. A. Ealey, 1990. "Development of an Active Member Using Piezoelectric and Electrostrictive Actuation for Control of Precision Structures," AIAA Paper No. 90-1085-CP.

The MIT SERC Interferometer CSI Testbed

Eric Anderson, Gary Blackwood, Tupper Hyde, and Ed Kim

MIT Space Engineering Research Center Department of Aeronautics and Astronautics

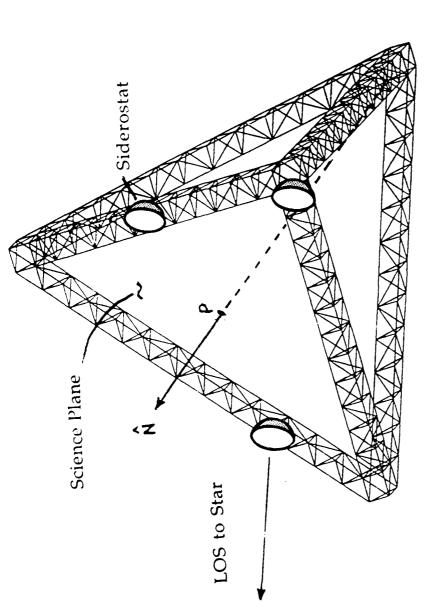
> MIT Room 37-351 Cambridge, MA 02139 (617) 253-8207

The MIT Space Engineering Research Center (SERC) has developed a controlled structures technology (CST) testbed based on one design for a space-based optical interferometer. The role of the testbed is to provide a versatile platform for experimental investigation and discovery of CST approaches. In particular, it will serve as the focus for experimental verification of CSI methodologies and control strategies at SERC. The testbed program has an emphasis on experimental CST-incorporating a broad suite of actuators and sensors, active struts, system identification, passive damping, active mirror mounts, and precision component characterization.

The SERC testbed represents a one-tenth scaled version of an optical interferometer concept based on an inherently rigid tetrahedral configuration with collecting apertures on one face. The testbed consists of six 3.5 meter long truss legs joined at four vertices and is suspended with attachment points at three vertices. Each aluminum leg has a 0.2m by 0.2m by 0.25m triangular cross-section. The structure has a first flexible mode at 31 Hz and has over 50 global modes below 200 Hz. Typical total light path length stability goals are on the order of 50 nanometers. It is expected that active structural control will be necessary to achieve this goal in the presence of disturbances. The internal laser metrology system has a resolution of 5 nanometers.



Space Science Basis



Fourth Vertex

Space-Based Optical Interferometer: Mission Requirements for

3 milli arc seconds 10th magnitude star

.5 µm

||

I meter diameter siderostats 10 second observation time Baseline = 35 meters

Actual Testbed: 3.5 meter baseline (1/10 scale)

Important Parameters for Science Objectives:

- Total Starlight Pathlength Stability
- Projected Baseline Stability

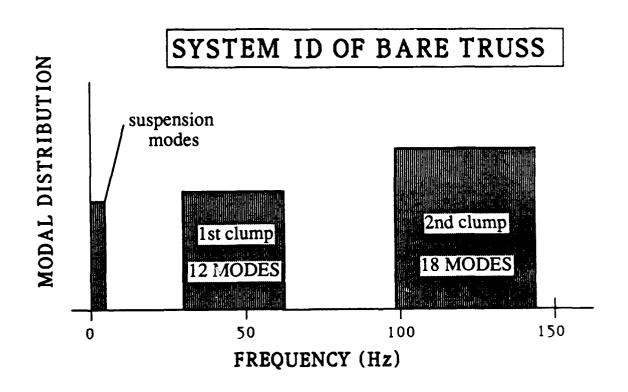
Dynamic Requirements on Pathlength and Baseline:

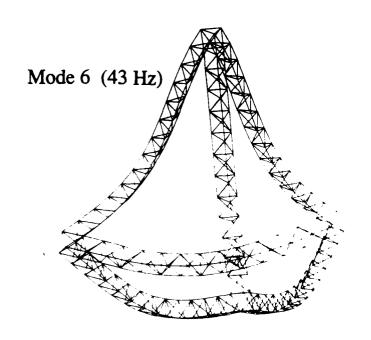
| f > 0.1 Hz | intensity errors drive requirements control to 50 nm rms independent of baseline |
|-------------|--|
| f < 0.1 Hz | phase error drive requirements measure to λ/20 or 25 nm rms |

Performance Metric of Testbed:

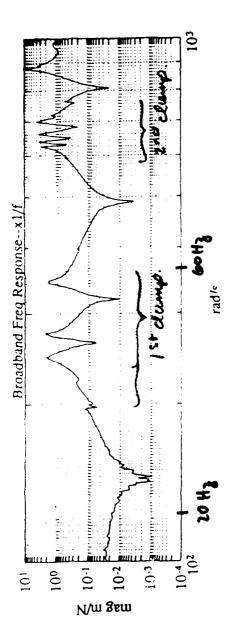
- control (total) internal pathlength and projected baseline to 50 nm r.ns for frequencies above 0.1 Hz (first mode is 30 Hz)
- · ignore rigid body, beam tilt and external pathlength errors

Dynamics of the Testbed





- Testbed suspended by 3 vertices
- Suspension bounce and pendulum modes are below 3 Hz.
- Dynamics of the bare truss have been experimentally characterized
- · Symmetry results in
- · nearly repeated eigenvalues (ID becomes more difficult)
- clumping of modes (12 modes between 31 Hz and 62 Hz)
- First two clumps of modes are characterized by combinations of first and second bending and first torsional modes of the individual legs.
- Further system ID to be carried out when optics are all mounted
- Typical open loop damping ranges from 0.03% to 0.3%.
- Typical transfer function (displacement/shaker force):



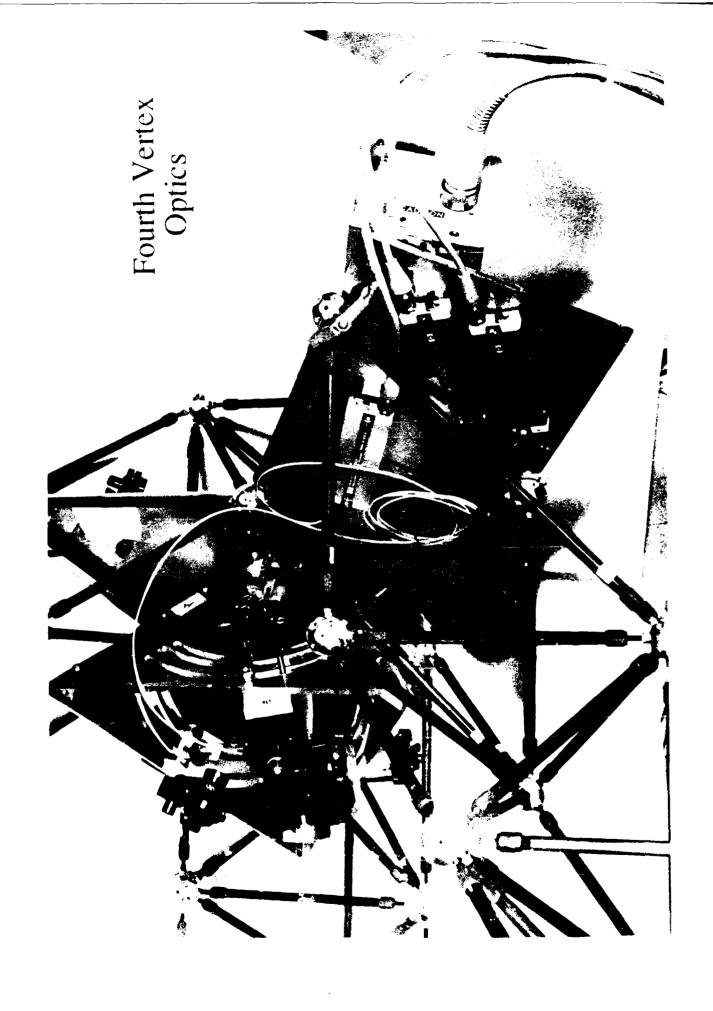
ADINA Finite Element Model

- One beam element per strut
- Stiffnesses based on component-level testing
- Bare truss has 696 struts and 228 nodes (1368 d.o.f.)
- Simple models of suspension have been included
- Comparison to measured frequencies:

| Error | + 7.3% | + 4.1 % |
|------------|---------|---------|
| Actual | 31.4 Hz | 94.1 Hz |
| Prediction | 33.7 Hz | 98.0 Hz |
| Mode | | 13 |

Optical Metrology System

- unique feature of testbed is multi-axis laser metrology
- 6 internal pathlength measurements used to define pathlength and baseline performance metrics
- resolution of 10 nm
- laser system powered by 670 µW laser from Hewlett Packard
- at 3 siderostat locations are precision 3 axis active mirror mounts holding common endpoint retroreflectors (cat's eyes)
- · VME based fringe counting provides seamless link to real time controller



Disturbances

Relevant Disturbances Affecting Space-Based Optical Interferometer (> 0.1 Hz)

- CMG broadband noise and harmonics
- RTG coolant flow
- · Solar array moment actuators
 - Siderostat motion

Scaled Disturbances Applied to Testbed

- frequency spectrum scaled to the fundamental mode
- jitter budget identical for full scale and testbed
- simulate same order of jitter disturbance in testbed as in full scale interferometer
- force magnitude scales proportional to the stiffness ratio

Hardware Implementation

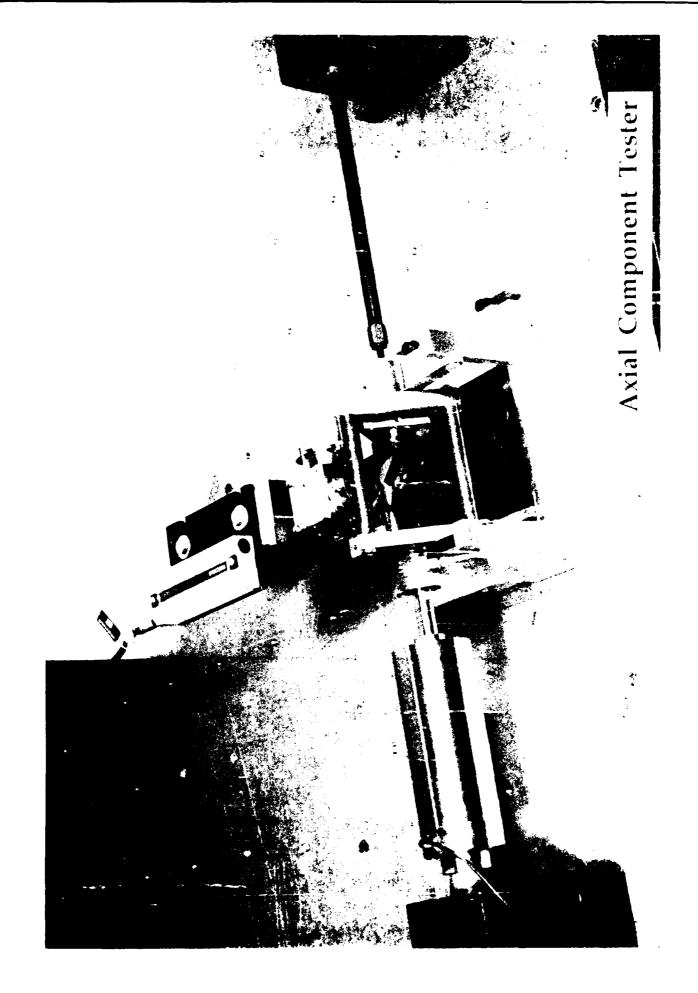
- linear shakers mounted at three vertices will introduce scaled disturbance spectrum and magnitude
- piezoelectric active struts may also be used for low and high frequency excitation

Axial Component Tester

An axial component tester has been constructed and is operational on an optics bench. This facility includes a Physik Instrumente piezoceramic strut to drive various test articles which represent subcomponents of the testbed. Mainly, these are passive or active replacements for the aluminum struts. Load and displacement are measured, the latter with a Zygo Axiom 2/20 interferometer system. The tester will be used in the 0.1-100 Hz frequency range, with displacements from 1 nm to 60 mm. Initial measurements to be conducted are:

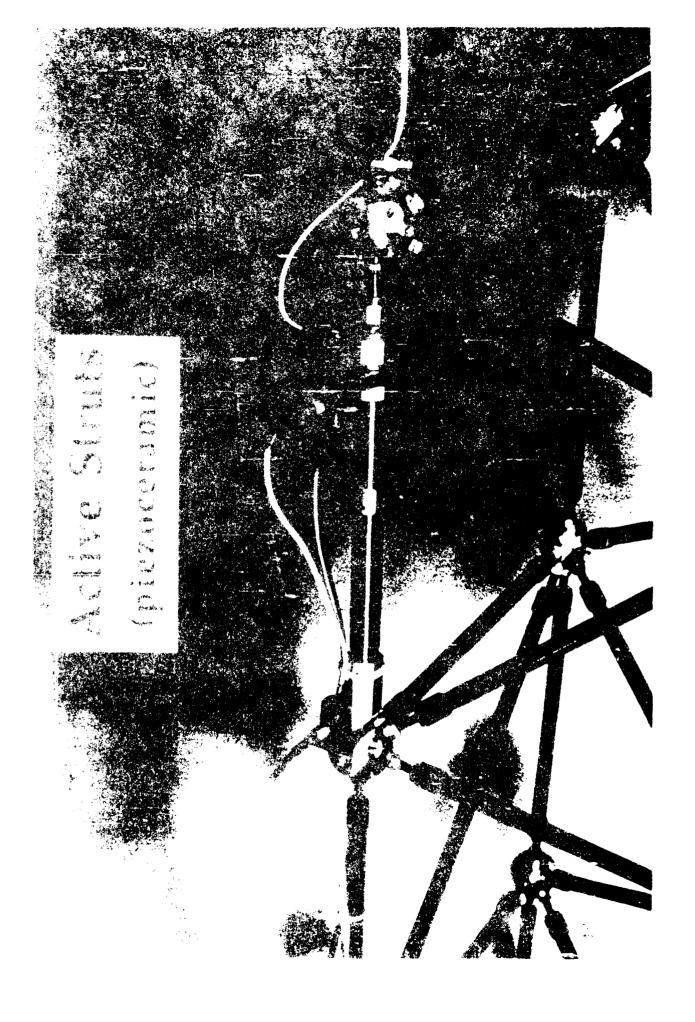
- stiffness of truss longerons and diagonals
- stiffness of active struts
- voltage/deflection plots of active struts
- viscoelastic strut characterization

The facility will be available in the future for characterization of other passive or active components.



Active Struts

There are currently three Physik Instrumente piezoceramic actuator struts available for electromechanical shunting or active control. The piezoceramic stack is preloaded and isolated from bending loads by a steel flexure. Each actuator includes an internal strain gage measurement. The actuator is placed in series with a load cell, and two accelerometers. The stiffness of the strut was chosen to nearly match the structural impedance. It has a free stroke of \pm 45 microns (\pm 30 in the truss) at a voltage of \pm 50 Volts with a 50 Volt bias. A fourth homemade strut is also available for disturbance generation, shunting, or control.



Active Mirror Mounts

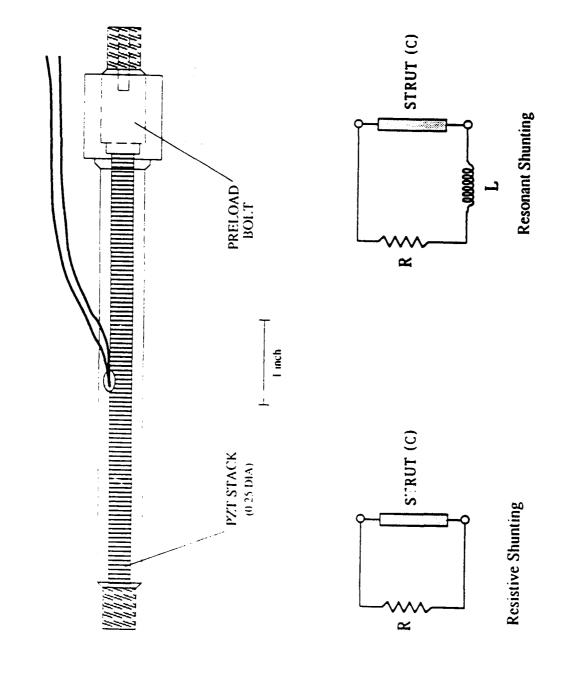
The active mirror mount (shown mounted to a rigid block in the figure) is a small stroke device intended to control only path length errors in the flexible truss. Active mirror mounts will be used to maintain to $\lambda/20$ the linear positions of the cat's eye retroreflectors, which are located at the three mock siderostat locations. Output position control will be achieved by moving the cat's eye and mounting table using three microactuators: 0.7" piezoelectric stacks for two of the active mirror mounts and 0.8" electrostrictive stacks for the third. The actuators will be run in common mode to actuate piston motion of the cat's eye. Lateral motion of the cat's eye will be induced by differential operation of the ceramic stacks. Simultaneous displacements of +/- 5 microns can be achieved in all three directions. The mirror mount design includes the flexibility to introduce additional mass to simulate the scaled mass of the reiroreflectors. Additionally, the mounts can later be modified to incorporate mass reactuation, where the the effect of moving the mass of the cat's eye is reduced or even cancelled. The result will be a reduction in the interaction between the mirror control system and the truss flexibility.



Passive Damping

- Underutilized to date in CSI studies and experiments
- Consider and incorporate passive damping to greatest extent possible
- system identification, robust control design, and in reducing controller less glamorous than active control, but it can only be beneficial for
- naked truss has < 0.1 % damping in most global modes
- damping options:
- constrained-layer viscoelastic struts
- shunted piezoelectric struts
- viscous dashpot
- proof mass
- problems:
- difficult to add significant damping due to large number of struts (700)
- viscoelastics are temperature and frequency dependent
- other options involve expensive hardware

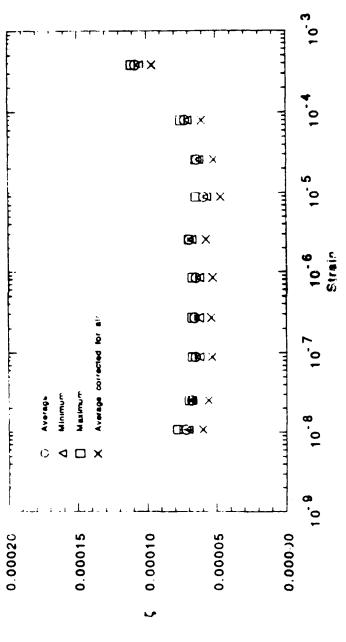
Shunted Piezoelectric Damping



Damping at Nanostrain Levels

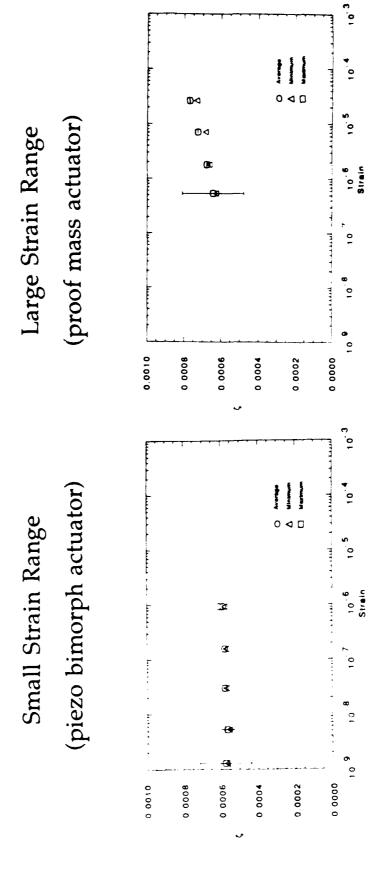
- Most structural dynamic tests conducted in 10 1000 microstrain range
- Approach:
- Test rectangular bar and cylindrical specimens of typical spacecraft materials to determine changes in material damping
- Graphite/Epoxy
- 6061-T6 aluminum tubes
- Acquire data directly on the Interferometer Testbed





Damping vs Strain in Interferometer Testbed

• mode in first clump of global modes (44.1 Hz)



Real-time Control Capability

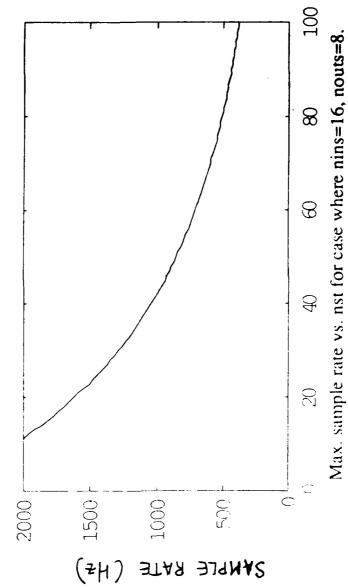
Real Time Control Hardware

- VME based digital control hardware
- 68030 processor
- CSPI vector processor
- Capability:
- 16 inputs
- 10 outputs
- 32 states at 1000 Hz; scales by (ns + ni) * (ns + no)
- Direct link to six HP laser measurement boards
- Control design in MATLAB on Sun SparcStation
- Analog: circuits for displacement and velocity feedback to active struts

Benchmark Results: (16 inputs, 8 outputs)

Min. Sample Time Formula:

dt(microsec) = 215 + 9*nins + 30*nouts + 0.15*nst(nst+nins+nouts)



Future Work

- Make six optics legs fully operational
- Experimentally identify dynamics after testbed reaches relatively stable state (after optics are fully integrated)
- Update finite element model
- Characterize uncertainty in plant dynamics
- Investigate structural tailoring and modification
- Explore and design additional passive damping devices
- Control loop input-output identification
- Control using passive and active isolation at siderostat locations, employing active mirror mounts
- Power flow control using local feedback around active struts
- Global shape control using active struts
- Investigate nonlinear thermal popping phenomenon

MODEL REFINEMENT / DAMAGE DETECTION USING MEASURED TEST DATA*

D.C. Zimmerman and M. Kaouk University of Florida Gainesville, Florida

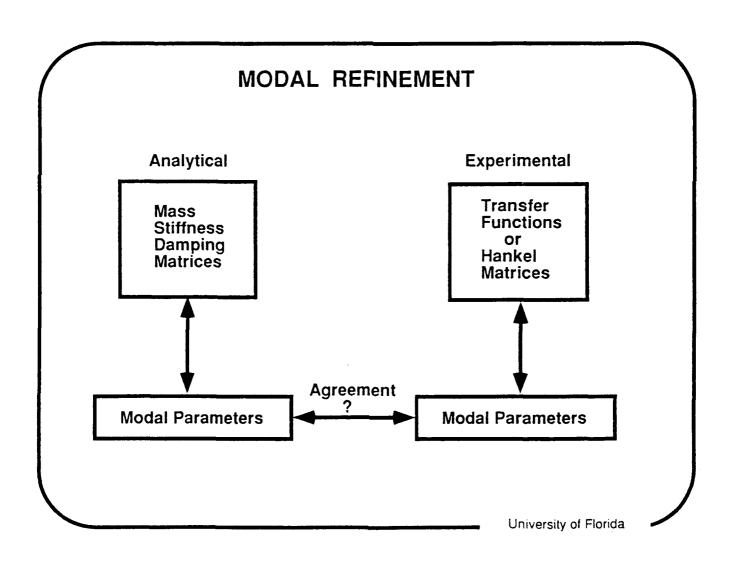
Fourth NASA/DOD CSI Technology Conference Orlando, Florida

5-7 November 1990

^{*}Sponsored by the Florida High Technology and Industry Council, Computer Integrated Engineering and Manufacturing Group

INTRODUCTION

The development of an analytical mathematical model for structural systems is one of the basic requirements of engineering analysis. It is widely accepted that these models must be experimentally "validated" before their acceptance as the basis for final design analysis. By properly comparing the Finite Element Model (FEM) predicted dynamic characteristics of the structure with direct measurements, errors in the original analytical model can be identified and corrected, so that the model is eventually capable of "predicting" the systems dynamic behavior accurately and reliably. Comparison of the dynamic system vibrational modal properties as obtained from Experimental Modal Analysis (EMA) to those predicted by the FEM is one such way to validate the analytical model. Unfortunately, in practice, the results of the comparison are often less than satisfactory, resulting in the need to modify or update the analytical model. This same modification technique can also be used to detect structural damage if the change in the model dynamic characteristic are due solely to damage, and not to errors in the original FEM.



SYMMETRIC EIGENSTRUCTURE ASSIGNMENT ALGORITHM

In the Symmetric Eigenstructure Assignment (SEA) algorithm [1], the mathematical framework of eigenstructure assignment typically used in designing control systems is adapted and extended to solve the model refinement/damage detection problem. The SEA method assumes a nonproportionally damped system, and shows considerable promise to deal with large order FEM's. In Ref. [2], it is proven that if a system described by the equations below is controllable and observable (which we can guarantee by proper selection of B₀, C₀ and C₁), then by proper selection of F, a maximum of (m,r) closed-loop eigenvalues and partial eigenvectors can be assigned with a minimum of (m,r) entries in each eigenvector being arbitrarily assigned where m and r are the row dimensions of u and y respectively (the number of pseudo actuators and sensors). The basis of the SEA algorithm is to design a "pseudo-controller" such that the closed-loop eigenvalues and eigenvectors match those determined experimentally. Manipulating the equations below, it is seen that the pseudo-controller adjusts both the damping and stiffness matrix.

MODEL REFINEMENT BASED ON CONTROL THEORY

o n-Dof Finite Element Model Mw + Dw + Kw = B₀u

Pseudo-Controller

- Pseudo-Sensor Measurements $y = C_0 w + C_1 \dot{w}$
- Pseudo-Controlleru = Fy
- Select B₀, C₀, C₁ and calculate F such that measured eigenstructure assigned to analytical model
 Mw + (D B₀FC₁)w + (K B₀FC₀)w = 0
- Occident of size of the finite element model)

EIGENVECTOR EXPANSION

Common to all model refinement algorithms, the dimension of the experimentally measured eigenvectors is usually much less than that of the FEM eigenvectors due to practical EMA testing limitations. One solution to this problem is to employ a model reduction technique such that the reduced dimension of the analytical model matches that of the experimentally measured eigenvector. The alternative approach, which is employed in this work, is to expand the measured eigenvector to the size of the analytical eigenvector. An examination of the eigenvalue problem reveals that the expanded eigenvector must lie in the space spanned by the columns of L_i , which depend both on the original FEM, the control influence matrix, and the measured eigenvalue.

EIGENVECTOR EXPANSION

- Dimension of measured eigenvector < Dimension of analytical eigenvector
- The ith experimental eigenvector to be assigned, V_{ie}, must lie in the subspace spanned by

$$L_i = (M\lambda_{ie}^2 + D\lambda_{ie} + K)^{-1}B_0$$

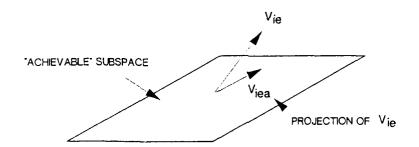
 λ_{ie} = experimental eigenvalue

LEAST SQUARES EXPANSION AND PROJECTION

Consider a fully expanded eigenvector, v_{ie} , that does not lie in the space spanned by the columns of L_i . Minimizing the 2-norm difference between v_{ie} and v_{rea} , the fully expanded and the fully expanded achievable eigenvector respectively. v_{rea} can be shown to be given as $v_{rea} = L_i(L_i^T L_i)^{-1} L_i^T v_{rea}$ [2]. If one proceeds in a similar manner and minimizes the 2-norm difference between only the experimentally measured components of v_{rea} and the corresponding components of v_{rea} , the resulting expanded and projected achievable eigenvector is given by $v_{rea} = L_i(\tilde{L}_i^T \tilde{L}_i)^{-1} \tilde{L}_i^T v_{rea}$, where v_{rea} is a vector containing only the measured components of the eigenvector. \tilde{L}_i are rows of L_i which correspond to the measured eigenvector components. With this method, each measured eigenvector must be expanded and projected individually. This requires the inversion of a nxn matrix, where n is the size of the FEM. For large order FEM's, this method may not be practical.

LEAST SQUARES SOLUTION

Projection and Expansion of V_{ie} into "achievable" subspace



- Comments
 - Expands and projects in single calculation
 - Works on single eigenvector
 - Calculation requires inversion of a nxn matrixundesirable

ORTHOGONAL PROCRUSTES EXPANSION

In the orthogonal procrustes problem, the possibility that the portion of the analytical modal matrix corresponding to the experimental measurement locations can be rotated into the experimental modal matrix is explored by solving the minimization problem described below. If they can be, a reasonable approximation to the unmeasured modal matrix components can be obtained by applying the same rotation matrix to the corresponding components of the analytical modal matrix. This expansion can be performed on all eigenvectors simultaneously. However, it is still necessary to perform a projection onto the achievable subspace L, for each eigenvector.

ORTHOGONAL PROCRUSTES SOLUTION

Expansion - minimize with respect to a rotation matrix

min V_{iem} - V_{iam}Q

where V_{iem} := Experimental eigenvector

V_{iam} := Corresponding analytical eigenvector component

Q := Rotation matrix

Unmeasured experimental components given by

 $V_{ieu} = V_{iau}Q$

where

V_{ieu} := Unmeasured experimental eigenvector components

V_{iau} := Corresponding analytical eigenvector components

Q := Rotation matrix

- Projection into achievable subspace as before
- Comments
 - Can work on multiple eigenvectors simultaneously
 - Requires nxn matrix inversion for projection operation
 - On test cases, appears to give closer expansions to experimental data

SELECTION OF B₀

The control influence matrix is a free variable. Three possibilities for its selection has been investigated. The first is that of viewing the elements of B_0 to be design variables. These design variables can then be adjusted using nonlinear programming to minimize an appropriate objective function. The objective function used to date is the Frobenius norm of the changes made to both the damping and stiffness matrix. This method is practical for small order FEM's. The second method is to select B_0 such that only the modes of vibration corresponding to measured modes is controllable. The method is practical because only the original analytical eigenvectors corresponding to the measured modes are required to determine B_0

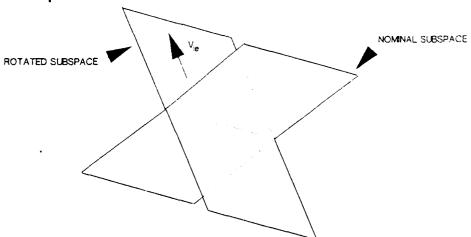
SELECTION OF CONTROL INFLUENCE MATRIX (B₀)

- Nonlinear Optimization
 - Minimize normed changes in damping and stiffness matrix with respect to elements of B₀
 - Disadvantage number of design variables proportional to size of FEM
- Modal Matrix Method
 - Choose B₀ such that analytical modes that correspond to unmeasured modes are nearly uncontrollable
 - Requires analytical eigenvectors corresponding to measured modes practical

SELECTION OF B₀ (cont'd)

The third algorithm tested is based on selecting B_0 such that the measured and expanded eigenvector lies in the achievable eigenvector subspace. In this method, the measured eigenvalues/vectors are assigned to the analytical model individually. Thus, each measured mode will have its own B_0 . Because the subspace can be rotated into the fully expanded eigenvector, there is no need for the projection operation. This eliminates the required inversion of the nxn matrix. Therefore, selecting B_0 in this manner in conjunction with the Orthogonal Procrustes expansion results in a computational procedure which is feasible for large order FEM's





- Select B_o such that expanded eigenvector lies in subspace
- <u>All</u> measured eigenvector components assigned independent of number of assigned eigenvalues
- In conjunction with OP expansion, <u>does not</u> depend on the size of FEM - Practical for large order FEM's

SYMMETRIC EIGENSTRUCTURE ASSIGNMENT

Arbitrary selections of the sensor influence matrices would result in adjusted damping and stiffness matrices which are no longer symmetric. It can be shown that a necessary condition on the C_i are that they satisfy a generalized algebraic Riccati equation. All real solutions to the Riccati equation are determined using Potters method [3,4]. From this set of solutions, different criteria can be used to select the optimal updated model.

SYMMETRIC EIGENSTRUCTURE ASSIGNMENT

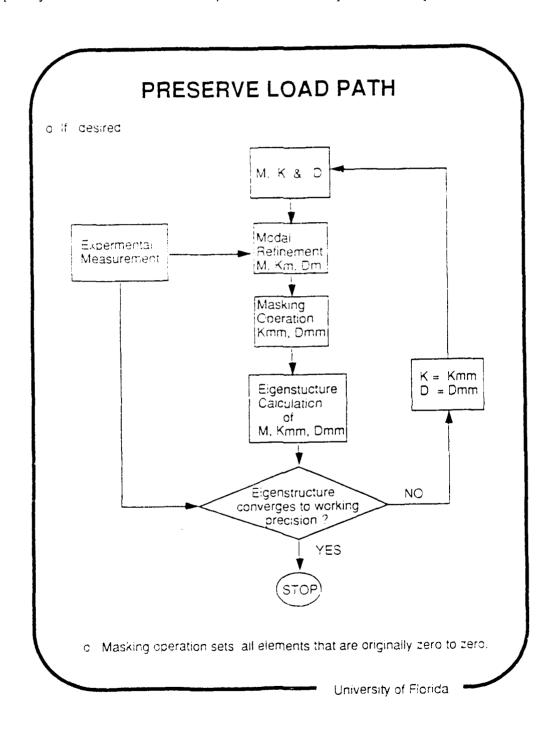
 Symmetry of adjusted stiffness and damping matrix places constraints on the output influence matrices C_i

$$C_i = G_i B_0^T$$
 $i = 0,1$
 $X = G_1^{-1} G_0$
 $A_1 X + X A_2 + X A_3 X + A_4 = 0$

- A_i dependent on measured eigenvalues/vectors and original analytical model
- Finite and countable number of real solutions X, each generating a different adjustment - selection based on a minimum model change criteria
- O Different criteria can be used to accomodate damage detection

LOAD PATH PRESERVATION

In some applications, it is required that the sparsity of the damping and/or stiffness matrix due to original load path be retained. The following iterative solution technique is one way in which to preserve the load path. At the model refinement stage (M,Km,Dm) the eigenstructure of the model and the experimental measurements match. When the terms in Km and Dm are set to zero to preserve load path (Kmm,Dmm), the eigenstructure of the model and experimental measurements no longer match. This mismatch can be viewed as a completely new model refinement problem and the procedure repeated.

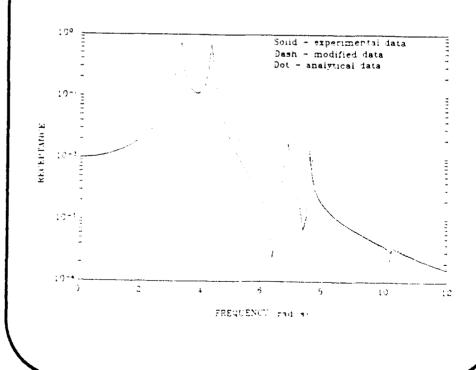


DAMAGE DETECTION

Consider a 5-dof of freedom structural model. The diagonal elements of the stiffness matrix are (100,120,200,94,124). Experimental damage is "simulated" by determining the "experimental" modal characteristic where the K(3,3) element has been changed from 200 to 70. This simulation of damage represents a case where a localized stiffness change has occurred due to damage. The receptance function below shows that the algorithm is able to detect both the location and extent of damage. In reviewing the modified model, the K(3,3) element has been determined to be 70.01

DAMAGE DETECTION

- 5-DOF model
- Damage simulated in single element (200 70)
- 1 mode, 4 eigenvector components



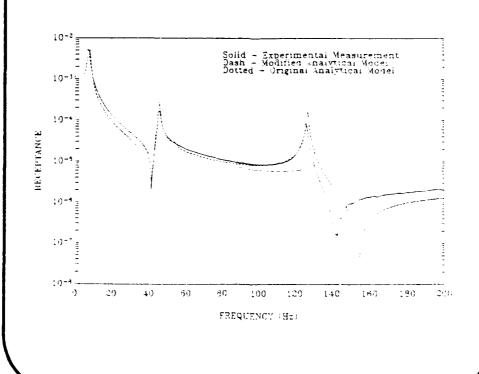
University of Flamaa

EXPERIMENTAL STUDY

The model refinement algorithm was applied to a simple cantilevered beam. The natural frequencies, damping ratios, and mode shapes of the first three bending modes were determined from a modal survey of the beam. Only the translational components of the eigenvectors were measured. A finite element model of the beam was constructed assuming a perfect cantilever condition at the beam root. Inspecting the receptance functions below, it is seen that the original analytical model is stiffer than the actual measurements. The model refinement algorithm was used to assign the first three bending mode modal characteristics. It is seen that the refined model more closely matches that obtained experimentally.

EXPERIMENTAL STUDY

- Cantilever beam
- First 3 bending modes measured (6 eigenvector components)



SUMMARY

A method has been developed to incorporate measured modal data into analytical FEM's such that the refined model more closely matches the experimental data. The method is founded on eigenstructure assignment theory. For large order FEM's, the pseudo-control influence matrix B_0 is chosen using an achievable eigenvector subspace rotation strategy. This greatly reduces the computational burden of measured eigenvector expansion and projection (projection is no longer required with subspace rotation). The pseudo-sensor influence matrices C_i are chosen to maintain system symmetry.

SUMMARY

- Model refinement approach from control theory perspective
- o Control influence matrix chosen to enhance eigenvector assignability
- Output influence matrices chosen to maintain system symmetry
- Intensive calculations (inverses, SVD,...) can be made <u>independent</u> of size of FEM (still have matrix multiplications)

REFERENCES

- Zimmerman, D.C. and Widengren, M., "Correcting Finite Element Models Using a Symmetric Eigenstructure Assignment Technique," <u>AIAA Journal</u>, Vol. 28, No. 9, 1990, pp. 1670-1676.
- [2] Srinathkumar, S., "Eigenvalue/Eigenvector Assignment Using Output Feedback," IEEE Transactions on Automatic Control, AC-23, 1 1978, pp. 79-81.
- [3] Potter, J.E., "Matrix Quadratic Solutions," <u>SIAM Journal of Applied Mathematics</u>, Vol. 14, No. 3, 1966, pp. 496-501.
- [4] Martensson, K., "On the Matrix Riccati Equation," <u>Information Sciences</u>, Vol. 3, 1971, pp. 17-49.

JPL CSI PHASE B TESTBED

M. O'Neal
J. Fanson
D. Eldred
Jet Propulsion Laboratory

JPL CSI PHASE B TESTBED

the Phase B Testbed. This testbed is being employed to investigate nanometer level optical pathlength control on a The Jet Propulsion Laboratory is developing an evolutionary chain of ground test facilities to develop and The most recent addition to the family flexible structure, simultaneous control and structure optimization, active structures, and disturbance isolation. validate several key emerging control/structure interaction technologies.

located anywhere on the structure. In addition, proof mass actuators and disturbance sources (with isolation stages) can be attached at any location. In the present configuration, there are four modes under 20 Hz, eight under 100 Hz, replaced with an active member or damper, and the modular nature of the design ensures versatility and expandability. Sensors, including accelerometers, proximity devices, and strain gages can be easily incorporated and Each strut can be easily removed and the frequencies can be modified as desired by adding mass to various locations. The structure is configured to resemble part of a stellar interferometer.

This system is a stellar The optical assembly consists of a cat's eye can be added to couple more structural motions into pathlength and wavefront tilt errors. The moving portion of this a wide retroreflector mounted on a voice coil actuator with its secondary mirror mounted on a two stage piezoelectric actuator. A laser interferometer is used to measure the pathlength through the optical train to a resolution of 2.5 system weighs approximately half of what the rest of the structure weighs, so significant interactions are assured. The challenge is to lock on to an interference fringe and maintain the desired pathlength in the face of a wide variety of disturbances. The challenge will be met by combining state of the art control of the optical elements, The fundamental structural mode (at 4 Hz) couples directly into pathlength changes. control of the structure itself (including vibration suppression), and disturbance isolation. The optical motion compensation system is attached to the end of one arm. interferometer delay line developed for an existing instrument.

Of key importance to controller performance is the accuracy of the control design dynamic Experimental model verification and direct transfer function determination are being employed at each step experiment to maintain a valid model.

and optimization approaches to develop the technology to enable the future generation of large space and lunar based missions. The JPL CSI Phase B Testbed mission is to explore several control

| ontact: | Mike O'Neal | (818) | (818) 354-2875 |
|---------|-------------|-------|----------------|
| | Jim Fanson | (818) | (818) 354-7014 |
| | Dan Eldred | (818) | (818) 354-6519 |

TESTBED CSI PHASE

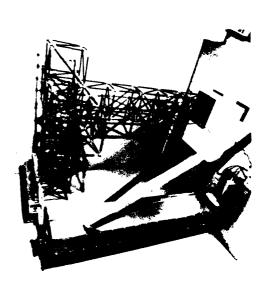


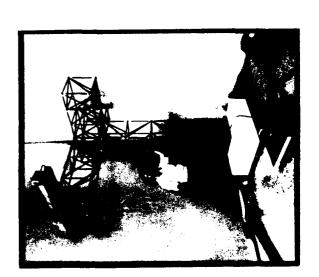












FAILURE DETECTION, IDENTIFICATION, AND CONTROL SYSTEM RECONFIGURATION (FDI&R) USING THE SEQUENTIAL PROBABILITY RATIO TEST (SPRT)

J. Shenhar and R.C. Montgomery NASA Langley Research Center Hampton, Virginia

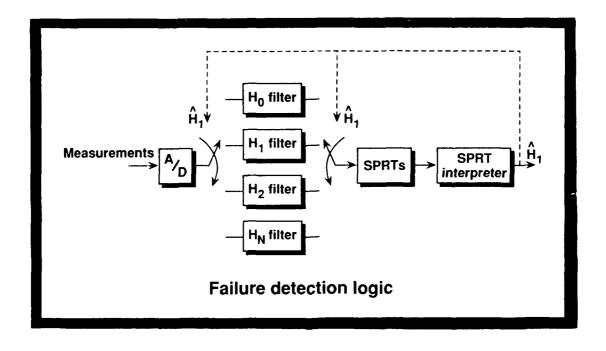
POSTER HIGHLIGHTS

Long life requirements, large numbers of sensors and actuators, and heavy dependence on the proper operation of the control system dictate that the control system for large flexible spacecraft must operate acceptably in the presence of component failures. The option of hardware duplication may not be feasible when large numbers of physically distributed components are attached to a lightweight, highly flexible spacecraft. Hence, sensors which measure dynamically different quantities and actuators which have different effects on the system need to be manuged using analytic models. The objective of this research is to develop analytic redundancy management concepts that would be incorporated in control procedures of large flexible spacecraft. effectively incorporate reliability into the design of spacecraft control systems, both the preliminary design and the on-orbit operation of the system must be considered. Preliminary design studies must be made on the effects of component placement on the probability of mission success. Also, since hardware duplication may not be viable, on-line automatic FDI&R algorithms based on analytical models need to be developed. For the application of the method at hand, the residual sequence of a single operating Kalman filter is used to detect and identify failures via the SPRT algorithm. After a failure has been identified, a Kalman filter previously designed for the remaining sensor set is used. The residual sequence of this filter is then processed to identify any further failures. The technique is suboptimal since only the residual from one Kalman filter is used and failure hypotheses are tested sequentially. Also, herein, only bias type sensor failures are considered. The technique is amenable, however, to handling any sensor failure that has a recognizable effect on the innovations (or estimated residuals) of the Kalman filter. The success of the method is conditioned on whether the deviation from the theoretical zero-mean character of the innovations sequence can be relied upon as an indicator of a component failure. The Spacecraft COntrol Laboratory Experiment (SCOLE) research facility will be used to evaluate the FDI&R concept in a real-time test. SCOLE is an experimental facility which was designed for research in the control of large, flexible structures. The experimental apparatus is a functional model of the Space Shuttle with a large, flexible, offset-feed antenna attached. SCOLE test results may be extrapolated to the on-orbit operational system.

FAILURE DETECTION LOGIC

Sensor measurements are sampled at uniform intervals and processed by one of the Kalman filters selected by the failure state estimate ${\rm H}_{\rm i}$.

The filters are designed for each anticipated failure condition. This enables the scheme to handle multiple simultaneous failures. The decision as to whether or not a failure has occurred is made by processing each scalar element of the innovations of the selected filter using the SPRT algorithm. Since failure of a single sensor affects more than one sensor innovations sequence, an interpreter is required to examine the innovations of the operating filter for the appropriate failure signature.



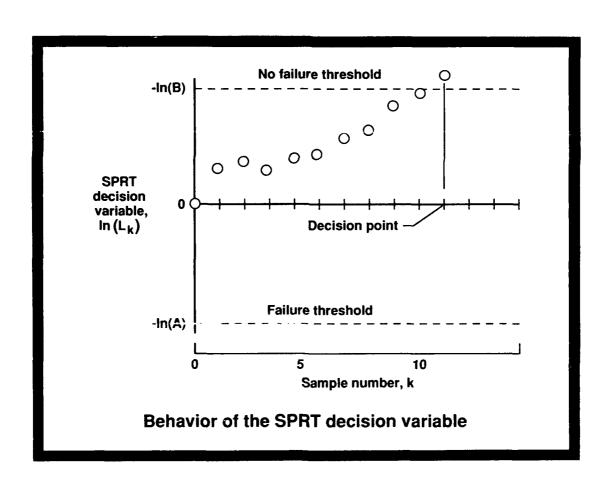
BEHAVIOR OF THE SPRT DECISION VARIABLE

Sequential testing of a sample was developed as a means to economize the number of observations required in a test procedure. The SPRT algorithm decides in favor of one hypothesis, H_0 , over another , H_1 , by

sequentially calculating the ratio of the probability of the input data sequence assuming one hypothesis to that of assuming the other. As sample data are taken, the magnitude of the SPRT decision variable is checked. If it is less than a predetermined threshold B, a decision is made in favor of the no failure hypothesis ${\tt H}_{0}$ and the test is

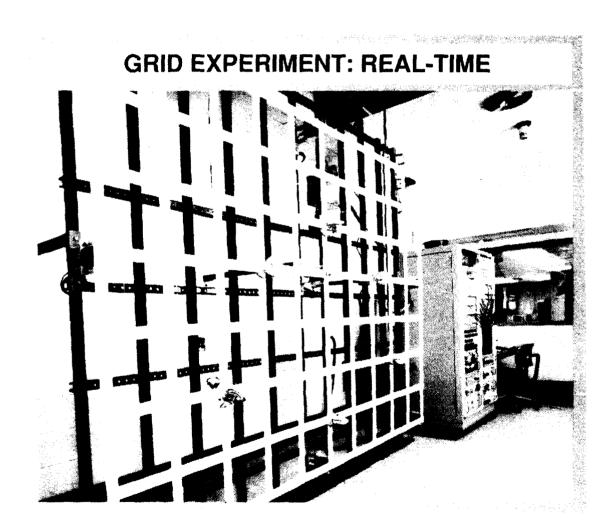
terminated. If it is greater than a threshold A, the decision is made in favor of the failure hypothesis ${\rm H}_{_1}$ and, again, the test is

terminated. No decision can be made as long as the SPRT variable is between A and B. In such a case more data are required to make a decision and the test continues. The thresholds A and B are selected by the designer and reflect his concern over the risk involved of missing a failure and the nuisance created by sounding a false alarm.



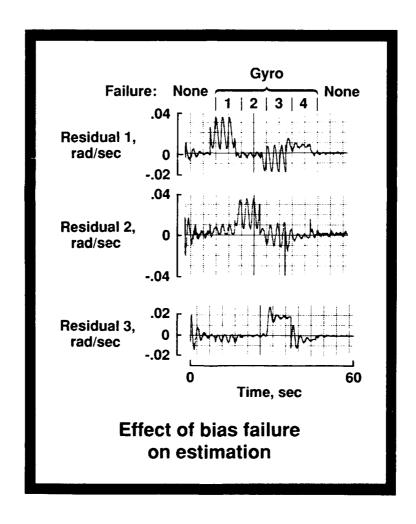
GRID EXPERIMENT

The grid apparatus has appreciable low frequency structural dynamics, inertial sensors and actuators, and microprocessor-based distributed computing components. The test article is a lattice of thin, flat, aluminum bars which are riveted and bonded at each intersection to form a planar structure with an overall dimension of 7x10 feet. It is suspended from a top bar by two cables. Twenty closely spaced modes of motion are below 10 Hz. The sensors and actuators are interfaced to an M68000-based microcomputer for implementation of control system algorithms.



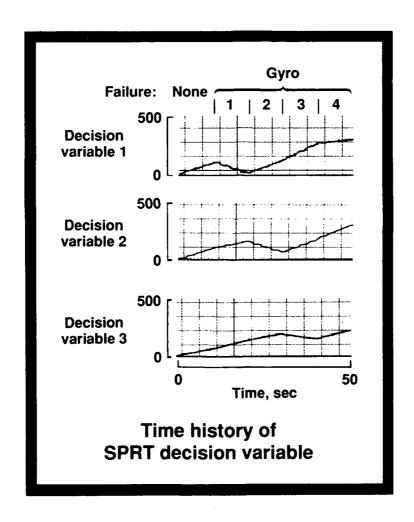
EFFECT OF A BIAS FAILURE ON ESTIMATION

The effect of sensor non-zero constant output failure of .01 rad/sec on the Kalman filter residuals is shown. It is noted that the failure of the third component results in a high-variance, low-mean error in the residual of the third estimate. This result is caused by the Kalman filter attempting to filter out the zero frequency signal since it is not included in the filter model.



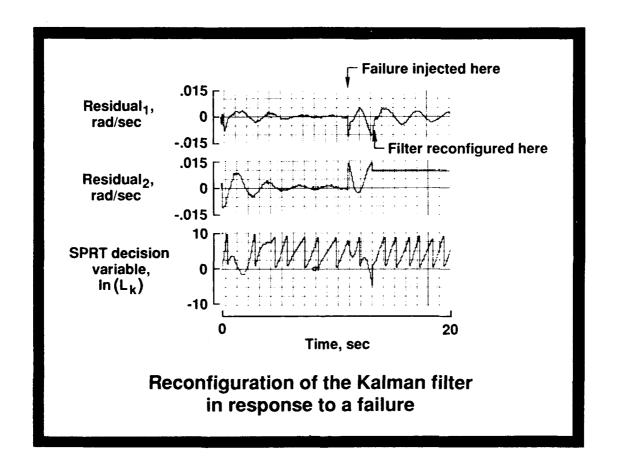
TIME HISTORY OF SPRT DECISION VARIABLE

The behavior of the SPRT decision variable for each residual sequence is shown. The individual sensors are failed one at a-time, with a .01 rad/sec constant signal. The decision variable is calculated continuously from time zero. Note that although the slope of the decision variable signal changes for all residuals for each failure of the first three sensors, only the one for the currently failed sensor tends towards the failure bound.



RECONFIGURATION OF THE KALMAN FILTER IN RESPONSE TO A FAILURE

Reconfiguration of the filter to accommodate failure of the second sensor is shown. The filter design is always based on the hypothesis of the most recent decision. Because failure of a sensor is uniquely reflected in the decision variable associated with that sensor, detection and identification may be accomplished simultaneously based on the outcome of a single decision variable.



SCOLE EXPERIMENT

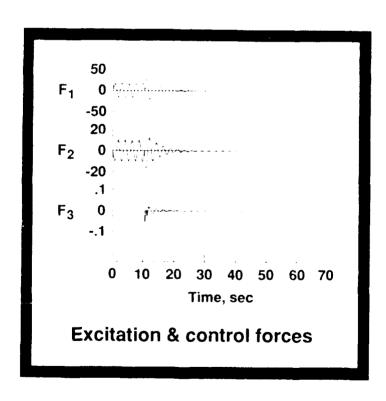
The SCOLE hardware shown in the figure, consists of three major elements: a platform representing the Space Shuttle; a planar, hexagonal, tubular structure representing an antenna reflector; and, a single tubular flexible mast connecting the antenna to the platform. The entire structure is suspended from a crane with an 11-foot long cable attached near the global system centroid via a low-friction universal joint that provides roll and pitch degrees of freedom. The system actuators consist of three torque wheels that produce torque in three mutually orthogonal directions. The sensors used herein are a three-axis rate sensor located at the tip of the mast and two accelerometers located at the center of the reflector. Experiments are run on SCOLE using a control computer that has analog-to-digital converters used to input the sensor data, digital-to-analog converters used to output command to the reaction wheels, and a process timer used to achieve precise timing of the data sampling process.

SCOLE EXPERIMENT: SIMULATION



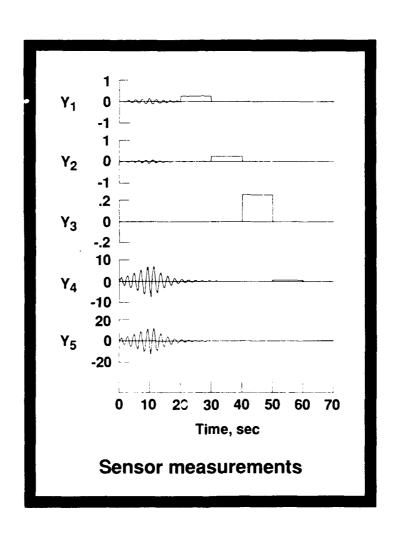
EXCITATION AND CONTROL FORCES

The figure illustrates the three actuator forces for the simulation. The section between 0 and 10 seconds displays the excitation segment while the section from 10 seconds and above introduces the associated control forces.



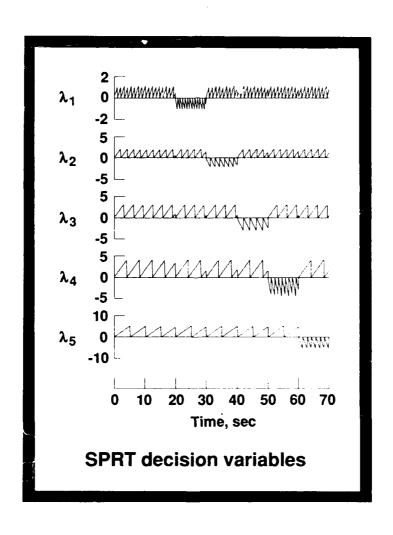
SENSOR MEASUREMENTS

The figure illustrates the five sensor measurements for the simulation. In the first three plots, Y_1 , Y_2 , and Y_3 , are the tip-of-the-mast three-axis rate sensor outputs, and the last two, Y_4 , and Y_5 , are the reflector accelerometer measurements. The square wave sections appearing in the figure represent bias signals imposed on the system to demonstrate sensor failures.



SPRT DECISION VARIABLES

The figure illustrates the five decision variables for the simulation. In the first three plots, λ_1 , λ_2 , and λ_3 , are the three-axis rate sensor decision variables, and the last two, λ_4 , and λ_5 , represent the reflector accelerometers decision variables. One at a-time, a failure was injected to a sensor and the associated decision variable responded accordingly. Sensor 1 failed between 20 - 30 seconds, sensor 2 between 30 - 40, sensor 3 between 40 -50, sensor 4 between 50 - 60, and sensor 5 between 60 - 70 seconds, as shown.



SUMMARY

A methodology that allows on-line failure detection, identification and reconfiguration using Kalman filter based approach has been presented. This FDI&R system involves sequential testing of the residuals of the single, active, Kalman filter using SPRT. Failure is isolated by examining the residuals for a pattern corresponding to the failure case involved. Individual failures obviously affect all innovations, but the nature of the filter and SPRT decision process allows trivial detection of the failure. The success of the method is conditioned on whether the deviation from the theoretical zero-mean character of the innovations sequence can be relied upon as an indicator of a component failure.

RELATED LITERATURE

- Montgomery, R. C. and Shenhar, J.: Analytic Redundancy Management for Systems with Appreciable Structural Dynamics. Proceedings of the IFAC/AIPAC'89 Symposium on Advanced Information Processing in Automatic Control, Nancy, FRANCE, July, 3-5, 1989, Vol. 2, pp. 1-6.
- Montgomery, R. C.: Management of Redundancy in Flight Control Systems Using Optimal Decision Theory. Chapter in AGARDograph No. 251, Theory and Applications of Optimal Control in Aerospace Systems, Ir. Pieter Kant, Editor, pp. 11-1 through 11-12, July 1981.
- Willsky, A. S.: A Survey of Design Methods for Failure Detection in Dynamic Systems. Automatica, Vol. 12, pp. 601-611, Pergamon Press, Great Britain, 1976.
- Montgomery, R. C. and Williams, J. P.: Testing of A Failure Accommodation System on A Highly Flexible Grid. Proceedings of the 1985 American Control Conference, Boston, MA, June 19-21, 1985, pp. 984-989.
- Williams, J. P. and Montgomery, R. C.: Failure Detection and Accommodation in Structural Dynamics Systems Using Analytic Redundancy. 24th IEEE Conference on Decision and Control, Fort Lauderdale, FL, December 11-13, 1985.
- Wald, Abraham: Sequential Analysis. J. Wiley & Sons, New York, 1947.
- Deckert, J. C., Desai, M. N.,., Deyst, J. J. and Willsky, A. S.: Reliable Dual-Redundant Sensor Failure Detection and Identification for the NASA F-8 DFBW Aircraft. Report No. R-1077, The Charles Stark Draper Laboratory, Inc., Cambridge, Massachusetts, May, 1977.
- Williams, J.P. and Rallo, R. A.: Description of the Spacecraft Control Laboratory Experiment (SCOLE) Facility. NASA TM-89057, January, 1987.

Robust LQG/LTR Control Design Synthesis of Discrete-Time Systems With Large Space Structural Control Application⁺

Peter M. Bainum⁺⁺ Xing Guangqian^{*} Aprille J. Ericsson^{**}

Department of Mechanical Engineering School of Engineering Howard University Washington D.C. 20059

Offered for Presentation at the Annual NASA/DOD CSI Conference Orlando, Florida, Nov. 5-7, 1990

⁺ Supported by AFSC / WRDC contract F 33615-89c-3225, Mr. Duane E. Veley, Project Engineer

Distinguished Professor of Aerospace Engineering, Associate Fellow AIAA: Fellow, AAS

^{*} Senior Research Associate

^{**} Graduate Research Assistant

Robust LQG/LTR Control Design Synthesis of Discrete-Time Systems With Large Space Structural Control Application

Peter M. Bainum, Xing Guangqian, and Aprille J. Ericsson Department of Mechanical Engineering, Howard University

Purpose

To develop analysis and design methods for robust control of large space structural sampled data stochastic systems with a specific application to the orbiting flexible shallow spherical shell system.

Focus

- * Extend the conditions of stability robustness for multivariable systems from continus-time systems to discrete-time systems;
- * Extend the LQG / LTR method(linear quadratic Gaussian synthesis loop transfer recovery) from continous-time systems to discrete-time systems;
- * Study the relationships between transient responses, robustness parameter, sensitivity parameter, and eigenvalues of the full order LQG controller and estimators during the process of robustness and sensitivity recovery;
- * Simulate full order and various reduced order LQG controllers, study the robustness of various reduced order LQG controllers for shallow spherical shell systems in the presence of unmodeled dynamics and parameter variations.

Methodology

- * The concept of the mathematically equivalent continous—time system for the discrete—time system is presented. It is proved that the relationship between the input and output is the same for both the equivalent continous—time systems and discrete—time systems. It is used for the extension of theoretical results from continous—time systems to discrete—time systems.
- * The theory of multi-input / multi-output transfer function matrix in the Z transformation space will be used for the analysis and design of multivariable discrete-time feedback control systems in the frequency domain.
- * The LQG / LTR method for continous-time will be extended to discrete-time systems, the H²-optimization theory and robustness / sensitivity recovery properties of the LQG problem will be used for studying the robust control of large space structures subject to sampled data inputs.

Introduction

1 Review of Past Works

- (1) H.Kwakernaak: "Optimal Low-sensitivity Linear Feedback Systems" Automatica, vol5, pp279-285, Pergamon Press, 1969.
- (2) J.C. Doyle and G. Stein: "Multivariable Feedback Design: Concepts for a Classical/Modern Synthesis" IEEE Trans. on AC,vol. AC-26 No.1.Feb. 1981.
- (3) G. Stein and M. Thans; "The LQG/LTR Procedure for Multivariable Feedback Control Design", IEEE Trans. vol. AC-32,No.2,Feb.. 1987.
- (4) Xing Guangqian and Peter M. Bainum: "The Optimal LQG Digital Control of Orbiting Large Flexible Beams", Journal of The Astronautical Sciences, vol. 37, No.1, 1989.
- (5) Xing Guangqian and Peter M.Bainum: "The Optimal LQG Digital Shape and Orientation Control of an Orbiting Shallow Spherical Shell System", 40th Congress of the International Astronautical Federation, Oct. 7-12, 1989. Also to appear in Acta Astronautica 1990.
- (6) Tan Zhaozhi and Peter M. Bainum: "The Optimal LQG Digital Control of an Orbiting Large Flexible Platform", The International Conference on Dynamics, Vibration and Control, Beijing, China, July, 1990.
- (7) Aprille J. Ericssion, Peter M. Bainum, and Xing Guangqian: "The Optimal LQR Digital Control of a Free-Free Orbiting Platform" 41st Congress of the International Astronautical Federation, Oct. 6-12, 1990/Dresden, GDR.

2 The Statement of LQG/LTR for Discrete-Time Systems

Given

State Eq.
$$X(k+1) = A X(k) + B U(k) + L \xi(k)$$
 (1)

Measurement Eq.

$$Y(k) = C X(k) + \mu I \eta(\kappa)$$
(2)

Control Output

$$Y_c(k) = H X(k)$$
 (3)

Assume

$$E\{\xi(\kappa)\xi(\kappa)^T\} = I$$
 $E\{\eta(\kappa)\eta(\kappa)^T\} = I$

Then

$$\mathsf{E}\big\{\big(\mu\mathsf{I}\eta(\kappa)\big)(\mu\mathsf{I}\eta(\kappa)\big)^{\mathsf{T}}\big\} \,=\, \mu^2\;\mathsf{I}\;\;,\quad \mathsf{E}\big\{\big(L\xi(\kappa)\big)\big(L\xi(\kappa)\big)^{\mathsf{T}}\big\} \,=\, \mathsf{L}\mathsf{L}^{\mathsf{T}}$$

Where

- L Noise input matrix
- μ Parameter of measurement noise
- H Control output matrix
- ρ Parameter of control weighting matrix

Find a controller depending only on Y(k),U(k) (k=0,1,2,3,...), to minimize

$$J = E \Sigma \left(Y_c^T(k) Y_c(k) + \rho^2 U(k)^T U(k) \right) \tag{4}$$

It is well known that if the system (A B H) is controllable and observable; the system (A L C) is controllable and observable. (The conditions may be reduced to stabilizable and detectable for the time-invariant system), then the closed-loop system of the LQG optimal regulator is asymptotically stable.

Control Law

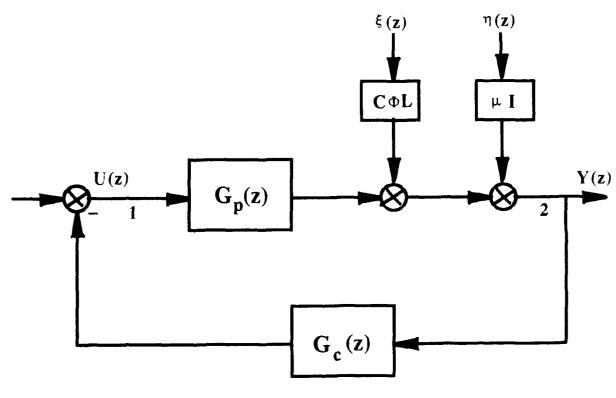
$$U(k) = - K_c \hat{X}(k/k-1)$$
 (5)

$$\hat{X}(k+1/k) = (A - K_f C - BK_c) \hat{X}(k/k-1) + K_f Y(k)$$
 (6)

where

Kalman filter gain $K_f = AK$ $K=P_eC^T(CP_eC^T + \mu^2 I)^{-1}$ $P_e = AP_eA^T - AP_eC^T(\mu^2I + CP_eC^T)^{-1}CP_eA^T + LL^T$ $K_c = (\rho^2 I + B^T P B)^{-1} B^T P A$ Regulator gain $P = A^T P A - (A^T P B)(\rho^2 I + B^T P A)^{-1} B^T P A + H^T H$

(1) (2) (5) (6) may be written in terms of the Z transformation, the diagram of the input and output is as follows;



$$G_p(z) = C(zI-A)^{-1}B$$

$$\Phi = (zI - A)^{-1}$$

$$G_c(z) = K_c(zI - A_c)^{-1}K_f$$
 $A_c = (A - BK_c - K_fC)$

$$A_c = (A - BK_c - K_fC)$$

3 Robustness Recovery and Sensitivity Recovery

 T_1 : The transfer matrix of the input loop-breaking point T_2 : The transfer matrix of the output loop-breaking point

$$I_1(z) = G_c(z)G_p(z)$$

$$T_2(z) = G_p(z)G_c(z)$$

 $K_{c}(zI-A)^{-1}B$: LQR loop transfer function

 $C(zI-A)^{-1}K_{f}$: Kalman filter loop transfer function

 $X \in \mathbb{R}^n \cdot U \in \mathbb{R}^m \cdot Y \in \mathbb{R}^r$

The following facts have been proven to be also true for the discrete-time system.

| Robustness Recovery | Sensitivity Recovery | |
|--|---|--|
| Let L=B r ≥ m | Let H=C r≤m | |
| Suppose $C(zI-A)^{-1}L$ is min. phase When $\mu - 0$ | Suppose $H(zI-A)^{-1}B$: is min. phase When $\rho - 0$ | |
| Then $T_1(z) \longrightarrow K_c(zI-A)^{-1}B$ | Then $T_2(z) \longrightarrow C(zI-A)^{-1}K_f$ | |
| Relationship between LQ regulator parameters and sensitivity weighting | Relationship between Kalman filter parameters and sensitivity weighting | |
| $H(zI-A)^{-1}B / \rho = W(z)$ | $C(zI-A)^{-1}L / \mu = W(z)$ | |
| A B H ρ : LQ-regulator parameters $W(z)$: Sensitivity weighting | A L C μ : Kalman filetr parameters $W(z)$: Sensitivity weighting | |

L Noise input matrix

Free Parameters: μ Parameter of measurement noise

H Control output matrix

p Parameter of control weighting matrix

Robustness Recovery

As we know, there are very nice properties (performance and robustness) for LQ-regulators and Kalman filters. Therefore the steps of design are as follows:

- (a) Design an LQ-regulator with desirable sensitivity, complementary sensitivity and loop transfer function by means of adjusting the parameters: H, ρ . The proper reduction of ρ (or proper increase of H) may improve the performance of the controller;
- (b) Let L=B, design a sequence of K-filters for $\mu \longrightarrow 0$, to approximate the function in step(a), to whatever accuracy is needed.

Sensitivity Recovery

The sensitivity recovery is dual with robustness recovery. We also use similar steps to design a compensator:

- (a) Design a K-filter with desirable sensitivity, complementary sensitivity and loop transfer function by means of adjusting the parameters: L, μ , The proper reduction of μ (or proper increase of L) may improve the performance of the control system.
- (b) L=B, design a sequence of LQ-regulator for $\rho \rightarrow 0$, to approximate the function in step(a) to whatever accuracy is needed.

When L=B, H=C the robustness / sensitivity of the control system only depends on two parameters: ρ (sensitivity parameter) and μ (robustness parameter).

4 The Effect of Varying the Free Parameters on the Transient Response of the Shallow Spherical Shell System with LQG Controller

(1) Simulation parameters of LQG robust control for orbiting shallow spherical shell system

The plant of the orbiting shallow shell: 26-dim (3 rigid+3A+1M+6C)

Controllers may be divided into 4 cases:

Case 1: 18-dim. controller (3 rigid+2A+1M+3C)

Case 2; 12-dim. controller (3 rigid+1A+1M+1C)

Case 3: 8-dim. controller (3 rigid+1M)

Case 4: 6-dim. controller (3 rigid)

Simulation noise of system: $\sigma_s = 10^{-3}$

Simulation noise of observation: $\sigma_0 = 10^{-2}$

Sampling time: 5 second

12 actuators (see Fig. 1 for locations and thrust directions)

Initial conditions:

$$\psi(0) = \phi(0) = \theta(0) = 0.2$$
 rad.

$$\dot{\psi}(0) = \dot{\phi}(0) = \dot{\theta}(0) = 0.02$$
 rad./sec

$$q_1(0)=q_2(0)=q_3(0)=q_4(0)=q_5(0)=q_6(0)=5$$
 meter

$$\dot{q}_1(0) = \dot{q}_2(0) = \dot{q}_3(0) = \dot{q}_4(0) = \dot{q}_5(0) = \dot{q}_6(0) = 0$$

A--axisymmetric M--meridional C--combined

(2) Modulus of Eigenvalues for Controller and Observer

| ρ^2 / μ^2 | Min. Modulus | | Max. Modulus | |
|--------------------|--------------|----------|--------------|----------|
| | Controller | Observer | Controller | Observer |
| 104 | 0.99042 | 0.99030 | 0.99999 | 0.99999 |
| 10^{3} | 0.99042 | 0.99033 | 0.99999 | 0.99999 |
| 10^{2} | 0.99038 | 0.99029 | 0.99996 | 0.99999 |
| 10 | 0.99004 | 0.98994 | 0.99991 | 0.99997 |
| 1 | 0.98805 | 0.98791 | 0.99973 | 0.99990 |
| 10^{-1} | 0.98165 | 0.98124 | 0.99929 | 0.99973 |
| 10^{-2} | 0.96773 | 0.96662 | 0.99831 | 0.99925 |
| 10^{-3} | 0.94354 | 0.94005 | 0.99623 | 0.99878 |
| 10^{-4} | 0.80428 | 0.87910 | 0.99523 | 0.98827 |
| 10^{-5} | 0.53367 | 0.58624 | 0.99641 | 0.99775 |
| 10^{-6} | 0.26839 | 0.01346 | 0.99860 | 0.99942 |

ρ – Sensitivity parameter , μ – Robustness parameter

From examination of the minimum moduli of the controller and observer and the condition that the min. modulus of observer must be less than the min. modulus of the controller, to provide a timely state estimate, we can construct Fig.2 to show the region of acceptable combinations of parameters ρ and μ . The points to the right of the curve are the points of acceptable combination for parameters (ρ,μ). The acceptable combination of (ρ , μ) means that the min. modulus of controller and observer satisfy the above constraint condition.

(3) Effect of ρ and μ on the Original (Full Order) System

```
Fig. 3a, Fig. 3b (\rho=100, \mu=1, full order) Point 1 on Fig. 2
Fig. 4a, Fig. 4b (\rho=100, \mu=0.1, full order) Point 2 on Fig. 2
Fig. 5a, Fig. 5b (\rho=1, \mu=1, full order) Point 3 on Fig. 2
Fig. 6a, Fig. 6b (\rho=1, \mu=0.1, full order) Point 4 on Fig. 2
Fig. 7a, Fig. 7b (\rho=0.01, \mu=0.1, full order) Point 6 on Fig. 2
```

Conclusions:

- * As $\rho \downarrow$ then the sensitivity weighting W \uparrow , performance gets better:
- * The reduction of ρ will be constrained by the condition: Min. modulus of estimator eigenvalues \leq that of controller
- (4) Effect of Different Combinations of ρ and μ on the Reduced Order Controller System

Fig. 8a, Fig. 8b ($\rho=100$, $\mu=0.1$, 12-dim.) Point 2 on Fig. 2 Fig. 9a, Fig. 9b ($\rho=1$, $\mu=0.1$, 12-dim.) Point 4 on Fig. 2 Fig. 10a, Fig. 10b ($\rho=0.01$, $\mu=0.1$,12-dim) Point 6 on Fig. 2

The conclusions are the same as for the above full order controller.

(5) Effect of the Size of the Reduced Order Controller for the Same Combination of ρ and μ on the Transient Response

```
Fig. 11a, Fig. 11b (\rho=1, \mu=1, 12-dim) Point 3 on Fig. 2
Fig. 12a, Fig. 12b (\rho=1, \mu=1, 8-dim) Point 3 on Fig. 2
Fig. 13a, Fig. 13b (\rho=1, \mu=1, 6-dim) Point 3 on Fig. 2
```

Conclusions:

- * The robustness of the 12-dim. reduced order controller is enough for unmodeled dynamics of shallow shell system;
- * The 6-dim and 8-dim reduced order controller can not be used for the optimal control of shallow shell system;
- * The controller based only on the rigid model will result in severe divergence for shallow shell system.
- (6) Effect of μ for a Fixed ρ on 12-dim Reduced Order Controller (robustness recovery)

```
Fig. 14a, Fig. 14b ( \rho=1, \mu=1 18-dim) Point 3 on Fig. 2
Fig. 15a, Fig. 15b ( \rho=1, \mu=0.1 18-dim) Point 4 on Fig. 2
Fig. 16a, Fig. 16b ( \rho=1, \mu=0.001 18-dim) Point 5 on Fig. 2
```

Conclusions:

- * After the parameters of controller have been selected, the robustness of system will be increased with the reduction of parameter μ :
- * When the reduction of μ is too much, the performance of system will be degraded.

5 Conclusions

- * The robustness recovery / sensitivity recovery properties have been proven to be also true for discrete-time systems;
- * The properties of robustness recovery(sensitivity recovery) may be used for the design of LQG robust controller for discrete—time systems. If let L=B,H=C, the robustness and performance of control system only depend on two parameters, ρ (sensitivity), and μ (robustness). The reduction of μ as $\mu \to 0$ (or of ρ , as $\rho \to 0$) must be constrained by the following relationship:

Min. modulus of eigenvalues for Observer ✓ Min. modulus of eigenvalues of controller

Otherwise, the closed loop responses will be characterized by divergence;.

* Simulations have certified the 12-dim reduced order controller will be enough for optimal LQG control of shallow spherical shell system in the presence of unmodeled dynamics. The performance of 8-dim reduced order LQG controller for shallow shell is unacceptable.

The 6-dim reduced order controller(only rigid modes) for shallow shell will result in the severe divergence of transient responses.

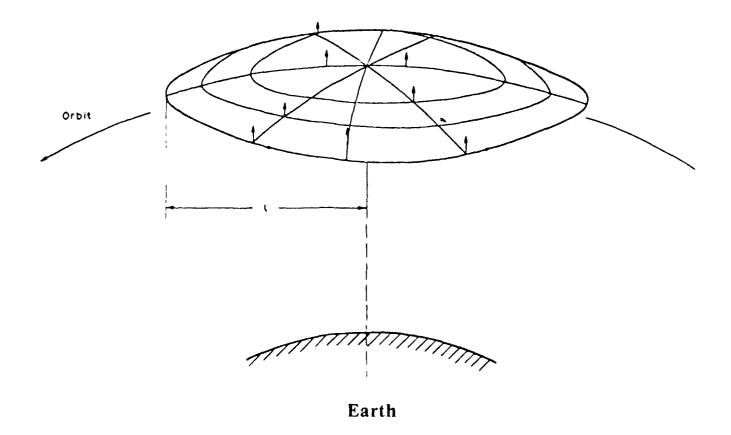


Fig. 1 Orbiting Shallow Spherical Shell System

Physical and Geometrical Parameters of Shallow Spherical Shell:

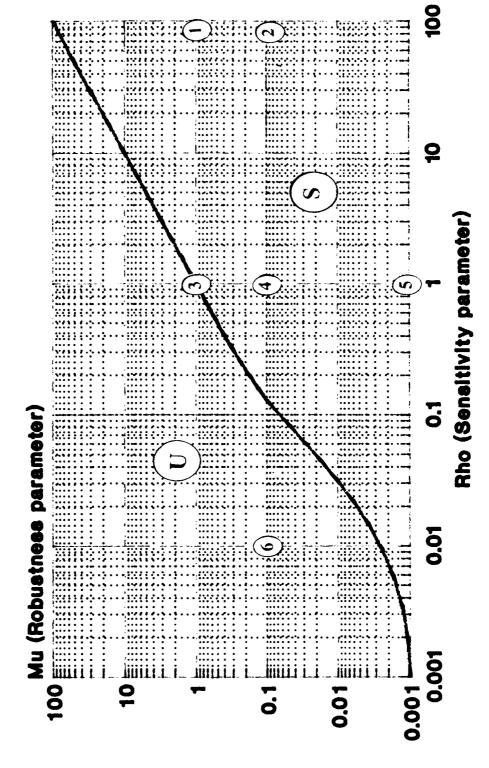
M(mass) = 10,000 kg. :

I (the base radius of shell) = 100 meter:

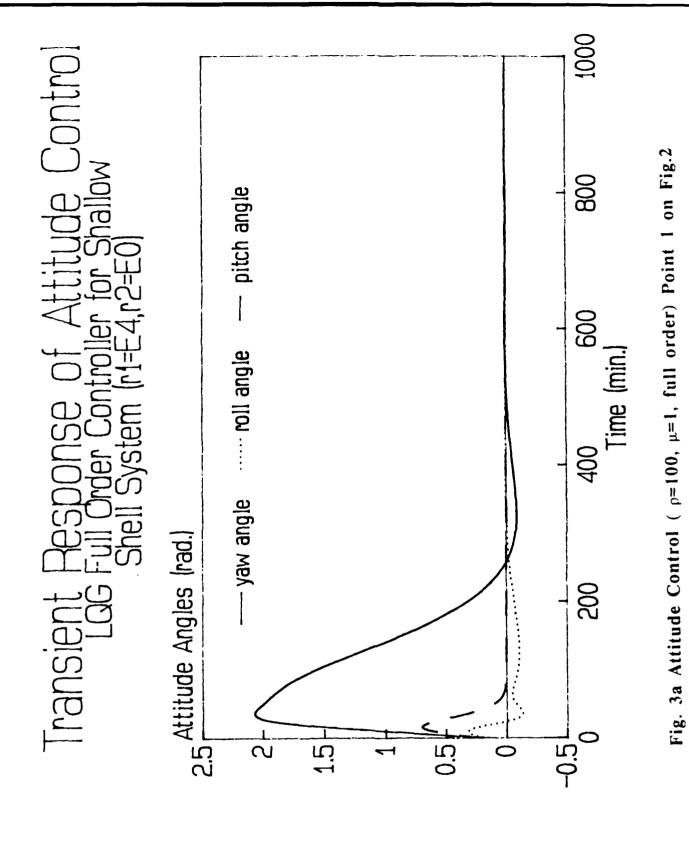
H(the height of shell) = 1 meter: R(radius of curvature for shell) = 5000 meter:

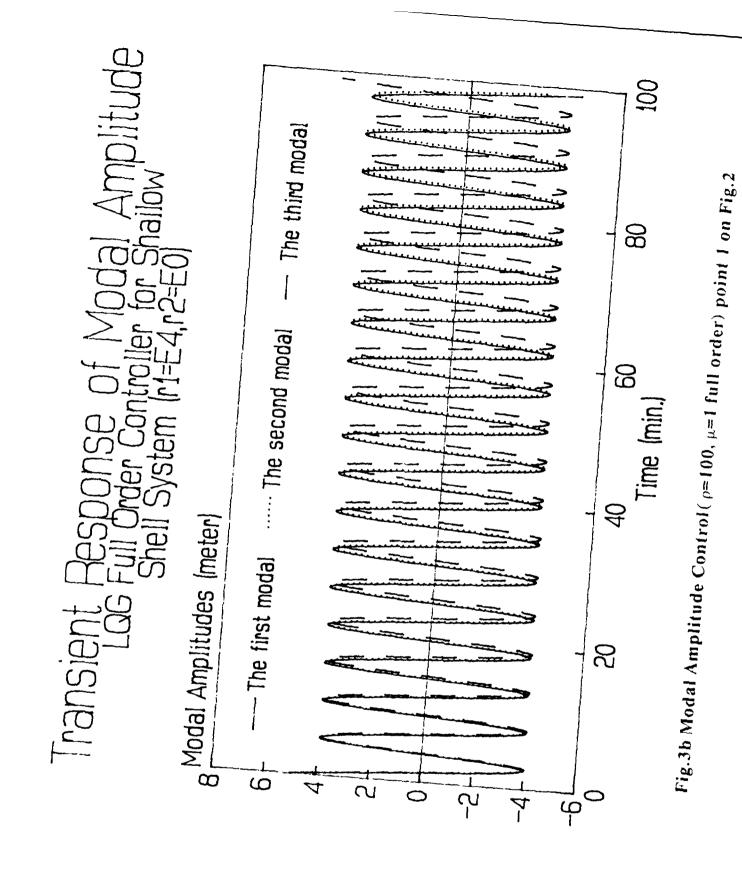
h(wall thickness of shell) = 0.01 meter

Mu & Rho for LQG Control of Orbiting The Acceptable Combinations of Shallow Shell System



g. 2 The Acceptable Combinations for ρ and μ





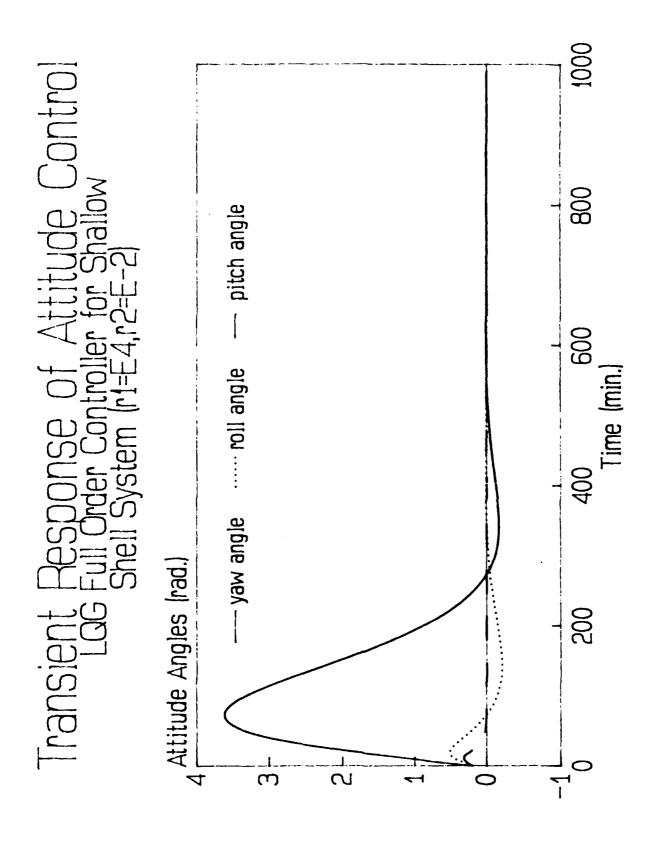


Fig 4a Attitude Control (ρ =100, μ =0.1 full order) Point 2 on Fig. 2

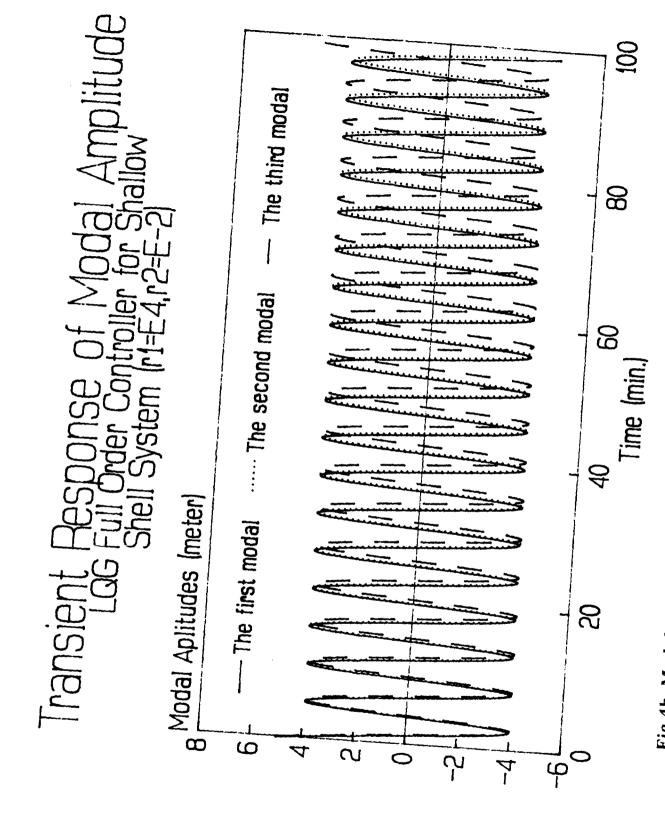


Fig.4b Modal Amplitude Control(ρ =100, μ =0.1 full order)Point 2 on Fig.2



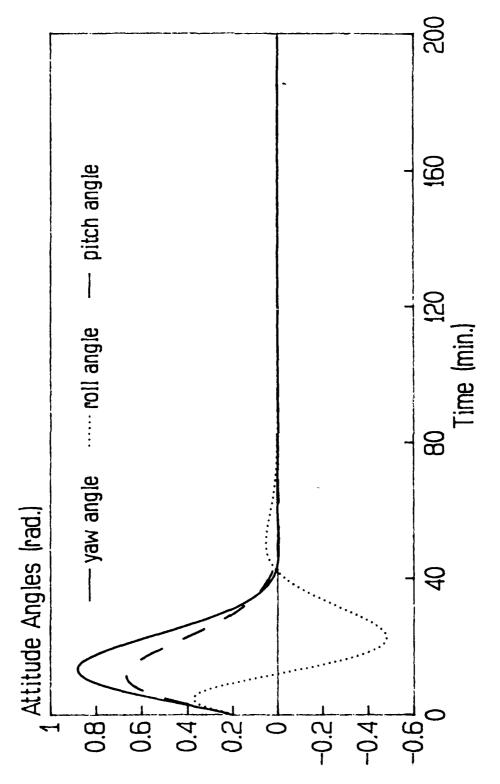


Fig. 5a Attitude Control ($\rho=1$, $\mu=1$, full order) Point 3 on Fig. 2

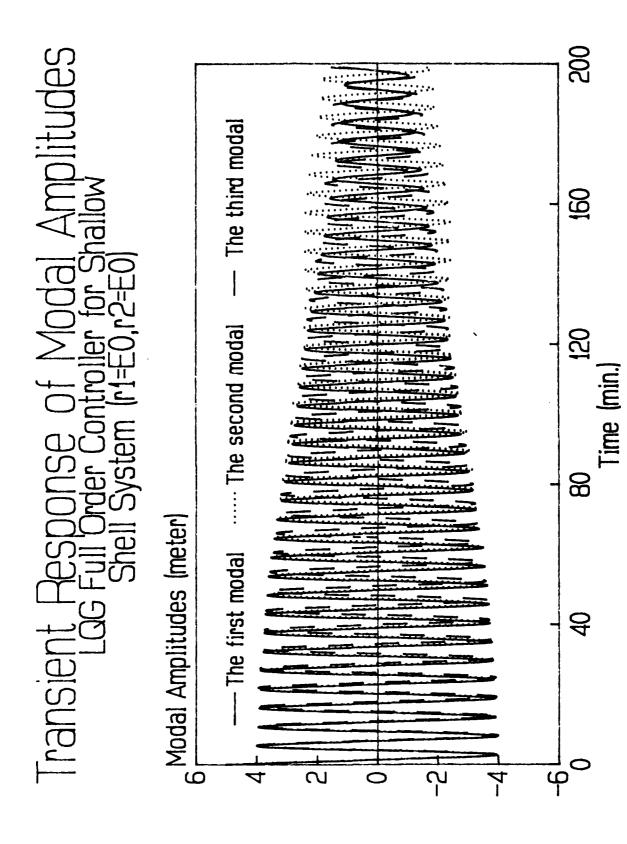


Fig. 5b Modal Amplitude Control($\rho=1$, $\rho=1$, full order)Point 3 on Fig. 2

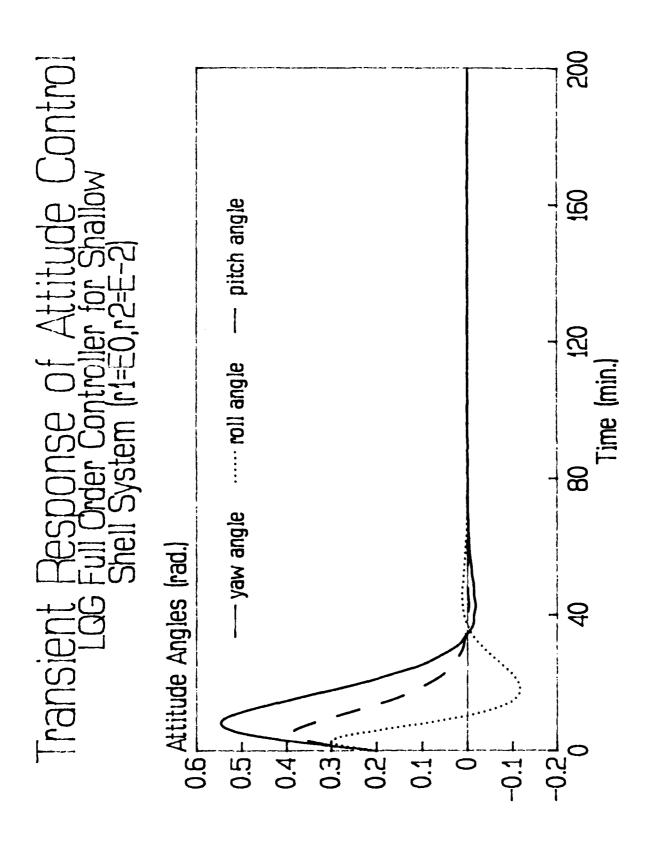


Fig. 6a Attitude Control ($\rho=1$, $\mu=0.1$ full order) Point 4 on Fig. 2



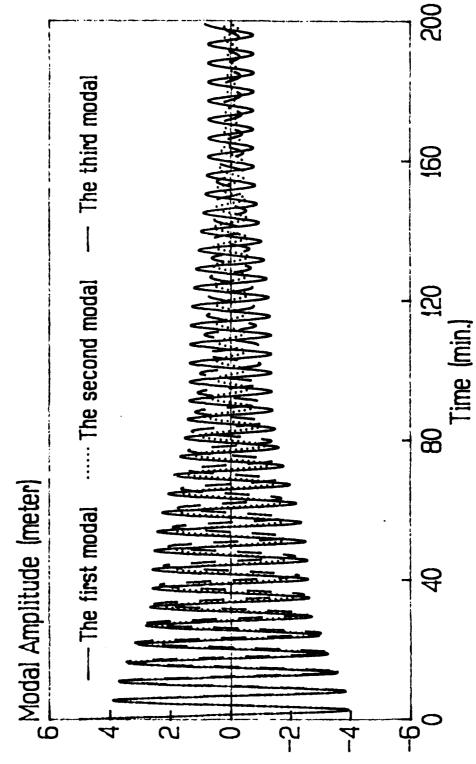


Fig. 6b Modal Amplitude Control ($\rho = 1, \ \mu = 0.1$ full order) Point 4 on Fig.2

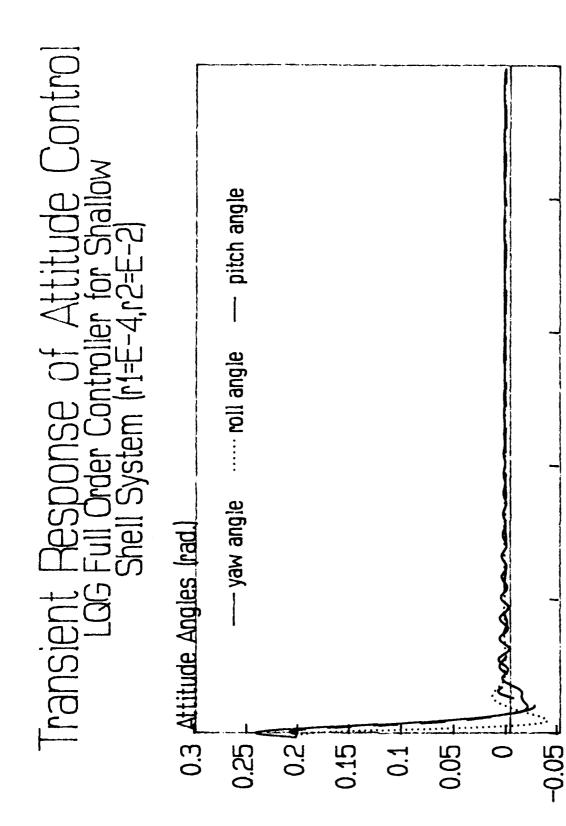


Fig 7a Attitude Control (ρ =0.01, μ =0.1, full order) Point 6 on Fig. 2

Time (min.)



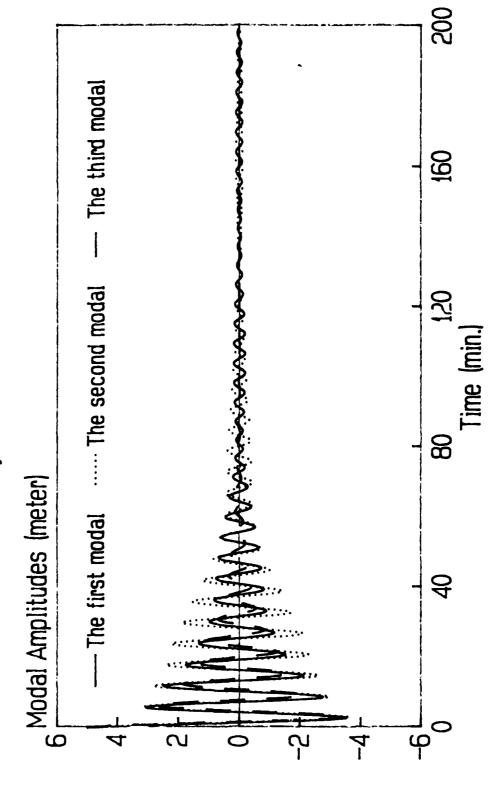


Fig. 7b Modal Amplitude Control (g=3.01, $\mu=0.1,$ full order) Point 6 on Fig.2



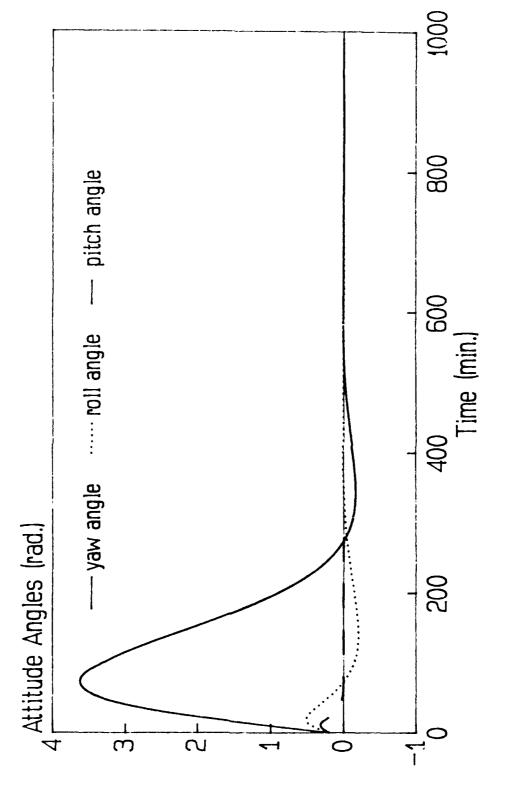


Fig. 8a Attitude Control (ρ =100, μ =0.1 12-dim) Point 2 on Fig. 2

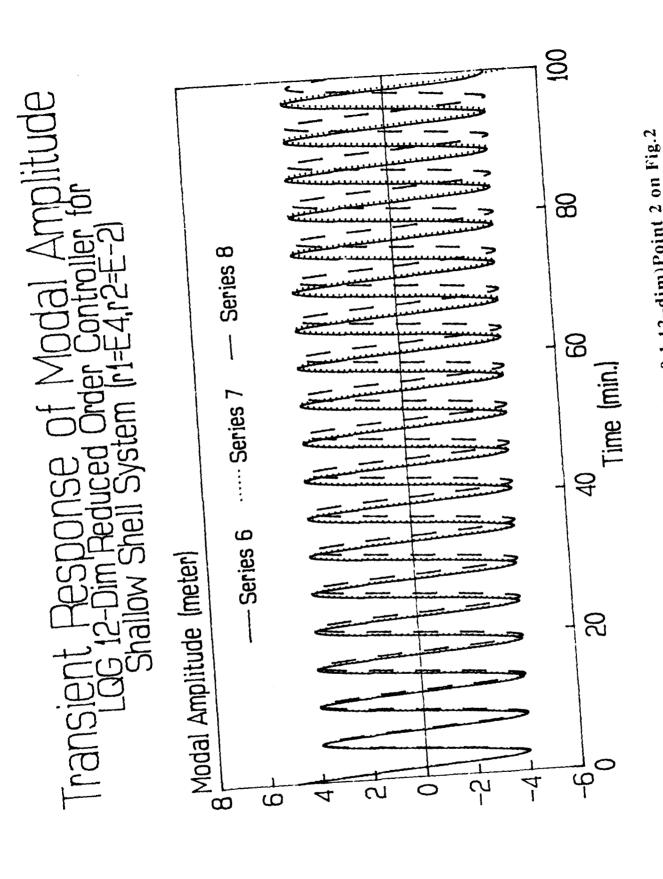


Fig. 8b Modal Amplitude Control ($\rho=100,\mu=0.1,12-dim$)Point 2 on Fig.2



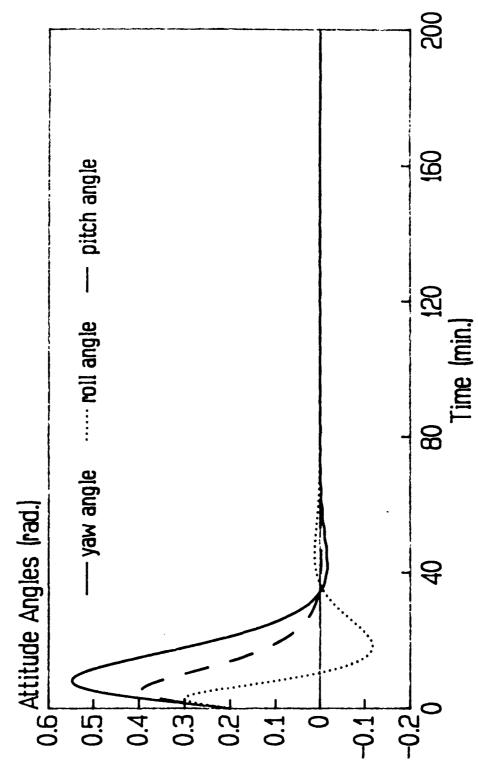


Fig. 9a Attitude Control ($\rho=1,~\mu=0.1~12-dim)$ Point 4 on Fig. 2



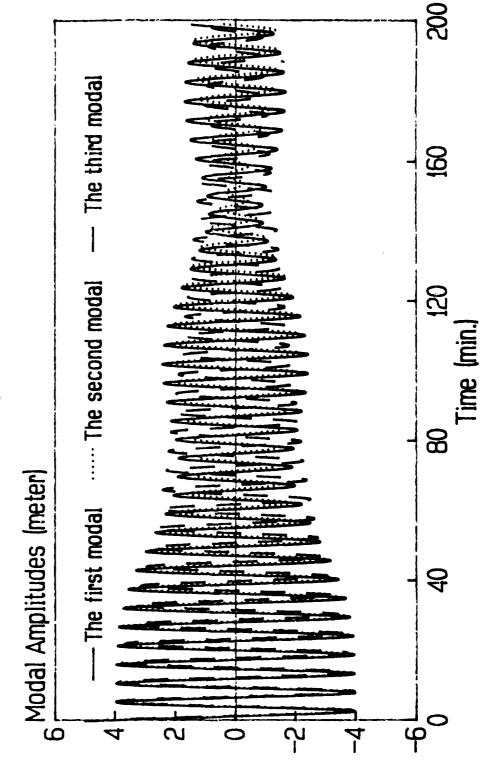


Fig. 9b Modal Amplitude Control (ρ =1, μ =0.1 12-dim) Point 4 on Fig.2



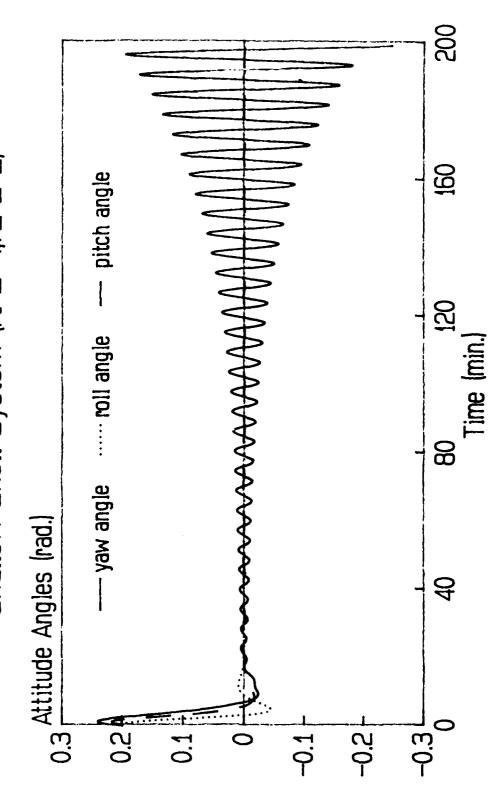


Fig. 10a Attitude Control (ρ =0.01, μ =0.1 12-dim) Point 6 on Fig.2



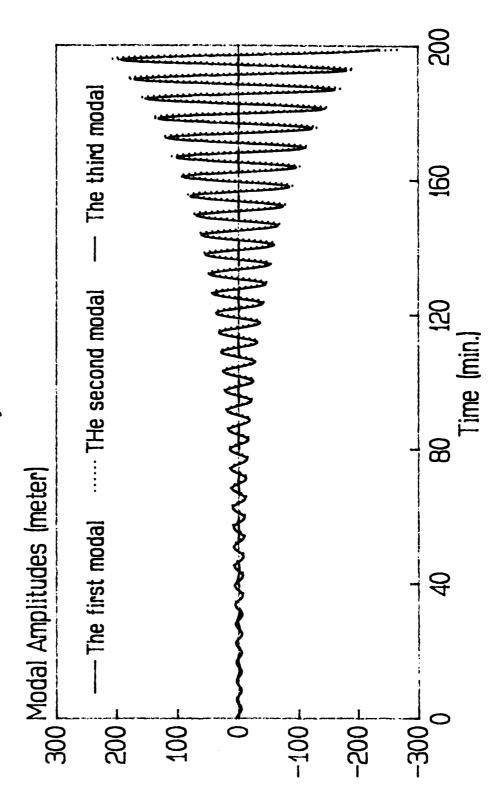


Fig.10b Modal Amplitude Control(ρ =0.01, μ =0.1,12-dim) Point 6 on



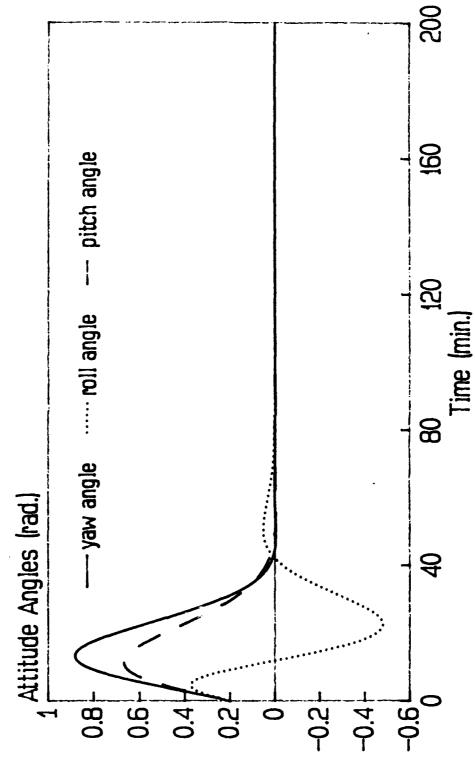


Fig.11a Attitude Control (ρ =1, μ =1, 12-dim) Point 3 on Fig.2

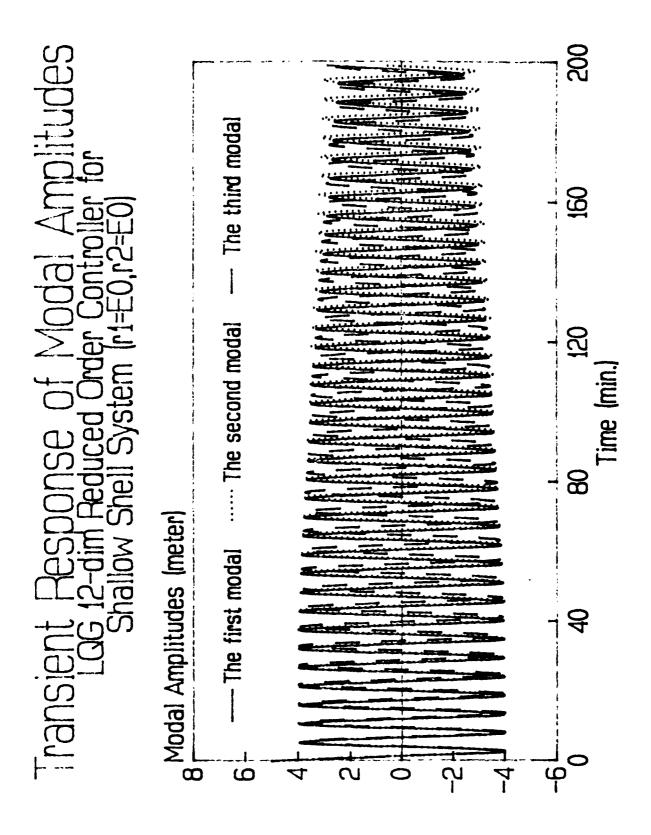


Fig. 11b Modal Amplitude Control (p=1, µ=1,12-dim) Point 3 on Fig. 2

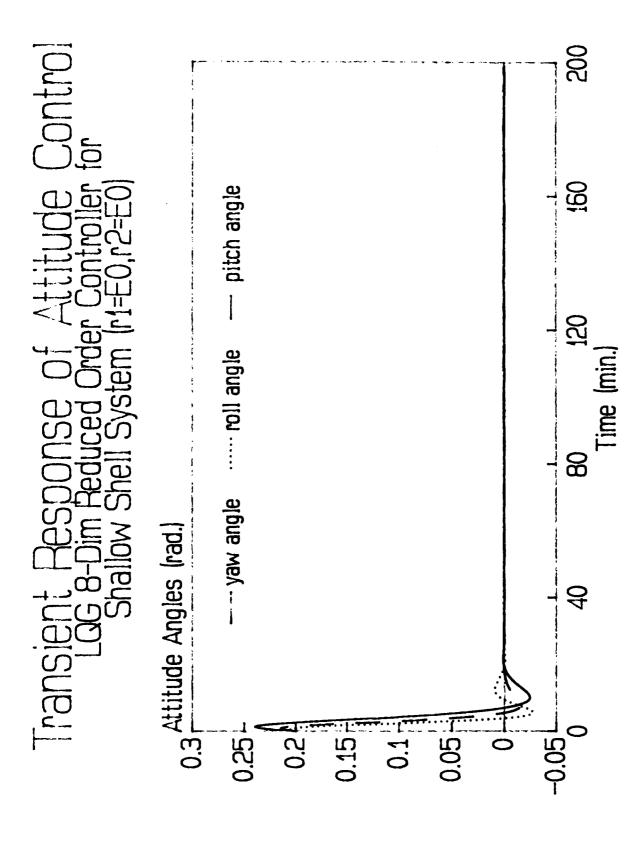


Fig. 12a Attitude Control ($\rho=1$, $\mu=1$, 8-dim) Point 3 on Fig. 2

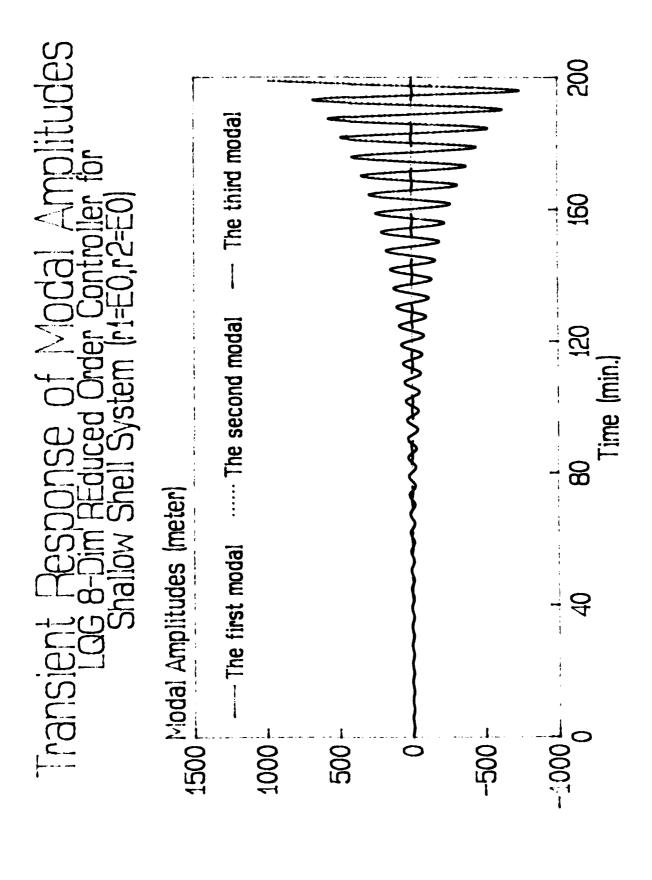


Fig. 12b Modal Amplitude Control(ρ =1, μ =1, 8-dim)Point 3 on Fig. 2.

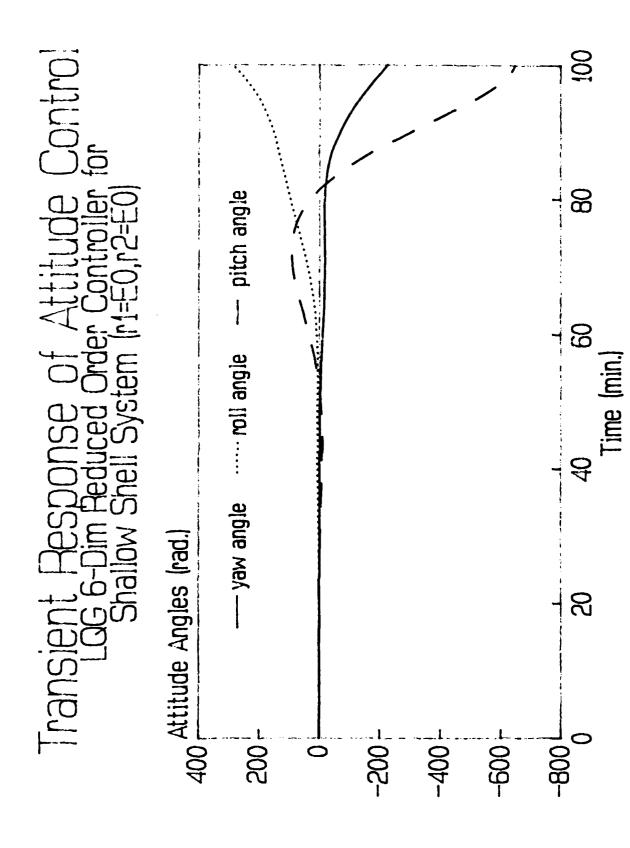


Fig. 13a Attitude Control ($\rho=1,\ \mu=1,\ 6-dim$) Point 3 on Fig. 2

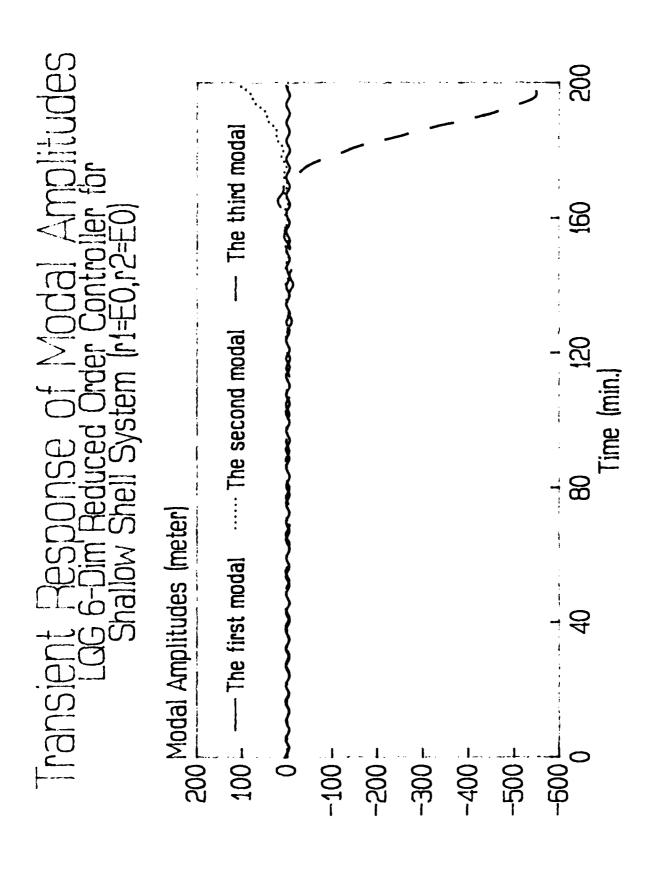


Fig. 13b Modal Amplitude Control($\rho=1, \mu=1, 6$ -dim)Point 3 on Fig.

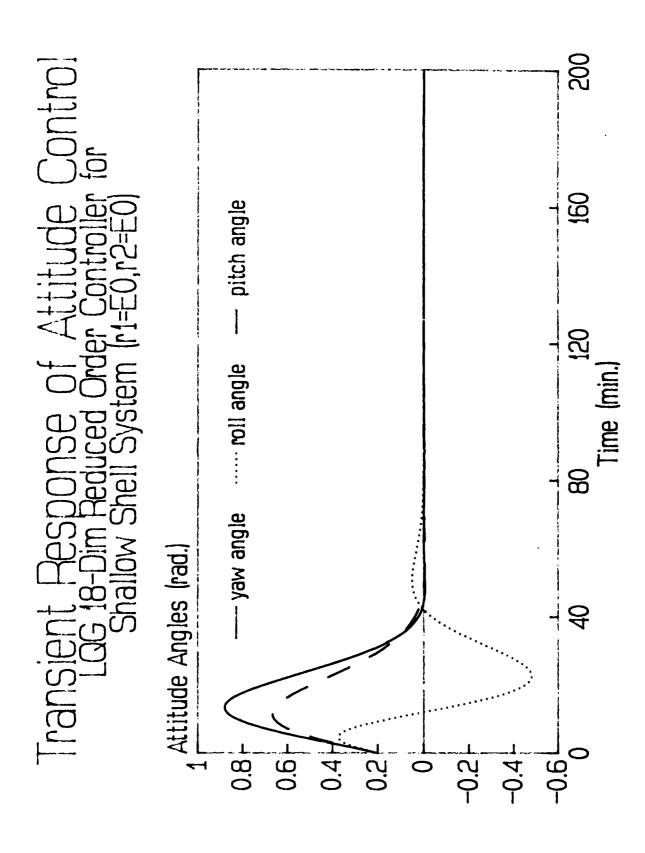


Fig. 14a Attitude Control (p=1, μ =1, 18-dim) Point 3 on Fig. 2



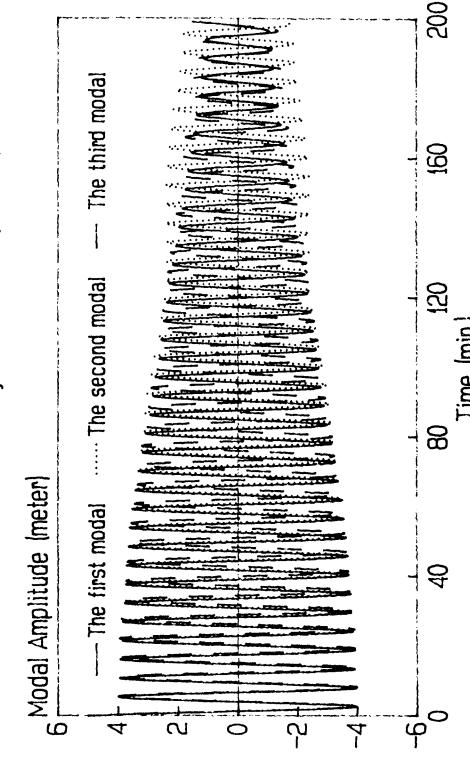


Fig. 14b Modal Amplitude Control(p=1, µ=1, 18-dim)Point 3 on Fig.2

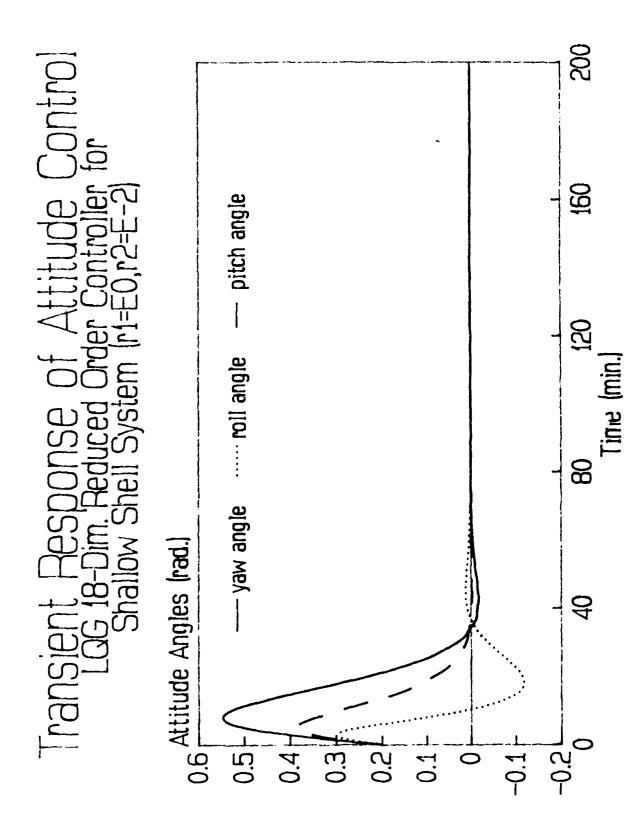


Fig. 15a Attitude Control (ρ =1, μ =0.1, 18-dim) Point 4 on Fig.2



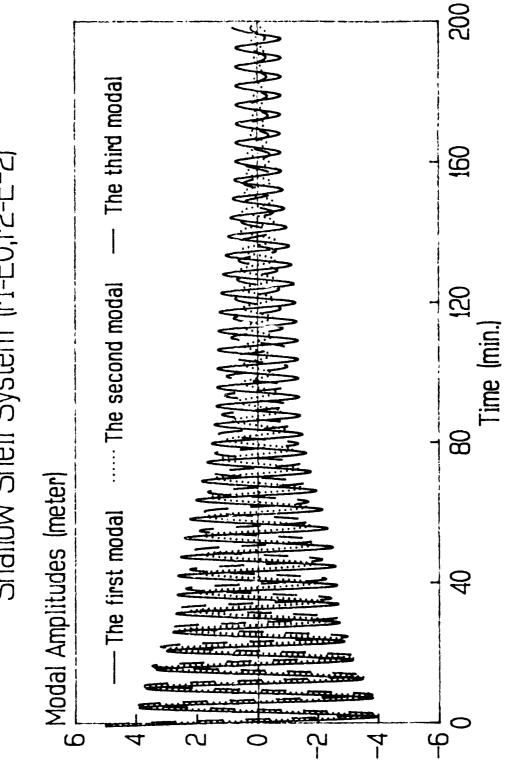


Fig. 15b Modal Amplitude Control (ρ =1, μ =0.1, 18-dim) Point 4 on Fig.2

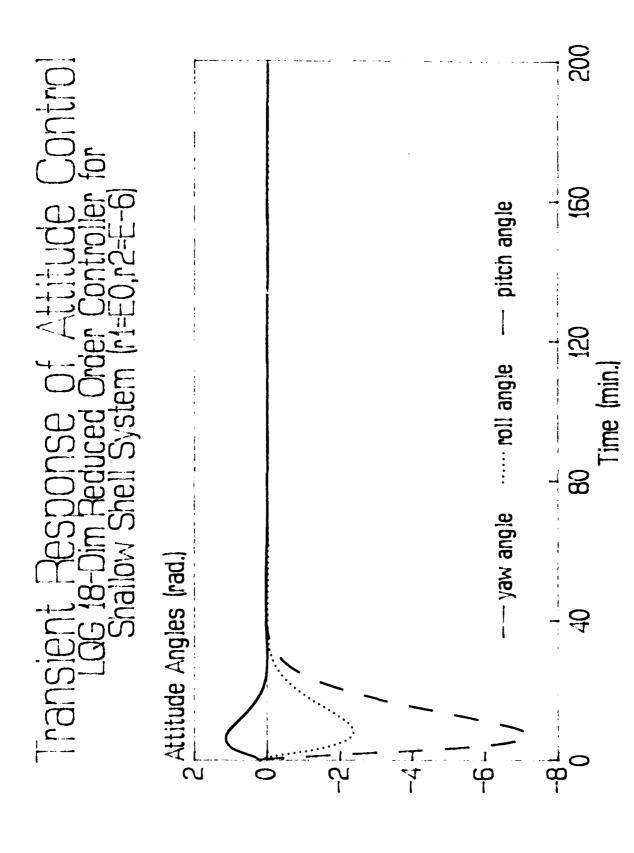


Fig. 16a Attitude Control (ρ =1, μ =0.001, 18-dim) Point 5 on Fig. 2



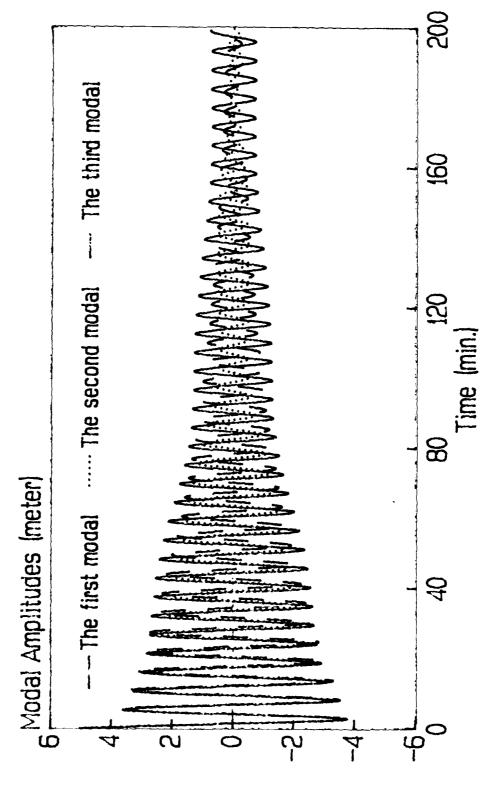


Fig.16b Modal Amplitude Control($\rho=1,\ \mu=0.001,\ 18$ -dim) Point 5 on Fig.2

PHOTOVOLTAIC ARRAY POINTING PERFORMANCE ANALYSIS FOR SPACE STATION FREEDOM ASSEMBLY COMPLETE CONFIGURATION

Ronald E. Graham NASA-Lewis Research Center 21000 Brookpark Road Cleveland OH 44135

Richard J. Lalonde Nathan L. Moseley Analex Corporation 21775 Brookpark Road Fairview Park OH 44126

Fourth Annual NASA/DoD CSI Technology Conference Orlando, Florida November 5-7, 1990

The work described here was performed under Engineering Directorate Job #85012, on behalf of the Systems Engineering and Analysis Branch, Space Station Freedom Directorate, NASA Lewis Research Center.

ABSTRACT

The purposes of the analysis described here are as follows: to verify that dynamic models and control law design chosen for the Space Station Freedom (SSF) photovoltaic (PV) array beta gimbals joints meet pointing accuracy requirements for the Assembly Complete (AC) SSF configuration; and to support structural dynamic loads analyses being performed for the same configuration.

The AC configuration was chosen for this study for the following reasons: when that configuration is achieved, it is expected to be unchanged for some time; structural models of AC are readily available; and its eight PV arrays provide a large number of structural degrees of freedom.

The simulation model for AC used contains structural system modes, transferred from NASTRAN to EASY5 via COSTIN. Modal ordering techniques were applied to reduce the order of this simulation model for use in Shuttle docking and orbit reboost analysis.

A full-order dynamic model of the beta gimbal assembly (BGA) control system has been developed and is presented here. It has not been applied to a system simulation model pending design changes proposed by Rocketdyne, the prime contractor. Instead, simple models were used for all gimbal control laws.

The results to be presented show that PV pointing requirements are met during reboost and Shuttle docking conditions for the model used, and that control forces and torques induced during these cases will not exceed structural load requirements.

Further study is being performed in the following areas: reduced-order dynamic modeling, nonlinear effects on beta gimbal dynamics, use of a displacement gyro for pointing error measurement, and determination and documentation of SSF stage disturbance environments.

NOMENCLATURE

AC - Assembly complete

BGA - Beta Gimbal Assembly

MB - Mission Build

MOR - model order reduction

PD - proportional-derivative (control)

PV - photovoltaic

RCS - Reaction Control System

ROM - reduced-order model

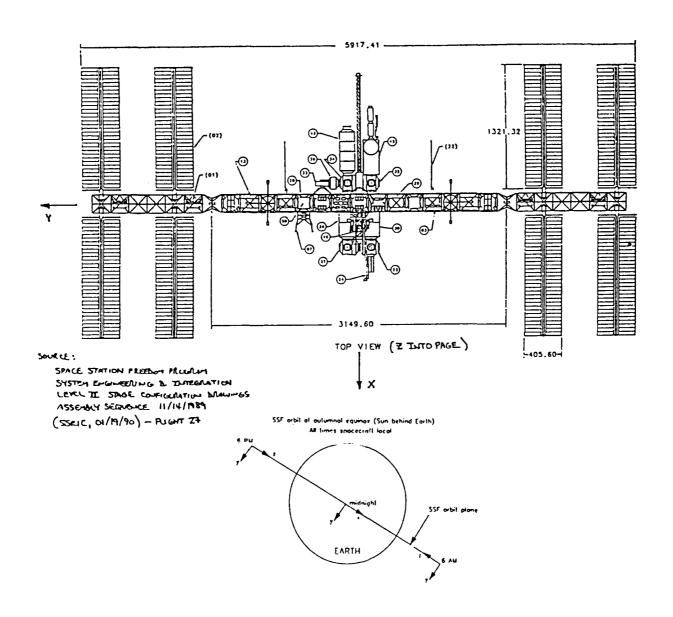
SD - Solar Dynamic

SSF - Space Station Freedom

STRUCTURAL MODEL

Description:

The model was developed by the Structural Systems Dynamics Branch at Lewis Research Center. The diagram below, taken from the Level II Stage Configuration Drawings (Assembly Sequence dated 11/14/89), illustrates the structure. There are eight PV arrays and no Solar Dynamic modules added in this configuration. The NASTRAN finite element model of this configuration gave 320 modes of vibration: 16 rigid body, and 304 flexible (with maximum natural frequency about 5 Hz).

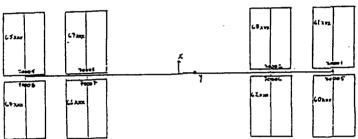


PV ARRAY CHARACTERISTICS

The array consists of two blankets of solar cells, a flexible mast (to which the blankets are rigidly attached at either end), a cylindrical canister (from which the arrays are deployed), and a container with cover.

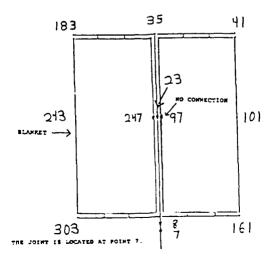
```
= 5.3 lbf-sec^2/in
mass
moment of inertia about rotational axis = 5.3e4 in-lbf-sec<sup>2</sup>
width
                                               = 33.8 ft
length
                                               = 107.9 ft
blanket width (each)
                                                 14.2 ft
blanket tension (each)
                                               = 75 lbf
                                               = 360 deg
rotational range
      (although a 52 deg zero-to-peak range is covered during
      nominal operation)
peak angular rate
                                               = 0.015 \text{ deg/seg}
peak angular acceleration
                                               = 0.01 \text{ deg/sec}^2
peak torsional moment (of BGA) = 7000 in-lbf
peak torsional moment (gravity-gradient disturbances)
                                               = 7000 in-lbf
                                               = 0.3 in-lbf
                                               = about 0.08 Hz
first torsional mode frequency
```

(HOOM CONFIGURATION, FRONT VIEW)



PV point numbering disgram

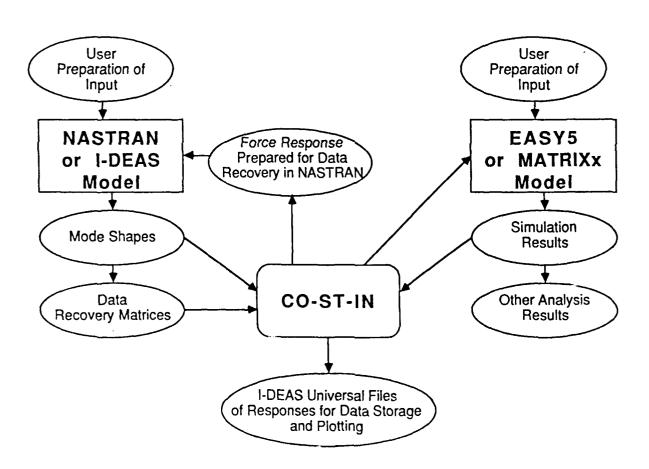
GRIDS 183,41,303, AND 161 REFRESENT MOTION OF BOTE THE BLANKET AND THE FRAME AS THEY ARE RECIDLY ATTACHED AN THE FINITE ELEMENT MODEL.



THE ROLE OF COSTIN IN MODEL REDUCTION AND ANALYSIS

The interface program COSTIN was developed by Dr. Paul Blelloch of the Structural Dynamics Research Corporation (SDRC) for use in analyses of this type. From the normal modes output of a NASTRAN finite element model, modal matrices are written into an EASY5 analysis file. Control loops are written within EASY5 for use in analysis and simulation. Time histories of control forces and torques are sent via COSTIN into a NASTRAN input deck for use in dynamic loads analysis.

COSTIN also has several mathematical techniques within its program for ordering modes on the bases of controllability and observability.



BGA MODEL & ANALYSIS

Description:

The model is composed of three main parts: motor electronics, motor dynamics, and array dynamics. The motor electronics consist of a single loop, RL circuit with negligible back EMF. The motor dynamics consist of a motor-produced torque, moment of inertia, damping relative to the SSF main structure, and a gear of small mass. The array dynamics consist of a large gear mounted on a shaft, damping relative to the SSF main structure, moment of inertia, and a disturbance torque acting on the array.

Parameters:

Variables:

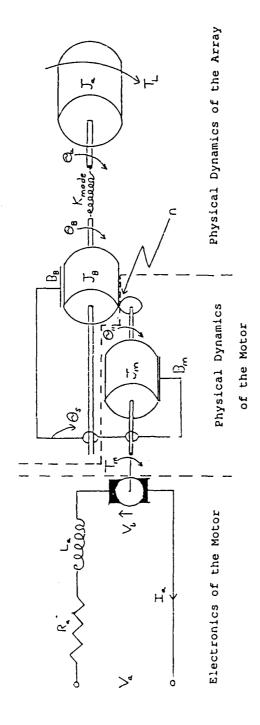
 $\begin{array}{lll} \textbf{V}_{a} &=& \textbf{motor input voltage (modeled as proportional to} \\ & \textbf{commanded torque} \\ \textbf{\Theta}_{S} &=& \textbf{SSF structure rotational velocity, rad/sec} \\ \textbf{\Theta}_{m} &=& \textbf{motor rotation, rad} \\ \textbf{\Theta}_{B} &=& \textbf{large gear rotation, rad} \\ \textbf{\Theta}_{m} &=& \textbf{array rotation, rad} \\ \textbf{T}_{L} &=& \textbf{array disturbance torque, in-lbf} \end{array}$

Note:

This BGA dynamic design was chosen to drive SD modules, which are much heavier than PV arrays. A requirement has existed for a common device to drive both PV and SD, and that requirement is currently under review. If the requirement is lifted, Rocketdyne will switch to a direct-drive system to rotate the PV arrays.

For this reason, although the current design is still being adapted to an SSF system model, no results of that adaptation will be presented here.

PV BETA GIMBAL ASSEMBLY



Modelling Assumptions:

- The back emf, V_b , is negligible. The small gear on the motor shaft has negligible moment of inertia. The parameter values for the motor are for a DC brushless motor.

This BGA design is **not** the most current version of the assembly. NOTE:

MODEL ORDER REDUCTION

Shuttle docking:

| stage | # modes | total modes | input(s) | output(s) |
|-------------|----------------|----------------|--------------------------------------|--------------------------------|
| 0 1 2 | 16 58 17 | 16 74 91 | none β torque α torque port | none β rot α rot port |
| 3 | 15 | 106 | α torque | α rot star |
| 2,3 | 14 10 | 120 130 | none docking forces, | none PV x,y rot |
| 5 | 10 | 140 | torques docking x rot torque | PV x rot inboard of β |
| 6 | 22 | 162 | docking y rot torque | PV y rot inboard of α |

Reboost:

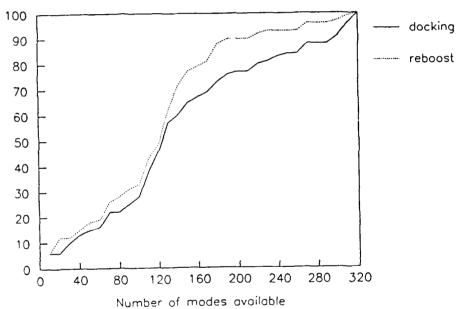
| stage | # modes | total modes | input(s) | output(s) |
|-------|---------|-------------|---------------------|-----------|
| 0 | 16 | 16 | none | none |
| 1 1 | 42 | 58 | β torque | β rot |
| 2 | 50 | 108 | RCS jets reboost | βrot |
| 3 | 10 | 118 | a torque | β rot |
| 4 | 10 | 128 | RCS jets reboost | |
| 5 | 8 | 136 | α torque | |

These tables show the stages in selection of modes for a reduced-order model for the two simulation cases. COSTIN was used to perform the modal selection and EASY5 to verify the selections. For both cases, the 16 rigid body modes were chosen at stage 0.

The following figure illustrates the frequency distribution of the modes selected for both docking and reboost. For both cases, modes were selected throughout the entire range of 320 available modes, for which the highest natural frequency was about Hz. If modes are selected according to order of natural frequency, the model either quickly becomes large or may ignore modes that impact control performance.

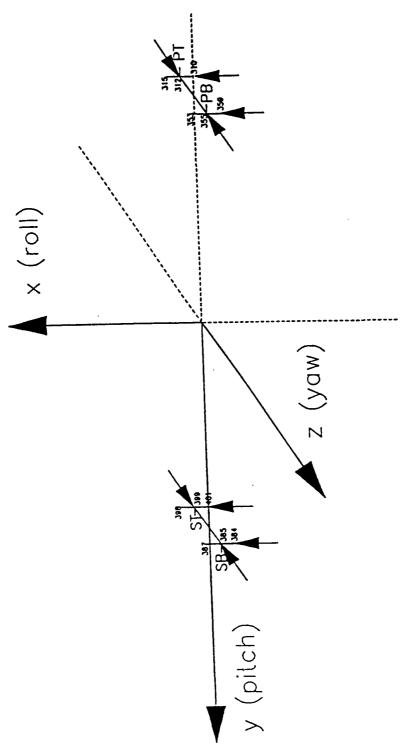
Percentage modes retained vs. modes available (for both docking and reboost)

Percentage of total modes retained



CONTROL SYSTEM USED IN DOCKING AND REBOOST ANALYSES

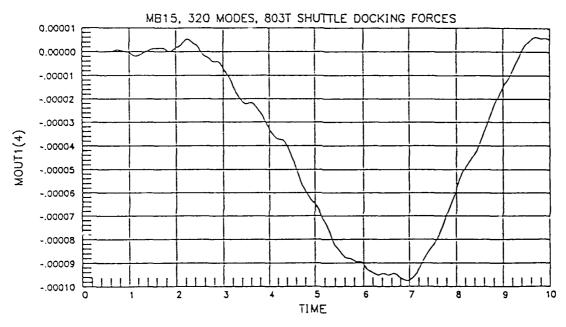
The figure below illustrates the layout of the SSF Reaction Control System (RCS), used in both docking and reboost analyses. The RCS is used after a Shuttle docking primarily for momentum reset on the SSF CMGs. Numbers on the diagram are NASTRAN node numbers for the finite element model.

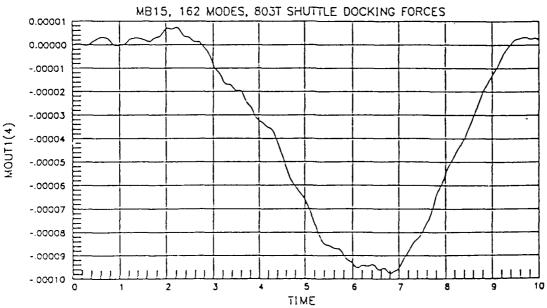


DOCKING RESULTS

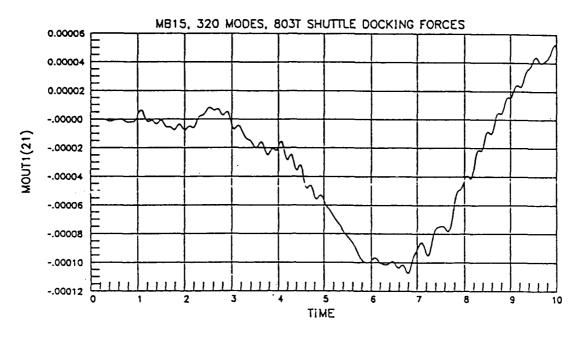
The results presented include: relative rotation of starboard alpha gimbal (rad) vs. time (sec); rotation about the pitch axis of node 243 (the middle of the blanket, maximum distance from the mast) on a certain PV array (rad) vs. time (sec). These plots are given for two cases: 162 (ordered) modes and 320 (all available) modes. The traces for the two cases are very similar.

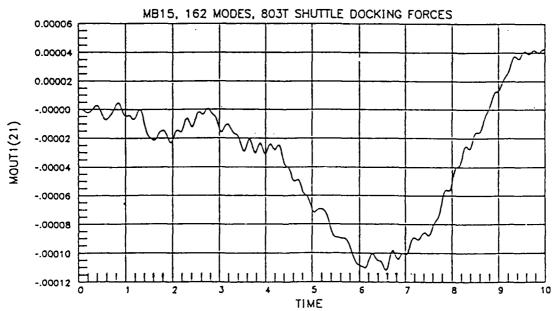
relative rotation of starboard alpha joint vs. time





y-direction rotation of array node point 243 vs. time

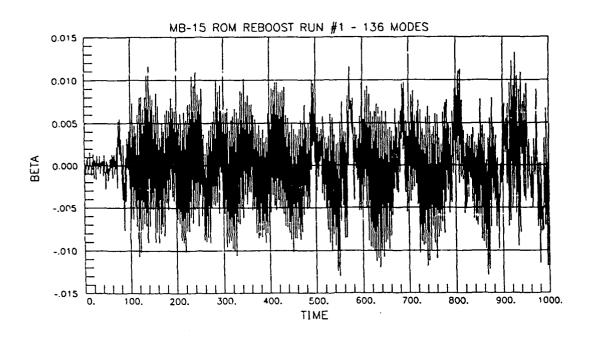


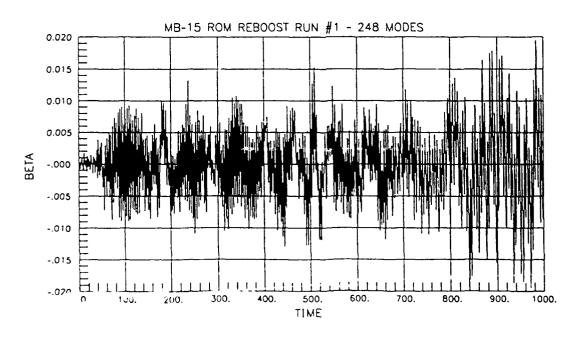


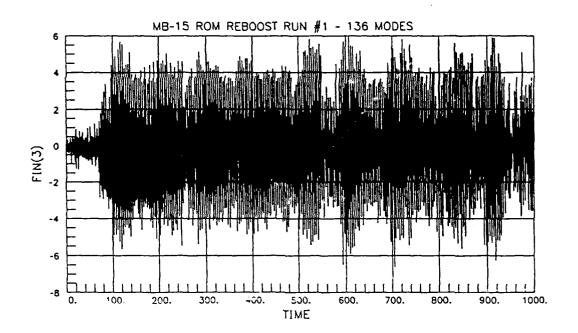
REBOOST RESULTS

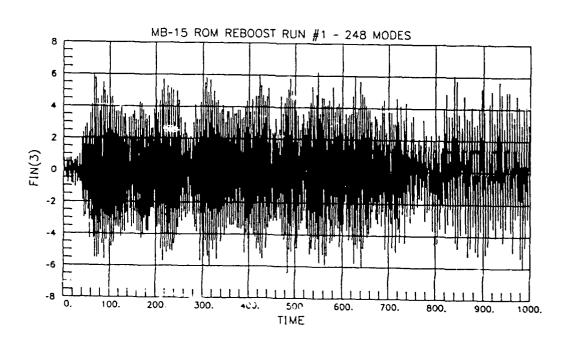
The results presented include: relative rotation of a single beta gimbal about its degree of freedom (deg) vs. time (sec); beta gimbal control torque for the same array (in-lbf) vs. time (sec). These plots are given for two cases: 136 (ordered) modes and 248 (ordered by frequency) modes. The traces for the two cases are similar. A more correct representation of the model may require more modes.

beta gimbal angle vs. time









NASA/DoD CSI Conference November 1990

H_{∞} CONTROL DESIGN FOR THE ASCIE SEGMENTED OPTICS TEST BED:

ANALYSIS, SYNTHESIS AND EXPERIMENT

- Dr. Alain CARRIER, Lockheed Palo-Alto Research Laboratory, Palo-Alto, CA
- Pr. Arthur E. BRYSON Jr., Stanford University, Stanford, CA
- Dr. Jean-Noel AUBRUN, Lockheed Palo-Alto Research Laboratory, Palo-Alto, CA
- Dr. Kenneth LORELL, Lockheed Palo-Alto Research Laboratory, Palo-Alto, CA

BACKGROUND

The performance of astronomical systems is directly related to the size of their reflectors. Since it is very difficult to cast mirrors larger than 7 meters in diameter from a single piece of glass, to reach unprecedented performance levels, it is planned to construct future optical systems with diameters in the 7-12 meters range from arrays of mirror segments. The Keck Ten Meter Telescope, presently under construction, is such a system.

The problem with segmented optics is to make them behave like the conventional ones made from a single piece of glass: optical performance requires positioning the mirror segments to a fraction of the wavelength of light. No support structure can provide the mechanical rigidity needed to maintain the position of the mirror segments to such an accuracy. To compensate for the mechanical imperfections, the deformations due to the gravity and thermal loads and to attenuate the seismic or maneuver induced vibrations, the mirror segments must therefore be actively controlled.

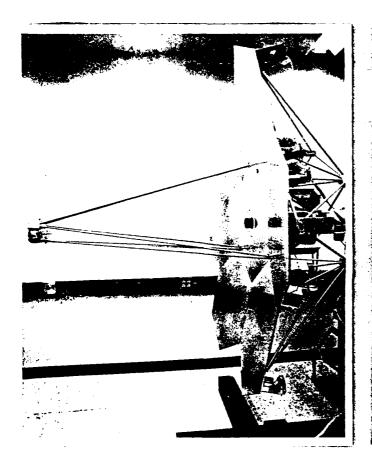
Some of these systems such as the NASA's Large Deployable Reflector [1] will be sent into space. Their support structure will be lightweight trusses.

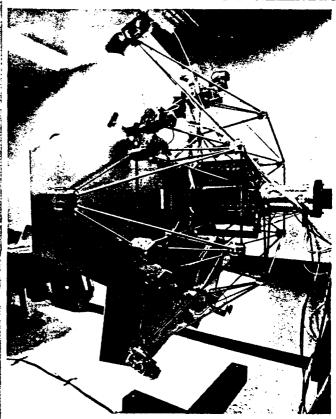
Both the high performance requirements and the increased flexibility contribute to merging the active control system and the structural dynamics. Earlier work done on the Keck Ten Meter Telescope [2] at the Lockheed Palo-Alto Research Center showed that, because of the control structure interaction, an integral control strategy that would have enough authority to compensate for the gravity sag, would worsen the effects of dynamic disturbances or even lead to instability. The success of the new optical systems depends on advances in multiple areas such as sensor and actuator technology, pointing/slewing, control/structure interaction, structural control and shape control. The shape control problem is one of the most challenging. It combines the difficulties of a large flexible space vehicle control problem with extreme performance requirements and high dimensionality (the Keck Ten Meter Telescope for example has 162 sensors and 108 actuators).

Because of the latest advances in microprocessor technology and robust, multivariable control theory [3], [4], it is now possible to address the shape control problem of segmented optics in its full complexity. At present, little work has been done to take advantage of the computing power of new microprocessors, or to demonstrate and familiarize the practicing control engineer with the new control techniques [6], [7], [8], [9].

To validate the new optical system concepts and the new control design methodologies, the Lockheed Palo-Alto Research Center has developed a control-systems-oriented test bed called the Advanced Structures/Controls Integrated Experiment (ASCIE) [10]. We report here on the modeling and the shape control design of the ASCIE segmented optics. The techniques developed and the experience gained are applicable to the control of large flexible structures in general.

ASCIE TEST BED





ASCIE TEST BED (CONTINUED)

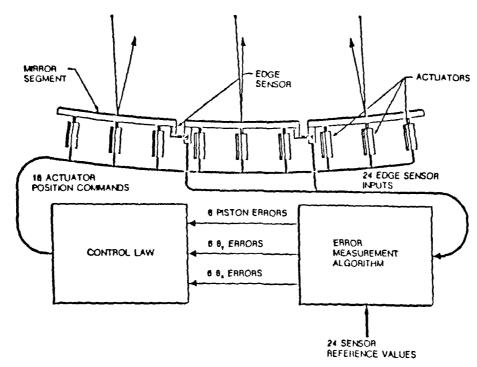


Figure 2: Schematic diagram illustrating operation of segment alignment control system

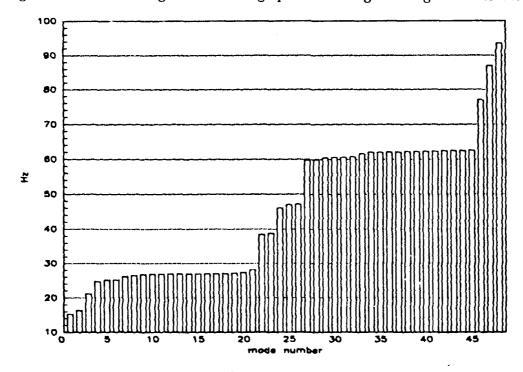


Figure 3: ASCIE structure modal frequency histogram

ASCIE TEST BED

The ASCIE emulates a f/1.25 Cassegrain telescope. Its seven-hexagonal-segment primary mirror is mounted on a light-weight flexible truss structure. The six peripheral segments are actively controlled in three degrees of freedom by 18 linear electromagnetic precision actuators. 24 inductance sensors (4 per actively controlled segment) are used to measure the relative displacements between the segments and generate commands for the actuators to keep the segments optically aligned, the central segment acting as a reference.

Sensing

The edge sensors measure the position of the segments with respect to each other. The central segment, instead of the support structure which lacks dimensional stability, is used as a reference. The edge sensors have a 15 nanometer resolution below 5 Hz, and a large measurement range $(\pm 1 \text{ mm})$ to accommodate the initially large misalignments. A laser optical system, not described, is used for initial calibration and system alignment. In future works, this system will also be useful for optical scoring.

Actuation

The actuators have been specially designed at Lockheed [11] to meet the strict resolution, dynamic range, smoothness of operation and bandwidth requirements. Each actuator is instrumented with an automatic system providing force offloading.

Truss structure

The structure was designed and optimized to emulate a large telescope structure while being able to support the mirror segments in a 1-g environment. Figure (3) shows the distribution of the modal frequencies of the ASCIE. The fundamental mode is at 15 Hz. 18 natural frequencies are tightly grouped around 26 Hz. The modal distribution is typical of segmented optical systems, and fundamentally different from the well-spaced distribution of beamlike structures.

MODELING OF THE ASCIE

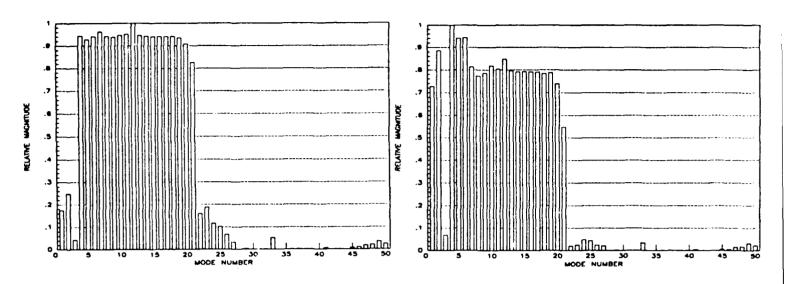


Figure 4: ASCIE modal controllability observability products

Figure 5: ASCIE modal disturbability

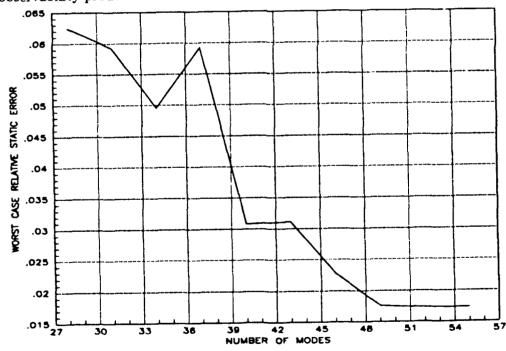


Figure 6: Worst case relative fidelity error caused by modal truncation model reduction

MODELING OF THE ASCIE

A 586 mode Finite Element Model was computed and then reduced by Guyan reduction to a 288 mode model using the Lockheed Astro Finite Element Analysis program [15].

The largest controller that the Array Processor can run at 200 Hz (about 4 times the frequency of the modes to control) has 100 states. Coincidentally, 100 is also the maximum order of a Riccati equation that can reliably be solved by current Schur Riccati solvers. To apply worst case control techniques with frequency dependent performance and stability requirements to the ASCIE, the model, if possible should contain less than 30 modes. The modeling objective is to meet this size requirement while keeping an accurate description of the static and dynamic characteristics of the system.

Three criteria (controllability/observability [13], disturbability and static fidelity) were used to select modes from the Finite Element Model to form the control design model.

Controllability of a state is measured by the minimum amount of control energy needed to bring the system from 0 to this particular state. Observability of a state is measured by the amount of energy delivered to the sensors as this state decays freely to 0. Controllability/observability is measured by the ratio of the above two energy quantities. For lightly damped systems [14], when the modes are well separated either spatially or in frequency, the controllability/observability measure of a mode is also the maximum singular value of the corresponding term in the pole residue expansion of the transfer function matrix from the controls to the measurements. Figure (4) shows the controllability/observability of the first 50 modes of the ASCIE. The controllability/observability measures are normalized with respect to the largest one to eliminate the contribution of the proportional damping which was set to 1% in all the modes.

Disturbability is measured like controllability/observability with the disturbances replacing the controls and the regulated variables (here three piston displacements per mirror segment) replacing the measurements. For lightly damped systems like the ASCIE, the modal disturbability measures nearly represents the maximum energy gain of the system from the disturbances to the regulated variables at the modal frequencies. Figure (5) shows the disturbability measures of the first 50 modes of the ASCIE normalized with respect to the largest one.

To produce given displacements of the ASCIE mirror segments, appropriate actuator forces must be applied to the system. Under these forces the full modal Finite Element Model will predict the correct displacements to the extent of its validity, but a reduced order model will not. The error is a static fidelity error. For optical systems, the static fidelity errors must be kept small (typically below 5%) because of the tight static performance requirements. Figure (6) shows the worst case static error versus the number of most controllable/observable modes kept in the reduced order model.

The above three tests show that a model formed from the 28 most controllable/observable modes describes accurately the dynamic and static characteristics of the ASCIE and is suitable for control design purposes.

MODELING: SYSTEM DECOUPLING

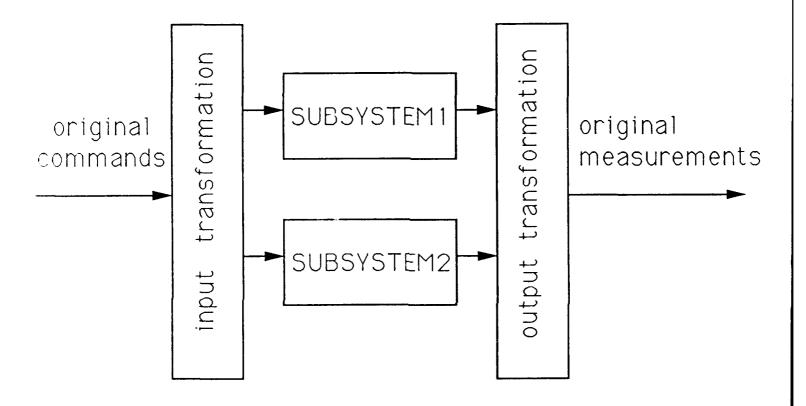


Figure 7: Open-loop system decoupling: SUBSYSTEM1 and SUBSYSTEM2 can be controlled independently of one another if the input and output transformations are invertible and nearly orthogonal.

MODELING: SYSTEM DECOUPLING

The ASCIE primary mirror, structure and tripode secondary mirror assembly has a three fold symmetry. However because of the stand support, the system is only symmetric with respect to a vertical plane. Like most symmetric systems, the ASCIE can be open-loop decoupled into several subsystems.

Open-loop decoupling reduces the difficulties of the synthesis problem in several ways: subcontrollers can be computed faster (the computation go down like the inverse of the cube of the number of subsystems when the subsystems have equal size) and more reliably than a controller for the global system, and they are easier to test. Furthermore, optimality is not lost in the synthesis process if the decouplings are nearly exact. Whenever possible, open-loop decouplings should be sought, especially for large systems like the ASCIE.

Open loop decoupling consists in partitioning the modes of a system into subsets of modes that can each be controlled and sensed by different combinations of the physical actuators and sensors. These actuator and sensor combinations define new fictitious sensors and actuators. The transformation from the fictitious to the physical actuators should be well conditioned so that the physical actuator and control specifications such as maximum actuator authority are applicable without any modification to the fictitious actuators.

Numerical algorithms have been devised to systematically sort out all the open loop decouplings in linear systems, using nearly orthogonal transformations in the control and the sensor spaces. These algorithms applied to the ASCIE 28 mode control design model returned two subsystems: one with 22 modes, 12 controls and 12 measurements, the other with 6 modes, 6 controls and 6 measurements. The condition numbers of the input and output transformations are 1.02 and 1.19 respectively. The 22 mode subsystem can be input decoupled but not output decoupled into two subsystems of equal size. The output coupling is the result of the sensor configuration: it would disappear if the sensors were only sensitive to the out of plane motion of the mirror segments.

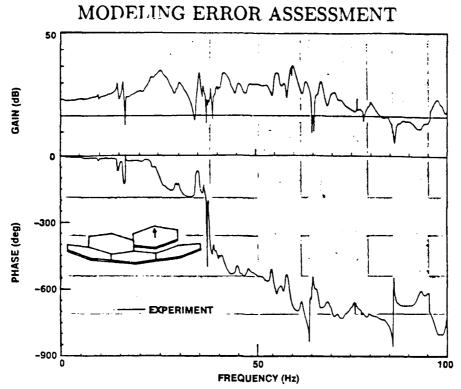


Figure 8: Experimental mirror segment piston response to a piston command

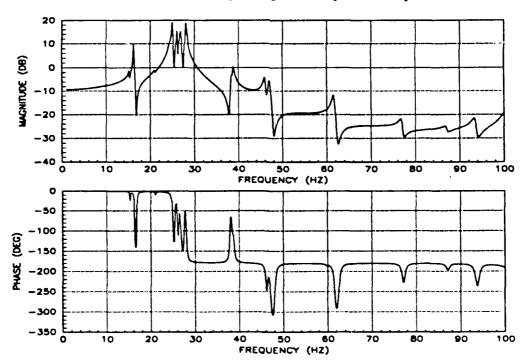


Figure 9: Theoretical mirror segment piston response to a piston command

MODELING ERROR ASSESSMENT (CONTINUED)

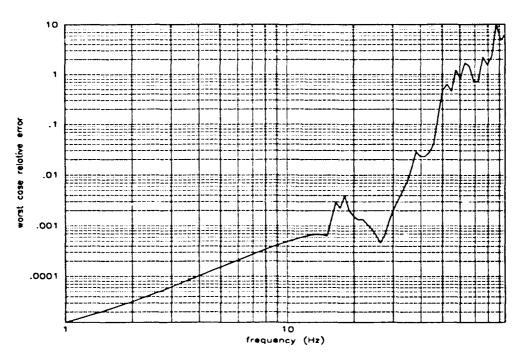


Figure 10: Worst case model reduction relative error

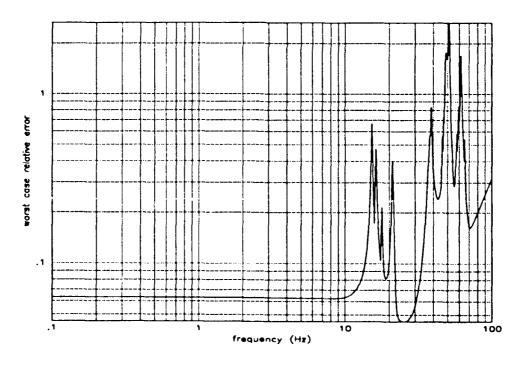


Figure 11: Worst case model decoupling relative error

MODELING ERROR ASSESSMENT

Some knowledge of the modeling errors is needed in control synthesis to define the stability robustness specifications that a controller must meet. Presently there are three important sources of modeling errors:

- inaccurate Finite Element Model
- model reduction
- input/output decoupling

Finite Element Model Preliminary model evaluation [16] revealed several significant differences between the Finite Element Model and the real system. This is illustrated by Figure (9) and Figure (8) which compare the piston response of one of the mirror segments submitted to a piston command predicted by the Finite Element Model to the actual response. The modal frequencies of the lowest frequency modes are known to no better than 10%. Beyond 35 Hz, the Finite Element Model is totally unreliable, the predicted and actual responses being 180 degrees or more out of phase. Also, the response of the Finite Element Model rolls off beyond 30 Hz while the actual response does not. The magnitude of the relative input error is about 10 at 35 Hz. 60dB per decade of roll-off starting at 16 Hz are therefore needed to avoid spillover. We expect that 16 Hz is the maximum achievable control bandwidth.

Model reduction

Figure (10) shows the worst case input relative difference between the 28 mode model and the Finite Element Model. The worst case static error is 0 because exact static fidelity was recovered by adding a feedthrough term to the 28 mode model. The worst case errors are much smaller than the Finite Element modeling errors.

Input/output decoupling

Figure (11) shows the worst case relative difference between the 28 mode model and the 28 mode decoupled model. The decoupling errors are negligible compared to the Finite Element modeling errors.

CONTROL OBJECTIVES AND CONSTRAINTS

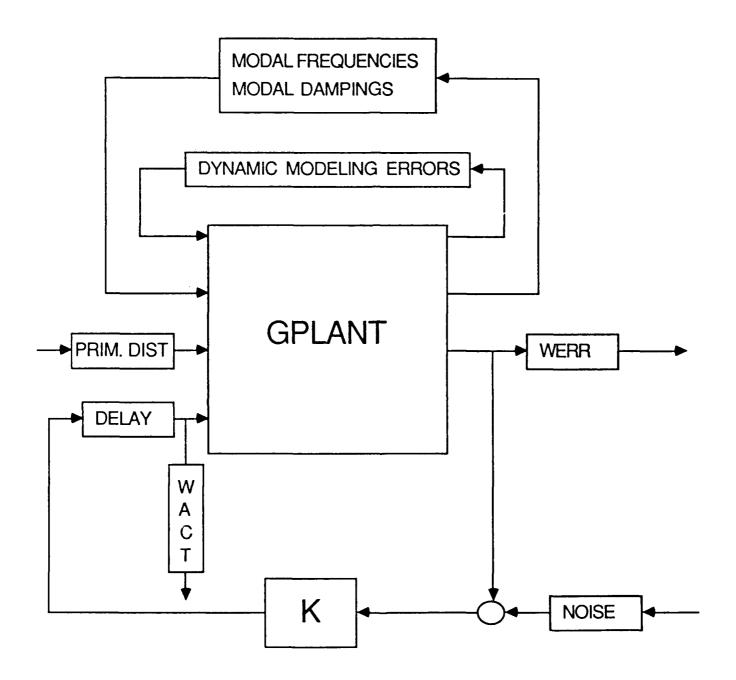


Figure 12: Summary of control design objectives and constraints

CONTROL OBJECTIVES AND CONSTRAINTS

Objectives

The segment alignment control system must achieve the optical quality of a single mirror in the segmented primary mirror. The expected segment piston errors are 50 nanometers and the expected tilt errors .1 arcseconds. The projected bandwidth is 16 Hz. Integral control action is needed to counteract the effects of gravity loads, thermal loads and quasi-static disturbances.

As the segment alignment bandwidth increases, the controls start exciting the resonant modes of the light-weight support structure. This control structure interaction may result in closed-loop instability. For satisfactory performance, the segment alignment requirements must therefore be coupled with modal vibration suppression requirements. In this respect, the objective is not to worsen the natural response of the system to disturbances outside the control bandwidth and if possible to damp out the natural vibration mode of the system.

In the laboratory, the air conditioning system is the main dynamic disturbance source. For ground telescopes, winds and secondary mirror motions would be the main sources. In this study, we have modeled the disturbances as 18 independent forces applied at 18 symmetrically and evenly distributed primary mirror nodes. Each force has a .1 Hz bandwidth. It can create a 1 mm mirror static displacement, equivalent to what we can expect from the gravity loads. Although quasi-static, the disturbance excites significantly all the mirror vibration modes, creating mirror displacements of the order of 10 μ m in the 15-30 Hz frequency range, equivalent to what we can expect from wind disturbances in ground telescopes [2]. The nominal performance objective is to bring the amplitude of the mirror displacements due to this theoretical disturbance below 100 nanometers at all frequencies.

Constraints

The controller must account for limited control authority and imperfect measurements:

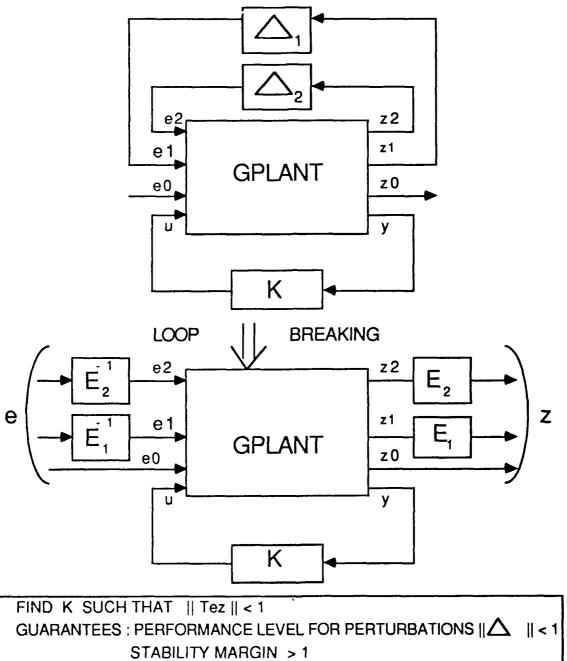
- The maximum available actuator force is 2 lbf. The actuators have a 140 Hz current loop bandwidth. Driven in current mode, they do not constrain the achievable control bandwidth.
- The sensors can measure displacements down to the 30 nanometers level up to 15 Hz.

The controller must satisfy strict robustness requirements:

- 10% stability margin with respect to modal frequency errors.
- 100% stability margin with respect to modal damping errors.
- 60 dB/decade of roll-off in the loop gain starting at 16 Hz to avoid spillover.

Finally the controller must account for any delay resulting from the digital implementation.

CONTROL DESIGN METHOD



STABILITY WARGIN > 1

Figure 13: H_{∞} robust control design methodology

CONTROL DESIGN METHOD

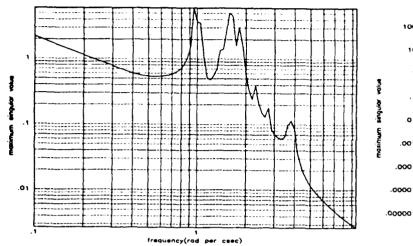
 H_{∞} design methods that trade performance, parameter stability margins, and spillover margins are used to synthesize the control laws which must provide form both integral control action to counter the effects of the gravity loads and low frequency disturbances, and for vibration suppression in 18 structural modes.

 H_{∞} design methods are fairly involved to put into practice. We have followed a progressive approach performing and analyzing a nominal performance design first, and introducing the stability requirements one after another. This approach gave us much insight into the nature of the performance/robust stability trade-offs. In particular, it demonstrated clearly that only the roll-off requirements significantly limit the achievable control bandwidth.

The designs were performed in the continuous time domain. The controllers were reduced using Safonov's balancing algorithm [12], and discretized using a Tustin transformation with prewarping at 140 rad/sec ($\sim 22 \text{ Hz}$).

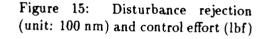
In the design process, we made several technical simplifications. The effect of the mirror surface deformations on the optical performance was not addressed directly, instead we required that the segments be individually oriented and positioned with a high degree of accuracy. Also, we replaced the 24 constrained physical edge sensor measurements by 18 unconstrained fictitious piston measurements of the mirror segments motion. The two sets of measurements are related by a geometrical transformation which, we checked, does not affect the control design.

SYNTHESIS RESULTS: 22 MODE SUBSYSTEM



100 TETT TO THE PROPERTY OF TH

Figure 14: Maximum open loop gain



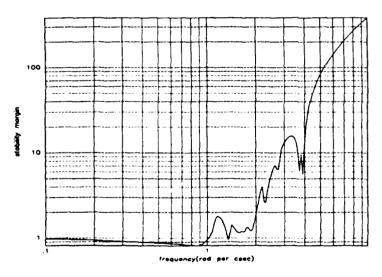


Figure 16: Stability margin to output plant multiplicative uncertainties

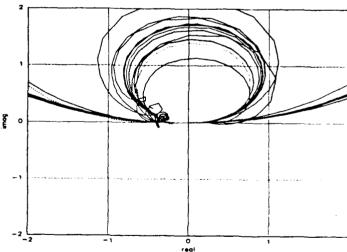


Figure 17: Stability margin to modal frequency errors

SYNTHESIS RESULTS: 22 MODE SUBSYSTEM

The control design for the 22 mode subsystem is most challenging. The subsystem contains two modes around 16 Hz which are 5 times more disturbable than controllable/observable. The lack of gain of the system at 16 Hz must be compensated by high controller gains to achieve the required disturbance attenuation. High gains in the cross-over region limit the achievable segment alignment bandwidth because of the need to get the proper phase margin to avoid instability. Both the theoretical and the experimental results concurred and showed that the control system is most sensitive at this frequency. In addition, the subsystem contains several modes laying outside the projected control bandwidth near the cross-over region which further complicates rolling off the loop gain.

Figure (14) shows the maximum open-loop gain of the controlled subsystem. The controller combines a 3 Hz bandwidth integral action for segment alignment with high gains in the 15-17 Hz and 20-30 Hz frequency bands for vibration suppression.

Figure (15) shows the open and closed loop responses of the subsystem to the theoretical disturbance used in the design (top curves), and the actuator authority needed to achieve the above disturbance attenuation (bottom curve). Up to 10 dB of vibration attenuation is achieved. Some disturbance amplification can be noticed in the 3-10 Hz frequency region.

Figure (16) shows the stability margin of the closed loop system to dynamic output plant multiplicative uncertainties. The loop gain rolls off at 60 dB per decade starting at 30 Hz. The minimum stability margin, .8 around 14 Hz, shows that any loop gain variation less than 80%, in any one or multiple channels at the output of the plant would not cause instability.

Figure (17) shows the stability margin of the closed loop system to individual modal frequency errors. Each curve is a Nyquist plot with respect to a modal frequency parameter. The parameters have been normalized so that whenever the Nyquist plot only crosses the real axis between +1 and -1, the stability margin is at least 10%. The figure shows that we have more than 10% stability margin in each modal frequency error, the worst margin, obtained for the first mode, being 20%.

The stability margin to simultaneous modal damping variations, not shown, is larger than 100%.

SYNTHESIS RESULTS: 6 MODE SUBSYSTEM

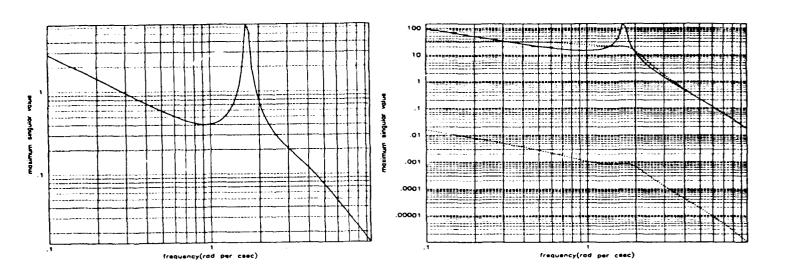
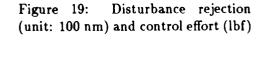


Figure 18: Maximum open loop gain



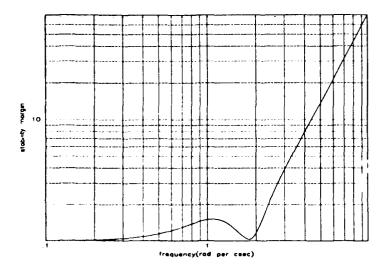


Figure 20: Stability margin to output plant multiplicative uncertainties

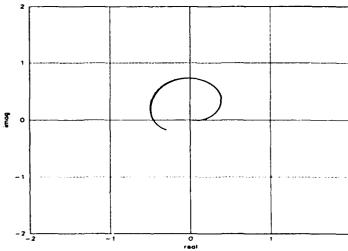


Figure 21: Stability margin to modal frequency errors

SYNTHESIS RESULTS: 6 MODE SUBSYSTEM

In contrast to the previous subsystem design, the control synthesis for the 6 mode, 6 input, 6 output subsystem is trivial: the subsystem is almost equivalent to 6 uncoupled oscillators. No mode lay in the 30-50 Hz frequency range to complicate the roll-off of the loop gain. The achievable control bandwidth is only limited by the roll-off requirements.

Figure (18) shows the maximum open-loop gain of the controlled subsystem. The controller combines a 5 Hz bandwidth integral action for segment alignment with high gains in the 20-30 Hz frequency range for vibration suppression.

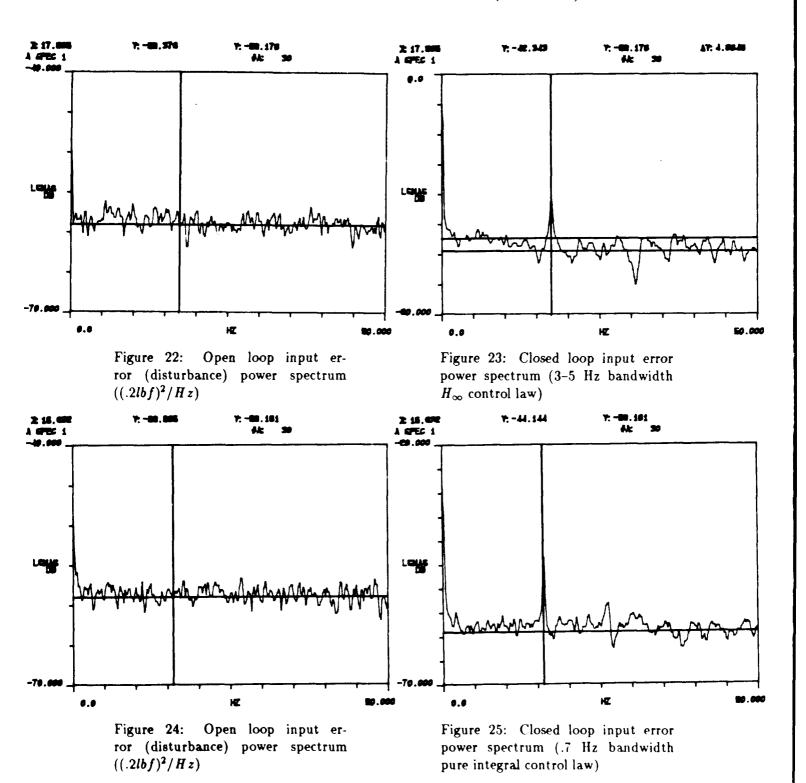
Figure (19) shows the open and closed loop responses of the subsystem to the design theoretical disturbance (top curves), and the actuator authority needed to achieve the above disturbance attenuation (bottom curve). Up to 20 dB of vibration attenuation is achieved. Some disturbance amplification can be noticed in the 6-20 Hz frequency region.

Figure (20) shows the stability margin of the closed loop system to dynamic output plant multiplicative uncertainties. The loop gain rolls off at 40 dB per decade starting at 30 Hz. Any loop gain variation less than 100%, in any one or multiple channels at the output of the plant would not cause instability.

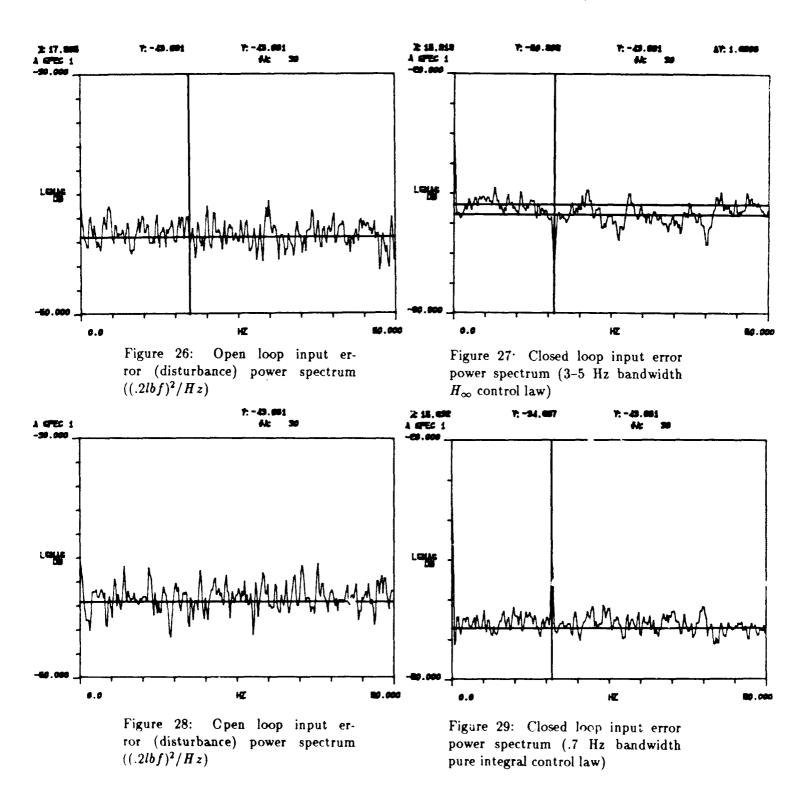
Figure (21) shows the stability margin of the closed loop system to individual modal frequency errors. We have achieved more than 20% stability margin in each modal frequency error.

The stability margin to simultaneous modal damping variations, not shown, is larger than 100%.

CSI EXPERIMENTAL RESULTS (MODE 1)



CSI EXPERIMENTAL RESULTS (MODE 2)



CSI EXPERIMENTAL RESULTS (MODE 17)

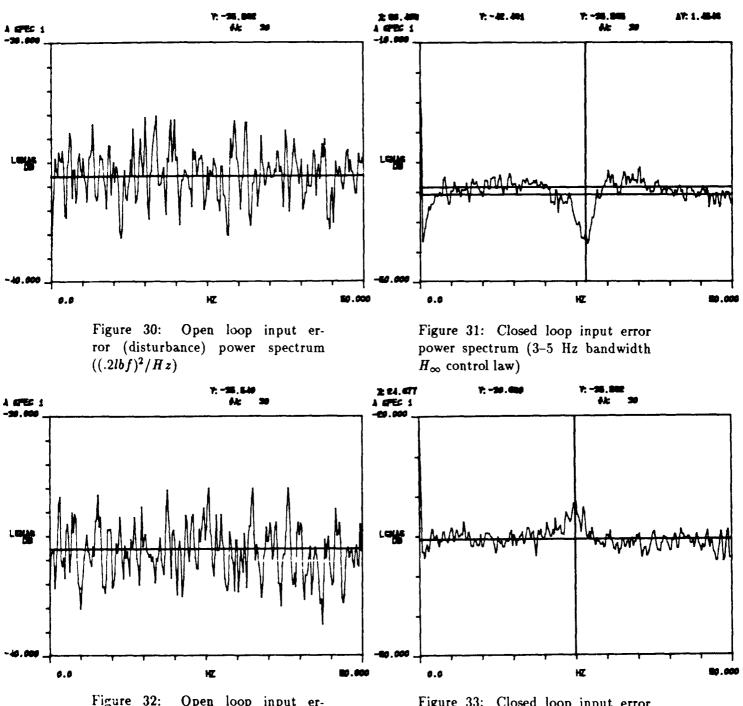


Figure 32: Open loop input error (disturbance) power spectrum $((.2lbf)^2/Hz)$

Figure 33: Closed loop input error power spectrum (.7 Hz bandwidth pure integral control law)

CSI EXPERIMENTAL RESULTS

In the CSI series of tests, we extracted the mode shapes of the first 28 modes from the Finite Element Model and forced white noise through each of them into the actuators. The evaluation was performed by comparing the open and closed loop power spectra of one of the ASCIE actuator input errors. The modes tested have frequencies in the 15 to 30 Hz range. The results show the attenuation or the amplification of dynamic input disturbances and demonstrate how well we were able to solve the Controls/Structures Interaction problem.

The results in the three modal input directions corresponding to mode 1 (15 Hz), mode 2 (16 Hz) and mode 17 (27 Hz) are reported and compared to those obtained for a .7 Hz segment alignment bandwidth pure integral control law (Figure (22-33)).

The first modal test reveals that the closed loop system is sensitive at 15 Hz (Figure (23)), the frequency of the fundamental mode. In fact the controlled system would be unstable for a 4 Hz segment alignment bandwidth in the 22 mode subsystem. The theoretical design evaluation shows that the design is most sensitive around 15 Hz, but does not explain the observed sensitivity. An erroneous position of the system zeroes (Figure (8)) which alternate very closely with the system poles around 15 Hz may explain the experimental results, but this will have to be confirmed by experimental model verification.

The H_{∞} control law shows 4 dB of disturbance amplification (Figure (23)) in the 5-10 Hz frequency region which is consistent with the analytical results (Figure (15)).

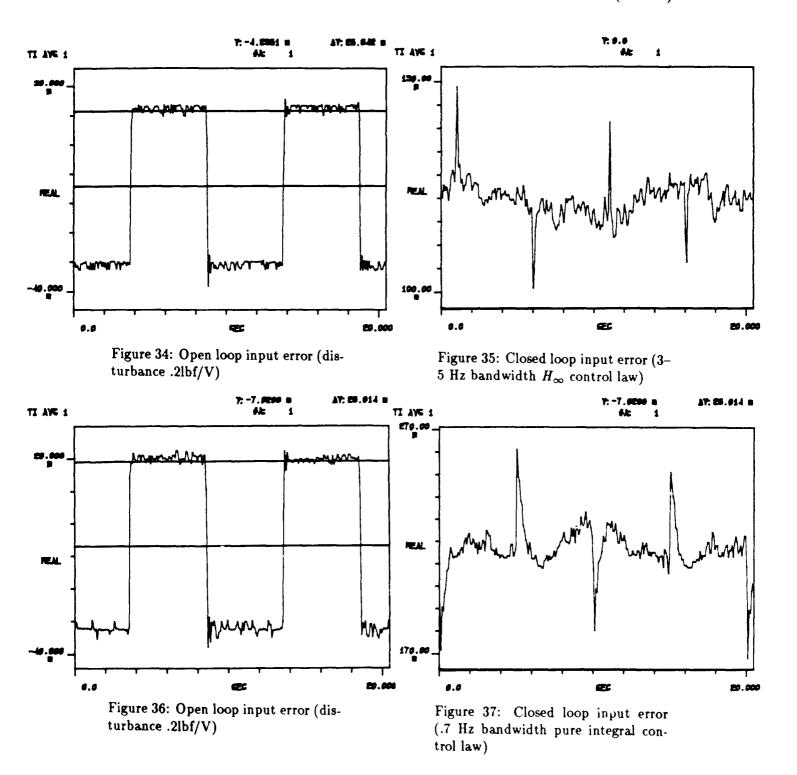
The H_{∞} control law and the pure integral control law show comparable control structure interaction for this first test, however the former has 5 times more bandwidth.

The second modal test (Figure (26-29)) shows that the H_{∞} control law achieves 10 dB of disturbance attenuation in the second mode shape input direction, while the pure integral control law amplifies the disturbances by 10 dB.

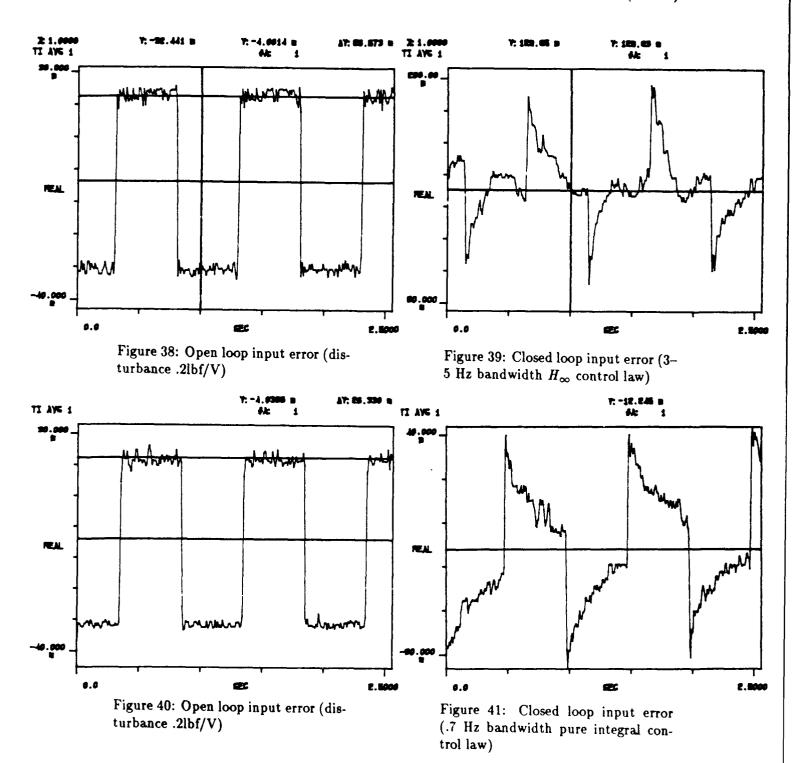
The seventeenth modal test (Figure (30-33)) shows that the H_{∞} control law achieves 10 dB of disturbance attenuation in the seventeenth mode shape input direction, while the pure integral control law amplifies the disturbance by a few dB.

The whole series of tests revealed that disturbance attenuation was achieved in 23 out of the 28 modes tested, the attenuation going from a few dB to 15 dB.

SEGMENT ALIGNMENT BANDWIDTH TEST RESULTS (.1 HZ)



SEGMENT ALIGNMENT BANDWIDTH TEST RESULTS (1 HZ)



SEGMENT ALIGNMENT BANDWIDTH TEST RESULTS

In the segment alignment bandwidth series of tests, we extracted the mode shape of some of the modes from the Finite Element Model and forced square waves through each of them into the actuators. The evaluation was performed by comparing the open and closed loop time and spectral responses of ones of the ASCIE actuator input errors. The tests show how well the control system rejects input step disturbances. They also give valuable information on the control bandwidth.

The time responses to .1 Hz and 1 Hz square waves in the modal direction corresponding to mode 17 are reported and compared to those obtained for a .7 Hz segment alignment bandwidth pure integral control law (Figure (34-41)).

Figure (34-37) show that the H_{∞} control law rejects the steps much faster than the pure integral control law does, as expected. The low frequency component of the closed loop responses correspond to the actuator command needed to reject the output disturbances. Without the controller, these disturbances would have caused a 15 to 25 μ m mirror segment piston misalignments (100 μ m/V in Figure (35,37)). The piston misalignments recorded during the test were only about 200 nanometers. This explains a posteriori why segmented optics need to be actively controlled to meet optical performance requirements.

The 1 Hz results (Figure (38-41)) show that the integral control law cannot fully reject the steps in .5 seconds while the H_{∞} control law needs less than half this time to perform the rejection. The H_{∞} control bandwidth is therefore larger than 4 Hz.

CONCLUSION

We have demonstrated the H_{∞} control design methodology on a very difficult structural control experiment: the ASCIE segmented optics test bed. We have increased the segment alignment bandwidth by a factor 5 to 7 over the maximum achievable bandwidth using a pure integral control strategy while solving most of the Controls/Structures Interaction problem. The results are supported by experimental data.

Most important, the control laws were obtained using only a mathematical model of the system which, we know, is very inaccurate. This demonstrates the potential of H_{∞} as a robust control design methodology.

Future, near term work will focus on eliminating the remaining Controls/Structures Interaction and increasing further the control bandwidth. We expect model verification to be an important part of this effort.

References

- [1] Swanson P., Gulkis S., Kuiper T. and Kiya M., 'Large Deployable Reflector (LDR): A Concept For An Orbiting Submillimeter-Infrared Telescope For The 1990s', Opt. Eng., Vol. 22, pp. 725-731, 1983.
- [2] Aubrun J., Lorell K., Havas T., Henninger W., "An Analysis Of The Segment Alignment Control System For The W. M. Keck Observatory Ten Meter Telescope", Keck Observatory report No 143, 1985.
- [3] Zames G., 'Feedback And Optimal Sensitivity: Model Reference Transformations, Multiplicative Seminorms, And Approximate Inverses', IEEE Trans. Aut. Contr., Vol. AC-26, April 1981.
- [4] Doyle J., 'Analysis Of Feedback Systems With Structured Uncertainties', IEE Proceedings, Vol 129, Part D, No 6, pp242-250, Nov 1982.
- [5] Glover K., Doyle J. 'State-Space Formulae For All Stabilizing Controllers That Satisfy An H_{∞} Norm Bound And Relations To Risk Sensitivity', Systems Control Letters, Sept. 1988.
- [6] Doyle J., Lenz K., Packard A., 'Design Examples Using μ-Synthesis: Space Shuttle Lateral Axis FCS During Reentry', IEEE Conf. Dec. Control, Dec. 1986.
- [7] Yue A., Postlethwaite I., ${}^{\prime}H_{\infty}$ -Optimal Design For Helicopter Control', Proceedings Amer. Control Conf., pp1679-1684, June 1988.
- [8] Safonov M., Chiang R., Flashner H., ${}^{\prime}H_{\infty}$ Robust Control Synthesis For A Large Space Structure', Proceedings Amer. Control Conf., pp2038-2045, June 1988.
- [9] Carrier A., 'Modeling And Shape Control Of A Segmented-Mirror Telescope', Stanford University PhD thesis, March 1990
- [10] Lorell K., Aubrun J.N., 'The Advanced Structures/Controls Integrated Experiment (Ascie): A Control Technology Test Bed For Large Segmented Reflectors', Proceedings of the SPIE Conference, 1990.
- [11] Lorell K., Aubrun J.-N., Zacharie D., Perez E., 'Development Of A Precision, Wide-Dynamic-Range Actuator For Use In Active Optical Systems', Proc. 23rd Aerospace Mechanisms Symposium, pp. 139-156, 1989.
- [12] Safonov M., Chiang R., 'A Schur Method For Balanced-Truncation Model Reduction', IEEE Trans. Aut. Contr., Vol. AC-34, No 7, July 1989.
- [13] Moore B. C., 'Principal Component Analysis In Linear Systems: Controllability/Observability And Model Reduction', IEEE Trans. Aut. Control, A.C. 26, No 1, Feb. 1981.

- [14] Gregory C., 'Reduction Of Large Flexible Spacecraft Models Using Internal Balancing Theory', Journal of Guidance and Control, Vol. 17, No 6, 1984.
- [15] Havas T., 'ASTRO Program Manual, Version I', Lockheed Missiles and Space Co. Inc., LMSC-DO51785, 1978.
- [16] Parsons E., 'Identification Of A Precision Segmented Reflector', Proceedings of the American Control Conference, 1990.

ASTREX CONTROLLER DESIGN: OVC AND OCC APPROACH

J. Ramakrishnan* and K.W. Byun*

R. Skelton[†]

Lt. D.F. Cossey

Abstract:

Controllers are designed for the Advanced Space Structures Technology Research Experiments (ASTREX) facility to minimize the control energy while satisfying inequality pointing constraints on the line-of-sight (LOS) outputs. The ASTREX facility consists of the test article (with primary, secondary, and tertiary substructures and mirrors) mounted on the air bearing of the supporting pedestal. The L_2 and L_∞ output constraint and the output correlation constraint (OCC) algorithms are applied to the reduced-order design model of ASTREX. The controllers are evaluated using the full order ASTREX evaluation model.

I. Introduction:

ASTREX was developed to provide the hardware for testing and validating emerging space structures technology. ASTREX has the desirable features of large precision structures laboratory namely three axis slew capability, three dimensional realistic mission representative test article, ability to change key structural members and add/delete sensors and actuators as desired together with a fully programmable real-time controller. The control objective for these precision structures is to maintain the root-mean-square (RMS) values of the LOS outputs within a prescribed set of limits. The hardware provides a test bed to verify the controller performance.

Similar variance constraint problems occur in many industrial processes and flexible structure systems design [1-3]. Toivonen [3] presented a self-tuning regulator for a variance constrained optimal control problem. The self-tuning regulator uses on-line identification followed by the computation of the optimal variance constrained strategy at each step. Makila et.al. [4], [5], and Toivonen [6] address extensions to the linear quadratic

mal or suboptimal full order self tuning and single step controllers. Newton's methods for solving parametric LQ control problems were also considered. Kalaba and Springarns [7] studied equality energy constraints for time varying finite interval systems leading to a large number of two point boundary value equations to be solved. In this work, the OVC approach of Skelton [8] and his co-workers [9] is used. The motivation for this approach is a consequence of the characterization of the requirements of the typical large space structure control problem. Performance requirements are stated in terms of RMS values of critical outputs rather than in terms of desired closed loop pole locations or LQ weighting matrices. The OVC approach shows the procedure for iterative weight selection is an LQ problem to solve another problem: a nonlinear mathematical programming problem with inequality constraints. The minimization of a quadratic function of the control vector subject to multiple inequality constraints on the output L_2 norms. L_{∞} norms, covariance matrix and maximum singular value of the output covariance matrix is addressed.

Gaussian (LQG) procedures such as algorithms for opti-

The paper is organized in the following fashion: Section II provides an overview of the OVC problem. The L_2 constraint problem and the L_∞ constraint problem are described. The output correlation constraint (OCC) method is described in section III. Section IV goes into details of the ASTREX hardware. Section V deals with the finite element and state space model of ASTREX. The controller design results are detailed in section VI. Finally the study highlights and conclusions are presented.

II. OVC Theory:

The OVC problem seeks to design a controller that minimizes input energy subject to inequality constraints on the output variances. The OVC theory is reviewed here for the state of completeness.

Consider the following time-invariant, stabilizable

^{*}Dynacs Engineering Co., Inc.

Purdue University

AFAL, Edwards AFB

and detectable continuous system state space model:

$$\dot{x}_p = A_p x_p + B_p u + D_p w_p
y = C_p x_p
z = M_p x_p + v_p$$
(1)

where $x_p \in R^{n_x}$, $y \in R^{n_y}$, $z \in R^{n_z}$, $u \in R^{n_z}$ are the state, output, measurement and control vectors respectively. The disturbance vector $w \in R^{n_w}$ is a zero mean white noise process with intensity $E\left\{w_p(t)w_p^*(\tau)\right\} = W_p\delta(t-\tau)$ while the measurement noise v_p has a intensity $V_p\delta(t-\tau)$. The objective is to design a full order controller

$$u = Gx_c$$

$$\dot{x}_c = A_cx_c + Fz \tag{2}$$

which minimizes the control energy

$$J = E_{\infty}(u^T R u)$$

$$= tr RG E_{\infty} x_c x_c^T G^T$$

$$= tr RG X_c G^T$$
(3)

subject to (1), (2) and satisfies the output inequality constraints

$$E_{\infty} y_i^2(t) \le \sigma_i^2 \quad i = 1, 2, \dots, n_y \tag{4}$$

Defining a new state vector x as

$$x = \begin{bmatrix} (x_p - x_c)^T & x_c^T \end{bmatrix}^T$$
 (5)

equations (1) and (2) can be written as

$$\dot{x} = Ax + Dw \tag{6}$$

$$y = Cx \tag{7}$$

where

$$A = \begin{bmatrix} A_p - FM_p & A_p - FM_p + B_pG - A_c \\ FM_p & A_c + FM_p \end{bmatrix}$$

$$D = \begin{bmatrix} D_p & -F \\ O & F \end{bmatrix}$$

$$C = [C_p C_p]$$

$$u = [0 G] x$$

$$w = \begin{bmatrix} w_p \\ v_p \end{bmatrix}$$
(8)

The state covariance matrix of the system (6) becomes

$$X \triangleq E_{\infty}(xx^*) = \begin{bmatrix} P & X_{12} \\ X_{12}^T & X_c \end{bmatrix}$$
 (9)

and the state covariance of the plant (1) becomes

$$X_p = P + X_c \tag{10}$$

where P is the error covariance matrix and

$$W = \begin{bmatrix} W_p & 0 \\ 0 & V_n \end{bmatrix} \tag{11}$$

The OVC problem can now be expressed as an equivalent nonlinear programming problem (NLP):

Given
$$\Omega \triangleq \text{admissible of } (X, G)$$

$$= \begin{cases} (X, G) & | AX + XA^T + DWD^T = 0 \\ [C_p X_p C_p^T]_{ii} \leq \sigma_i^2 \\ i = 1, 2, \dots, n_y \\ X > 0 \end{cases}$$

find $X, G \in \Omega$ minimizing

$$J = tr RGX_cG^T$$
 (12)

Let

$$\Delta_{ij} = [AX + XA^T + DWD^T]_{ij}$$

$$T_i = [C_p X_p C_p^T]_{ii}$$
(13)

then the augmented cost function can be written as

$$\dot{J} = trRGX_cG^T + \sum_{i,j}^{(n_x + n_x)} K_{ji}\Delta_{ij} + \sum_{i=1}^{n_y} q_i(T_i - \sigma_i^2)
= J + trK\Delta + trQ[C_pX_pC_p^T - \Psi]$$

where

$$K = \begin{bmatrix} \bar{K} & K_{12} \\ K_{12}^T & K_c \end{bmatrix} = \text{Lagrange multipliers}$$

$$Q \triangleq diag[q_1, q_2, \dots, q_{n_y}] = \text{Lagrange multipliers}$$

$$\Psi \triangleq diag[\sigma_1^2, \sigma_2^2, \dots, \sigma_{n_y}^2]$$
(14)

The necessary conditions for a minimum are

$$\frac{\partial \dot{J}}{\partial X} = 0$$

$$\frac{\partial \dot{J}}{\partial K_{ji}} = 0 \quad \text{for all } i, j$$

$$\frac{\partial \dot{J}}{\partial G} = 0$$

$$\frac{\partial \dot{J}}{\partial A_{c}} = 0$$

$$\frac{\partial \dot{J}}{\partial F} = 0$$

$$q_{i} \geq 0, \quad q_{i}(T_{i} - \sigma_{i}^{2}) = 0$$
(15)

where the inequality variance constraint is handled via Kuhn-Tucker conditions. The solution of the necessary conditions results in the following algorithm.

OVC Algorithm:

Given data $\{A_p, B_p, C_p, D_p, M_p, W_p, V_p, Q_o, R, \sigma_i, \epsilon_i, n\}$ where $Q_o > 0$ is a diagonal matrix

Step 1: Compute the Filter gains F

$$0 = PA_{p}^{T} + A_{p}P - PM_{p}^{T}V_{p}^{-1}M_{p}P + D_{p}W_{p}D_{p}^{T}$$

$$F = PM_{p}^{T}V_{p}^{-1}$$
(16)

Step 2: Compute the maximal accuracy solution

$$y_i^2 \text{ (Max. Accuracy)} = \left[C_p P C_p^T\right]_{ii}$$
 (17)

If $\sigma_i^2 < [C_p P C_p^T]_{ii}$ for any i, STOP.

go to step 3.

Step 3: Compute the controller gains

$$0 = \tilde{K}A_{p} + A_{p}^{T}\tilde{K} - \tilde{K}B_{p}R^{-1}B_{p}^{T}\tilde{K} + C_{p}^{T}Q_{k}C_{p}$$

$$G = -R^{-1}B_{p}^{T}\tilde{K}$$
 (18)

Solve the controller covariance equation

$$0 = X_c (A + BG)^T + (A + BG)X_c + FVF^T$$
 (19)

Compute the output variance

$$(y_{i_{RMS}})^2 = [C_p(P + X_c)C_p^T]_{ii} = [C_pX_pC_p^T]_{ii}$$
 (20)

Step 4: Verify the convergence condition

$$[y_{i_{RMS}}^2 - \sigma_i^2]Q_{ii} \le \epsilon_i$$
 for all i STOP

Else

Update Q_k

$$Q_{k+1} = \left[\begin{array}{c} \frac{y_{i_{RMS}}^2}{\sigma^2} \end{array} \right]^n Q_k \tag{21}$$

and return to step 3.

The necessary condition for the OVC problem is the same as that of the LQ class of problems with some diagonal output weighting matrix that is iteratively updated. From equation (21), it turns out that if $E_{\infty}y_{\alpha}^2(t) < \sigma_{\alpha}^2$, then the corresponding weighting q_{α} is 0. Physically this means that this particular output $y_{\alpha}(t)$ is not critical to the design and the constraint $T_{\alpha} \leq \sigma_{\alpha}^2$ is not necessary. It is, of course, not known a priori which constraints will be binding, and so all constraints must be stated in the problem. More details on the OVC method can be found in reference [9]. While there is no convergence proof for the algorithm, experience shows that the algorithm will converge if the tuning parameter n is sufficiently small.

Deterministic L_2 and L_{∞} Interpretations:

A deterministic interpretation of the OVC controller can be obtained from the Linear Quadratic Impulse (LQI) theory. If the set of r excitations include impulsive inputs $w_p(t) = W_i\delta(t), v_p(t) = V_i\delta(t)$ of strengths W_i and V_i that are applied one at a time, then the deterministic cost index can be expressed as

$$J = \sum_{i=1}^{r} \int_{\sigma}^{\infty} u^{T}(i,t)Ru(i,t)dt \qquad (22)$$

$$r = n_{z} + n_{w}$$

The output L_2 constraint for continuous system (OL_2) is cast as

$$\min_{A_c,F,G} J = \sum_{i=1}^r \int_o^\infty u^T(i,t) Ru(i,t) dt$$

subject to (1), (2), and

$$y_{\alpha_{RMS}} \stackrel{\triangle}{=} \left[\sum_{i=1}^{r} \int_{\sigma}^{\infty} y_{\alpha}^{2}(i,t)dt \right]^{1/2}$$

$$\leq \sigma_{\alpha}, \alpha = 1, 2, \dots, n_{y}$$
(23)

The algorithm is identical to the stochastic version of the OVC problem listed in equations (16) - (21).

The OL_2 controller has the following L_{∞} property ($|[\cdot]|$ denotes absolute value of $[\cdot]$),

$$||y_{\alpha}(\cdot)||_{\infty} \stackrel{\triangle}{=} \max_{t>0} |y_{\alpha}(t)|$$

 $< \epsilon_{\alpha} \quad \alpha = 1, 2, ..., y$

where $\epsilon_{\alpha}=\sigma_{\alpha}\mu$ for any disturbance satisfying the L_2 constraint,

$$\| \begin{bmatrix} w_p^T(t) & v_p^T(t) \end{bmatrix} \|_2^2 \stackrel{\triangle}{=} L_2$$
 norm of noise

$$\triangleq \int_{o}^{\infty} \left[w_{p}^{T}(t) \ v_{p}^{T}(t) \right] \left[\begin{array}{cc} W_{p} & 0 \\ 0 & V_{p} \end{array} \right]^{-1} \left[\begin{array}{cc} w_{p}(t) \\ v_{p}(t) \end{array} \right] dt \leq \mu^{2}$$
(24)

The importance of these properties stems from physical system requirements. The L_2 constraints are soft constraints such as RMS pointing accuracies for the n_y different output channels. The L_∞ constraints, on the other hand, are hard constraints and limit the signal range such that saturation limits are satisfied. This becomes critical to prevent burnout in actuators and sensors and keep them working in the linear range. The Lemmas pertaining to the output L_∞ constraints are now stated:

Lemma 1:

For the asymptotically stable closed-loop system, the output time correlation matrix is

$$Y = \sum_{i=1}^{r} \int_{o}^{\infty} y(i,t)y^{T}(i,t)dt$$
$$= CXC = C_{p}X_{p}C_{p}^{T}$$

where X is the state correlation

$$X \triangleq \sum_{i=1}^{r} \int_{o}^{\infty} x(i,t) x^{T}(i,t) dt$$

satisfying (with $r = n_w + n_z$)

$$0 = XA^T + AX + DWD^T$$

Let $w(\cdot)$ in equation (8) be any L_2 disturbance

$$\|w(\cdot)\|_2^2 \stackrel{\triangle}{=} \int_0^\infty \omega^T(t) W^{-1} w(t) dt = \mu^2$$

Then the square of the L_{∞} norm of $y(\cdot)$ satisfies

$$||y(\cdot)||_{\infty}^{2} \stackrel{\triangle}{=} \max_{y>0} y^{T}(t)y(t) \le \bar{\sigma}(Y) ||w(\cdot)||_{2}^{2}$$
 (25)

A proof of Lemma 1 is available in [10]

Lemma 2:

The bound given by (24) can be written in the following form

$$\tilde{\sigma}[Y] = \sup_{\||w(\cdot)\|_2^2 = \mu^2} \frac{\||y(\cdot)\|_{\infty}^2}{\mu^2}$$
 (26)

Equation (25) can be applied to each output $y_i(i = 1, 2, ..., n_y)$.

$$C_i X_p C_i^T = \bar{\sigma}(C_i X_p C_i^T) \ge \frac{|y_i(\cdot)|_{\infty}^2}{||w(\cdot)||_2^2}$$
 (27)

where C_i is the i^{th} row vector of the C_p matrix. By Lemma 2, we also have

$$C_{i}X_{p}C_{i}^{T} = \sup_{\||w(\cdot)\|_{0}^{2} = \mu^{2}} \frac{|y_{i}(\cdot)|_{\infty}^{2}}{\mu^{2}}$$
 (28)

Define

$$\epsilon_i^2 \stackrel{\triangle}{=} \sup_{\||\boldsymbol{w}(\cdot)\|_2^2 \le \mu^2} ||\boldsymbol{y}(\cdot)||_{\infty}^2$$
$$i = 1, 2, \dots, n_{\eta}$$
 (29)

$$\sigma_i^2 \stackrel{\triangle}{=} \frac{\epsilon_i^2}{\mu^2} \tag{30}$$

Then solving the OL_{∞} problem

$$|y_i(\cdot)|^2_{\infty} \le \epsilon_i^2 \quad i = 1, 2, \dots, n_y$$

is equivalent to solving the OL_2 problem

$$C_{i}X_{p}C_{i}^{T} \leq \sigma_{i}^{2}$$

where σ_i^2 is given in equation (30). The OVC algorithm is used to solve the L_{∞} problem with σ_i^2 as defined in equation (30). Although the above lemmas are based on LQI theory where the noise applies one at a time, the lemmas also apply to the case where the noises with bounded L_2 -norm apply simultaneously.

III. OCC Problem:

The output time correlation matrix Y defined in Lemma 1 is related to system robustness issues. The determination of an assignable matrix Y satisfying the desirable system properties is an open problem. The output time correlation constraint approach, however, can be used to determine controller such that a given upper bound on matrix \bar{Y} (which is not necessarily assignable) is satisfied using minimum control energy.

The OCC control problem is

$$\min_{A_{\epsilon}, F, G} \sum_{k=1}^{r} \int_{o}^{\infty} u^{T}(k, t) Ru(k, t) dt$$

subject to (1), (2) and the output time correlation constraints

$$Y = \sum_{k=1}^{n} \int_{0}^{\infty} y(k,t) y^{T}(k,t) dt \le \bar{Y}$$
 (31)

Consider the case where \bar{Y} is given by

$$\bar{Y} = \sigma I \tag{32}$$

Then constraint (31) is equivalent to the constraint

$$\bar{\sigma}(Y) = \rho(Y) \le \sigma \tag{33}$$

where $\bar{\sigma}(\cdot)$ and $\rho(\cdot)$ denote the maximum singular value and the spectral radius of (\cdot) .

Some robustness properties can be described in terms of the largest singular value of Y and the constraint (31) plays an important role in designing a robust controller Constraint (33) can be generalized to constraint (31) in order to include different weightings in the selected output coordinates. The Cholesky decomposition of Y as $\overline{Y} = LL^T$ yields the relation

$$L^{-1}YL^{-T} \leq I \tag{34}$$

or

$$\sigma(L^{-1}YL^{-T}) \le 1 \tag{35}$$

From equation (35), we have constraints on the correlation matrix of the transformed output $L^{-1}y$.

The OCC problem has a full Q matrix unlike the OVC problem but otherwise yields identical necessary conditions. The only step that is replaced in the CL_2 algorithm is step 4. The OCC algorithm uses the following:

Step 4:

$$Y_k = C_p X_k C_p^T$$
Else,
$$Q_{k+1} = \tilde{Y}^{-1} Y_k Q_k Y_k \tilde{Y}^{-1}$$
If $||(Y_k - \tilde{Y}) Q_k|| \le \in STOP$
Go to step 3

Convergence of the algorithm implies that the column vector of Q matrix will be in the null space of $Y-\bar{Y}$, which satisfies the Kuhn-Tucker condition for the OCC problem.

IV. Modal Cost Analysis (MCA)

The evaluation model is reduced to Riccati solvable dimensions by the MCA method. The reduced order model is called the design model. The controller is designed based on this model. The contribution of the mode i to the scalar cost function is called "modal cost." Modes are truncated such that the design model retains a percentage of the cost of the evaluation model.

Consider the system in modal coordinates

$$\dot{\eta}_i = \lambda_i \eta_i + b_i^* u \qquad i = 1, \dots, n_x U_{\sigma}(t) = \mu_{\sigma} \delta(t)$$

$$y = \sum_{i=1}^{n_x} C_i \eta_i \qquad \eta_i(0) = 0$$

with the scalar cost function is

$$V = \sum_{t=0}^{n_{\bullet}} \int_{2}^{\infty} y^{\alpha^{\bullet}}(t)Qy^{\alpha}(t)dt$$

where $y^{\alpha}(t)$ is the response to $u_{\alpha}(t) = \mu_{\alpha}\delta(t)$. For the modal coordinate η_i , the modal cost is given by

$$V_{n_{1}} = [X_{m} C_{m}^{*} Q C_{m}]$$

where

$$0 = X_m A_m^* + A_m X_m + E_m \mathcal{U} B_m^*$$

$$\mathcal{U} = diag \begin{bmatrix} \mu_1^2 & & \\ & \ddots & \\ & & \mu_{nu}^2 \end{bmatrix}$$

and $A_m = diag[\dots \lambda_1 \dots]$ with B_m and C_m being corresponding modal input/output coefficient matrices. From the computational viewpoint, closed form solutions of the Lyapunov equation in modal coordinates

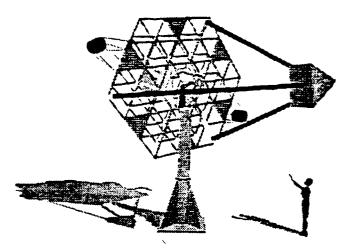


Figure 1: ASTREX Facility

are used. Furthermore, some of the calculations are carried out in the real Jordan form coordinates yielding the appropriate design model.

The controller design iterations use the integrated MCA-OVC formulation. The design model determined by MCA approach depends on the output weighting matrix Q, which reflects the importance of each output. The OVC approach iteratively determines the Q matrix that yields a controller satisfying output inequality constraints. So both the design model and the controller are influenced by the weighting matrix. Thus the model reduction procedure is influenced by the designed controller. The integrated procedure is implemented as follows. Based on an initial weighting matrix Q_o , MCA approach is used to design a reducid-order model which is followed by the OVC loop. The OVC loop yields a new Q matrix. This matrix Q is now used in the MCA procedure to design a new reduced order model. Controller design is repeated until the reduced-order model ceases to change. This approach is again referred to in section VII.

V. ASTREX Hardware Description:

The ASTREX facility consists of a pedestal with an air bearing system on which the test article is placed. The pedestal comprises of pneumatic components, electronics, power supplies and computer at its base and an air bearing with the cable follower and electronics at the other end as illustrated in Figure (1). The desired specifications of the air bearing system are:

- Load capacity 14,500 lbs
- ± 20° Pitch and Roll. ± 180° Yaw
- Measure attitude to within 1 arc second at rates up to 10°/sec and accelerations up to 10°/sec/sec.

• Cable follower to bring supply lines from "Ground" to test article; Crossover frequency of at least 5 Hz

The mirror mass simulator consists of a support truss with the primary mirror, secondary mirror and a termary mirror. The state space model is obtained from the finite element model of the pedestal and the test article. For the sake of ampletoness, the ASTREX pardware is summarized below:

ASTRIX Hardware-Summary

Facility: 10 ft. × 40 ft. × 40 ft. laboratory Overhead Grane, temperature control

Air Bearing: Spherical (3-Axis) Air Bearing, 19 inch ball, cable follower: Two gimbal - 3 axis mechanical arrangement Rigid Body Attitude Sensing - 1 arc sec acturacy

Computer: Real time Control and Data Acquisition Computer 32 Inputs, 32 Outputs, 1000 Hz + Sampling Rate 10-15 MFLC Parallel Processor based System

Structure: 3 Mirror Beam Expander, 1/3 - 1/2 Dynamically scaled structure, Modular Graphite Epoxy Construction

Sensors/Actuators: Throttleable Cold Gas Thrusters, upto 200 lb force

- · Proof Mass Actuators
- · Reaction Wheels
- Provision for Centrol Moment Gyros (CMGs)
- Accelerometers
- Optical Line of Sight Sensor

VI. ASTREX Models:

The ASTREX finite element model consists of the pedestal and test article models. The model is constructed using bar triangular and quadrilateral elements together with rigid connections. The pedestal and test article models are shown in Figures (2) and (3). The test article is connected to the pedestal via elastic elements. The air bearing cushion is modeled to support 8100 lbs with a 50 Hz stiffness.

The model has 2064 degrees of freedom (DOF) of which 1518 are associated with the test article. In addition to imposing specific constraints at some nodes, the city manic constraint generation facility of NASTRAN is used. The first eleven pedestal modes range in frequency from 37.7 Hz to 92.6 Hz while the test article's range from 3.06 Hz to 31.82 Hz. The combined model



Figure 2: ASTREX Pedestal (FE Model)

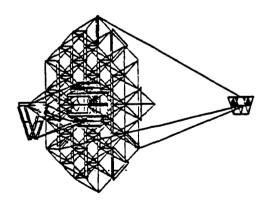
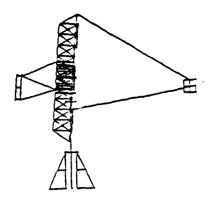
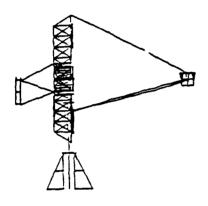


Figure 3: ASTREX Test Article (LE Model)



Mode: 3.78 Hz

Figure 4: System Eigenvector 3.78 Hz

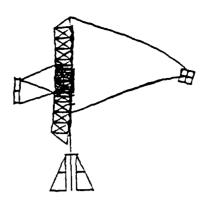


Mode: 9.95 Hz.

Figure 5: System Eigenvector 9.95 Hz

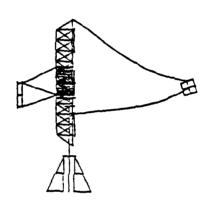
has frequencies starting from 3.78 Hz. The first four mode shapes of ASTREX are plotted in Figures (4) - (7). The reader is directed to references [11], [12] for more details.

The ASTREX state space model is synthesized using the NASTRAN generated system eigenvector matrix (2056 \times 40). The 40 modes range in frequency from 3.8 Hz to 90 Hz. A Rayleigh damping model with a low frequency damping of 0.2% to a high frequency damping of 5% was used. Four cold gas thrusters and four moment actuators were located on the primary mirror truss to provide actuation forces. The thrusters provide a maximum thrust of 200 lbs in the z direction. The actuator locations are shown in Figure (8). Twenty-four (24) accelerometer sensors are located on the primary, secondary and tertiary structures and on the structural interconnections between them. A simplified sketch of their locations is shown in Figure (9). The output matrix C (Line-of-Sight) (LOS)) is formulated by combin-



Mode: 11.66 Hz.

Figure 6: System Eigenvector 11.66 Hz



Mode: 13.98 Hz

Figure 7: System Eigenvector 13.98 Hz

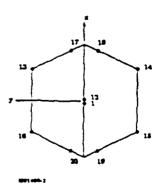


Figure 8: Actuator Locations

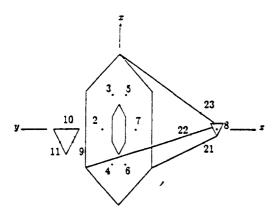


Figure 9: Sensor Locations

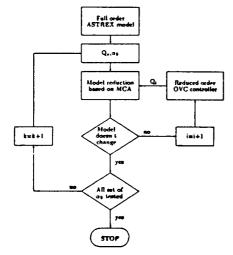


Figure 10: MCA-OVC Design Loop (α-study)

ing the optical sensitivity data (provided by Boeing) with various displacements at selected node locations on the primary, secondary and tertiary mirrors. This procedure is used to estimate the mirror motion for each of these three mirrors. The procedure of constructing the output matrix C has been detailed in [11]. The resulting state space model is:

$$\dot{x}_p = A_p x_p + B_p u + D_p w
y = C_p x_p
z = M_p x_p + H_p u$$

where $A_P \in \Re^{80 \times 80}$, $B_p \in \Re^{80 \times 8}$, $D_p \in \Re^{80 \times 8}$, $C_p \in \Re^{6 \times 80}$, $M_p \in \Re^{24 \times 80}$, $H_p \in \Re^{24 \times 8}$.

VII. ASTREX Controller Design

The MCA and OVC approaches are integrated to form a model and controller design loop. The procedure for the L_2 and L_∞ OVC controllers is referred to as the α -study. The α -study design loop is sketched in Figure (10) and consists of the following steps:

- 1. Given the plant and noise intensity matrices, define a set of feasible output variances σ_i^2 . The nominal output variances may be specified by the user. These variances must be larger than the maximal accuracy solution (17)
- 2 Using the given initial weighting matrices, a reduced-order design model is formed using the MCA approach.

$$\dot{x}_r = A_r x_r + B_r u + D_r w
y = C_r x_r
z = M_r x_r + H_r u + v$$

3. The given variances are tuned by scaling them by α

$$y_{RMS}^{i2} \leq \alpha \sigma_i^2 \quad i = 1, \dots, n_y$$

- 4. The OVC design loop is executed and iterations are performed till convergence is achieved. This gives us a converged controller for the current value of $\alpha = \alpha_1$. The appropriate LQ weighting matrices for this controller are also determined.
- 5. Using the updated weighting matrices, MCA is repeated to yield a new design model. The α parameter is changed and a set of OVC controllers are iterated on. The OVC loop converges to the controller corresponding to $\alpha = \alpha_2$. Steps 2, 3 and 4 are repeated till very high bandwidth controllers are designed. The variance curve asymptotically approaches the maximal accuracy solution.
- The reduced-order controllers thus designed are evaluated using the evaluation model. From the cost curve for the evaluation model, suitable set of controllers are selected.

The thrusters and CMGs as actuators for ASTREX control have actuator dynamics explained in the Appendix. The augmented open-loop system has 92 states, 8 controls, 16 process noises, 8 measurements. 8 sensor noises, and 24 controller outputs.

Noise intensity matrices of the augmented system are given by

$$W = diag \left[r_1^2 r_1^2 r_1^2 r_1^2 r_2^2 r_2^2 r_2^2 \right]$$

$$V = r_3^2 \times I_{24}$$

The values for r_1 , r_2 , r_3 are determined by the actuator and sensor performance and are given as

$$r_1 = 8.88 N$$
, $r_2 = 0.949 Nm$, $r_3 = 0.005 g$

where g is the gravity constant.

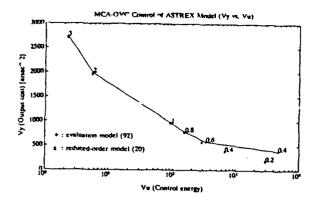


Figure 11: Output Cost V_y vs. Input Cost V_u

The desired output RMS values for the noise intensities are determined as

The a-study procedure is tested for

$$0.2 \le \alpha \le 16$$

For each α , iterative MCA and OVC process yields a 20^{th} -order design model and corresponding OVC controller (See Table 1). Figure (11) shows the plots of unweighted output cost V_y vs. input cost V_u . The dotted curve is the α -study curve for the design models while the solid curve is for the evaluation model with the reduced-order controllers. The result of the α -study indicates that the closed-loop systems for the design model and evaluation model behave like open-loop systems for large α . For small α (tighter specifications) the design model reaches to maximal accuracy solution while the evaluation model has minimum output cost around α =0.4 and becomes unstable for α =0.2.

Figures (12) and (13) show the plots of output variances vs. V_u and input variances vs. V_y for the evaluation model. Each output variance can be specified using Figure (12). If, for example, the variance of y_4 is to be bounded above by $2.3 \times 10^3 \, \mathrm{arcsec^2}$, then the α must be taken from the range $0.4 \le \alpha \le 3$. On the other hand, each control variance can be specified using Figure (13). For example the variances of the thruster and CMG inputs are to be bounded by $10^3 \, \mathrm{lb^2}$ and $30 \, (\mathrm{ft\text{-}lb})^2$, respectively, then the α must be taken from $\alpha \ge 0.6$. The set of controllers satisfying input and output constraints can be tested further for other closed-loop specifications.

In this paper, $\alpha = 0.6$ is chosen for the 20^{th} -order controller. MCA algorithm selects 10 modes with first

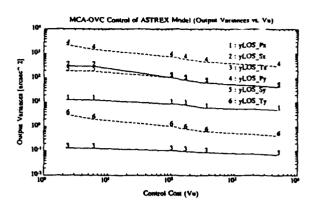


Figure 12: Output Variances vs. Input Cost Vu

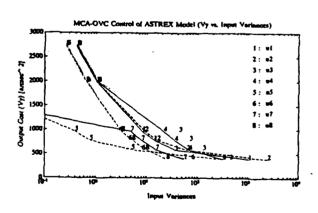


Figure 13: Output Cost vs. Input Variances

Table 1: Retained Modes in the Reduced Order Models

| α | 3 | 2 | 1 | 0.8 | 0.6 | 0.4 | 0.2 |
|----------|----|-----|-----|-----|-----|-----|-----|
| | 1 | l | 2 | 2 | 2 | 2 | 1 |
| | 4 | 4 | 1 | 1 | 1 | 1 | 2 |
| | 3 | 3 | 7 | 7 | 7 | 7 | 7 |
| | 17 | 17* | 4 | 4 | 4 | 4 | 4 |
| Retained | 8 | 8 | 3 | 3 | 10 | 10 | 10 |
| Modes | 18 | 18* | 6 | 6 | 3 | 3 | 3 |
| | 16 | 16* | 9* | 9 | 9 | 9 | 9 |
| | 6 | 6 | 22* | 22 | 6 | 6 | 6 |
| | 2 | 2 | 10- | 10 | 22 | 22 | 22 |
| | 7 | 7 | 8 | 8 | 8 | 8 | 8 |

^{*} The modes 17, 18 and 16 for $\alpha=2$ are replaced by the modes 9, 22, and 10 for $\alpha=1$.

10 highest output modal costs. The modes retained are

where the numbers identify the modes with ascending order of frequencies.

The 20^{th} order controller corresponding to $\alpha=0.6$ is tested on the evaluation model with pulse noises applied simultaneously. The duration of the pulses is 0.02 sec and the pulse amplitudes are given by

$$w_i = 62.79 \ N \ i = 1, ..., 4$$

 $w_i = 6.71 \ Nm \ i = 5, ..., 8$
 $v_i = 0 \ i = 1, ..., 24$

The weighted L_2 -norm of the noises is

$$\mu^2 = ||w(t)||_2^2 = 8$$

Guaranteed L_{∞} -norms of the LOS outputs and control inputs are computed as

$$||y_i(\cdot)||_{\infty}^2 = T_i \cdot \mu^2 \ (i = 1, ..., 6)$$

 $||u_j(\cdot)||_{\infty}^2 = S_j \cdot \mu^2 \ (j = 1, ..., 8)$

where T_i and S_j are the i^{th} output variance and the j^{th} input variance.

Table (1) and (2) list the input output variances and guaranteed L_{∞} -norm bounds. The tables also show the simulated L_{∞} -norms of the inputs and outputs. Figure (14) shows the time response plot of typical output. The guaranteed L_{∞} -norm bounds are shown to be satisfied, although the bounds are conservative for the given pulses.

OCC Controller

The α -study in this section can also include OCC controller instead of OVC controller. For comparison, the

Table 2: Input and Output Variances and l_{∞} -norms

| Output | Output | Guaranteed | Simulated |
|---------|------------------------|------------|-----------|
| i | Variances | Bounds | Bounds |
| | [arcsec ²] | [arcsec] | [arcsec] |
| ì | 5.77 | 6.79 | 0.44 |
| 2 | 61.66 | 22.21 | 1.11 |
| 3 | 0.09 | 0.83 | 0.03 |
| 4 | 449.26 | 59.95 | 1.49 |
| 5 | 62.29 | 22.32 | 2.87 |
| 6 | 0.61 | 2.21 | 0.08 |
| Control | Input | Upper | Simulated |
| i | Variances | Bounds | Bounds |
| | $[N^2]$ | [N] | [N] |
| 1 | 36.74 | 17.14 | 1.62 |
| 2 | 62.26 | 22.32 | 2.00 |
| 3 | 129.77 | 32.22 | 1.66 |
| 4 | 68.89 | 23.48 | 1.32 |
| 5 | 5.10 | 6.39 | 0.40 |
| 6 | 8.25 | 8.13 | 0.56 |
| 7 | 15.37 | 11.09 | 0.75 |
| 88 | 9.83 | 8.87 | 0.92 |

Table 3: Comparison of OVC and OCC Control Design

| Design Goal | | Output | Variances | Eigenvalues |
|----------------|--------------------|--------|-----------|------------------------|
| $[\sigma_i^2]$ | $diag[\sigma_i^2]$ | | | $\lambda_i(\bar{Y}-Y)$ |
| OVC | OCC | OVC | OCC | OCC |
| 5.40 | | 5.40 | 5.24 | 336.32 |
| 60.00 | | 60.00 | 57.62 | 17.25 |
| 0.60 | | 0.09 | 0.08 | 2.14 |
| 539.98 | | 443.09 | 205.26 | 0.13 |
| 60.00 | | 60.00 | 41.79 | 0.49 |
| 0.60 | | 0.60 | 0.28 | 0.00 |

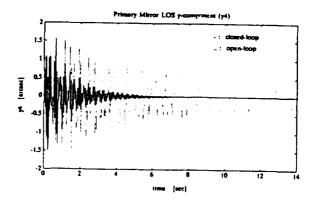


Figure 14: Time Responses to Pulse Noises

same reduced order model for $\alpha=0.6$ resulting from MCA-OVC controller is used for the OCC controller design. The desired variances for OVC control design for $\alpha=0.6$ are used as the diagonal elements of the matrix bound \bar{Y} (31). Table 3 compares the OVC and OCC control design results.

Table 3 shows that the inequality constraint on the output variance is satisfied. The matrix $(\bar{Y} - Y)$ is positive semi-definite.

Conclusions:

The L_2 , L_∞ and output correlation constraint controllers are state space model. The design approach reduces to the LQI method with a special choice of weights. The proper choices for these weighting matrices cannot be specified a priori, but require iteration. The modeling aspects are introduced in the design loop via the integrated MCA-OVC approach.

The designed controllers satisfy the bounds imposed on the RMS values of the output, due to impulsive inputs. Both soft constraints and hard, saturation type constraints are handled. The OCC controller is significant since it relates to covariance assignability work. While the OCC approach does not assign a given output covariance matrix (\bar{Y}) , it provides an output covariance matrix (\bar{Y}) which is bounded by (\bar{Y}) .

Work in progress includes the verification of the controller performance on the AFAL ASTREX hardware, multibody modeling and control verification for ASTREX and the development covariance control design techniques. Currently we are working on model identification and covariance controller design for ASTREX.

Appendix: Actuator Dynamics

1. Actuator Dynamics

For thrusters,

First order dynamics with time constant $\tau = 5$ msec. Limit: 200 lbs

For CMGs (Moment Actuators),

Second order dynamics with bandwidth 20 Hz and damping factor $\zeta = 0.707$ Limit: 70 ft-lb

2. Augmented Equation

Actuator:

$$\dot{x}_a = A_a x_a + B_a (u_c + w)$$

$$u = C_a x_a$$

Plant:

$$\dot{x}_p = A_p x_p + B_p u
z_p = M_p x_p + H_p u$$

3. Augmented System

$$\dot{x} = Ax + Bu + Dw
z = Mx + Hw + v
y = Cx$$

where

$$x = \begin{bmatrix} x_p^T & x_a^T \end{bmatrix}^T,$$

$$A = \begin{bmatrix} A_p & B_p C_a \\ 0 & A_a \end{bmatrix}, B = \begin{bmatrix} 0 \\ B_a \end{bmatrix}, D = \begin{bmatrix} 0 \\ B_a \end{bmatrix}$$

$$M = \begin{bmatrix} M_p & H_p C_a \end{bmatrix}, H = H_p, C = \begin{bmatrix} C_p & 0 \end{bmatrix}$$

Acknowledgement

The authors wish to thank Mr. Joel Berg, AFAL for his help with the ASTREX NASTRAN modeling. Ms. Linda Large's help in typesetting the document is appreciated.

References

- 1. R.E. Skelton, and M. DeLorenzo Space Structure Control Design by Variance Assignment, J. Guidance, vol. 8, No. 4, pp. 454-462, 1985.
- 2. P.E. Moden, and T. Soderstrom, Stationary Performance of Linear Stochastic Systems Under Single Step Optimal Control, IEEE Trans. Automat. Contr., vol. AC-27, No. 1, pp.214-216, Feb. 1982.
- 3. H.T. Toivonen, Variance Constrained Self-Tuning Control, Automatica, vol. 19, No. 4, pp. 415-418, 1983.
- 4. P.M. Makila, T. Westerlund, and H.T. Toivonen. Constrained Linear Quadratic Gaussian Control with Process Applications, Automatica, vol. 20. No. 1, pp. 15-29, 1984.
- 5. P.M. Makila, Self-tuning Control with Linear Input Constraints, Optimal Contr. Appl. & Meth., vol. 3, pp. 337-353, 1982.
- 6. H.T. Toivonen, Suboptimal Control of Discrete Stochastic Amplitude Constrained Systems, Int. J. Contr., vol. 37. No. 3, pp. 493-502, 1983.
- R. Kalaba and K. Spingarn. Design of Linear Regulators with Energy Constraints. Proceedings of IEEE CDC, pp. 301-305, 1980.

- 8. R.E. Skelton, Dynamic Systems Control, Chapter 8, New York, Wiley, 1988.
- 9. C. Hsieh, R.E. Skelton and F.M. Damra, Minimum Energy Controllers with Inequality Constraints on Output Variance, Opt. Control Appl. & Methods, vol. 10, pp. 347-366, 1989.
- 10. G. Zhu and R. Skelton, Mixed L_2 and L_{∞} Problems By Weight Selection in Quadratic Optimal Control,
- 11. Updated ASTREX Finite Element Model, Dynacs Eng. Co., Sept. 90, Report submitted to AFAL.
- 12. ASTREX Eigenanlaysis Dynacs Eng. Co., Oct.90, Report submitted to AFAL.

USING INPUT COMMAND SHAPING

TO SUPPRESS MULTIPLE MODE VIBRATION

IN FLEXIBLE STRUCTURES

Professor Warren P. Seering

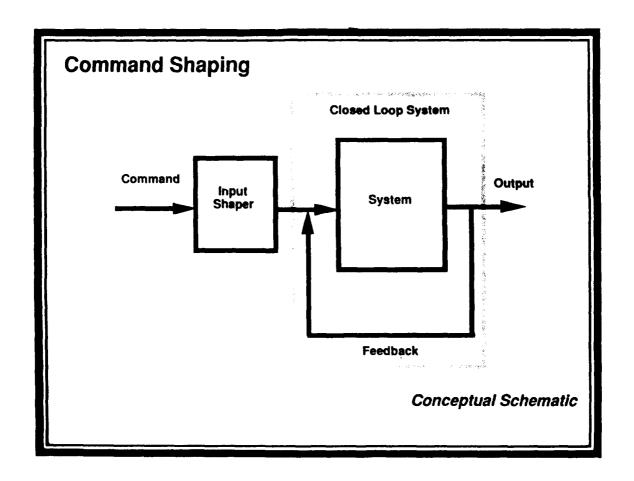
James M. Hyde Research Assistant

Mechanical Engineering Department Massachusetts Institute of Technology

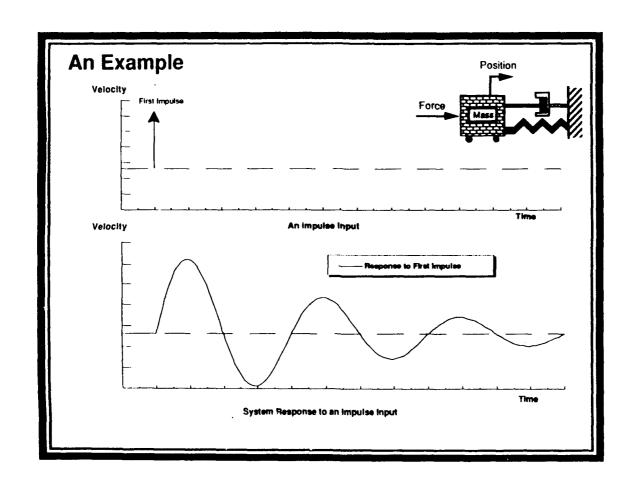
Abstract

Spacecraft and space-borne robotic systems often utilize lightweight materials and configurations that give rise to vibration problems. Prior research has led to the development of input command pre-shapers that can significantly reduce residual vibration. These shapers exhibit marked insensitivity to errors in natural frequency estimates and can be combined to minimize vibration at more than one frequency. The shaping methods has demonstrated significant vibration reduction in laboratory flexible systems and in NASA's Manipulator Development Facility. We have also developed multiple mode input shapers which are simpler to implement than previous designs and produce smaller system response delays. The new technique involves the solution of a group of simultaneous non-linear impulse constraint equations. The resulting shapers were tested on a finite element model of MACE, an MIT/NASA experimental flexible structure.

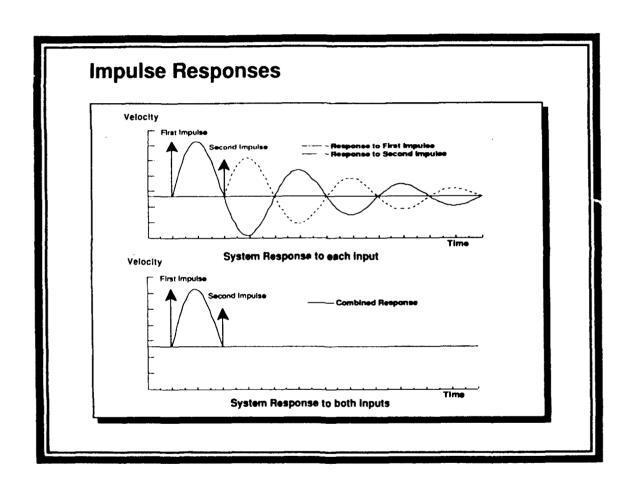
During this presentation, a strategy will be presented for modifying system command inputs to reduce system residual vibration.



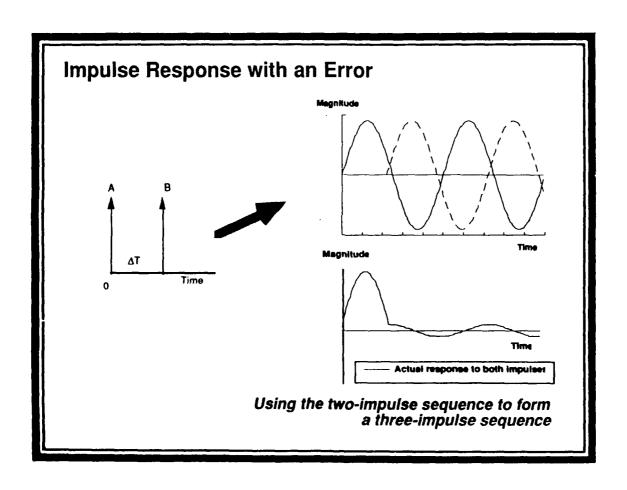
Assume that a single mode system includes a point of actuation and another point whose vibration we wish to minimize. A velocity impulse applied by the actuator will cause a sinusoidal velocity response at the point of interest.



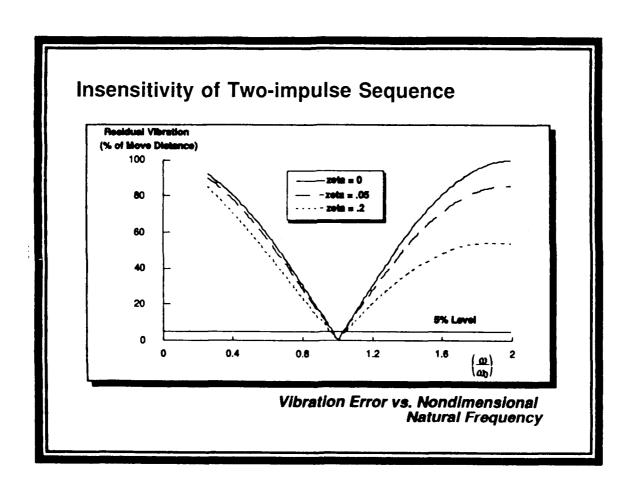
A second impulse applied 1\2 period later will cancel the vibration caused by the first.



However, if our estimate of the resonant frequency is off; the second impulse will not occur at the correct time and consequently will not fully cancel the vibration.



In fact, for small errors in estimated frequency, the residual vibration can be large. It grows rapidly for small increases in estimate error.

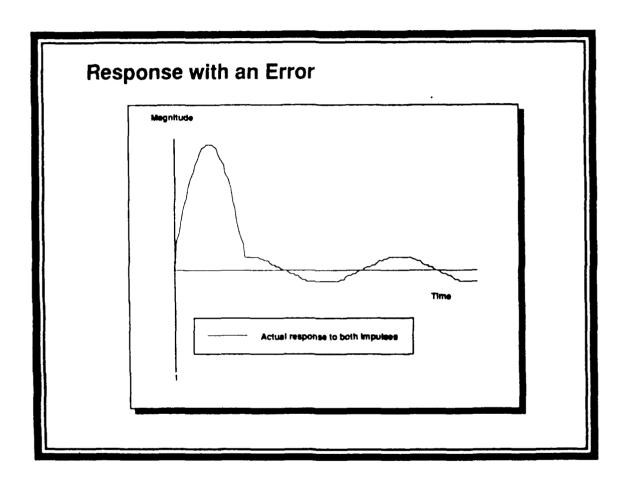


Command shaping methods have traditionally been seen as having a variety of problems. They are not perceived as useful for application to controlled systems. As shown above, their effectiveness is very sensitive to quality of the system mode. And it can be difficult to extend them to handle multiple modes. The first of these is simply not true. They can be very effective when applied to controlled systems. They must, though, be designed to account for the closed loop poles of the system. Other problems will be addressed in the viewgraphs which follow.

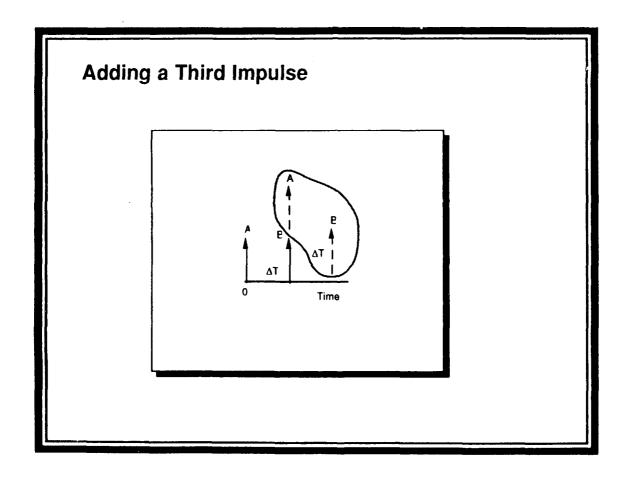
Problems with Command Shaping Methods

- They do not work for systems with controllers.
- Response is sensitive to modeling errors.
- Actuators can't (shouldn't) apply impulses to flexible systems.
- Shaping strategies cannot suppress multiple modes of vibration.

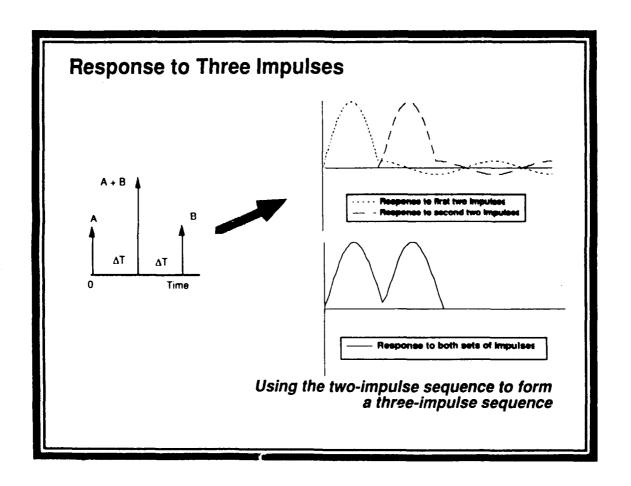
The command shaping algorithm presented above was shown to leave a residual vibration if the system model was not perfectly accurate. However it can be assumed that this residual error can be obtained repeatably.



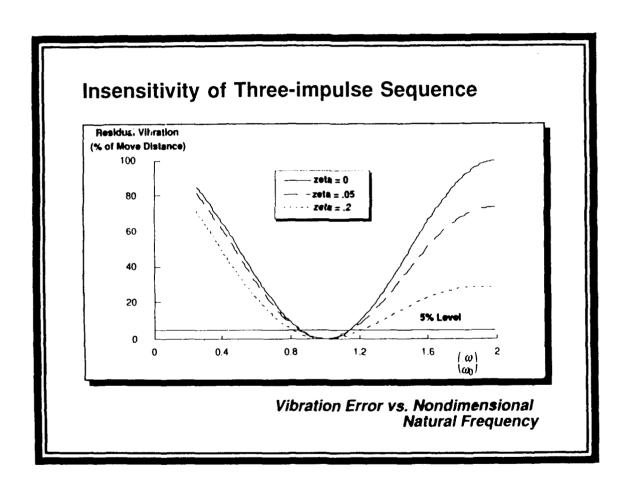
It is possible to command the system with a two impulse sequence and then to immediately issue a second identical sequence so that the first impulse of the second sequence overlaps the second impulse of the first sequence.



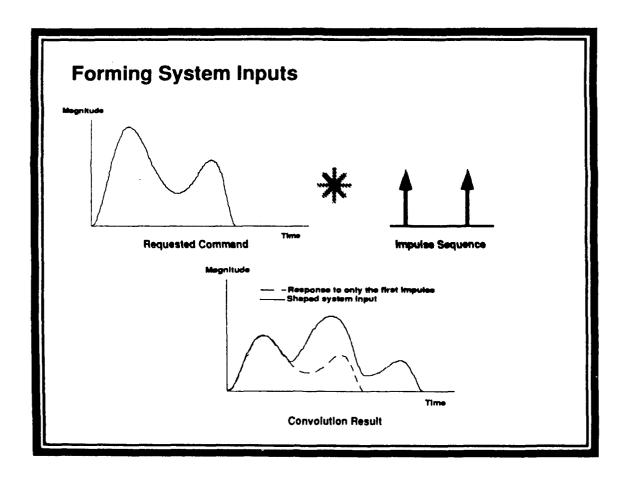
The vibratory response of the second sequence will tend to cancel the vibration caused by the first.



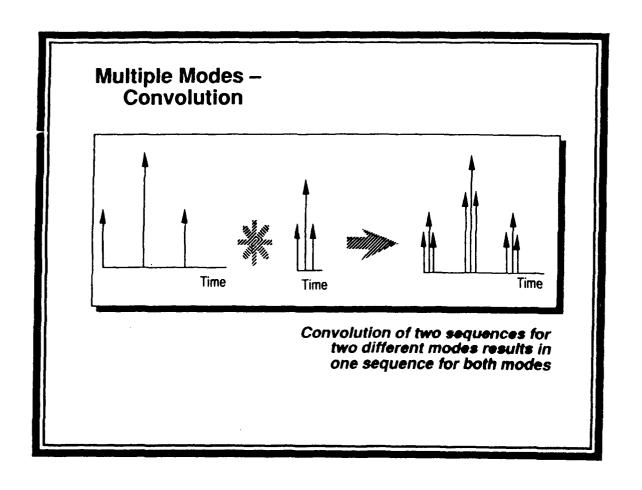
For this new sequence, now made up of three impulses, sensitivity to errors in the system model is much less than for the two impulse sequence.



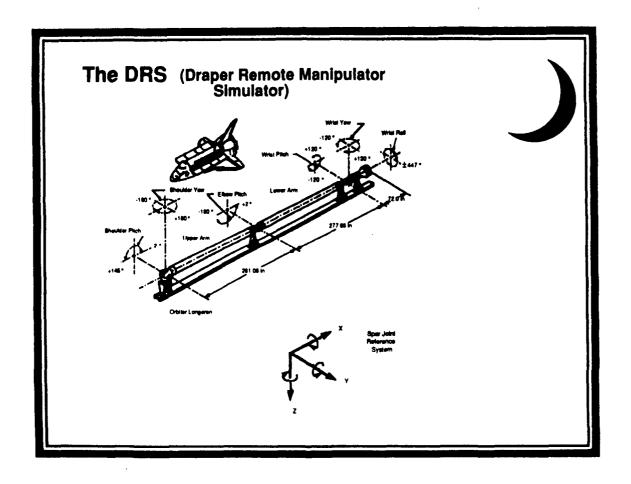
Of course, impulses cannot in practice be applied by finite actuators. A realizable command sequence can be convolved with an impulse sequence, producing a new command sequence which resembles the original sequence but does not cause residual vibration.



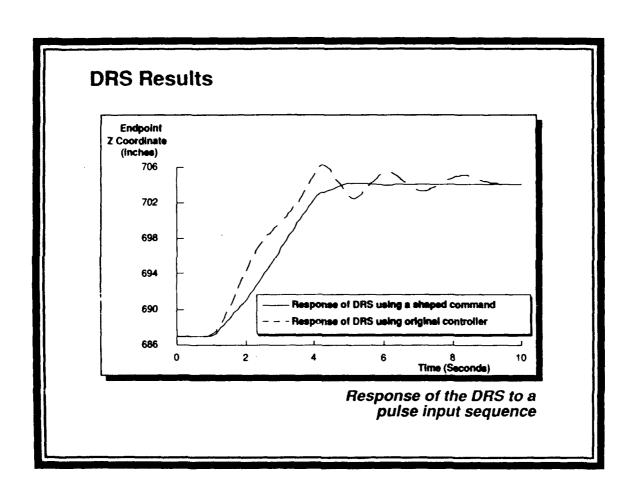
Response at more than one resonant frequency can be minimized by convolving a desired command sequence with an impulse train which itself is the convolution of sequences each designed to reduce residual vibration at a single frequency.



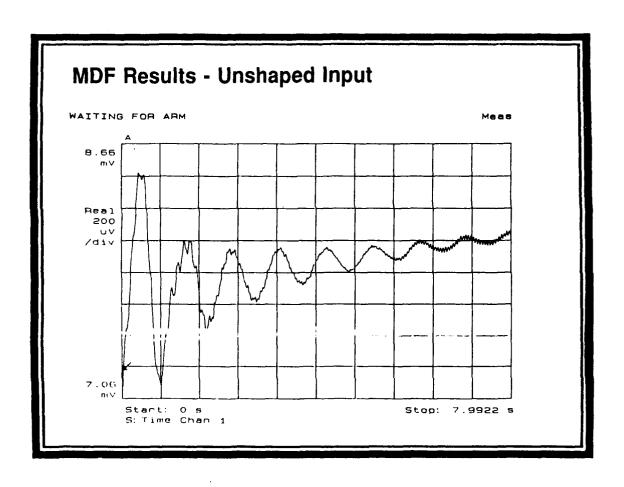
Performance of shaped inputs has been evaluated in simulation using the model of the shuttle manipulator created for NASA at the Draper Laboratory.



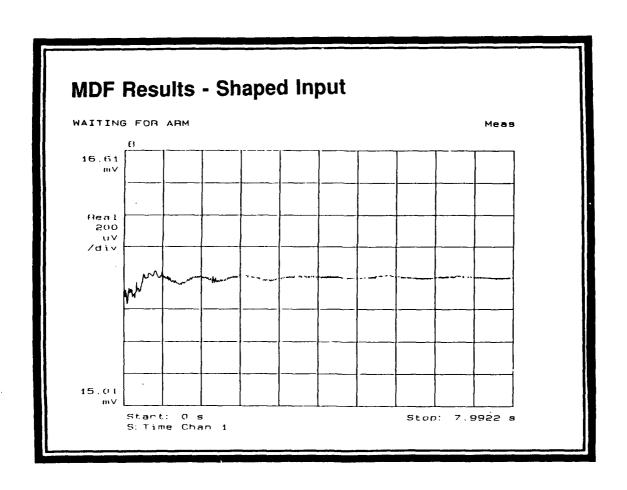
With the existing controller, a one meter tip motion will typically require four seconds of actuation and will result in 10 to 15 seconds of residual vibration. The same command convolved with a shaping impulse sequence will require five seconds of actuation but will cause almost no residual vibration.



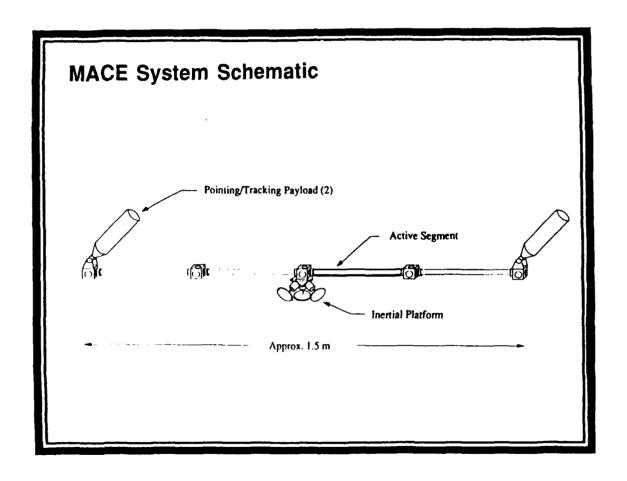
The arm in the Manipulator Development Facility at the Johnson Space Center may vibrate for 12 to 15 seconds after completion of an input command.



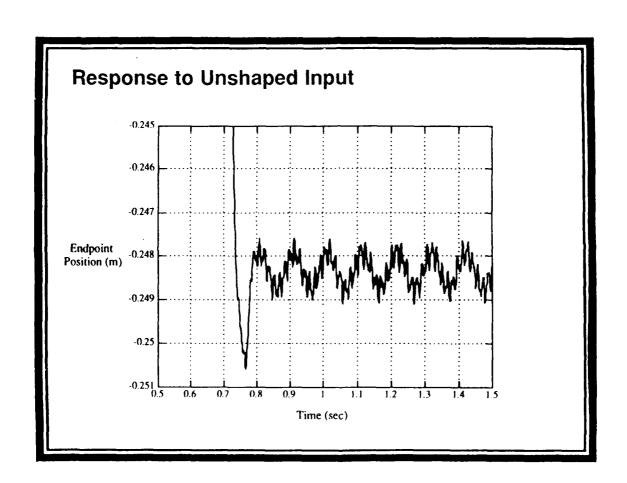
If a comparable command is shaped, residual vibration is reduced by as much as 95%.



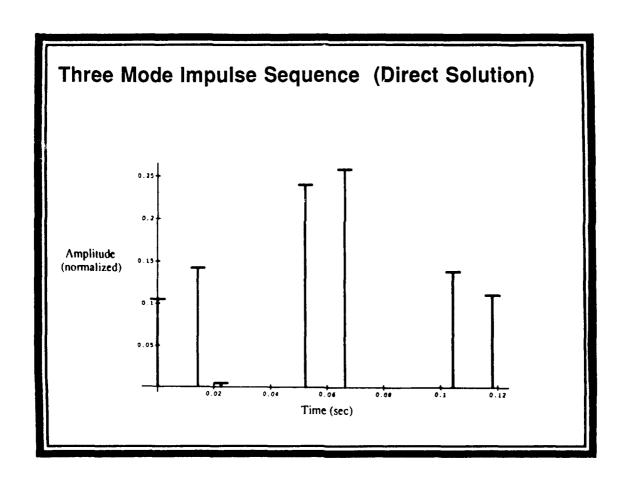
Shaping algorithms are currently being designed for experiments on a Mid-deck Active Control Experiment. The structure is 1.5 meters long and is made up of four segment. At each end is a two-axis gimbal with a payload.



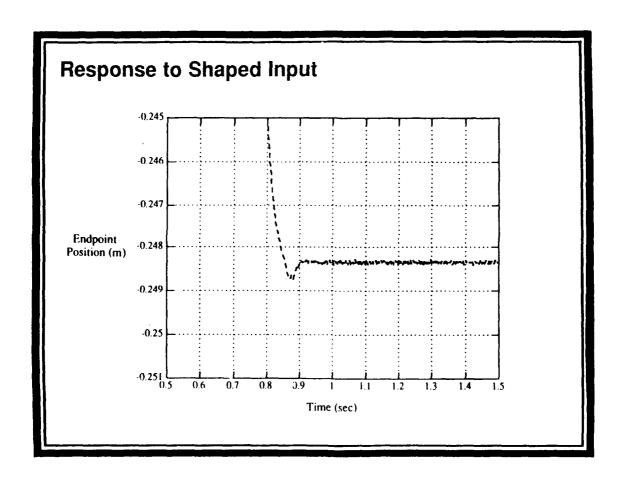
A finite element model of the system exhibits about one millimeter of residual vibration at the conclusion of a step input.



By directly solving a system of impulse constraint equations, a seven impulse shaping sequence can be created to eliminate vibration in the first three modes of this structure. This "Direct Solution" sequence is easier to implement and causes smaller time delays than the convolved multiple mode sequences shown earlier.



When the step command described previously is shaped before being sent to the system, residual vibration is reduced by more than 90%.



EVALUATION OF SY. EM IDENTIFICATION WITH CONTROL LAW UPDATE FOR THE CONTROLS, ASTROPHYSICS, AND STRUCTURES EXPERIMENT IN SPACE

Raymond C. Montgomery*, Dave Ghosh*
Michael A. Scott*, and Dirk Warnaar*

Fourth NASA/DOD CSI Technology Conference Sheraton Orlando North Hotel and Towers, Orlando, FL November 5-7, 1990

ABSTRACT

This presentation describes an evaluation of on-orbit testing and system identification followed by a control system design for a potential flight experiment being considered by NASA — the Controls, Astrophysics, and Structures Experiment in Space (CASES). The evaluation uses a system simulator based on a NASTRAN finite element structural model of the Space Shuttle with the fully deployed CASES payload. The simulation model is constructed by selecting a finite number of modes to represent the structural dynamics. In addition to the structural model, the system simulator also includes models of the electronics, actuators, sensors (including an optical sensor that can measure deflections at locations along the CASES boom), the digital controller and the internal and external disturbances.

The paper includes data from a series of simulated on-orbit tests performed for system identification. System identification is accomplished on each simulated on-orbit test data set by using a parameter identification algorithm, the eigenvalue realization algorithm (ERA), least squares, or other system identification techniques. The results of the individual parameter identification analyses are then assembled into an aggregate system model.

The control system design method used in this study, is based on optimal multi-input/output linear quadratic Gaussian theory (LQG). An LQG control design has been accomplished based only on the identified model and its performance is evaluated based on the time for a vibration to decay to a certain amplitude as compared with the uncontrolled structure for the same initial amplitude.

^{*} Aerospace Technologist, Spacecraft Controls Branch.

[†] Structural Dynamics Analyst, Lockheed Engineering and Sciences Co., Hampton, VA.

Principal Engineer, Lockheed Engineering and Sciences Co., Hampton, VA.

PRESENTATION OUTLINE

This presentation is organized as follows. First, CASES is described and the on-orbit configuration used for system identification and control studies is described. This is followed by an overview of the modelling process and the system simulator. Next, the system identification procedure and control law design are described together with the results of the system identification and closed-loop performance of the control system. This control system design procedure follows that successfully used for the facility readiness control law demonstration on the Mini-Mast (reference 1).

Presentation Outline

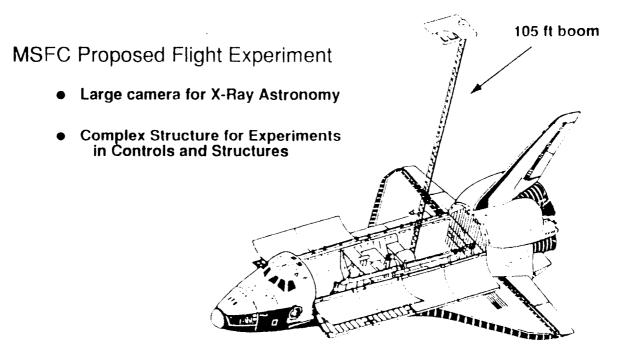
- Introduction and CASES Overview
- System Modelling and Simulation
- System Identification
- Control System Design
- Simulation Results
- Concluding Remarks

CASES - Controls, Astrophysics, and Structures Experiment in Space

CASES is an experiment that is proposed by the Marshal Space Flight Center and is, in effect, a very long focal-length, space-based, camera. The "film" of the camera is in the payload bay of the Space Shuttle and the "lens" is at the opposite end of the 105 ft. boom extending from the payload bay. The "lens" is actually a pinholed plate and the "film" is an X-ray photon counter. The goals supported by this configuration are identifying energy sources from the galactic center, and the energy release mechanisms during solar flares. Precision pointing and stability of the optical axis are required when high energy photons are counted so that image reconstruction can be made.

CASES also accommodates research in controls and structural dynamics. The structural dynamics research capability is enhanced by a Parameter Modification System which is designed to alter the mode shapes and frequencies while in orbit. Advanced control law research can be accomplished using a variety of sensors and actuators provided by CASES, covered in the next chart. The role of the NASA Langley Research Center in this proposed experiment is to conduct on-orbit system identification and to redesign the control system based on the results of the identification so that the high precision pointing stability and vibration damping requirements of the science can be guaranteed.

Controls, Astrophysics, and Structures Experiment in Space



Larc CASES ACTIVITY

The purpose of the work reported in this paper is to determine whether or not NASA Langley Research Center can fulfil its role to conduct on-orbit system identification and to redesign the control system based on the results of the identification so that the high precision pointing and vibration stability requirements of the science can be guaranteed. To do that, we elected to conduct on-orbit system identification and control system redesign evaluations based on a high-fidelity simulator.

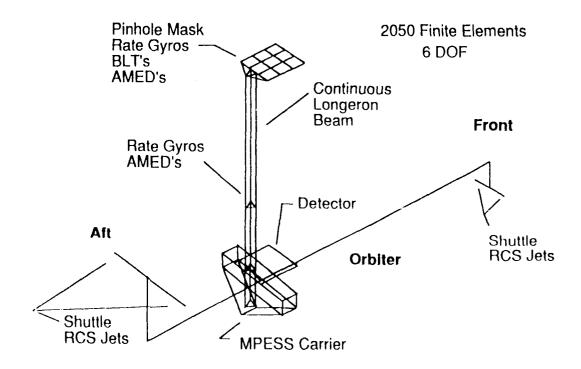
LaRC CASES Activity

- Purpose -- Evaluate the Proposed Flight Experiment Relative to the LaRC CSI Mission
- Approach -- Evaluate the Ability of the Experiment to Support the System ID and Control Law update by means of System Simulation

CASES MODELLING

The space shuttle, experiment carrier, and experiment hardware constitute the structural elements for the CASES finite-element model. The space shuttle is modelled as a stick model. However, the carrier that interfaces the experiment hardware to the space shuttle, the multi-purpose experiment support structure (MPESS), is a detailed model. The complete finite-element model of the on-orbit CASES configuration includes 2050 beam elements and is a NASTRAN model. The location and type of sensors and actuators available on CASES are indicated on the accompanying sketch. The actuators include small cold gas thrusters (bi-linear thrusters, BLT's) and angular momentum exchange devices (AMEDs). AMEDs are electric motors with flywheels attached to the armatures to effect moment control. The sensors include rate gyros, accelerometers, and a novel remote optical sensor that detects motion of optical targets distributed along the mast.

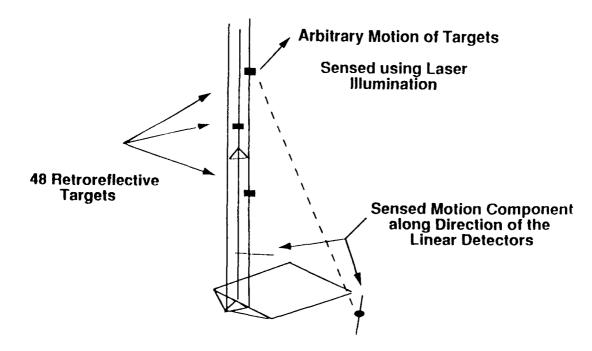
CASES Modelling



REMOTE OPTICAL SENSOR

The remote optical sensor employs a laser to illuminate retroreflective targets. The reflection from the laser targets is focused onto linear CCD (charge-coupled device) detectors. Two single-axis linear detectors are mounted on orthogonal axes at the base of the experiment platform. The discrete projections of the target images as perceived from the detectors are used in the control system. The system is capable of optically sensing multiple target locations. Twenty-four targets are distributed along the 105 foot boom to monitor boom motion and the tip displacement. Additional targets placed on the tip-plate allow determining the rigid-body rotation and translation of the plate.

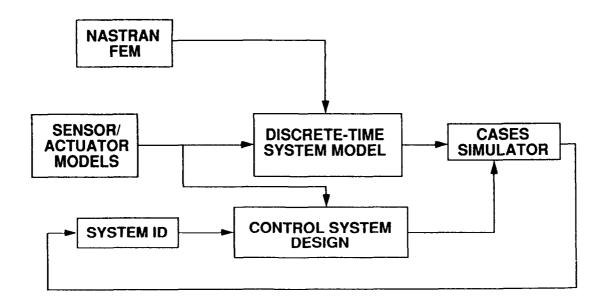
Remote Optical Sensor Model



SYSTEM SIMULATION

The design procedure presented here is applied to the CASES configuration. This is done by developing a system simulator capable of accurately representing the on-orbit environment. For this purpose NASTRAN model data are passed to a preprocessor that generates a discrete-time model of the CASES dynamics suitable for digital control. Actuator and sensor data is also input to this module. These data are used in the control system design module along with output from the system identification which is conducted using simulated open-loop, on-orbit data. The discrete-time model and the control system design are passed on to the simulator for the closed-loop control system performance evaluation. Thus, the control system design is based only on results of the system identification and prior knowledge of sensor and actuator characteristics (assumed to be obtained from bench tests and geometrical mounting data for locations of the components).

System Simulation



SIMULATOR FEATURES

The finite-element model of the CASES configuration includes 663 grid points, 2050 beam elements, and lumped masses representing the actuator and sensor components at the tip and mid boom assemblies.

NASTRAN used to compute the modes with frequencies less that 10 Hz.

Open-loop eigensolution analysis provided the necessary mode shapes and frequencies to build the system simulator. Based on the 40 Hz sample frequency fourteen modes were used in the simulator. The chart lists the frequencies and description of these modes (0.5 percent structural damping was assumed for each mode). In addition to the structural model, the system simulator also includes detailed models of the electronics, actuators, sensors (including RAMS) and the digital controler. Sensor noise and disturbances are modelled as Gaussian random noise. The procedure for modelling the in-situ noise characteristics of the sensors caused by uncertainty in modelling, mounting, and quantization will be discussed later in this paper.

Features Modelled In Simulator

 $\omega = (.033,.034,.165,.431,.441,1.412,1.543,2.744)$ Hz Modal Model -- 6 Rigid, 8 Flexible Modes

Detailed Model of the Optical Sensor

Digital Controller with 40 Hz Sample Rate

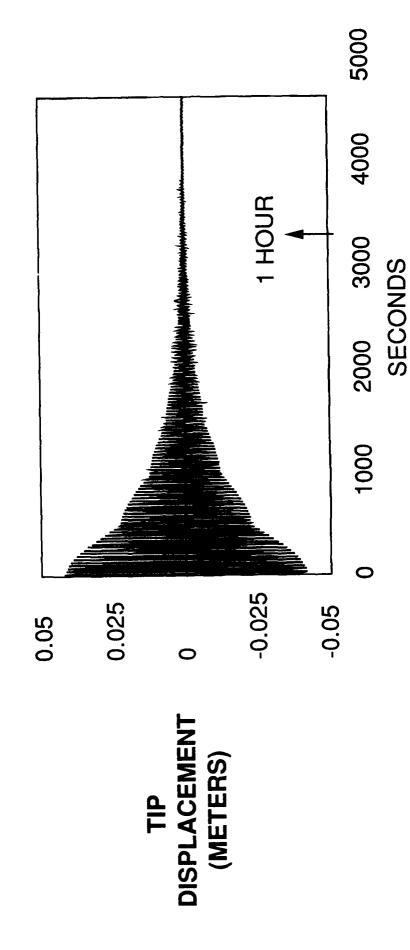
Quantization from Digital Conversion

Sensor Noises and Ranges

OPEN-LOOP RESPONSE TO AN IMPULSE OF 1 N-SEC

The response of the system to an impulse of 1 N-sec is shown in the figure. The important characteristic is that the system does not damp to an undetectable motion for 4,000 sec and does not fall below 1 cm at the tip plate for over 1,000 sec.

CASES OPEN - LOOP RESPONSE TO AN IMPULSE OF1 N-SEC



SENSOR RANGES, NOISE LEVELS, AND ACTUATOR LIMITS

The actuator limits were determined based on the maximum allowable loading on the structural components of the CASES flight experiment. In the case of the bilinear thrusters (BLTs), their maximum force is almost equal to the static buckling limit of the boom. Applying the industry-standard safety factor of 2.5, the maximum commanded value of the thrust is 1 N.

The sensor range and noise levels used in the system simulator are shown in the chart. The expected range of the sensors is determined during the excitation period of the system identification tests (SID). Therefore, prior to assigning values for the sensor noise a complete simulation was performed to determine the peak response of the sensors to each of the PID (parameter identification) test. To prevent sensor saturation, the expected range is defined as six times the peak of the actual response of the test. Thus, the data was carefully inspected, peak displacements were identified, noise levels, were determined and added to the data prior to performing system identification on the data. The three-sigma noise range levels correspond to one percent of the expected range for the inertial sensors. The optical sensor noise levels correspond to 0.1 percent of the expected range. The open loop excitation tests indicated the peak displacements are highest near the tip of the boom. Thus, the noise levels added to the optical sensor increase near the tip of the boom.

Sensors and Actuators

Actuator Limits --

- MEDs -- 1 N-m (141.2 oz-in)
- BLTs -- 2 N (.43 lbf, safety factor of 2.5 over static buckling)

Sensor Ranges --

- Accelerometers -- .012 m/s/s
- Rate Gyros -- .06 1/s
- Optical -- .04 m to 1 m depending on target location

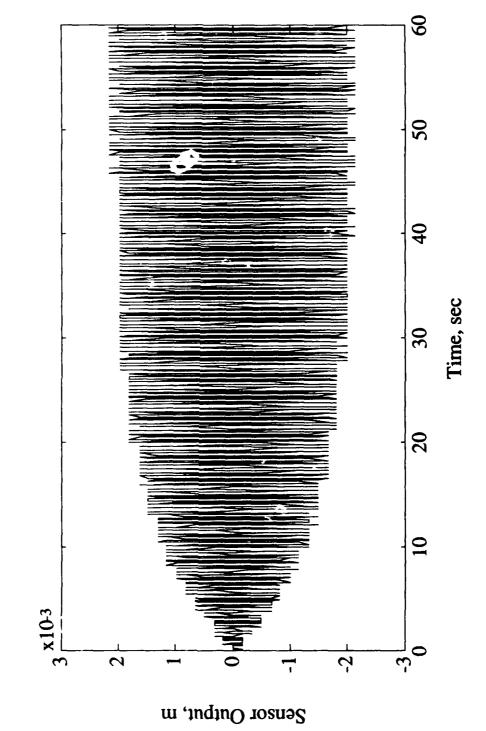
Sensor Noise Levels --

- Accelerometers -- 3 σ is 1 % of range
- Rate Gyros -- 3 o is 1 % of range
- Optical -- 3 o is .15 % of range

EFFECTS OF QUANTIZATION MID-BOOM DEFLECTION

This chart shows the character of the signals that resulted from application of the actuator comma. i limits of the previous chart. Here the boom is excited with the mid-station torque wheel at the mode 8 resonant frequency. The effect of quantization in the signal is apparent by the step-like nature of the sensor output. The maximum amplitude of the signal is approximately 4 mm peak-to-peak and the quantization is approximately in .2 mm increments.

Effects of Quantization Mode 8 at Mid-Station Maximum AMED Excitation



SYSTEM IDENTIFICATION APPROACH

A complete system identification procedure requires the identification of modal frequencies, damping ratios, mode shapes, and actuator influence coefficients. An unsuccessful attempt was made to identify the mode shapes using the sine-sweep and random excitation tests. Because of actuator input limitations dictated by flight safety requirements, sine-sweep and random excitation techniques do not excite the structure sufficiently to identify mode shapes and actuator influence coefficients. However, the modal frequencies can be identified. First, ERA (reference 2) was used to determine the frequencies from a sine-sweep test. It was used again to identify the mode shapes, frequencies, and damping ratios from 28 sine-dwell tests. (These tests were determined from the finite-element predictions to eliminate unnecessary data processing.) In an actual flight the complete matrix of tests (number of modes by the number of actuators) would be used. The least squares method (reference 3) and a closed form solution method (the b-coefficient method, explained herein) were used on the data to determine the actuator influence coefficients. The results of the individual parameter identification analyses are then assembled into an aggregate system model for use in the control system design phase.

The actuator influence coefficients were identified using least squares estimation and a closed form solution method. Both techniques analyze single-input, single-output data. The sensor with the highest signal-to-noise ratio was selected for determining the actuator influence coefficient for the corresponding mode-actuator combination. For the higher frequency modes, quantization effects and low levels of excitation prohibited the least squares estimation from converging. For these modes the b-coefficient method was used. This method is based on fitting the the envelope of the forced response curve. The equation governing the envelope for this method is

$$y(t) = \frac{b \left[1 - e^{-\zeta \omega_n t}\right]}{\omega_n (2\zeta \omega_n)}$$

which assumes zero initial conditions, small damping, and the presence of a single mode. The unknown b-coefficient is determined from the knowledge of a sensor output y at time t. The damping coefficient ζ and the natural frequency $\omega_{_{\! L}}$ were previously determined using ERA.

The closed form method accurately predicts the magnitude of the coefficient. However, it does not predict the sign of the coefficient. The sign is determined by examining the phase relationship of the senser output to the excitation input. If the output lags the input by 90° , the influence coefficient is positive. If the output leads the input, the coefficient is negative.

System ID Approach

Frequency, Damping, and Mode Shapes

- Free Decay Following Sinusoidal Excitation
- Algorithms -- ERA

Actuator Influence Coefficients

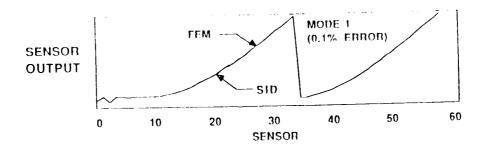
- Sinusoidal Excitation at Predicted Resonances
- Algorithms -- Least Squares, Log Decrement, Parametric Fitting of Response

SYSTEM IDENTIFICATION RESULTS

Using ERA, the mode shapes, frequency, and damping coefficients of the 8 lowest frequency flexible modes were identified. Shown here are results of the ERA analysis and a line graph of the sensor output shape function for the first mode (plotted against sensor number). For the line graph, the first 4 sensors are rate gyros. The next 24 are laser retroreflective targets using one of the detectors and the last 24 are the retroreflective targets for the other detector. Also plotted is the finite-element simulated value of the parameter. It cannot be destinguished from the parameter identification value on this chart.

The identified damping differs substantially from the system in the lower frequency modes. Although there has been no attempt to identify the source of this problem, it is believed that the cause is the limited amount of data used in the sytem identification. The data runs were limited because of system software problems incurred on the host computer of the simulator. For this reason the number of complete cycles of the identified mode decreased with frequency and, consequently, the variance of the estimated damping ratio increased. This problem would be overcome for a flight experiment and more data would be used in the system identification. For this exercise it is the challenge of the control system design process to tolerate such disparities between the system and the design model.

SYSTEM IDENTIFICATION RESULTS

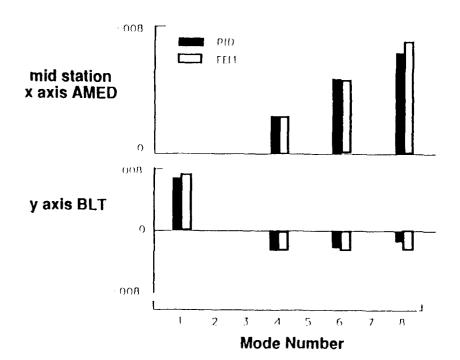


| FLEXIBLE MODE | SYSTEM | | SYSTEM IDENTIFICATION | |
|----------------------------|--|---|--|--|
| | FREQUENCY (HZ) | DAMPING (%) | FREQUENCY (HZ) | DAMPING (%) |
| 1 2 3 4 5 6 | 0.033 0.034 0.165 0.431 0.441 1.412 1.543 2.744 | 0.5 0.5 0.5 0.5 0.5 0.5 0.5 | 0.033 0.034 0.165 0.431 0.441 1.412 1.543 2.743 | 1.674 1.013 0.667 0.463 0.297 0.501 0.482 0.540 |

ACTUATOR INFLUENCE COEFFICIENTS

This chart shows the actuator influence coefficients used in the simulator (the finite-element model, FEM) and those identified using parameter identification (PID). For the actuator influence coefficients, the worst estimates occur in the higher frequency modes. This is because of the limited control authority of the actuators. This resulted in very low levels of signals from which the estimates were extracted. In this case, The problem is not a function of the software on the simulator's host computer (as was the limitation on test data set size) and, therefore, is one to be expected if a flight test is made using the CASES hardware as assumed herein. Again for this exercise it is the challenge of the control system design process to tolerate such disparities between the system and the design model.

Actuator Influence Coefficients



CONTROL DESIGN PROCESS

The vibration suppression control law is developed using the linear quadratic Gaussian analytic design method (reference 4). This procedure uses a linear, steady-state minimum-variance estimator to obtain the states for use in a linear fixed gain regulator. The control law minimizes the time integral of the weighted, square, modal amplitude and the weighted, square, the control signals. The weighting matrix for the modal amplitude is the identity matrix divided by the modal frequency squared. The weighting matrix for the control input is the identity matrix.

Control Design Process



DESIGN CRITERIA: ESTIMATION -- MINIMUM VARIANCE

CONTROL LAW -- QUADRATIC IN BOTH REGULATION ERROR AND CONTROL

DESIGN MODEL --- 8 LOWEST FREQUENCY VIBRATION MODES

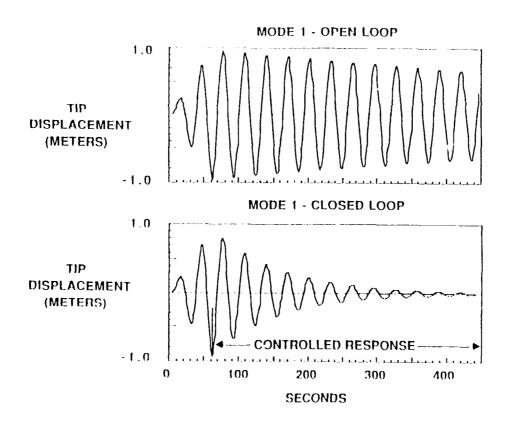
ACTUATORS --- 2 BLTs (1 N) 5 AMEDs (1 Nm)

SENSORS --- 24 LASER TARGETS
5 RATE GYROS
3 ACCELEROMETERS

CLOSED-LOOP PERFORMANCE

The closed loop performance of CASES was evaluated with the results of the system identification information. An updated regulator and a state estimator based on the SID results were obtained. This chart shows the tip displacement (in meters) of the CASES mast due to sinusoidal excitation (using the tip thruster) at the first resonant frequency of the structure. The upper graph shows the forced response for the first 60 seconds and free decay response after 60 seconds. The lower graph shows the forced response to the same input disturbance with the controlled response after 60 seconds. The open-loop system (0.5 percent damping) takes approximately 10 times longer to achieve the same level of damped response as the closed-loop system (5 percent damping). This would be a significant savings in set-up time for science experiments and settling-time for CSI experiments for CASES.

CLOSED LOOP PERFORMANCE



CONCLUDING REMARKS

A procedure has been presented for the on-orbit design of a control system for flexible space structures. This procedure has been successfully implemented in a CASES flight experiment simulation. Results indicate that, due to the large number of actuators and modes, low levels of allowable excitation, and long test times, system identification will be difficult but can be done. The actuator influence coefficients are difficult to obtain with the levels of actuator force allowed. With current actuator force levels, 5 percent damping can be added to the system.

Concluding Remarks

System ID can be done but will be difficult

Many Actuators and Modes Low Levels of Excitation Long Test Times

 5% Damping can be achieved with current Actuator force levels

REFERENCES

- 1. Montgomery, R. C.; and D. Ghosh: LQG Control for the Mini-Mast Experiment. Proceedings of the Sixth VPI&SU/AIAA Symposium on Control of Large Structures. June 29, 1987.
- 2. Juang, J.; and R. S. Pappa: An Eigensystem Realization Algorithm for Modal Parameter Identification and Model Reduction. Journal of Guidance, Control, and Dynamics, vol. 8, no. 5, pp 620-627, 1985.
- 3. Sparks, D. W., Jr.; Montgomery, R. C.; Elder, R. C.; Lenox, D. B.: Parameter Identification for Vibration Control of SCOLE. ASME Paper No. 88-WA/DSC. Presented at the 1988 ASME Winter Annual Meeting, Chicago, Ill. Nov-Dec 1988.
- 4. Kwakernaak, H. and R. Sivan: <u>Linear Optimal Control Systems</u>. Wiley Interscience; New York, N.Y.

Surprises in Open Section Smart Structures

Presented by:

Dean Jacot Tyler Anderson

The Boeing Company
Aerospace & Electronics Division

3rd NASA/DOD CSI Conference Orlando, FL Nov 3-5, 1990

SURPRISES IN OPEN SECTION SMART STRUCTURES

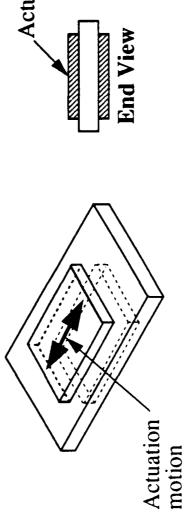
Smart structures include actively controlled materials such as piezoelectric, NiTiNOL, or fiber optics that are embedded in, or attached to, the primary structural material. This can provide active damping, shape control, system identification, and health monitoring/damage assessment. that has limited the previous application of actively controlled structures (i.e., smart materials have cost, weight and reliability advantages over proof mass actuators). In some applications, smart structures will offer advantages over conventional precision structural materials and fabrication Smart materials and structures promise to significantly reduce the high cost, weight and unreliability

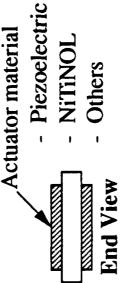
This paper describes two newly observed phenomena in actively controlled smart structures with open section elements. Most of the previous smart structure research has used solid core structural elements, whereas real applications utilize open section elements with relatively thin walled tubes or box elements for weight efficiency. Both attached and embedded possibilities are embedded sensors/actuators in Graphite Epoxy materials that are electrically conductive, so the electrically controlled sensor/actuator material must be insulated from the structure. This fabrication location, the actuator/sensor material could be attached to the inside (or outside with adequate protection) of the structure as the last step in the fabrication process. The results of this research are appliciable for either attached or embeddeed sensors/actuators, but place significant constraints on Illustrated at the bottom of the adjoining figure. Most of Boeing's smart structure experience is with process introduces the possibility for breaking the piezo material, either during layup, curing, or removal from the mandrel. As an alternative for reducing fabrication costs or increasing flexibility of attached concepts.

Surprises in Open Section Smart Structures

Boeing Aerospace & Electronics

- Smart structures incorporate
- Sensor/actuators embedded in, or bonded to, structural elements
- Useful for active damping, shape control, system ID, and health monitoring
- Most testing has been done with solid structural elements





Open section elements are normally used due to weight efficiency



ACTIVE CONTROL BEAM

electrical connection between the metallized face of the piezo and the Al beam. This allowed using the beam as an electrical return signal. The nonconducting epoxy transfers the shear stress to the beam, while minimizing the chance of arching across the thin 10 mil piezo (a few hundred volts are successfully demonstrate a high level of active damping of the first mode of beam vibration. The controllable piezoelectric elements, (20 on each side), were used on the aluminum beam. The piezoelectric material was bonded to the beam with a small dot of conductive epoxy (BMS 35D Type 1, Grade A), surrounded by non-conducting epoxy (BMS 5-92D). The conductive epoxy provided an open section box beam with piezoelectric actuators and sensors was previously used to adjacent figure illustrates the test beam, mounted in a cantilever configuration. Forty separately normally used to actuate the piezo material). When a voltage is applied to the free face of the piezo, it expands transversely through the d31 effect as illustrated at the lower right of the adjacent figure. If an opposite polarity voltage is applied to the piezo on the opposite face of the beam it will contract. The expansion and contraction forces then combine to form a moment that will cause the beam to deflect as illustrated at the upper right

sensing (ref 1 to 5). The basic objective of this research was to compare the previous active damping results with that obtainable with piezo sensing. In both series of tests, the measured first The beam was initially fabricated to explore active damping using a fiber optic and NiTiNOL cantilever mode was 30 hz, which is somewhat lower than the theoretical 35 hz. The lower frequency was traced to base mounting compliance.

Active Control Beam

Boeing Aerospace & Electronics



6061 Al beam

0.125 wall thickness 57" length, 3" x 3"

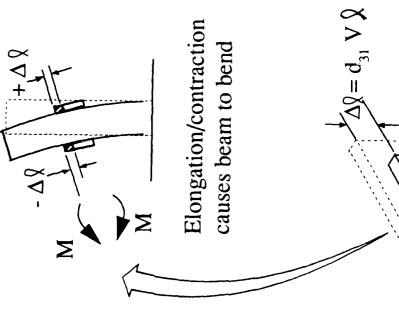
20 on each side - 0.6" x 1.55" piezos - 0.01" thick G1195 Piezoelectric

255a

- .25" gap between elements

- Individually wired

to elongate (contract) Voltage causes piezo





ACTUATION AUTHORITY/RELAXATION

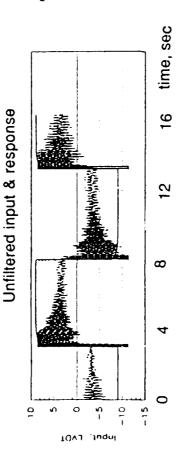
line in the upper left trace, but the ringing still dominated the response. By careful examination of the The beam was deflected using all of the piezos as actuators. The motion of the tip was sensed a Linear Variable Differential Transformer (LVDT), mounted to another adjacent post. When a low frequency (0.1 hz) square wave excitation of 90 volts was applied to the piezo's, the first traces, there appeared to be a relaxation phenomena that caused the beam deflection to decrease deflection of the beam. The square wave commanded voltage was rounded as shown by the solid mode dynamic ringing of the beam tip, as measured by the LVDT, masked the steady during the 5 second period of constant voltage.

data more clearly illustrates this relaxation. The general shape of the FFT filtered response was The test data was then collected through a 250 samples per second, 12 bit A/D converter. It was cocessing, the signal content from 4 to 100 hz was removed, and the signal inverse transformed plotted as shown, along with the commanded voltage to the piezo's. The filtered response then passed through a bandpass Fast Fourier Transform (FFT) filtering operation. After FFT verified by conventional analog filtering.

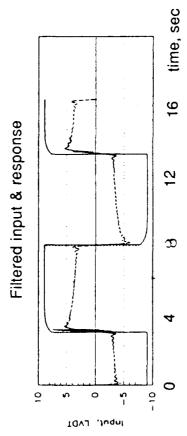
expected from theoretical calculations, and was found to be lower than expected. On talking to To understand this relaxation phenomena, the steady state deflection was compared to that the piezo manufacturer and Boeing experts in adhesives, it was concluded that the cause was a poor selection of Epoxy adhesive and its incomplete curing. It was discovered that the bonding adhesive used was a general purpose Epoxy with relatively low modulus and poor visco-elasticity. viscosity characteristics, and that is consistent with Incompletely cured Epoxy can retain some the general relaxation characteristic observed.

Measured tip deflection with LVDT





- Tried several techniques to see steady offsets
- rounding corner on excitation
 - filtering of signal
- FFT post processing(filtering)



- Presently think relaxation is due to Epoxy adhesive
 - viscosity effect if inadequately cured
- shows less beam deflection per volt than expected

ACTIVE DAMPING

the plots). This data was for a single strain rate sensor, which included a first order rolloff filter at 800 adequate "holes" in the continuously increasing frequency response to place this filtering is the By using a low impedance sensor amplifier, strain rate sensing was used, as this should provide the output is illustrated at the middle right of the figure. The increasing strain rate response at very high frequencies illustrates the difficulty associated with using collocated rate feedback (the sparseness of the experimental datapoints near the resonances is the cause of the ragged appearance of hz. At some frequency, filtering must be introduced to avoid high frequency instabilities. Finding major limitation of rate feedback. This is one of the motivations for positive position feedback that As illustrated at the upper right of the adjacent figure, the piezo can either sense strain or strain rate. proper phase for active damping. The overall frequency response from actuator input to sensor inherently rolls off this response (ref. 6).

tests to be very successful in duplicating the previous active damping results. The time damping ratio of 0.003. This was increased by about a factor of 5 in the actively damped case without any significant effort being made to optimize this damping. Because of the simplicity of this histories at the left illustrate the effectiveness of this damping. The undamped beam had a structure, adequate high frequency rolloff was obtained by placing 3 first order filters at 80 hz (between The dominance of the first mode allowed the initial piezoelectric sensor and actuator damping the first and second modes).

Active Damping

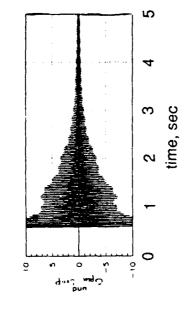
· Boeing Aerospace & Electronics

Undamped

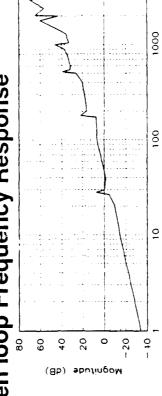
Technologies

(4) sirospace

System



- Piezo Sensing
- $\triangle V = K(\triangle L)$
- open circuit position sensing
- $\Delta I = K(\Delta \dot{L})$
- short circuit rate sensing
- Open loop Frequency Response



Actively Damped

- Experimentally selected piezo phase
 - Damp first mode
- Top piezo sensing
- Required positive rate feedback

വ

۵۱**۰**: رکام: time, sec

DYNAMICS ANOMALY

to control the phase of the signal at the first mode. This was necessary because of the phase change caused by a zero before the first pole. The open loop responses illustrated at the left of the adjacent figure illustrate this phenomena. These responses were obtained by using all piezos on both sides as actuators, except the single one being used as a sensor. The consistency of the lower In conducting the previous damping tests, it was found that positive rate feedback was necessary frequency zero is shown despite the location of the sensing piezo.

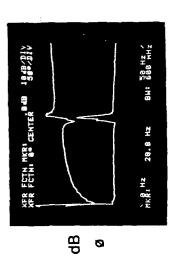
example, it can be argued that the deflection of the first cantilevered mode should be in phase with the excitation (positive C1). This results in the zero (Wn), being at a higher frequency than the lowest mode (W1), for the expected values of C2 (the second mode). For non-collocated measurements, zeros can be found below poles, or even non-minimum phase zercs are possible, but these are unusual input/output conditions. The zero before pole for the collocated measurements led to theoretical beam response is illustrated at the upper right of the figure, and shows an expected pole before zero phenomena. The model directly below further illustrates this dilemma. For considerable consternation over the source of the dynamic anomaly.

Dynamics Anomoly

■ Boeing Aerospace & Electronics

Theoretical Response

Test Data



piezo top

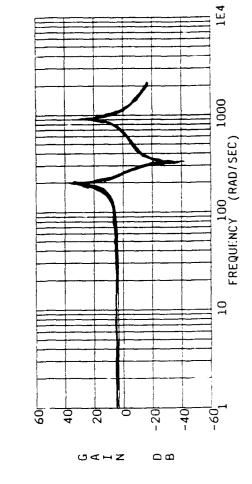
Sensing

Sensing middle piezo

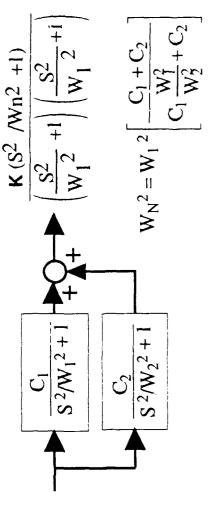
50

μz

freq,



Equations



Sensing bottom

ф

Ø

20

μz

freq,

BW1 588 HZ /

28.8 Hz

piezo 50 28.4 Hz BH: 688 HZ μz freq,

ik R. Hz

0

ST/kwo/ADJ/4410/9002-4

фB

Ø

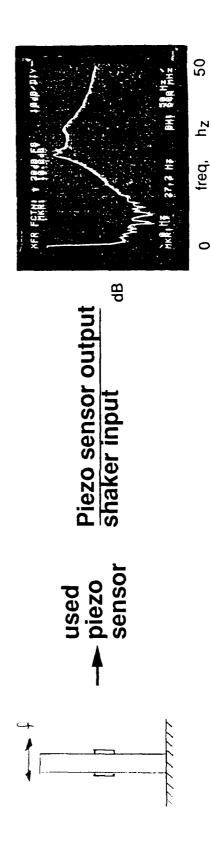
KFR FCTN MKR: 1.84B 1848/DIV

ANOMALY INVESTIGATION

Several different tests were investigated in attempting to resolve this anomaly. At first, it the piezo actuators. An insulated piezo was attached to rule out this effect, as well as any cross coupling pickup from the other axis of vibration. A piezo is sensitive to either direction of transverse strain and the thought was that the other axis could be vibrating at a slightly lower frequency. The insulated piezo was mounted at the top of the piezo actuator area, and was placed on two insulators that were bonded to the beam, thus making it insensitive to transverse beam bending (similar to that used in ref 7). The long axis of the piezo was along the beam which further would further diminish The new piezo however, exhibited the same dynamic anomaly was suspected that the anomaly was from EMI, caused by using the beam as the ground return for any transverse axis effects.

The next step was to conduct some tests to identify if the phenomena was associated with the exhibit this phenomena, which pointed to the piezo sensor as being the cause of the anomaly. To actuator or sensor. To rule out any coupling from the LVDT friction or its mounting post dynamics, it was not used in the anomaly investigation. We first mounted an accelerometer on the tip of the beam, validate this, we mounted a small shaker (speaker core) at the tip of the beam. The shaker to piezo and compared the piezo signal with the integrated accelerometer signal. The accelerometer did not or accelerometer sensor transfer function showed the zero at a higher frequency as expected. these tests we concluded that the basic anomaly was somehow caused by the piezo actuator.

- Several blind alleys were investigated while trying to understand
- · EMI
- Piezoeletric/beam cross coupling
 - Beam torsion
- Depoted piezoelectrics
- Additional tests were performed
- Added small shaker and accelerometer at tip to execite/sense beam



TM 10/90 MrdaHD

HYPOTHESIZED PHENOMENA

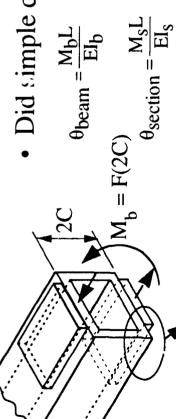
calculations about an alternative explanation. The overall beam bending illustrated is a result of the local skin bending from the piezoelectric actuators. The initial thought was associated with the nitial square section deformation ("ovaling") as the beam was bent. This led to some simple moment (piezo force times the beam depth, 2*c = 3 inches), acting on the beam inertia (c*c*A, where inertia to the 2.25 in**4 illustrated). This led to some simple calculations of the effects of the piezo section inertia (t*t*A/12), which is 4610 times smaller that the beam inertia. The ratio of these two deflections shown in the middle of the adjoining figure indicates the skin should bend about 96 times inertia, this leads to much higher local deformations that eventually get reversed by the beam. This considerable head scratching, we began to suspect that the anomaly was associated A is the beam section area, plus the beam sidewall inertia contribution which brings the bearn section skin moment (force times skin thickness/2, t/2 =0.0625 inches). The skin moment is 48 times smaller than the beam moment. The local resistance to the skin moment is provided by only the skin more that the beam should. Since the overall deflection has to be governed by the beam section reversal of deflection requires a change in direction of the bending slope that the piezo sensor detects. This in turn, leads directly to the phase reversals necessary for the observed low frequency

area, a single piezo was energized. The location of the actuation signal was varied down the beam, and the responses shown at the hottom supported this theory. As the actuator became isolated from A series of tests was done to confirm this theory. Using the isolated piezo at the top of the actuation the sensor, the lower zero phenomena vanished, as would be expected from a local skin effect phenomena. These tests also illustrate the high sensivity of the piezo as a sensor, as it detected the very small beam bending caused by a single piezo actuator.

Hypothisized Phenomena

Boeing Aerospace & Electronics





$$\theta_{beam} = \frac{M_bL}{EI_b}$$

$$M_b = F(3.0)$$

Beam Beam depth

depth
$$M = F(.062)$$

$$M = F(.062)$$

Section Section Solution

$$I \approx \frac{bh^3}{12} = \frac{3(.125)^3}{12}$$

Section

Skin section

$$\frac{\theta_{\text{section}}}{\theta_{\text{bean}}} = \left(\frac{Ms}{Mb}\right) \left(\frac{lb}{ls}\right) = 96$$

$$\left(\frac{l}{48}\right) (4610)$$

 θ_{beam}

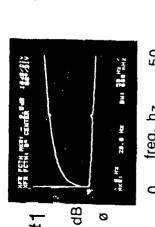
 $M_{S} = F({}^{l},{}_{7})$

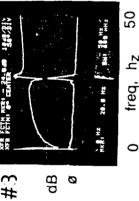
Piezo

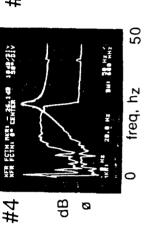
thickness

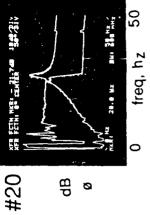
Reversal leads

• Did tests - sensing top piezo, actuating single piezo #4 #3









ST/kwo/ADJ/410/9002MII

PLATE BEAM STRUCTURAL MODEL

up to a frequency of 1263 Hz were obtained from a NASTRAN analysis, and solved using EASY5. The A plate model of the beam was then constructed to insure and quantify our understanding of this phenomena. The first model had plate elements somewhat larger than the piezo elements themselves, and the whole beam was modeled with 512 of these plate elements. Fifteen modes results did not snow the localized skin strain phenomena, even though all the modes were included. This was not too much of a surprise, because we expected to encounter modal truncation problems.

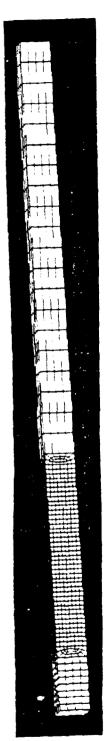
actuation area was modeled by smaller plate elements, and the rest of the beam was modeled by the storage capabilities. The residual stiffness matrix (total stiffness minus that associated with the 15 of the important plate nodes, the stiffness matrix size was still 30x97, or 2910 of the available 984,169 stiffness elements. The use of the Integrated System Modeling (ISM) software was of considerable utility in selecting and keeping track of the proper nodes and their stiffness elements/degrees of freedom, the nodal (XYZ) coordinates, and for communication between analysis programs. EASY5 A higher fidelity model was then developed as illustrated at the top of the adjoining figure. The original larger plates. This resulted in 1968 nodes and 9840 DOF. Even with the use of larger plates except in the area of importance, it was difficult to keep the system order within computer and modes) of 987 of the more important plate elements was then developed. By retaining only a few (97) MATRIXx used to generate the plots at the bottom which confirm the suspected local deformation. was then used to assemble the data and generate the predicted local skin deformations,

The plots show the large deflections at the point of application of the piezo moment. If the sensor is a small distance from the actuator, the phase of the bending can be opposite of that of the total beam bending, thus providing a signal cancellation sensed as a zero near the first mode. Applying only forces did not show this phenomena, the previously described skin moments are responsible for the skin strain phenomena.

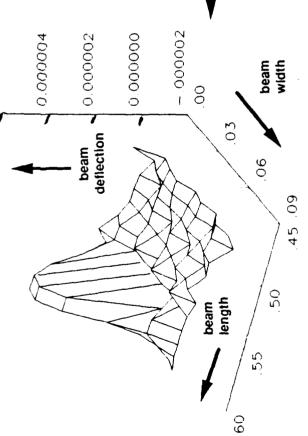
Plate Beam Structural Model

Started development of plate type structural model

Boeing Aerospace & Electronics



- Got 15 modes (to 1263 hz) didn't show phenomena
- Got Stiffness Matrix from Model



- 987x987 matrix
- Used ISM to select 2910 of 984, 169 elements for EASY5/MATRIX_x analysis
- Applied piezo force/moment
 Force alone doesn't
 show phenomena
- Force & Moment does show phenomena

Skin Strain Phenomena

SUMMARY

The two unexpected results of this series of tests were the relaxation phenomena, and the low frequency zero or local skin strain effect. The relaxation is suspected to be caused by viscosity of the Epoxy adhesive used to attach the piezo's to the beam. The local skin strain effect was shown by analysis to be the effect that caused the dynamic causes phase reversals of the deflection of the beam wall for sensors located near actuators. The anomaly. A variety of potential causes were investigated before the successful explanation was which is then counteracted by the smaller gross bending motion of the beam. This counteraction uncovered and proved. The phenomena is due to high amplitude local deformation of the thin wall, effect did not preclude very effective active damping in the simple test article.

model description even with this very detailed model (1968 nodes) could not capture this phenomena. Since we knew the phenomena we were attempting to validate, we were successful in This theory was proved by developing a detailed plate model of the beam. A conventional modal capturing this effect by dealing with the total system stiffness matrix. This requires dealing with very high dimensionality data sets for which the ISM program was very useful.

Normally open section structural elements are used, and if embedded, the actuators would be processes will result in some degree of local skin strain effect. With other fabrication concepts such as attaching the actuators on the interior of the structure, it is necessary to closely consider this The understanding of the dynamic anemaly is important to the design of smart structures. placed near the skin neutral axis. Uncertainties however in material properties and fabrication phenomena in selecting the sensor/actuator placement and control concept. Boeing Aerospace & Electronics

- Observed Relaxation Phenomena
- Think due to adhesive viscosity
- Came Across & Explained Skin Strain Phenomena
- Moment on skin induces local deformation
- Phenomena is significant if doing colocated or near colocated strain sensing
- Understanding is useful to assess necessity of actuation near skin neutral axis

REFERENCES

- 1) "Smart Structures Using Shape Memory Metals", R. Ikegami et al.
- 2) "Positive Position Feedback Control for Large Space Structures", J Fanson and T.K. Caughley
- 3) "Embeddable Interferometric Strain Sensor for Active Damping", R.D. Rempt and D.G.Wilson
- 4) "Shape Memory Alloys and Fiber Optics for Flexible Structure Control", D.G.Wilson et. al., SPIE San Jose Symposium, OE/FIBERS 90 Conference, Sept 17,1990

Optimal Active Member and Passive Damper Placement and Tuning

Cheng-Chih Chu James L. Fanson Mark H. Milman Daniel B. Eldred Jet Propulsion Laboratory California Institute of Technology Pasadena, CA 91109

Fourth NASA/DOD CSI Conference Orlando, Florida November 5 — November 7 , 1990

structure, it may be necessary to use a combination of isolators, passive dampers, actuators, and sensors to accomplish the In addition, it is assumed that the sensor configuration (including number, type, and location) has been given. Although the desirable performance requirements. In this study, only the passive damping and active control method will be considered. flexible structures where the vibrations are introduced into the structure by both internal and external disturbances. There are various ways for vibration control, for example, by isolation, by passive damping method, or by active control. In a physical Structural vibration control is necessary to satisfy the stringent pointing and shape requirements for future large precision sensor selection/placement problem is also very critical for control design, it will not be treated in this study.

or positive position feedback). For simplicity, only the passive dampers will be considered here. The active control, on the as viscoelastic/viscous dampers), or close the local actuator/sensor pairs passively (such as collocated velocity feedback loops, other hand, involves designing a closed-loop feedback control law using a number of sensors/actuators such that the resulting The passive damping method considered here can be treated as a control problem where the objective is to increase the level of modal dampings associated with critical flexible modes. This can be usually achieved either using passive dampers (such closed-loop system achieves performance requirements while preserving stability.

In either passive or active placement, the following fundamental problems needed to be addressed are:

- 1. How many passive dampers and actuators are necessary?
- 2. What types of actuators will be required?
- 3. Where the dampers and actuators should be placed in the structure? and
- 4. What is the "optimal" strategy (control law) to utilize selected dampers and actuators control law to achieve performance requirements?

the selection of types and locations for placing passive/active control elements is highly coupled with the associated control performance problem. In this study, we will not consider the problem (1) and (2) listed above. The number of passive dampers Because the effectiveness of passive dampers and/or actuators is decided by the performance of closed-loop systems, it is extremely difficult, if not impossible, to judge a priori which configuration (number, type, and locations) of passive and actuation devices is most effective without solving the related control performance for all possible configurations. Therefore, and the number/type of actuators are assumed to be given.

Introduction

Robust structural vibration control is critical to the success of future high precision large flexible structures.

Ways for vibration control include:

- Passive Damping (viscous and viscoelastic dampers).
- Active Damping (sensor/actuator colocation).
- Active Control (active feedback control law where sensors and actuators may or may not be colocated).
- Isolation.

(To meet the stringent mission requirements, some combination of these approaches may be necessary.)

Effectiveness of these methods will depend on:

- location(s) to be applied (placement problem), and
- the optimal strategy to be utilized (control problem).

Objective

to rolloff at a lower frequency. Hence, the performance at the torsion mode (approximately at 11.4 Hz) will be poor. The bandwidth while demanding performance in the same frequency range may also cause stability problems. All these difficulties the control bandwidth is too close to 35 Hz, the controller will not be able to rolloff fast enough in order not to excite the higher frequency modes. On the other hand, if the control bandwidth is too close to 12 Hz, then the controller must begin have been observed when our preliminary designed controller are implemented. One possible remedy to our control design is to It is a fact that any model is at best an approximation of the physical system. Hence, there is always some uncertainty present, even when the underlying process is essentially linear. This is especially the case of flexible space structures. If the uncertainties are not properly accounted for in control system design, the controller may cause instability or the performance of the closedloop system may be limited severely. Therefore, tight uncertainty bounds are required to provide robust control designs which achieve high performance when implemented on the physical system. However, tight uncertainty bounds are difficult to get. This is particularly true for lightly damped systems. Our recent experience in modeling and designing the control system for the Precision Truss where the non-collocated accelerometers and active elements are used as the measurement and actuation devices provides a good illustration for these difficulties. The control objective is to provide good performance for the first three flexible modes (<12 Hz) while not destabilizing the higher frequency modes (>35 Hz). It is extremely difficult, if not impossible, to achieve such an objective since there is not much space in frequency for allowable control bandwidth. If problem is further compounded by the extremely lightly-damped nature of the torsion mode which makes the identification of corresponding modal damping and frequency very difficult. Therefore, small error in modal parameter near the control place passive damper(s) such that the damping in the torsion mode is significantly improved. This will reduce the uncertainty associated with the torsion mode drastically. These previous experiences have motivated us to develop practical placement techniques for both passive dampers and actuators.

damp modes with large participation in the transfer functions of interest. In particular, our emphasis on the placement of controlled passively. This will make the design of active control systems less troublesome but more robust. The performance metrics to be used in the placement of passive dampers will be in the form of weighted system energy (passive). For the Since there are only a limited number of passive and actuation devices available, our strategy is to place passive dampers to passive dampers should be focused on flexible modes in the vicinity of the desired control bandwidth so that these modes can be placement of actuators, a weighted performance index of the quadratic form will be used where the variables are output errors (to be minimized) and control inputs.

Objective

- of passive and active elements to facilitate structural vibration control design. To develop meaningful and practical techniques for the placement and tuning
- To demonstrate placement techniques developed on CSI's Testbed structures.

The Placement Problem

be described by a linear, second order matrix differential equation. Note that it is common in structural analysis to model the In this study, it is assumed that number of passive dampers and actuators are fixed and the dynamics of the structures can D_v damping matrix as proportional damping .i.e.,

$$D_v = \alpha M + \beta K \quad (\alpha, \beta \ge 0, \ \alpha + \beta \ne 0).$$

In this case, the structural model can be rewritten in terms of modal coordinates The mass matrix is normalized to unity, and damping and stiffness matrix are both diagonalized. However, in general, this assumption will not be necessary in our approach.

The Placemen: Problem

In this study, the placement problem associated with passive damping and active control is considered.

Assumptions:

- Viscous dampers are used to introduce passive damping which is modeled as a spring (k_p) in parallel with a dashpot (k_v) .
- ullet Number of passive dampers (n_p) and actuators (n_a) are fixed.
- Number and locations of sensors for active control are given.
- Dynamic model of the structure can be described by:

$$M\ddot{z} + Dv\dot{z} + Kz = B_f f$$

where

z = the generalized coordinates $(n \times 1)$,

f = the external forced input vector $(l \times 1)$,

$$M = M^T > 0, K = K^T \ge 0,$$
 and

 $D_v = lpha M + eta K$ is the proportional viscous damping matrix

$$(\alpha, \beta \ge 0, \alpha + \beta \ne 0).$$

Dynamic Model for the Passive Placement Problem

as a device with collocated sensor and actuator where the sensor measures the relative velocity and displacement between two end points of the damper, and the actuator will apply an axial force at two nedal points with equal magnitude but in opposite directions. Therefore, to include a viscous damper in the structure, the damping and stiffness matrix in the dynamic model Suppose that a discrete viscous damper is placed between two nodal points in the structure. Ideally, the damper can be treated will be changed. The control force applied by the actuator can be regarded as constant position plus velocity feedback.

Dynamic Model for the Passive Placement Problem

The dynamic model with the inclusion of a viscous damper can be described as:

$$M\ddot{z} + Dv\dot{z} + Kz = bpup + B_f f$$

where u_p is the force generated by the damper:

$$u_p = -b_p^T (k_p z + k_v \dot{z}) \quad (k_v > 0).$$

Rewritten as:

$$M\ddot{z} + (D_v + k_v b_p b_p^T)\dot{z} + (K + k_p b_p b_p^T)z = B_f f.$$

With n_{p} dampers,

$$M\ddot{z} + (D_v + B_p K_v B_p^T)\dot{z} + (K + B_p K_p B_p^T)z = B_f f.$$

where

$$Kv = diag \left[kv_1 \ kv_2 \ \dots \ kv_{np} \right], \quad Kp = diag \left[kp_1 \ kp_2 \ \dots \ kp_{np} \right].$$

Combined Placement Model

In case that both the problems of passive damper and actuator placement are considered, the corresponding dynamic model can be generated easily

$$M\ddot{z} + (D_v + B_p K_v B_p^T) \dot{z} + (K + B_p K_p B_p^T) z = B_a u_a + B_f f.$$

As mentioned in the introduction, the problem of sensor placement will not be considered in this study. It is assumed that the types of sensors and their locations are given. Typically, the measurements can be expressed as

$$y_m = C_{mp}z + C_{mv}\dot{z} + \eta$$

where y_m is a $m \times 1$ vector and η is a $m \times 1$ sensor noise vector.

Instead, they are expressed as functions of some sensor measurements, for example, pathlength and wavefront tilt in the FMI [1]. These variables are called the controlled outputs. Typically, the controlled output can be expressed or approximated as It is common in the control problems, variables which we wish to control, may not be measurable directly from specific sensors. linear combinations of measurements. Therefore, the controlled output y can also be written in the following form:

$$y_o = C_{op}z + C_{ov}\dot{z}$$

where y_o is the controlled output vector $(r \times 1)$.

Under the assumption of proportional viscous damping, the dynamic model can then be written in the state-space form where the state vector consists of a modal coordinate vector and its derivative.

Dynamic Model for the Actuator Placement Problem

The dynamic model with the inclusion of n_a actuators can be described as:

$$M\ddot{z} + Dv\dot{z} + Kz = B_a u_a + B_f f$$
 (u_a is $n_a \times 1$ actuator input vector).

The measurements and the controlled output can be written as:

$$y_m = C_{mpz} + C_{mvz} + \eta$$
 (η is the sensor noise vector),

$$y_0 = Copz + Cov\dot{z}$$
.

Combined Placement Model

Under the assumption of proportional viscous damping, the combined dynamic model can be represented in the state-space formulation:

$$\dot{x} = \left[-(\Omega^2 + \Phi^T B_p K_p B_p^T \Phi) \right. \\ \left. -(2\Lambda\Omega + \Phi^T T_p E_p K_v B_p^T \Phi) \right] x + \left[\begin{array}{c} 0 \\ \Phi^T B_a \end{array} \right] u_a + \left[\begin{array}{c} 0 \\ \Phi^T B_f \end{array} \right] f$$

$$ym = [Cmp\Phi \quad Cmv\Phi]x + \eta$$

$$y_O = [C_{Op} \Phi \quad C_{Ov} \Phi] x$$

where

$$= \Phi_q, \quad x = \begin{bmatrix} q \\ \dot{q} \end{bmatrix}, \quad \Phi^T M \Phi = I, \quad \Phi^T K \Phi = \Omega^2, \quad \Phi^T D_v \Phi = 2 \Lambda,$$

$$\Omega = diag[\omega_1 \omega_2 \ldots \omega_n], \quad \Lambda = diag[\zeta_1 \zeta_2 \ldots \zeta_n], \quad \text{and } \zeta_i = \frac{1}{2}(\frac{\alpha}{\omega_i} + \beta\omega_i).$$

Criterion for the Optimal Placement

A reasonable strategy to the optimal placement problem is to use physically meaningful and numerically tractable measures of performance. If only the passive dampers are considered and no explicit control objective is specified, a reasonable quantity to be considered in the optimization problem is the total energy E_T in the system which is the sum of kinetic energy and strain

To capture this energy type of criterion in a numerically tractable way, 13t's define a fictitious vector

$$y_{\scriptscriptstyle E} = rac{\sqrt{2}}{2} \left[egin{matrix} \Omega q \\ \dot{q} \end{array}
ight].$$

Hence, $y_E^T y_E = E_T$, and

$$\|y_E\|_2^2 = \int_0^\infty E_T \ dt$$

where $||y_E||_2$ is the \mathcal{H}_2 -norm of y_E .

 $x_0 = \begin{bmatrix} q(0) \\ \dot{q}(0) \end{bmatrix}$. To avoid the dependency of $\|y_E\|_2$ on x_0 , one could take a weighted average over the set of possible x_0 . This The advantage of this formulation is that it is expressed as the integral of a quadratic function in the state vector. The integral thus can be computed through the solution of a Lyapunov equation from any stabilizing control law. In the case of passive dampers, the control law is simply the collocated negative velocity feedback. Although using the integral of total energy of the averaging process results in a criterion which in the stochastic sense could be interpreted as the steady state RMS energy due to a white noise input with appropriate intensity. This type of criterion is applicable to the optimal placement problem of the system as the criterion for the optimization is computationally attractive, the quantity $\|y_E\|_2$ depends on the initial conditions, passive dampers if there are no inputs/outputs specified in the problem. However, this situation does not happen very often.

From the perspective of control system design, the main reason to place passive and active devices in the structure is to improve performance in the presence of uncertainties. The performance of a system is measured in terms of the behavior of the output or error signals. For example, a good performance measure for the vibration control problem is to attenuate the level of disturbance effects on some well-defined variables associated with the system. The uncertainties, on the other hand, consider external input signals such as disturbances and noises, and unavoidable modeling errors between the physical system and its corresponding mathematical model. In fact, to resolve the fundamental tradeoffs of performance and uncertainty was the primary motivation for the development of feedback theory. Therefore, to make the placement problem meaningful, the controlled output variables should be clearly defined, and external disturbance inputs should also be characterized A reasonable criterion to the optimal placement problem is to use physically meaningful and numerically tractable measures of performance.

Example:

$$\int_0^\infty E_T \ dt$$

where E_{T} is the sum of kinetic energy and potential energy:

$$E_T = \frac{1}{2} \dot{z}^T M \dot{z} + \frac{1}{2} z^T K z = \frac{1}{2} \dot{q}^T \dot{q} + \frac{1}{2} q^T \Omega^2 q \ .$$

This criterion is applicable for the passive damper placement if no inputs/outputs are specified.

meaningful, the controlled output variables must be clearly defined, and external From the perspective of control system design, to make the placement problem disturbance inputs should be suitably characterized.

Optimal Placement for the Passive Dampers

specified. Then, $\|y_o\|_2$, the \mathcal{H}_2 norm of y_o , can be used as the criterion for the optimization problem. If colored disturbances Assume that the disturbance inputs are modeled as uncorrelated white noises, and in addition, the controlled output y_o is are assumed, the dynamics of coloring filters can be absorbed into the state equation.

Since there are only a limited number of passive elements available, the passive elements should be placed in such a way that the criterion used in the passive placement should focus more in certain ranges of frequencies. For example, in the Precision Truss experiment [2,3], if the passive damper can be inserted in such a way that the damping of the torsional mode is significantly As previously discussed, from the control perspective, both the placement of passive and active devices should be considered. increased, then the active control design will not be compromised too much to avoid the potential stability problem. This will enhance the robustness in the active control and and the performance will be improved.

Optimal Placement for the Passive Dampers

tion, the controlled output y_0 is specified. Then, $\|y_0\|_2$, the \mathcal{H}_2 norm of y_0 , can be used as the criterion for the optimization problem, and the associated optimal placement problem Assume that the disturbance inputs are modeled as uncorrelated white noises, and in addiof passive dampers can be posed as

$$\min_{Bp \in \mathcal{B}_{\mathcal{P}}} \|y_0\|_2$$

subject to

$$\dot{x} = \left[-(\Omega^2 + \Phi^T B_p K_p B_p^T \Phi) \right. \\ \left. -(2\Lambda\Omega + \Phi^T B_p K_v B_p^T \Phi) \right] x + \left[\Phi^T B_f \right] f$$

7

$$y_0 = [C_{op} \Phi \quad C_{ov} \Phi] x$$
.

where

$$\mathcal{B}_{\mathcal{P}} \triangleq \{(b_{i_1}, b_{i_2}, \dots, b_{i_{n_p}}) : i_1, i_2, \dots, i_{n_p} \in \mathcal{N}_{\mathcal{P}}, \ i_j \neq i_k, \ \forall \ j, k = 1, 2, \dots, n_p(j \neq k)\}$$

 $b_{i_{k}}$ is the influence vector corresponding to $i_{k}^{\ th}$ location.

 $N_{m p}$ is the total number of candidate locations for placement,

$$\mathcal{N}_{\mathcal{P}} \stackrel{\triangle}{=} \{1, 2, \ldots, N_p\}.$$

Optimal Placement for the Passive Dampers (Cont'd)

One reasonable way to improve damping only on selected modes is to introduce a weighting function W, into the quadratic cost function. The frequency response of W_p will have relatively large magnitude in the frequency range of interest

the frequency response of y_o most effectively in the region indicated by W_p . For the current control design of the Precision The solution of the above optimization problem will attempt to place the passive dampers in a configuration which improves uncertainty near the crossover frequency may not be an issue. In this case, W_p can be used to improve dampings of flexible Iruss, this region will be in the vicinity of crossover frequency (approximately at 20 Hz). However, for other control problems, design model could result from a "poor" identification of the physical system within the control system bandwidth. Another possibility is to use W_p in the region of the first few flexible modes beyond the control bandwidth so that the controlled system modes at lower frequencies so that the performance within the control bandwidth will be enhanced. For example, the nominal will be much more robust against higher frequency uncertainty.

Another interesting issue associated with optimal passive damper placement is "optimal tuning" of damper parameters where typically the damping rate and damper stiffness can be tuned. In this case, the "placement+tuning" optimization problem becomes a combined continuous-discrete optimization problem, i.e.,

 $\min_{K_v,K_p} \min_{B_p \in \mathcal{B}_P} \|W_pG_p(s;B_p)W_f\|_2$

Optimal Placement for the Passive Dampers (Cont'd)

Alternatively, the optimization problem can be posed as:

$$\min_{Bp \in \mathcal{B}_{\mathcal{P}}} \|G_p(s; B_p)\|_2$$

where $G(s;B_p)$ is defined as the transfer matrix from the f to y_O with a given damper configuration corresponding to $B_{p}.$

- For a given B_p , the above \mathcal{H}_2 -norm can be accurately computed in closed-from by solving a Lyapunov equation.
- For colored noises, one can solve

$$\min_{B_p \in \mathcal{B}_{\mathcal{P}}} \|G_p(s; B_p) W_f \|_2$$

where \boldsymbol{W}_f is the corresponding color filter.

Weighting matrix (W_p) can be used to improve the performance over certain frequency range, the optimization problem can then be further generalized as:

$$\min_{B_p \in \mathcal{B}_{\mathcal{P}}} \|W_p G_p(s;B_p) W_f\|_2$$

ullet k_v and k_p of a given damper can also be tuned such that the performance is optimized:

Optimal Placement for the Actuators

For the actuator placement problem, the same performance measure, i.e. $\|y_o\|_2$ should also be included in the optimization criterion. In addition, any physical actuation device can only provide finite control energy, which is usually described in terms of saturation level (magnitude) and finite bandwidth. Therefore, to avoid saturation, the control energy should be penalized appropriately in the optimization problem.

If the actuator placement problem is posed for active control, the following optimization problem can be formulated:

$$\min_{B \in \mathcal{B}} \min_{K \in \mathcal{K}} \| \frac{W_a y_o}{W_u K y_m} \|_2$$

signals which not only penalizes the control energy but also indicates the desired spectral content in actuator signals. Again, if the disturbance inputs are independent colored noises, the dynamics of color filters can be augmented into the model. Note where W_a is the weighting function for the desired controlled output y_o , and W_u is the weighting function for the actuator that the inclusion of actuator dynamics into the state-space model can also be done in a similar manner as that in the coloring At this point, one may wonder if it is possible to pose a combined optimal placement problem which considers both passive dampers and actuators. A natural candidate is to form the following "bi-objective" optimization problem:

$$\min_{B \in \mathcal{B}} \min_{K \in \mathcal{K}} \min_{B \in \mathcal{B}_{\nu}} \gamma \|w_{p} y_{o}\|_{2} + \lambda \|\frac{W_{a} y_{o}}{W_{u} K y_{m}}\|_{2} \qquad (\alpha > 0, \beta > 0).$$

It is not clear at this stage to see the advantages of the above formulation toward achieving our objective. Instead, in this study, it is proposed to solve the two placement problems separately. The passive placement problem will be solved first. The active placement problem will then be solved with the inclusion of passive dampers placed at the locations resulted from the solution of the passive placement problem.

Optimal Placement for the Actuators

In our approach, the actuator placement problem is carried out in the context of active control, the associated optimal placement problem can be posed as a \mathcal{H}_2 optimization problem:

$$\min_{Ba \in \mathcal{B}_{\mathcal{A}}} \min_{K \in \mathcal{K}} \| \frac{W_{pyo}}{WuKym} \|_2$$

subject to

$$\dot{x} = \begin{bmatrix} 0 & I \\ -\Omega^2 & -2\Lambda\Omega \end{bmatrix} x + \begin{bmatrix} 0 \\ \Phi^T B_a \end{bmatrix} u_a + \begin{bmatrix} 0 \\ \Phi^T B_f \end{bmatrix} f ,$$

$$y_m = [C_m p \Phi \quad C_m v \Phi] x + \eta ,$$

and

$$y_o = [C_{op} \Phi \quad C_{ov} \Phi] x$$
.

 W_{p} is the weighting function for the performance.

 $oldsymbol{W}_u$ is the weighting function for actuator signals.

$$\mathcal{B}_{\mathcal{A}} \stackrel{\triangle}{=} \{ (b_{i_1}, b_{i_2}, \dots, b_{i_{n_a}}) : i_1, i_2, \dots, i_{n_a} \in \mathcal{N}_{\mathcal{A}}, \quad i_j \neq i_k, \ \forall \ j, k = 1, 2, \dots, n_a (j \neq k) \}$$

 $\mathcal{K} \stackrel{\triangle}{=} \{K: \text{ any } n_a imes m \text{ stabilizing feedback controller } \}$

 b_{i_k} is the $i_k{}^{th}$ column of the B_a matrix.

 $N_{oldsymbol{a}}$ is the total number of candidate actuator locations for placement, and

$$N_{\mathcal{A}} \stackrel{\triangle}{=} \{1, 2, \ldots, N_d\}.$$

Approach

It is clear that each of the optimization problems includes solving (i) an "optimal control" problem, and (ii) a "combinatorial optimization" problem. In the passive case, the associated "optimal control problem" only involves computing the performance measure $\|v_p y_o\|_2$. Since the damping rate constant k_v is fixed, given any possible combination in $\mathcal{B}_{\mathcal{P}}$, it is well-known that the norm $\|W_p y_o\|_2$ can be computed through the solution of a Lyapunov equation. The solution of the associated combinatorial optimization problem is the combination in $\mathcal{B}_{\mathcal{P}}$ corresponding to the minimal norm $\|w_p y_o\|_2$.

For the actuator placement problem, the "optimal control" problem is more involved. For each possible combination in $\mathcal{B}_{\mathcal{A}}$, through standard LQG theory by solving two Riccati equations. Again, the combinatorial optimization problem is simply to For the actuator process, where $\frac{V_a y_o}{V_b}$ is simply an optimal LQG problem where the performance measure $\|\frac{W_a y_o}{W_a K y_m}\|_2$ can be computed choose the combination with minimal cost function.

In both optimization problems, the corresponding "optimal control" problem is relatively easy. However, the corresponding combinatorial optimization problems are both notor ous problems. This is due to the fact that the potential number of candidate locations for placement (N_p, N_a) will be large in large space flexible structures. However, relatively few passive and actuation devices (n_p, n_a) will be available. In general, $N_p >> n_p$, $N_a >> n_a$, and total numbers of combinations, $\frac{N_{p^{\perp}}}{(N_{p}-r_{p})!}$ and $\frac{N_{q^{\perp}}}{(N_{q}-r_{q})!}$ respectively, are usually very large. Therefore, it is impractical, if not completely impossible, to try the exhaustive search.

step to limit the set of possible candidate locations to a smaller subset, say N_a' where $N_a >> N_a'$. In [2], the active A heuristic approach [2] was developed for the active-member placement for the Precision Truss which involves a "pruning" member placement was done by first solving a LQR problem where all candidator active member locations are used. The pruning step is simply to select N_a ' elements which contribute most "energy". An exhaustive combinatorial search is then conducted throughout this subset to find the "optimal" combination of elements which yields the smallest \mathcal{H}_2 -norm cost.

For the passive placement problem, a "pruning" process could be developed based on the modal strain energy ranking method used in the study of the FMI [1]. The pruning process is simply to choose the top N_p ' candidate structural element locations according to the ranking where $N_p >> N_p' > n_p$. Again, the exhaustive combinatorial search can then be done throughout this smaller subset.

statement regarding the solutions of these sub-optimal approaches as compared to the optimal ones. In recent years, the probabilistic approach to the combinatorial programming problem have gained popularity and have been applied on various These ad hoc pruning approaches have been demonstrated to be quite useful ([1],[2]). However, it is difficult to make a general disciplines with impressive results. Two notable methods in this area are simulated annealing [4,5,6] and genetic algorithm [7]. In particular, the method of simulated annealing has been applied to the optimal passive members problem for CSI Phase B Testbed. The preliminary study showed very encouraging results.

Approach

The optimal placement problem includes:

- "optimal control" problem,
- "combinatorial optimization" problem.

Solution to the optimal control problem:

- Solve Lyapunov equation for the passive damper placement.
- Solve an nonlinear programming problem for optimal tuning of damper coefficients.
- Solve two Riccati equations for the actuator placement.

Solution to the combinatorial optimization problem:

- Simulated Annealing
- Genetic Algorithm
- •

Passive Damper Placement for JPL's CSI Phase B Testbed

The proposed approach for the placement has been applied to select the damper locations for JPL's CSI Phase B Testbed

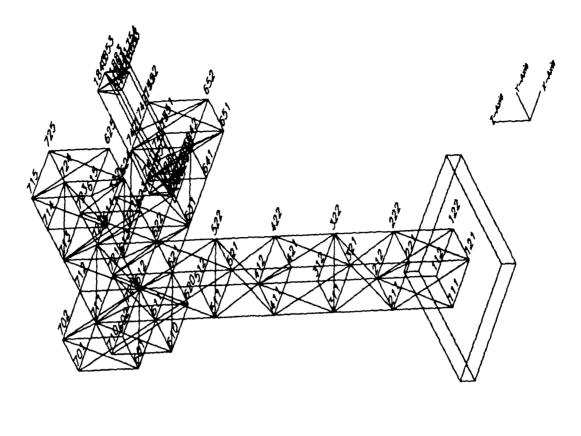
There are 186 candidate locations on the main truss structure to be considered for placing 4 passive dampers. In this preliminary study, the values of the damping and stiffness parameter (respectively) for all 4 dampers are assumed to be the same. Therefore, the optimal passive damper placement problem is simply a combinatorial optimization problem which can be solved using the simulated annealing technique. Note that this simplified assumption may constrain the effectiveness of dampers. A more feasible approach is to allow the "tuning" of damping and stiffness parameters for dampers to be placed. This is a much harder optimization problem since it includes both the "discrete" optimization problem (selection of damper location) and "continuous" optimization problem (tuning). This will be considered in our future study.

234 Hertz. Our goal is to minimize the motions at the truss bay where the trolley is mounted. In particular, displacements in x, y, and z direction at the 8 grid points of the truss bay under consideration are chosen as the controlled outputs. In addition, a 6^{th} order butterworth filter with a bandwidth of 25 Hertz is used as a weighting function in the performance measure. As Since the passive damper will have no impact on the rigid body modes, the dynamic model includes only 18 flexible modes below discussed before, this weighting function was constructed to emphasize our desire to place dampers in locations where the dampers will be most effective in the frequency range less than 25 Hertz.

3 translational degrees of freedom. It is further assumed that the disturbance inputs are uncorrelated white noises. The performance measure (referred as energy in this paper) is then the \mathcal{L}_2 -norm of the weighted controlled outputs, or equivalently, Two locations, grid 412 and 715, are considered as the disturbance input sources where the forces can be applied at all the H2-norm of weighted transfer matrix from disturbance inputs to the controlled outputs which can be computed reliably through the solution of a Lyapunov equation. In the following, two studies, corresponding to applying disturbance at grid 412 and 715 respectively, are considered for the placement of passive dampers on JPL's CSI Phase B Testbed. The damping and stiffness coefficients of the viscous dampers used in this study are equal to 750 lb-s/in and 8000 lb/in respectively.

Passive Damper Placement for CSI Phase B Testbed

- 186 candidate locations for placement.
- 4 viscous passive dampers available.
- constant damping and stiffness parameters for all dampers.
- 18 flexible modes (< 234 Hz) considered.
- 0.1% uniform modal dampings for all modes.
- the disturbance inputs forces applied at grid 412 and 715 in x, y, and z direction.
- the controlled outputs displacements at 8 grid points of the truss bay supporting trolley (641, 642, 651, 652, 741, 742, 751, and 752).
- performance measure H₂-norm (energy)
 of the controlled outputs.



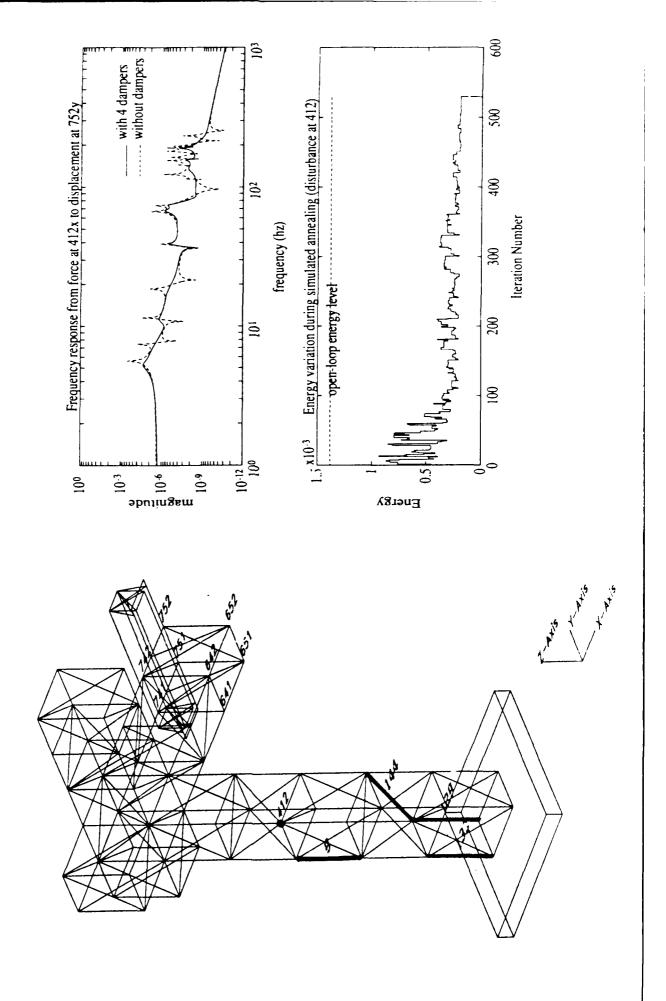
Summary of Results: Case A - Disturbances at Grid 412

In the first study, optimal passive damper placement problem is considered where the disturbance input forces are applied at grid 412 in x, y, and z direction. To initialize the simulated annealing procedure, energy values for 20 randomly chosen combinations for placing 4 dampers are computed, and the average energy variation is used as the initial temperature. The combination which results in the lowest energy so far is chosen as the initial passive damper configuration. For each following iteration, only one location is allowed to change. Since there is more than one damper to be placed, our approach is to first decide randomly which damper location among 4 previously selected locations will be replaced. A new location will then be randomly generated.

It took 528 iterations to find the "optimal" combination which does not include the 20 combinations used in initialization. The 4 optima! damper locations are 9, 129, 133, and 144, and the corresponding energy is equal to 1.964805e-04. Note that the energy of the system with no dampers (called open-loop system) is equal to 1.382392e-03. It is clear from the comparison of frequency responses that there is significant improvement in disturbance responses with 4 "optimally placed" dampers. It is worth mentioned that element 144 vas also identified in a separate study of viscous damper effects on Phase B Testbed by Andy Kissil of JPL using the strain energy ranking method. For the first flexible mode, element 144 has the highest element strain energy among all the long diagonal elements.

is equal to 2.213588e-04. If only 2 campers are to be placed in the structure, the optimal locations are 132 and 133, and the corresponding energy is equal to 5.451702e-04. These results are interesting since using more dampers always results in For the case that only 3 dampers are available, the optimal locations are 35, 133, and 141, and the corresponding energy better performance. However, the ma gin of performance improvement may decrease if more dampers are used.

An interesting exercise was carried out by randomly generated 600 combinations for placing 4, 3, and 2 dampers. The minimal energy are 2.437498e-04, 2.44949470e-04, and 2.626762e-04, respectively. The results show the optimal solutions obtained through simulating annealing always generate better results in all three cases.



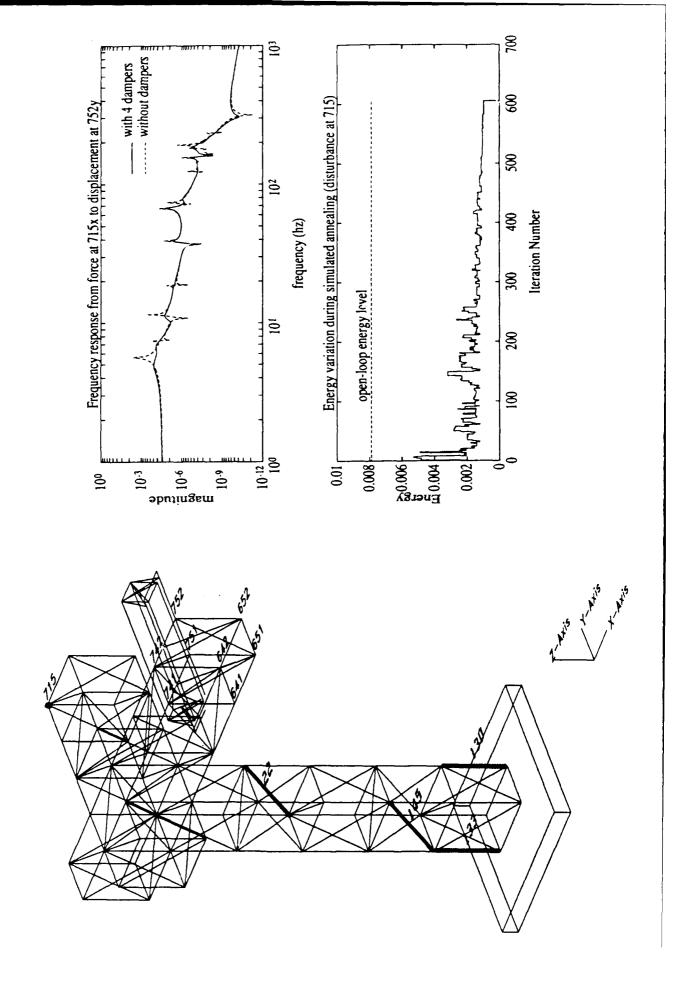
Summary of Results: Case B - Disturbances at Grid 715

The second study is similar to the first one except that the disturbance input forces are applied at grid 715 in x, y, and z

locations are 22, 130, 133, and 145, and the corresponding energy is equal to 9.681566e-04. Note that the energy of the system with no dampers (called open-loop system) is equal to 7.883377e-03. Again, the comparison of frequency responses Following the same approach as in the first study, the "optimal" solution was found after 603 iterations. The 4 optimal damper indicate that there is significant improvement in disturbance responses with 4 "optimally placed" dampers.

is equal to 1.023244e-03. For the case that only 2 dampers are available, the optimal locations are 130 and 131, and the For the case that only 3 dampers are available, the optimal locations are 130, 132, and 133, and the corresponding energy corresponding energy is equal to 2.451702e-04.

Again, similar exercise was done by comparing the randomly generated best solution with the optimal solution using the simulated annealing technique. The latter always yields better performance.



Conclusions and Future Work

Conclusions:

- A well-posed optimization problems for the actuator and passive damper placement and turing is proposed.
- The optimal placement problem includes
- (i) an optimal control problem where the optimization criterion can be computed reliably.
- (ii) a combinatorial optimization problem where reasonable solution can be obtained using simulated annealing techniques.
- The approach is used to place passive dampers to JPL CSI Phase B Testbed. The "optimal" locations chosen yield significant performance improvement.

Future Work:

- To include tuning of damper's parameters in the passive damper placement. (This will result in combined continuous-discrete optimization problem).
- To apply the optimal placement techniques for placing passive dampers and active members on Phase B Testbed.
- To study and evaluate other approaches toward solving the combinatorial programming problem.

Acknowledgements

The research described in this paper was carried out by the Jet Propulsion Laboratory, California Institute of Technology, under contract with the National Aeronautics and Space Administration. The authors wish to express their appreciation to Dr. Moktar Salama, Ms. Robin Bruno, and Mr. Andy Kissil of JPL for their contributions to this work.

References

- 1. Laskin, R.A., ed. "Focus Mission Interferometer: Business-as-Usual Design Document," October 31, 1989.
- 2. Fanson, J.L., G.H. Blackwood, and C.C. Chu, "Active-Member Control of Precision Structures," AIAA Paper No. 89-1329, 30th Structures, Structural Dynamics and Materials Conference, Mobile, AL, 1989.
- Chu, C.C., R.S. Smith, and J.L. Fanson, "Robust Control of An Active Precision Truss Structure," Proc. American Control Conference, Vol. 3, pp. 2490-2495, 1990. **دن** .
- Metropolis, N., A. Rosenbluth, M. Rosenbluth, A. Teller, and E. Teller, "Equations of State Calculations by Fast Computing Machines," J. Chem. Phys., 21, pp. 1087-1093, 1953. 4
- 5. Kirkpatrick, S., C. Gelatt, and M. Vecchi, "Optimization by Simulated Annealing," Science, Vol. 220, No. 4598, May, 983, pp. 671-680.
- Chen, G.S., R. Bruno, and M. Salama, "Optimal Placement of Active/Passive Members in Truss Structures Using 89-1287, 30th Structures, Structural Dynamics and Materials Conference, Simulated Annealing," AIAA Paper No. Mobile, AL. 9
- 7. Goldberg, D.E., "Genetic Algorithms in Search, Optimization, and Machine Learning," Addison-Welley Publishing Company, Inc., 1989.

Modal Domain Optical Fiber Sensors for Vibration Sensing in Large Flexible Truss Structures

Douglas K. Lindner Richard O. Claus
Bradley Department of Electrical Engineering
and
Harley Cudney
Department of Mechnical Engineering

VIRGINIA TECH

Prof. Douglas K. Lindner
Bradley Department of Electrical Engineering
Virginia Tech
Blacksburg, VA 24061
(703) 231-4580

Prof. Richard O. Claus
Fiber & Electro-Optic Research Center
Bradley Department of Electrical Engineering
Virginia Tech
Blacksburg, VA 24061
(703) 231-4580

Prof. Harley Cudney

Department of Mechnical Engineering

Virginia Tech

Blacksburg, VA 24061

(703) 231-7088

OUTLINE

- * Experiment / Research Objectives
- * Modal Domain Optical Fiber Sensors
 - * Identification and Control Results
 - * Conclusions / Future Work

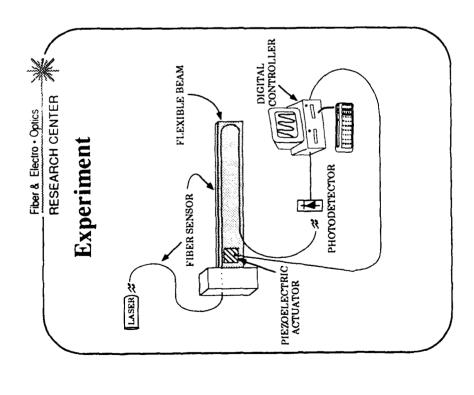
Recently, it been shown, both theoretically and experimentally, that modal domain (MD) optical fiber sensors can be used for identification and control of flexible structures. In this paper we review the current state-of-the-art of MD sensors for sensing vibrations in flexible structures.

First, we describe an experiment which incorporated an MD sensor into a control loop for vibration suppression in a cantilevered beam. The objective of this experiment was to develop a model of the sensor for control system design and verify this model experimentally.

Next, we describe the basic operating principles of MD sensors and integrate the sensor model into the beam model. The result is a standard design model to which any of the usual system theoretic methodologies may be applied.

Then we present the results of the experimental investigation.

Finally, we suggest several future applications of MD sensors.



This experiment consisted of a flexible cantilevered beam instrumented with a piezoelectric actuator and an MD optical fiber sensor.

The modal domain (MD) sensor consisted of a source laser, an insensitive lead in fiber, a sensing fiber attached along the length of the beam, an insensitive lead out fiber, and a photodetector.

This sensor is called a **distributed-effect** sensor because the sensor responds to strain over a significant gage length.

The steel beam was approximately 27 inches long and 1/32 inch thick.

The actuator was a standard piezoelectric ceramic patch.

A PC was used to collect data and implement the control law. The sampling frequency was sufficiently high that the sampling effects could be ignored.

This experiment and the results in this paper are described in detail in

Cox, D. E. and D. K. Lindner, "Active Control for Vibration Suppression in a Flexible Beam Using a Modal Domain Optical Fiber Sensor," accepted for the ASME Journal of Vibration and Acoustics, 1990.

RESEARCH OBJECTIVES

- * Verify the Modal Domain Sensor Model
 - -For Control System Design
 - -For Other System Theoretic Applications

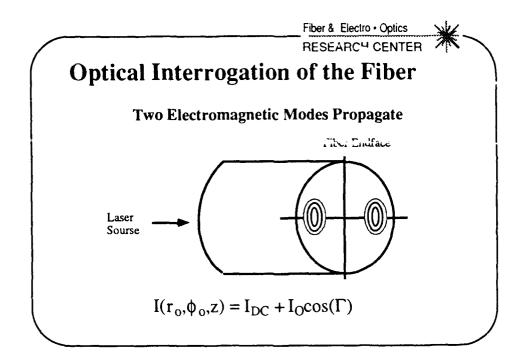
The purpose of this research was to derive the model of a distributed-effect MD optical fiber sensor, integrate this model into the dynamic model of a flexible beam, and verify this analysis by experiment.

MODAL DOMAIN SENSOR MODEL

- * Optical Interrogation of the Fiber
 - Interferometric
- * Strain Transfer Between the Optical Fiber and the Beam
- * Strain-Optic Interaction
- * Detection Schemes

The output of the optical fiber sensor is related to to strain in the beam. The derivation of this relationship can be split into the four components identified above.

Below we will discuss modal domain optical fiber sensors. Other types of optical fiber sensors can be obtained by reconfiguring the source and detection electronics differently, or by using different fibers. However, all of these sensors follow the general principles outlined above.

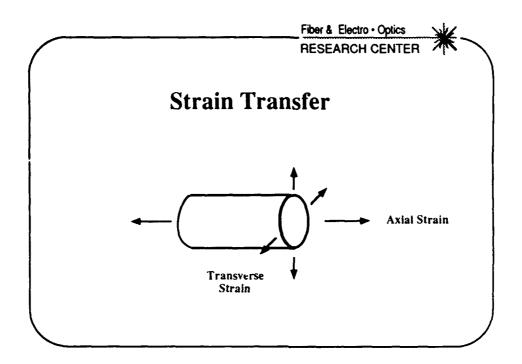


The intensity at the endface of the optical fiber depends on the electromagnetic modes propagating in the fiber. Which modes propagate depends on the geometry of the fiber, the wavelength of the source laser, and the launch conditions. In MD sensors, two modes propagate.

These two modes establish a well defined two lobe intensity pattern in any cross section of the fiber; in particular, at the endface of the fiber. When the fiber is subjected to strain the power shifts between these lobes. By monitoring the intensity at a point on the fiber endface with a photodetector, vibrations in the beam can be detected.

The intensity pattern is generated by the interference of the two modes as they propagate down the fiber. Hence, this sensor is of the interferometric type. The operation of this sensor is described in detail in

Murphy, K. A., M. S. Miller, A. M. Vengasarkar, and R. O. Claus, "Elliptical-Core Two Mode, Optical Fiber Sensor Implementation Methods," Journal of Lightwave Technology, Vol. 8, 1990, pp. 1688-1696.



The strain in the beam is transferred to the optical fiber through the mechanical attachment of the fiber to the beam. At each point along the sensing section of the fiber the strain in the fiber is resolved into axial and transverse components. A detailed discussion of strain transfer is given in

Sirkis, J. S. and H. W. Haslach, Jr., "Complete Phase-Strain Model for Structurally Embedded Interferometric Optical Fiber Sensors," submitted for publication, 1990.

In the experiment above, the axis of the fiber was aligned with the strain field of the beam. We assumed perfect bonding of the fiber to the beam. Thus, the intensity at the fiber endface changed in response to axial strain in the optical fiber.

Strain - Optic Interaction

Strain effects the propagation constant of the electromagnetic modes through:

- * Changing the core radius
- * Changing the fiber length
- * Photo-elastic Effect; Changing the indices of refraction

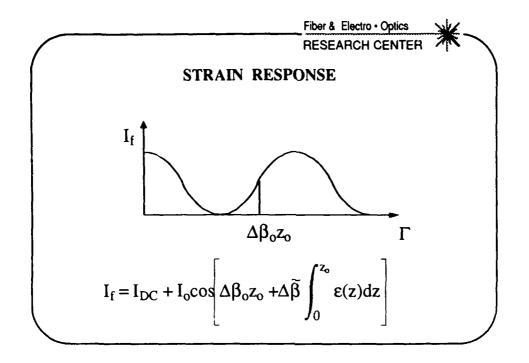
The electromagnetic modes which propagate in the fiber depend on the the source wavelength, core radius, and the indices of refraction. These parameters determine the propagation constants of the two modes which propagate in the fiber.

The two modes which propagate set up an interference pattern which varies sinusoidal along the length of the fiber. The axial variation of the interference pattern is determined by the difference in the propagation constants of the two modes. The particular pattern observed at the fiber endface depends on the nominal gage length of the sensor.

When the fiber is subjected to strain the core radius changes due to mechanical deformation. Also, the indices of refraction change because of the photoelastic effect. These two changes in the fiber parameters cause a differential change in the propagation constants of the two propagating modes resulting in a different axial variation in the interference pattern.

Finally, when the fiber is subjected to strain the gage length changes.

All of these changes are resolved into a net change in the interference pattern at the endface of the fiber.



The change in phase of each differential element of the fiber is determined according to the effects discussed in the previous slide. The total change in phase is obtained by integrating over the gage length of the fiber. The exact nonlinear expression is then linearized about zero strain. The resulting expression is shown above.

This graph shows the two most important features of the dependance of the output of the sensor on the strain in the structure. First, the sensor output depends on the integral of strain along the path of the fiber. Secondly, for large strains the sinusoid nonlinearity is significant.

For the results reported here, the sensor was operated in its linear region. The effect of the nonlinearity on the sensor output and on the control system performance is discussed in

Lindner, D. K., G. A. Zvonar, W. T. Baumann, and P. Delos, "Nonlinear Effects of a Modal Domain Optical Fiber Sensor in a Vibration Suppression Control Loop for a Flexible Structure," submitted to the ASME Journal of Vibration and Acoustics, 1990.

Detection Electronics

Small Strains--Analog Detection

Large Strains--Fringe Counting

If the level of strains in the beam is such that the sensor output is in the linear range of the sinusoid, the analog output of the photodetector can be used directly as a feedback signal in the control loop.

In the experiment described here we used direct analog feedback.

For large strains, it is possible to count the number of 2π phase shifts in the intensity ("fringe counting"). The hardware required to count fringes is described in

Murphy, K. A., M. S. Miller, A. M. Vengasarkar, and R. O. Claus, "Elliptical-Core Two Mode, Optical Fiber Sensor Implementation Methods," Journal of Lightwave Technology, Vol. 8, 1990, pp. 1688-1696.

Integration of the Sensor Model with the Beam Model

$$M\ddot{\eta}(t) + D\dot{\eta}(t) + K\eta(t) = Qv(t)$$

$$I_{f}(t) = \Delta \widetilde{\beta} \int_{0}^{z_{o}} \frac{\partial^{2}}{\partial z^{2}} y(t,z) dz$$

$$I_{f}(t) = \Delta \widetilde{\beta} \sum_{i=1}^{N} \eta_{i}(t) \left[\psi_{i}'(z_{o}) - \psi_{i}'(0) \right]$$

$$I_f(t) = C\eta(t)$$

Assuming perfect strain transfer between the beam and the optical fiber, the strain at the surface of the beam is equal to the axial strain in the fiber. Let the displacement of the beam be y(z,t). Then the output of the sensor in terms of the beam coordinates is found by substituting the strain at the beam surface in terms of y(z,t) into the integral expression of a previous slide.

Here we have assumed that the flexible beam is represented by a finite dimensional model derived from a modal expansion of y(z,t). Substituting this modal expansion into the model of the sensor results in a finite dimensional model of the fully instrumented beam in standard form. Now all of the standard identification and control algorithms can be applied in the usual way.

In the experiment below we compared simulated and experimental responses for both the open and closed loop system to verify the the sensor model above.

The graph above shows the open loop MD sensor output for wideband excitation.

0.5

sec

0.6

0.7

0.8

One plot corresponds to experimental data.

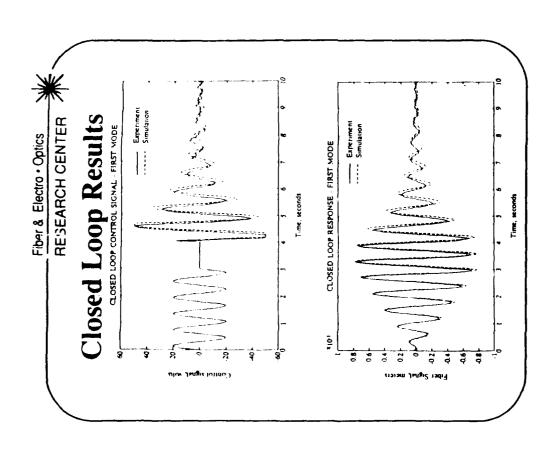
The plot which corresponds to the simulated response was obtained by directly measuring the system parameters for the analytical model.

The last plot was obtained from a model that was identified using the ERA algorithm.

These results are described in

·1.5

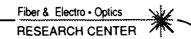
Furness, C. Z., S. Bingulac, D. K. Lindner, and R. O. Claus, "Parameter Identification of a Flexible Beam Using a Fiber Optic Sensor," to appear in the Proceeding of the and USAF/NASA Workshop on System Identification and Health Monitoring of Precision Space Structures, California Institute of Technology, Pasadena, CA, 1990.



These plots show the simulated and actual responses for the experiment above.

The top plot shows the control signal. First, the beam was driven open loop with a sinusoid at the first mode frequency. Then the excitation was turned off and the beam was allowed to free decay. Finally, the control loop was closed.

The bottom plot shows the output of the MD sensor.



Conclusions

Integrated Distributed-Effect Optical Sensors into a Vibration Control System

Future Work

Combined Communication / Sensing Network

Analog Optics for Compensator Implementation

- While optical fiber sensors suggest many new applications in identification and control, two ideas seem particularly interesting.
- If optical fiber sensors are going to be used as distributed sensors, they could be used to network the actuators on complicated space structures. This configuration would yield a communication network dedicated to identification and control of the structure.
- Secondly, if the local sensor response to strain could be varied along its length, the result would be a distributed control gain. Recently, it has been shown (Lindner, et. al., 1990) that a distributed control gain can be used to dramatically reduce the complexity of the compensator. In other words, analog optics can be used to replace digital computation.
- Lindner, D. K., K. M. Reichard, W. T. Baumann and M. F. Barsky, "Measurement and Control of Flexible Structures Using Distributed Sensors," *Proc. of the 29th IEEE Conf. on Decision and Control*, Honolulu, HI, December, 1990.

FOR LARGE FLEXIBLE ANTENNAS

C. W. Gillard and L. L. Ames

Electro-Optical Systems, O/62-46, B/151 Lockheed Missiles & Space Co., Inc. P. O. Box 3504, Sunnyvale, CA 94088

Introduction

This paper examines electro-optical means for measuring the figure of high-gain, deployable, space-based microwave antennas, permitting a variety of active corrections which significantly enhance the antenna performance. Sufficient accuracy may be obtained with appropriate instrumentation to correct the figure of a distorted antenna, and thereby to achieve diffraction-limited performance at even the shortest millimeter wave wavelengths. A simple one-dimensional measurement, monitoring points where the surface phase-error from a nominal configuration is measured at predetermined radii, is sufficient to sense the antenna figure, although it needs a five-dimensional fitting routine to fit an optimal parabolic surface to the measured points of the surface. A simple algorithm, based on an optical analogy, provides a quick method of analyzing the resulting antenna pattern, including any difficult-to-remove residual errors in the antenna figure.

Background

For large reflective antennas, high efficiency is obtained when the rms of the surface irregularities do not exceed approximately 1/20 of the shortest operating wavelength. This constrains the upper frequency at which an antenna of a given size may be operated, since current materials and structural fabrication techniques limit the rms surface-error-to-diameter ratio to approximately one part in ten thousand, although this limit might be stretched somewhat for antennas fabricated from new, low CTE materials such as graphite epoxy. Other practical limitations also approximate this bound: fabrication and deployment tolerances, dynamic and thermal stress, and material creep. As on earth, materials degrade in space: long-term effects of high-energy charged particles, intense UV, repeated thermal cycling, and micrometeoroids present hazards which, over time, will affect the physical as well as mechanical properties of materials. The current trends toward larger antennas and shorter wavelengths are already reaching the limits of conventional fabrication technology. Optically instrumented and accurized antennas will provide a means of breaking beyond the bounds imposed by established material and fabrication limits, giving higher frequency/higher gain antennas.

¹ See NASA Conference Publication 2269, "Large Space Antenna Systems Technology - 1982", Pg. 77.

Numerous structural concepts have been studied as candidate designs for large, space-based antennas. Three in particular have been studied extensively: the radial rib, the hoop/column, and the truss structure. Each offers specific and somewhat unique attributes. The truss structure is simple and offers high stiffness; the hoop/column is easily deployed and is potentially controllable by adjustments of the guy lines; the radial rib features a compact package, reliable deployment, and a simple but limited figure control by pivoting the ribs at the hub. A generic approach allows the antenna figure sensor to be devised largely independent of the structure. As will be apparent from the following design details, the electro-optical sensor described herein may be employed with any dish-type reflector or flat, phased array.

Antenna Surface Error Effects

Aperture efficiency for reflective antennas is composed of several components: blockage due to the subreflector or feedhorn assembly and support struts, spillover, the illumination function, leakage through the surface, and deviation of the surface from the ideal figure. For large antennas operated at short wavelengths, surface error effects can represent the most significant loss. A measure of antenna surface error is given by the parameter $\kappa = D/\epsilon$, where ϵ represents the rms surface error and D is the diameter. Figure 1, taken form Ref. 1, illustrates the κ -values which have been achieved using contemporary, passive control technology. Note that the best values for the most accurate antennas are between 1 and 2×10^4 .

Ruze² presents a theoretical prediction of aperture efficiency, experimentally confirmed using a special model constructed to test the theory. The model was limited to areas-of-coherence small relative to the aperture diameter, restricted to small phase errors (which are the only errors of interest here), and only for shallow (large f/D) reflectors. Under these conditions, Ruze shows that:

$$\eta_s = e^{-(4\pi\epsilon/\lambda)^2},\tag{1}$$

where:

 η_s = surface roughness component of aperture efficiency, and ϵ = rms surface error.

² J. Ruze, "Antenna Tolerance Theory - A Review", Proc. IEEE, Vol 54, No. 4, April 1966, pp. 633-640.

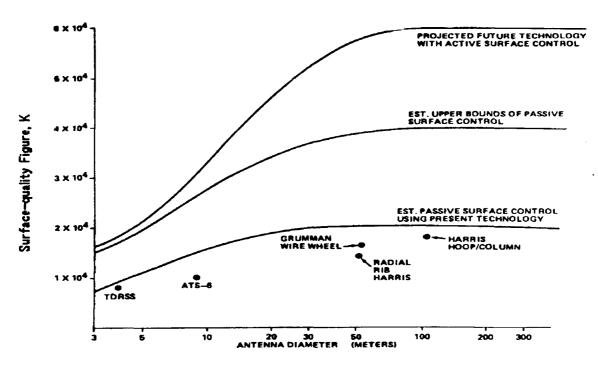


Figure 1. Antenna Surface Tolerance Effects

Figure 2 illustrates η_s as a function of rms surface error in units of λ . It constitutes a universal curve for all surface-type antennas subject to the beforementioned restrictions. The curve indicates that the antenna performance degrades quickly when surface errors exceed $\lambda/15$.

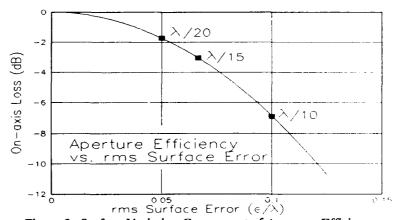


Figure 2. Surface Variation Component of Aperture Efficiency

It is instructive to express the product of aperture gain G and the surface roughness (i.e., phase variation) component η_s of the aperture efficiency in terms of the dimensionless value D/λ and the surface-quality variable, κ :

$$G\eta_s = \pi^2 (D/\lambda)^2 \exp\left(-\left(\frac{4\pi}{\kappa} \cdot \frac{D}{\lambda}\right)^2\right). \tag{2}$$

where:

 $G = 4\pi A/\lambda^2 = (\pi D/\lambda)^2$ (classical expression for gain of any aperture antenna), D = aperture diameter, and

A =aperture area in units of λ^2 .

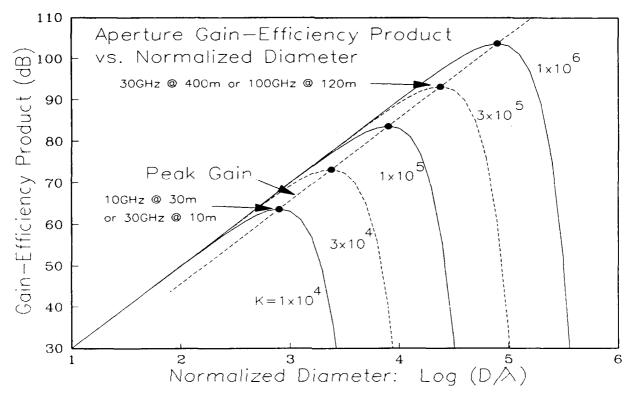


Figure 3. Aperture Gain-Efficiency Product vs. Normalized Diameter

Figure 3 illustrates an important effect: for a given aperture diameter the gain increases as the operating wavelength decreases, until a point is reached where the phase error effects (destructive interference) begin to dominate. Decreasing the operating wavelength beyond this point results in a rapid reduction in gain. This implies that, for an antenna of given diameter, there exists a specific wavelength which results in maximum gain, and that this maximum gain is determined only by the κ -value, i.e., by the accuracy of the surface. As previously mentioned, the effects due to surface roughness are only one component (albeit the major component) of the overall efficiency: the curves shown in Figure 3 ignore the effects of the illumination function, blockage, and other efficiency components, since they are design-dependent and can be kept relatively small.

Maximum gain is achieved at a wavelength of

$$\lambda_{\text{mex}} = 4\pi D/\kappa, \tag{3}$$

where the loss relative to a perfect surface is e⁻¹ (4.3 dB). Maximum gain is thus

$$(G \eta_s)_{\text{max}} = \kappa^2 / 16e. \tag{4}$$

Note that the maximum gain is proportional to the square of the κ -value, i.e., to the square of the surface accuracy. Thus, for high-gain antennas, increasing surface accuracy results in a large reward.

Sensing the Antenna Figure

For purposes of illustration, a means of applying electro-optical accurization to a radial rib antenna will be discussed. Figure 4 illustrates a typical radial rib antenna.

A convenient and relatively stable location, such as the antenna hub as illustrated in Figure 4, is selected for the antenna figure sensor; location of the figure sensor on, and alignment with, the antenna axis of symmetry is nice but not essential. The sensor system consists of an axially symmetric, omnidirectional optical system: a biconical reflector, or "bicone", in conjunction with a telescope and detector arrays. This system views light emitted from the ends of fibers attached at known points on either the antenna surface or its supporting structure. The elevation angles of the lights, relative to a reference plane normal to the sensor system axis, are measured as linear positions of images on the detector arrays. The product of elevation angle and radial position of a given light source yields the axial position of that point, and the deviation between the observed and nominal positions gives a measure of the distortions. Information derived from the figure sensor for many light sources may be used to determine the best fit parabola to the surface and/or to provide feedback data for actively controlling the antenna in order to constrain it to a specified shape.

The light sources in the example shown in Figure 4 are arranged in two concentric rings, one at the rib tips and the other at mid-rib position, although this is generally not an optimal configuration for the lights. An optimal configuration depends on whether the surface is to be actively controlled, the location of possible nodal flexure points of the structure, the illumination function, and various other design considerations. Many more light sources than are implied by the illustration may be used; indeed, the use of several thousand lights is not out of the question for very large antennas.

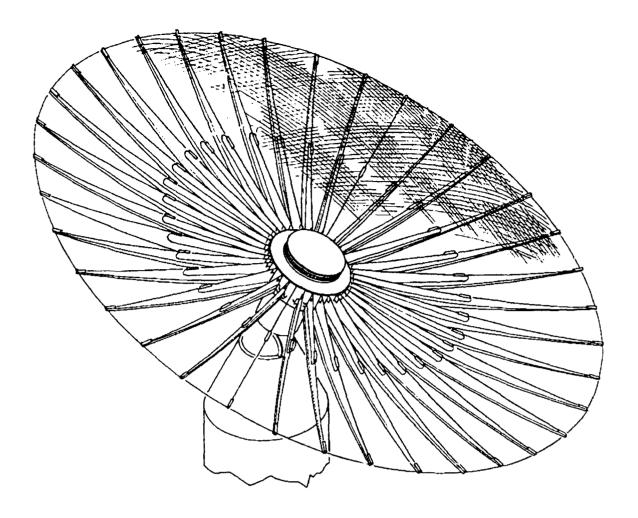


Figure 4. Accurization of a Radial Rib Antenna

The bicone-telescope system, the key element of the antenna figure sensor, is detailed in Figure 5. The biconical reflector, a diamond-turned optical surface fabricated from a single piece of aluminum alloy, is symmetrically mounted atop a Schmidt-Cassegrain telescope as illustrated. Divergent light from a point source on the antenna is bent and collimated by the auxiliary lens and prism assembly, doubly reflected by the bicone, directed into the telescope, and focused as a slightly curved, diffraction-limited line on the focal plane (two pairs of linear CCDs coaligned with a beamsplitter). Fabricating the biconical reflector from a single piece of aluminum offers two important advantages: it is thermally stable (i.e., it is an isothermal unit), and the two reflective surfaces are accurately and

permanently aligned. The double reflection of the bicone gives precision sensor performance independent of any small misalignments of the bicone relative to the telescope, a practical (even essential) feature of the bicone-telescope assembly.

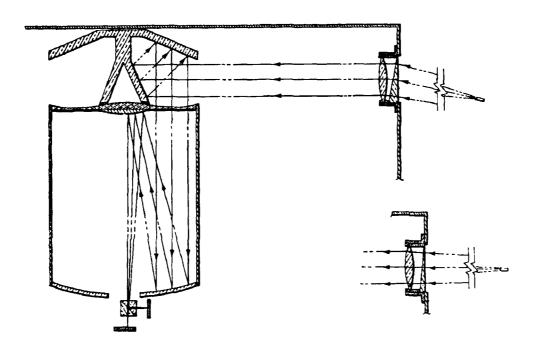
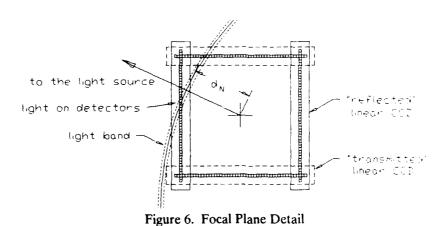


Figure 5. Details of Bicone-Telescope Assembly and Auxiliary Optics

Details of the focal plane are illustrated in Figure 6. As shown in the Figure, the four CCDs appear as a square array with the corners overlapping when viewed through the beamsplitter. Shown is light from a typical source that is focused as a band crossing the array. The distance dN



from the center of the square, normal to the light band and calculated from the centroid positions on the illuminated CCDs in the array, provides a measure of the elevation angle of the light source, and thus the axial position of that point on the antenna to which it is attached. The normal vector points in the direction of the light source and may be used to provide a low-resolution measure of torsional surface motion. Laboratory tests show that the light band is sharp enough that d_N can be measured with an rms accuracy of approximately 0.02 pixels for 13 micron pixels and a 2 m focal length telescope, such as might be employed with a large antenna, providing a measurement accuracy of 0.13 microradians.

Once the position for a particular light has been determined, it is turned off, another is turned on, and the measurement process repeats, eventually measuring the entire antenna. To increase the sample rate, several light sources may be viewed simultaneously by the bicone-telescope provided the resulting light bands do not overlap on the array of CCDs. The lights are grouped by first mapping the light sources individually on the CCD arrays, and then assigning potentially conflicting light sources to separate groups. These groups are then turned on sequentially. Allowing a few milliseconds to collect light, process the signal, and determine the positions, times about a dozen groups of lights, gives a complete measure of the antenna at better than a 100 Hz rate. Combine that with the 0.13 microradian resolution, corresponding to a surface-quality figure of $\kappa = 10^7$, and you have a system more than fast and accurate enough to control even the largest antennas at the shortest achievable wavelengths.

Data Processing

Simply measuring an antenna will not improve the gain--something has to be done with the information. A straight-forward course of action is to use the information in a servo-control feedback loop, forcing the antenna to conform to the ideal figure. Other less costly strategies exist that are adequate for many situations.

If the antenna is a planar phased-array antenna, the task is simple; use the measurements as a basis for electronic phase correction of individual elements in the array, rather than mechanically adjusting the supporting structure. Figure 7 illustrates the manner in which the antenna figure sensor can map a planar surface to provide the data.

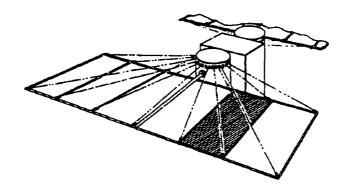


Figure 7. Electro-Optical Accurization of a Phased-Array Antenna

For curved reflective antennas, the situation is more complicated. For purposes of illustration, Fig. 8 shows an idealized, perfect antenna. When it's nominal symmetry axis is pointed at a transmitter, the received signal focuses on the feedhorn at the nominal focus, as it should.

Figure 9 exaggerates reality: upon measuring, it is found that the antenna is warped. When it is pointed in nominal alignment, the received signal does not focus at the nominal focus. The feed-horn could be moved to where more of the received signal converges, but analysis of the measurement data provides better alternatives.

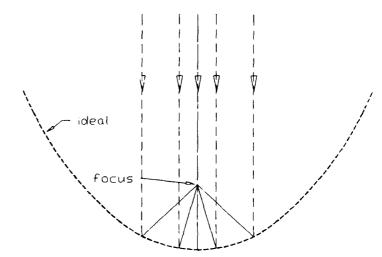


Figure 8. Ideal Antenna

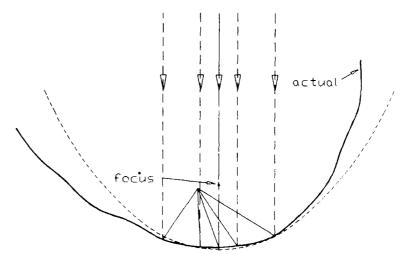


Figure 9. Warped Antenna.

Figure 10 shows a "bestfit" parabolic surface to the actual distorted antenna, with a new symmetry axis and a new focal point. This best-fit paraboloid is the homological equivalent of the warped antenna, with the "degree of homology"³ describing the goodness of the fit. **Optimal** performance without active control of the antenna surface itself is obtained by moving the feedhorn to the new focus, and aiming the antenna using the new symmetry axis.

If the feedhorn can not be moved from its original nominal position, it is still possible to improve performance by using the measurements. As shown in Fig. 11, the antenna can be "point-aligned", whereby the antenna (and usually the entire satellite) is aimed in a direction different from the nominal pointing. The optimal pointing can be calculated based on the antenna's f/D ratio once the actual symmetry axis is found.

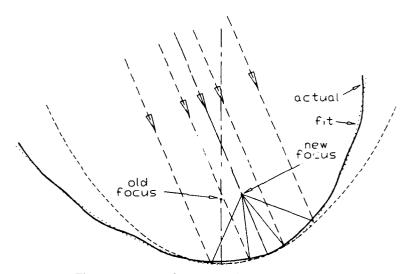


Figure 10. Homological Equivalent Paraboloid

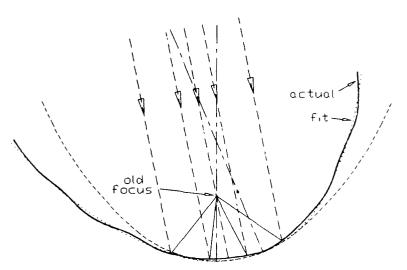


Figure 11. Point Alignment

Five parameters must be varied to find the best fit: two to describe the direction of the symmetry axis and three for the location of the focus (or, equivalently, the location of the paraboloid's vertex and the focal length). Traditionally, the best-fit is searched for by

³ Deviations of Microwave Antennas from Homology, Krystyna Kiedron, NASA Tech Briefs vol. 12, no. 3, item #22 (1988)

⁴ include the beam deviation proportionality factor: see p. 488, Microwave Antenna Theory and Design, ed. by Silver, 1949.

repeatedly calculating the antenna pattern, or gain as a function of beam direction, as various choices for feedhorn location are sequentially tried. Besides being time consuming, the optimal parameters were seldom found by the discreet steps in feedhorn location. Note that the best-fit is independent of wavelength, but does vary with illumination function.

Rather than employing the traditional method, we adapted a least-squares fitting routine⁵ to search over the five parameters. The function to be minimized is the square of the phase difference between the measured and ideal paraboloids, summed over numerous representative surface patches and weighted by the amplitude illumination function. The phase differences are proportional to the differences in the path lengths of the reflected radiation, which are different from the Δz errors that a straight-forward surface fitting routine would likely use. The resulting program runs on a desktop computer in a matter of minutes, and in test cases found solutions that antenna engineers hadn't considered but later verified to be superior.

Since we didn't have access to a large, warped antenna, we simulated the measurements in order to test the fitting routine and explore the implications of various possible corrective measures. We chose as a representative example an average-depth paraboloid (f/D=0.5) with a typical illumination function of $\cos^{3.6}(\theta)$. We distorted it with a gentle warp by using the function

$$z = (1/4f)(1 + \beta\cos\alpha)r^{2},$$
 (5)

where α is the azimuthal angle and β gives the distortion. The example presented here used $\beta = 1/600$, which amounts to a $\pm 1/2$ " distortion at the rim of a 200' diameter antenna.

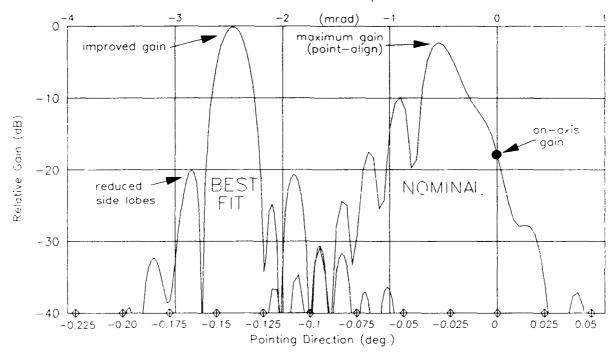
The best fit to the simulated data of the example at first was surprising: the vertex of the fitting parabola is shifted by 5.6" from the nominal vertex, a number large compared to the distortion. The situation is as illustrated in Fig. 10: the vertex moves, the symmetry axis tilts, and the antenna works best if the feedhorn is moved to the focus of the homologically equivalent paraboloid.

⁵ A Rapidly Convergent Descent Method for Minimization, R. Fletcher and M. Powell, Computer Journal, vol. 6, 1963

Figure 12 shows the antenna patterns calculated for the simulated warped antenna, for a wavelength λ of 1/2". The curve labelled "nominal" has the feedhorn at the nominal location, while the "best fit" has the feedhorn shifted by 2.6". Several points are worth noting:

Pattern of Warped Antenna

Feedhorn at nominal and optimal locations



Power III. func $\cos^3 .6$ F/D = 0.5; lambda=D/4800; warp=1/600

Figure 12. Antenna Patterns for a Warped Antenna

- (1) If nothing is done, then the feedhorn is antenna at the nominal focus and the antenna is aimed along the nominal (0°) axis. The gain is reduced by 17 dB.
- (2) If the feedhorn is not allowed to be moved, the whole antenna can still be pointed in the optimal direction, which can be found by analyzing the antenna measurements. Point-aligning improves the gain by 14 dB in this example, down only 3 dB from the ideal.
- (3) Moving the feedhorn and properly aiming the antenna gives virtually the full gain (down only 0.1 dB), without requiring active control of the surface itself.

(4) Aside from higher gain, the best-fit configuration also has a narrower pattern and the side lobes are reduced (by 10 dB in this example), which can be significant in distinguishing between adjacent sources and in avoiding cross-talk.

Figure 13 presents this information from a different point of view: the better the antenna, the higher the frequency at which it can be used. Again for the simulated 200' warped antenna, the three curves show the gain as a function of wavelength for (a) nominal alignment (no corrections), (b) point alignment (feedhorn fixed), and (c) best fit (pointing

and moving the feedhorn). For low frequencies, anything will do, and the nominal antenna is sufficient; somewhat higher frequencies can be accommodated simply by point-aligning the antenna. Tilting and shifting the feedhorn permits the antenna to perform at thirty times the nominal frequency limit. If even higher frequencies are required. then the surface must be actively controlled.

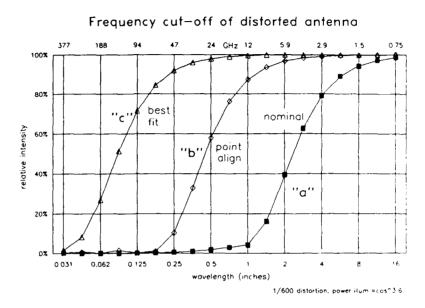


Figure 13. Gain vs. Wavelength for a Distorted Antenna.

As mentioned at the beginning of this section, once the antenna is measured, the data can be used to control servos that push and pull the antenna back into the proper shape. However, if the data is fit, then the surface can be shaped into the homologically equivalent paraboloid. As can be seen in Fig. 10, the corrections required to force the antenna surface into a perfect paraboloid are much smaller when the goal is the best-fit paraboloid than when the goal is the original nominal shape. Rephrased: it is easier (and probably cheaper) to control the antenna surface to obtain a perfect antenna if one is willing to move the feedhorn and tilt the antenna as well.

Antenna Patterns

As an aside, the antenna patterns of Figs. 12 and 13 were calculated in minutes on a desktop computer, using a simple program based on an optical analogy. As can be seen in Fig. 14, this program gives answers quite similar to the traditional program that calculates induced currents and reradiated fields, and that runs overnight on a mainframe.⁶

Comparison of Antenna Pattern Calculations F/D=0.5, lambda/D=0.001, feedhorn offset = 10 std. beamwidths

To 60

50

optical analysis methods

20

10

Figure 14. Comparison of Computational Results

0.6

angle (degrees)

0.7

8.0

0.9

0.5

The antenna pattern software is inspired by the Huygen's principal of optics, which dealt with adding the phases of wavelets. The program calculates the path length of rays, starting from a plane, travelling in the incident beam direction, reflecting off of the surface, and then proceeding to the desired feedhorn location. A refinement to adjust for the reflecting angle of the ray slows the computation but does not significantly modify the results. Numerous rays (e.g., about 2000) sample the entire surface, each weighted according to the

0.4

0

0.2

0.3

⁶ thanks to Ken Jablinskey at LMSC for the mainframe calculations.

amplitude illumination function. The path lengths convert to wavelengths, resulting in various phase differences, with each ray giving a contribution $w\cos(2\pi L/\lambda)$, where L is the path length. The various rays add in amplitude, constructively or destructively depending on their phases; the amplitude is squared to give the power intensity. The offset phase due to the arbitrary starting plane is removed by repeating the summation over all rays, using the sine in place of the cosine, and adding the square of this sum to the intensity sum. The results are normalized by dividing by the sum of the weighting factors w. The calculations are repeated over a range of parameters (e.g., pointing direction), and plotted.

The results are quite good when the wavelength λ is small compared to the antenna diameter (λ <D/100), and are better for shallower paraboloids; the traditional approach may be better for polarized radiation or anisotropic antenna surfaces. As this code runs quickly on a desktop machine, engineers are able to play with the antenna design, trying various "what-ifs" that the slow mainframe calculations would inhibit.

Conclusions

A simple device, basically blinking lights and mirrors, gives quick and precise measurements of an antenna figure. A best-fit to the data gives the optimal configuration (feedhorn location and/or pointing direction). A simple code gives the resulting antenna pattern. The combination allows and simplifies the design, construction, and optimization of large, high-gain, high-frequency antennas.

A Velocity Command Stepper Motor for CSI Applications

by

Jeff Sulla Lockheed Engineering and Sciences Co. Hampton, Va. 23665

> Jer-Nan Juang, Lucas Horta Mail Stop 230 NASA Langley Research Center Hampton, Va. 23665

Fourth NASA/DOD CSI Conference Orlando, Florida November 5-7, 1990 The application of linear force actuators for vibration suppression of flexible structures has received much attention in recent years. A linear force actuator consists of a movable mass that is restrained such that its motion is linear. By application of a force to the mass, an equal and opposite reaction force can be applied to a structure. In this presentation, the use of a linear stepper motor as a reaction mass actuator is described. The outline of this presentation includes the objective of this work, description of the hardware utilized, analytical application of this device, test beam and Mini-Mast experimental results, future applications, and concluding remarks.

OUTLINE

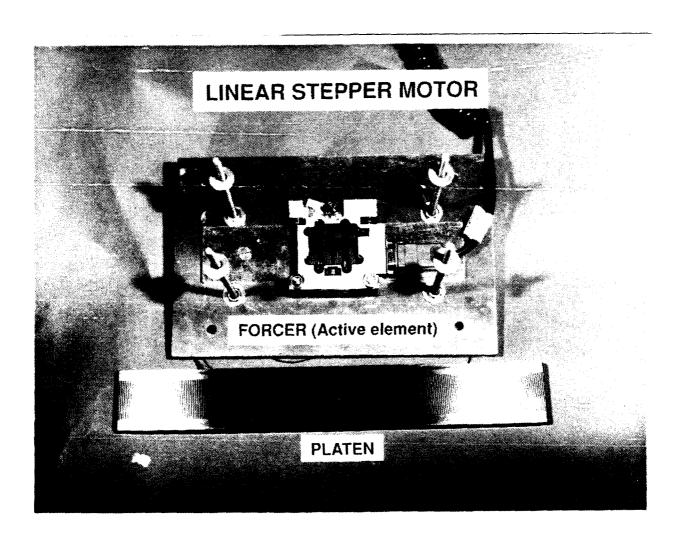
- OBJECTIVES
- HARDWARE OVERVIEW
- COMMAND MODE ANALYSIS
- EXPERIMENTAL RESULTS
- FUTURE APPLICATION
- CONCLUSIONS

The development of reaction mass actuators is not a trivial undertaking, with much design and analysis effort (and cost) required in the development of prototype reaction mass actuators. The first objective of this work is to demonstrate the ability of an "off the shelf" industrial linear stepper motor system to operate as a reaction mass actuator for CSI applications. The second objective is to utilize the relative velocity command capability of this reaction mass actuator using various output feedback schemes to provide damping augmentation of a flexible structure. This is demonstrated on a simple test beam and the NASA Mini-Mast.

OBJECTIVES

- Demonstrate use of an industrial "off the shelf" linear stepper motor system as a reaction mass actuator.
- Demonstrate use of the actuator velocity command mode in flexible structure vibration suppression.

A linear stepper motor is conceptually a very simple device that consists of two elements. The linear motor used is a Compumotor L5A manufactured by the Parker-Hannifin Corporation. In this application as a reaction mass actuator, the stationary part is the forcer and the moving part is the platen (the reaction mass). The forcer consists of two electromagnets and a permanent magnet. The platen is a passive element with teeth cut into its surface (100 per inch) to form pole faces which concentrate the magnetic flux lines generated by the forcer. The platen rides on the forcer supported by ball bearings that maintain the required air gap. By selectively applying current to the two winding of the forcer, magnetic force can be concentrated at the poles faces to cause relative motion between the two motor elements. The motor is classified as a two-phase permanent magnet hybrid linear motor.



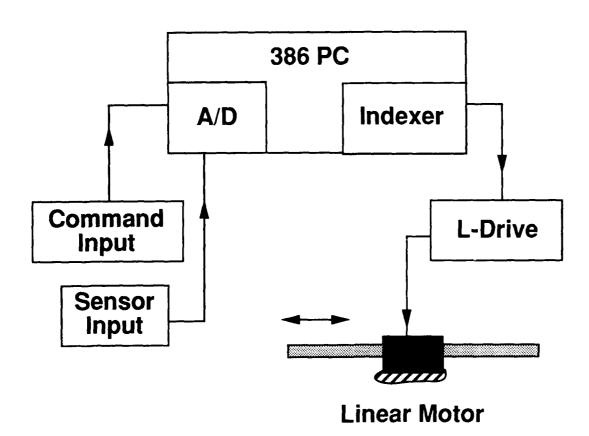
The motor step resolution obtained by the tooth spacing on the platen is increased by the motor control system digitally proportioning the motor current to the winding, resulting in an effective step resolution of 12500 steps per inch. This greatly improves the smoothness of motor operation. The control system also allows the user to command the velocity of the motor with a resolution of approximately 15 steps/sec. The weight breakdown of the linear motor system in its current reaction mass actuator application is 3.5 lbs for the reaction mass, 0.8 lbs for the forcer, and 1.95 lbs for mounting/adapter plates required to interface to the test articles, for a total weight of 6.25 lbs. Each actuator with its associated drive electronics cost about \$3000.

ACTUATOR CHARACTERISTICS

- 12500 steps per inch
- Velocity command capability
- Total Weight 6.25 Lbs
 - 3.5 Lbs reaction mass
 - 0.8 Lbs stationary element
 - 1.95 Lbs mounting/adaptor plates
- Cost approx. \$3000 each

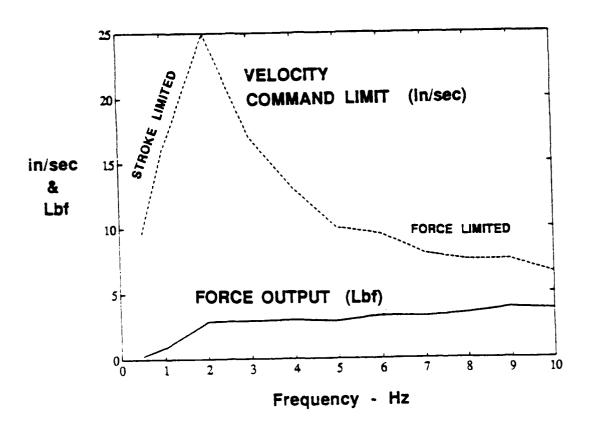
The linear motor system hardware is interfaced as follows. A Compumotor PC23 microprocessor-based three axis indexer is installed in a PC-AT compatible card slot. This device provides the step pulses to the motor drive in response to operator commands. A motion control mode defined as velocity streaming is used to provide real-time control of the linear motor velocity. The motor command step pulses are sent to a L series bipolar, micro-stepping drive specifically designed for two-phase permanent magnet hybrid linear motors. The digital proportioning of the motor drive current is done here allowing motor step resolution to be effective increased to 12500 steps per inch. The use of a DT2811 analog to digital converter card in another PC-AT card slot allows the input of various analog signal inputs such as sensors and analog velocity commands to the actuator, depending on the software program used. Software drivers for the stepper motor were converted to C and combined with A/D board software to allow operation of the linear motor in several operating modes. These include indexer based or analog potentiometer relative position measurement, and analog command input with one or two independent linear motors.

HARDWARE INTERFACE



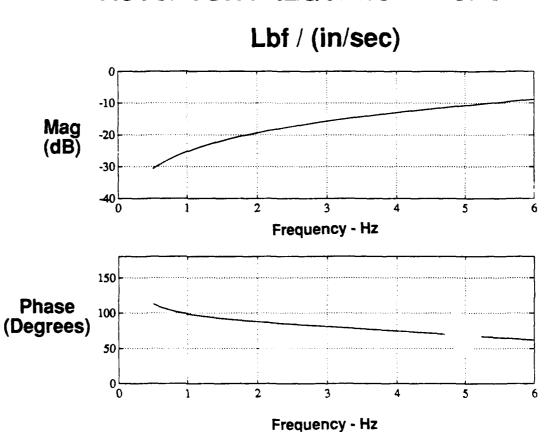
Bench testing of various actuator configurations was performed. The relative smoothness of the linear motors operation was used as a guide to determine the "best" operating mode of the system to use. Since indexer operation was the limiting factor in determining the velocity command update rate (or frame rate), these commands were kept to minimum by using the indexer to only output velocity commands to the motor, instead of also using the indexer to keep track of the reaction mass relative position. By using the analog reaction mass relative position measurement, a velocity command update rate of 232 Hz was obtained. With this configuration, operational limits of the actuator were determined by commanding various velocity command amplitudes at a given frequency. When the linear motor exceeded its stroke limits or began to stall/slip, this velocity command amplitude was used as the maximum velocity command for a given frequency. This procedure was used over the frequency range of 0.5 to 10 Hz. The actuator in this configuration is stroke limited under 2 Hz and force limited over 2 Hz. A calculated actuator force output is shown derived from the sinusoidal frequency and amplitude of the velocity command and the mass of the reaction mass.

ACTUATOR LIMITS 232 Hz Command Update

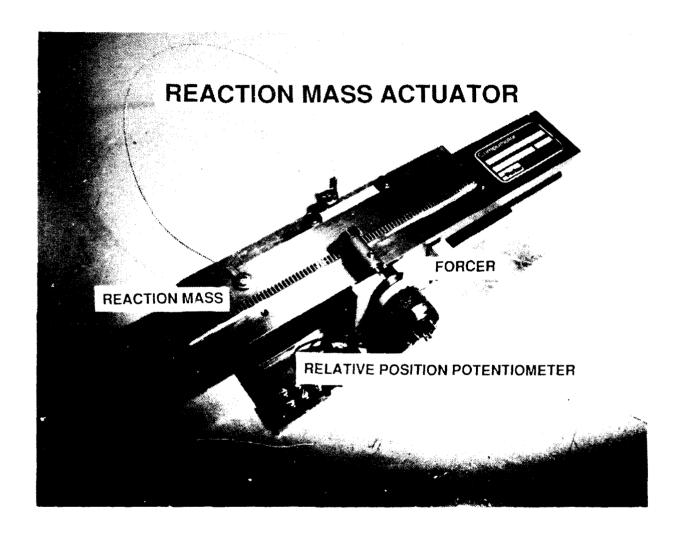


Using two actuators connected to the indexer causes the command update rate to decrease to approximately 106 Hertz. With the analog command input mode used and an accelerometer attached to the reaction mass, a dynamic signal analyzer was used to perform sine sweep tests over a frequency range of 0.5 to 6 Hz. The transfer function shown is actuator force output over velocity command input. This frequency response shows the expected results using a velocity command actuator.

ACTUATOR FREQUENCY RESPONSE



This photo shows the current configuration of the actuator assembly. A crude rack and pinion drive is used to provide an analog feedback signal proportional to the relative position of the reaction mass to ensure the reaction mass remains centered at low velocity command frequencies. A steel cable is attached between the reaction mass and base to prevent the reaction mass from exceeding its stroke limits. Total weight as shown here is 6.25 lbs.



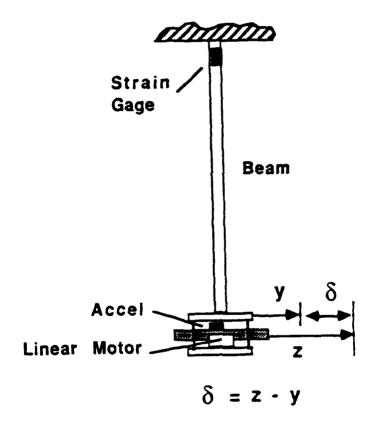
The usual implementation of reaction mass actuators for vibration suppression requires that the actuator be considered a force command or a relative position command device. The use of a velocity command reaction mass actuator allows some simple output feedback schemes to be implemented. Analytically, it can be shown that using direct output feedback, a velocity command device requires displacement or acceleration signals to augment the damping of a flexible structure. This is in contrast to the velocity feedback signal required for a force command actuator to provide additional damping in a flexible structure.

COMMAND MODE ANALYSIS

- Force command actuator requires velocity feedback to augment damping in a flexible structure.
- Velocity command actuator requires displacement or acceleration feedback to augment damping in a flexible structure.

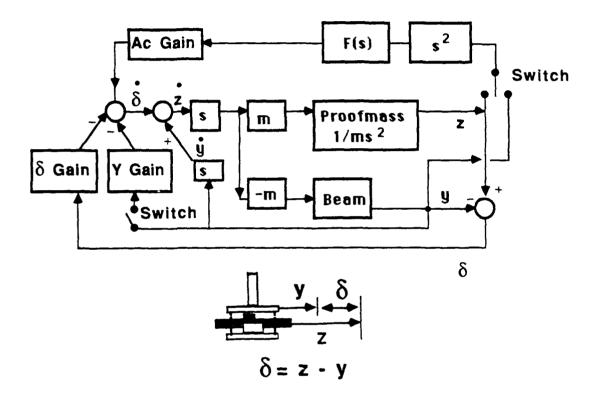
The linear motor was first tested on a simple test beam. The test beam was a vertically cantilevered seven foot aluminum tube (beam) with an actuator mounting plate attached. The mass of the beam was approximately five times that of the reaction mass. The first bending mode of this system was 1.8 Hz. The feedback sensors used were a strain gage at the beam root which provided a signal proportional to beam displacement, and a servo accelerometer which was used to measure beam or reaction mass inertial acceleration.

TEST BEAM



A block diagram of the feedback loops demonstrated on the test beam is shown here. For all tests, reaction mass relative position feedback was used to ensure the reaction mass remained centered. For damping augmentation of the beam, strain gage, beam acceleration, or reaction mass acceleration was used.

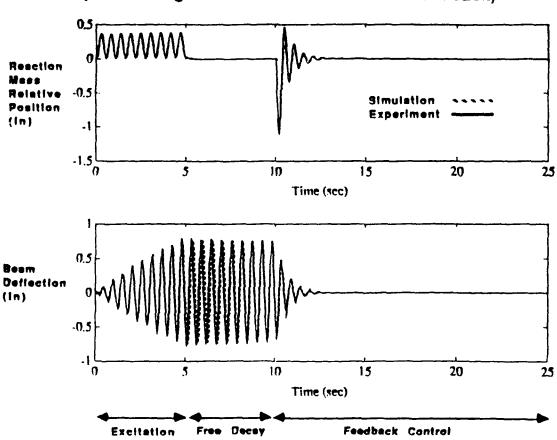
CLOSED LOOP SYSTEM BLOCK DIAGRAM



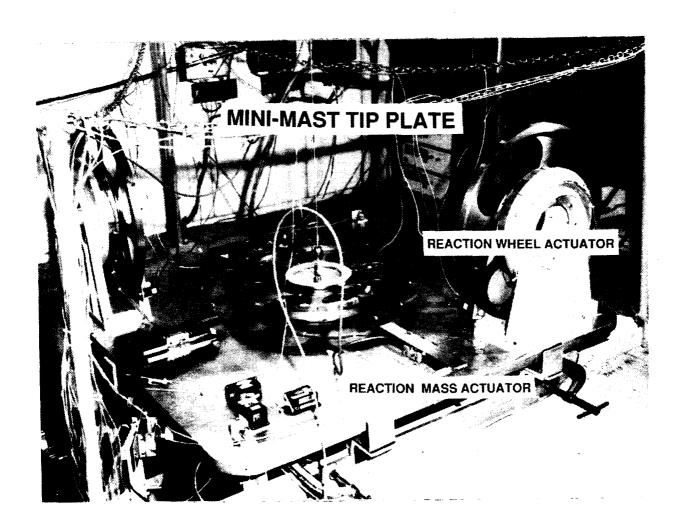
The beam was excited at its first mode frequency for five seconds, with no feedback loops closed. From five to ten seconds, the reaction mass relative position feedback loop was closed. At ten seconds, the damping augmentation feedback loop was closed, with a total test time to twenty-five seconds. A command update rate of 55 Hz was used. The following figure shows a comparison of simulated and experimental results for the case using strain gage and reaction mass relative position feedback. In this case, a closed loop damping of 14.5% is achieved. Similar results were obtained for the acceleration feedback cases.

TEST BEAM EXPERIMENTAL RESULTS

(Strain Gage and Relative Position Feedback)

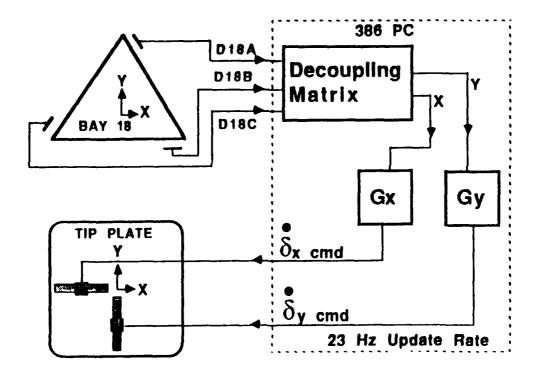


The second test article used was the NASA Mini-Mast, which is a 20 meter vertically cantilevered near-flight quality truss beam. For these tests two linear motors were used to provide two axis control. The linear motors were mounted on the tip plate to provide control forces along the Mini-Mast global X and Y bending axis (see next chart). The first five modes of the Mini-Mast are as follows: 1st X & Y bending (0.85 Hz), 1st Torsion (4.2 Hz), and 2nd X & Y bending (6.2 Hz). A interesting comparison between the two types of actuators shown (reaction wheel vs. reaction mass) can be made. Given the 50 ft-lbf torque output of the reaction wheels and the 0.7 lbf force output of the linear step motor, the torque available for application to the structure is equivalent, but the weight of the reaction wheels is 13 times that of the reaction mass actuator.



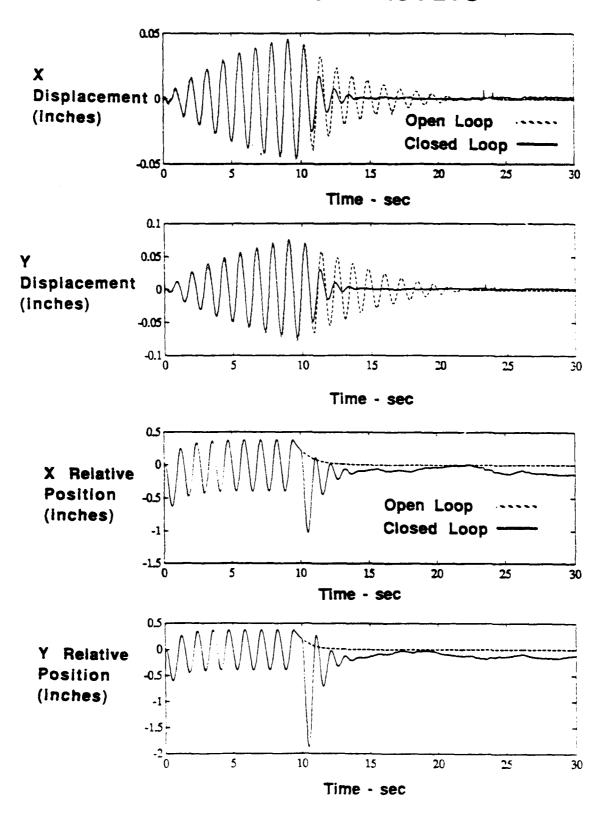
The Mini-Mast tip displacement feedback loop implemented is shown below. Mini-Mast tip deflection detected by three non-contacting displacement probes are input to the 80386 PC system. The displacement inputs are multiplied by a geometric de-coupling matrix to obtain X and Y displacement of the Mini-Mast tip plate with respect to the global bending axis. These global X and Y displacements are multiplied by their respective gains to generate the corresponding reaction mass actuator relative velocity command. The frame cycle for this process was only 23 Hz, since the indexer was used for relative position measurement. The reaction mass relative position feedback loops are not shown for clarity.

MINI-MAST FEEDBACK LOOPS



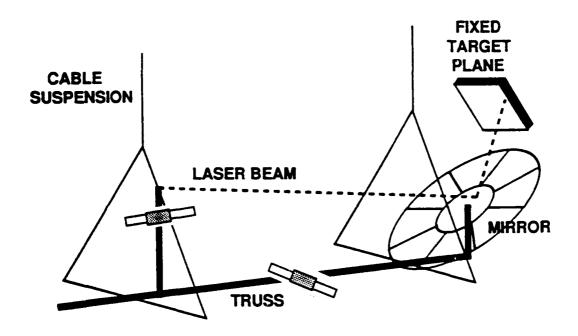
The Mini-Mast was excited for 9.8 seconds at the 1st bending mode frequency (.85 Hz) with both reaction mass actuators, followed by the feedback control at 10 seconds. The structural damping was increased from the $4.5\ \%$ free decay damping to approximately 15 % with displacement feedback.

MINI-MAST TEST RESULTS



Plans are currently underway to use these linear stepper motor actuators on the CSI Evolutionary Model at NASA Langley Research Center. Initially, they will be used as inertial disturbance sources. Later, closed loop control of the 1.4 to 1.7 Hz flexible modes will be conducted.

CS! EVOLUTIONARY MODEL TESTS



In conclusion, this presentation has shown that an industrial linear stepper motor system can be utilized as a reaction mass actuator for CSI applications. The use of a velocity command reaction mass actuator allows simpler output feedback implementation for vibration suppression since common sensor outputs are used. The performance of these actuators was demonstrated by closed loop tests on a simple test beam and the NASA Mini-Mast.

CONCLUSIONS

- Industrial linear stepper motor system can be used as a reaction mass actuator.
- Velocity command actuator allows use of displacement or acceleration measurements for direct output feedback to augment damping for vibration suppression of flexible structures.
- Actuator vibration suppression capability demonstrated on a test beam and the NASA Mini-Mast.

Optics for Control/Structures/Optics Integration

David C. Redding

C.S. Draper Lab

B. Martin Levine, W.G. Breckenridge, H.C. Briggs,

R.A. Laskin

Jet Propulsion Lab,

California Institute of Technology

Context

to dynamic motions that affect the beam train geometry. Whether due to deformations of the restoring image quality, lowering or raising signal-to-noise ratio, reducing or improving the directors, or any optical instruments incorporating articulating optical elements, are subject instrument structure or to controller actions, these dynamic disturbances change the beam Large optical instruments such as spaceborne astronomical telescopes, laser beam train alignment and element figure, altering the instrument line-of-sight, distorting or visibility of interference fringes, or decreasing or increasing wavefront quality.

parameters, structural configuration and stiffness parameters, structural thermal qualities and statically, as is usual in optical design, and dynamically, with optical performance calculated control system sensor, actuator and control loop parameters. To acheive the best system design, it is necessary to trade-off optical, structural and control system design variables against their effect on optical performance. This performance should be quantified both For these instruments, optical performance is equally a function of optical design as a function of time, as driven by structural and controller dynamics

This paper presents an approach to modeling optics for integrated optics/structures/ controls design and analysis.

Integrated Design and Analysis Tasks

mentioned here. Error analysis is required to determine basic feasibility of the system and to sensitivities of the observational error - be it line-of-sight (LOS) pointing, wavefront or other misalignments. Calibration can be performed by conducting a sequence of observations and the error equations can be inverted in a least-squares sense to estimate the component errors Several of the tasks the spaceborne instrument system designer must perform are error - to individual structural, control, or optical component errors, such as structural develop and track a system-wide error budget. The error equations consist of the

Optical controllers, such as gimballed-mirror controllers, typically are driven by optical may require motions over large angles or positions. The control designer needs to know the sensors, such as CCD focal planes, to keep certain signals at a commanded condition. This optical effect of motions of the controlled element - the optical gains. These are computed as the optical sensitivities projected into particular sensor and actuator coordinates.

parameters in each subsystem and recompute performance to perform trade studies that cross time and frequency domains to determine total system performance. The designer can alter structure subjected to vibrational disturbances, LOS and wavefront quality are functions of he configuration and stiffness of the truss elements, the size of control actuators, and the disciplinary boundaries. For instance, for a large telescope distributed on a flexible truss performance of a design. Response to dynamic disturbances can be analyzed in both the power of individual optical elements. The optimal system design picks values for these Dynamic simulation of the integrated system is extremely useful for determining parameters that minimize LOS and wavefront errors over time, while also maximizing energy received at the focal plane and minimizing system mass and controller power.

Multi-objective optimization techniques provide a method for automating the design optimization process, as discussed in Refs. 1 and 2.

Integrated Design and Analysis Tasks

- Error analysis: optical/structural tolerancing
- Error equations derived from optical, structural sensitivities
- Calibration algorithm design
- Error equations "inverted" to estimate errors from observations
- Controller design
- Optical gains transform sensor signals to actuator coordinates
- Dynamic simulation and analysis
- Exercise complete system model to determine end-to-end performance vs. time and frequency
- Integrated design optimization
- Cross-disciplinary trade studies
- Automated design optimization

Integrated Analysis

performance. The optics form part of the C matrix or function, transforming the state vector The basic form of the equations used in integrated analysis tasks is summarized here. into measurements y. These measurements in turn drive the controllers through the gain For an instrument consisting of optics mounted on flexible or articulating structures, the linear and nonlinear dynamical equations take the first-order (linear or nonlinear) form indicated. The dynamical equations can be directly integrated to simulate system matrix K.

Another use of optical models is in designing optical control systems. As is indicated, calculations, in this case for a linear-quadratic regulator. Other modern or classical control optical performance can be directly incorporated into a cost function for controller gain design approaches will benefit by detailed performance modeling as well.

uncertainties into a cumulative measurement or performance error. Error analysis uses the C varying nonlinearly over different operating configurations. They couple the optics together Error equations are transformations from the error states to the performance objectives functions to predict system performance based on expected component error statistics. The process of calibration inverts the measurement equations C in a sequence of observations in with the structural and control geometry, summing component-level misalignments and or measurements. These C transformations depend on the system geometry, generally different operating configurations to estimate the component errors.

Integrated Optics/Structures/Controls Analysis

Simulation:

Linear

$$\dot{x} = A\dot{x} + B\dot{u}$$

$$\vec{y} = C\vec{x} + D\vec{u}$$

$$\ddot{\mathbf{x}} = \mathbf{A}(\ddot{\mathbf{x}}, \ddot{\mathbf{u}}, \ddot{\mathbf{d}}, t)$$
$$\ddot{\mathbf{y}} = \mathbf{C}(\ddot{\mathbf{x}}, \ddot{\mathbf{u}}, \ddot{\mathbf{d}}, t)$$
$$\ddot{\mathbf{u}} = -\mathbf{K}(\ddot{\mathbf{y}}, t)$$

Control Design:

$$\min J = \int_{0}^{\infty} \left(\vec{x}^{T} C^{T} Q C \vec{x} + \vec{u}^{T} R \vec{u} \right) dt$$

Error Analysis:

$$d\vec{y} = C(\vec{x}, \vec{u}, t) d\vec{x}$$

Calibration:

$$d\vec{x} = \begin{bmatrix} C_{obs1} & \cdots & C_{obsn} \end{bmatrix}^{-1} \vdots$$

Controlled Optics Modelling Package

Controlled Optics Modelling Package (COMP). COMP is being developed as a module for The modelling approach we describe in this paper is realized in a computer tool, the capabilities for a number of the standard structures, controls, thermal and optics analysis the AFWL/Boeing Integrated Structural Modelling computer tool. The ISM facilitates integrated system analysis by providing a common workspace and data manipulation

system simulation. COMP-generated optical gains can also be exported for integration with indicated. These models can be exercised within the COMP stand-alone tool to trace rays, compute sensitivities, or to perform other standard optical tolerancing analyses. They can also be exported to be integrated with structural and control models to form an integrated COMP can be used to generate a number of different types of optical models, as a real-time controller.

perform exact ray-tracing and diffraction calculations as functions of structural geometry and The form of COMP models depends on the modelling task. For systems that undergo motions, nonlinear models are required. We are developing the capability for COMP to generated in the form of "C-matrices," or fixed data. For systems that experience large directly generate optical models in the form of Fortran subroutines. These routines will only small motions, constant-coefficient linear models can be very useful. These are actuator inputs over large articulations of the system.

COMP models provide the essential functionality of a standard optical modelling tool, but in a form that can be run in-line with other code.

Controlled Optics Modelling Package (COMP)

optical models for integration with structures and controls models We are creating an optical model generation tool for computing

- Ray-trace geometric models
- Chief-ray only or full wavefront
- Linear (small-motion) C-rnatrix models
- Non-linear (large-motion) models are subroutines driven by structural and controller parameters
- Diffraction models
- Hybrid ray-trace/diffraction models

COMP is available as a module of the Integrated Structural Modeling computer tool

Geometric Optics Approach

The niathematical approach underlying the COMP linear and non-linear ray-trace models is sketched out in the following few charts.

notation, indicated by boldface type, with arrows and hats distinguishing general vectors and user-defined coordinate frame, usually the structural frame, as indicated on the linearized The exact ray-trace equations are summarized in coordinate-free vector/dyadic unit-vectors, respectively. Actual calculation is done using matrices in an arbitrary ray-trace chart.

require numerical differentiation to generate optical sensitivities for all ray perturbation state also the factor that enables COMP to directly generate Fortran subroutines for calculation of components. This capability appears to be unique among the most-used optical tools. It is optics. It is also convenient for differentiation. The optical sensitivities used in linearized ray-tracing have been derived in closed form. As a consequence, COMP models do not The use of coordinate-free notation enables a very general expression of ray-trace optical gains in real time.

The fact that we do not use multiple coordinate systems to trace rays can lead to considerable savings in computation time.

A detailed description of the analysis is provided in Ref. 3.

COMP Geometric Optics

COMP uses a new ray-trace analysis of optical beam trains

- This analysis is coordinate-free
- Modular vector/dyadic representation of rays and elements
- Simple, general exact ray-trace equations
- Valid over large motions of the elements
- Linear ray-trace equations in closed form
- Used to create small-motion models
- Exact optical gains for optical controllers
- Approach is not restricted to paraxial rays or centered or symmetric systems

Coordinate-Free Ray Trace-Equations

optical element. The optical element surface is defined by the dyadic M and vector NO. The geometry yields the point of incidence. The surface normal is computed from M, N and p, which is the vector from the surface vertex to the point of incidence. Finally, the reflected surface is a solution to the scalar quadratic equation shown. Having determined L, simple incident ray starts at point p, and has direction r(i-1). The length of the ray from p to the These equations govern the propagation of a single ray past a conic-of-revolutior and refracted ray directions are computed.

system model for execution within the COMP application or externally to COMP, perhaps as providing the starting point p for each succeeding surface, to trace the full optical beam train from entrance pupil to focal plane. COMP realizes this process in subroutine form for many rays simultaneously. COMP routines can be combined to construct a full nonlinear optical These equations are applied repeatedly, with each successive point of incidence part of a simulation.

Coordinate-Free Ray-Trace Equations

Conic surface defined by

$$\overline{\mathbf{N}}_0 = -\mathbf{f}(1+\mathbf{e})\widehat{\boldsymbol{\Psi}}$$

$$\mathbf{M} = \mathbf{I} - \mathbf{e}^2 \widehat{\psi} \widehat{\psi}$$

Ray segment length

$$\left(\widehat{\mathbf{r}}_{i-1},\ \mathbf{M}\cdot\widehat{\mathbf{r}}_{i-1}\right)\!L^2 + 2\widehat{\mathbf{r}}_{i-1}\cdot\left(\mathbf{M}\cdot\widehat{\mathbf{p}}+\widetilde{\mathbf{N}}_0\right)\!L$$

$+ \widehat{\mathbf{p}} \cdot \left(\mathbf{M} \cdot \widehat{\mathbf{p}} + 2 \overline{\mathbf{N}}_0 \right) = 0$

Point of incidence

$\vec{\rho} = \vec{p} + L\hat{r}_{i-1}$

Normal at incidence point
$$\widehat{\mathbf{N}} = \mathrm{unit}(\widehat{\mathbf{N}}_0 + \mathbf{M} \overrightarrow{\rho})$$

Reflection of incident ray

$$\widehat{\mathbf{r}}_{\mathbf{i}} = \left(\mathbf{I} - 2\widehat{\mathbf{N}}\widehat{\mathbf{N}}\right) \cdot \widehat{\mathbf{r}}_{\mathbf{i}-1}$$

Refraction of incident ray

$$\hat{\mathbf{r}}_{i} = \mu \hat{\mathbf{r}}_{i-1} - \frac{1 - \mu^{2}}{\sqrt{1 - \mu^{2} + \mu^{2} (\hat{\mathbf{N}} \cdot \hat{\mathbf{r}}_{i-1})^{2}} - \mu \hat{\mathbf{N}} \cdot \hat{\mathbf{r}}_{i-1}} \hat{\mathbf{N}}$$

focus point \hat{p}_i reflected \hat{r}_{i-1} surface $\hat{\psi}$ $\hat{\psi}$ \hat{r}_i \hat{h} \hat{r}_i \hat{r}_i \hat{r}_i \hat{r}_i \hat{r}_i \hat{r}_i \hat{r}_i \hat{r}_i \hat{r}_i

Exact Ray-Trace Geometry

Linearized Ray-Trace Equations

equations for computing optical sensitivities. A perturbation-state vector x is used to express the differential motion of the rays, as shown. The relevant perturbations include element tilt and translation. The perturbation equation provides 2 linearized ray-trace equation valid for The exact ray-trace equations have been differentiated to obtain differential ray-trace small perturbations about the nominal rays. Sensitivities of any ray to perturbations in an upstream element or ray can be computed by chaining the partial derivatives as indicated.

fast enough and compact enough to be run in-line as part of other codes, such as simulations optical codes rely on numerical differentiation to determine sensitivities. This is typically a COMP is unique in providing this closed-form differential ray-trace capability. Other more time-consuming process. The COMP routines that calculate optical sensitivities are and controllers.

Linearized Ray Trace Equations

In the structural coordinate frame...

Perturbed ray state

Linearized ray-trace equation

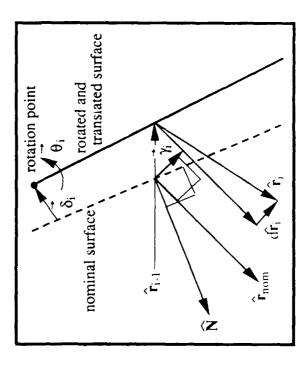
$$\vec{x}_i = \frac{\partial \vec{x}_i}{\partial \vec{x}_{i-1}} \vec{x}_{i-1} + \frac{\partial \vec{x}_i}{\partial \vec{u}_i} \vec{u}_i$$

Sensitivity of jth ray segment to perturbations of the ith element

$$\frac{\partial \vec{x}_j}{\partial \vec{u}_i} = \frac{\partial \vec{x}_j}{\partial \vec{x}_{j-1}} \cdots \frac{\partial \vec{x}_{j+1}}{\partial \vec{x}_i} \frac{\partial \vec{x}_i}{\partial \vec{u}_i}$$

Element perturbation

$$\vec{u}_i = \begin{bmatrix} \vec{\theta}_i \\ \vec{\delta}_i \end{bmatrix} \quad \text{tilt} \\ \text{translation} \label{eq:unitarity}$$



Linearized Ray-Trace Geometry

Map Optical Element Perturbations Into Structural Degrees of Freedom

This chart expands upon the connection between the optical model and the structural dynamic model by illustrating the equivalency of the degrees of freedom in the two models. The inputs to the optical model are the u; which are the rotations and displacements of the optical elements. These motions might be caused either by control actuators or motion of the structural attachment point and must be extracted from the structural dynamic model to compute the optical system response. The example illustrated in the chart is taken from an analysis of the CSI Phase B Test Bed. The optical delay line is supported by an arm on the truss structure, as shown in the lower left. The figure on the right shows a portion of the finite element model that contains the support arm structure and the dynamic model of the delay line. The figure also contains the optical model rays which enter from the left, reflect off the parabolic mirror on the right end of the delay line down to a flat mirror at the focal point, back to the parabolic mirror and out the left side of the delay line. The structural dynamic model computes the motions at the three reflection points that must be extracted for use as inputs to the op ical model. These structural degrees of freedom are d₁₉₀ through d₁₉₆ and consist only of displacements since the truss is modeled with rod elements. The absence of rotational degrees of freedom can be shown by setting θ_i for the flat and the two parabola points to zero or eliminating the corresponding columns of [C].

The collection of these structural degrees of freedom must be programmed in the language of the finite element analytical program and the resulting u vector exported to the system analysis program. In Pro-Matlab at JPL, both optics and structures are available as tool boxes and the computation is simply

[u] = [zeros(3,1); d(190:192,:); zeros(3,1); d(193:195,:); zeros(3,1); d(196:199,:)];

Into Structural Degrees of Freedom

Element Pertuhation

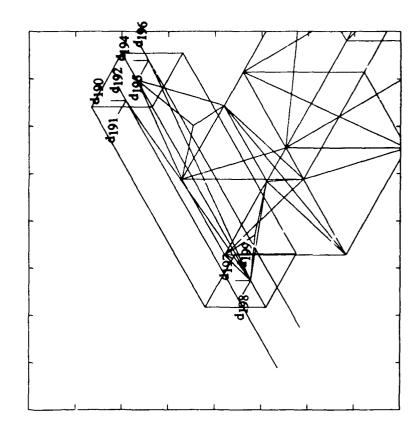
$$\vec{u_i} = \begin{vmatrix} \vec{\theta_i} \\ \vec{\delta_i} \end{vmatrix} \leftarrow \text{Rotation Degrees of Freedom}$$

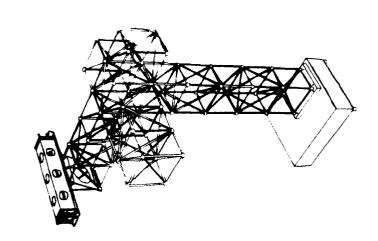
For Example, For the CSI Phase B Optical Delay Lin?

$$\delta_{\text{FLAT}} = \begin{cases} d_{197} \\ d_{198} \end{cases} \qquad \delta_{\text{PARAB1}} = \frac{\delta_{\text{PARAB1}}}{d_{199}}$$

$$\frac{d_{194}}{\delta_{PARAB2}} = \frac{d_{194}}{d_{196}}$$

d190 d191 d192





COMP Linear Models

at the focal plane (the nth element) to small motions of the input ray x0 and to small motions single-ray models to compute the wavefront phase, the blur spot, and other parameters at the The way in which optical sensitivities are combined to form linear ray-trace models is shown here. The single-ray C-matrix optical model consists of the partials of the chief ray of each element (the u's). The multiple-ray C-matrix optical model combines many final surface.

Linear Optical Models

Single-ray line-of-sight model

Single-ray line-of-sight model
$$\vec{x}_{n_{chiefray}} = C_{LOS} \begin{bmatrix} \vec{x}_0 \\ \vdots \\ \vec{u}_1 \\ \vdots \end{bmatrix} = \begin{bmatrix} \vec{\partial}\vec{x}_n & \vec{\partial}\vec{x}_n \\ \vec{\partial}\vec{x}_0 & \vec{\partial}\vec{u}_1 \\ \vdots \\ \vec{u}_n \end{bmatrix}_{chiefray} \begin{bmatrix} \vec{x}_0 \\ \vec{u}_1 \\ \vdots \\ \vec{u}_n \end{bmatrix}$$
Multiple-ray wavefront model

Multiple-ray wavefront model

$$\begin{bmatrix} \vec{x}_{n_{ray \, 1}} \\ \vdots \\ \vec{x}_{n_{ray \, m}} \end{bmatrix} = C_{WF} \begin{bmatrix} \vec{x}_0 \\ \vec{u}_1 \\ \vdots \\ \vec{u}_n \end{bmatrix} = \begin{bmatrix} \left[\frac{\partial \vec{x}_n}{\partial \vec{x}_0} \frac{\partial \vec{x}_n}{\partial \vec{u}_1} \cdots \frac{\partial \vec{x}_n}{\partial \vec{u}_n} \right] \\ \vdots \\ \left[\frac{\partial \vec{x}_n}{\partial \vec{x}_0} \frac{\partial \vec{x}_n}{\partial \vec{u}_1} \cdots \frac{\partial \vec{x}_n}{\partial \vec{u}_n} \right] \begin{bmatrix} \vec{x}_0 \\ \vec{u} \\ \vdots \\ \vec{u}_n \end{bmatrix}$$

Cost functional

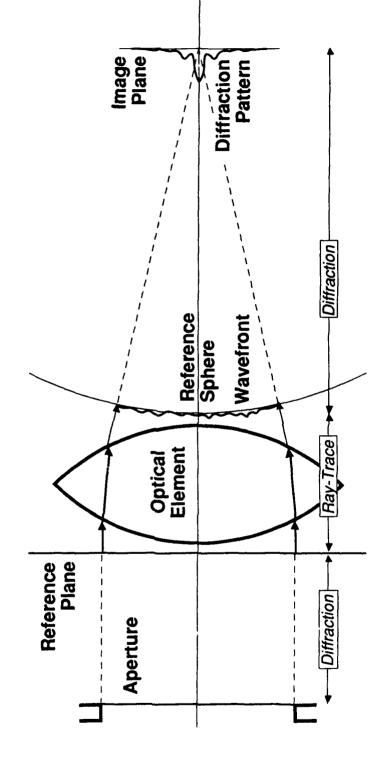
$$dJ = \frac{1}{m} \left[\vec{u}_1 \dots \vec{u}_n \right] C_{WF} R C_{WF} \left[\begin{array}{c} \vec{u}_1 \\ \vdots \\ \vec{u}_n \end{array} \right]$$

COMP Physical Optics

COMP has a developing capability to perform surface-to-surface diffraction analysis in from the last element to the focal plane. The sensor-measured intensity is represented by the modeling optical systems for which diffraction effects are important. Obscurations, segment gaps, long wavelengths and small optics are some of the conditions that lead to diffraction conjunction with ray-trace propagation through a beam train. This capability is useful for effects. Detailed modeling of focal-plane sensors requires diffraction propagation at least point-spread function (PSF). In a detailed sensor simulation, the PSF can be quantized deformable mirror controller, a segmented-mirror controller, or some other controller. image-recognition algorithm, which in turn may drive a steering mirror controller, a according to a particular pixel layout and the resulting signal fed to a centroiding or

COMP Physical Optics

Surface-to-surface diffraction capability



Ray-trace through optical elements

COMP Diffraction Analysis

reference surfaces tangent to the optics. There the phase function is calculated based on the through individual elements, however. The rays are traced through the optical elements to COMP uses a Fresnel Diffraction Theory approach to calculating the propagation of propagation. Optics are handled using the ray-trace approach to carry the diffraction grid light (Ref. 4). Both near- and far-field propagation methods are employed for free-space wavefront to the next element, which has another reference surface tangent to its surface. ray paths and the complex wavefront is reconstructed. Fresnel propagation carries the Tracing rays from this surface through the new element, the process is repeated. This approach is consistent with the thin-phase approximation for optical elements. It has a couple of advantages: it allows the use of diffraction analysis in a fully-folded optical system geometry; and it is compatible with the COMP computational structure.

COMP Diffraction Approach

COMP uses a Fresnel diffraction theory approach that exploits its ray-trace capabilities

- Near-field or far-field diffraction propagation between reference surfaces tangent to optical elements
- Ray-trace to optical element and then to next reference surface
- More general than thin-phase approximation for optical

Rays can translate, expanding or contracting grid

- Rays not necessarily paraxial
- Enables use of COMP segmented- and deformableelement capabilities

Nonlinear Optical Models

The COMP ray-trace and diffraction models can be run in-line as part of other codes. They are assembled - currently by hand - from the COMP Fortran subroutine package. This process will be automated in the future.

Nonlinear Optical Models

CALL LOS_MODEL(CHIEF_RAY_OUT, X_STRUCTURE, U_ACTURTORS,

CHIEF_ RAY_IN) ŏ

CALL WF_MODEL(WAVE_FRONT_OUT, CCD_PSF, X_STRUCTURE,

U_ACTUATORS, MAUE_FRONT_IN) ŏ

CALL DIFF_MODEL(WAVE_FRONT_OUT, CCD_PSF, X_STRUCTURE, ॐ

U_ACTUATORS, MAUE_FRONT_IN)

CALL OPTICAL_GAINS(DSDU, DUDS, X_STRUCTURE, U_ACTUATORS, ٥ŏ

CHIEF_ RAY_IN)

Examples

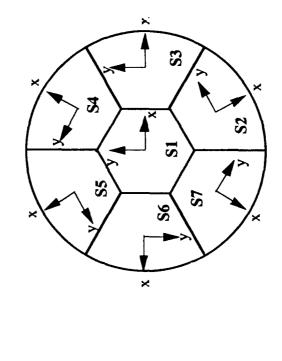
The following several charts illustrate the effect of a coordinated displacement of the wavelength Cassegrainian telescope, as sketched. Each segment is moved 100 microns outer 6 segments of a segmented mirror. The mirror is the primary of a 100 micron along the local x-axis, as illustrated.

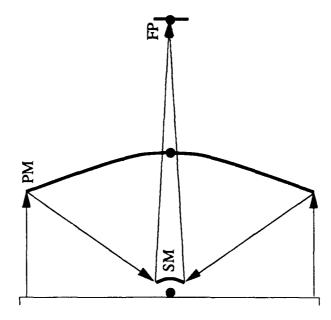
The plot that follows this chart shows the nominal and perturbed spot diagrams (the spread function projected onto the focal-plane sensor but without sensor quantization or nominal is a single spot in the center of the focal plane). The next plots are of the point other noise sources. They are shown in gray-scale and wire-frame form.

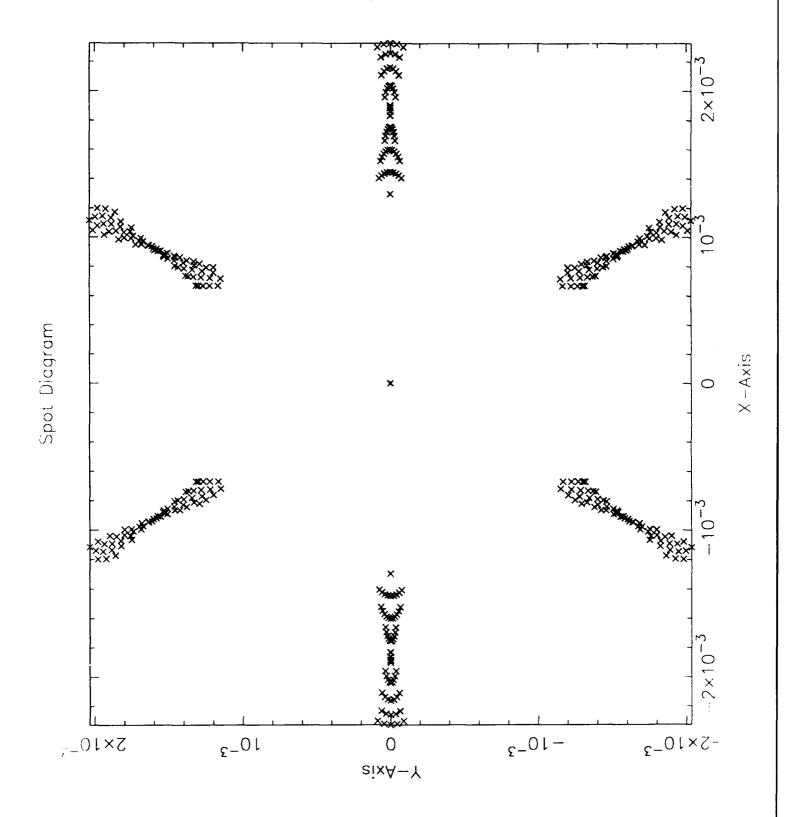
in a test setup. The main result is a wrinkling of the surface, causing a spreading of the blur The second example illustrates the effect of a deforming actuator on a single segment spot, as seen in several ways.

Segmented Mirror Example

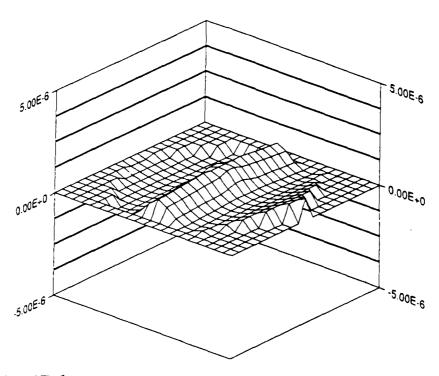
A Far-IR astronomical telescope



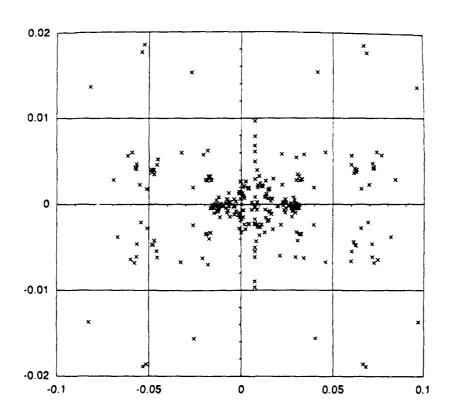


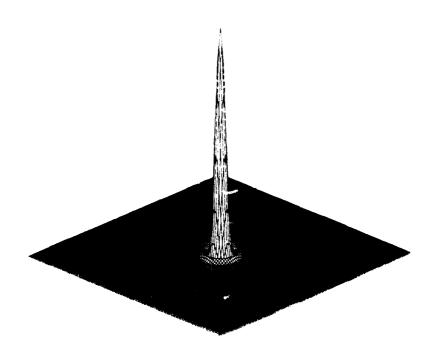


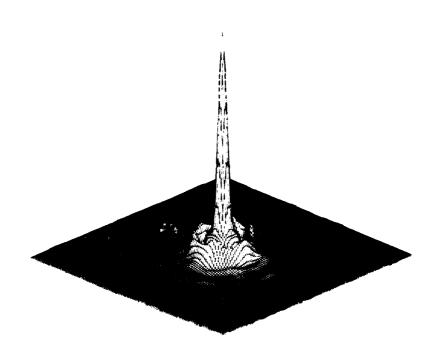
REFLECTOR PANEL OPD MAP AND SPOT DIAGRAM CENTER ACTUATOR LOAD

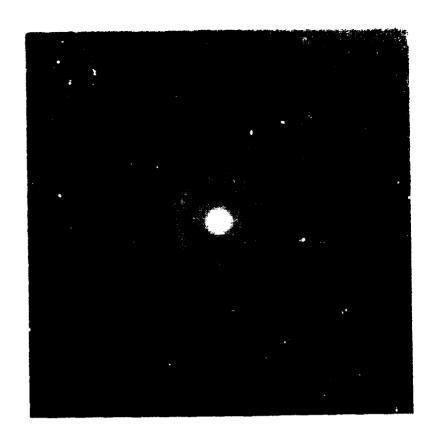


Wavelength = 1E-6 m rms Wavefront Error = 0.47E-6 m



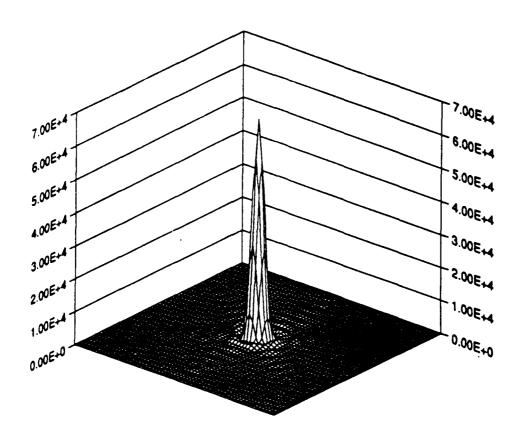




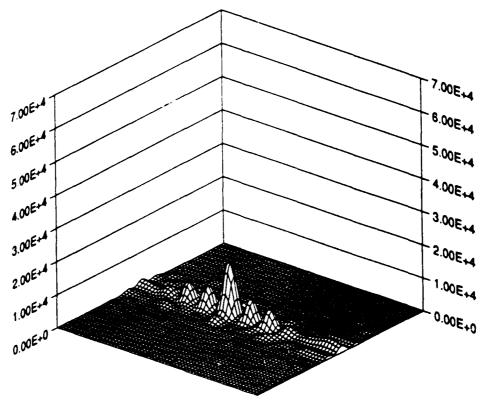




REFLECTOR PANEL PSF



NOMINAL vs. CENTER ACTUATION LOAD
Wavelength = 1E-6 m



Telescope Models and Disturbance Excitation

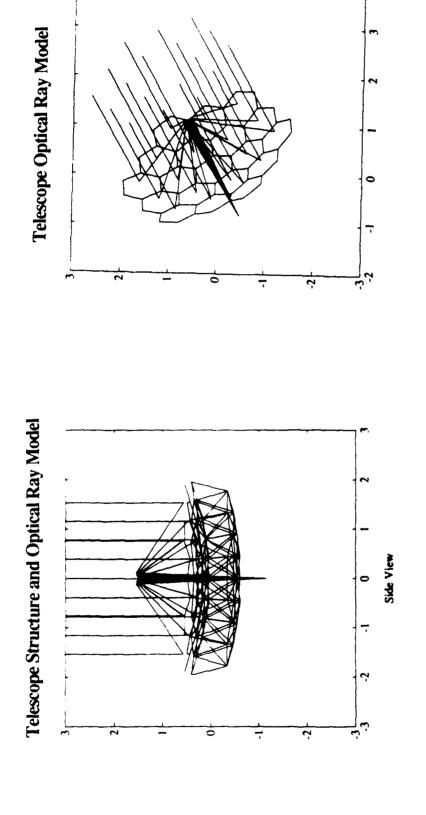
a Precision Segmented Reflector Telescope" by C. C. Ih, H. C. Briggs, and S. J. Wang. The optical model and the simulation results few slides. The model of the structure, the panels and the panel supports is described in "3D Dynamic Modeling and Simulation of As another example of this new capability, analysis results from a segmented telescope design are presented in the next are described in the companion paper "Integrated Control/Structure/Optics Dynamic Performance Modeling of a Segmented Reflector Telescope" by H. C. Briggs, D. C. Redding, and C. C. Ih. Both papers can be found in the Proceedings of the Twenty First Annual Pittsburgh Conference on Modeling and Simulation, 3-4 May, 1990.

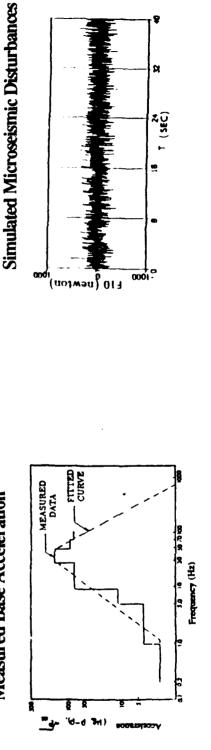
inner ring are positioned by three linear actuators with lateral restraining flexures while the outer ring panels are simply attached to concentrated mass supported by a tripod of truss elements. The structural dynamic model contains 300 degrees of freedom which The telescope model is shown in the facing slide and contains the typical elements of a controlled optic structure. The primary reflector is supported by a truss paneled by 18 curved hexagonal reflector segments. Each of the six segments of the the truss. The panels are assumed rigid and are modeled by stiff elements. The structural model of the secondary mirror is a are reduced to 102 vertical displacements for subsequent analysis.

The optical model consists of a segment principal ray that enters parallel to the telescope axis. The primary segments are represented by conic optical elements that reflect the rays to an output detector behind the primary. The output of the optical model is the pair of ray displacements, for each of the six rays of the inner panel ring, in the plane of the detector.

mirrors due to truss dynamics and the action of the control system. Specifically, the six active primary segments have piston and two tilt freedoms and the secondary elements have three translation freedoms to be associated with the structural motion of the Optical degrees of freedom have been included in the model to represent the motion of the primary and secondary secondary mirror. For this telescope, the primary segment freedoms represent control inputs while the secondary reflector freedoms represent the coupling induced by structurally supported optical elements. To illustrate the use of the optics model in the system dynamic simulation, a seismic disturbance has been applied to the present and the inner ring panels bounce freely on their soft support fixtures. The spectral content of the seismic acceleration is base of the truss to analyse expected conditions in the technology validation laboratory. In this analysis, no control system is shown in the chart along with a typical time history of the input force.

Telescope Models and Disturbance Excitation





Measured Base Acceleration

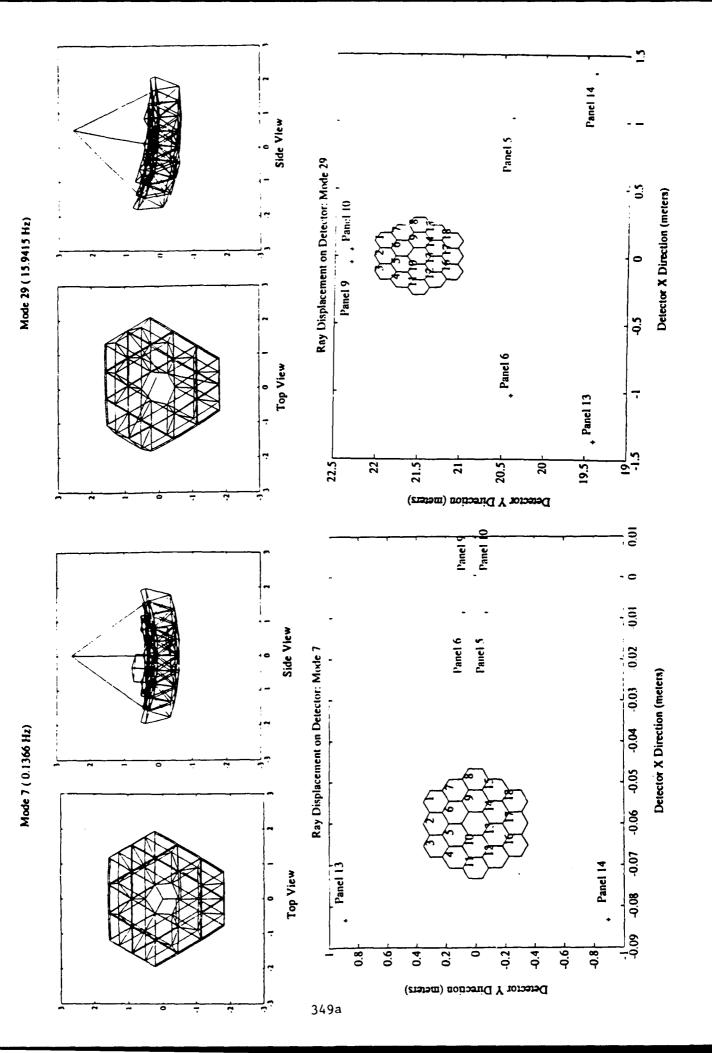
Effect of Structural Modes on Panel Chief Rays

modes are shown in the facing chart. On the left is one of the 18 panel modes in which panels 13 and 14 show a strong asymetric The time domain simulation utilized a reduced order model with 23 dominant modes out of 102. These consisted of 18 panel modes ranging from 0.1366 Hz to 0.1718 Hz, and 5 truss modes with frequencies from 15.8 Hz to 74.3 Hz. Two typical motion. The right figure show a truss bending mode.

Since no dampling data for the demonstration test article were available, a modal dampling ratio of 5% was assumed for all modes. Tests of the panel suspension controller have demonstrated a capability to damp the panels at this level, although no data for the truss is available. The simulation was executed in ACSL and the results transferred to Pro-Matlab for this analysis.

mode shape. That is, [C]*[Φ_i] provides the x and y displacements of each segment principal ray in the plane of the detector for The modal cost in terms of the optical performance can be measured by the ray displacements resulting from a given mode i. The bottom half of the facing chart shows these displacements for the panel mode and the truss mode.

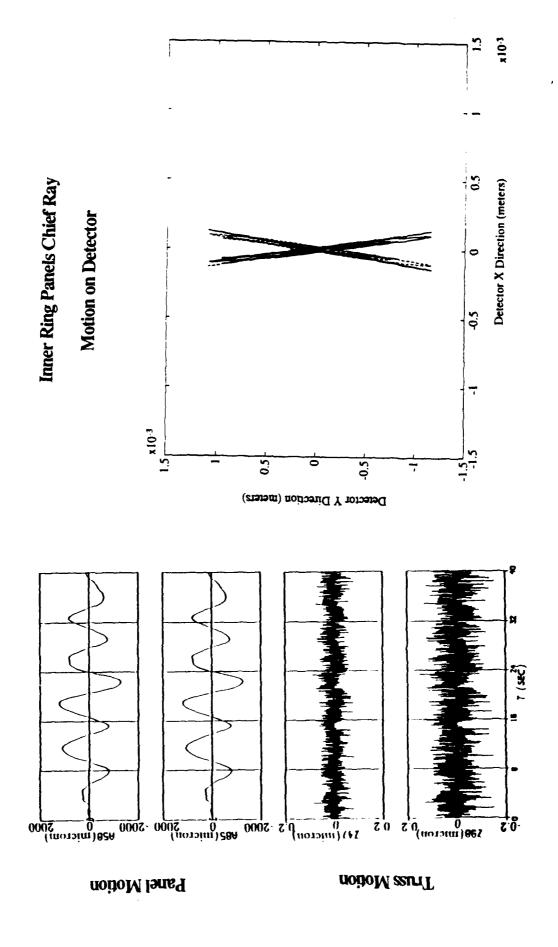
Effect of Structural Modes on Panel Chief Rays



Open Loop Time Response

response of the panel passive support system at approximately 0.1 Hz. The excitation contained a small spectral energy below 1 Hz The time histories from the simulation are shown in this chart along with motion of the rays in the detector. The left which is its design function. The lower plots show the motion of a typical truss node and clearly shows the spectral content of which is exciting the panel support mode. The panel support system effectively eliminates all disturbances above this frequency plots show typical panel motions caused by the base accelerations with no panel control system. The notion is dominated by the disturbance.

The right plot show the traces of the six inner panel rays in the detector plane. These show the basicly sinusoidal motion of the panel responses on the left.



Current Activities

- Precision Segmented Reflector Project
- Figure initialization control design and simulation
- Figure maintenance control design and simulation
- Reflector panel fabrication and test
- Control Structures Interaction Project
- Stellar Interferometer integrated calibration and performance analyses
- Laser metrology performance analysis
- Testbed analysis and design
- Integrated structures/optics/controls optimization
- Hubble Space Telescope/Wide Field and Planetary Camera **Project**
- Image Inversion study

Summary

- optical/structural/controls analysis and design is a necessity For large, controlled optical instruments integrated
- Linear ray-trace models are useful for controller design, error analysis, calibration, performance analysis
- Nonlinear ray-trace models are required for large articulations
- Computing optical performance
- Computing optical sensitivities
- Physical optics models are required for diffraction-dominated cases
- COMP computes each of these types of models in forms suitable for integrated simulation and analysis

References

- Control-Structure Design: A Multi-Objective Approach," JPL Report D-6767, January, M. Milman, M. Salama, R. Scheid, R. Bruno, and J. Gibson, "Integrated
- 2. M. Wette, M. Milman, and D. Redding, "Experiences in Integrated Structure/Optics/Control Design Optimization," to appear.
- D. Redding and W. Breckenridge, "Modeling Optics for Dynamics and Control Analysis," Paper No. 90-3383, AIAA/AAS Guidance and Control Conference, Portland OR, August 1990. 3
- 4. J. Goodman, Introduction to Fourier Optics, McGraw-Hill, 1968.

Selection of Sensors and Actuators with Applications to the ASTREX Facility

A. Hu
Dynacs Engineering, Co., Inc.
and
R.E. Skelton
Purdue University
and
Capt. G.A. Norris, and Lt. D. F. Cossey
AFAL, Edwards AFB

Abstract

This paper presents sensor and actuator selection (SAS) algorithm as applied to the reduced order model of Advanced Space Structures Technology Research Experiments (ASTREX) developed at Edwards AFB. The AS-TREX facility is a test bed for conducting precise pointing and shape control to validate the rapidly emerging space structures control technology. The existing method of sensor and actuator selection is modified to consider the effect of direct transmission from plant input to measurement as well as that of actuator dynamics. Basically, the SAS algorithm employs a linear quadratic Gaussian controller, an efficient weightselection or Output Variance Control design (OVC) technique, and a criterion to measure the effectiveness of actuators and sensors based on their contributions to the quadratic performance metric. When applying the SAS algorithm to the ASTREX model, actuators and sensors are deleted one-at-a-time until the closed-loop system degrades or the system becomes uncontrollable or unobservable. The SAS algorithm is then integrated with the output variance constraint algorithm, and sensor/actuator deletion followed by controller design is performed. The results demonstrate the efficacy of the approach to design problems.

1.0 Introduction

In the past, the sensor and actuator selection algorithm has been mainly used to located perfect (infinite bandwith) sensors and actuators on large scale systems [1,2]. In addition, the actuator and sensor noise have usually been assumed to be uncorrelated. Norris and Skelton [3] extended SAS algorithm so that it can be applied to the linear system using imperfect sensors and actuators with correlated excitation and measurement noise. This makes it possible to investigate the effects of the

sensor and actuator dynamics on the optimal selection of sensors and actuators. However, if a large number of sensors and actuators are present, to include the dynamics of both sensors and actuators in the control design at the same time would significantly increase the dimension of the system and complicate the calculation. In fact, for many practical control problems such as the control design of ASTREX facility, the sensors can usually respond much faster than the actuators. This suggests that for such type of problem we may only consider actuator dynamics and assume that the sensors have instantaneous response. Therefore, we can improve sensor and actuator selection results without significantly increasing the computational burben.

The purpose of this paper is to apply SAS algorithm to ASTREX reduced order model when imperfect actuators are used. The basic theory for SAS algorithm developed in [1-4] are briefly reviewed for completeness. The optimal controllers with correlated noise have been modified to consider the effects of direct transmission from plant input to its measurement.

This paper is organized as follows. Section 2 presents optimal controller with correlated noise due to direct transmission from plant input to its measurement. Section 3 provides the ingredients of sensor and actuator selection algorithm when imperfect actuators are used. Section 4 applies the SAS algorithm to the reduced order model of ASTREX facility and compares the results using non-dynamic and dynamic actuators.

2.0 Optimal Controllers with Correlated Noise Due to Direct Transmission

Consider the following tandem connection of dynamic actuators and plant using perfect sensors.

The actuators are described by the dynamics

$$\dot{x}_a = A_a x_a + B_a (u + w_{in})$$

$$y_a = C_a x_a$$
(1)

the plant described by the dynamics

$$\dot{x}_p = A_p x_p + B_p (y_a + w_{out})
y_p = C_p x_p$$
(2)

$$z = M_p x_p + H_p (y_a + w_{out}) + v$$

where the term H_p reflects the direct transmission from the plant input to its measurement. The dimensions of the vectors are

$$x_a \in \mathbb{R}^{n_*}, \ x_p \in \mathbb{R}^{n_p}, \ u \in \mathbb{R}^{n_*}, \ w_{in} \in \mathbb{R}^{n_*}, \ w_{out} \in \mathbb{R}^a$$

$$y_a \in \mathbb{R}^a, \ y_p \in \mathbb{R}^p, \ z \in \mathbb{R}^{n_*}, \ v \in \mathbb{R}^p$$

The tandem system described by eqns. (1) - (2) can be reorganized into an augmented open-loop form in the following manner

$$\dot{x} = Ax + Bu + Dw
y = Cx
z = Mx + Hw + v
= Mx + \mu
\mu \triangleq Hw + v$$
(3)

where

$$A \stackrel{\triangle}{=} \begin{bmatrix} A_a & 0 \\ B_p C_a & A_p \end{bmatrix}, \tag{4}$$

$$B \triangleq \begin{bmatrix} B_a \\ 0 \end{bmatrix}, \tag{5}$$

$$D \triangleq \begin{bmatrix} B_a & 0 \\ 0 & B_p \end{bmatrix} \tag{6}$$

$$C \triangleq \begin{bmatrix} C_a & 0 \\ 0 & C_p \end{bmatrix}, \tag{7}$$

$$M \triangleq [H_p C_a, M_p] \tag{8}$$

$$H \triangleq [0 H_p] \tag{9}$$

$$x \triangleq \begin{bmatrix} x_a \\ x_p \end{bmatrix}, y \triangleq \begin{cases} y_a \\ y_p \end{cases}$$
 (10)

where

$$x \in \mathbb{R}^n$$
, $n \triangleq n_a + n_p$

$$\boldsymbol{w}^{T}(t) \triangleq [\boldsymbol{w}_{in}^{T}(t), \boldsymbol{w}_{out}^{T}(t)] \tag{11}$$

Note that although w and v are still uncorrelated, the state excitation noise w and the measurement noise μ are correlated white noise processes, that is,

$$E\begin{bmatrix} w(t) \\ \mu(t) \end{bmatrix} [w^{T}(\tau), \mu^{T}(\tau)]$$

$$= \begin{bmatrix} W & WH^{T} \\ HW & HWE^{T} + V \end{bmatrix} \delta(t - \tau)$$
(12)

In the augmented open-loop system of eqn. (3), both the outputs of the actuators y_a and plant y_p are included in the output of the augmented open-loop system. The Output Variance Control algorithm [6] (also see Appendix) is used to provide an LQG control law such that

$$\min E_{\infty} u^T R u, \ E_{\infty} \stackrel{\triangle}{=} \lim_{t \to \infty} E$$

subject to

$$E_{\infty}y_i^2(t) \leq \sigma_i^2$$

The controllability and observability properties are essential for designing optimal controllers for the open-loop system in eqn. (3). Specifically, the matrices A, B, C, D and M in eqn. (3) must satisfy the following stabilizability and dectability condition.

stabilizable: (A, B), (A, D)detectable: (A, C), (A, M)

Furthermore, the controllability and observability of the system should be ensured in the process of sensor and actuator deletion. In general, the controllability and observability of each of the individual component in a tandem connection do not guarantee the controllability and observability of the resultant composite system. It was shown in [3] that if the actuator and plant do not have common eigenvalues, then the augmented system is controllable (observable) if the plant and actuator are individually controllable (observable) and the eigenvalues of the plant are not the transmission zeros of the actuator system.

In order to provide expressions for the closed-loop input and output costs, it is first necessary to put the fully augmented system, under closed loop steady-state optimal state-estimate feedback control, in the following state space form:

$$\dot{\mathbf{x}}(t) = \mathbf{A}\mathbf{x}(t) + \mathbf{D}\mathbf{w}(t)
\mathbf{y}(t) = \mathbf{C}\mathbf{x}(t)
V = E_{\infty}V_{o}(t), V_{o}(t) = \mathbf{y}^{*}(t)\mathbf{Q}\mathbf{y}(t).$$
(13)

where

$$\mathbf{x}^{T} = [x^{T}, x_{c}^{T}], \mathbf{y}^{T} = [y^{T}, u^{T}], \mathbf{w}^{T} = [w^{T}, v^{T}]$$

$$\mathbf{A} = \begin{bmatrix} A & BG \\ FM & A + BG - FM \end{bmatrix}, \mathbf{D} = \begin{bmatrix} D & 0 \\ 0 & F \end{bmatrix},$$

$$\mathbf{C} = \begin{bmatrix} C & 0 \\ 0 & G \end{bmatrix}$$

$$\mathbf{Q} = \begin{bmatrix} Q & 0 \\ 0 & R \end{bmatrix}, \mathbf{W} = \begin{bmatrix} W & WH^T \\ HW & HWH^T + V \end{bmatrix}$$

$$Q = diag [Q_a, Q_p], \ Q > 0$$

$$G = -R^{-1}B^{T}K$$

$$0 = KA + A^{T}K - KBR^{-1}BK + (14)$$

$$C^{T}QC \text{ for } K \ge 0$$

$$F = (PM^{T} + DWH^{T})(HWH^{T} + V)^{-1} (15)$$

$$0 = P[A - DWH^{T}(HWH^{T} + V)^{-1}M]^{T}$$

$$+ [A - DWH^{T}(HWH^{T} + V)^{-1}M]P$$

$$- PM^{T}(HWH^{T} + V)^{-1}MP + DWD^{T} (16)$$

$$- DWH^{T}(HWH^{T} + V)^{-1}HWD^{T}$$

The optimal filter solution in eqn. (15) and (16) has been generalized to include the possibility of noise correlation due to the presence of direct transmission term H from input to measurement while the optimal regulator is not affected by the noise characteristics. This optimal filter can be easily obtained using Theorem 4.6 of [5]. The only modification required here is to substitute WH^T for the non-zero cross-correlation term between state excitation and measurement noise and use $HWH^T + V$ for the measurement noise intensity. Specifically, comparing with the standard filter Riccati equation, the following changes have been made by replacing

A with
$$A = LWH^{T}(HWH^{T} + V)^{-1}M$$

V with $(HWH^{T} + V)$

and

$$F = PM^TV^{-1} \text{ with}$$

$$F = (PM^T + DWH^T)(HWH^T + V)^{-1}$$

3.0 Sensor and Actuator Selection

In this section we provide the ingredients of sensor and actuator selection algorithm when imperfect actuators are used. Specifically, we shall discuss the concept of closed-loop input and output cost analysis, and provide the expressions for input cost reduction as well as those for actuator and sensor effectiveness values.

3.1 Input/Output Cost Analysis

For the system in eqn. (13) the "output costs" $V_i^{\mathbf{y}}$ is defined by

$$V_{i}^{\mathbf{y}} \triangleq (1/2) \{ E_{\infty}(\partial V_{o}/\partial \mathbf{y}_{i}) \mathbf{y}_{i} \}$$

where

$$V_o = E_{\infty}[||y(t)||_O^2 + ||u(t)||_R^2],$$

and

The "output costs" V_i^y are calculated as follows

$$V_i^{\mathbf{y}} = [\mathbf{C}\mathbf{X}\mathbf{C}^T\mathbf{Q}]_{ii} \tag{17}$$

where X is the steady state covariance satisfying

$$0 = \mathbf{AX} + \mathbf{XA}^{\prime} + \mathbf{DWD}^{T} \tag{18}$$

The input costs are defined by

$$V_i^{\mathbf{W}} \triangleq (1/2) \{ E_{\infty} (\partial V_o / \partial \mathbf{w}_i) \mathbf{w}_i \}$$

and are found from

$$V_i^{\mathbf{W}} = [\mathbf{D}^T \mathbf{S} \mathbf{D} \mathbf{W}]_{ii} \tag{19}$$

where S satisfies

$$0 = \mathbf{A}^T \mathbf{S} + \mathbf{S} \mathbf{A} + \mathbf{C}^T \mathbf{Q} \mathbf{C} \tag{20}$$

Furthermore the closed-loop covariance X may be written as

$$\mathbf{X} = \left[\begin{array}{cc} P + N & N \\ N & N \end{array} \right]$$

where P satisfies eqn. (16) and N satisfies

$$0 = N(A + BG)^{T} + (A + BG)N + F(V + HWH^{T})F^{T}$$
(21)

Also, S has the following form

$$\mathbf{S} = \left[\begin{array}{cc} K + L & -L \\ -L & L \end{array} \right] \tag{22}$$

where K satisfies eqn. (14) and L satisfies

$$0 = L(A - \vec{A}M) + (A - FM)^{T}L + G^{T}RG$$
 (23)

The input and output costs represent the in situ contributions that the noise inputs and the system outputs make in the cost function. We may also wish to know the amount by which the cost function will be reduced if a noise input is eliminated. This amount, $\Delta V_1^{\mathbf{w}}$, is defined as

$$\Delta V_i^{\mathbf{w}} = V - V_{Ri} \tag{24}$$

where V_{Ri} is the value of the cost function after the i^{th} noise input is eliminated, (but the controller is not redesigned), and $\Delta V_i^{\mathbf{W}}$ is the cost reduction due to eliminating w_i .

It is shown in [1] that after partitioning the matrices \mathbf{W} and \mathbf{D}_i , the cost reduction $\Delta V_i^{\mathbf{W}}$ is

$$\Delta V_i^{W} = 2V_i^{\mathbf{W}} - d_i^T \mathbf{S} d_i \mathbf{W}_{ii} \tag{25}$$

Note that a positive value for $\Delta V_i^{\mathbf{W}}$ indicates that elimination of the i^{th} noise input will reduce the cost, while a negative $\Delta V_i^{\mathbf{W}}$ indicates that a cost increase will follow noise elimination. It is shown in [4] that $\Delta V_i^{\mathbf{W}}$ may be positive or negative in the presence of noise correlation, and some noise source may be beneficial in the linear system.

Output Cost

The equations used to derive the output costs are based on eqn. (17)

$$V_i^{\mathbf{y}} = [\mathbf{C}\mathbf{X}\mathbf{C}^T\mathbf{Q}]_{ii}$$

where $\mathbf{X} = \begin{bmatrix} P+N & N \\ N & N \end{bmatrix}$ (26)

For convenience the state covariance P+N is partitioned as follows

$$[P+N] = \left[\begin{array}{cc} X_a & X_{12} \\ X_{12}^T & X_p \end{array} \right]$$

Recall that the output for the closed-loop system in eqn. (13) is

$$\mathbf{y}^T = [y^T, \ u^T] = [y_a^T, \ y_r^T, \ u^T]$$

and

$$\mathbf{C} = \left[\begin{array}{cc} C & 0 \\ 0 & G \end{array} \right], \quad C = \left[\begin{array}{cc} C_a & 0 \\ 0 & C_p \end{array} \right]$$

$$\mathbf{Q} = \begin{bmatrix} Q & 0 \\ 0 & R \end{bmatrix}, \quad Q = \begin{bmatrix} Q_a & 0 \\ 0 & Q_n \end{bmatrix}$$

Hence the output costs are

$$V_i^{y_a} = [C_a X_a C_a^T Q_a]_{ii}, \quad i = 1, ..., a$$

$$V_i^{y_p} = [C_f X_p C_p^T Q_p]_{ii}, \quad i = 1, ..., p \qquad (27)$$

$$V_i^{y_a} = [GNG^T R]_{ii}, \quad i = 1, ..., n_a$$

Input Cost

The equations used to derive the input cost are based on eqn. (19)

$$V_i^{\mathbf{W}} = [\mathbf{D}^T \mathbf{S} \mathbf{D} \mathbf{W}]_{ii}$$

where

$$\mathbf{S} = \left[\begin{array}{cc} K + L & -L \\ -L & L \end{array} \right]$$

Recall that the input costs for the closed-loop system in eqn. (13) is

$$\mathbf{w}^{T} = \begin{bmatrix} w_{in}^{T}, w_{out}^{T}, v^{T} \end{bmatrix}$$

$$\mathbf{D} = \begin{bmatrix} D & 0 \\ 0 & F \end{bmatrix},$$

$$\mathbf{W} = \begin{bmatrix} W & WH^{T} \\ HW^{T} & HWH^{T} + V \end{bmatrix}$$
(28)

Hence the input costs are

$$V_{i}^{u_{in}} = [D^{T}(K+L)DW - D^{T}LFHW^{T}]_{ii}$$

$$i = 1, ..., n_{u}$$

$$V_{i}^{u_{out}} = [D^{T}(K+L)DW - D^{T}LFHW^{T}]_{n_{u}+i, n_{u}+i, i}$$

$$i = 1, ..., a$$

$$V_{i} = [F^{T}LF(V+HWH^{T}) - F^{T}LDWH^{T}]_{ii}$$

$$i = 1, ..., n_{z}$$
(29)

3.2 Input Cost Reduction

With direct substitution of input cost expressions of eqn. (29), into (25) we obtain

$$\Delta V_{i}^{u_{in}} = 2V_{i}^{u_{in}} - [D^{T}(K+L)D]_{ii} W_{ii}$$

$$i = 1, \dots, n_{u}$$

$$\Delta V_{i}^{u_{out}} = 2V_{i}^{u_{out}} - [D^{T}(K+L)D]_{n_{u}+i,n_{u}+i}$$

$$W_{n_{u}+i,n_{u}+i}$$

$$i = 1, \dots a$$

$$\Delta V_{i} = 2V_{i} - [F^{T}LF]_{ii}[HWH^{T} + V]_{ii}$$

$$i = 1, \dots, n_{z}$$
(30)

A direct approach to the selection of sensors and actuators leads to integer programming. This approach is extremely time-consuming for a large set of actuators and sensors. Therefore, we sek a suboptimal alternative. Equations (27), (29) and (30) provide the ingredients to a "cost decomposition" approach which motivates our approach.

3.3 Actuator and Sensor Effectiveness

Now that the closed-loop input and output costs have been determined for systems with dynamic actuators, it remains to use the cost decomposition results in eqns. (27) - (30) to define expressions which reflect the contribution that each sensor and actuator is making to the minimization of the cost functional V. These effectiveness values will provide the guide-lines for the sensor and actuator selection problems.

Actuator Effectiveness

As noted in the previous discussion, V_i^u represents the contribution that u_i is making to V. On the other hand, ΔV_i^w represents the amount by which the cost function will be reduced if a noisy input is eliminated. That is, a positive value for ΔV_i^w indicates that elimination of the i^{th} input will reduce the cost, while negative ΔV_i^w would indicate an increase in the cost after elimination.

Based on the above discussion we define "actuator effectiveness", V_i^{act} , by subtracting the contribution of i^{th} actuator's noise in the cost function from the contribution of control signal.

That is,

$$V_i^{aci} = V_i^u - \Delta V_i^u \tag{31}$$

Applying the definition in eqn. (31) to systems with dynamic actuators, some necessary modifications are in order. It should be noted that in eqn. (3), there are two noise sources associated with each actuator: command noise w_{in} , which is filtered by the actuator dynamics; and output noise, w_{out} , which is additive to the actuator output. Thus, the noise contribution associated with the i^{th} actuator is given by the sum of $\Delta V_i^{w_{in}}$ and $\Delta V_i^{w_{out}}$.

The beneficial control cost (such as V_i^u in eqn. (31)) for each actuator also needs clarification. First, recall that it is the actuator output $y_a(t)$, not its input u(t), that drives the system. Next, note that the contribution of the i^{th} actuator's output in the cost function, $V_i^{y_a}$, includes the effect of w_{in} that must be excluded in order to define the net contribution of u_i to $V_i^{y_a}$, denoted by $[V_i^{y_a}]^u$,

$$[V_i^{y_o}]^u = V_i^{y_o} - [V_i^{y_o}]^w$$

=
$$[C_a(X_a - \underline{X}_a)C_a^T Q_a]_{ii}$$
(32)

where

$$[V_i^{y_a}]^u = [C_a \underline{X}_a C_a^T Q_a]_{ii}$$

Note that X_a is a partition of (P+N) and the open-loop covariance of actuator state X_a satisfies

$$0 = A_a X_a + X_a A_a^T + B_a W_{in} B_a^T$$

Finally, eqn. (31) is generalized to account for both the "good" and "bad" contributions discussed above to get an effectiveness formula for dynamic actuator

$$V_{i}^{act} = [V_{i}^{y_{a}}]^{u} - \Delta V_{i}^{u_{in}} - \Delta V_{i}^{u_{out}}, \quad i = 1, \dots a \quad (33)$$

Sensor Effectiveness

Unlike the actuator noise, the noise associated with sensors reach the system only through the Kalman filter, whereas the actuator noise has a direct path to the output independently of the controller influence. It is known that the gains in the Kalman filter represent an optimal trade-off of each sensor's (beneficial) measurement information versus the (performance degrading) impact of its noise ($\mathbf{W} = \text{diagonal}$). For this reason, the following definition for the effectiveness of the i^{th} sensor has been used in the sensor selection when the sensor and actuator noises are uncorrelated ($\mathbf{W} = \text{diagonal}$).

$$V_i^{sen} \stackrel{\triangle}{=} V_i^v = \Delta V_i^v \tag{34}$$

But from [3] ΔV_i^v is sign-indefinite in the case of correlated noise, so that sensor effectiveness V_i^{sen} given by eqn. (34) is sign-indefinite as well. Hence, eqn. (34) will not necessarily lead to deletion of the sensor whose noise is making the smallest impact on the cost. Therefore, when the sensor and actuator noises are correlated a more general definition for sensor effectiveness values is needed to reflect the measurement information/noise trade-off of Kalman filter, i.e.,

$$V_i^{sen} = |\Delta V_i^v| \tag{35}$$

With the expressions for sensor and actuator effectiveness values chosen the sensor and actuator selection problem will be solved by iteratively deleting the sensor or actuator with the algebraically lowest effectiveness values, recalculating the effectiveness values for the remaining devices, and continuing the procedure until the desired number of sensors and actuators is reached.

4.0 Application of SAS Algorithms to ASTREX Model

This section presents the results of applying integrated Output Variance Control (OVC) and Sensor/Actuator Selection (SAS) algorithms to the reduced order model of ASTREX facility. The OVC algorithm seeks to design a controller that minimizes input energy subject to output inequality constraints and adjusts the weighting matrices Q and R. The SAS algorithm selects the

sensor and actuator by iteratively deleting the sensor or actuator with the algebraically lowest effectiveness values.

In this section we shall briefly discuss the main features of ASTREX and its reduced order model. We shall also compare the results of sensor and actuator selection for ASTREX model using non-dynamic and dynamic actuators.

4.1 ASTREX Facility

The Advanced Space Structures Technology Research Experiments (ASTREX) is illustrated in Figure 1. It was developed to provide the hardware for testing and validating emerging space structures technology. ASTREX has the desirable features of large precision structures laboratory, namely, three-axis slew capability, three dimensional realistic misssion representative test articles, ability to change key structural members and add/delete sensors and actuators as desired together with a fully-programmable real-time controller.

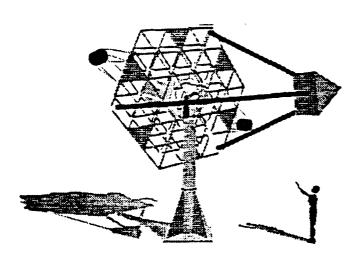


Figure 1: ASTREX Facility

The full order model of ASTREX is synthesized using the NASTRAN and can be found in [7,8]. It has 8 actuators, 24 measurements and 6 outputs. The control objective for these structures is to maintain the rootmean-square (RMS) values of the Line-of-Sight (LOS) outputs within a prescribed set of limits.

The eight actuators were located on the primary mirror truss to provide actuation forces. Four cold gas thrusters provide maximum capacity of 200 lbs in z direction. Four CMG moment actuators provide maximum capacity of 70 ft-lb along x and y directions. The

actutaor locations are shown in Figure 2. Twenty-four (24) accelerometer sensors were located on the primary, secondary and tertiary structures and on the structural interconnnections between them. A simplifying sketch of their locations is shown in Figure 3. The line-of-sight (LOS) is formulated by combining the optical sensitivity data with various displacements at selected node locatins on the primary, secondary and tertiary mirrors.

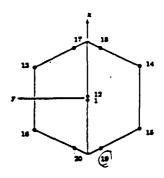


Figure 2: Actuator Locations

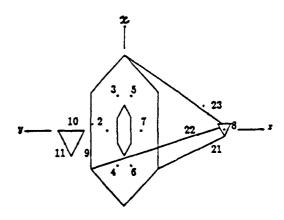


Figure 3: Sensor Locations

4.2 Non-Dynamic Actuator

The reduced order ASTREX model is obtained using Modal Cost Analysis [9], and is briefly described as follows.

$$\dot{x}_r = A_r x_r + B_r u + D_r w$$

$$y = C_r x_r$$

$$z = M_r x_r + N_r u + H_r w + v$$

In this section the actuators are assumed to be non-dynamic and u is a 8×1 vector, y is a 6×1 vector of line-of-sight (LOS) errors (XLOS and YLOS at primary, secondary, and tertiary mirrors), and z is 24×1 vector of acceleration in g's. The matrices A_r , B_r , D_r , C_r , M_r , N_r , and H_r can be found in [7,8]. The presence of direct transmission terms N_r and H_r is due to the use of accelerometers for measurement. The state excitation noise w and measurement noise $(H_rw + v)$ are correlated, although there is no cross-correlation between w and v with noise intensities as follows.

Actuator noise intensity matrix

$$W = diag[78.8544*I(4), 0.9010*I(4)]$$

Sensor noise intensity matrix

$$V = 25 * 10e-6 * I(24)$$

Note that the units for the first 4 W_{ii} are $Newton^2$ and the unit for the last four W_{ii} are $(Newton.Meter)^2$. The unit for all V_{ii} are the same as g^2 's.

The general flow of OVC/SAS procedure can be found in Figure 4.

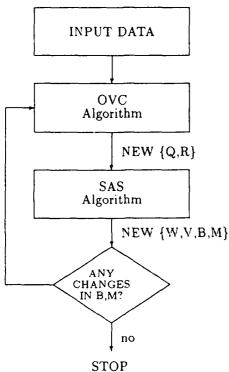


Figure 4: The OVC/SAS Algorithm

When using the OVC algorithm, the open-loop, desired, and minimum achievable output variances can be found and are listed in Table 1 for the case of nonzero direct transmission H_r .

Table 1: Output Variances $(H \neq 0)$

| Open-Loop | Desired | Minimum |
|-----------|----------|----------|
| 4.35e-10 | 2.11e-10 | 1.67e-11 |
| 8.60e-09 | 2.11e-10 | 1.44e-10 |
| 3.77e-12 | 2.11e-12 | 1.09e-13 |
| 1.21e-07 | ? 35e-09 | 1.88c-09 |
| 5.52e-09 | 2.35e-09 | 9.51e-11 |
| 1.62e-10 | 2.35e-11 | 2.51e-12 |

Note that the desired output variances expressed in arcseconds is as follows.

In combining OVC and SAS algorithms, the following three steps were taken for the reduced order model of ASTREX.

- (1) Apply OVC/SAS algorithms to the "original" system with 8 actuators and 24 sensors. Compute and rank actuator and sensor effectiveness values.
- (2) Apply OVC/SAS algorithms to the "original" system and delete actuators one at a time while retaining all 24 sensors, as long as the reduced system remains controllable and continues to improve (or does not degrade) its closed-loop performance.
- (3) Apply OVC/SAS algorithms to the "reduced" system obtained from step 2 with 5 actuators including 1 thruster (No. 1) and 4 CMG's (No. 5-8), and delete sensors one at a time while retaining all 5 actuators. We continueed this calculation as long as the closed-loop system performance index does not increase and the system remains observable.

When applying OVC/SAS algorithm to ASTREX model, two important facts concerning the impact of actuator and sensor noise on sensor and actuator deletion should be emphasized: (1) the deletion of a noisy actuator may or may not degrade the closed-loop system performance, or in other words, it is possible for an LQG controller to do better (i.e., maintain lower output specification at the same input power or maintain the same output specification with the lower input power) when a noisy actuator is deleted; (2) the deletion of a noisy sensor cannot reduce the closed-loop system performance index, or in other words, noisy sensors never degrade the performance of an LQG controller.

Step 1:

In this step we apply the combined OVC/SAS algorithms to the "original" system with a full set of actuators and sensors. We then compute and rank the

magnitude of the effectiveness values, V_i^{act} and V_i^{sen} , such that they are in ascending order.

After using SAS routine we obtain the following results

Actuator effectiveness in acsending order (v^{act1})

- -4.0781e+04
- -1.9169e+04
- -2.7129e+03
- 9.0315e+01
- 4.3497e+02
- 5.7586e+02
- 6.4173e+02
- 3.6356e+03

The ranking of actuator effectiveness in ascending order is: [3, 4, 2, 1, 6, 5, 8, 7] and the ranking of sensor effectiveness is: [24, 4, 13, 23, 15, 11, 16, 2, 10, 12, 22, 14, 3, 6, 20, 5 1, 18, 7, 9, 8, 19, 21, 17]. This implies that the 3rd actuator (thruster) or the 24-th sensors have least effectiveness values and are the first candidates for deletion if the system controllability or observabilty is not disturbed.

Note that the effectiveness values are negative for actuators 3, 4, 2 but are positive for actuators 6, 5, 8, 7. In other words, actuators 3, 4, 2 are contributing more noise than control action and should be either deleted or their signal-to-noise ratio should be improved. On the contrary, actuators 1,6,5,7.8 are contributing more control action than noise and should be retained in the closed-loop system.

Step 2:

In this step we apply OVC/SAS algorithms to the ASTREX model and delete actuators one at a time while retaining all sensors. We repeatedly use OVC/SAS algorithms according to the procedure shown in Figure 4. That is, we started with a full set of 8 actuators and 24 sensors and use OVC algorithm to select weighting matrices. Then using the new Q and R matrices we apply SAS algorithm to the ASTREX system. We compute the closed-loop system performance, rank the actuators and delete the smallest V_i^{act} . We also check the controllability property of the modified closed-loop system and continue this iterative process until the closed-loop system performance metric ceases to improve, or the system loses its controllability. The results in this step are listed in Tables 2 and 3.

Table 2 shows the the closed loop system performance metric vs. the number of actuators retained. For example, the rankings of the 8 actuators are [3, 4, 2, 1, 6,

5. 8. 7] in the first iteration, and the 3rd actuator has the least actuator effectiveness value (negative values with the biggest magnitude), and was to be deleted. In the second iteration, the rankings of the 7 actuators are [4,2,1,5,6,8,7], and the 4th actuator was to be deleted. It is noted that the rankings in the successive iterations are not the same from each other, which clearly shows that the relative importance of sensors and actuators depends on the weighting matrices Q and R, and the deletion of sensors and actuators will, in turn, change Q and R.

Table 2 - Closed Loop System Performance vs. No. of Actuators Operating (Non-Dynamic Actuators) (Norris-Skelton Approach)

| No. of Act. Operating | Actuator Deleted | $V_{\mathbf{u}}$ | V_{cls} |
|--------------------------|---------------------|------------------|-----------|
| 8 | | 3.34e+04 | 1.82e+05 |
| 7 | 3 | 2.08e+03 | 7.12e+03 |
| 6 | . 3,4 | 2.22e+02 | 9.00e+02 |
| 5 | 3,4,2 | 3.52e+01 | 1.15e+02 |

Note:

$$V_{y} \triangleq \Sigma(E_{\infty}y_{i}^{2})$$

$$V_{u} \triangleq \Sigma(E_{\infty}u_{i}^{2})$$

$$V_{ols} = \Sigma E_{\infty}y_{i}^{2}q_{i} + \Sigma E_{\infty}u_{i}^{2}r_{i}$$

The result in Table 2 also suggests that, comparing to the 8-actuator closed-loop system configuration, a 7-actuator, (or 6, 5-actuator) configuration can achieve a same level of output cost V_y with a lower control effort V_u . All the reduced actuator configurations have better closed-loop system performance than the 8-actuator system.

As a partial check of the optimality of the above actuator selection procedure, the reduced order model of ASTREX was iteratively operated with each one of the 8 actuators deleted while all the remaining 7 actuators remained. The results are summarized in Table 3.

From Table 3 it is apparent that deleting actuator 3 would be the optimal decision if only 1 actuator were to be deleted. That is, to achieve the same output variance specifications, the control effort required is more than one order of magnitude greater if we instead delete any other single actuator. This result agrees with that in Table 2. To check the complete optimality of the SAS algorithm empirically, the analysis of Table 3 would have to be repeated for any 2, 3,..., actuators deleted for the entire set when different number of sensors are retained. Clearly, the computation burden will be formidable if this trial-and-error approach is used instead of SAS algorithm.

Table 3 Closed-Loop System Performance with Only One Actuator Deleted (Non-Dynamic Actuators)

| Actuator | | | |
|----------|----------|------------------|----------|
| Deleted | V_y | $V_{\mathbf{u}}$ | Vcls |
| No. 0 | 3.37e-09 | 3.34e+04 | 1.82e+05 |
| No. 1 | 3.33e-09 | 3.01e+04 | 1.61e+05 |
| No. 2 | 3.20e-09 | 2.90e+04 | 1.51e+05 |
| No. 3 | 3.70e-09 | 2.08e+03 | 7.12e+03 |
| No. 4 | 3.48e-09 | 9.07e+03 | 3.81e+04 |
| No. 5 | 3.39e-09 | 3.38e+04 | 1.87e+05 |
| No. 6 | 3.38e-09 | 3.38e+04 | 1.85e+05 |
| No. 7 | 3.35e-09 | 3.76e+04 | 2.09e+05 |
| No. 8 | 3.37e-09 | 3.40e+04 | 1.89e+05 |

Step 3:

Table 4 Closed-Loop System Performance vs. No. of Sensors Operating (5 Non-Dynamic Actuators)

| (5 Non-Dynamic Actuators) | | |
|---------------------------|------------------|------------|
| No. of Sensors | | |
| Operating | $V_{\mathbf{u}}$ | Vels |
| 24 | 3.52e+01 | 1.15e+02 |
| 23 | 3.52e+01 | 1.15e+02 |
| 22 | 3.52e+01 | 1.15e+02 |
| 21 | 3.52e+01 | 1.15e+02 |
| 20 | 3.52e+01 | 1.15e+02 |
| 19 | 3.52e+01 | 1.15e+02 |
| 18 | 3.52e+01 | 1.16e+02 |
| 17 | 3.53e+01 | 1.16e+02 |
| 16 | 3.53e+01 | 1.16e+02 |
| 15 | 3.55e+01 | 1.17e+02 |
| 14 . | 3.58e+01 | 1.19e + 02 |
| 13 | 3.61e+01 | 1.20e+02 |
| 12 | 3.63e+01 | 1.21e+02 |
| 11 | 4.11e + 01 | 1.46e+02 |
| 10 | 4.24e+01 | 1.54e+02 |

The procedure in this step is very similar to that of step 2, except that we now delete sensors one at a time by retaining 5 actutators obtained from step 2: 1 thruster (No. 1) and 4 CMG's (No 5 - 8). In each iteration, we design an OVC controller and proceed to apply SAS algorithm to the ASTREX model. We continue this iterative process until the system loses its observability, or the control power needed starts to increase significantly. It was found that when there are 12 sensors remained, the control power needed begins to increase significantly, and therefore we decided not to continue sensor deletion. The results are summarized in Table 4.

The remaining twelve sensors are listed as follows.

Sensor No. 1: on the primary mirror

Sensor No. 7: on the secondary mirror

Sensors No. 10, 12, 14: on the tertiary inirror

Sensors No. 16 - 22 located on the trusses connecting primary and secondary mirror.

4.3 Dynamic Actuator

The following model of actuators dynamics is used for imperfect actuators.

$$\dot{x}_a = A_a x_a + B_a (u + w_{in})
y_a = C_a x_a$$

where x_a a 12 × 1 vector. The first four thruster actuators are modeled by the first order dynamics having same time constant of 5 milli second and the next 4 CMG actuators are all modeled by second order dynamics with $\omega_n = 20$ Hz and $\zeta = 0.707$.

Several possibilities exist for the characteristics of the white noise associated with the actuators; white noise may be an input to (and thus be filtered by) the actuator, or it may be additive with the actuator output (thus unfiltered), or both. In this example four representative actuator noise models are considered. Recalling that the non-dynamic actuators had additive white noise with intensity W, the following noise cases were studied for dynamic actuators:

- 1. white actuator input noise of intensity $W_{in} = W$:
- 2. white actuator input noise of intensity $W_{out} = W$;
- 3. both input and output noise, each white and of intensity W;
- 4. both input and output noise, each white and of intensity W/2;

Table 5 - Maximal Accuracy for Different Actuator Noise

| Noise | Max. Acc. |
|----------------------------------|-----------|
| Perfect Actuators | 2.13e-09 |
| $W_{in} = W, W_{out} = 0$ | 2.08e-09 |
| $W_{out} = W, W_{in} = 0$ | 2.13e-09 |
| $W_{out} \equiv W_{in} \equiv W$ | 2.57e-09 |
| $W_{out} = W_{in} = W/2$ | 1.96e-09 |

From Table 5 it is clear that the addition of actuator dynamics along with retention of the white noise input to the system states (actuator output noise only, $W_{out} = W$) does not change the theoretical maximal accuracy; that is, V_y is equal for the non-dynamic and the $W_{out} = W$ case. Also from the table, filtering of the

actuator noise by passing it through finite actuator dynamics clearly improves the maximal accuracy. Finally it is noted that for case (3), $W_{out} = W_{in} = W$, the minimal LOS error is greater than the case of non-dynamic actuator. All these results are expected. It seems to us that among the four cases presented in Table 5, case 4 is most representative. Therefore, we proceed to apply OVC/SAS procedures to reduced order ASTREX model to delete actuators and sensors as in steps 2 and 3 of section 4.2.

Table 6 - Closed Loop System Performance vs. No. of Actuators Operating (Dynamic Actuators)
(Norris-Skelton Approach)

| No. of Act. Operating | Actuator Deleted | V _u | Vcis |
|--------------------------|---------------------|----------------|----------|
| 8 | | 5.09e+04 | 3.01e+05 |
| 7 | 3 | 2.53e+03 | 9.88e+03 |
| 6 | 3,4 | 2.82e+02 | 1.35e+03 |
| 5 | 3,4,2 | 2.71e+02 | 9.51e+02 |

As is in the case of non-dynamic actuator, similar procedures are used for actuator deletion for ASTREX model with dynamic actuators. The quantity $V_{y_{\bullet}}$ in Table 6 represents the output cost for the plant model of reduced order ASTREX which is equivalent to V_y in Tables 2 - 4. Similar to the results of step 2 in the previous section, a 7-actuator, (or 6, 5-actuator) configuration can achieve same level of output cost $V_{\mathbf{v}}$ with a much lower control effort V_u comparing to the 8-actuator closed-loop system configuration. All the reduced actuator configurations have better closed-loop system performance than the 8-actuator system. As is the case of non-dynamic actuators, the least effective actuators are [3,4,2,1], all of them are thrusters. This shows that for the current choise of actuator dynamics and noise characterritics ($W_{in} = W_{out} = W$), the effect of actuator dynamics on actuator selection is not significant. But it may dsiplay more signifucant impact for other situations.

The sensor selection with dynamic actuators are very similar to that with non-dynamic actuators discussed in step 3 of Section 4.3. We proceed to delete sensors one at a time while retaining 5 dynamic actuators obtained from step 2 of the previous section. The five actuators are: 1 thruster (No. 1) and 4 CMG's (No 5 - 8). The control power remains almost unchanged until there are only 14 sensors left. Recall that in sensor deletion with non-dynamic actuators, the 12 remaining sensors are. No. 1.7.10.12.14, and No. 16 - 22. Almost all the abovementioned sensors except sensor No.1 are retained now.

Three additional sensors retained are sensors No 4, 5, and 8. Note that sensor No 4 and 5 are located on the primary mirror, and Sensor No. 8 is on the secondary mirror. The results are summarized in Table 7.

Table 7 Closed-Loop System Performance vs. No. of Sensors Operating (5 Dynamic Actuators)

| No. of Sensors Operating | V _u | Vcia |
|-----------------------------|----------------|----------|
| 24 | 2.72e+02 | 9.51e+02 |
| 23 | 2.72e+02 | 9.51e+02 |
| 22 | 2.72e+02 | 9.56e+02 |
| 21 | 2.73e+02 | 9.57e+02 |
| 20 | 2.73e+02 | 9.57e+02 |
| 19 | 2.73e+02 | 9.58e+02 |
| 18 | 2.73e+02 | 9.60e+02 |
| 17 | 2.75e+02 | 9.65e+02 |
| 16 | 2.77e+02 | 9.80e+02 |
| 15 | 2.78e+02 | 9.95e+02 |
| 14 | 2.84e+02 | 1.00e+03 |
| 13 | 2.90e+02 | 1.05e+03 |
| 12 | 2.92e+02 | 1.07e+03 |
| 11 | 2.94e+02 | 1.08e+03 |
| 10 | 2.97e+02 | 1.09e+03 |

Conclusion

This paper applies the integrated Output Variance Control (OVC) and Sensor and Actuator (SAS) algorithms to the reduced order model of ASTREX facility. The existing method of sensor and actuator selection is modified to consider the effect of direct transmission from plant input to measurement as well as that of actuator dynamics. The OVC algorithm seeks to design a controller that minimizes input energy subject to output inequality constraints and selects the weighting matrices Q and R. The SAS algorithm determines the critical sensors and actuators from the admissible sets. When applying OVC/SAS algorithm to the ASTREX model. we are able to achieve same output specification with less control power when noisy actuators are deleted, or we may need slightly more control power to achieve similar specification. For the noise intensity used for this example, the inclusion of actuator dynamics does not alter the actuator ranking, neither does it have significant impact on the results of sensor selection.

APPENDIX

The Output Variance Control (OVC) algorithm (LQG weight selection)

For a system with direct transmission from input to measurement and correlated noise such as follows

$$\dot{x} = Ax + Bu + Du$$

$$y = Cx$$

$$z = Mx + Nu + Hw + v$$

$$= Mx + Nu + \mu$$

$$\mu \triangleq Hw + v$$

$$\begin{split} E\left[\begin{array}{c} w(t) \\ \mu(t) \end{array}\right] \left[w^T(\tau), \mu^T(\tau)\right] \\ = \left[\begin{array}{cc} W & WH^T \\ HW & HWH^T + V \end{array}\right] \delta(t-\tau) \end{split}$$

the OVC problem solves the following design problem:

$$\min E_{\infty} u^T R u$$

subject to

$$E_{\infty}y_i^2(t) \leq \sigma_i^2$$

OVC Algorithm

1. Solve

$$0 = P[A - DWH^{T}(HWH^{T} + V)^{-1}M]^{T}$$

$$+ [A - DWH^{T}(HWH^{T} + V)^{-1}M]P$$

$$- PM^{T}(HWH^{T} + V)^{-1}MP + DWD^{T}$$

$$- DWH^{T}(HWH^{T} + V)^{-1}HWD^{T}$$

for P > 0

and $[CPC^T]_{ii} \leq \sigma_i$? (If not STOP, if yes, continue)

$$F = (PM^T + DWH^T)(HWH^T + V)^{-1}$$

$$Q_o = diag[\dots \sigma_i^{-2} \dots], \text{ set } k = 0$$

2. Solve

$$0 = K_k A + A^T K_k - K_k B R^{-1} B K_k + C^T Q_K C \text{ for } K \ge 0$$

$$G_K = -R^{-1} B^T K_k$$

$$0 = X_k (A + B G_k)^T + (A + B G_k) X_K + F (HWH^T - V) F^T$$

3. $\hat{\sigma}[C(X_k + P)C^* - C(X_{k-1} + P)C^*]_{ii} < \epsilon$ If yes STOP. If not, continue

4.

$$[Q_{k+1}]_{ii} = [Q_k]_{ii} \left\{ \frac{[C(X_k+P)C^*]_{ii}}{\sigma_1} \right\}$$

where

$$Ey_i^2(k) = \left[\left[C(X_k + P)C^* \right]_{ii} \right]$$

Return to Step 2

In summary, step 1 computes the standard Kalman filter and contains maximal accuracy tests for LQG. Step 2 computes the standar LQG gain, given a weighting matrix Q_k . Step 3 determines whether the iterations have converged. Step 4 updates the weighting matrix to Q_k

REFERENCES:

- 1. R.E. Skelton and M. L. DeLorenzo, Selection of Noisy Sensors and Actuators in Linear Stochastic Systems, Journal on Large Scal Systems, Theory and Application, Vol. 4, April 1983, pp. 109-136.
- M.L. DeLorenzo, Sensor and Actuator Selection for Large Space Structures Journal of Guidance, Control, and Dynamics, p.p 249-257, Vol. 13 No. 2, March-April, 1990.
- 3. G.A. Norris and R.E. Skelton, "Selection of Dynamic Sensors and Actuators in the Control of Linear Systems", Journal of Dynamic Systems, Measurement, and Control, p.p. 389-397.
- 4. R.E. Skelton and G.A. Norris, Selection of Noisy Sensors and Actuators in the Presence of Correlated Noise, Journal of Control Theory of Advanced Technology, to appear.
- 5. H. Kwakernaak and R. Sivan Linear Optimal Control Systems, John Wiley, 1972.
- C. Hsieh, R.E. Skelton and F.M. Damra, Minimum Energy Controllers with Inequality Constraints on Output Variance, Opt. Control Appl. & Methods, vol. 10, pp. 347-366, 1989.
- 7. Dynacs Engineering Co., Updated ASTREX Finite Element Model, Report submitted to AFAL, Sept, 1990.
- 8. Dynacs Engineering Co., ASTREX Eigen-analysis, Report submitted to AFAL, Oct, 1990.
- 9. J. Ramakrishnan, K.W. Byun, R.E. Skelton and Lt. D.F. Cossey, ASTREX Controller Design OVC and OCC Approach, 4-th NASA/DOD CSI Conference, Orlando, FL, Nov, 1990.

ANALYTICAL AND EXPERIMENTAL ISSUES IN THE DESIGN OF INTELLIGENT STRUCTURES

Edward F. Crawley
Jonathan P. How
David J. Warkentin
MIT Space Engineering Research Center

Fourth NASA/DOD CSI Conference Orlando, Florida November 5-7, 1990

Technology Objectives

The development of *Intelligent structures* technology offers an appealing approach to the design of precision space structures, which are typically difficult to control because of the high modal densities and low levels of damping. These two difficulties are usually compounded by large uncertainties in the structural model, and the unreliability of ground based testing. Since conventional control techniques typically employ only a small number of high authority actuators, they cannot achieve high levels of spatial resolution and tend to be susceptible to spillover problems. In comparison, the alternative approach of using intelligent structures, with high densities of sensors, actuators, and processors, offers several advantages for the control of space structures: good spatial resolution, shape control at both micro and macro levels, and a relatively simple means of tuning the closed loop performance.

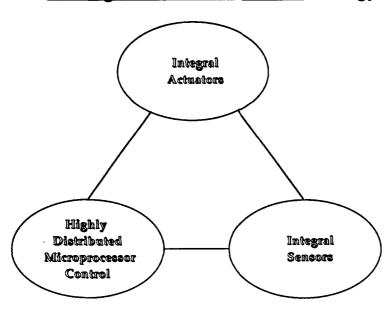
Technology Objectives

- Difficulties with structural control:
 - High modal densities, lightly damped.
 - Potentially large modal uncertainties.
 - Ground testing difficult and unreliable.
- Conventional control approaches typically use a small number of high authority actuators.
- Alternative approach: develop technology to enable a high density distribution of sensors, actuators, and processors in the structure.
 - Enables good spatial resolution.
 - Achieves shape control over micro and macro vibrations.
 - Software changes can modify or tune closed loop performance.
 - Allows tailoring of the actuators/sensors.

Intelligent Structures Technology

Intelligent structures are comprised of three main components: the highly distributed processor network, the integral actuators, and the integral sensors. The technology also includes the modelling and analysis techniques, and the manufacturing processes.

Intelligent Structures Technology



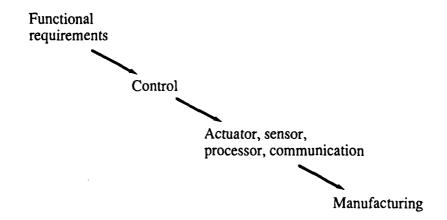
Plus - Modeling and analysis techniques - Manufacturing technology

Talk Objectives

The aim of this paper is to examine the development of the technology for intelligent structures from the perspective of the overall system requirements. In particular, the aim is to report progress on efforts at MIT Space Engineering Research Center (SERC) to respond to these requirements. The objective is to discuss the influence of the overall functional requirements on the design of each subsection of the technology group.

Talk Objectives

- Examine the development of Intelligent Structures from a perspective of the overall system requirements.
- Report progress on efforts at MIT SERC to respond to these requirements.
- Address issues from a "concurrent engineering approach" of design and manufacturing.



Hierarchic Control

Associated with the control of space structures are several difficulties arising from the fact that the plant is typically flexible, modally dense, and lightly damped. Intelligent structures, with the associated high densities of both sensors and actuators, are even more complicated to control because of the large amount of information that must be measured and organized. Traditional centralized control designs are typically computationally infeasible for these types of structures, and purely decentralized approaches tend to lack the overall performance capabilities required by most objectives. Our solution is to employ a two-level architecture with a centralized controller to handle the slower, longer wavelength motions, and distributed regional controllers to govern the local vibration dynamics. The two levels are virtually decoupled by the spatial filtering process inherent in the architecture, which allows the design processes to be performed almost independently. The hierarchic architecture is designed to aggregate the measurements and distribute the control commands in such a way that real-time control with stringent overall performance objectives is computationally feasible, even with a large number of sensors and actuators.

Hierarchic Control

- Requirement: To efficiently control an "intelligent structure" with high density of actuators/sensors.
 - Centralized designs are computationally infeasible.
 - Decentralized designs lack overall performance capabilities.
- One Approach: A multi-level control architecture with:
 - Centralized controller for long wavelength, low frequency vibrations.
 - Regional processors for short wavelength, high frequency vibrations.

· Key Points:

- Makes real time control with many sensors/actuators computationally feasible.
- Hierarchic architecture aggregates measurements, which reduces communication requirements.
- Global control design independent of lower level, and based on full state feedback approaches.
- Various approaches available for the lower level design.

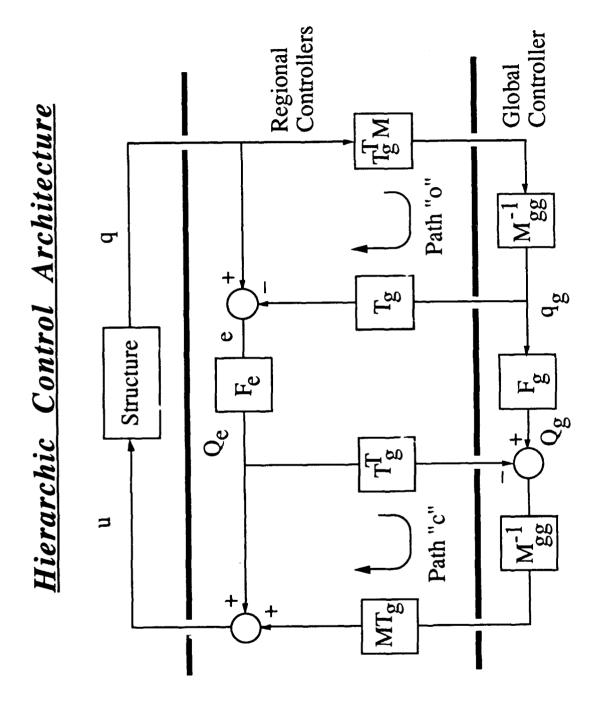
Hierarchic Control Architecture

The architecture consists of two levels of controllers operating at different rates and acting on different forms of the sensor measurements. The notation is defined by Hall et al. [1] and to some extent in the figure; briefly, T_g is an aggregation matrix constructed from some assumed shape functions, M is the finite element model mass matrix, q_g is a vector of states for a coarser global model of the structure, and e is the vector of residuals which remain after the aggregation/interpolation steps in path "o." The set of controls applied to the structure u is computed by combining the filtered and extrapolated commands from the two levels. The aggregation process combines the measurements into a smaller number of weighted averages that are associated with the states of the coarser global model. As shown in the figure, the architecture consists of two main feedback loops connected by the paths o" and "c." Path "o" computes

$$e = \left(I - T_g T_g^{-L}\right)_I = \left(I - T_g M_{gg}^{-1} T_g^T M\right) q$$

which eliminates the observational spillover between the two control levels. In a similar fashion, path "c" removes the control spillover.

One advantage of this architecture is the spatial filtering process performed when the large number of sensor measurements are aggregated before they are passed to the central controller. In this way, the higher level, which controls the longer wavelength modes, receives only the information actually required. Since the states of the design model for the global controller are based on weighted averages, which are all available, the model order is significantly reduced, and full state feedback design techniques can be employed. The influence of the filtering inherent in the architecture also means that the global design can be done independently of the lower level. The main advantage of this approach is that the feedback is done in parallel with several computers performing the necessary calculations.



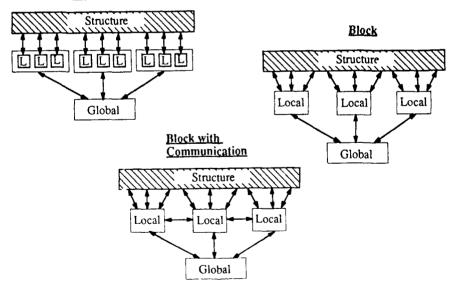
Local Control Approaches

The lower level controllers of the hierarchic architecture are designed to govern the shorter wavelength, localized dynamics of the structure. Some possible design techniques include both spatially discrete and continuous LQR/LQG algorithms, impedance matching based on wave models, or feedback based on acoustic models (Statistical Energy Analysis). In the hierarchic architecture, each controller of the distributed lower level is associated with a region of the structure called a finite control element. An important consideration in the design of the lower level controllers is the constraints placed on the achievable performance levels and the implementation requirements by the allowable amount of communication between neighbors. Controllers with several types of constraints – no shared of information (collocated), information shared within a region of the structure (block), and information shared with neighboring regions (block with communication) – have been designed. As discussed by How [2], these designs were done for structures like circular mirrors, which possess a high degree of spatial symmetry.

Local Control Approaches

- Requirement: Constrained architecture local control to perform:
 - Shape control of a region of the structure.
 - Measurement aggregation/global control distribution.

Collocated

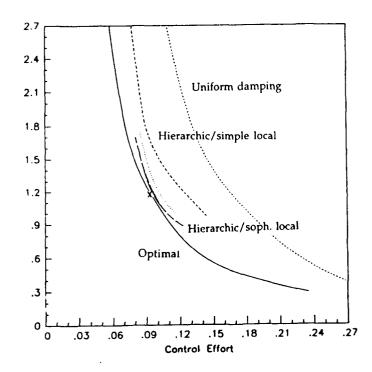


Performance Comparison

The three competing design approaches were compared in terms of the computational requirements at the lower level, the implementation requirements (especially communication), and the achievable performance. The results for this last category are shown in the figure. These were obtained from a beam simulation with a cost function including line-of-sight, displacement, and energy weights. The overall comparison indicated that feasible approaches can be designed to provide near optimal closed loop performance [2].

Performance Comparison

- Simulate the performance of several local controllers applied to a beam.
- Objective includes line-ofsight, displacement, and energy penalties.
- Conclude that feasible lower level controllers can be designed to provide near optimal closed loop performance.



Functional Analysis Control Approaches

Another way to approach the control of intelligent structures is to use functional analysis techniques on the LQR control problem with models of the approximately continuous structure, sensors, and actuators [3]. The resulting explicit expressions for the optimal gains provide insight to the appropriate sensor/actuator selections that will maximize the collocated nature of the feedback, and thus reduce implementation difficulties. Typical results indicate that, for a beam with induced strain actuators and diagonal state penalty matrices, the optimal LQR gains for both strain and velocity sensors are completely collocated.

Functional Analysis Control Approaches

- Spatially continuous control design approach:
 - Model structure, sensors (S), and actuators (A) as spatially continuous functions.
 - Use functional analysis techniques on LQR problem.
 - Develop explicit expressions for dependance of feedback gains on S/A type.
 - Complexity of implementation reduced with S/A pair that maximizes collocated nature of gains.
 - Discretize control gains for implementation with finite number of S/A.
- Results for a beam with strain actuation, diagonal state penalties:
 - Optimal feedback gains are completely collocated for strain and velocity sensors.

Distributed Sensing

The main requirement of the distributed sensors is that they provide measurements that can be used locally for controlling vibrations and globally for inferring overall displacements. The displacements associated with these longer wavelength modes can be used to interpolate motions at intermediate points, or extrapolated to provide contributions to the performance objective.

A variety of sensors have been used at MIT SERC to meet these requirements. Pointwise embedded resistive and piezoceramic strain gauges have been used extensively to provide local measurements [4]. Piezoelectric accelerometers are alternative distributed discrete sensors. Spatially tailored piezopolymer convolving sensors have been used to provide integrated strain measurements with a built-in modal filter [5]. Shaping the width of the sensor as a sinc function results in spatial filtering which exhibits high order roll-off and little phase lag. To infer knowledge of the overall displacements from discrete sensors, it is necessary to spatially integrate the available measurements. In Reference [6], various numerical algorithms are investigated to compare and predict the error bounds on the integrated displacement as a function of the distribution pattern and density of the sensors. These analytic predictions are shown to compare well with the static experimental results. The results shown in the figure give a measure of the sensitivity of the trapezoidal integration scheme to strain gage uncertainty and misplacement.

Distributed Sensing

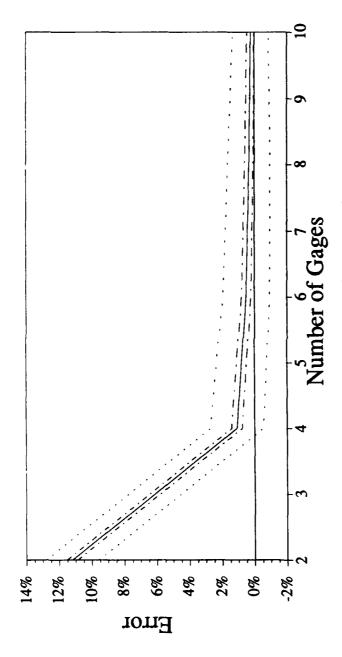
· Requirements:

- 1) Provide local measurements for lower level control designs.
- 2) Infer knowledge of longer wavelength motions for
 - interpolation between other autonomous measurements.
 - extrapolation to locations important for the performance objective.

Approaches:

- Pointwise embedded resistive, piezoceramic, piezopolymer strain gauges.
- Shape tailored piezopolymer strain gauges for spatially convolving, modal filtering sensors.
- Local accelerometers.
- Area averaging (integrating) sensors.
 - Discrete long gauges.
 - Continuous fiber optic.

Displacement Error vs. Strain Gage Number



- Trapezoidal integration scheme with short strain gages, on a cantilevered beam.
- Results:
- Solid line integration errors only.
- Dashed line integration errors + 1% gage factor error + 0.2% placement error.
- Dotted line integration errors + 5% gage factor error + 1% placement error.

Actuation requirements

Since the concept of intelligent structures to some extent involves an attempt to control higher frequency modes of flexible structures, high actuator bandwidth is desirable. Similarly, a high spatial bandwidth or resolution is needed to selectively control complex mode shapes. The linearity of actuator properties and their insensitivity to such environmental variables as temperature are also important in selecting a suitable mechanism.

Actuation Requirements

Among the desired properties for the actuators of an intelligent structure are:

- Large control authority (stroke)
- · High bandwidth
- · High spatial resolution
- Linearity/low hysteresis
- · Low temperature sensitivity

Actuation approaches

This table illustrates some of the properties of strain actuation materials which have been used or suggested for intelligent structures. While the large strains attainable with shape memory alloys allows them to produce gross structural deformations, their low bandwidth limits their use in dynamic control. There are significant problems associated with the application of the magnetic fields required for magnetostrictive materials, and the "fair" linearity of the electrostrictives degrades rapidly with decreasing temperature. Of the two piezoelectric candidates, the higher modulus of the ceramic types allows for better structural impedance matching than with the film varieties. The higher maximum temperature also makes them better suited for embedding in composites requiring an elevated temperature cure. The hysteresis can present difficulties, but these can be mitigated by means of feedback loops or charge rather than voltage control.

<u>Actuation Approaches: A Comparison of Actuation</u> <u>Strain Materials</u>

| | PZT G1195 | PVDF | PMN-BA | TERFANOL DZ | NITINOL |
|------------------------|--------------|------------------|-----------------|-----------------|-----------------------|
| Actuation Mechanism | piezoceramic | piezo. film | electrostrictor | magnetostrictor | shape memory alloy |
| L max. (µstrain) | 1300 | 230 DC 690 AC | 1300 | >2000 | 80000 DC 20000 AC |
| E (Msi) | 9.14 | 0.29 | 17.5 | 7.0 | 4.35 (m) 12.9 (a) |
| e max (µstrain)* | 448 | 11 | 653 | 575 | 8520 (a) |
| T max (°C) | 360 | 80-120 | high | 380 | 45 |
| linearity | good | good | fair | fair | роог |
| hysteresis | 10% | >10% | <1% | 2% | 5% |
| temp. sensitivity | .05 | .8 | .9 | high | - |
| bandwidth | high | high | "high" | moderate | low |

^{*}for a sheet of actuator material bonded to aluminum beam ($t_s/t_a=10$) in bending assuming ac value of L

⁽m) = martensite (a) = austenite

Processing: Requirements and Approaches

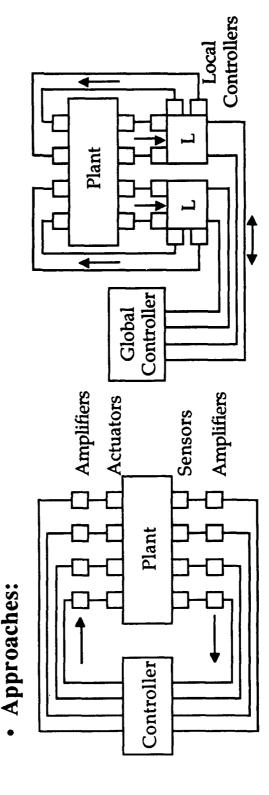
If the term "processing" is taken to include all the steps of signal manipulation required in a control system, different levels of functionality may be identified. In gathering information from sensor devices, some kind of signal conditioning is required. One example of this is a strain gage signal conditioner, which supplies the bridge circuit necessary to detect the change in gage resistance, and gives a signal proportional to the strain, allowing desired adjustments of offset level and amplification. A similar level of functionality is present for actuators as well; generally some power amplification of the low-level controller signal is necessary. Furthermore, assuming the use of a digital computer or computers for the implementation of the control algorithm, conversion of signals from analog to digital and from digital to analog is required. The control system of an intelligent structure, if it is to achieve greater performance by controlling short-wavelength, high frequency motion, must also have a greater bandwidth at lower level. Some means of communication among system components is also needed, whether it be a simple analog connection between a sensor and a signal conditioner, or a digital connection between control processors.

The diagrams illustrate two extremes in the spectrum of possible system architectures. On the left is a system in which a single controller gathers information from all the sensors, performs the control algorithm, and sends commands to all the actuators. On the right, a number of local controllers are used to perform short-wavelength, high speed control tasks and at the same time condense state information which is sent to a global controller. The global controller executes a control algorithm on this coarse information and sends commands back to the local controllers, which add the desired effort to their local actuator commands. Although either of these schemes could implement the hierarchic control algorithm suggested earlier, the second is clearly chosen with such an algorithm in mind. The use of distinct local controllers in the place of a single serial machine has the added advantage of increasing the control system bandwidth by parallel processing. The local processors also serve to reduce the number of connections to the global controller, which is a significant consideration in the case of a system with many tens of sensors and actuators. These digital connections could be implemented by means of a single serial or parallel bus rather than by point-to-point connections, further simplifying the architecture. The signal conditioning and amplification functions are shown integrated with the local controllers, reducing the number of chips required.

Processing: Requirements and Approaches

· Requirements:

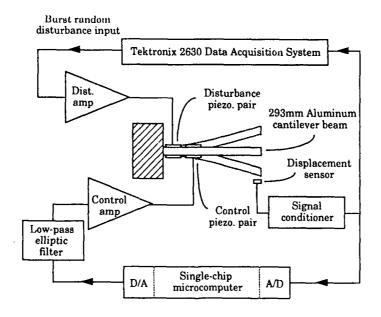
- Signal conditioning (amplification)
- Analog/digital and digital/analog conversion
 - Bandwidth
- Communications



Single-chip Microcomputer Control Experiment

A simple experiment has been performed using a single-chip microcomputer [7]. The purpose of this experiment was to demonstrate control of a simple structure [8] using a control processor which incorporates on a single piece of silicon an unusually large subset of the functions required for a control system. Piezoceramic plates were bonded to an aluminum cantilever beam, whose tip deflection was measured by an induction sensor. One pair of piezoceramic plates was used to excite the beam. The tip deflection measurement was digitized and passed through a digital filter by the microcomputer, producing a command signal which, when applied to the other pair of piezoceramics, acted to reject the disturbance and damp out the vibrations. Although some circuitry external to the microcomputer (power, clock, and signal conditioning and amplification) was required in this experiment, the on-chip A/D and D/A conversion greatly simplified the arrangement. Further advances in the integration of signal processing on the chip could be expected in a custom device.

Single-chip Microcomputer Control Experiment

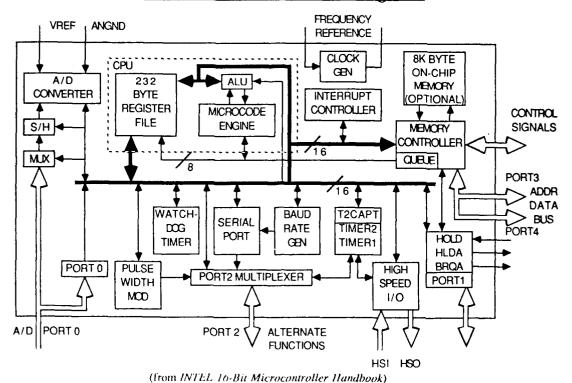


Intel 87C196KB Block Schematic

A block schematic of the Intel single-chip microcomputer shows its non-traditional characteristics. In conventional microcomputer systems, the central processing unit (CPU) would by itself constitute a single chip, the microprocessor. In the 87C196KB, however, A/D and D/A (pulse-width modulated) functions are included, as are the memory and a substantial amount of I/O capability. The simple control experiment described here took advantage of the on-chip A/D, D/A, and memory. The on-chip I/O functions could make this microcomputer (or a derivative) applicable as a local controller in a hierarchic control architecture.

Single-chip microcomputers like the 87C196KB are designed for a wide variety of controller applications such as games, appliances, and automobiles, and as such must still require additional external circuitry to preserve flexibility. A similar microcontroller, designed with specific sensors and actuators in mind, could integrate more of the signal processing functions within itself, thus further simplifying the system interconnections and reducing the chip count.

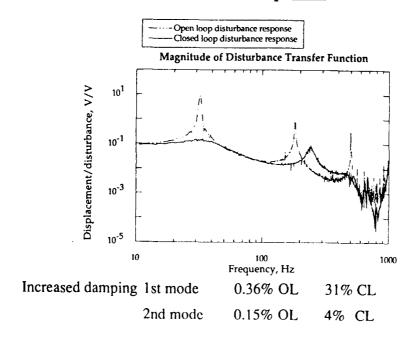
Intel 87C196KB Block Diagram



Performance Achieved with Single-chip Microcomputer

This figure illustrates the performance achieved with an in-circuit emulator development version of the single-chip microcomputer. By digitally implementing a compensator consisting of a zero at the origin and a double real pole at 400 Hz (at a 15400 Hz sampling and control loop rate), a reduction of nearly 20 dB was achieved in the RMS tip displacement due to white noise excitation from DC to 1000 Hz. Ring-down tests were used to characterize both open and closed loop modes. Open loop damping was 0.36%, 0.15%, and 0.20% in the first three modes. Upon closing the loop, 31% and 4% damping was achieved in the first and second modes, while the third became undetectable as it approached cancellation with a zero in the actuator transfer function (not shown). The second mode shows a frequency shift from 182 Hz to 242 Hz, corresponding to a modal stiffness change of 77%, illustrating the authority of the actuators. Increasing the loop gain shifted the second mode still higher, eventually pushing it unstable at 266 Hz, for a 114% change in modal stiffness.

<u>Performance Achieved with Single-chip</u> <u>Microcomputer</u>



Manufacturing Requirements

The manufacture of an intelligent structure involves the physical integration of structural materials such as graphite/epoxy composites. If the components are physically embedded in the structure, they must be able to survive the temperatures and pressures involved in the composite cure schedule. The embedded components must also withstand the stresses induced by operational loads on the structural member. The mechanical interface must take into consideration the different nature of the devices; while sensors and actuators require stress and strain transfer to function, the delicate metal and oxide structures on brittle silicon chips must be mechanically isolated. Protection from the surrounding structure must also be provided in the form of electrical insulation (in the presence of conductive graphite fibers) and, for electronic circuits, chemical isolation from ionic contamination from the structural epoxy resin. The structure must also be protected from the embedded devices; the inclusions should present the smallest possible interruption of structural plies in order to avoid the production of stress concentrations and delamination sites.

Manufacturing Requirements

Manufacturing procedures must be developed so that the control system components of the intelligent structure can:

- Survive manufacturing (autoclave) pressures and temperatures
- Withstand mechanical stresses generated during operation
- Be electrically insulated from conductive elements (e.g. graphite fibers)
- Survive ionic contamination IC lifetime is typically limited by corrosion
- Present a minimal disruption of structural plies

Manufacturing Approaches

One possible approach to the control of structures consists of a centrally located processor or processors and surface-mounted or embedded actuators. This allows servicing of the electronics, but could require an unwieldy number of lengthy (and hence noise-susceptible) connections to a large number of sensors and actuators. The option in which processing is distributed on the structures surface but not embedded can simplify these connections and reflects the natural computational division of the hierarchic control architecture. This approach could not be used, however, in cases where surface properties (e.g. optical or aerodynamic smoothness) require a clean surface, or when environmental conditions (e.g. potential damage, presence of fuel) prohibit such a placement of sensitive components. The connection of surface-mounted processors with embedded sensors or actuators would pose a further problem, as the connecting leads would create cracks in the structure leading to the surface. These objections are met by the third, most physically integrated (and most technically challenging) option, in which sensor, actuator, and processor components are all embedded within the structure.

Manufacturing Approaches

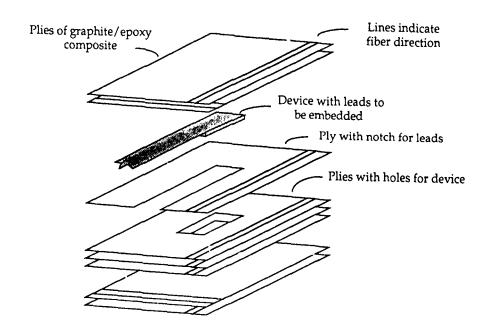
Three basic levels of distribution and embedding may be distinguished:

- Processing centrally located, sensors and actuators surfacemounted or embedded
- Processing physically distributed, but not embedded
- Processing embedded within structure along with sensors and actuators

Embedding Devices within Composite Structures

Techniques have been developed for embedding piezoelectric ceramics [3] and integrated circuits [7] in laminated composite structures. Holes are cut in plies to accommodate the devices and their leads, as shown in the figure. Protective layers of insulating polyimide film are used to shield the piezoceramics from conductive graphite fibers. A similar function is performed for the integrated circuit chip by a layer of electronics grade epoxy or silicone rubber, which also serves to protect the circuitry from ionic contamination by impurities in the structural epoxy. The silicone rubber layer also mechanically isolates the chip from the surrounding load-bearing structure, preventing fracture of the leads, the circuit structures, and the silicon chip itself.

Embedding Devices within Composite Structures

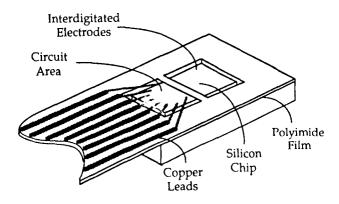


Integrated Circuit Chip Packaged for Embedding

The requirement that plies be disturbed as little as possible points to the need for a low profile, minimal packaging technique for the integrated circuit chips. Shown is a chip packaged in what could be described as a variation on tape automated bonding (TAB). TAB involves etching conductive leads on a polymer tape carrier, which is then aligned with the chip so the leads can be bonded to the chip. At this stage, electrical connection is complete, and the packaging is not much bulkier than the chip itself. The thickness of the assembly shown is approximately 0.5 mm.

The device chosen for the embedding feasibility demonstration was a sensor manufactured by Micromet for process monitoring of epoxy curing. A number of these sensors were embedded in a $[0^{\circ}/90^{\circ}/0^{\circ}_{2}]_{S}$ layup of Hercules AS4/3501-6 graphite/epoxy pre-preg tape. An extended, reduced temperature cure was used to improve the yield of functioning devices. The resulting laminates were machined into test specimens for use in quasi-static and cyclical extensional stress experiments and for a test involving exposure to a high temperature, high humidity environment. A metal-oxide-semiconductor field effect transistor (MOSFET) present in the on-chip circuitry was monitored during these tests; as a building block of digital circuitry, the simple MOSFET served to demonstrate the feasibility of applying the embedding technique to more complicated devices.

Integrated Circuit Chip Packaged for Embedding

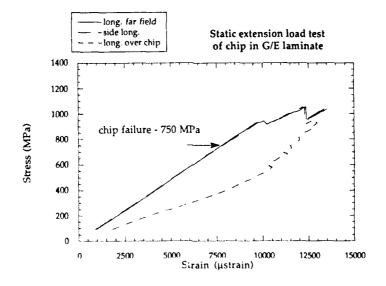


Test of Embedded Chip in G/E Coupon

The plot shows longitudinal strain gage measurements taken on a coupon with an embedded chip while under extensional load. The coupon was 356 mm long, 50 mm wide, and 1.07 mm thick. The measurements from the "side" gage, located 19.6 mm from the embedded chip and 5.4 mm from the coupon edge, are nearly indistinguishable from the far field measurements, taken with a gage 50 mm away. This shows that the disturbance in the stress and strain fields due to the chip was very localized. The remaining curve shows the strain measured at the spot on the surface of laminate directly over the chip; this typically showed strain concentration factors of 1.6 to 2.3 over the far field values.

The failure of the embedded chip occurred at a nominal stress level of 750 MPa, and was distinguished by a loss of signal to a circuit monitoring the MOSFET characteristic curve. Electrical tests of mechanical specimens and visual examination of cured and uncured devices led to the conclusion that the failure mode was the breaking near the chip or the debonding of one or more of the fine conductive leads. In those specimens in which a silicone rubber layer was substituted for the protective epoxy before laminate assembly and cure, electrical failure occured at or very near the maximum laminate stress (over 1000 MPa). In the cyclic tests, the specimen with the silicone rubber withstood 123 cycles of loading up to 420 MPa, while the specimens with the epoxy layer failed within 4 cycles. The results of the mechanical tests indicate the benefits of using a mechanical isolation layer and also suggest that improved performance could be achieved by using more rugged lead connections.

Test of Embedded Circuit in G/E Coupon



Conclusions

The overall functional requirements for intelligent structures have been shown to have a significant influence on the design of each of the subsystems of the technology group. As demonstrated, MIT SERC has addressed these issues from the perspective of the overall requirements, and has made progress in each of the control, actuator, sensor, processor network, and manufacturing subgroups. The feasibility of each of these designs has been demonstrated in either computer simulations or laboratory testbeds.

Conclusions

- Overall functional requirements for intelligent structures significantly influence the design of each subgroup.
- MIT SERC has:
 - Addressed these issues from perspective of the overall requirements.
 - Made progress in each of the control, actuator, sensor, processor network, and manufacturing subgroups.
 - Demonstrated feasibility of these designs on either computer simulations or laboratory testbeds.

References

- [1] Hall, S. R., Crawley, E. F., How, J. P., and Ward, B., "A Hierarchic Control Architecture for Intelligent Structures," November 1989. To be published in the AIAA Journal of Guidance, Navigation, and Control.
- [2] How, J. P., Local Control Design Methodologies for a Hierarchic Control Architecture, SM Thesis, MIT Department of Aeronautics and Astronautics, (Space Engineering Research Report #5-90), June 1990. Paper submitted to the AIAA Journal of Guidance, Navigation, and Control.
- [3] de Luis, J., Design and Implementation of Optimal Controllers for Intelligent Structures using Infinite Order Structural Models, Phd Thesis, MIT Department of Aeronautics and Astronautics, (Space Systems Laboratory Report #3-89), January 1989.
- [4] Ting, J. M., Characterization of Damping of Materials and Structures at Nanostrain Levels, SM Thesis, MIT Department of Aeronautics and Astronautics, (Space Engineering Research Report #1-90), June 1990.
- [5] Collins, S., Sensors for Structural Control Applications using a Piezoelectric Polymer Film, SM Thesis, MIT Department of Aeronautics and Astronautics, (Space Engineering Research Report #12-90), October 1990
- [6] Crawley, E. F., Andersson, M. S., Schaffner, G., and Sadlowski, M., "Structural Shape Determination by Discretely Distributed Strain Sensing," to be submitted, October 1290.
- [7] Warkentin, D. J., Embedded Electronics for Intelligent Structures, SM Thesis, MIT Department of Aeronautics and Astronautics, December 1990.
- [8] Hagood, N. H., Chung, W. H., von Flotow, A., "Modelling of Piezoelectric Actuator Dynamics for Active Structural Control," Journal of Intelligent Materials Systems and Structures, Vol. 1, No. 3, p. 327, July 1990.

INTEGRATED CONTROLS-STRUCTURES DESIGN FOR A CLASS OF FLEXIBLE SPACECRAFT

Peiman G. Maghami Suresh M. Joshi Sandeep Gupta

NASA Langley Research Center

Fourth NASA/DOD CSI Conference Orlando, Florida November 5-7, 1990 Many future space missions will require large structures to be assembled, deployed and maintained in space with high precision in attitude and shape. Control systems design for such structures is a difficult problem because of their special dynamic characteristics which include a large number of low-frequency, closely-spaced elastic modes, and small inherent damping. The traditional "sequential" design approach for large spacecraft is to design the structure first, and then to optimize the control system for the fixed structure. However, the best achievable performance with this approach is limited and may not satisfy the stringent specifications of future missions. Moreover, significant coupling exists between the structural design and control design problems. Therefore, it would be highly desirable, if not necessary, to perform the structural design and control design simultaneously to optimize common objectives.

MOTIVATION

- Control of flexible spacecraft is a difficult problem
 - -- Large number of elastic modes
 - -- Low value, closely-spaced frequencies
 - -- Very small damping
- Traditional design approach:
 - -- Design the structure first
 - -- Design the control system next
- Best achievable performance with traditional approach is limited
- To obtain better overall design, it would be necessary to design the structure and control system simultaneously.

In this paper, the integrated controls-structures design problem is considered for a class of flexible spacecraft which have no articulated payloads. Such spacecraft (e.g., large space antennas) are required to satisfy stringent fine-pointing and vibration suppression requirements. The objective of this research is to develop a methodology for simultaneous controls-structures design, as well as, to develop computational tools for practical integrated design. Two formulations are considered, which are based on single-objective and multi-objective optimization.

OBJECTIVE

- Develop an integrated controls-structures design methodology for spacecraft requiring fine attitude pointing and vibration suppression
 - -- Address controls-structures interaction issues
 - Develop computational tools for practical integrated design (CSI-DESIGN Code)

The approach taken in this paper is to pose the integrated controls-structures design problem as a simultaneous controls-structures optimization. Both, single-objective and multi-objective optimization approaches are considered. In single-objective optimization, an objective function such as, cost or performance, etc., is optimized while the remaining design requirements and specifications are formulated as constraints. The multi-objective optimization approach is used when more than one objective needs to be optimized, which naturally leads to a trade-off between the objectives. The feasibility of the proposed integrated design methodology is demonstrated by applying it to a generic space platform. Plans are also underway for experimental validation via application to the Controls-Structures-Interaction (CSI) program's Evolutionary Model at NASA Langley Research Center.

APPROACH

- Formulate the integrated design problem as a simultaneous controlsstructures optimization problem
 - -- Single-Objective optimization
 - -- Multi-Objective optimization
- Validate the methodology through an integrated design of the CSI Evolutionary Model

The basic problems in control systems design for flexible spacecraft arise because i) the order of a practically implementable controller is generally much lower than the number of elastic modes, and ii) The parameters, i.e., frequencies, mode-shapes and damping ratios, are not known accurately. The type of controller used in the integrated design should be robust (i.e., should maintain stability, and possibly performance) to unmodeled dynamics and parametric uncertainties mentioned above. In addition, it should be practically implementable, as well as be amenable for inclusion in an optimization process. One class of controllers which has these desired properties is the dissipative controllers [1], and includes "static" and "dynamic" dissipative controllers. The static (or constant-gain) dissipative controller employs collocated and compatible actuators and sensors, and consists of feedbacks of the measured attitude vector y_p and the attitude rate vector y_r using constant, positive-definite gain matrices G_p and G_r . This controller is robust in the presence of parametric uncertainties, unmodeled dynamics and certain types of actuator and sensor nonlinearities [1]. However, the performance of such controllers is inherently limited because of their structure.

CANDIDATE CONTROLLERS

Static Dissipative Controllers

$$u = -G_r y_r - G_p y_p$$

- Collocated sensors and actuators
- Positive definite gain matrices
- Robust in presence of model uncertainties
- Limited Performance

In order to improve the performance of static dissipative controllers, an additional dynamic outer loop can be introduced as shown below, where z is the compensator state vector. The matrices A_c , B_c , and G denote the compensator system, input, and output matrices, respectively. These matrices satisfy certain additional conditions to establish dissipativity as described in Ref. 2. The resulting two-level controller is called "dynamic dissipative controller", and is guaranteed to be robustly stable in the presence of unmodeled dynamics as well as parametric uncertainties. It should be noted that standard high-performance model-based controllers (e.g., $H_2(LQG)$ or H_{∞} designs) are generally not robust to real parametric uncertainties [2], which makes dynamic dissipative controllers distinctly advantageous.

CANDIDATE CONTROLLERS

Dynamic Dissipative Controllers

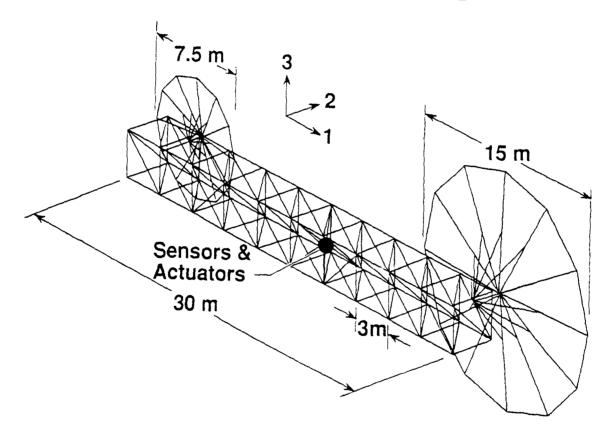
$$u = -Gz - G_r y_r - G_p y_p$$

$$\dot{z} = A_c z + B_c y_r$$

- Collocated sensors and actuators
- Robust in presence of model uncertainties
- Enhanced performance

A generic model of a multi-user platform shown below is used as a focus problem for describing and demonstrating the integrated design methodology. The model is composed of a ten bay bus structure with two antennas at either end (a 7.5m diameter antenna and a 15.0m diameter antenna). A three-axis control moment gyro (CMG) is used for actuation of the control inputs, along with collocated attitude and rate sensors.

STRUCTURAL MODEL



Eleven structural design variables are chosen for the integrated design process. These include the outer diameters of the longerons, battens and diagonals for three sections of the bus structure (nine design variables), as well as, the outer diameters of the antenna support members (two design variables). The number of control design variables vary depending on the type of controller used. For static dissipative design the elements of the Cholesky factorization matrix of the positive-definite position and rate gain matrices are chosen as design variables. In dynamic dissipative designs, the elements of the gain matrices, as well as the compensator matrices are used as design variables.

DESIGN VARIABLES

- Structural design variables:
 - -- Outer diameters of the longerons, battens and diagonals (nine design var.)
 - -- Outer diameters of the antenna support members (two design var.)
- Control design variables:
 - -- Static: elements of the gain matrices (Cholesky Factors)
 - -- Dynamic: elements of the gain matrices and compensator matrices

In the first design problem, the integrated controls-structures design is posed as a single-objective optimization wherein a closed-loop performance measure, the steady-state root-mean-square (rms) pointing error at the large antenna due to white-noise disturbance of unit intensity at the inputs, is minimized. In order to achieve a reasonable design, constraints are placed on the steady-state control energy and the total structural mass. It is noted that the steady-state rms pointing error and control energy are obtained from a solution of a Liapunov equation as explained in detail in Ref. 3. Additional side constraints are also placed on the structural design variables for safety and practicality concerns. Lower bounds are placed on these variables to satisfy structural integrity requirements against buckling and stress failures. On the other hand, upper bounds are placed on these variables to accommodate manufacturing limitations.

DESIGN PROBLEM

ullet Objective function: minimize the steady-state rms pointing error at the large antenna

$$J \equiv \min_{d} \{E\{Trace\{\gamma\gamma^T\}\}\}^{\frac{1}{2}}$$

subject to

$$E\{Trace\{uu^T\}\} \le E_a$$

$$M_{str} \leq M_o$$

Side constraints on design variables for safety and practicality

The following table summarizes the results for the first design problem, i.e., a singleobjective formulation using a static dissipative controller. An initial design based on a nominal structure and a controller to achieve good rigid-body performance was first obtained. The nominal structural mass is 442.06 kg, while the actuator masses are assumed constant at 150 kg. The initial design gives an rms pointing error of 73.6 \(\mu rad\) with the control energy constrained at 3. The conventional design approach was next followed, wherein only the control design variables were optimized. This "control-optimized" design yielded an rms pointing error of 26.9 \(\mu rad\). Next, an integrated controls-structures design was obtained by allowing both, structural and control design variables, to change simultaneously. This resulted in an rms pointing error of $16.9\mu rad$ (a 37% reduction over the conventional design) with a slightly lower structural mass, clearly demonstrating the advantage of the integrated design over the traditional design. Furthermore, in an attempt to evaluate the effect of varying actuator mass on the integrated design process, the actuator masses were allowed to vary by relating them to the infinity norms of the attitude rate and position gair. matrices (a worst case scenario). Although, the actuator masses increased from 150 kg to a conservative mass of 298.7 kg, the rms pointing error and structural mass were not affected. This is due to the structure being rather stiff, i.e., it is not affected by small

CONVENTIONAL VS. INTEGRATED

(Static Dissipative Controller)

| | RMS Pointing | Structural Mass | Actuator Mass | Control Energy |
|---------------------------------------|-----------------|--------------------|------------------|-------------------|
| Initial Design | 73.6 | 442.06 | 150 | 2.9804 |
| Control-Optimized Design | 26.9 | 442.06 | 150 | 2.9995 |
| Integrated Design (without act. mass) | 16.94 | 404.21 | 150 | 2.9998 |
| Integrated Design (with act. macs) | 17.01 | 400.32 | 298.73 | 2 9991 |

In the second design problem, the integrated design is posed as a dual-objective optimization problem in which both, a measure of closed-loop performance represented by the sum of the time constants of the closed-loop system (a measure of transient response), and the total mass representing a cost measure are optimized. To achieve this dual-objective optimization, a single objective, formed by a linear combination of the two objectives, is optimized. The coefficient β allows for a trade off between the two objectives. As β is varied from 1 to 0, more emphasis is placed on the closed-loop performance and less on the total mass or the cost. Furthermore, in order to satisfy certain fine pointing requirements, an upper bound constraint is placed on the rms pointing error at the large antenna due to white-noise disturbances at the position and rate sensors. Additional side constraints are also placed on the structural design variables for safety and practicality concerns.

DESIGN PROBLEM

 Objective function: minimize the total mass while maximizing a measure of the controlled response (sum of the time constants of the closed-loop system)

$$J \equiv \min_{d} \{\beta * Total \;\; Mass + (1-\beta)/Controlled \;\; Performance\}$$

subject to a constraint on the steady-state RMS pointing error at the large antenna

$$E\{Trace\{\gamma\gamma^T\}\}^{\frac{1}{2}} \le RMS_d$$

• Side constraints on design variables for safety and practicality

Using a sixth-order dynamic dissipative controller, an initial design based on rigid-body performance was obtained, first. Further results are normalized with respect to the initial design. Then, with the β parameter chosen at 0.15, a conventional or control-optimized design was performed by optimizing the control design variables only. This results in a 30% increase in the control performance, but it also increases the total mass by 18%. Next, an integrated controls-structures design was carried out, resulting in a four folds increase in the control performance along with slightly lower total mass over the initial design (21% less than the total mass of the conventional design). Here, the mass of the structure is reduced by 34% while mass of the actuators is increased by 44%. Again, these result demonstrate that the integrated design can produce a better overall design than the conventional approach.

CONVENTIONAL VS. INTEGRATED

(Dynamic Dissipative Controller)

RMS < 10 μ rad

| | Controlled Performance | Structural Mass | Actuator Mass | Total Mass |
|---|---------------------------|--------------------|------------------|---------------|
| Initial Design | 1.0 | 1.0 | 1.0 | 1.0 |
| Control-optimized Design $\beta = 0.15$ | 1.30 | 1.0 | 1.45 | 1.18 |
| Integrated Design $\beta = 0.15$ | 4.03 | 0.66 | 1.44 | 0.97 |

Another approach for the integrated controls-structures design is by employing multiobjective optimization with several objectives. The approach used here for multi-objective
optimization follows the goal attainment technique [4]. For this approach, a set of functions, $g_j(\mathbf{x})$, are derived from the objective functions, $f_j(\mathbf{x})$, as shown below. The parameters a_j are certain reference values or goal values of the objectives, and b_j are scaling parameters so that various objectives become commensurable, and some weights are assigned
to the objectives. As seen from the expression for $g_j(\mathbf{x})$, the weight of each objective
depends inversely on b_j . A solution to the multi-objective optimization problem is then
given by minimizing over \mathbf{x} the maximum of g_j 's. Problems with this approach are that
the maximization function is non-differentiable, which disrupts most numerical nonlinear
programming algorithms. Also, the solution from this approach may not be Pareto optimal
[4].

Goal Attainment Approach for Multi-objective Optimization

$$g_j(\mathbf{x}) = \frac{f_j(\mathbf{x}) - a_j}{b_j}$$
 for $j = 1, 2, ..., m$,

where a_j are reference values or goal values, b_j are scaling parameters so that various objectives are commensurable.

$$\min_{\mathbf{x}} \ [\ \max_{j} \{ \ \mathbf{g_{1}(x)}, \ \mathbf{g_{2}(x)}, ..., \ \mathbf{g_{j}(x)}, ..., \ \mathbf{g_{m}(x)} \} \]$$

Problems:

- 1) nondifferentiable max function
- 2) solution may not be Pareto optimal

The Kreisselmeier-Steinhauser (KS) function [5] given by the expression below provides an approximation for the maximum of a set of functions $g_j(\mathbf{x})$. Values of the KS function remain within the interval $g_{max} \leq KS \leq g_{max} + (\ln m)/\rho$, where g_{max} is the maximum of the set and ρ is a positive scalar parameter of the KS function. Furthermore, this function is differentiable with respect to the design variable, x_i . Thus, the KS function provides a differentiable approximation for the maximization function. Our approach to multi-objective optimization is to use the KS function instead of the maximization function in the goal attainment approach. Minimization over \mathbf{x} of the KS function of $g_j(\mathbf{x})$ gives a multi-objective optimal solution. With this approach the problem is reduced to an unconstrained minimization (apart from side constraints on the design variables) of a differentiable function, which is very amenable to numerical nonlinear programming algorithms. Furthermore, the minimum KS solution is a Pareto-optimal solution.

Multi-objective Optimization Approach

$$\min_{\mathbf{x}} \left\{ g_{\text{max}} + \frac{1}{\rho} \ln \left(\sum_{j} \exp \left[\rho \left(g_{j}(\mathbf{x}) - g_{\text{max}} \right) \right] \right) \right\}$$

where
$$g_{j}(\mathbf{x}) = \frac{f_{j}(\mathbf{x}) - a_{j}}{b_{j}}$$
 for $j = 1,...,m$

gives a multi-objective optimal solution.

- --> unconstrained minimization of a differentiable function
- --> min KS solution is a Pareto-optimal solution.

To demonstrate the use of this approach in the integrated controls-structures design, a redesign of the generic space platform, described earlier, was performed. The objective of this redesign was minimizing the root-mean-square pointing error due to a zero-mean white-noise disturbance at the actuators, along with reasonable bounds on control energy and structural mass. The bounds on control energy as well as structural mass are implemented as supplementary objectives. Desired values for these objectives are the limits on the respective variables, and very small values are chosen for the scaling parameters, b's, so that these objectives, i.e. g_2 and g_3 , are highly emphasized. Some desirable value is chosen for the rms pointing error, which is essentially arbitrary at first but can be chosen judiciously in subsequent optimizations. The scaling parameters are selected to emphasize the supplementary objectives, so that whenever the optimization algorithm tends to increase these variables beyond their bounds, the supplementary objectives dominate the overall KS function and do not allow the optimization to proceed in that direction. By varying the values of the goal values and the scaling parameters, different trade-off studies among the various objectives can be performed, with a Pareto-optimal solution at each design. Side constraints on the design variables are needed for safety and practicality.

DESIGN PROBLEM

Minimize the RMS pointing error, the control energy and the structural mass

$$g_1 = rac{RMS - RMS_d}{b_{RMS}}$$
 $g_2 = rac{E - E_d}{b_E}$ $g_3 = rac{M_s - M_{s_d}}{b_{M_s}}$

• Side constraints on design variables for safety and practicality

Numerical studies for the redesign of the space platform using the multi-objective optimization approach described above were compared with the conventional design approach. Using a static dissipative controller, an initial design based on rigid-body performance was obtained. The results of other designs were normalized with respect to this initial design. A control-optimized design was developed by optimizing only the control design variables in the optimization process, while using the nominal structure. For this design, the rms pointing error was reduced by 27 % while the cost in terms of the control energy went up by 29 %. The structural mass is unchanged, since the nominal structure is used. In the integrated design, the structural variables were also free to be changed, so that the optimizer could modify the structure as needed. In this case, the rms pointing error was reduced by 59 % for approximately the same penalty of 28 % in control energy, with the structural mass also about the same as the initial design. Thus, this numerical design study again demonstrates the benefits of integrated design as opposed to conventional design or control-optimized design.

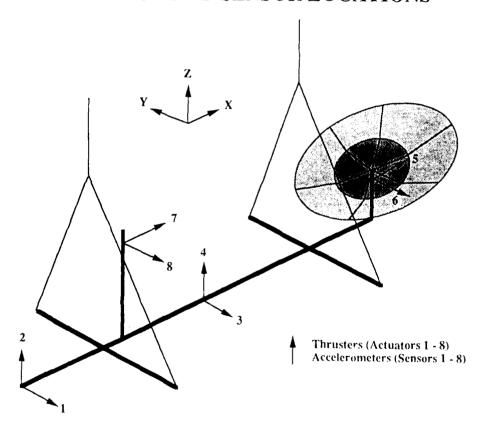
CONVENTIONAL VS. INTEGRATED

(Static Dissipative Controller)

| | RMS Pointing | Structural Mass | Control Energy |
|-----------------------------|-----------------|--------------------|-------------------|
| Initial Design | 1.0 | 1.0 | 1.0 |
| Control-optimized Design | 0.73 | 1.0 | 1.29 |
| Integrated Design | 0.41 | 0.994 | 1.28 |

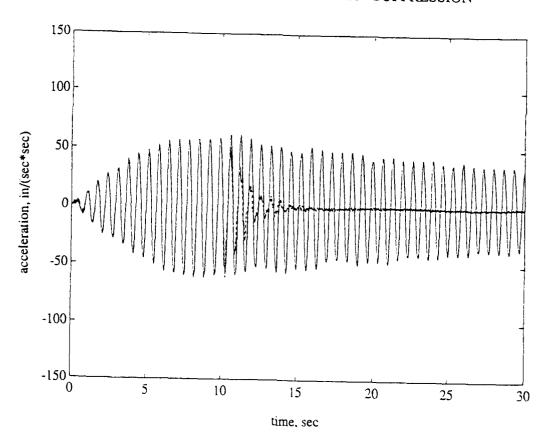
An important part of the CSI program is the experimental validation of the design methods developed. Therefore, in order to validate the dissipative control designs, both static and dynamic dissipative designs were performed for the CSI Evolutionary Model, an experimental testbed at NASA Langley Research Center (see figure below). The Evolutionary model consists of a 62-bay truss bus (each bay at 10 inches), two towers and several appendages. At the end of one of the towers a laser is mounted, and at the end of the other a reflector with a mirrored surface. A laser beam is reflected by the mirrored surface unto a detector surface above (660 inches above the reflector). Eight proportional bi-directional gas thrusters provide the input actuation, while collocated servo accelerometers provide output measurements.

ACTUATOR AND SENSOR LOCATIONS



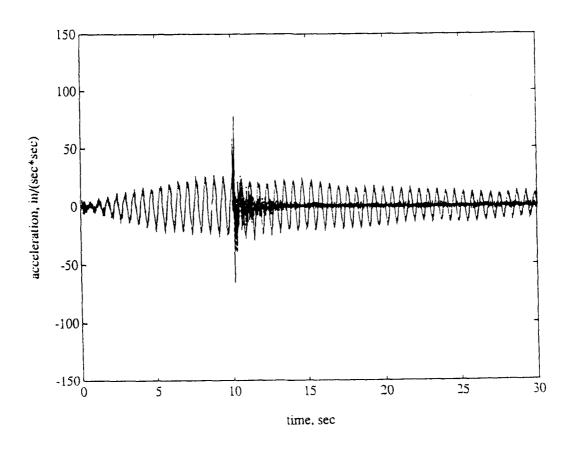
The objective chosen for the design was to minimize the steady-state variance of the control input (i.e., average control energy) with a constraint on the maximum of the real parts of the closed-loop eigenvalues. Washout filters were included in the design for asymptotically removing the accelerometer biases. Because of discrete-time implementation, it was found necessary to include low-pass filters (in static dissipative control design) to attenuate high-frequency modes. The dynamic dissipative controller, however, includes a built-in low-pass filter, whose parameters are determined through the optimization process. The best design was obtained using a 16th-order dynamic dissipative controller. The figure below shows the experimentally obtained acceleration response at sensor no. 8, wherein excitation inputs are applied for 9 seconds to excite the first two pendulum modes and the first two flexural modes. The control law is turned on at the 10 seconds mark, and shows a satisfactory closed-loop response (predominantly the first flexural mode). The closed-loop damping achieved for this mode is about 8.5%, as opposed to the open-loop damping ratio of 0.1-0.2%.

EXPERIMENTAL RESULTS: VIBRATION SUPPRESSION



The closed-loop damping ratios for the other modes were much higher. The experimental response at sensor no. 7 for the excitation described earlier is shown below. The sensor output predominantly consists of the second flexural mode, for which the closed-loop damping ratio of about 14% is observed.

EXPERIMENTAL RESULTS: VIBRATION SUPPRESSION



An integrated controls-structures design methodology for a class of flexible spacecraft has been developed. This methodology formulates the design problem as a simultaneous controls-structures optimization. It has been demonstrated that the integrated design methodology can result in a better overall design as opposed to the traditional sequential design approach. Moreover, the automated nature of the integrated optimization approach is quite attractive since it can accommodate almost any type of design specification and requirements, and it is quite amenable to computer aided design implementations. Two dissipative controllers have been considered for the integrated design process. Both, static and dynamic dissipative controllers have been experimentally validated through implementations on an actual test article. Currently, research is underway to verify the feasibility of the integrated design methodology by using it to redesign the CSI Evolutionary Model at NASA Langley Research Center.

CONCLUDING REMARKS

- Integrated design approach can result in a better overall design
- The automated nature of the design is desirable, particularly for CAD implementations
- Dissipative controllers are good candidates for use in the integrated controls-structures design
- Research is underway to continue and verify the integrated design for this class of problems

References

- [1] Joshi, S. M.: Control of Large Flexible Space Structures, Berlin Springer-Verlag, Vol. 131, Lecture Notes in Control and Info. Sciences, 1989.
- [2] Joshi, S. M. and Maghami, P. G.: Dissipative Compensators for Flexible Spacecraft Control, Proc. 1990 American Control Conference, San Diego, CA, May 23-25, 1990.
- [3] Kwakernaak, H. and Sivan, R.: Linear Optimal Control Systems, Wiley-Interscience, Wiley & Sons, Inc., 1972.
- [4] Gembicki, F. W. and Haimes, Y. Y.: Approach to Performance and Sensitivity Multiobjective Optimization: The Goal Attainment Method, pp. 769-771, IEEE Transactions on Automatic Control, December 1975.
- [5] Kreisselmeier, G. and Steinhauser, R.: Systematic Control Design by Optimizing a Vector Performance Index, pp. 113-117, Computer Aided Design of Control systems, Zurich, Switzerland, August 1979.

AN OPTIMIZATION METHOD FOR CONTROLLED SPACE STRUCTURES WITH VARIABLE ACTUATOR MASS

Stanley E. Woodard and Sharon L. Padula NASA Langley Research Center

> Philip C. Graves Vigyan Research Associates

Benjamin B. James
Lockheed Engineering and Sciences Company

Fourth Annual NASA/DOD CSI Conference Orlando, Florida November 5 - 7, 1990

Introduction

The historical necessity for controls-structures design methodology dates back to Explorer 1, the first U.S. satellite. Explorer 1 was intended to be spin stabilized about its minor axis of inertia. However, unexpected structural energy dissipation due to the flexibility of four whip antennas perpendicular to spin axis caused the satellite to tumble undesirably about its major axis of inertia. This could probably have been prevented if the controls aspects and the structural aspects of the design were mutually integrated. More recently, are the controls-structures issues of the Galileo spacecraft which involved the vehicle analysis and ground testing. Galileo is a spin stabilized gyrostat. Its structural frequencies were close to the pointing control bandwidth. Uncertainty in the dynamic model due to model reduction and 1g effects on ground tests and uncertainty in the stability margin led to a two year extension in the control design phase of the project. Because of the uncertainties in the dynamic model, an inflight system identification capability was added to the design to establish confidence in Galileo's control system. The Explorer 1 and Galileo examples of Controls-Structures Interaction (CSI) issues were cited to illustrate that CSI problems could occur at any time in a spacecraft's life cycle (1).

Current design methods do not often detect problems in the early phases of the design where more leverage for solution exists and more options are available, and when the impact of cost, risk, and time scheduling are least (1). Future spacecraft will be lightweight and very flexible. Their structural frequencies will overlap their controller bandwidth. Along with the complications of their design due to flexibilty will be added complexity due to higher performance specifications. Traditional methods of spacecraft design (developing optimal control laws for a structural design that has been structurally optimized) will not be able to produce spacecraft capable of meeting future mission specifications. Instead of the traditional approach, new design methods are being developed that consider the structural design to be integrated with the control design, thereby allowing for trade-offs between structural design parameters and control design parameters.

A fundamental problem facing controls-structures analysts is a means of determining the trade-offs between structural design parameters and control design parameters in meeting some particular performance criteria. Developing a general optimization-based design methodology integrating the disciplines of structural dynamics and controls is a logical approach (2-3). The objective of this study is to develop a general Controls-Structures Interaction design methods for coupled systems. These are systems that have control variables that are mutually and implicitly coupled to the structural design variables.

An outline of this presentation is given below:

Research Objective

Develop general Controls-Structures Interaction design methods for coupled systems.

Outline

- Technical Approach
- Optimization Scheme
- Structure/Reference Configuration
- Controls
- Optimization Results
- Concluding Remarks/Future Work

Technical Approach

A derivative of the Earth Observing System (EOS) is used for optimization studies. This model is an adequate representation of a "real world" application that can benefit from CSI-motivated trade-off. The EOS derivative model allows results from this study to be intuitively compared with other studies which are using the same model as a reference. The dynamic analvsis of the problem is maneuver-dependent. Torque actuators are sized to control the elastic deformation of the spacecraft resulting from the chosen maneuver. These co-located elastic controllers (CEC) have mass which is non-neglible. The actuator mass couples the analysis because it is both a structural variable and a control variable. Thus, the optimization problem is multidisciplinary and coupled. The Global Sensitivity Equations (GSE) (4) can be used for an optimization problem such as this. These equations produce globally coupled partial derivatives from uncoupled partial derivatives. Off-the-shelf programs such as CONMIN (used for optimization) and the Engineering Analysis Language (EAL, used for structural analysis) are used whenever possible.

- Earth Observing System derivative spacecraft
- Maneuver dependent
- Controller and structure coupled via actuator mass
- Global Sensitivity Equations \Rightarrow Multidisciplinary and coupled optimization
- Off-the-shelf programs

Optimization Problem

The design objective for this problem is to minimize the total spacecraft mass which includes that of the structure and the actuators. Although with modern launch vehicles the total mass of a spacecraft similar to the one under consideration does not constitute a critical design driver, the actuator mass does play a key role in the entire system behavior. The goal of this analysis is to develop and validate a method for optimizing systems with implicitly coupled design variables. In this problem, the actuator mass plays the role of both a control variable and a structural variable, thereby coupling the analysis. Real parts of the closed-loop eigenvalues are constrained to be below some prescribed value. This constraint addresses mission performance such as pointing. The design performance question is whether structural mass can be traded for actuator mass to meet design objective and constraint.

Design objective: Minimize the total spacecraft mass (structure and actuator) while constraining vibration decay rate using both structural variables and control variables.

$$\min[\mathbf{m}_{\text{actuator}} + \mathbf{m}_{\text{structure}}] \quad \text{while} \quad \mathbf{Re}\{\lambda'\mathbf{s}\} \leq -\delta$$

Performance question: Can structural mass be traded for actuator mass to meet design objective and constraint?

OPTIMIZATION STRATEGY

The strategy for the optimization problem is to have the total spacecraft mass as an objective and to have required vibration decay rate as a constraint. There are three structural design variables and twelve control design variables. Structural variables include the diameter of truss members, the diameters of the antenna support members, and the diameter of the antenna ribs. Control variables are the elements for the position and rate gain matrices. These matrices are symmetric and positive definite. Thus, there are six design variables in each matrix. Another important consideration are gradients necessary to perform the analysis.

When systems are implicitly coupled there are two possible approaches for producing gradient information. A conventional approach uses sequential linear programming. The conventional method connects an optimizer with a linear approximation to the full analysis. It consists of calculating the derivative approximations by perturbing the each design variable and then repeating the full analysis Another method consists of using sequential linear programming with the Global Sensitivity Equations to calculate improved approximations using derivatives of the component analyses. The optimizer is connected with a linear approximation to the full analysis. Gradients of the objectives and the constraints are provided by performing a single full analysis followed by a sensitivity analysis for the structures and controls.

Objective: Constraints:

Design Variables: Gradients:

Total mass

Required vibration decay rate

3 structural - 12 control Two possible approaches for implicit coupling

(1) CONVENTIONAL

Calculate derivative approximations by perturbing design variables and repeating full analysis

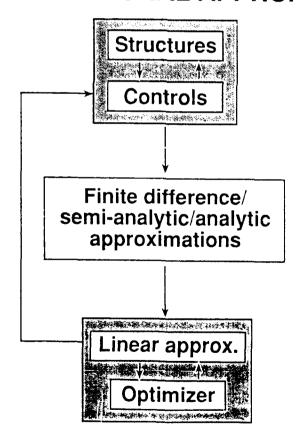
(2) GSE

Calculate improved approximations using derivatives of component analyses and Global Sensitivity Equations (GSE)

Conventional Approach

The optimization scheme for the Conventional Approach is illustrated below. The full analysis consists of the structural analysis and the control analysis. Global derivatives can be produced using either finite differencing, semi-analytic approximations, and/or fully analytic approximations. After linear approximation, these derivatives are used in the optimizer. The strengths to this approach are that it is straight-forward to implement using FORTRAN codes and operating command language, and easy to start regardless of cause for abnormal termination. Weaknesses include the necessity to choose proper perturbation step size which may be difficult or even impossible. The complete convergence of the full control-structural analysis loop is critical. Poor values of the gradients may cause the optimizer to maltunction. And, the optimizer must allow the move limits, the allowed upper and lower bounds to changes in the design variables, to initially be loose and then gradually tightened.

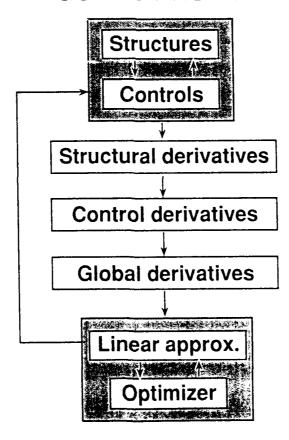
CONVENTIONAL APPROACH



GSE Approach

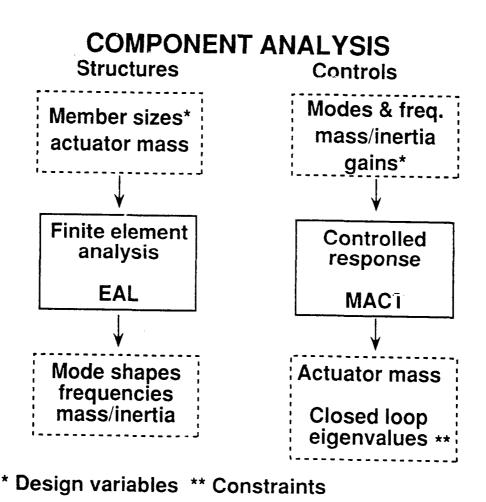
The GSE optimization scheme is illustrated below. The full analysis is the same as that used in the conventional approach. Once the full analysis has converged, the control and structural gradients are estimated as uncoupled partial derivatives. The Global Sensitivity Equations use the uncoupled partial derivatives to approximate the appropriate coupled partial derivatives. These coupled partial derivatives are used by an optimizer to develop an optimal solution based on the design objectives and contraints. Move limits are imposed so that the linear approximations to the full analysis remains valid. One strength of this approach is that it provides accurate gradients even if the full analysis is not completely converged. Restart is very simple. Control sensitivity derivatives can be calculated reliably and accurately. This approach finds an optimum and feasible solution even if the initial values of the design variables are poorly chosen. Weaknesses include the necessity for calculation of controls sensitivity derivatives which can be expensive because of the numerous inputs and partial derivatives of the actuator mass and closed-loop eigenvalues that are required. Assembly of the GSE matrix requires proper scaling of local derivatives and involves complicated programming logic. This problem is further complicated because of closely-spaced and repeated eigenvalues. And, the optimizer must allow the move limits to initially be loose and then gradually tightened.

GSE APPROACH



Component Analysis

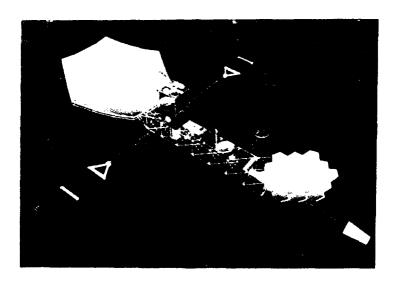
Because the actuator mass is non-negligible, it couples the open-loop finite element model with the control analysis, thereby requiring an iterative solution. The iteration is an "inner loop " within the optimization "outer loop." The inner loop contains control analysis and structural analysis. The structural analysis produces mode slopes, frequencies, and the system inertia matrix. These are used by the control analysis to produce a value for the actuator mass based on required torque. This actuator mass value is then used in the structural analysis to regenerate the mode slopes, frequencies, and inertia matrix. The iterative process of computing actuator mass requires system mass matrix updating and recalculation of the eigensolution until the calculated actuator mass converges on a value relative to its prior value. Once a converged value for actuator mass is generated, structural and control gradients are estimated as uncoupled partial derivatives.



W-CMP

Earth Observing System

A derivative of the Earth Observing System (EOS) is used for optimization studies. The features of this vehicle used for the reference configuration are the two antennas mounted outboard on the structural support truss and the truss.

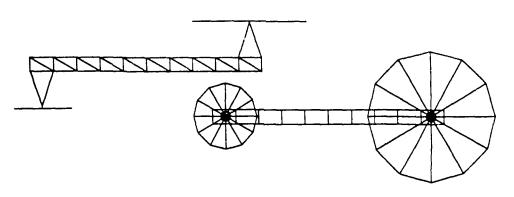


Reference Configuration

The reference configuration is illustrated below. There are fifteen design variables. Three include the diameters of the antennas, diameters of the antenna support mounts and, the diameters of the truss members. Three-axis co-located elastic control torquers are located beneath the antenna mounts. The remaining design variables are the elements to the rate and position gain matrices. Each matrix is a 3 by 3 symmetric and positive-definite matrix with six elements used as control design variables each.

REFERENCE CONFIGURATION

15 design variables: 3 truss sizing variables, 12 gain matrix variables



3-axis torquers

I-REF. CONFIG-90-118

Estimating Accuator Mass

The spacecraft's rigid-body motion and elastic behavior are used in the control and structural analysis. The analysis of the spacecraft's dynamics considers having the vehicle rotated from its initial attitude to a new attitude. After the rotation it is desired that any vibration that has occurred because of the maneuver be suppressed. The knowledge of the dynamics is used to size the controllers which are used to rotate the spacecraft and suppress its vibration.

Torque wheels with bang-bang control slew the spacecraft during attitude maneuvers and, consequently, excite the structure. The maneuver is considered to be linear (i.e., small angular displacement over a long duration). In addition to the torque wheels used for the attitude maneuver, two collocated elastic controllers are located in the bays below the antenna supports. The modal representation of the elastic response, q, of the spacecraft due to the bang-bang maneuver and the collocated elastic controllers is governed by the following equation of motion:

$$\ddot{q} + D\dot{q} + \Lambda q = -\Psi^T G_{\rm p} \Psi q - \Psi^T G_{\rm r} \Psi \dot{q} + \Gamma^T M$$

Modal damping and stiffness are D and Λ , respectively. The first two terms on the right side of the equation above constitute the input due to the collocated elastic controller. These terms are proportional to the position gain, G_p , and the rate gain, G_r , and to the difference of mode slopes, Ψ , at the two elastic controller locations. The last term on the right-hand side of the equation above is due to the bang-bang control maneuver. This torque is propertional to the mode slope, Γ , at the point where the bang-bang torque of magnitude M is being applied. M, produced by the torque.

- Bang-Bang maneuver (reference excitation only)
- CEC torque sized proportional to angular deformation at actuator location
- CEC torque sized proportional to gains and modal elastic response
- Size torque after slew maneuver is completed
- Modal contribution

Elastic Response History

The elastic response can be calculated as:

$$x(t) = A^{-1}[e^{At} - I]BM \qquad 0 \le t \le t_{\rm f}/2$$

$$x(t) = A^{-1}[e^{At} - 2e^{A(t - t_{\rm f}/2)} + I]BM \qquad t_{\rm f}/2 \le t \le t_{\rm f}$$

$$x(t) = A^{-1}[e^{At} - 2e^{A(t - t_{\rm f}/2)} + e^{A(t - t_{\rm f})}]BM \qquad t \ge t_{\rm f}$$

$$A = \begin{pmatrix} 0 & I \\ [-\Lambda - \Psi^T G_{\rm f} \Psi] & [-D - \Psi^T G_{\rm p} \Psi] \end{pmatrix}$$

$$B = \begin{bmatrix} 0 & \Gamma^T \end{bmatrix}^T$$

where A and B are the system plant matrix and control input matrix, respectively.

The torque output, u, for each actuator is resolved to three orthogonal directions according to the following relation:

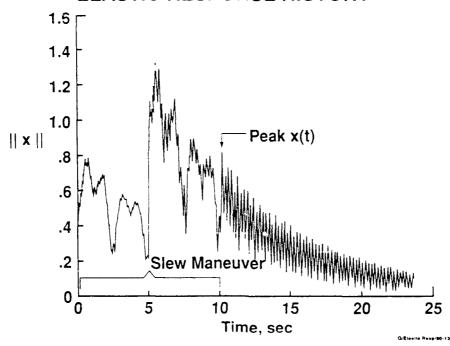
$$u = -[G_p \Psi - G_r \Psi] x(t)$$

Total mass, m_a , for both actuators is proportional to the maximum torque magnitude along each direction $(u_{1\max}, u_{2\max}, u_{3\max})$ such that:

$$m_{\mathbf{a}} = 2m_{\mathbf{t}}(u_{1\max} + u_{2\max} + u_{3\max})$$

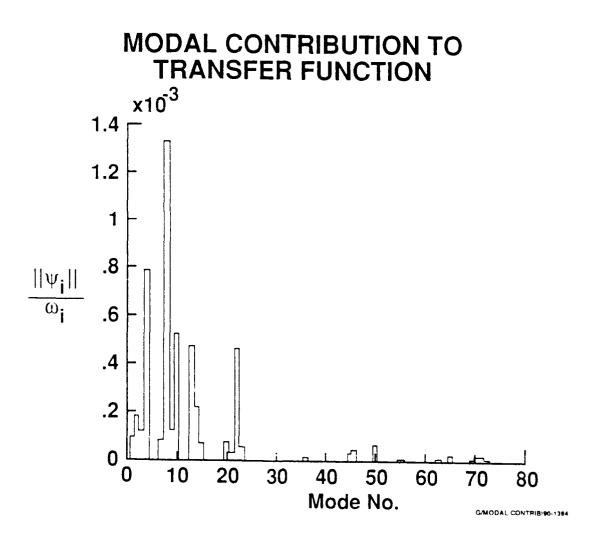
where m_i is a scaling factor for mass per unit torque.

ELASTIC RESPONSE HISTORY



Modal Contribution to Transfer Function

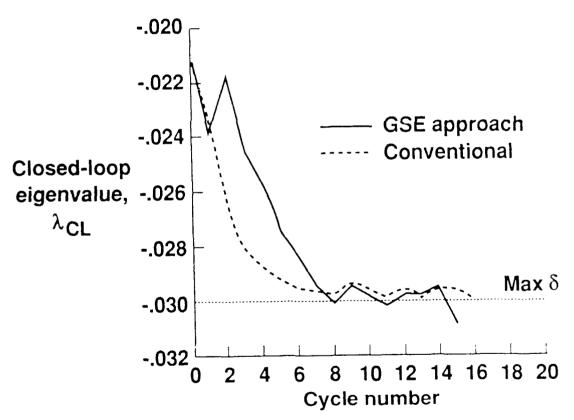
Because the actuator mass calculation depends upon the number of modes selected, it is necessary to know which modes significantly contribute to the transfer function. The highest contribution to the transfer function occurs within the first 25 modes. If some of the major contributors are truncated or ignored, then the derived value of the actuator mass will be lower than necessary to control the flexible modes.



GSE vs. Conventional Approach: Constraint

The aggregate results of the overall optimization analysis illustrates that both the GSE method and the conventional method try to meet the optimization constraint even though both started with the same infeasible design variables. The constraint on the design is that the real part of all closed loop eigenvalues be less than $\delta = -.030$. As depicted below, this constraint is initially satisfied at cycle 8 of the outer loop using the GSE method. The oscillation of the solution after cycle 8 is due to the changing move limits.

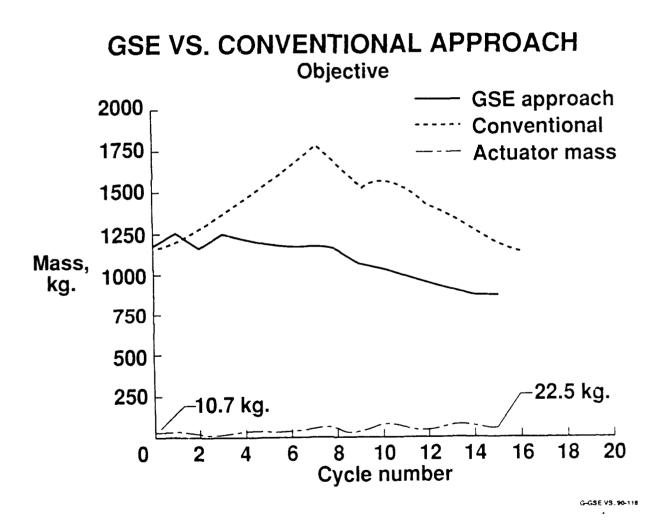
GSE VS. CONVENTIONAL APPROACH Constraint



G-GSE VS. CON 90-118

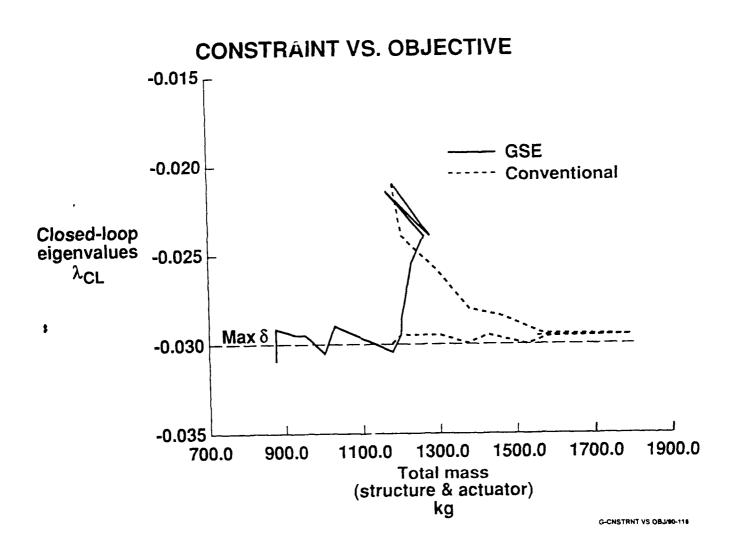
GSE vs. Conventional Approach: Objective

When the initial design variables do not satisfy the constraint, the conventional approach sacrifices the objective (total mass) in an effort to meet the constraint. However, the GSE method tries to concurrently minimize the total spacecraft mass while satisfying the optimization constraint. The effect that the GSE approach has on the spacecraft design is that it redistributes the spacecraft mass. The diameters of the antenna and the antenna mount have increased while the diameter of the truss members has decreased. The GSE method has also increased the total actuator mass by approximately 11 kg. But, such an increase of actuator mass is worthwhile since the total spacecraft mass has decreased by approximately 250 kg.



Constraint vs. Objective

The aggregate results of the overall optimization analysis illustrate that the GSE method outperforms the conventional method. The figure below illustrates that the GSE method tries to concurrently minimize the the total mass while trying to satisfy the constraint. However, the conventional approach sacrifices minimizing the objective in order to satisfy the constraint.



Concluding Remarks

A method has been presented that combines structural analysis and control analysis for implicitly coupled systems using the Global Sensitivity Equations integrated as a single optimization problem. This technique takes advantage of trade-offs between control variables and structural variables to meet a performance objective. In the method illustrated the actuator mass value was prescribed to depend on the modal representation of the spacecraft motion. Modal selection has been shown to be a very important factor in determining the actuator mass. Knowing the elastic response was also a key factor. Aggregate results of the entire optimization loop have illustrated the effectiveness of using an integrated approach to meet performance objectives. Trading structural mass for actuator mass reduced the total spacecraft mass while improving its performance. The approach using the Global Sensitivity Equations outperformed the conventional approach for systems with implicit coupling. The controls-structures integrated design approach also facilitates cooperation between controls and structures design teams. Integration of the methods of control analysis and structural analysis to obtain optimal performance will result in a viable tool for designing flexible spacecraft of the future.

- Trading structural mass for actuator mass reduces total mass and improves performance
- GSE approach outperforms conventional approach for systems with implicit coupling
- CSI method facilitates cooperation between controls and structures design teams

References

- 1. Ketner, G.L.: "Survey of Historical Incidences with Controls-Structures Interaction and Recommended Technology Improvements Needed to Put Hardware in Space," Report prepared for NASA Langley Controls-Structures Interaction Office, March 1989.
- 2. Woodard, S.E.; Padula, S.L.; Graves, P.C.; James, B.B.; "A Multidisciplinary Approach to Optimization of Controlled Space Structures," Proceedings from the Third Air Force/NASA Symposium on Recent Advances in Multidisciplinary Analysis and Optimization, San Francisco, CA, September 24-26, 1990.
- 3. Maghami, P.G.; Joshi, S.M.; Walz, J.E.; Armstrong, E.S.; "Integrated Control-Structure Design Methodolgy Development for a Class of Flexible Spacecraft," Proceedings from the Third Air Force/NASA Symposium on Recent Advances in Multidisciplinary Analysis and Optimization, San Francisco, CA, September 24-26, 1990.
- 4. James, B.B.; "An Alternative Formulation of the Global Sensitivity Equations," Proceedings from the Third Air Force/NASA Symposium on Recent Advances in Multidisciplinary Analysis and Optimization. San Francisco, CA, September 24-26, 1990.



INFLUENCE OF UTILITY LINES AND THERMAL BLANKETS ON THE DYNAMICS AND CONTROL OF SATELLITES WITH PRECISION POINTING REQUIREMENTS

PR-297

The Fourth NASA/DOD Controls Structures Interaction Conference Orlando, Florida **Presented at**

Presented by J.M. Hedgepeth R.K. Miller M.W. Thomson Astro Aerospace Corporation Carpinteria, California

November 5-7, 1990

(sunshade) of the envisioned 20-meter-diameter infrared telescope (LDR) shown in Figure 1. The shroud is taken to be a flexible multilayer insulation blanket supported by a truss framework. Of course, the member size of the framework would be dependent on the tension in the blanket. Thus, the need became apparent for rational design criteria for the tension in such secondary mechanical systems as thermal blankets and utility lines. Such criteria can be related to the effect of the The study reported herein was motivated by the need to perform a rational quantitative conceptual design of the shroud dynamics of these masses on the dynamics and control of the spacecraft.

systems. Hence, development of design criteria for such secondary systems which tend to minimize these deleterious precision pointing. Many planned future missions call for very high precision in pointing and station-keeping, which results troublesome due to the inherent lack of observability and controllability of the state variables associated with such After completing a rapid slewing maneuver, mission requirements for a high performance satellite usually demand high in unprecedented demands on pointing control systems. In such cases, the residual oscillations caused by residual strain energy in such secondary and ill-managed systems as wiring harnesses and thermal blankets may be particularly effects on control-structure interactions is of considerable importance.

appendage is presented. Finally, application is made to the design of a sunshade (thermal blanket) for the LDR satellite is The paper is organized along the following lines. First, a study of the residual oscillations after "bang-bang" reorientation Next, a generalization to the case of a membrane maneuvers of a rigid satellite with a string appendage is presented.

LARGE DEPLOYABLE REFLECTOR (LDR) CONCEPT

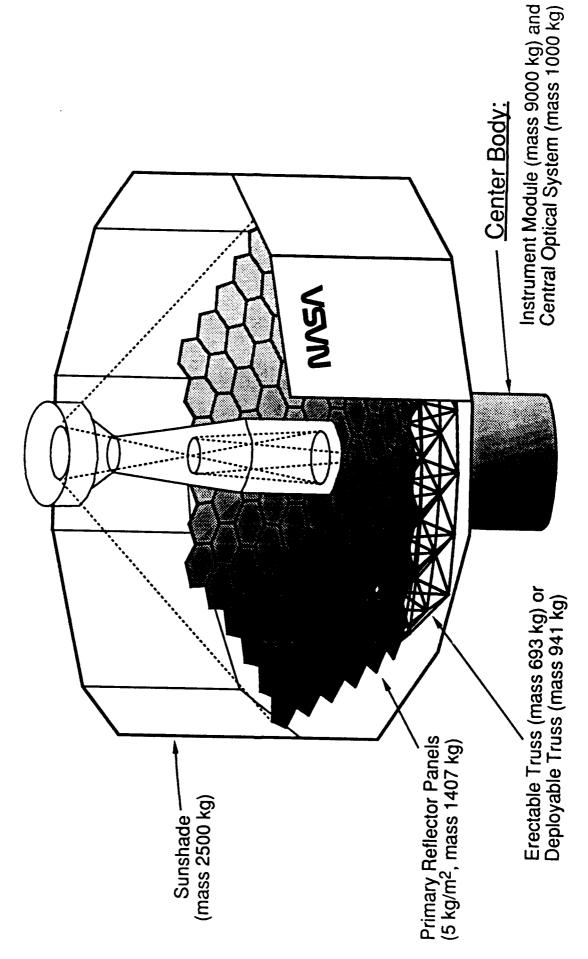


Figure 1

In this section, the equation of motion of a string is presented with an initial elongation which may be either (1) finite and positive (initial taut behavior), (2) finite and negative (initial slack behavior), or (3) anywhere in between these extremes, including zero elongation (zero bending stiffness) Consider an elastic string attached at the ends to rigid supports which are separated by a distance 1. Let the unstretched length of the string be &, where &, may be either larger or smaller than &. Then the initial unit elongation & is defined For string motions which do not involve axial waves, the string tension T has negligible variation along the length of the string. In such cases, T may be approximated as:

$$T = \begin{cases} EAE_{Avg} : \varepsilon_{avg} \ge 0 \\ 0 : \varepsilon_{avg} < 0 \end{cases}$$

where E is the modulus of elasticity of the string material, and ϵ_{avg} is the average load strain over the length of the string. In particular, E and may be computed as shown below. Employing a Galerkin approximation to discretize the equation of motion using a simple parabolic shape function shown in Figure 2 gives

$$\epsilon_{\text{avg}} = \epsilon_{\text{o}} + \frac{1}{6} \left(\frac{\eta}{\ell} \right)^2$$

and

$$T(\eta) = \begin{cases} EA\varepsilon_o + \frac{EA}{6} \left(\frac{\eta}{t}\right)^2 ; \eta^2 \ge \eta_o^2 \\ 0 ; \eta^2 < \eta_o^2 \end{cases}$$

where

$$\eta_o = \begin{cases} \ell\sqrt{-6\varepsilon_o} ; \varepsilon_o < 0 \\ 0 & ; \varepsilon_o \ge 0 \end{cases}$$

STRING DYNAMICS

Initial unit elongation:

$$\varepsilon_0 = \frac{\ell - \ell_0}{\ell_0} \ll 1$$

String tension:

$$T = EA\varepsilon_{ave}$$

$$\varepsilon_{ave} = \varepsilon_0 + \frac{1}{2\ell} \int_0^{\ell} V_X^2 dx$$

Wave equation:

$$Tv_{xx}=\rho Av_{tt}$$

Single-mode assumption:

$$V = \eta(t) \frac{x}{\ell} \left(1 - \frac{x}{\ell} \right)$$

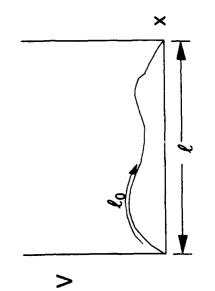


Figure 2

The single-degree-of-freedom yielded by the Galerkin process is given in Figure 3.

The nonlinear character of the free vibrations of the string governed by this equation may be revealed by exploring the amplitude-frequency behavior. Although in principle this may be done exactly by integrating the approximate equation form approximation of adequate accuracy is obtained by employing the method of equivalent linearization. In this method, the linear equation below is used to approximate the nonlinear one. The validity of the approximation depends critically on the choice of the "equivalent linear stiffness," k. This is accomplished by selecting k to minimize the square of the time average of the difference term obtained by subtracting the two equations. The resulting estimate of k is shown in the figure. Let the time history of η(t) be approximated as shown below where Δ represents the (non-negative) amplitude of motion and ω and φ respresents the circular frequency and phase, respectively. Then the least mean of motion, the actual evaluation of the integral is quite tedious due to the nature of the nonlinearity. Instead, a closedsquare procedure yields

$$k = \rho A \ell \omega_n^2$$

where

$$\frac{\omega_n^2 \ell^2}{10c^2} = \begin{cases} \varepsilon_o + \frac{1}{8} \left(\frac{\Delta}{\ell}\right)^2 ; \varepsilon_o \ge 0 \\ \varepsilon_o \frac{(2\beta + \sin 2\beta)}{\pi} + \frac{1}{6} \left(\frac{\Delta}{\ell}\right)^2 \frac{\left(\frac{3}{2}\beta + \sin 2\beta + \frac{1}{8}\sin 7\beta\right)}{\pi} ; \varepsilon_o < 0 \end{cases}$$

$$\beta = \cos^{-1} \left(\frac{\sqrt{-6}\varepsilon_o}{(\Delta/\ell)}\right)$$

$$c = \sqrt{\frac{E}{\rho}}$$

EQUIVALENT LINEARIZATION

$$\rho A\ell \ddot{\eta} + 10\eta \frac{T}{\ell} = 0$$

Replace by: $\rho A\ell \ddot{\eta} + k\eta = 0$

where

$$k = \frac{10}{\ell} \frac{\left\langle \eta^2 T \right\rangle}{\left\langle \eta^2 \right\rangle}$$

<u>et</u>

$$\eta = \Delta \cos(\omega t - \phi)$$

natural frequency increases with increasing amplitude. The qualitative differences in behavior caused by different levels the linear theory. For the unstretched string, note from the figure that the effective natural frequency is directly proportional to the amplitude of motion, with the implication of an infinite penod of oscillation at zero amplitude. Finally, for the initia ly slack string, note that no oscillatory motion is possible until the amplitude of motion reaches a threshhold of initial strain are confined to the small amplitude domain. In the case of an initially taut string, the effective natural frequency becomes independent of amplitude for small motions, and is determined solely by the positive initial strain, as in determined by the negative initial strain. For amplitudes below this threshhold value, no tension is developed in the string, Shown in Figure 3 are representative curves for the amplitude-frequency behavior of the string. In particular, three curves initially slack (ε_o < 0) string. The global behavior in all three cases is that of a "hardening system," in which the effective are shown: one corresponding to an initially taut string $(\varepsilon_o > 0)$, one for a string with no initial strain $(\varepsilon_o = 0)$, and one for an so that no restoring forces are available to permit oscillation.

corresponding to higher "modes" of oscillation. These were not considered herein in order to concentrate instead on the dynamic interaction between the string in its fundamental mode, and the slewing motion of a rigid body whose residual The complete amplitude-frequency behavior of the string would include additional curves at higher frequencies oscillations are of primary concern, as presented in the following section.

NONLINEAR STRING VIBRATION

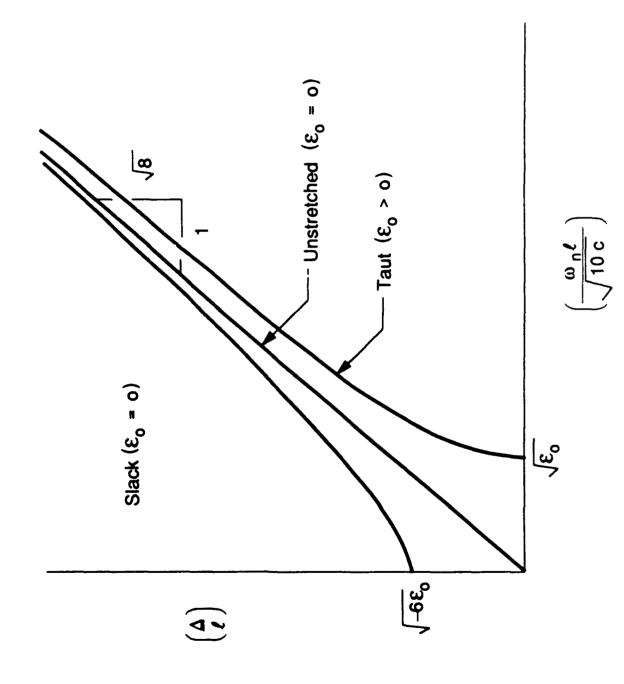


Figure 3

Consider the mechanical configuration shown in Figure 4. The system consists of a rigid body with mass moment of inertia I about its axis of rotation, two rigid massless supports extending radially a distance R from the axis of rotation, and an elastic string appendage attached to the supports. The angular position θ(t) of the rigid body relative to an inertial reference frame, as well as the externally applied torque M(t) about the axis of rotation are assumed positive in the direction shown. All motion of the string is assumed to be confined to the transverse plane which is normal to the radial supports. A view of the string in this plane is shown in Figure 4. The lateral deflection of the string relative to the chord line between supports is denoted v(x, t), where x represents the position along the chord line and t represents time. The supports are separated by a distance (.

Due to the rotation of the rigid body, the supports at the ends of the string are subject to motion. The support motion is denoted y(t). For the configuration shown in the figure, the absolute motion of the string is the superposition of v(x, t) and y(t). Thus, for this case with moving supports, the string motion is governed by:

$$T\frac{\partial^2 v}{\partial x^2} = pA \frac{\partial^2 v}{\partial t^2} + pA \frac{d^2 y}{dt^2}$$

$$F(t) = 2T \frac{\partial v}{\partial x} \int_{x=0}^{\infty} (2)$$

The total inertial force F(t) exerted on the rigid supports by the string may be expressed as since the motion contemplated involves only symmetric modes.

$$F(t) = 2T \frac{\partial v}{\partial x} I_{-\alpha}$$
 (2)

The equation of motion for fixed axis rotation of the rigid body is $M(t) + F(t)R = I\ddot{\theta}(t)$.

Furthermore, the support motion
$$y(t)$$
 may be expressed as $y(t) = R\theta(t)$.

<u>4</u>

ල

Substituting equations (2) and (4) into equations (1) and (3) to eliminate y(t) and F(t) yields

$$T\frac{\partial^2 v}{\partial x^2} = \rho A \frac{\partial^2 v}{\partial t^2} + \rho A R \ddot{\theta}$$
 M(t) + 2RT $\frac{d}{dt}$

$$M(t) + 2HT \frac{\partial v}{\partial x} \Big|_{-\infty} = I \ddot{\theta}$$

as the coupled equations of motion for the system in Figure 4.

The Galerkin procedure yields the following equations governing single degree of freedom motion of the string coupled with body

$$\rho A \ell \ddot{\eta} + 10 \eta \frac{T(\eta)}{\ell} = -5 \rho A \ell R \ddot{\theta} \qquad M(t) + 2R \eta \frac{T(\eta)}{\ell} = I \ddot{\theta}$$

DYNAMICS OF STRING APPENDAGE

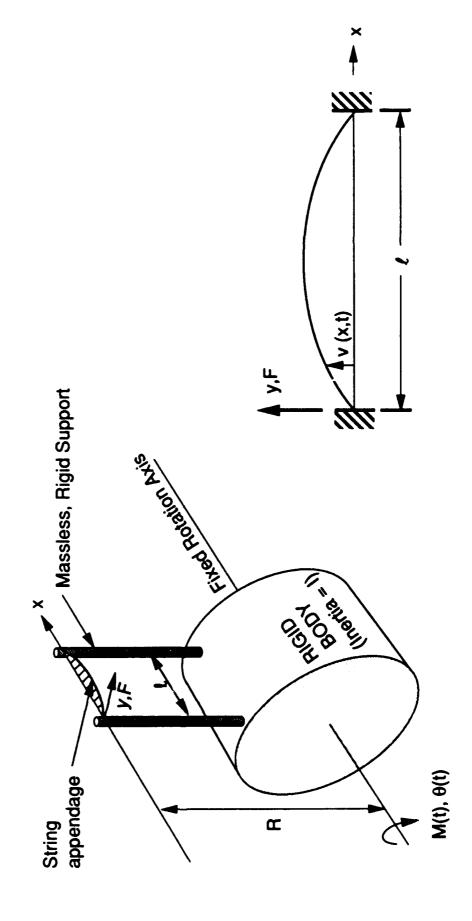


Figure 4

the total stored energy in the string at the end of maneuvers is the primary objective, an energy approach will be in the angular orientation of the rigid body (e.g., pointing errors), are of primary concern, and are considered later. Since employed. Furthermore, a simple approximation will be used to estimate the maximum total energy remaining in the body-string system after the slewing maneuver is completed. These residual oscillations, which result in periodic motion stored in the string at the end of maneuvers. Such total stored energy then feeds residual oscillations of the coupled rigid In this application, the string response during slewing maneuvers is important only insofar as it determines the total energy

the string. Since considerable uncertainty surrounds these variables, any estimate which is sensitive to them is of little in the absence of any energy dissipation, the residual string energy is a strong function of the duration of angular acceleration pulses relative to the natural period of vibration of the string, in addition to the initial position and velocity of practical value.

bang-bang maneuvers clearly lead to response predictions which are conservative since pulse smoothing to remove sharp In view of these difficulties, the following approximation is adopted. The residual string energy will be determined as the contains an adequate degree of conservatism for two reasons. First, the abrupt changes in acceleration associated with corners is common in real applications. In addition, the coincidental relation between acceleration pulse duration and while beginning from rest in a position along the chord line between supports. Although this approximation provides only peak strain energy developed in a string subjected to a single acceleration pulse of infinite duration (e.g., step response) one-half the upper bound displacement value for a linear system, with bang-bang acceleration, it is believed that it string natural period required to achieve the theoretical upper-bound response is highly unlikely.

RESIDUAL MOTIONS AFTER SLEWING

- · During slewing acceleration the slack, if any, is taken up. Then the string is strained.
- dependent on the detailed slewing history but can be practically bounded by doubling the strain which would be caused by The amount of strain energy remaining after slewing is very applying the maximum accelerations statically.
- The residual strain energy is (conservatively) assumed to result in a single-mode residual oscillation.

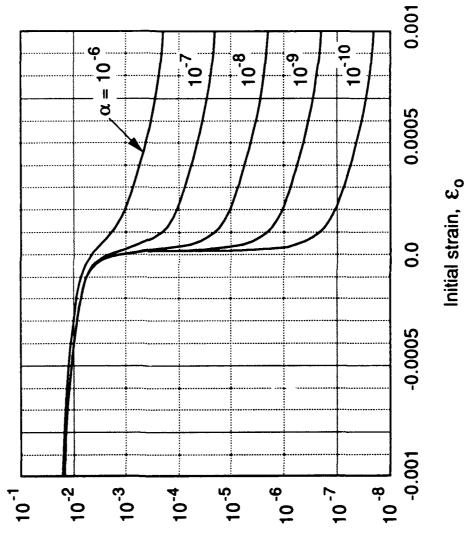
The results for the general nonlinear case are shown in Figure 5 as curves of $\overline{\Theta}_0$ versus $arepsilon_0$ for different levels of reorientation angular acceleration $\ddot{\theta}_o$, as determined by the nondimensional parameter α shown in the figure. In general, increases in the initial strain ϵ_o are accompanied by corresponding decreases in the peak amplitude of angular oscillation $\overline{ heta}_o$. The five curves, corresponding to five different levels of excitation $\overline{ heta}_o$ through the parameter lpha, demonstrate that in all cases increasing levels of excitation lpha are accompanied by increasing levels of response, $\overline{\Theta}_{
m p}$. Furthermore, dramatic changes in string behavior occur near $\varepsilon_o = 0$. For positive initial strain ε_o , the five curves appear to separate and fall to the right in this region of linear behavior. Careful inspection of the curves in this region will reveal that the response $\overline{\theta}_{
m b}$ is proportional to lpha for $arepsilon_{
m o}$, as expected.

of excitation a. In fact, as e, becomes large and negative, all five curves coalesce into a single curve which is independent of α , and less dependent on ϵ_0 than in the linear case where $\epsilon_0 > 0$. Careful examination of the curves in For negative initial strain ε_o (initial slack behavior), the curves show that the response is much less sensitive to the level

$$\overline{\theta}_{p} \sim \frac{\alpha}{\varepsilon_{o}}$$
; $\varepsilon_{o} \approx 0$
 $\overline{\theta}_{p} \sim \sqrt{-\varepsilon_{o}}$; $\varepsilon_{o} \approx 0$

RESIDUAL OSCILLATION AFTER SLEWING

 $\alpha = \rho R \theta_0 / E$



Scaled oscillation amplitude, $\bar{\theta}_p$

Motivated by the limiting behavior, consider the following change of variables:

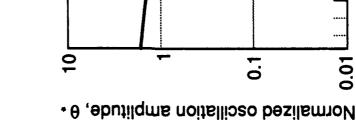
$$\varepsilon_{\bullet} \equiv \varepsilon_{0}$$

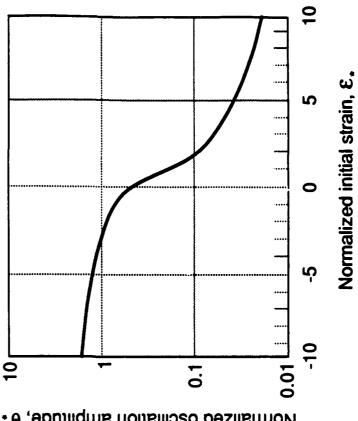
As shown in Figure 6, the family of curves falls on a single one. Figure 6 includes a detail of the behavior of the curve near £. = 0, with a magnification of the horizontal scale by a factor of 50.

NORMALIZED RESIDUAL OSCILLATION

$$\mathbf{E}_{\bullet} = \mathbf{E}_{0}/\alpha^{2}$$

$$\theta_{\star} = \overline{\theta}_{\rho}/\alpha^{\frac{1}{3}} \qquad \qquad \xi_{\star} = \xi_{0}/\alpha^{\frac{2}{3}}$$





Normalized initial strain, E.

400

200

-200

400

0.00001

0.0001

0.000001

Detail near E.

Figure 6

0.1

0.01

Normalized oscillation amplitude, 0.

0.001

100

10

In this section, the analysis is extended from a string appendage to a membrane appendage. Specifically, the effects of maneuver of a rigid satellite are investigated. The motion is considered to consist of a "bang-bang" reorientation phase membrane appendage (capable of a full range of initial strain) on the residual oscillations after a slewing reorientation followed by a residual oscillation phase. In summary, it is found that within the limitations of the assumptions used, the results for both the string case and the membrane case are determined from the same normalized equations, with the following interpretations:

$$u = \begin{cases} \left(\frac{R}{\ell}\right) \left(\frac{\ell^2 \ddot{\theta}_o}{c^2}\right) & \text{; string case} \\ \frac{5}{2} \left(\frac{R_o}{\ell}\right) \left(\frac{\ell^2 \ddot{\theta}_o}{c^2}\right) \left(1 + \frac{2}{3} \frac{h}{R_o}\right) & \text{membrane case} \end{cases}$$

 $\{2 \mid \ell \mid \mathbb{C}^2 \mid \exists \mathbb{R}_o\}$; string case $\epsilon_o \equiv \begin{cases} \text{initial strain} & \text{initial strain at } x_2 = h; \text{ membrane case} \end{cases}$

 $\frac{1}{\theta_{p}} = \begin{cases}
\left(\frac{R}{\ell}\right)\left(1 + \frac{1}{1_{1}}\right)\theta_{p} & \text{; string case} \\
\frac{3}{2}\left(\frac{R_{o}}{\ell}\right)\left(1 + \frac{2}{3}\frac{h}{R_{o}}\right)\left(1 + \frac{1}{1_{1}}\right)\theta_{p}; \text{ membrane case}
\end{cases}$

I, $\equiv \left\{ \frac{5}{6} \text{ mR}_{o}^{2} \left(1 + \frac{3}{4} \frac{h}{R_{o}} \right) \left(1 + \frac{2}{3} \frac{h}{R_{o}} \right) \right\}$ membrane case

 $m \equiv \begin{cases} pAl ; string case \\ pt_ohl'; membrane case \end{cases}$

Figure 7

In typical applications involving the structural design of large space structures, such parameters as the initial tension (or strain $arepsilon_o)$ and the unsupported length $oldsymbol{\ell}$ must be selected. In some cases, the analysis presented in this report may be used to develop some insight into the selection of structural design parameters which provide satisfactory performance by purely

As an illustration of these design implications, consider the LDR, a baseline telescope with a 20-meter aperture, shown in Figure 1. The sunshade is expected to exert substantial influence on the pointing and slewing performance of the LDR. Potential materials for fabrication of the sunshade include a layered thermal blanket consisting of alternate layers of Kapton film and insulation material. The effective mass per unit area of the blanket may vary widely, depending on the number and composition of layers included in the blanket. For purposes of illustration, we consider a blanket design with a unit mass of 1 kg/m². We assume that the effective modulus of elasticity of the blanket is one-half that of Kapton, while the mass density is equal to that of Kapton. Furthermore, we assume that the height h of the sunshade is 10 meters, and the unsupported length & is also 10 meters, corresponding to a hexagonal support structure with six equally spaced vertical struts around the perimeter of the reflector. We assume that the total blanket area is 1100 m2. In addition, we assume an effective base radius R_o of 4 meters for the sunshade.

The LDR mission requirements might include a peak slewing acceleration of 1 milliradian/sec2. We estimate the LDR mass mornent of inertia about a slewing axis (not including the sunshade) to be about 150,000 kg-m 2 .

Figure 8 graphs the resulting dependence of the required initial strain ε₀ to achieve a given level of maximum residual pointing error. Each figure displays two curves, one based on linearized membrane behavior for large initial tension, and one based on the nonlinear analysis presented earlier. Note that the two curves diverge in the neighborhood of $\theta_p \equiv 1$ milliradian. Furthermore, the value of $\theta_{\mbox{\scriptsize p}}$ corresponding to zero initial strain is

$$\theta_{\rm s} = 0.971 \, \text{millirad}$$

sunshade will produce pointing errors in this range. Of course, the linear model, which is based on the assumption of large For $\theta_p > \theta_{po}$, the minimum required initial strain ϵ_o is actually negative, indicating that designs with an initially slack initial strain, is incapable of predicting this behavior.

FOR LIMITED RESIDUAL OSCILLATION INITIAL TENSILE STRAIN REQUIRED

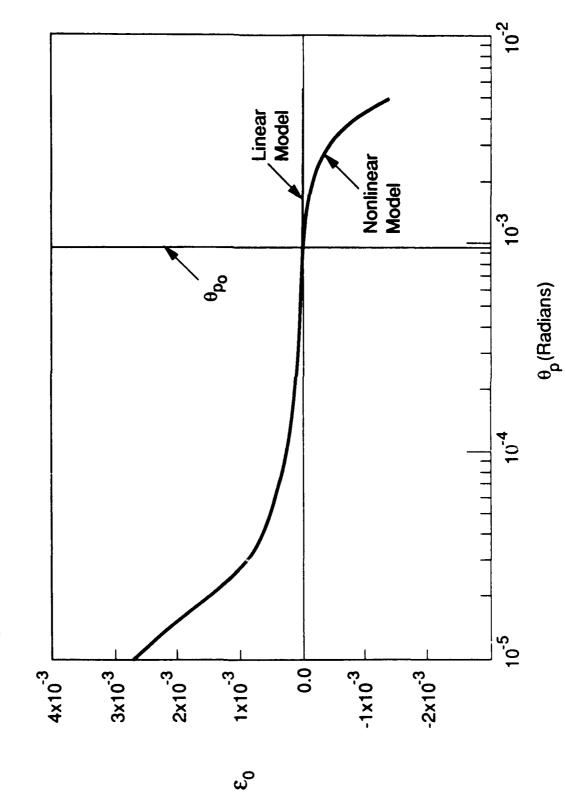


Figure 8

Another design parameter of major importance is the peak force F which the sunshade exerts on one of its supports during and after the reorientation maneuver considered herein. This force plays a central role in the structural design of the struts used to support the membrane.

Shown in Figure 9 is a graph of the normalized support force (F/F.) as a function of the normalized residual pointing error (θ_p/θ_{po}) , where

$$F_{\bullet} = \frac{\alpha^{\frac{2}{3}}Et_{0}h}{3}$$

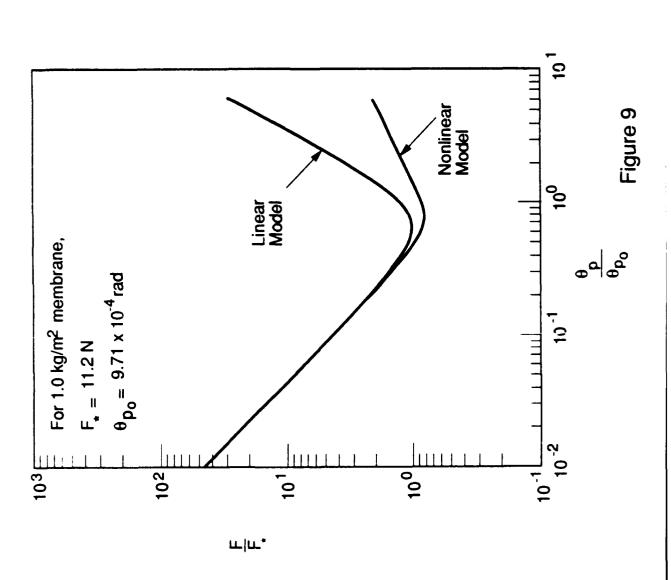
The figure contains two curves, one generated from the nonlinear model and one from the linear approximation. Note that both curves predict a minimum in F near $\theta_p = \theta_{po}$. In this range, however, the linear model is not accurate.

The minimum support force F predicted by the nonlinear model is located at the following approximate values:

For the case of the sunshade with areal density of 1 kg/m², this would result in $F_{min} \equiv 93$ N at $\theta_D \equiv 1.14$ milliradians.

Of interest is the fact that for initially slack behavior $(\theta_p > \theta_{po})$, the dynamic effects caused by nonlinear membrane oscillations involving periodic slack and taut behavi or cause increased peak support forces even though no initial forces are

PEAK FORCES ON THE MEMBRANE SUPPORTS FOR LIMITED RESIDUAL OSCILLATIONS



CONCLUSION

then a quite reasonable sunshade and support structure may be designed to avoid both excessive structural mass and The results shown in Figure 9 indicate that if a residual oscillatory pointing error as large as 1 milliradian may be tolerated undesirable pointing behavior using only passive means. However, it is clear that very high precision requirements would lead to very different conclusions. For example, if the required pointing error is reduced to $\theta_D = 1 \times 10^{-5}$ radians, then the results indicate that a very large initial strain of $\epsilon_o = 0.3$ percent is required. Note that many thermal blanket materials are not able to sustain such large strains without either rupturing or creeping excessively. Even if such high strain were tolerable, additional serious problems are created for the sunshade support struts which must be designed to withstand very large forces. In particular, the results indicate that a peak supports. Clearly, if high pointing accuracy is needed, the supporting truss in the shroud must be more closely spaced so as meeting the performance objectives associated with very high pointing accuracies. In such cases, use of appropriate active to reduce the unsupported length of the blanket. Indeed, passive structural design of the sunshade may not be capable of control techniques must be explored

Experiences in Integrated Control/Structure/Optics Design Optimization

Matt Wette, Mark Milman Jet Propulsion Laboratory, Caltech

> Dave Redding Charles Draper Laboratory (currently on site at JPL)

Fourth NASA/DOD Control/Structures Interaction (CSI) Technology Conference November 5-7, 1990 Orlando, Florida

M. Wette, M. Milman, D. Redding: Experiences in Integrated Structure/Optics/Control Design Optimization

Increasingly complex spacecraft will benefit from integrated design and optimization of structural, optical, and control subsystems, allowing designers to make tradeoffs in objectives and constraints across these subsystems. For example, structural element stiffness could be traded off against telescope focal ratio and control actuator size to minimize mass while meeting optical wavefront quality and pointing stability performance requirements.

This paper presents experiences with the development of a multiobjective optimization tool for integrated design. This technology is being developed with the intent of providing an environment for aiding initial design trade studies. A description of the framework for the integrated design optimization tool is given along with a brief overview of the theory developed for the multiobjective optimization approach. This framework and theory is then used as a basis for the generation of a software tool for design of controlled hub-truss structures with attached optical elements, as a simple illustration. Experience and insights gained with this tool on a few example problems is discussed along with projections of required future efforts.



- Objectives and Requirements
- Framework
- Theory
- Algorithms and Software
- Examples
- Conclusions and Future Directions

M. Wette, M. Milman, D. Radding: Experiences in Integrated Structure/Optics/Control Design Optimization

In this talk we will cover objectives of the design tool and requirements for the development of the tool. We will then provide a framework for solution of the associated optimization problems. This will be followed by brief review of the theory and strategy used. Then we will overview the algorithms and software which make up the design tool. This will be followed by examples. Finally, we will conclude with a discussion of possible further work.

Objectives and Requirements

- Objective:
 - Develop tools for studying tradeoffs in early stages of advanced spacecraft design.
 - Use multiobjective optimization to get idea of "best" designs.
- Requires interdisciplinary approach:
 - Structures
 - Optics
 - Control
 - Optimization
- Requires several development phases:
 - Framework
 - Theory
 - Algorithms
 - Software
 - Experience

M. Wette, M. Milman, D. Redding: Experiences in Integrated Structure/Optics/Control Design Optimization

The object of this work is to provide a tool for the design of spacecraft systems during early phases of flight projects when the consideration of tradeoffs becomes important under tight cost and performance requirements. This problem will be approached using multiobjective optimization, allowing designers to study behavior of optimal design under conflicting design objectives.

The development of such a tool requires incorporation or development of tools for structural design, optical system design, control system design as well as optimization.

The development of tools for such a capability requires the formulation of the problem in a clean way, the development of theory to provide solid ground for the solution of the problems, the algorithms and software to provide a reliable implementation of a design tool, and experience to provide guidelines and insight into design.

Framework

• Structure Modeling:

• $M(\alpha)\ddot{z} + F(\alpha)\dot{z} + K(\alpha)z = G_1(\alpha)u + G_2(\alpha)\dot{u}, \quad y = H_1(\alpha)z + H_2(\alpha)\dot{z}$

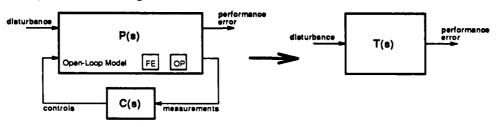
• gradient: $\frac{\partial M}{\partial \alpha}$, $\frac{\partial F}{\partial \alpha}$, $\frac{\partial K}{\partial \alpha}$, $\frac{\partial G_1}{\partial \alpha}$, $\frac{\partial G_2}{\partial \alpha}$, $\frac{\partial H_1}{\partial \alpha}$, $\frac{\partial H_2}{\partial \alpha}$

• Optics Modeling:

• $e = C_{\alpha}z$

• gradient: $\frac{\partial C_{\alpha}}{\partial \alpha}$

• Control System Modeling:



M. Wette, M. Milman, D. Redding: Experiences in Integrated Structure/Optics/Control Design Optimization

In our development of the system, we assume that we can generate parameterized linear second order structure models whose coefficient matrices are smooth functions of the parameters. We also assume that the analytic gradients can be computed in an efficient manner. This imposes some careful thought, for example, in the production of reduced order models. The production of reduced order models becomes a requirement for complex systems modeled by finite element models.

We assume that an optics model is available which provides measurement and performance output as a function of optical element motions. Parameterizations of the model are assumed smooth and that the models and thier gradients can be calcu-

lated with reasonable efficiency.

In our framework a linear feedback control system appears as in the figure on the left. This framework is a "linear fractional" one and provides us a clean, flexible design environment. For example, the framework allows inclusion of tracking and bandwidth requirements. The transfer functions are all multi-input multi-output and the signals are vector-valued. C(s) is the controller which maps measurement signals to control signals, P(s) is a transfer function which is constructed as an interconnection of models for the spacecraft structure, the optical elements, any sensors or actuators, and performance-motivated weighting functions. Inputs to P(s) consist of disturbances, additive noise and control signals. Outputs from P(s) consist of performance-motivated error signals (which must include some form of control effort measure), as well as the measurements. When a controller is placed in the system the resulting transfer function T(s) provides an object with which to measure overall system performance.

Framework (cont'd)

- Control system modeling (cont'd)
 - Plant, P(s), and controller, C(s):

$$\begin{bmatrix} E_{\alpha}\dot{x} \\ y \\ e \end{bmatrix} = \begin{bmatrix} A_{\alpha} & B_{\alpha,1} & B_{\alpha,2} \\ C_{\alpha,1} & D_{\alpha,11} & D_{\alpha,12} \\ C_{\alpha,2} & D_{\alpha,21} & D_{\alpha,22} \end{bmatrix} \begin{bmatrix} x \\ u \\ d \end{bmatrix} \qquad \begin{bmatrix} E_{\alpha}\dot{\hat{x}} \\ u \end{bmatrix} = \begin{bmatrix} A_{C\alpha} & K_{F\alpha} \\ K_{C\alpha} & D_{\alpha,21} \end{bmatrix} \begin{bmatrix} \hat{x} \\ u \end{bmatrix}$$

- gradient: $\frac{\partial E_{\alpha}}{\partial \alpha}$, $\frac{\partial A_{\alpha}}{\partial \alpha}$, $\frac{\partial B_{\alpha,1}}{\partial \alpha}$, $\frac{\partial B_{\alpha,2}}{\partial \alpha}$, $\frac{\partial C_{\alpha,1}}{\partial \alpha}$, $\frac{\partial C_{\alpha,2}}{\partial \alpha}$, $\frac{\partial D_{\alpha,11}}{\partial \alpha}$, ..., $\frac{\partial D_{\alpha,22}}{\partial \alpha}$
- Wish to minimize
 - structure mass and open-loop dynamic response

$$J_{st}(\alpha) = W_{mas} \cdot \mathbf{M} + W_{dyn} \cdot ||P_{11}(s)||_2^2$$

• Squared H_2 -norm of T(s) (or LQG control performance index)

$$J_{co}(\alpha) = ||T(s)||_2^2$$

M. Wette, M. Milman, D. Redding: Experiences in Integrated Structure/Optics/Control Design Optimization

The plant P(s) and controller C(s) discussed on the previous page are represented as parameterized generalized (or extended) state space models. Smoothness of the underlying structure and optical system models provides an overall model whose coefficient matrices are smooth functions of the design parameters.

The advantage of the extended state-space model arises in the use of second order models which appear in structure control problems. A second order model of the form

$$M\ddot{q} + F\dot{q} + Kq = Gu$$
, $y = H_1q + H_2\dot{q}$

has an equivalent extended state space model of the form

$$\begin{bmatrix} I & 0 \\ 0 & M \end{bmatrix} \dot{x} = \begin{bmatrix} 0 & I \\ -K & -F \end{bmatrix} x + \begin{bmatrix} 0 \\ G \end{bmatrix} u, \qquad y = \begin{bmatrix} H_1 & H_2 \end{bmatrix} x$$

Note that M^{-1} does not appear in the model. Thus, this formulation allows us to avoid explicit inversion of the mass matrix and preserve sparsity in M, F, and K, a property which is lost when M^{-1} is used. The real magic is that the optimal controller, its cost, and the analytic gradient of the cost can be found without ever explicitly inverting M.

The structure mass and its rms dynamic response to external disturbances (or squared H_2 norm of the open-loop plant) form the basis for the structure cost. The squared H_2 -norm of the closed-loop system (equivalent to a corresponding LQG problem) forms the basis for the control cost. The H_2 optimal control problem provides a smooth optimization function for which gradients can be computed fairly simply (i.e., by solution of linear matrix equations).

Theory

- ullet multiobjective optimization: consider $\left[egin{array}{c} J_{st}(lpha) \ J_{co}(lpha) \end{array}
 ight]$
 - Definition: α^* is Pareto optimal if there exists no α for which both

$$J_{st}(\alpha) < J_{st}(\alpha^*)$$
 and $J_{co}(\alpha) < J_{co}(\alpha^*)$

ullet Theorem: If $lpha^*$ is Pareto optimal, then there exists $\lambda \in [0,1]$ for which

$$\left. \frac{\partial}{\partial \alpha} \left\{ (1 - \lambda) J_{st}(\alpha) + \lambda J_{co}(\alpha) \right\} \right|_{\alpha^*} = 0$$

• Strategy: search for necessary conditions on minimum of

$$J(\alpha) = (1-\lambda)J_{st}(\alpha) + \lambda J_{co}(\alpha)$$
 for $0 \le \lambda \le 1$

M. Wette, M. Milman, D. Redding: Experiences in Integrated Structure/Optics/Control Design Optimization

Our approach to design optimization in the presence of multiple conflicting objectives is to apply results from multiobjective optimization theory. Given a vector-valued objective function $J(\alpha) = \begin{bmatrix} J_1(\alpha) & J_2(\alpha) \end{bmatrix}^T$ we can induce a partial ordering of $J(\alpha)$ by defining \leq such that

$$J(\alpha) \leq J(\beta)$$
 if $J_1(\alpha) \leq J_1(\beta)$ and $J_2(\alpha) \leq J_2(\beta)$

In this ordering the parameter vector α^* is (strongly) Pareto optimal if $J(\alpha) \leq J(\alpha^*)$ implies $J(\alpha) = J(\alpha^*)$.

A necessary condition for Pareto optimality due to Lin [1] states that if α^* is Pareto optimal then there exists a vector $\begin{bmatrix} z_1 & z_2 \end{bmatrix}^T$ with $z_1, z_2 > 0$ such that $z^T \frac{\partial J}{\partial \alpha}\Big|_{\alpha^*} = 0$. This is equivalent to the condition that if α^* is Pareto optimal then there exists a $\lambda \in [0,1]$ such that

$$\frac{\partial}{\partial \alpha} \left\{ (1 - \lambda) J_1(\alpha) + \lambda J_2(\alpha) \right\} \Big|_{\alpha^*} = 0$$

This result implies that a reasonable strategy for finding Pareto optimal solutions is to search for necessary conditions for the optimal solution of the scalar objective criterion

$$\overline{J}(\alpha) = (1-\lambda)J_{st}(\alpha) + \lambda J_{co}(\alpha)$$
 for $0 \le \lambda \le 1$

[1] J. G. Lin, "Maximal vecotrs and multi-objective optimization," J. of Opt. Theory and Appl., Vol. 18, 1976, pp. 41-65

Algorithms and Software

• Program written in Fortran77:

Control-Structure-Optics program: 10K lines
ARE's, matrix op's, I/O utilities: 12K lines
Optimization library: 11K lines

Optimization

• BFGS algorithm for Quasi-Newton approach to unconstrained optimization

• ADS (Automated Design Synthesis) Fortran library

• Input file used to "tune" optimization parameters, specify range of λ , etc.

• Structure Modeling:

• Custom Fortran code to produce finite element model and gradients for hub-truss structure with added masses, Rayleigh damping

• Structure configuration from input file specifying properties, parameters limits, inputs, and outputs

• Outputs are second order model matrices and gradients

$$M\ddot{z} + F\dot{z} + Kz = G_1u + G_2\dot{u}, \quad y = H_1z + H_2\dot{z}$$

M. Wette, M. Milman, D. Redding: Experiences in Integrated Structure/Optics/Control Design Optimization

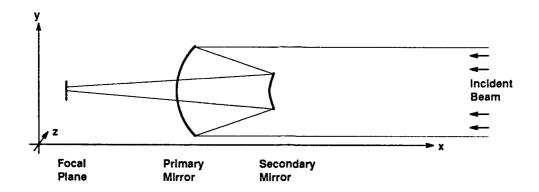
To provide the multiobjective design capability, a Fortran77 program has been written for optimization of controlled hub-truss structures with attached optical elements. About 50 routines have been written, at JPL as a part of the CSI project, for the generation of models, computation of analytic gradients, and running through the the optimization. These 50 routines constitute about 10,000 lines of code. The program makes use of additional libraries collected from past work. One library provides routines for the solution of generalized algebraic Riccati equations, generalized Lyapunov-type equations, various matrix operations as well as input-output utilities. The routines used from this library consist of about 12,000 lines of code. In addition, we make use of the ADS (Automated Design Synthesis) optimization library. This library constitutes about 11,000 lines of code.

We used the BFGS (Broyden-Fletcher-Goldfarb-Shanno) quasi-Newton method for unconstrained optimization. This algorithm is available in the ADS fortran library. An input file is used to provide the user the ability to "tune" optimization parameters, such as convergence criteria, initial step sizes and a range for the parameter λ .

The structure model is provided by a finite element subroutine which constructs a model of the system using rod elements, nonstructural masses, and a rigid body hub. Damping is assumed to be Rayleigh damping. That is, the damping matrix takes the form $F = a_0M + a_1K$ where M is the mass matrix and K is the stiffness matrix. The model is parameterized by the rod element cross-sectional areas and the nonstructural masses. The structural model is specified by the user through an input file to the program. This file specifies the grid points and connecting elements, the material properties, the parameterization for the model (with lower and upper bounds) and the model inputs and outputs. The output from the structure modeling routines is a second order model of the form shown.

Algorithms and Software (cont'd)

- Optical system modeling
 - Uses "Controlled Optics Modeling Package" (COMP)
 - Input file to specify configuration of optical elements, input motions, and output image error
 - Output is "C-matrix" and gradient (via finite difference)



M. Wette, M. Milman, D. Redding: Experiences in Integrated Structure/Optics/Control Design Optimization

The optical system modeling is accomplished by COMP (Controlled Optics Modeling Package) which is described in a companion paper. This package allows optical systems to be modelled using mirrors, lenses, focal planes, and other elements. Optical properties are established by tracing a beam through the train of optical elements. The optical system is specified through an input file to the program. The user specifies optical elements, their properties (focal length, eccentricity, location), and sets up a sample beam to trace. Also specified in the input file are input motions for the optical elements (usually resulting from motions in the structure) and output properties of the optical image at the focal point. Optical image quality is typically measured by translations and rotations of the image, and pathlength error of rays at the focal plane. Output from COMP subroutines consists of a constant matrix which maps optical element motions to these measures of image quality.

Algorithms and Software (cont'd)

- Control system modeling
 - Input file to specify control and disturbance inputs, performance error and measurement outputs, and connections with structure and optics models
 - Output is generalized state space model
- H2 (equiv. LQG) optimal controller and cost
 - ullet QZ with ordering (or real Schur) method to solve generalized algebraic Riccati equation, providing H_2 cost

$$A^{T}XE + E^{T}XA - E^{T}XBR^{-1}B^{T}XE + C_{2}^{T}C_{2} = 0$$

ullet Bartels-Stewart-type algorithm to solve generalized Lyapunov equation to get gradient of H_2 controller and cost

$$A_c^T \frac{\partial X}{\partial \alpha_i} E + E^T \frac{\partial X}{\partial \alpha_i} A_c + \frac{\partial A^T}{\partial \alpha_i} X E + \dots = 0$$

M. Wette, M. Milman, D. Redding: Experiences in Integrated Structure/Optics/Control Design Optimization

The control system model is constructed with the structure and optical system models are specified with an input file to the program. In this file the user specifies control and disturbance inputs to the open-loop system performance and measured outputs from the open-loop system and connections between these inputs, outputs, and the inputs and outputs of the structure model and the optical system model. The output from the system modeling routine is an extended state space model as described in a previous slide. Other routines are provided to generate the analytic gradients of the open-loop and closed-loop models.

The optimal control cost and its gradient are computed through solution of generalized algebraic Riccati equations (GAREs) shown in the slide. The associated cost is given by

$$||T(s)||_2^2 = \operatorname{trace}(B_2^T X_2^B) + \operatorname{trace}(D_{21} K_c Y K_c^T D_{21}^T)$$

where K_c is the state feedback gain and Y is the solution to the filtering GARE. The GARE solvers use eigenstructure type techniques based on the Schur method for the regular ARE but make use of the QZ generalized eigenvalue algorithms along with software for ordering eigenvalues in the generalized Schur form. The software also provide routines for Newton iteration to refine the Riccati solutions and routines to compute the optimal feedback gains and controllers. The gradient of the H_2 optimal control cost is computed through solution of generalized Lyapunov-type equations. These solvers use the QZ algorithm along with a Bartels-Stewart-type backsolver.

Examples dieturbance truss hub Incident Beam Secondary Focal Primary Plane Mirror Mirro: P(s) OP FE performance disturbance

M. Wette, M. Milman, D. Redding: Experiences in Integrated Structure/Optics/Control Design Optimization

10

To check out the design tool and gain some experience with it we have run through a few design examples. The system we are working with is a controlled hub-truss with attached primary and secondary mirrors. The control effort is a torque on the hub. The system is subjected to a disturbance at the end of the truss. Measurements for the control system consist of the hub angular position and rate and the structure tip position and rate. These measurements are corrupted by additive white noise. The truss is equipped with a primary mirror on the end of the first bay and a secondary mirror mounted on the end of the second bay. The performance of the system is measured by the pathlength error of eight rays from the incident beam. The parameters for the optimization were cross sectional areas of the struts.

controls

C(s)

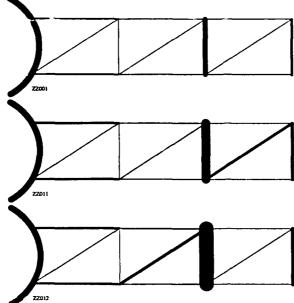
Currently we are working on a new case where an additional parameter is the aperture of the primary mirror. The aperture of the secondary mirror varies with that of the first mirror to make the clear aperture constant. That is, the area of light striking the primary mirror is constrained to be constant.

The problem is set up by creating files for specifying the layout and parameterization of the structure and optical system models. The interconnection of these subsystems and the layout of the control system is specified through another file. The control system layout of this particular model is shown in the lower figure.

In running cases of the above problem we found that wide variations in the parameter sometimes resulted in ill-conditioned forms of the filtering algebraic Riccati equation. One workaround for this problem was to bypass the filtering Riccati equation and use LQR (i.e., full state feedback) control instead of H_2 or LQG control. The results shown in the following slides reflect results from LQR runs. We feel that addition of a model reduction capability will provide more reliable solutions to the design equations.

Examples (cont'd)

•
$$R = 10^{-4}$$
, $\lambda = \frac{\zeta}{1+\zeta}$



$$\zeta=10^8$$

M. Wette, M. Milman, D. Redding: Experiences in Integrated Structure/Optics/Control Design Optimization

For these examples the structure mass was used as the structure cost and the LQR performance index was used as the control cost. For this case the optimization objective takes the form $J(\alpha) = (1-\lambda)J_{st}(\alpha) + \lambda J_{co}(\alpha)$.

 $\zeta = 10^6$

 $\zeta = 10^7$

To see variations in the λ we reparameterized the optimization with respect to a new parameter ζ where λ is given in terms of ζ by the expression shown. Running these with the optimization tool provided the Pareto optimal solutions displayed in the above slide. The following table provides values for the corresponding mass, rms control torque, and rms wavefront error: m mmmm

| | total mass | control torque | wavefront error |
|------------------|---------------|---------------------|---------------------|
| $\zeta = 10^6$ | 75.5 | $6.7\cdot 10^{-3}$ | $5.6 \cdot 10^{-3}$ |
| $\zeta = 10^7$ | 226 | $1.6 \cdot 10^{-3}$ | $1.8 \cdot 10^{-3}$ |
| $\zeta = 10^{8}$ | 555 | $1.3 \cdot 10^{-4}$ | $8.3 \cdot 10^{-4}$ |

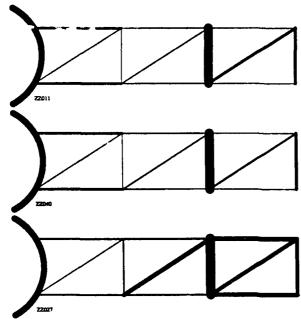
We should also mention that for the top design the optimal control cost is about 10% of a structure with the same mass, but all struts of equal cross sectional area.

For $\lambda=0$ ($\zeta=0$) the strut areas are at their lower limit. If ζ is increased to 10^6 two of the struts are made heavier. We consider this case to still be dominated by the mass cost. It seems as if the end strut has been made heavier to resist the external disturbance and the strut on the second bay has been made heavier to sturdy the secondary mirror. When ζ is increased to 10^7 more mass is added to the entire structure in general. The struts near the hub become stiffer and the diagonal strut between the secondary mirror and the truss end becomes stiffer. Finally, if ζ is still increased to 10^8 the strut on which the secondary mirror sits becomes quite heavy.

The overall effect here seems to suggest that the control is not effective in stabilizing the secondary mirror and that mass must be added to its support strut to isolate disturbances from the truss end.

Examples (cont'd)

• $\zeta = 10^7$



$$R = 10^{-4}$$

$$R = 1$$

$$R = \infty$$

M.Wette, M.Milman, D.Redding: Experiences in Integrated Structure/Optics/Control Design Optimisation

1:

This set of diagrams shows the effect of changing the weight on the control energy in the H_2 control cost. We show the control weighting R for the equivalent LQG problem. The following table shows total mass, rms control effort and rms wavefront error:

| | total | control | wavefront |
|---------------|-------|---------------------|---------------------|
| | mass | torque | error |
| $R = 10^{-4}$ | 226 | $1.6 \cdot 10^{-3}$ | $1.8 \cdot 10^{-3}$ |
| R = 1 | 235 | $1.9 \cdot 10^{-7}$ | $1.8 \cdot 10^{-3}$ |
| $R = \infty$ | 555 | 0 | $2.8 \cdot 10^{-3}$ |

The above can be considered as Pareto optimal solutions to a three objective (mass, rms control effort, rms wavefront error) problem. The effect we see is that there exists a strong tradeoff between control effort and mass with little influence on performance (wavefront error). Thus, we conclude that significant improvement in performance may be achieved only by adding both mass and control effort.

Conclusions and Future Work

Conclusions

- Developed design tool for controlled structured with attached optical elements
- Studies show sensitivities in the design parameters to differing emphasis on different design objectives
- Experience show some wide variations in parameters can lead to ill-conditioned Riccati equations.

Future Work

- Additional experience with optimization of optical parameters
- Use of reduced order models
- Addition of robustness objective
- Apply tool to CSI Phase B truss experiment

M. Wette, M. Milman, D. Redding: Experiences in Integrated Structure/Optics/Control Design Optimization

In conclusion, we have presented an overview of a new tool for integrated design of controlled structures with attached optics. We have shown some design examples which show a sensitivity in design parameters to changes in the weight on design objectives. In addition, in the solution of these problems we have experienced some problems in the solution of certian of the Riccati equations associated with the optimization problem. Further study has shown that under certain circumstances the associated Riccati equations become very ill-conditioned. Scaling of the system equations has shown to be effective in solution of some of these problems, but not a overall cure. We feel that the addition of model order reduction techniques will provide better performance.

Several directions exist for future work. We have implemented a robust objectives and are in the process of developing model order reduction techniques for use in optimization. In addition, current plans include the application of the design tool to an experimental facility at JPL, the CSI Phase B truss.

COMBINED CONTROL/STRUCTURE/OPTICS OPTIMIZATION:

ANALYSIS AND MATHEMATICAL METHODS

Mark Milman

Moktar Salama

Robert Scheid

Jet Propulsion Laboratory

California Institute of Technology

Pasadena, California

4th NASA/DoD Control/Structures

Interaction Technology Conference

Orlando, Florida

November 5-7, 1990

coordinated multidisciplinary effort to design and integrate the various optical, structural and control elements of the system. The need for multidisciplinary integration of design arises partly because of the competing goals and resources that impact design decisions. As an example of this consider the simple system depicted on the opposite page. The primary objective is to minimize the wavefront error at the focal plane. However, to accomplish this goal there are several competing objectives The problem of designing large space structures to support future large telescopes or interferometers will require a tightly such as the minimization of power consumption and total spaceraft mass that must also be factored into the design.

choice of structure parameters, control element locations and gains. Our objective is to develop tools to optimize measures It is evident that many variables contribute to the design of the system, ranging from system topology to the the of performance with respect to these variables with an emphasis toward impacting the early design phase of the integrated system development. Correspondingly, our focus is not on detailed point design, but on the generation of a family of optimized designs to enable trade studies covering a spectrum of the design space.

PROBLEM OVERVIEW

GOALS

- -Minimize wavefront error at focal plane
- -Minimize total mass of system
- -Minimize power consumption
- -Others (e.g., max stress constraints, etc.)

DESIGN VARIABLES

- -System topology (number of bays, geometry,...)
- -Structure parameters, control gains, optical design variables ("smooth" problems)
- -Placement of elements (actuators, sensors, dampers,...)

multidisciplinary design. The general approach to this problem is to begin with a dynamical system defined by a finite element model with mass, stiffness, and damping matrices dependent on a vector of design parameters a, and a known disturbance (and/or initial condition). The problem is to determine a control input function $u(\cdot)$ from a class of admissible controllers and a design variable a to minimize certain objective functionals that reflect system performance (e.g., wavefront In recent years a number of papers have appeared in the area of combined optimization to address the problem of quality, total system mass), while maintaining constraints that are imposed on the system (e.g., maximal deformations, mininal eigenvalues, maximum stresses in members, etc.).

to the closed loop as opposed to performing an open loop optimization followed by the control design. The approach in [6] is LQR cost as the control objective. Hale recognizes the potential use of the convexity of the structure cost and the value of varying the weights between the objectives, although he does not pursue these ideas. In [10] an LQG performance index reflecting line-of-sight pointing error as a function of structural member thickness is minimized with respect to a total mass constraint. These studies demonstrate the improved performance attained by optimizing structure parameters with respect to the approach we have taken. Hale and Salama appear to be the first to use an additive combination of structural and control objectives in the optimization cost functional. Both papers use total system mass as the structure objective and an most extensive in that the design variables include structural parameters, actuator locations and the feedback gain matrix. Constraints are imposed in the form of closed loop eigenvalue locations and scusitivities, and structure constraints. Since all Among the combined optimization papers that have appeared, the papers [2], [6], [10], [12] are probably closest in spirit the constraints cannot be simultaneously satisfied, a homotopy approach is used to relax them.

Physical Process (FEM Model): $M(a) \vec{r} + D(a)\vec{r} + K(a) \vec{r} = G_1 u + G_2 d \qquad (4)$ Design Variables: $A(a) \vec{r} + D(a)\vec{r} + K(a)\vec{r} = G_1 u + G_2 d \qquad (5)$ Design Variables: $a \in R^1, u(\cdot) \in \text{Admissible class of controllers}$ Objective Functionals: $J_1(a, u(\cdot), r(\cdot), \vec{r}(\cdot)), J_2(a, u(\cdot), r(\cdot), \vec{r}(\cdot)), \dots$ Constraints: $H(a, u(\cdot), r(\cdot), \vec{r}(\cdot)) \geq 0, \quad G(a, u(\cdot), r(\cdot), \vec{r}(\cdot)) = 0$ Basic problem statement: $\min_{a \in R} J_1(a, u(\cdot), r(\cdot), \vec{r}(\cdot)) = 0$ (**)

 H_2 control cost criteria. The rationale behind the choice of the H_2 formulation stems from the fact that the formulation is rich enough to capture significant problem features, such as partially observed states, disturbance spectra, and bandwidth The approach we have chosen for the combined optimization problem is based on a vector optimization formulation with considerations, while at the same time retains relative computational simplicity.

it is assumed that the structure objective is a convex, coercive function of the design variable a, and the control cost is an LQR cost, i.e., we are assuming full state feedback. In accordance with the objective of determining a family of design On the facing page we show the problem setup in a simplified situation involving just two objective functionals. Here options, we seek Pareto optimal solutions to the optimization problem. That is we wish to find the set $\{\alpha * : J_s(\alpha) \le J_s(\alpha *) \}$ and $J_c(\alpha) \leq J_c(\alpha*)$ implies $J_s(\alpha) = J_s(\alpha*), J_c(\alpha) = J_c(\alpha*)$. The standard necessary conditions for Pareto optimality interpreted for this bi-objective problem is the vanishing of $\nabla_{\alpha}J_{\lambda}$ [13]. Thus our goal is to solve

$$\nabla_{\alpha}J_{\lambda}(\alpha)=0, \qquad \lambda \in [0,1].$$

The basic strategy we adopt is straightforward: Given the solution at a value λ_0 , smoothly propagate it to a new solution at $\lambda_0 + \Delta \lambda$. The process is initialized by determing the global minimum of J_s . Then to insure a smooth propagation of solutions, we assume that the mappings $\alpha \to A, B, Q, R$ are all smooth.

MULTIOBJECTIVE H_2 APPROACH (Simplified Setup)

First Orc'er Form:

$$\dot{x} = A(\alpha)x + B(\alpha)u$$

$$A = \begin{pmatrix} 0 & I \\ -M^{-1}K & -M^{-1}D \end{pmatrix}, B = \begin{pmatrix} 0 \\ M^{-1}G_1 \end{pmatrix}$$

Problem: Find stationary values of

$$J_{\lambda} = (1 - \lambda)J_{s}(\alpha) + \lambda J_{c}(\alpha); \qquad \lambda \in [0, 1]$$

 $J_s(\alpha)=$ convex, coercive (e.g. total mass, quadratic form on a priori design)

 $J_c(\alpha) = LQR \cos t$,

$$J_c=min_{u(\cdot)}\int_0^\infty < x, Qx>+< u, Ru>dt$$

set of Riccati equations, Lyapunov equations, and gradient equations. The term Vie reflects averaging the LQR cost over a positive definite matrices, and Σ is the space of symmetric matrices. Thus the zeros of H correspond to the zeros of a coupled denotes the domain of the homotopy parameter λ , R^{n_r} is the domain of the design variable α , Σ_+ denotes the space of It can be shown that the stationary conditions are the zeros of the function H defined on the facing page. Here [0,1] set of initial conditions.

using standard analytical, geometric and algebraic techniques. An important feature that emerges from this analysis is that in a certain generic sense the set of Pareto optimal solutions are contained in a finite collection of smooth curves in the larger n,-dimensional design space. Thus the Pareto solutions constitute only a "small" subset of the design space, and the much What is of interest now is the structure of the solution set $H(\lambda,x)=0$. In the next few slides we will analyze this set arger complementary set of values of the parameter α lead to inferior designs.

STATIONARY CONDITIONS

Stationary conditions are the zeros of the function $H:[0,1]\times R^{n_p}\times \Sigma_+\times \Sigma_+\to$

$$H(\lambda, \alpha, Z, P) = \begin{bmatrix} H_1(\lambda, \alpha, Z, P) \\ H_2(\lambda, \alpha, Z, P) \end{bmatrix},$$

$$H_1 = (1 - \lambda) \frac{\partial J_s(\alpha)}{\partial \alpha_i} + 2\lambda tr(ZP \frac{\partial A}{\partial \alpha_i})$$

$$H_2 = A_c Z + ZA_c^T + V_{ic}; \qquad A_c = A - BR^{-1}E^TP$$

$$H_3 = A^TP + PA + Q - PBR^{-1}B^TP$$

QUESTION: What can be said about the solution set $H(\lambda, x) = 0$?

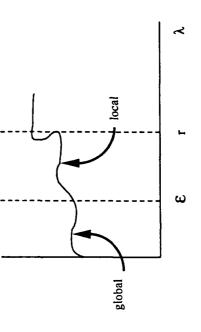
The two propositions on the opposing page describe the solution curve emanating from the minimum of the structure objective functional J_s at $\lambda = 0$. Both of these results rely on the implicit function theorem to generate a smooth solution path that is parameterized by λ . The first result asserts that in a neighborhood of $\lambda=0$ the solution path is actually a increasing values of λ , the path is guaranteed to remain at least locally optimal for J_{λ} . We will see later an interesting result global minimum of J_{λ} . The second result states that so long as the solution path can be continued to be parameterized by concerning the behavior of paths when there is a "fold" in λ , i.e. a value where the curve begins to move in a negative λ

LOCAL SOLUTIONS

PROPOSITION 1. For ϵ sufficiently small there exists a unique global solution to the optimization problem

$$min_{\alpha}J_{\lambda}(\alpha) = (1-\lambda)J_{s}(\alpha) + \lambda tr(P(\alpha)V_{ic})$$

for all $\lambda < \epsilon$.



PROPOSITION 2. If $det\{\frac{\partial H(\lambda,x(\lambda))}{\partial \lambda}\}$ is nonzero for $\lambda \in [0,r]$ then $\alpha(\lambda)$ is a local minimum for J_{λ} for all $\lambda \in [0, r]$.

known value at λ_0 to a new value at λ_1 is given on the opposite page. We have implemented this scheme in a simple combined optimization problem involving a flexible beam attached to a rotating hub [14]. When compared to solutions obtained using Assuming that the solution path can be parameterized by λ , an efficient path following scheme consisting of a tangent predictor step followed by a Newton correction step can implemented. The iteration scheme of advancing the solution from a the ADS (Automated Design Synthesis) program with the BFGS option (which included analytically determined gradients), an approximate ten-fold speedup was observed in convergence when both methods were started with the same initial conditions.

FOLLOWING THE OPTIMALITY PATH (invertibility of $\partial H/\partial x$)

 $\lambda \to x(\lambda)$ smooth and $H(\lambda, x(\lambda)) = 0$ implies

$$x'(\lambda) = -(\frac{\partial H}{\partial x})^{-1}(\frac{\partial H}{\partial \lambda})$$

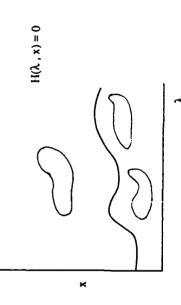
• Implemented Newton Predictor-Corrector Scheme:

$$x^{0}(\lambda_{1}) = x(\lambda_{0}) - (\lambda_{1} - \lambda_{0}) \left[\frac{\partial H(\lambda_{0}, x(\lambda_{0}))}{\partial x} \right]^{-1} \frac{\partial H(\lambda_{0}, x(\lambda_{0}))}{\partial \lambda}$$
$$x^{k+1}(\lambda_{1}) = x^{k}(\lambda_{1}) - \left[\frac{\partial H(\lambda_{1}, x^{k}(\lambda_{1}))}{\partial x} \right]^{-1} H(\lambda_{1}, x^{k}(\lambda_{1}))$$

ullet Newton scheme results in approximately $10\times$ speedup over BFGS optimization using same starting values and analytical gradients The Newton path following scheme requires that the solution curve be parameterized by A. This is not always the case, and the Newton approach may fail. However, a somewhat more general path following technique utilizing an arclength parameterization can be shown to be generically applicable for the combined optimization problem. (The precise meaning of this can be found in [8].) In this reference it is shown that "with probablity one" the zero set of H is a smooth onedimensional manifold, as shown on the opposing page. That is, the zero set is comprised of smooth non-intersecting curves, each of which is diffeomorphic to either a circle or the real line. Using results from algebraic geometry (making use of the fact that the H₂ formulation leads to Lyapunov and Riccati equations that may be interpreted as a set of algebraic equations), it can be shown that there are only a finite number of these curves and that none of them can become unbounded in a closed λ-interval contained in [0,1). Also, the regularity of the solution set can be used to obtain a stability result which states that small perturbations in the problem data lead to small perturbations of the solution set [9].

When using the more general path following technique, an algebraic differential equation determines the evolution of $x(\lambda)$ as opposed to the differential equation shown in the previous slide which is applicable only when $\partial H/\partial x$ is invertible.

GENERIC SITUATION



THEOREM. Let $\epsilon>0$, and suppose M, K, and D are polynomials in α . If H(0,x)=0 has a unique solution x_* , then

- (i) $H^{-1}(0)$ contains only finitely many connected components
- (ii) Each component is bounded for $\lambda < 1 \epsilon$
- (iii) The solution curve containing x* can be continued for $\lambda < 1$
- (iv) The solution set is stable with respect to perturbations in H

There are a number of challenging topics to pursue in this area, and four very natural extensions are outlined on the opposite page. The first two of these will be discussed in subsequent slides. In this paragraph we will briefly touch upon some possibilities for the latter two.

example of this can be found in [9].) Thus there is practical value in locating other components of $H^{-1}(0)$. One approach is to find new local minima for a fixed value of λ (and hence, locate a new solution path) by varying initial conditions. Other A very interesting result due to Henderson and Keller [4] shows that folds and isola centers (corresponding to where the λ parameterization ceases to be strictly increasing) result in complex bifurcations that lead to new real solution paths. The possible for optimal solutions to lie on curves other than the principal curve emanating from $\lambda = 0$ (cf. previous slide). (An As we noted earlier, for the bi-objective problem, the Pareto optima are contained within the zero set of H. It is indeed alternatives include deflating out the current solution, or to employ a global Newton method [5] that locates multiple zeros. extent to which this phenomenon may be exploited remains to be investigated.

Our discussions thus far have concerned bi-objective problems. Extending the approach to more objectives requires some manifold for the solution set. A simple natural extension in this case is just to follow a number of one dimensional paths to continuation methods to determine a simplicial triangulation of the manifold. These methods generate a multidimensional modification of these ideas. Assuming certain regularity conditions, a p- objective problem would yield a p-1 dimensional reconstruct the optimality surface. Another approach due to Allgower and Schmidt [1], and Rheinboldt [11] uses simplicial grid of the solution space, which may have some computational advantages over the one dimensional curve following approach.

FURTHER QUESTIONS AND ISSUES

- -Maintaining computational efficiency for large order problems
- -Extending results to problems with constraints
- -Finding other zero curves for generating Pareto optima
- -Extending results to problems with greater than two objectives

One of the major numerical bottlenecks in the combined optimization problem is the evaluation of the cost functional and its sensitivity. These calculations require solving Riccati and Lyapunov equations on the order of twice the number of degrees of freedom of the system. For relatively small problems it is possible to retain the full mass and stiffness matrices in the model, and still efficiently carry out these computations. However, the situation degrades considerably for larger systems, and some sort of model reduction is necessary.

The desirable attributes of a reducing transformation $I(\alpha)$ for this problem are summarized on the facing page. Firstly, loop sense). And secondly, because optimization efficiency is enhanced by the use of analytical gradients, we require that for accurate approximation of the cost functional, a good approximation of the full system is required (especially in the closed $T'(\alpha)$ be easily computed to reduce the overhead in computing approximate cost sensitivies.

MODEL REDUCTION FOR THE COMBINED OPTIMIZATION PROBLEM

Problem Statement: Given $M(\alpha),K(\alpha),D(\alpha)\in R^{n\times n}$, find family of transformations

 $T(\alpha): R^{n_r} \to R^n, \quad n_r << n$

such that:

(i) The transfer function $G_T=CT(s^2M_r+sD_r+K_r)^{-1}T^tB$ is a "good approximation" to $C(s^2M+sD+K)^{-1}B$ where

$$M_{\tau} = T^{t}(\alpha)M(\alpha)T(\alpha), \qquad K_{\tau} = T^{t}(\alpha)K(\alpha)T(\alpha)$$

(ii) $T(\alpha)$ and $T'(\alpha)$ are easily computed

One way of achieving the attributes described in the previous slide in a neighborhood of a nominal parameter value is by modal truncation, where the modes that are retained contribute most to the nominal transfer function. The resulting Ritz transformation should perform well in a small neighborhood of this value. Furthermore since this transformation is independent of a it certainly satisfies the desired attribute of having an easily computed derivative. An obvious extension of this transformation is to introduce a first order correction term in terms of the derivatives of the eigenvectors about the

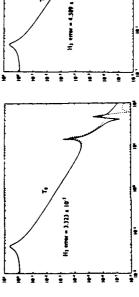
first order correction term. Significant improvement is clearly observed, and this improvement is quantified by the respective The plots contained on the facing page are indicative of the kind of improvement that is attained by including the first order correction term in the reducing transformation. In these plots we extracted the first three modes of a nominal nine-mode model of a planar two bay hub-truss system. These modes were used to develop the constant Ritz transformation T_0 and the first order correction transformation $T(\alpha) = T_0 + T_1(\alpha - \alpha_0)$, where T_1 is formed from the derivatives of the extracted eigenvectors. The design vector α consists of eight components each representing the cross-sectional area of a given rod element of the truss. In the nominal model all of these parameters were set to unity. In the plots that are shown a new full order model was developed by setting the values of the longerons of the first and second bays to 2.0, the first bay diagonal to 4.0, the second bay diagonal to 2.0, the first bay vertical to 7.0, and the second bay vertical to 4.0. The figure on the left contrasts the full transfer function of this perturbed model with the one obtained via the Ritz reduction T_0 . The figure on the right contrasts this same full order transfer function with the reduced order transfer function incorporating the H₂ transfer function error achieved by each of these reductions. Similar good results have been obtained in closed loop

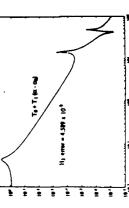
PARAMETERIZED MODEL REDUCTION SOLUTION APPROACH

 $T_0 = \text{matrix consisting of } n_r \text{ selected eigenvectors of nominal system } (M^{-1}(\alpha_r)K(\alpha_r)).$

 $T_1 = linear$ map of selected eigenvector derivatives at α_0







Lyapunov equations; equations in the same spirit as in the unconstrained problem. However, the generic topology of the zero sign of a Lagrange multiplier (this leads to a bifurcation [5]), and of course violation of the constraints. A number of articles The situation becomes somewhat more complicated when inequality constraints are introduced. Consider for example the case when maximal rms strain energy in selected members is imposed. These constraints can be generated by solving set of necessary conditions is much different in the constrained case. Although each subset of active constraints can again be shown to "generically" lead to a one-dimensional manifold of solutions, in the constrained setting the Pareto optima are now found to lie in the union of all subsets of constraints. However, since the union of one-dimensional manifolds is not necessarily a manifold, the possibility of intersecting curves corresponding to constraints becoming active/inactive arises. Several "nonthese intersections -loss of strict complementarity (an active constraint with zero associated Lagrange multiplier), a change in deal with the smoothness of parameterized Kuhn-Tucker curves, the numerical aspects of following these curves through smooth" things can happen when curves intersect nontangentially, and there are various indicators that can be used to detect oifurcation points, and applications to optimization problems [4], [7], [15].

INEQUALITY CONSTRAINTS (STRAIN ENERGY EXAMPLE)

- Include inequality constraints: $h_i(Z) \ge 0$; $h_i = \gamma_i tr(ZE_i)$
- K. T. Conditions

 $H(\lambda, \mu, x) = 0, \quad \mu_i h_i = 0, \quad \mu_i \ge 0$

GENERIC SITUATION

-Optima contained in union of 1-dim'l manifolds generated by power set of active constraints -At intersections constraints become active/inactive, lose strict complementarity;

-Change in sign of μ_i implies bifurcation

SUMMARY

- -Established optimization framework for multidisciplinary design
- -Investigated mathematical aspects of resulting bi-objective optimization problem
- -Developed and implemented efficient numerical schemes for solving bi-objective optimization problem
- -Defined future areas of research

References

- 1. E. L. Allgower, P. H. Schmidt, An algorithm for piecewise-linear approximation of an implicitly defined manifold, SIAM J. Numer. Anal., 22, (1985), pp. 322-346.
- 2. A. L. Hale, R. J. Liskowki, W. E. Dahl, Optimal simultaneous structural and control design of maneuvering spacecraft, AIAA J. Guid. 8, (1985), pp. 86-93.
- 3. M. E. Henderson, H. B. Keller, Complex bifurcation from real paths, SIAM J. Appl. Math., 50, (1990), pp. 460-482.
- 4. H. Th. Jongen, P. Jonker, F. Twilt, One-parameter families of optimization problems: Equality constraints, J. Opt. Theory and Appl., 48, (1986), pp. 141-161.
- 5. H. B. Keller, "Lectures on Numerical Methods in Bifurcation Problems," Springer-Verlag, Berlin, 1987.
- 6. K. B. Lim, J. L. Junkins, Robustness optimization of structural and controller parameters, AIAA J. Guid., Contr. and Dynamics, 12, (1989), pp. 89-96.
- 7. B. N. Lundberg, A. B. Poore, Bifurcations and sensitivity in parametric nonlinear programming, in Third Air Force/NASA Symposium on Recent Advances in Multidisciplinary Analysis and Optimization, Sept. 24-26, 1990, San Francisco, CA.
- 8. M. Milman, M. Salama, R.E. Scheid, R. Bruno, J. S. Gibson, Combined control-structure optimization, J. Comp. Mech.,
- 9. M. Milman, M. Salama, R. E. Scheid, R. Bruno, J. S. Gibson, "Integrated Control-Structure Design: A Multiobjective Approach", JPL D-6767, January, 1990.
- 10. S. K. Morrison, Y. Ye, C. F. Gregory, Jr., R. Kosut, M. E. Regelbrugge, Integrated structural/controller optimization for large space structures, AIAA Guid. and Contr. Conf., Minneapolis, MN, 1988.
- 11. W. C. Rheinboldt, On the computation of multi-dimensional solution manifolds of parameterized equations, Numer. Math., 53, (1988), pp. 165-181.
- 12. M. Salama, M. Hamidi, L. Demsetz, Optimization of controlled structures, JPL Workshop on Identification and Control of Flexible Space Structures, 1984, pp. 311-327.

- 13. Y. Sawaragi, H. Nakayama, T. Tanino, "Theory of Multiobjective Optimization", Academic Press, New York, 1985.
- 14. R. E. Scheid, M. Milman, M. Salama, A homotopy approach for combined control-structure optimization: Constructive analysis and munerical examples, 28th Aerospace Sciences Meeting, Jan. 8-11, 1990, Reno, Nevada.
- 15. Y. S. Shin, R. T. Haftka, L. T. Watson, R. H. Plaut, Tracing structural optima as a function of available resources by a homotopy method, Computer Methods in Appl. Mech. and Eng., 70, (1988), pp. 151-164.

Optimal Simultaneous Control and Structure Design With Discrete Structural Parameters

Scot K. Morrison

Ywh-Pyng Harn

Robert L. Kosut *†

September 13, 1990

Abstract The problem addressed is the development of optimization-based design tools for simultaneous control and structure design. Due to practical considerations, the structure design parameters are to be chosen from a discrete set.

1 Introduction

Many envisioned missions for large space structures (LSS) must satisfy stringent performance demands and will thus require feedback control. These performance requirements may be more effectively achieved by integrating the structural design with the control design to accrue significant performance benefits with less costly controller hardware, e.g., actuators, sensors, computers, etc. Therefore, for the development of large space structures, it becomes apparent that control and structural interaction (CSI) is of primary importance to achieving the desired performance requirements. One approach to this problem is to combine the controller and structural design using optimization techniques. This allows a great deal of flexibility in the tradeoff between design features, such as weight and power requirements, entirely through cost function selection. Research has been conducted in the area of combined controller and structural design, e.g. [4], [5]. The book chapter [1] contains an excellent bibliography. Typically, both the controller gains and structural parameters are allowed to vary continuously over some specified range. Although the controller design parameters can vary continuously, it is not feasible to construct a structure where the members have arbitrary physical dimensions. Structural elements are restricted to a finite discrete set.

In this paper, we present an optimization-based control/structure design methodology for LSS with the structural elements selected from some predefined set of available elements. Our approach is to use the branch-and-bound optimization technique [7] combined with the linear quadratic gaussian (LQG) design technique, or \mathcal{H}_2 -design, to solve the optimal control/structure design problem. The controller design could have been accomplished with other techniques without loss of generality or gain of difficulty, e.g., \mathcal{H}_{∞} -design.

Other approaches dealing with the combinatorial selection of the discretely varying parameters can also be found, e.g., in [6, 8]. These approaches require solving a sequence of approximation problems. Though the branch and bound approach requires solving many optimization subproblems, it does not make approximations and guarantees to get the global optimal solution.

We model the plant and formulate the design problem in Section 2. In Section 3, we present the simulation results for a truss structure with eleven elements to illustrate our design approach. We present conclusions and suggest future work in Section 4.

All the numerical results were obtained by using MATRIXx software tools from Integrated Systems, Inc.

^{*}Authors are all with Integrated Systems, Inc. , Santa Clara

 $^{^{\}dagger} Research supported by NASA LaRC under Contracts NAS1-19015 and NAS1-19096$

2 System Modeling and Problem Formulation

2.1 System Modeling

Consider a dynamic LSS system governed by:

$$M(p)\ddot{q} + D(p)\dot{q} + K(p)q = Gu + Jv_d,$$
(2.1)

$$y = H_1 q + H_2 \dot{q} + F v_s$$
, (2.2)

where q is an $n \times 1$ vector of nodal coordinates, p is an $n_p \times 1$ design vector of structural parameters, u is an $n_i \times 1$ control vector, v_d is an $n_{v_d} \times 1$ stochastic disturbance vector, y is an $n_o \times 1$ output vector, v_d is an $n_{v_o} \times 1$ stochastic sensor-noise vector, and $M(\cdot)$, $D(\cdot)$, $K(\cdot)$, G, J, $(H_1 \ H_2)$ and F are the mass, damping, stiffness, control influence, disturbance influence, output influence, and sensor-noise influence matrices of appropriate dimensions, respectively. $M(\cdot)$, $D(\cdot)$ and $K(\cdot)$ are functions of structural parameters p. $M(\cdot)$ is a positive definite matrix. $D(\cdot)$ and $K(\cdot)$ are nonnegative definite matrices.

We assume that each component of p belongs to a set of available elements. In addition, there may be other constraints on the choice of p, e.g., a constraint on the total mass. Thus,

$$p \in \mathcal{P}$$
, (2.3)

where \mathcal{P} is a discrete set of $n_p \times 1$ vectors.

For each $n_p \times 1$ vector p, we can find the mode shape matrix Φ and the modal frequency matrix $\Omega = \text{diag}(\omega_1, \dots, \omega_n)$ such that [3]

$$K(p) \Phi = M(p) \Phi \Omega^2, \qquad (2.4)$$

$$\Phi^T M(p) \Phi = I_n , \qquad (2.5)$$

$$\Phi^T K(p) \Phi = \Omega^2 , \qquad (2.6)$$

where I_n is an $n \times n$ identity matrix and Φ^T denotes the transpose of Φ . We assume that the system has a proportional damping term with a constant scalar modal damping ratio ζ , i.e.,

$$\Phi^T D(p) \Phi = 2\zeta \mathfrak{L}. \tag{2.7}$$

Transforming to modal coordinates via

$$q = \Phi \eta , \qquad (2.8)$$

the LSS dynamics (2.1-2.2) are equivalently:

$$\ddot{\eta} + 2\zeta \Omega \dot{\eta} + \Omega^2 \eta = \Phi^T G u + \Phi^T J v_d,$$
(2.9)

$$y = H_1 \Phi \eta + H_2 \Phi \dot{\eta} + F v_s$$
. (2.10)

Letting $x = [\eta \ \dot{\eta}]^T$, we transform (2.9-2.10) into the state-space form:

$$\dot{x} = Ax + Bu + Ev_d, \quad (2.11)$$

$$y = Cx + Fv_s, \qquad (2.12)$$

where

$$A = \begin{pmatrix} 0 & I_n \\ -\Omega^2 & -2\zeta\Omega \end{pmatrix}, B = \begin{pmatrix} 0 \\ \Phi^T C \end{pmatrix},$$
(2.13)

$$E = \begin{pmatrix} 0 \\ \Phi^T J \end{pmatrix}, C = (H_1 \Phi H_2 \Phi). \tag{2.14}$$

2.2 Problem Formulation

Consider the augmented LSS model shown in Figure 2.1, where

$$y_p \stackrel{\triangle}{=} Cx \tag{2.15}$$

are the vibration outputs of the plant that will be measured by sensors,

$$w \triangleq \begin{pmatrix} v_d \\ v_s \end{pmatrix} \tag{2.16}$$

is the disturbance and noise input, and

$$z \triangleq \left(\begin{array}{c} y_p \\ W_u u \end{array}\right) \tag{2.17}$$

is the vector of performance variables with W_u being a constant $n_i \times n_i$ weighting matrix.

The augmented design model in Figure 2.1 can be redrawn in the more compact form shown in Figure 2.2. From (2.11-2.14), the augmented plant, $P(\cdot)$, can be described by:

$$\dot{x} = Ax + Bu + (E \ 0)w$$
, (2.18)

$$z = \begin{pmatrix} C x \\ W_u u \end{pmatrix}, \qquad (2.19)$$

$$y = Cx + (0 F)w. (2.20)$$

The feedback system is configured as shown in Figure 2.3, where K denotes the compensator. Let H_{zw} denote the transfer function from w to z. The simultaneous control and structure design can be cast as the following optimization problem:

$$\min_{z \in \mathcal{P}} \min_{K} ||H_{zw}||_2^2 , \qquad (2.21)$$

where $||H_{z...}||_2$ is the \mathcal{H}_2 -norm of the transfer matrix H_{zw} , that is,

$$||H_{zw}||_2^2 \stackrel{\triangle}{=} \frac{1}{2\pi} \int_{-\infty}^{\infty} \operatorname{tr}[H_{zw}(j\omega) H_{zw}(-j\omega)^T] d\omega,$$

where $tr(\cdot)$ is the trace of a matrix.

For each $p \in \mathcal{P}$, let $\widetilde{K}(p)$ denote the optimal \mathcal{H}_2 -compensator and let $\widetilde{H}_{zw}(p)$ denote the corresponding optimal closed-loop transfer function matrix, i.e.,

$$\widetilde{K}(p) \stackrel{\triangle}{=} \arg\min_{K} ||H_{zw}(p)||_2^2$$
 (2.22)

and

$$\widetilde{H}_{zw}(p) \stackrel{\triangle}{=} H_{zw}(p) \mid_{K = \widetilde{K}(p)}$$
 (2.23)

 $\widetilde{H}_{zw}(p)$ is the transfer matrix of the feedback system in Figure 2.4.

The optimal compensator $\tilde{K}(p)$ is the so-called \mathcal{H}_2 -optimal compensator and is obtained by solving two uncoupled algebraic Ricatti equations [2].

The optimization problem in (2.21) is then equivalent to the following parameter optimization problem:

$$\min_{p \in \mathcal{P}} \|\widetilde{H}_{zw}(p)\|_2^2 . \tag{2.24}$$

2.3 Branch-and-Bound Algorithm

Since \mathcal{P} is a discrete set, we introduce the branch-and-bound algorithm for the purpose of efficiently solving the combinatorial problem in (2.24) [7].

As described in [7], the branch-and-bound optimization technique entails construction of a multi-node tree which subdivides the solution space of the problem. The technique then relies on being able to calculate a lower bound at any node on the tree, which then applies to any branch below that particular node as well. This allows us to eliminate the tree below any node which either has a bound that is greater than the best solution achieved so far or has no feasible points¹. Only those branches which hold the possibility of containing feasible points and a more optimal solution need be explored. This is

a very effective technique for enumerating all of the feasible points of a combinatorial optimization problem.

The development of the tree depends on two capabilities:

- Branching: the ability to partition the solutions set at a particular node into mutually exclusive sets.
- Lower Bounding: the ability to calculate a lower bound of the cost of any solution set.

The partitioning of solution sets into subsets is done by dividing the allowable structural members into subgroups. The lower bounding is possible by letting the structural parameters become free parameters in the range of the parameters in the current node and resorting to a continuous optimization procedure to find the lower bound for the current node. We will discuss this more in the next section. Now we introduce the basic branch-and-bound algorithm which is shown below [7]:

begin

```
activeset := 0;
currentbest := p_0, some point of \mathcal{P};
U := \cos t value corresponding to p_0;
while activeset is not empty do
   begin
       choose a branching node, node k \in
       remove node k from activeset: generate
       the children of node k, child i, i = 1,
       \dots, n and the corresponding lower
       bounds, z_i;
       for i = 1, ...n do
          begin
              if z_i \geq U then kill child i
              else if child i is a complete so-
              lution then
                 U:=z_i, currentbest:= child i
                 else add child i to activeset
          end
   \mathbf{end}
```

2.4 Implementation

Observe that the branch-and-bound algorithm requires computing a lower bound z_i for each

 $^{^{1}}$ By feasible points, we mean those points which satisfy all the constraints .

branch node containing a discrete set of structural design parameters. To determine the lower bound, we first let the structural parameters become free parameters in the range of the parameters in the current branch node which is assumed to be $[p_l \ p_u]^2$. Assume that there are equality and inequality constraints for the design parameters which are expressed in terms of the vectorvalued functions $g(\cdot)$ and $h(\cdot)$, respectively. We denote the lower and the upper limits of the inequality constraints by h_l and h_u . The following optimization problem is then solved to get the lower bound for each branch node:

$$\min_{p} \| \widetilde{H}_{zw}(p) \|_2^2 \qquad (2.25)$$

subject to

$$g(p) = 0, \qquad (2.26)$$

$$h_l \leq h(p) \leq h_u , \qquad (2.27)$$

$$h_l \le h(p) \le h_u$$
, (2.27)
 $p_l \le p \le p_u$. (2.28)

We have written software for the above optimization procedure and have implemented it into the MATRIXx software library. This has provided us with a very convenient environment to implement the branch-and-bound algorithm.

Using the nomenclature of the pseudo-code in Section 2.3, observe that a good choice of initialbest will keep the activeset small during the execution of the algorithm for system design, and, hence, enhance the efficiency of the algorithm. To achieve this, we solve the optimization problem in (2.25-2.28) with p_l and p_u being, respectively, the lower and the upper limits of the available structural elements to get a continuous optimal solution, and then find a currentbest point in P, which is nearest to this continuous optimal solution in the R^{n_p} Euclidean space. The initial cost is then equal to the value of $||H_{zw}||_2^2$ (see (2.23)) corresponding to the chosen initialbest point. Next, if we have to generate children for each branch node, we always generate two children as follows: (i) we find the optimal continuous solution \bar{p} for the current branch node, which gives us the lower bound of the cost for that node, (ii) we choose any integer i such that the ith elements of the points in the current branch node have the biggest number of possible values³, (iii) Suppose \hat{p}_i is the *i*th element

of \bar{p} and $\bar{p_i} \in [s_i^k, s_i^{k+1})$ where s_i^k and s_i^{k+1} are the consecutive possible values for the ith structural element in the current branch node. We then generate two children: one child contains the points of the current branch node with the ith element no greater than s_i^k , and the other contains the points of the current branch node with the *i*th element no less than s_i^{k+1} .

3 Simulation Results

Plant Description

In this section, we apply the branch-and-bound algorithm to the simultaneous control and structure design of a 11-beam truss structure as shown in Figure 3.1. Note that joint #1 is fixed. Joint #2 is fixed in the x-direction, but can be moved in the y-direction. The configuration of the ith beam is shown in Figure 3.2., where r is the radius of the beam and is assumed to be the same for all beams, and p_i is the width of the annular area of the ith beam. We will find the optimal solution for the structural parameters,

$$p \stackrel{\triangle}{=} [p_1, p_2, \cdots, p_{11}] \tag{3.1}$$

from a discrete, but very large set.

In this simulation example, we assume that the beams are made of aluminum. The mass density is therefore chosen to be $2770 kg/m^3$, and Young's modulus is $7 \cdot 10^{10}$. The radius of the beams, r, is chosen to be 0.02 meter. The length of the beams is chosen to be 10 meters, except the four diagonals whose length is $10\sqrt{2}$ meters. The constant damping ratio ζ in (2.7) is assumed to be 0.001 for all beams.

Actuators are placed at joints #3 and #4 (see Figure 3.1) for both the x and y directions. We therefore have four input forces. The disturbance force v_d , exerted on joint #2 (y-direction only), is assumed to be white noise with unit intensity,

$$\mathcal{E}(v_d(t_1)v_d(t_2)) = \delta(t_1 - t_2), \text{ (newton}^2)$$
(3.2)

where $\mathcal{E}(\cdot)$ denotes the mean value. Displacement sensors are located at joint #6 to measure the xaxis and y-axis motions. We assume that the

²Note that p_l and p_u are vectors. By $[p_l \mid p_u]$, we mean the set of vectors with each of their components lying between the corresponding ones of p_l and p_u .

³For the simulation example considered in the next

section, the integer $i \in \{1, 2, \dots, 11\}$, and the biggest number of possible values for any branch node is 4.

sensor noises are white noises with

$$\mathcal{E}(v_s(t_1) v_s^T(t_2))$$
= $10^{-14} \delta(t_1 - t_2) I_2$ (meter²)
= $10^{-2} \delta(t_1 - t_2) I_2$ ((μ -meter)²),

where μ -meter denotes 10^{-6} meter. In the notation of (2.2), $F = I_{n_{v_s}}$. We have found that the sensor noises v_s are small enough to be neglected during the execution of the branch-and-bound algorithm. Hence, the \mathcal{H}_2 or LQG feedback compensator design mentioned in Section 2.2 is then reduced to the linear quadratic regulator (LQR) (optimal state-gain) design during the execution of the branch-and-bound algorithm⁴. However, a Kalman filter is used when evaluating the closed-loop frequency responses and calculating cost functions in all of the figures and tables in this section.

The optimal control/structure design goal is to suppress the axial vibrations at the outputs for this structure. In terms of Figure 3.1 we have

$$y_p = [q_{x_6} \ q_{y_6}], \ u = \begin{bmatrix} f_{x_5} \\ f_{y_5} \\ f_{x_4} \\ f_{y_4} \end{bmatrix}, \ v_d = [d_{y_2}],$$

where q_{x_6} and q_{y_6} denote the axial vibrations at the joint #6 in the x and y directions respectively, $(f_{x_3}, f_{y_3}, f_{x_4}, f_{y_4})$ are the input forces at joints #3 and #4 in the x and y directions respectively, and d_{y_2} is the disturbance force at joint #2 in the y direction. The axial vibrational motion of the truss was analyzed by the finite element method [3]. For this case, the vector $q(\cdot)$ in (2.1) is a 9×1 vector, and the mass and the stiffness matrices are assumed to be linear in the structural parameters p^5 , i.e., [3]

$$M(p) = \sum_{i=1}^{11} p_i M_i,$$

$$K(p) = \sum_{i=1}^{11} p_i K_i,$$

where M_i and K_i are 9×9 constant matrices.

In this example, there are four possible choices for the width of each beam (in meters),

$$p_i \in \{0.001, 0.002, 0.003, 0.004\},$$

 $i = 1, 2, ..., 11.$ (3.3)

In addition, the mass of the truss structure is constrained. Since the mass of the *i*th beam is proportional to p_i , and each beam is made of the same material, we can express the mass constraint in terms of the width of the truss beams by the following inequality:

$$\sum_{i=1}^{11} \alpha_i p_i \leq w_0 \stackrel{\triangle}{=} 0.0253 \, (\text{meter}) \,, \quad (3.4)$$

where

$$\alpha_i = \begin{cases} \sqrt{2} & \text{for } i = 3, 4, 8, 9 \\ 1 & \text{others} \end{cases}$$

The number $w_0 = 0.0253$ on the right hand side of (3.4) is the nominal value of $\sum_{i=1}^{11} \alpha_i p_i$ with $p_i = 0.002$ (meter) for all *i*. The feasible set \mathcal{P} is then defined as

$$\mathcal{P} = \left\{ p \in R^{11} : p_i \in 10^{-3} \cdot \{1, 2, 3, 4\}, \right.$$
$$\sum_{i=1}^{11} \alpha_i p_i \le w_0 \right\}. \quad (3.5)$$

3.2 Numerical Results

In the following discussion, the unit of LOS errors is μ -meters $(10^{-6} \cdot m)$ and the unit of control u is newtons.

3.2.1 Nominal Design

To establish a nominal design, we set $W_u = 10 I_4$ and set $p_i = 0.002$ for all i, i.e.,

$$p = 10^{-3} \cdot [2 \ 2 \ 2 \ 2 \ 2 \ 2 \ 2 \ 2 \ 2 \ 2] .$$
 (3.6)

Thus each beam has equal cross-section area. An optimal controller is designed for this truss structure to minimize $||H_{zw}||_2^2$. Recall from Figure 2.3 that H_{zw} is the transfer function from disturbance/noise inputs w to controlled outputs z.

⁴ In this way, we have saved considerable computational time by avoiding handling a closed-loop system whose order is double that of the plant.

⁵ If we choose the radius, p_t , as the distance to the center of the tube wall, then the mass and stiffness matrices, as well as the mass constraint, are exactly linear in p_i . In this example, we chose to define p_i as an outside radius as shown in Fig. 3.2 because most available aluminum tubing is available with a constant outside diameter and variable wall thicknesses. M(p) and K(p) are therefore quadratic functions of p. However, the design methodology works just as well if the contribution of the quadratic term is less than 5%.

The optimal cost value in terms of $\|\widetilde{H}_{zw}\|_2^2$ in 3.2.3 Optimal Sequential Design (2.23) is

$$\|\tilde{H}_{zw}\|_2^2 = 1716. \tag{3.7}$$

The mean square values of LOS errors and inputs of this nominal structure are shown in Table 3.1 for both the open-loop and closed-loop systems. The first five modal frequencies and damping ratios of both the open-loop and closed-loop systems are shown in Table 3.2.

The frequency responses from the disturbance input v_d to line-of-sight (LOS) error outputs y_n for both the open-loop and closed-loop systems are shown in Figure 3.3. We also plot the frequency responses from disturbance input v_d to plant inputs u of the closed-loop system in Figure 3.4.

3.2.2 Optimal Control/Structure Design

With W_u fixed at $10 \cdot I_4$, the branch-and-bound algorithm as described in Sections 2.3 and 2.4 yields the following optimal structural parameters:

$$p^* = 10^{-3} \cdot [4 \ 1 \ 1 \ 1 \ 3 \ 3 \ 1 \ 1 \ 3 \ 4]$$
. (3.8)

The optimal cost value is

$$\|\widetilde{H}_{zw}^*\|_2^2 = 58.6. \tag{3.9}$$

The mean square values of LOS outputs and inputs of this optimal structure are shown in Table 3.3 for both the open-loop and closed-loop systems. The first five modal frequencies and damping ratios of both the open-loop and closed-loop systems for this case are shown in Table 3.4.

The frequency responses of the open-loop and closed-loop systems from v_d to y_p for this structure are shown in Figure 3.5.

To compare Figures 3.3 and 3.5 effectively, the frequency responses from v_d to y_p for the structures from the nominal design and the optimal control/structure design are plotted again in the same figures in Figures 3.6 and 3.7. Observe that there are $10 \sim 15$ db improvements in terms of the highest peak values of the frequency responses for the optimal control/structure design compared to the nominal design. The frequency responses from v_d to u of the closed-loop system are plotted in Figure 3.8 which can also be compared with those in Figure 3.4.

It is interesting to compare the optimal control/structure design with the structurecontroller sequential design. By structurecontroller sequential design, we mean that the structure and the controller designs are done in two steps. (1) First find the optimal structural design by using the branch-and-bound algorithm to minimize the \mathcal{H}_2 -norm of the open-loop transfer function from v_d to y. (2) Then, design an optimal controller for this structure. The optimal parameters obtained via this approach are

$$\tilde{p} = 10^{-3} \cdot [4 \ 4 \ 2 \ 1 \ 1 \ 2 \ 1 \ 1 \ 2 \ 4] \quad (3.10)$$

and the corresponding cost value is equal to

$$\|\widetilde{H}_{zw}\|_2^2 = 127.9, \qquad (3.11)$$

which is more than twice the cost value of optimal control/structure design. The mean square values of LOS outputs and inputs of this structure are shown in Table 3.5 for both the open-loop and closed-loop systems. The first five modal frequencies and damping ratios of both the openloop and closed-loop systems are shown in Table 3.6.

Figure 3.9 shows the open-loop and the closedloop frequency responses from v_d to y_p . Figures 3.10 and 3.11 shows the frequency responses from v_d to y_p for the sequential design and the optimal control/structure design. Observe that even though the highest peak values of the frequency responses in Figure 3.9 are lower than those in Figure 3.5 by $5 \sim 10$ db, the highest peak values of closed-loop frequency responses in Figure 3.9 are higher than those in Figure 3.5 by 5 db. The provides evidence that the interactions between structure design and controller design are significant to the overall performance of the system.

3.2.4 Performance Trade-offs

In this section, the mass constraint and the control weight are varied to study the performance trade-off. We assume that the mass constraint is

$$\sum_{i=1}^{11} \alpha_i p_i \le \beta w_0 , \qquad (3.12)$$

$$W_{\mathbf{u}} = w_{\mathbf{u}} \cdot I_{\mathbf{4}} \,. \tag{3.13}$$

Recall from (3.4) that $w_0 = 0.0253$. In the folcalculation of cost values. lowing figures, we choose

$$\beta \in \{0.75, 1, 1.25, 1.5\}$$
 (3.14)

and

$$w_u \in \{2.5, 5, 10, 20\}. \tag{3.15}$$

For each choice of (β, w_u) above, the branchand-bound algorithm is used to obtain an optimal control/structure design.

Figure 3.12 shows the cost $\|\widetilde{H}_{xw}\|_2^2$ versus β for various values of w_u . It can be observed that the curves move downward when the value of w_u decreases. This is due to the fact that decreasing w_u results in more allowable input energy and, therefore, less mean-square LOS error. Intuitively, by increasing the total structural mass, the cost should decrease. But it is interesting to observe from Figure 3.12 that the increase of β will not lower the cost much after β has reached some value around 1.2 in this numerical example. This phenomenon can also be observed in the next figure. This does not indicate that adding more mass is in general no longer effective in reducing the cost. It does, however, indicate that the constraints on how the mass can be added limit its effectiveness. The critical constraint is the maximum amount of mass that can be concentrated in one element of the truss. After a few key elements reach their maximum allowable mass, more mass is added in other elements, but the cost reduction is less pronounced. However, for this case, we did find that the increase of total mass helps reduce vibrations at joints other than joint #6 where the sensors reside.

Figure 3.13 shows the mean square values of LOS error versus input force for the four different values of allowable maximum total mass. This figure shows how much input energy is needed to achieve a specified LOS error, or how small the LOS error can be if a certain amount of input authority is given. In effect, these curves facilitate the design tradeoff between control energy and the total mass required to achieve a certain level of vibration suppression. Observe that the trade-off curve of $\beta = 1.5$ almost overlaps that of $\beta = 1.25$, because of the previously mentioned constraint on the mass of each element.

Note that every point on the curves in Figures 3.12 and 3.13 is optimal, and that they differ only because of different mass constraints and different control weights for the input energy in the

In Figure 3.14, we plot the curves of meansquare values of LOS error versus the input energy for nominal designs and optimal control/structure designs with $\beta = 1, 1.5$. In the case of $\beta = 1.5$, for the nominal design, $p_i = 0.003$ for i = 1, 2, ..., 11. We observe that the optimal control/structure design has significantly improved the system performance in the sense that it achieves much lower LOS error and requires much less input energy.

Conclusions 4

The branch-and-bound technique is an effective method for combined structural and controller optimization with structural elements restricted to a discrete set. In all cases, the designs achieved were better than those produced by performing the structural and controller design successively.

Potential future work includes application of the technique to a larger finite element model. The model used, although very lightly damped, was not truly representative of an LSS because of its low order. It is envisioned that analysis on an LSS would require an additional step to reduce the model order, such as that used in [5]. The most effective implementation of such a tool is probably an integration of the branchand-bound algorithm with parametric optimization algorithms for optimal control/structure design, and a finite element analysis program such as NASTRAN.

References

- [1] J. L. Junkins and D. W. Rew, chapter-"Unified Optimization of Structures and Controllers," from Large Space Structures: Dynamics and Control, Springer-verlag, New York, 1987.
- [2] H. Kwakernaak and R. Sivan, Linear Optimal Control Systems, John Wiley & Sons, 1972.
- [3] L. Meirovitch, Elements of Vibration Analysis, McGraw-Hill, 1975.
- [4] D. F. Miller and J. Shim, "Gradient-Based Combined Structural and Control Optimiza-

- tion," Journal of Guidance and Control, 10, May-June 1987, pp. 291-298.
- [5] S. K. Morrison, Y. Ye, C. Z. Gregory, Jr., R. L. Kosut and M. E. Regelbrugge, "Integrated Structural/Controller Optimization of Large Space Structures," AIAA/AAS Astrodynamics Conference, 1988.
- [6] G. R. Olsen and G. N. Vanderplaats, "Method for Nonlinear Optimization with Discrete Design Variables," AIAA Journal, Vol. 27, No. 11, November 1989, pp. 1584-1589.
- [7] C. H. Papadimitriou and K. Steiglitz, Combinatorial Optimization: Algorithms and Complexity, Prentice-Hall, 1982.
- [8] L. A. Schmit and C. Fleury, "Discrete-Continuous Variable Structural Synthesis Using Dual Methods," AIAA Journal, Vol. 18, 1980, pp. 1515-1524.

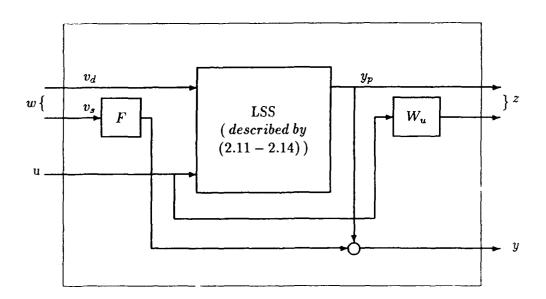


Figure 2.1: The augmented structure model

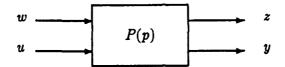


Figure 2.2: The augmented plant model

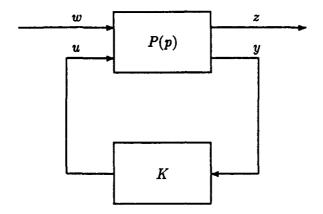


Figure 2.3: The closed-loop feedback system

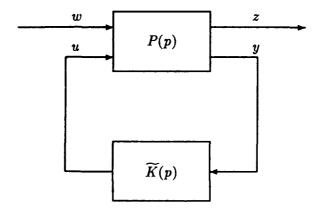


Figure 2.4: The optimal feedback system

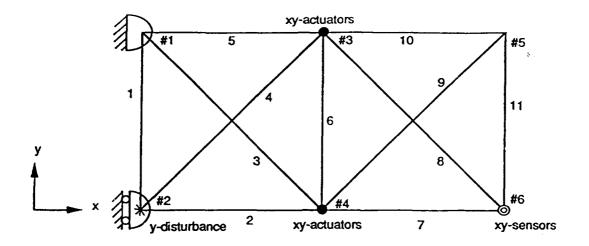


Figure 3.1: An 11-beam truss structure: xy-actuators at #3, #4; xy-displacement-sensors at #6; y-disturbance at #2

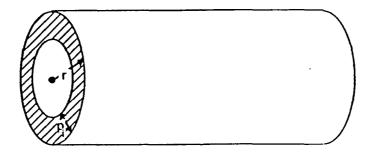


Figure 3.2: The cross section of the ith beam

| | mean-square values of y_p | mean-square value of u |
|-------------|-----------------------------|--------------------------|
| open-loop | 10,015 | - |
| closed-loop | 1,133 | 5.84 |

Table 3.1: Mean-square values of LOS outputs and inputs of the structure from the nominal design for both the open-loop and closed-loop systems

| | 1st mode | 2nd mode | 3rd mode | 4th mode | 5th mode |
|-------------|----------|----------|----------|----------|----------|
| open-loop | 20.0 | 53.1 | 59.1 | 114 | 116 |
| system | (0.001) | (0.001) | (0.001) | (0.001) | (0.001) |
| closed-loop | 20.4 | 28.7 | 52.6 | 53.1 | 59.2 |
| system | (0.153) | (0.75) | (0.072) | (0.015) | (0.026) |

Table 3.2: The first five modal frequencies (hz) and damping ratios (in parentheses) of both the open-loop and closed-loop systems of the nominal design

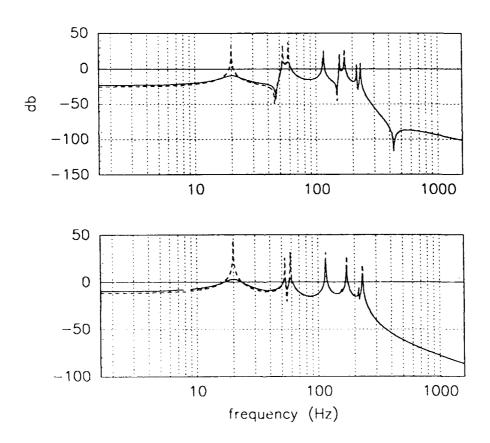


Figure 3.3: Magnitude (db) of frequency responses from v_d to y_p with the nominal parameter values $p_i = 0.002$, $\forall i$. Upper plot: v_d to x-direction output; Lower plot: v_d to y-direction output; '---' denotes open loop frequency response; '---' denotes closed-loop frequency response.

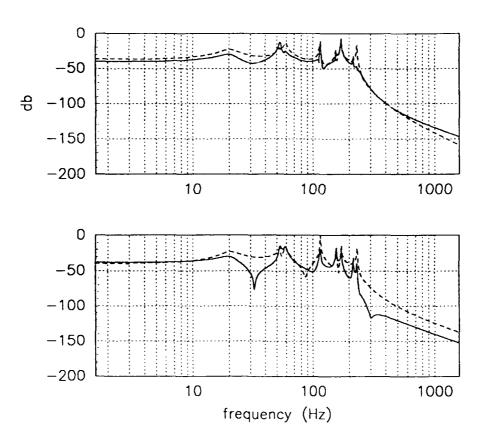


Figure 3.4: Magnitude (db) of frequency responses from v_d to structure inputs u with the nominal parameter values $p_i = 0.002$, $\forall i$. Upper plot: v_d to structure inputs at joint #3; Lower plot: v_d to structure inputs at joint #4; '---' denotes v_d to y-direction input; '—' denotes v_d to x-direction input

| | mean-square values of y_p | mean-square value of u |
|-------------|-----------------------------|--------------------------|
| open-loop | 986.4 | |
| closed-loop | 40.96 | 0.177 |

Table 3.3: Mean-square values of LOS outputs and inputs of the structure from the optimal control/structure design for both the open-loop and closed-loop systems

| | 1st mode | 2nd mode | 3rd mode | 4th mode | 5th mode |
|-------------|----------|----------|----------|----------|----------|
| open-loop | 12.4 | 42.5 | 44.4 | 75.4 | 133 |
| system | (0.001) | (0.001) | (0.001) | (0.001) | (0.001) |
| closed-loop | 13.2 | 15.9 | 41.7 | 42.5 | 44.4 |
| system | (0.264) | (0.55) | (0.073) | (0.0245) | (0.034) |

Table 3.4: The first five modal frequencies (hz) and damping ratios (in parentheses) of both the open-loop and closed-loop systems of the optimal control/structure design

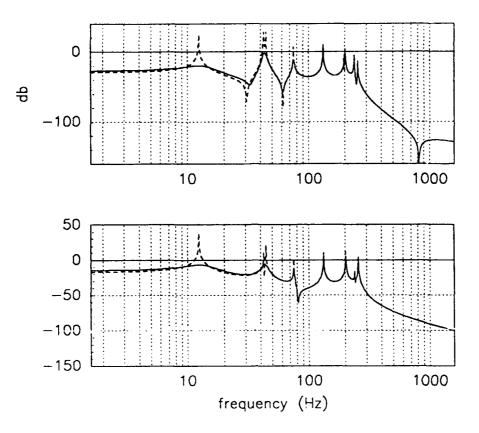


Figure 3.5: Magnitude (db) of frequency responses from v_d to y_p with the parameter values from the optimal control/structure design, $p = 10^{-3} \cdot [4\ 1\ 1\ 1\ 3\ 3\ 1\ 1\ 3\ 4]$. Upper plot: v_d to x-direction output; Lower plot: v_d to y-direction output; '---' denotes open-loop frequency response; '--' denotes closed-loop frequency response.

| | mean-square values of y_p | mean-square value of u |
|-------------|-----------------------------|--------------------------|
| open-loop | 351.4 | |
| closed-loop | 104.2 | 0.238 |

Table 3.5: Mean-square values of LOS outputs and inputs of the optimal structure from sequential design for both the open-loop and closed-loop systems

| | 1st mode | 2nd mode | 3rd mode | 4th mode | 5th mode |
|-------------|----------|----------|----------|----------|----------|
| open-loop | 15.8 | 51.3 | 63 | 104 | 132 |
| system | (0.001) | (0.001) | (0.001) | (0.001) | (0.001) |
| closed-loop | 16.1 | 16.6 | 51.33 | 51.37 | 63 |
| system | (0.161) | (0.299) | (0.0066) | (0.074) | (0.027) |

Table 3.6: The first five modal frequencies (hz) and damping ratios (in parentheses) of both the open-loop and closed-loop systems of the optimal sequential design

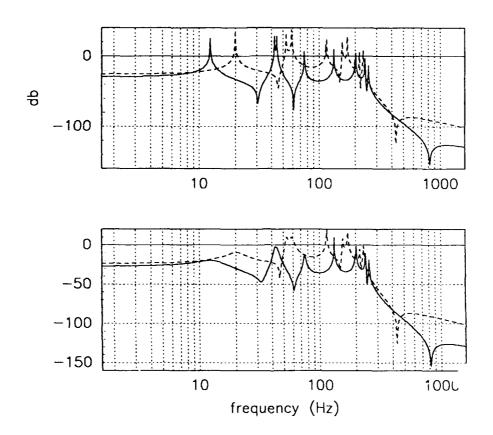


Figure 3.6: Comparison of the optimal control/structure design and the nominal design in magnitude (db) of frequency responses from v_d to y_p in x-direction. Upper plot open-loop frequency responses; Lower plot: closed-loop frequency responses; '--' denotes nominal design; '-' denotes optimal control/structure design

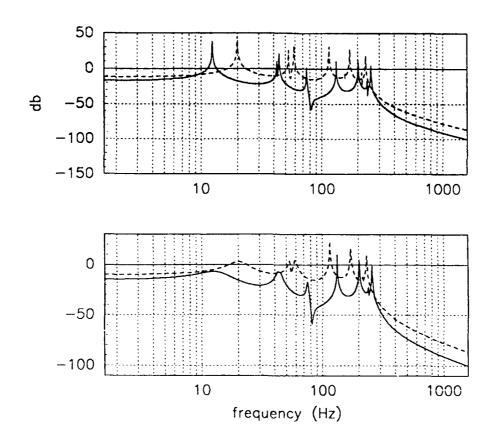


Figure 3.7: Comparison of the optimal control/structure design and the nominal design in magnitude (db) of frequency responses from v_d to y_p in y-direction: Upper plot: open-loop frequency responses; Lower plot: closed-loop frequency responses; '--' denotes nominal design; '--' denotes optimal control/structure design

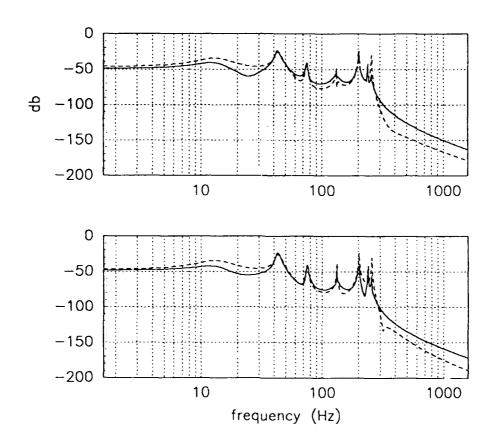


Figure 3.8: Magnitude (db) of frequency responses from v_d to structure inputs u with the parameter values from the optimal control/structure design, $p = 10^{-3} \cdot [4 \ 1 \ 1 \ 1 \ 3 \ 3 \ 1 \ 1 \ 3 \ 4]$. Upper plot: v_d to structure inputs at joint #3; Lower plot: v_d to structure inputs at joint #4; '---' denotes v_d to y-direction input; '--' denotes v_d to x-direction input

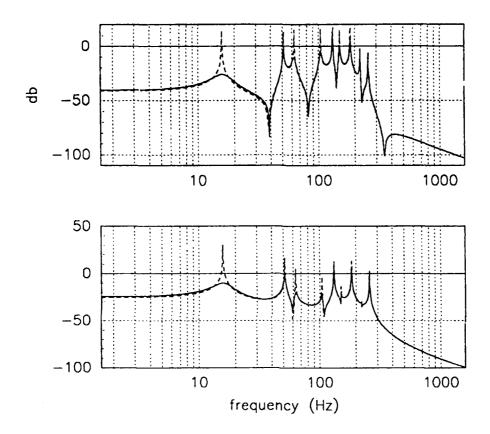


Figure 3.9: Magnitude (db) of frequency responses from v_d to y_p with the parameter values from the optimal sequential design, $p=10^{-3}\cdot[4\ 4\ 2\ 1\ 1\ 2\ 1\ 1\ 2\ 4]$. Upper plot: v_d to x-direction output; Lower plot: v_d to y-direction output; '---' denotes open-loop frequency response; '—' denotes closed-loop frequency response.

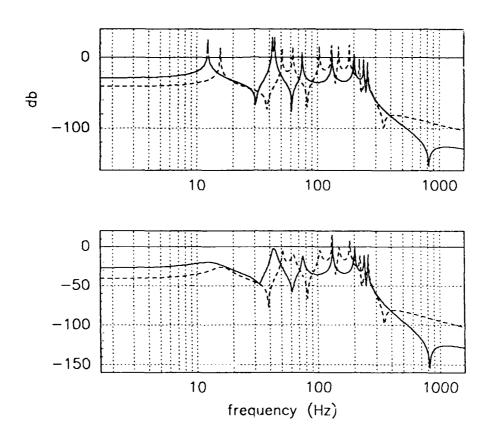


Figure 3.10: Comparison of the optimal control/structure design and the optimal sequential design in magnitude (db) of frequency responses from v_d to y_p in x-direction. Upper plot: open-loop frequency responses; Lower plot: closed-loop frequency responses; '-- ' denotes optimal sequential design; '-- ' denotes optimal control/structure design

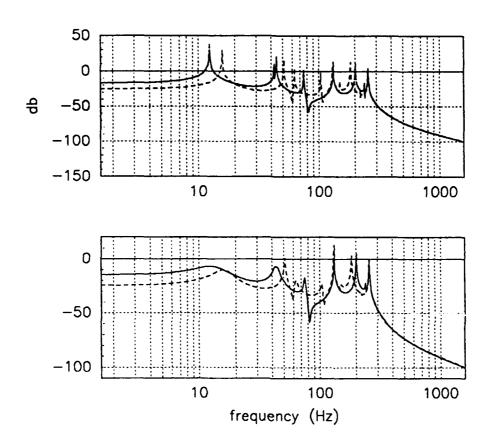


Figure 3.11: Comparison of the optimal control/structure design and the optimal sequential design in magnitude (db) of frequency responses from v_d to y_p in y-direction. Upper plot: open-loop frequency responses; Lower plot: closed-loop frequency responses; '---' denotes optimal sequential design; '---' denotes optimal control/structure design

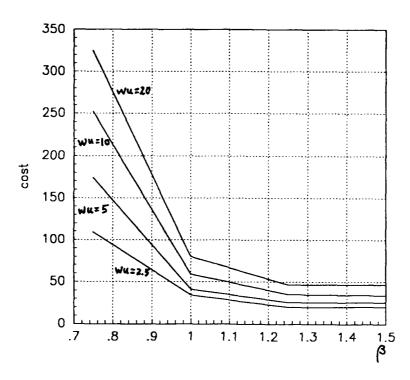


Figure 3.12: The cost value vs. the total mass β and the input weighting factor w_u

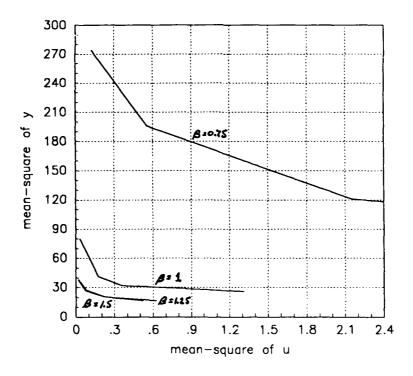


Figure 3.13: The mean-square values of LOS error (y_p) vs. the mean-square values of structure inputs (u) and the total mass β

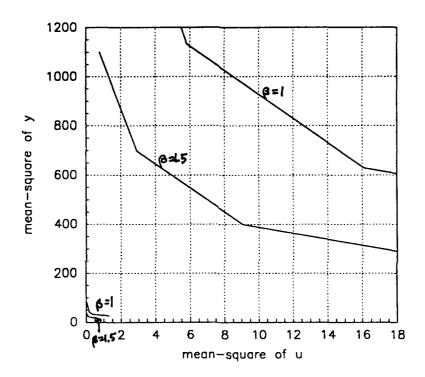


Figure 3.14: Comparison of the nominal design and the optimal control/structure design in the mean-square values of LOS error (y_p) vs. the mean-square values of structure inputs (u) with $\beta=1,1.5$. The upper two come from the nominal design; The lower two come from the optimal control/structure design

12 METER TRUSS ACTIVE CONTROL EXPERIMENT

WRIGHT RESEARCH AND DEVELOPMENT CENTER FLIGHT DYNAMICS LABORATORY

Robert W. Gordon WRDC/FIBGC

Umit Ozguner and Stephen Yurkovich The Ohio State University

Introduction

The Structures Division of the Wright Research and Development Center's Flight Dynamics Laboratory is conducting an experiment in the active vibration control of large, flexible structures. This presentation summarizes recent activity on the experiment including design, analysis and testing of open-loop and closed-loop configurations. Experiment design and analysis was performed in the Structural Dynamics Branch. Support for active control design, simulation and testing is provided by the Ohio State University, under contract.

Background

The 12 Meter Truss Experiment is part of an inhouse exploratory development program investigating the dynamics and control of flexible space structures. The program, entitled "Large Space Structures Technology Program," was begun in 1985 to investigate technical areas important to the development of future space vehicles. These areas include suspension and test methods for simulating the effects of zero-g during ground testing, passive damping and active vibration control approaches and hardware. The overall objective of the Large Space Structures Technology Program is to experimentally evaluate flexible space structures dynamics and control technologies for ground testing, passive damping and active vibration control. The program approach is to conduct a series of experiments on dynamically representative test articles. The Figure shows three experiments which have been completed in the program. The Advanced Beam Experiment, shown as the slender vertical beam at the left of the Figure, was our first experiment in active vibration control. It incorporated linear momentum exchange actuators to control the bending and torsion response of a cantilevered aluminum beam. The 12 meter trusses, two long, slender truss beams depicted at the right of the Figure, have provided a test bed for several experiments in ground testing and vibration control of large, flexible structures. One of the trusses is designed to have low inherent damping typical of future space vehicle while the other has significant passive damping designed in. The trusses have undergone extensive modal testing both vertically cantilevered from the floor and horizontally suspended on a soft spring suspension. The undamped truss was also tested in a microgravity environment on board a NASA test aircraft as shown at the bottom of the Figure.

LARGE SPACE STRUCTURES TECHNOLOGY

INHOUSE EXPERIMENTS

Ground Test Methods
Low Restraint Suspension Systems
Zero-G Testing

Viscoelastic Damping Analysis
Damped Structures Testing

Active Vibration Control Approaches
Active Control Hardware

4.5

CS1902

12 Meter Truss Active Control Experiment

The 12 Meter Truss Active Control Experiment was begun in 1988 as a second generation active vibration control experiment at the Flight Dynamics Laboratory. The objective of the experiment is to test the performance of leading active control approaches on a representative test article. In addition, the experiment will be used to evaluate the effects of added passive damping on active controller performance and check out a new digital control computer. The approach to the experiment is to configure the undamped 12 meter truss with sensors and actuators for active control. We emphasized the use of existing control hardware so we could concentrate on control testing and not hardware development. The level of passive damping in the truss will be tailored by adding damped diagonal members. Active control approaches can then be tested on a well characterized structure at two levels of passive damping.

12 METER TRUSS ACTIVE CONTROL EXPERIMENT

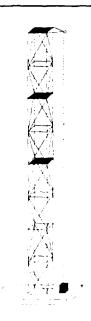
OBJECTIVES AND APPROACH

OBJECTIVES

- * Test Performance Of Leading Control Approaches on a Representative Test Article
- * Measure the Effect of Passive Damping On Controller Performance
- * Evaluate Performance of New Control Computer

APPROACH

- * Configure the Undamped 12 Meter Truss with Control Hardware
- * Tailor Modal Damping by Adding Damper Members
- * Test Controllers at Two Levels of Passive Damping



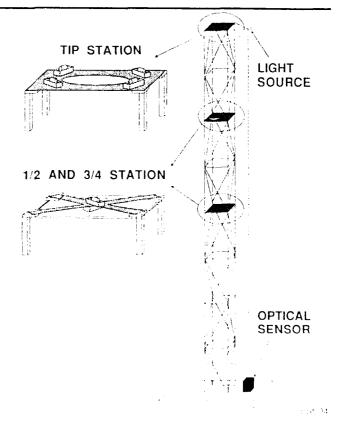
Experiment Design Features

The 12 meter truss is a welded aluminum frame with a 20 inch square cross section. The truss has four bolt-together sections with four truss bays in each section. The diagonal members are made of Lexan plastic and are bolted in place for easy removal. Damped diagonal members incorporating a viscoelastic damping material can be substituted for the Lexan diagonals to increase passive damping in the truss modes. The truss is equipped with 8 linear momentum exchange actuators to provide control forces. The actuators are located at the 1/2, 3/4 and tip stations of the truss and are oriented to control both bending and torsion modes of the truss. An accelerometer sensor is collocated with each actuator to sense truss motion. Disturbance forces are applied at the truss tip with an additional actuator for small force inputs (1 pound maximum) and an electromechanical shaker for larger force inputs. truss is also equipped with a small light source at the tip for optical sensing of truss motion. displacement of the light source is measured with an optical sensor mounted at the base of the truss. Truss tip motion is used as a figure-of-merit for controller performance.

12 METER TRUSS ACTIVE CONTROL EXPERIMENT

DESIGN FEATURES

- * 12 Meter Aluminum Frame 20" Square Cross Section Plastic Diagonal Members
- * 8 Linear Actuators with Colocated Accel Sensors
- * 9th Actuator and Shaker at Tip for Disturbances
- * Tip Light Source for Optical Sensing of Truss Tip Position Figure-of-Merit



12 Meter Truss in the Test Chamber

The photograph shows the 12 Meter Truss Active Control Experiment in a test chamber at the Flight Dynamics Laboratory. A scaffolding is located beside the truss to provide access to active control hardware at the 1/2, 3/4 and tip stations of the truss. Video cameras are mounted on the scaffolding at each actuator station to allow visual monitoring of truss and actuator motion. The digital control computer and supporting electronic equipment are located in an adjacent control room.



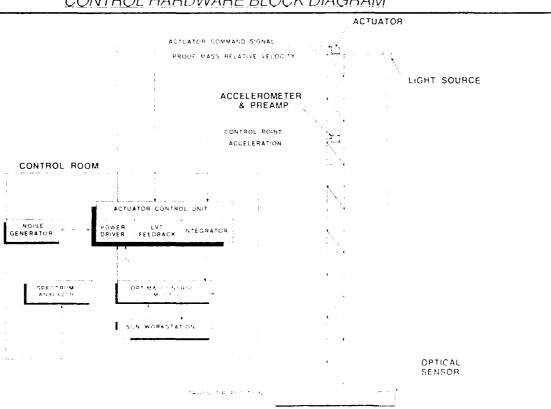
Control Hardware Block Diagram

The Figure shows a block diagram of the active control system hardware. The control system is made up of eight sensors and signal conditioners, a 12 channel real-time digital control computer, and eight actuators with power drivers and velocity feedback circuitry. Each accelerometer produces a signal proportional to the truss acceleration at its attachment point. acceleration signal is integrated to form a velocity signal which is fed to the control computer. The computer reads the vector of eight velocity signals and uses a control law to generate a vector of eight actuator command signals to minimize truss motion. Each actuator command signal is fed to a current drive which powers the actuator and generates the desired control force. Each actuator is also equipped with a relative velocity sensor which is used to provide velocity feedback damping to the actuator moving mass. An optical photodiode array sensor is used to track the motion of a small light source offset to one side of the truss tip. The sensor produces signals proportional to the x and y axis displacement of the light source. The displacement signals are then input to the control computer and stored for off-line analysis. Sensor inputs and actuator commands are also stored in the control computer for parameter identification and performance evaluation. The control computer is connected to a Sun graphics workstation which is used for control law development and simulation, remote download of control code and upload of experiment results, and analysis of recorded data.

12 METER TRUSS ACTIVE CONTROL EXPERIMENT

10.60

CONTROL HARDWARE BLOCK DIAGRAM



Real-Time Control Computer System

The real-time control computer used in the 12 meter truss experiment is shown schematically in the Figure. The system, produced by Systolic Systems, consists of two major components; the development system and the real-time controller. The development system, a Sun Microsystems graphics workstation, is used for software development, simulation, downloading of control code to the controller and analysis of test data. The real-time controller is a VME-based computer with a fast host processor, 12 channels of 16 bit analog input and output, a high speed vector processor and 4 Mbytes of memory for code and data storage. The controller provides the real-time control code execution as well as data acquisition and disturbance signal generation. The controller is fully programmable in the C language which allows a wide range of nonlinear or time varying control laws with concurrent sampling and storage of desired time histories.

0.90

12 METER TRUSS ACTIVE CONTROL EXPERIMENT

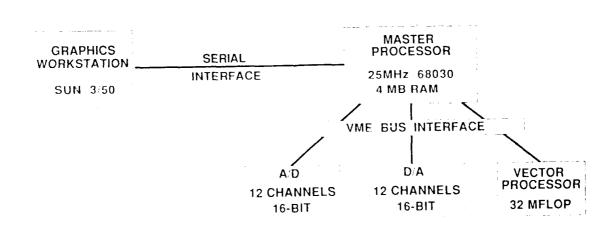
REAL-TIME CONTROL COMPUTER SYSTEM

Development System

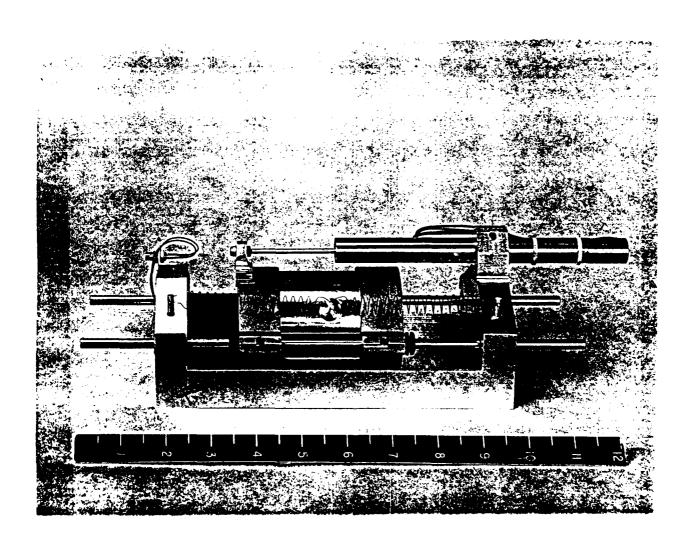
- Software Development
- Simulation
- Data Analysis (Matlab)

Real-Time Controller

- Real-Time Control
- Data Acquisition
- Fully Programmable in C

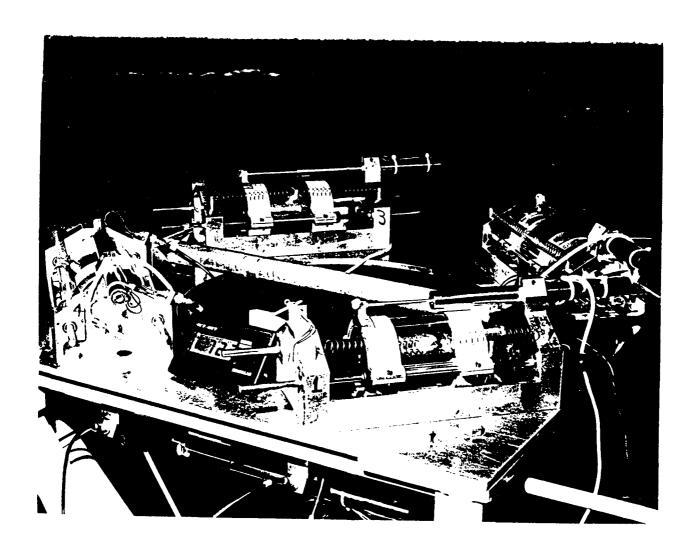


Eight linear momentum exchange actuators are used to generate control forces for active control of the truss. The actuator, shown in the Figure, is based on a design developed by Martin Marietta Corporation on the Passive and Active Control of Space Structures (PACOSS) contract. It incorporates a linear DC motor mounted on dual shafts and linear bearings. Light springs provide a small force to center the moving mass. A linear velocity transducer (LVT) senses the relative velocity between the moving mass and the structure which is fed back to the motor to produce viscous damping to control moving mass resonant response. The actuator weighs approximately 5 pounds and is capable of a 1 pound peak force output.



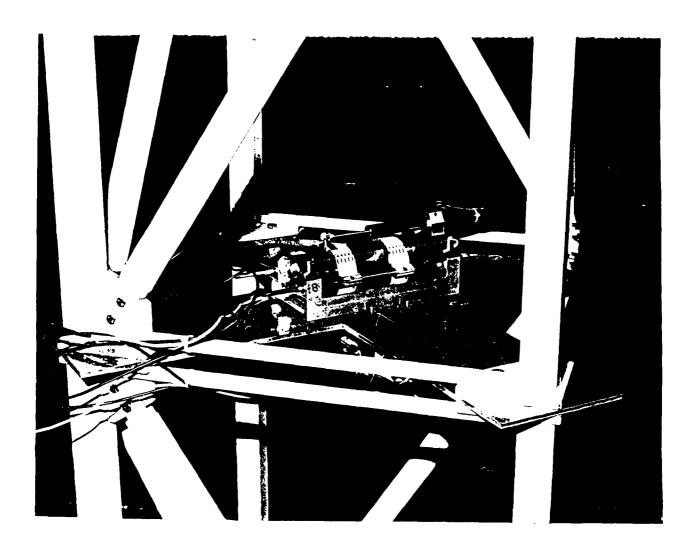
Actuator Configuration at the Truss Tip

The Figure is a photograph of the control hardware at the tip of the truss. The four control actuators, mounted on top of the truss, are arranged in two pairs, with one pair aligned along each bending axis. Each pair can be used to control motion in one bending axis while either or both pairs can be commanded in opposition to control torsional motion. The disturbance actuator can been seen in the foreground mounted under the plate and aligned at a 45 degree angle to the bending axes. The aluminum tube fastened to the tip plate positions the tip light source 24 inches from the truss center out of view to the left in the Figure.



Actuator Configuration at the Intermediate Stations

This figure shows the actuator configuration at the 1/2 station of the truss. A pair of actuators can be seen; one actuator aligned with each bending axis. The actuator configuration at the 3/4 truss station is identical to that shown here.



Open-Loop Modelling

Design and analysis of the open-loop behavior of the 12 meter truss were performed with finite element analysis on a personal computer. The damped and undamped trusses were originally modelled as full frame structures with one element per structural member. However, for analysis of the active control configuration, the truss was modelled as an equivalent continuous beam with sixteen elements, one for each truss bay. The equivalent beam element properties of an individual truss bay were determined from a detailed finite element model of a single bay. The beam elements were then 'stacked' in the proper orientation to assemble the full model. A beam model was used to reduce computation time and enable independent tuning of truss bending and torsional stiffnesses. The beam model without actuators has 96 degrees of freedom (DOF) while the full frame model has over 400 DOF. Bending and torsional stiffnesses of the equivalent beam elements were tuned to match frequencies measured for the truss and thus provide a more accurate model for control design. The actuators were included in the model as 1-DOF spring/mass/damper systems with a 1 Hz natural frequency and 10% modal viscous damping. The resulting truss open-loop model has eight structural modes and nine actuator modes in the frequency range of 0 - 20 Hz.

10/90

12 METER TRUSS ACTIVE CONTROL EXPERIMENT

OPEN-LOOP MODELLING

- * Open-Loop Analysis Performed With a PC-Based Finite Element Code
- * Truss Modelled as an Equivalent Continuous Beam
 - Reduced Computation Time
 - Independent Tuning of Bending and Torsion
- * Bending and Torsional Stiffness Tuned to Match Measured Frequencies
- * Actuators Modeled as 1-DOF Systems
 - 10% Viscous Damping
 - 1 Hz Natural Frequency
- * 8 Structural Modes and 9 Actuators Modes Below 20 Hz

Testing Approach

The approach to open-loop and closed-loop testing of the 12 meter truss consists of modal parameter identification and performance evaluation. Modal parameters, primarily natural frequencies and modal damping, are identified from two test conditions; single mode free decay and continuous, broadband random excitation. For the free decay test, the mode of interest is excited by one or more actuators or the shaker. The free decay response of the mode is then analyzed to extract modal information. A Hilbert transform fit method is used as well as a direct fit of decay response to a 1-DOF model. For the random test, the truss is excited by the shaker with a 0 - 50 Hz band random force. Frequency domain transfer functions are computed between all sensors and the measured shaker force input. Modal parameters are then extracted from the transfer functions using a 1-DOF circle fit. The performance of the active controllers is measured by exciting the truss with the same random signal and measuring the optical sensor's X and Y axis outputs.

10.00

12 METER TRUSS ACTIVE CONTROL EXPERIMENT

TEST APPROACH

PARAMETER I.D.

- * Single Mode Free Decay
 - Shaker or Actuator Force Input
 - Hilbert Transform Curve Fit
 - Exponential Decay Curve Fit
- * Transfer Functions from Random Force Input
 - Circle Fit

PERFORMANCE EVALUATION

- * Shaker Random Force Input, 0-50 Hz, 2 lb RMS
- * RMS Response of Tip Light Source as Measured by the Optical Sensor

Open-Loop Test Results

The Table displays the results of the open-loop modal parameter tests and compares them with predictions from the finite element model. Natural frequencies and modal damping values are listed for the lowest 8 bending and torsion modes of the truss and a composite of the 9 actuator modes. Measured natural frequencies agree very well with predictions for all modes listed. This is expected since the truss model was tuned based on bare truss test data. Modal damping values are under-predicted for the two first bending modes by 50%. This disagreement is likely due to the nonlinear damping present in the actuators from coulomb friction. Damping in the open-loop truss is modeled by viscous dampers representing actuator relative velocity feedback and by a 0.5% modal damping applied to all modes to account for nominal structural damping. Measured damping in the higher modes is below 1% which is representative of values expected in future space structures.

12 METER TRUSS ACTIVE CONTROL EXPERIMENT

OPEN-LOOP FREQUENCIES AND DAMPING

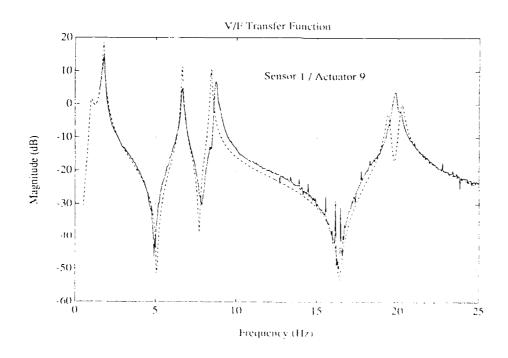
| | Mode Frequency (Hz) | | Damping (%) | | |
|---------------|---------------------|-------|-------------|-------|------|
| Mode | Number | Model | Test | Model | Test |
| Actuator | 1-9 | 1.00 | 0.91 | 10.0 | 6-10 |
| 1st X Bending | 10 | 1.74 | 1.75 | 1.7 | 3.8 |
| 1st Y Bending | 11 | 1.75 | 1.77 | 1.7 | 3.3 |
| 1st Torsion | 12 | 6.65 | 6.61 | 0.5* | 0.5 |
| 2nd X Bending | 13 | 8.45 | 8.48 | 0.5* | 0.5 |
| 2nd Y Bending | 14 | 8.45 | 8.74 | 0.5* | 0.7 |
| 3rd X Bending | 15 | 19.39 | 19.20 | 0.5* | 0.4 |
| 3rd Y Bending | 16 | 19.41 | 19.72 | 0.5* | 0.2 |
| 2nd Torsion | 17 | 20.22 | 20.06 | 0.5* | 0.2 |

^{*} Nominal unmodeled damping in truss

Truss Open-Loop Response

The measured open-loop response of the truss was compared with the finite element model results. The Figure shows measured and predicted transfer functions between velocity sensed at the truss tip to a force at the disturbance actuator. Good agreement in natural frequencies is evident in the Figure, but modal amplitudes agree less well with the model results, the model showing higher values. The differences in modal amplitudes may be due to unmodelled damping in the structure in the form of actuator coulomb friction and base mounting effects.

12 METER TRUSS ACTIVE CONTROL EXPERIMENT OPEN-LOOP RESPONSE: MODEL VS TEST



Active Control Design Approach

Active controllers have been designed for the 12 meter truss with two control objectives. The first objective is to generally increase passive damping in all controlled modes. This includes the lowest it truss bending modes and the lowest torsion mode. The second objective is more typical of a real system; minimize the truss tip displacement as measured by the optical sensor. The first objective weights all controlled modes as equally important while the second considers only those modes which affect truss tip motion; primarily the first bending modes with some reduced emphasis on first torsion and second bending. Actuator LVT damping values of 10% and 50% were used in the controller designs. The 10% value was used initially and the 50% valued was added after it was observed that the global controllers tended to reduced actuator damping to near zero for some cases.

12 METER TRUSS ACTIVE CONTROL EXPERIMENT

CONTROL DESIGN APPROACH

Control Objectives

- Maximize Damping in Controlled Modes
- Minimize Truss Tip Displacement Response to a Random Force Input

Model Truncated to 7 Modes

- 1st and 2nd Bending Pairs
- 1st Torsion
- One Actuator Mode in each Bending Plane

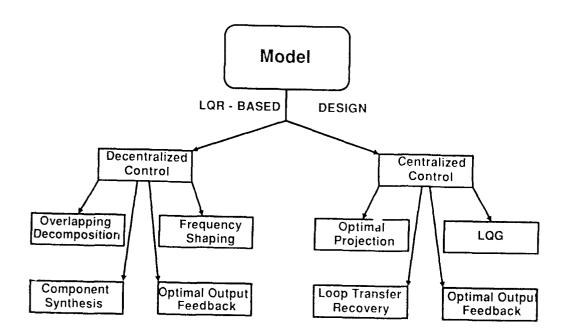
10% and 50% Damping in Actuator Modes

Active Controller Design

Active control design for the experiment was performed by professors Ozguner and Yurkovich and their students at the Ohio State University. Both centralized and decentralized controller designs were accomplished. All designs were based on linear quadratic regulator theory. As the Figure shows, several controllers of each type were designed using direct output feedback and full state feedback. The controllers which have been tested to date are shown as shaded boxes in the Figure.

12 METER TRUSS ACTIVE CONTROL EXPERIMENT

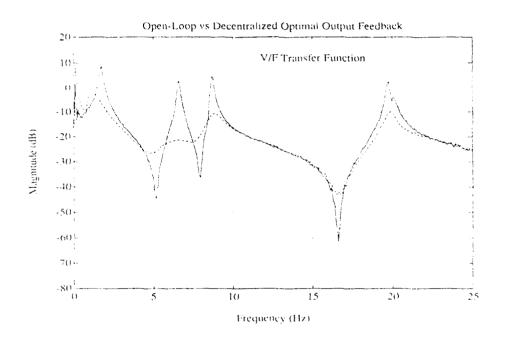
CONTROLLER DESIGN - OHIO STATE UNIVERSITY



Comparison of Open-Loop and Closed-Loop Frequency Response

The Figure shows a comparison of open-loop truss frequency response with a decentralized optimal output feedback controller. Good attenuation of response amplitude is seen for the modes in the 0 - 10 Hz control bandwidth. A substantial reduction is also evident in the modes near 20 Hz which are outside the control bandwidth. Also notice the increase in response of the actuator modes near 1 Hz due to the destabilizing effect of the global controller on the actuator modes.

12 METER TRUSS ACTIVE CONTROL EXPERIMENT CLOSED-LOOP VS OPEN -LOOP RESULTS



Closed-Loop Performance Results

The closed-loop performance of three active controllers in reducing truss tip motion is shown in the Table. The RMS displacement error of the tip light source is shown along with the RMS actuator force level required. Truss open-loop performance is also shown for comparison. First, it can been seen that all three controllers provide approximately a 40% reduction in tip motion compared to open-loop. Remember that the truss has approximately 4% damping in the first pair of bending modes which dominate the tip displacement response. The active controllers would show a much larger attenuation in a structure with damping levels of less than 1% as is expected in future systems. Even though the three controllers produce nearly equal performance, they require very different force levels to achieve this performance. The decentralized optimal output feedback controller uses over 50% more force than the overlapping decomposition decentralized approach with the centralized optimal output feedback controller somewhere in between.

12 METER TRUSS ACTIVE CONTROL EXPERIMENT

CLOSED-LOOP PERFORMANCE RESULTS

| Controller | RMS LOS* Error (inches) | RMS Actuator Force (pounds) |
|---------------------------------|----------------------------|-----------------------------|
| Open-Loop | .028 | 0 |
| Decentralized Outpu Feedback | ut .017 | .620 |
| Centralized Output Feedback | .0165 | .573 |
| Overlapping Decom | p .9165 | .400 |

^{*} tip light source position

Future Tasks

Evaluation of active controller performance on the 12 meter truss is underway and should continue through the end of 1990. In addition, efforts to identify and actively cancel actuator friction effects will continue. After controller evaluation on the current truss configuration is completed, a passively damped configuration will be designed and tested. Active controllers will then be tested on the passively damped truss and the active control energy required to achieve the same level of performance will be determined. The results of the damped truss testing will directly show the benefits to be gained from a combined passive and active control approach.

:0.90

12 METER TRUSS ACTIVE CONTROL EXPERIMENT

FUTURE TASKS

- * Evaluate Performance of Remaining Controllers
- * Test Controllers with Actuator Relative Velocity Feedback
- * Implement and Evaluate Active Friction Cancellation
- * Design and Test Passively Damped Configuration
- * Design and Test Controllers on Passively Damped Truss

Summary

The 12 Meter Truss Active Control Experiment is now operating. All control hardware is functioning well. Open-loop test results agree reasonably well with finite element model predictions. Coulomb friction in the actuators has been identified as an unmodelled source of damping in the truss. The friction has been characterized and an approach to minimizing its effects has been planned. The Optima digital control computer is performing very well. Active controllers with over 20 states have been run at sampling rates in excess of 500 samples per second. Finally, active controllers have been designed and tested which reduce truss tip motion by more than 90% over an open-loop structure with nominal modal damping levels of 0.5%.

12 METER TRUSS ACTIVE CONTROL EXPERIMENT

SUMMARY

- * Active Control Hardware is Operational
- * Open-Loop Test Results Agree Well with Model
- * Actuator Friction has been Identified and an Approach Defined to Minimize its Effect
- * Control Computer is Performing Well
- * Active Controllers Tested to Date Have Shown up to 10X Reduction in Truss Tip Response

PACOSS: The Final Chapter

Dr. K. E. Richards, Jr.
Martin Marietta Astronautics Group
Denver, Colorado

Fourth NASA/DoD Controls-Structures Interaction (CSI) Technology Conference November 5-7, 1990 Future large space systems (LSS), both civilian and military, will have performance objectives which require stringent pointing accuracies, relatively fast retargeting times, short settling times, accurate dynamic shape requirements, or combinations thereof. Many of these structures will be large but lightweight, and will exhibit a dense, low-frequency modal spectrum with significant content within the control bandwidth.

Although it is possible in principle to achieve structural vibration control with purely active means, experience with complex structures has shown that the realities of plant model inaccuracies and real sensor and actuator dynamics frequently combine to produce disappointing results.

It has been shown that a combination of passive and active control will result in a simpler system which can be expected to be more reliable and less expensive than a corresponding system utilizing active control exclusively.

The goals of the PACOSS (Passive and Active COntrol of Space Structures) program consist of a thorough investigation of the relative roles of passive and active vibration control, and the development of validated means of vibration control.

Introduction

- Future Large Space Systems Require Vibration Control
- Passive/Active Approach Most Effective
- Major Goals
 - Investigate Relative Roles for Passive and Active Vibration Control
 - Develop Validated Vibration Control Techniques

The PACOSS Program completed the original statement of work, termed the Phase 1 effort, in late calendar year 1988. Phase 2 began in April, 1989, and all technical work will be completed in March, 1991.

This presentation will follow the outline shown in Figure 2. We will briefly review the major accomplishments of the Phase 1 effort to establish the context for Phase 2. We will then discuss in some detail the three major Phase 2 ground test activities: the establishment of the DTA as a test bed, the investigation of passive fluid dampers, and some results of recent passive/active control experiments.

Outline

- Phase 1 Review
- Phase 2 Description
- DTA Testbed
- Viscous Fluid Damper
- Passive/Active Control Results
- Summary

A major objective of PACOSS is to develop vibration suppression technology for application to as broad a spectrum of military and civilian large space systems as possible. This objective has been realized in part by conducting extensive analytic investigations of the relative roles of passive damping and active vibration control, and the experimental validation of selected vibration control strategies.

Program Approach

- Broad, Generic Applications
- Extensive Analytic Investigations
- Experimental Validation

Fundamental to this objective is the selection of analytic and test articles of broad applicability. These articles are then designed by analysis, and hardware components are fabricated and tested to validate design and analysis practices.

The Dynamic Test Article (DTA), shown in Figure 4, is the principal testbed for PACOSS. It consists of seven substructures - a ring truss, a box truss, a beam-like truss known as the equipment platform, a tripod, an antenna, and two solar array simulators. All substructures except the ring truss have passive damping treatments.

Because the DTA is a validation device, it is important that no sources of inadvertent damping are present. For this reason, the DTA design makes extensive use of bonded joints. There are also several bolted joints which are designed to reduce the possibility of joint component flexing contributing to damping. The PACOSS team also chose to avoid complicated suspension techniques for the DTA to reduce inadvertent damping due to the extensive cabling required for distributed suspension systems. A consequence of this decision was that it was necessary to stiffen the DTA to permit it to survive the one-g test environment.

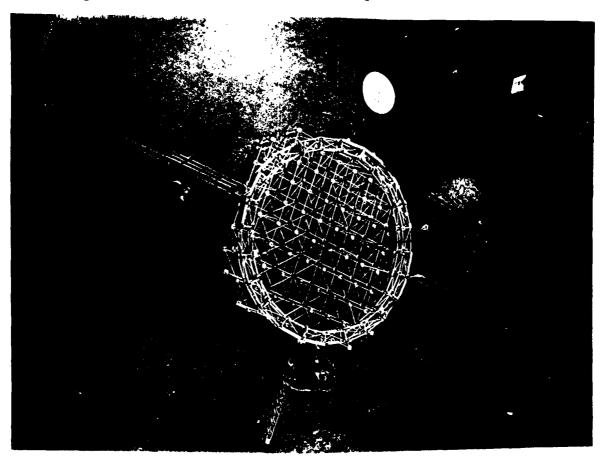


FIGURE 4

Six different types of viscoelastic damping treatments were applied to the DTA, and are shown in Figures 5a-5c. The design and placement of each treatment was based on the modal strain energy method. Each treatment is effective in damping those modes which have a significant portion of the modal strain energy in the viscoelastic elements.

Extensional shear dampers are placed throughout the box truss and equipment platform, and are effective in damping the lower truss modes. Rotational shear dampers are placed at each tripod leg/secondary mirror interface to damp modes involving relative rotation between the legs and mirror. Constrained layer treatments are used on the tripod legs, antenna legs, and solar array masts to damp modes involving flexure of these items. The antenna dish has an integral damping treatment to damp bending of the dish. Viscoelastic shear straps to damp in-plane bending and tuned-mass dampers to suppress out-of-plane blanket motion are used on the solar arrays.

DTA Dampers

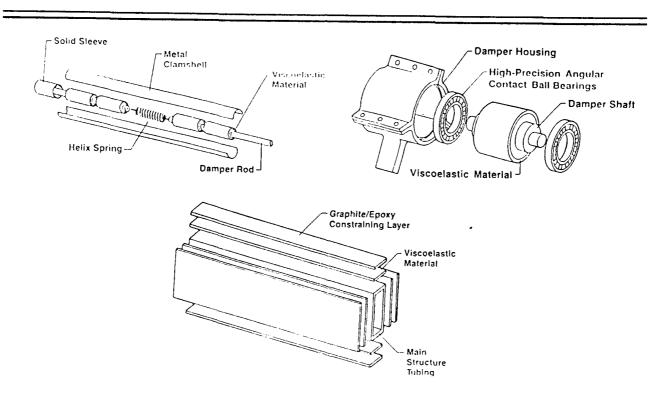


FIGURE 5a



FIGURE 5b

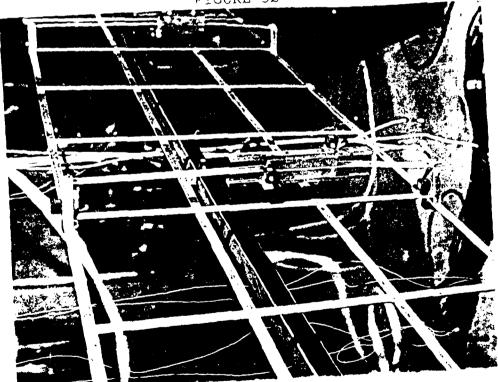


FIGURE 5c

The active control system used in Phase 1 consisted of six proof mass actuators located on the ring truss with active directions normal to the plane of the ring truss, as shown in Figure 6. Each actuator consists of a linear motor with an LVT to measure the relative velocity between the motor mass and actuator frame and an accelerometer to measure inertial acceleration. The springs provide a gravity offload for the motor mass, and result in an open-loop actuator frequency of approximately 1.5 Hz.

Each actuator has its own analog control box. The accelerometer signal is integrated to provide inertial velocity. The output from the LVT is fed back through an adjustable gain to provide damping to the actuator. The inertial velocity is fed back through an adjustable gain to implement the local direct velocity feedback (LDVFB) control algorithm specified by the Phase 1 SOW.

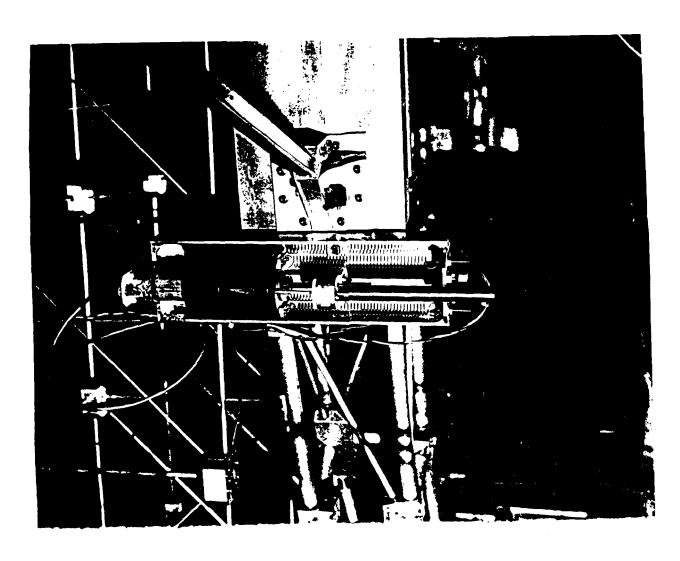


FIGURE 6

The DTA was assembled, the modal control system was installed, and open and closed loop modal testing were performed with multipoint burst random excitation in the specially constructed test chamber shown in Figure 7. The suspension system consisted of mechanical zero spring-rate mechanisms (ZSRMs). Test instrumentation consisted of a mix of PCB302, PCB308, and Endevco accelerometers. The PCB accelerometers were borrowed from other programs as a cost-savings measure.

During testing, the temperature in the test chamber was controlled to within +/- 2 degrees F to minimize VEM property changes during testing.

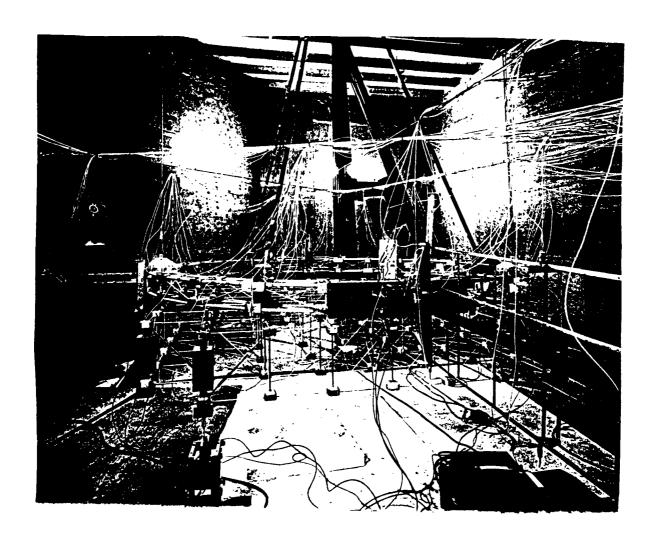


FIGURE 7

The results of open loop tests are compared with analytic results in Figure 8. Corrections have been made for VEM frequency effects and the effects of geometric stiffness and the deformed shape of the structure due to the one-g loading.

The high density of heavily damped modes (45 modes below 10 Hz), experimental noise due to the low frequencies and low excitation levels, and different phase characteristics of the modal test accelerometers joined together to provide a challenging parameter identification problem. Modal analysis requires curve fits of the experimental data, and the damping levels identified by apparently equally good attempts frequently vary by 20 percent, i.e., if the true value of damping for a given mode is 10 percent, apparently equally good curve fits can produce results between 8 percent and 12 percent.

Most of these results fall within the 20 percent band of parameter identification uncertainty.

DTA Open-Loop Global Modes

| System Mode | Global Mode | f, Hz | | ζ, % | |
|----------------|----------------|-------|----------|--------|----------|
| | | Test | Analytic | Test ' | Analytic |
| 15 | 1 | 2.61 | 2.61 | 3.6 | 2.8 |
| 20 | 2 | 3.25 | 3.29 | 5.0 | 4.4 |
| 21 | 3 | 3.53 | 3.50 | 8.8 | 8.2 |
| 22 | 4 | 3.72 | 3.70 | 5.2 | 4.7 |
| 26 | 5 | 4.83 | 4.60 | 4.5 | 7.8 |
| 27 | 6 | 5.04 | 4.81 | 11.4 | 10.4 |
| 35 | 7 | 6.48 | 6.12 | 12.7 | 10.0 |
| 37 | 8 | 9.40 | 7.52 | 10.3 | 6.0 |
| 42 | 9 | 8.92 | 9.04 | 7.0 | 6.8 |
| 45 | 10 | 9.26 | 9.28 | 8.6 | 7.0 |

Accuracy Approximately ± 20%

The global mode at approximately 2.6 Hz was targeted for active damping augmentation through local direct velocity feedback. Other modes with significant displacements at the actuator locations also receive some damping from the actuators. Figure 9 shows the analytic and measured results for the modes which received significant damping from the active augmentation. The agreement between predicted and measured values is excellent. We note, however, that the same 20 percent band as in the open loop case must be applied to the experimental damping levels.

DTA Closed-Loop Global Modes

| | Global Mode + | f, Hz | | ζ, % | |
|---------------|------------------|-------|----------|--------|----------|
| | | Test | Analytic | Test * | Analytic |
| Open- Loop | 1 | 2.61 | 2.61 | 3.6 | 2.8 |
| | 6 | 5.04 | 4.81 | 11.4 | 10.4 |
| | 7 | 6.48 | 6.12 | 12.7 | 10.0 |
| | 10 | 9.26 | 9.28 | 8.6 | 7.0 |
| Closed- | 1 | 2.55 | 2.54 | 7.5 | 8.4 |
| Loop | 6 | 5.00 | 4.68 | 15.0 | 15.8 |
| | 7 | 6.40 | 5.98 | 17.0 | 18.2 |
| | 10 | 9.30 | 9.30 | 13.0 | 12.0 |

⁺ Other Modes Not Appreciably Affected by Active Damping

FIGURE 9

^{*} Accuracy Approximately ± 20%

Several important conclusions can be drawn from work performed during Phase 1 of the PACOSS program. Most importantly, the best technique for control of large, flexible space structures is a combination of passive and active control. Passive augmentation is critical because the inherent damping in untreated precision structures is very small and unpredictable. It is possible, however, to design significant, predictable levels of passive damping into large space structures. Finally, the effects of active augmentation of a passively damped structure are predictable, at least for the case of LDVFB control systems.

Phase 1 Results

- Best Technique is a Combination of Active and Passive Control
- Untreated Precision Structures Have Low, Unpredictable Inherent Damping
- Significant, Predictable Damping Can Be Designed into Complex Structures
- Closed-Loop Performance with LDVFB Is Predictable

Knowledge gained from Phase 1 provided motivation for additional research, and development in related technologies provided the opportunity to significantly extend and enhance the Phase 1 results. Specifically, the Phase 2 activity included efforts to improve test data quality, to extend the passive/active vibration control strategy to include modern control algorithms, to provide a well-characterized test article for other researchers, to provide baseline data for the evaluation of modal parameter identification methods, to extend passive damping techniques to include viscous fluid dampers, and to quantify the benefits of the passive/active approach on a selected future system.

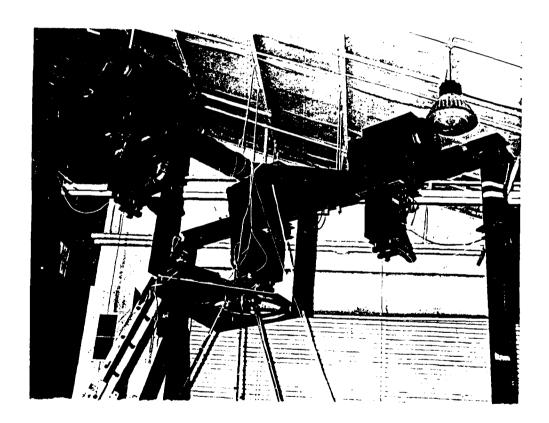
The system study was performed on a Grumman concept for a neutral particle beam spacecraft. This study was highly detailed, involving extensive analysis and simulation. Time does not permit a meaningful discussion of that study, so the rest of this presentation will concentrate on details of the enhanced DTA hardware and some of the more important experimental results.

Phase 2 Activities

- Improve Test Data Quality
- Passive/Modern Control
- National Testbed
- Baseline Parameter ID Data
- Viscous Fluid Dampers
- System Study

Major enhancements were made to the DTA. To improve data quality, 200 Kistler 8632A5 accelerometers were purchased to replace the PCB and Endevco accelerometers used during Phase 1. These accelerometers have a lower noise floor than those originally used, and virtually eliminate the phase differences between measurements.

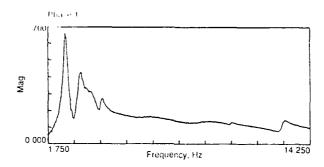
The mechanical ZSRM suspension system was replaced with three pneumatic suspension devices recently developed by CSA Engineering, Inc. The CSA devices provide a virtually friction-free suspension. The DTA was the first application which used more than one such device. Once a few initial bugs were eliminated, the pneumatic suspension devices provided many trouble-free hours of service during the extensive Phase 2 testing. Rigid body suspension frequencies for the 800 lb DTA are approximately 0.2 Hz.

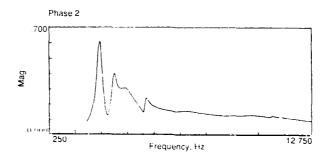


A comparison between typical Phase 1 and Phase 2 FRFs show the improvement in data quality. No effort was made to determine if the improvement was solely due to either the suspension system or the accelerometers.

The high density of heavily damped modes provides a challenge for existing parameter identification schemes. To provide an opportunity for researchers to test their algorithms, the PACOSS program provided a complete set of modal test data from Phase 2 testing, including geometry data and open-loop FRFs, to the Air Force. The FRFs are written on 1600 bpi magnetic tapes in universal file format.

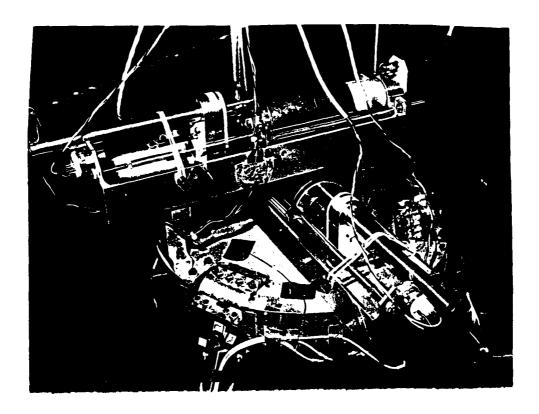
Phase 1/Phase 2 FRF Comparison





Several additional enhancements to the DTA were made to support the passive damping/modern control vibration suppression investigation. Four additional actuators were installed. Two of these actuators are identical to the Phase 1 versions, and are installed on corners of the box truss with active axis normal to the plane of the ring truss. The other two are modified versions with active axes in horizontal directions, and are installed on the secondary mirror. The horizontal actuators have open-loop frequencies of approximately 0.8 Hz. The control electronics for all actuators now also include the capability for position feedback.

To provide for non-collocated sensors, three Sundstrand accelerometers identical to those on the actuators were installation on the DTA, one on each of the solar array tips and one on the end of the box truss.



Control algorithms are implemented on a Systolic Systems Optima/3 digital controller. The Optima/3 is hosted by a Sun workstation with Pro-Matlab software. This controller has 32 inputs and 32 outputs, and is identical in capability to one in use at WRDC. Examples of the capabilities of this controller will be given in a later portion of this presentation.

At the conclusion of PACOSS, all DTA hardware including control sensors and actuators, pneumatic suspension system, and Kistler accelerometers will be delivered to WRDC. The PACOSS team will set up the DTA in the Vibrations Lab at WRDC, and train Air Force personnel on its use. The intent is to make use of this hardware available at WRDC to interested organizations.



Phase 1 of the PACOSS program demonstrated that viscoelastic shear dampers provide a highly effective, predictable mechanism for damping trusses and space frames. The mechanical properties of viscoelastics, however, are typically temperature sensitive. Viscoelastics are also prone to outgassing, which may limit their use in certain applications.

To provide an alternative to VEM dampers, the PACOSS program investigated one viscous fluid damper, the Honeywell D-Strut. The D-Strut concept was developed by Porter Davis and Jim Wilson, and is an extension of the vibration isolator in use on the Hubble Space Telescope. Dave Cunningham was the Honeywell technical lead. Brad Allen of CSA did the prototype testing for Honeywell and the acceptance testing of the delivery units for Martin Marietta. Technical direction was provided by Dan Morgenthaler of Martin Marietta, who also performed the system level tests.

The D-Strut investigation consisted of designing a hardware testbed representative of applications for D-Struts, and deriving performance requirements for the D-Struts from the testbed. The D-Strut design was then completed, and a prototype built and tested. Following satisfactory prototype testing, the delivery units were fabricated and tested individually. A modal survey of the undamped testbed was performed to verify that no significant inadvertent damping was present. The D-Struts were then incorporated into the testbed, and a modal surveys of the damped testbed were completed.

D-Strut Investigation

- Design Hardware Testbed
- Derive Performance Requirements
- Design D-Strut
- Prototype Fabrication and Testing
- Delivery Unit Fabrication and Testing
- System Level Testing

The D-Strut mechanism is shown schematically in the accompanying Figure 17, together with a five parameter model used to design the strut. K1 represents the stiffness of the outer tube, K2 is the stiffness of the inner tube, K3 is the shunt stiffness of the diaphragm, K4 is the series stiffness of the diaphragm/spring assembly and the fluid, and C is the damping constant for the orifice and fluid.

The purpose of the spring is to maintain a positive pressure on the fluid during extensional motion of the D-Strut to avoid cavitation of the fluid.

Requirements for the design are established by use of the modal strain energy method to determine an equivalent stiffness and loss factor (i.e., a complex stiffness) for the D-Strut which will provide the required damping in the test article. The mechanical impedance of the network is related to the complex stiffness of the D-Strut, and the values of the network parameters can be selected to produce the required performance.

D-Strut Design

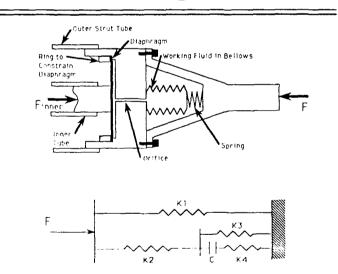


FIGURE 17

The five parameter network can be reduced to three independent parameters, a stiffness in parallel with another stiffness in series with a dashpot. This redundancy provides freedom to optimize components while achieving a design that will provide the desired characteristics. Physically, we can set three independent characteristics. Typical sets that could be specified are low frequency stiffness, high frequency stiffness, and frequency at which peak phase lead (or damping) occurs. Another set that can be used is static stiffness, frequency for peak damping, and phase lead.

The design goals for the PACOSS D-Strut were a static stiffness of 78,000 lb/in, the frequency for peak damping of 5.6 Hz, and a phase lead of 23.1 degrees. Making use of standard materials, the actual predicted values for the design were a static stiffness of 73,200 lb/in, the frequency for peak damping of 5.2 Hz, and a phase lead of 22.1 degrees.

After several prototype tests and modifications, fourteen delivery D-Struts were fabricated and tested. Results of those tests are shown below. As can be seen from the data, the phase angles measured were only about two-thirds of the desired value, with some scatter in all the parameters.

D-Strut Unit Tests

| \$S/N | Kstatic | φ PK; (deg) | 10, Hz |
|-------|---------|-------------|--------|
| 1 | 75K | 16.5 | 6.5 |
| 2 | 71K | 13.5 | 5.0 |
| 3 | 76K | 14.5 | 5.0 |
| 4 | 74K | 14.5 | 4.5 |
| 5 | 74K | 15.5 | 6.0 |
| 6 | 69K | 12.0 | 6.5 |
| 7 | 74K | 13.0 | 6.5 |
| 8 | 71K | 16.0 | 5.1 |
| 9 | 77K | 16.7 | 6.5 |
| 10 | 73K | 15.7 | 5.8 |
| 11 | 73K | 16.0 | 6.2 |
| 12 | 72K | 15.5 | 6.5 |
| 13 | 70K | 15.0 | 6.0 |
| 14 | 72K | 15.5 | 6.5 |

The loss in damping is due to additional compliance in some of the D-Strut components. Additional testing and analysis revealed that the additional compliance was due to difficulties in achieving good diaphragm clamping, a low modulus for the material of the inner tube, additional compliance in the spring housing and end fittings, and a low shear modulus of bonding material.

Program resources and schedule did not permit additional design refinement, so the best twelve units were selected for incorporation into the test article at Martin Marietta.

Additional D-Strut Compliance

- Poor Diaphragm Clamping
- Low Modulus Aluminum
- Spring/Housing
- Low Modulus Bonding Material

The test article for the D-Struts was an 8-bay, back-to-back K truss manufactured in three sections, two of three bays and one of five bays. One three bay section was undamped, and the other contained the 12 D-Struts as longerons. All joints with the exception of those joining the two sections were bonded. To provide a frequency separation in the first two modes (transverse bending), diagonally opposite longerons in the top five bays were constructed of aluminum for one pair and steel for the other. Several different tip weights were used to provide a range of fundamental frequencies from 3.5 Hz to 11.0 Hz.

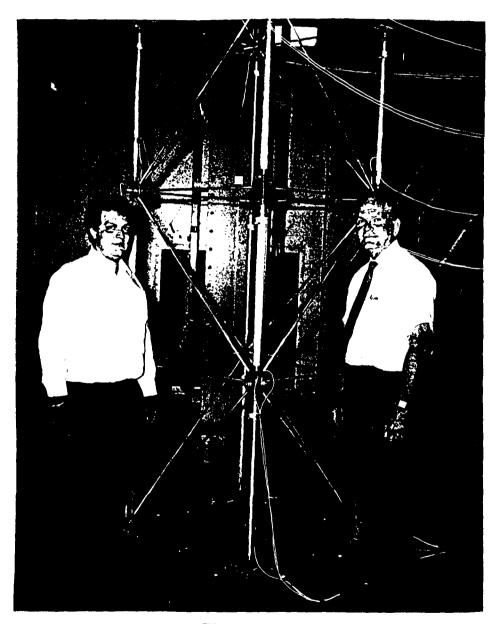


FIGURE 20

Results for one tip weight on the undamped and damped trusses are shown in Figures 21a and 21b, respectively. Examination of Figure 21a shows that virtually no inadvertent damping was present.

The analytic damped truss predictions shown in Figure 21b are based on complex modes derived from D-Strut network models based on parameter fits of the actual D-Strut data. Testing revealed that the D-Struts behaved linearly throughout the range of excitations applied. The smallest on-diagonal term exhibited in cross-orthogonality checks was 0.99, and the largest off-diagonal term was 0.03.

Undamped Truss Analysis/Test

| Measured Mode No. | Analytic Frequency, Hz | Measured Frequency, Hz | Measured Damping Ratio, % |
|----------------------|------------------------------|------------------------------|---------------------------------|
| 1 | 4.62 | 4.61 | 0.07 |
| 2 | 4.78 | 4.79 | 0.08 |
| 3 | 13.64 | 13.72 | 0.08 |
| 4 | 26.46 | 27.10 | 0.08 |
| 5 | 29.32 | 28.84 | 0.08 |
| 6 | 31.86 | 31.55 | 0.08 |
| 7 | 43.24 | 43.74 | 0.11 |

FIGURE 21a

D-Strut Truss

| | Analytic | | Measured | |
|----------|-------------------|----------------------|-------------------|----------------------|
| Mode No. | Frequency (Hz) | Damping Ratio (%) | Frequency (Hz) | Damping Ratio (%) |
| ~ | 4.98 | 7.23 | 5.00 | 6.59 |
| 2 | 5.10 | 9.62 | 5.25 | 9.43 |
| က | 13.61 | (0.1 | 13.68 | 0.11 |
| 4 | 26.20 | 0.72 | 26.79 | 0.79 |
| 2 | 28.42 | 0.28 | 28.16 | 0.39 |
| 9 | 30.77 | 0.49 | 30.67 | 0.52 |
| 7 | 40.70 | 0.22 | 40.99 | 0.26 |

Figure 21b

To provide a comparison of VEM dampers and D-Struts, a design for each was developed. The design goal was to have equal loss factor at 5 Hz. The VEM selected was Dyad 606, and the fluid selected was Dow Corning 200 Fluid (350cs).

One important advantage of D-Struts is that they exhibit a larger tolerance for temperature variations. The range for each damper that would result in a 10% change in loss factor or dynamic stiffness at 5 Hz was calculated.

Figure 22 shows that the current D-Strut design has a much lower static strength than the corresponding VEM damper, and adds more weight to the structure.

Comparison of Important Damper Characteristics

| | D-Strut | VESD |
|--------------------------------|----------------|---------------|
| Peak Loss Factor/Frequency | 0.275/6.0 Hz | 0.285/4.0 Hz |
| Loss Factor at 5.0 Hz | 0.270 | 0.280 |
| Equivalent Stiffness at 5.0 Hz | 96,000 lb/in. | 94,000 lb/in. |
| Static Stiffness | 78,000 lb/in. | 54,000 lb/in. |
| Static Strength | 600 lb | 5,70C lb |
| Damped Element Weight | 2.71 lb | 1.74 lb |
| Added Weight/Undamped Weight | 2.31 | 1.13 |
| Required Temperature Control | <u>+</u> 40° F | ±5° F |

FIGURE 22

In summary, D-Struts can provide effective damping treatments for truss structures. They provide an increased temperature range over VEM dampers and do not outgas. Although the current design adds more weight than the corresponding VEM damper and has lower strength, indications are that enhanced designs being developed both at Martin Marietta and Honeywell will overcome these limitations. In addition, both new designs should be less expensive to manufacture and exhibit much lower unit-to-unit variation.

D-Strut Summary

- Provide Effective Damping Treatment for Truss Structures
- Wider Temperature Range Than VEM
- Do Not Outgas
- Enhanced Designs Should Improve Strength and Reduce Cost and Weight

The active vibration control studies performed under Phase 2 are intended to extend the level of experience in vibration suppression to include the design, implementation, and testing of modern control algorithms as applied to dynamically complex structures in the presence of high levels of passive damping.

This effort was divided into two phases. First, a simplified control design experiment (CDE) was designed and implemented to provide a low-cost checkout of the Optima/3.

Then, several algorithms were implemented on the DTA. First, a digital implementation of LDVFB was implemented on the OPTIMA/3 to provide confidence that the DTA had remained unchanged, and the new suspension system was functioning properly. At the time of this presentation, modal space control with state estimator (MSC/EST), LQG/LTR, two versions of H-infinity, and LQG with residual mode filtering (LQG/RMF) have been implemented successfully. Some representative results will be presented here.

Phase 2 Active Control Studies

- Simplified Control Design Experiment (CDE)
- DTA Implementation
 - LDVFB
 - MSC/EST
 - LQG/LTR
 - H∞
 - LQG/RMF

Figure 25 shows the CDE. It consists of a latticework of thin beams suspended from cables and springs to ceiling trusswork. Light constrained layer passive damping treatments were applied over a small portion of the structure to give approximately 1-2% modal damping as an aid to stability. No effort was made to achieve high damping levels, and the finite element modal was relatively simple. The ceiling trusswork was much softer than anticipated, but modal frequencies were accurate to within less than 5%. As this was only a checkout and familiarization exercise, no effort was expended to refine the model.

Three of the DTA actuators were installed in symmetric positions on the structure. They served to provide excitation as well as control effort. In addition, one accelerometer for use in evaluating the LQG/LTR algorithm was installed on the right tip of the closest left-to-right member.

Control Design Experiment

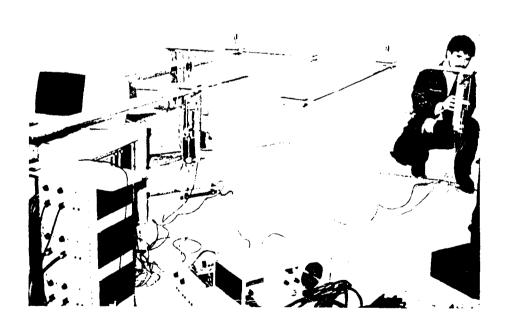


FIGURE 25

Figure 26 is a schematic of a top view of the Phase 2 version of the DTA, and shows the actuator and sensor locations. Only the 6 ring truss actuators were installed for the LDVFB and MSC/EST tests.

Each of the 10 actuators has two sensors, an accelerometer which measures incrtial acceleration and an LVT which measures the relative velocity between the actuator motor mass and the actuator frame. In addition, three non-collocated accelerometers are present, one each on the equipment platform and solar array tips. Thus, the DTA is suitable for implementation of control algorithms with as many an 23 inputs and 10 outputs.

Dynamic Test Article

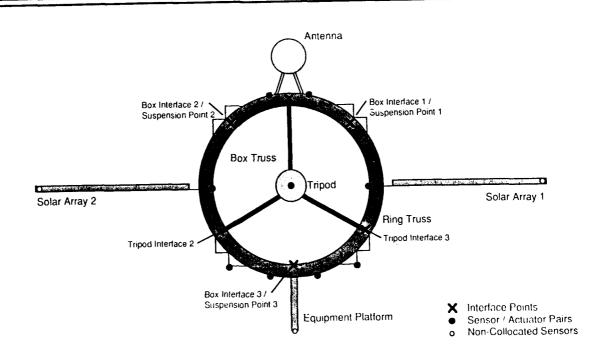


FIGURE 26

Figure 27 is a block diagram showing the MSC/EST algorithm as implemented on the CDE and the DTA. A Kalman filter is used to estimate the states, which are fed back through the feedback matrix K. The feedback matrix G is for damping in the actuator loops. Three collocated sensors/actuators were used on the CDE. Six collocated pairs were used on the DTA.

MSC permits targeting specific modes for active damping, the number of targeted modes being limited by the number of actuators used. Unlike LDVFB, other modes are unaffected, so all control effort is used on the selected modes. Thus, higher damping levels than from LDVFB may be attained.

Modal Space Control

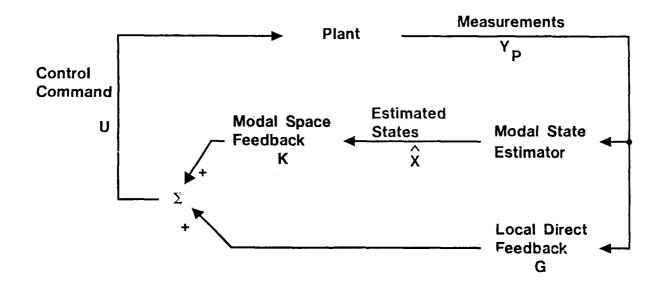
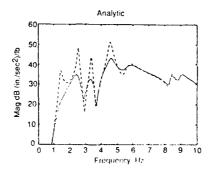


FIGURE 27

Figure 28 shows the open loop and MSC/EST closed loop analytic and measured FRFs on the CDE at the excitation point. The 1.5 Hz mode shown in both analytic plots is the actuator open-loop resonance. The next three modes were targeted for passive damping, and the agreement between analytic and measured FRFs is excellent. We note also that the modes in the 8-10 Hz range are not changed, demonstrating the selective nature of this algorithm.

CDE MSC/EST Closed-Loop



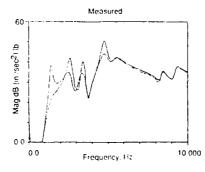


FIGURE 28

Figure 29 shows the open loop and MSC/EST closed-loop measured and FRFs at one of the DTA control points. The agreement is very good, although the control effectiveness is a little less than predicted.

DTA MSC/EST Closed-Loop

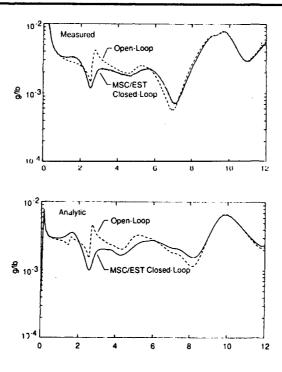


FIGURE 29

The MSC/EST performance on both structures agreed very well with analytic predictions. The design procedure for this algorithm naturally band limits control action due to the fact that specific modes are targeted for active damping. Thus, the algorithm can be made to ignore rigid body modes, and to roll off at high frequencies.

The roll-off, together with the collocated sensors and actuators, provided a stable controller. The performance of this strategy, however, is limited to what can be achieved by modal viscous damping.

MSC/EST Summary

- Excellent Agreement with Analytic Predictions
- Naturally Band-Limited
 - Ignore Rigid Body Modes
 - High-Frequency Roll-Off
- Performance Limited By What Can Be Achieved Through Modal Viscous Damping

FIGURE 30

Figure 31 is a block diagram of the LQG/LTR algorithm as implemented on the CDE and the DTA. A full state optimal regulator (K_c) is designed. Loop transfer functions are recovered at plant inputs (ii) by a Kalman-Bucy filter with gains (K_f) designed to estimate the states of the nominal plant model G(s). Increasing the gains improves the performance and more closely approximates full-state feedback. With this process, the gains in (K_f) can get very large, tending to reduce stability and requiring an excellent plant model.

LQG/LTR

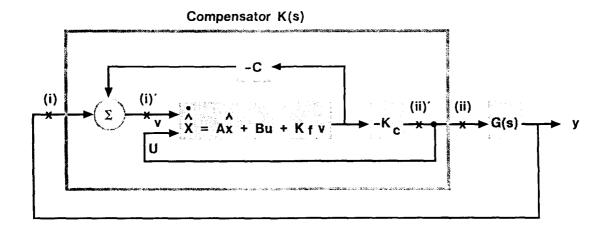


FIGURE 31

The LQG/LTR controller implemented on the CDE attempted to minimize the response at the tip accelerometer described previously due to an excitation on the centerline. Effectively, the algorithm attempts to achieve the desired performance by modal cancellation at the response point. Even though the hardware differed only slightly from the model used to design the algorithm, Figure 32 shows that the results were poor. Additional investigation showed that the poor performance was in fact due to the model/hardware discrepancy. Redesign of the controller using measured plant frequencies produced some improvement, but performance was still poor compared to analytic prediction, probably due to analytic mode shape errors.

CDE LQG/LTR Closed-Loop

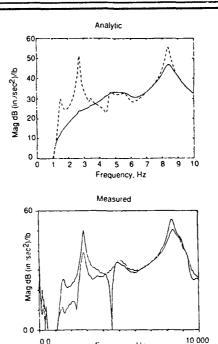


FIGURE 32

Frequency, Hz

The LQG/LTR controller implemented on the DTA attempted to minimize line of sight error and control effort. All 23 sensors and 10 actuators were used in the design. The open and closed loop analytic and measured results for one control point are shown. In Figure 33, we note that the measured performance is much lower than predicted, and has reduced the stability of the mode near 6 Hz. In fact, several modes were destabilized due to very small model/hardware differences and non-collocated sensors. In these cases, passive damping kept the closed loop system stable.

DTA LQG/LTR Closed-Loop

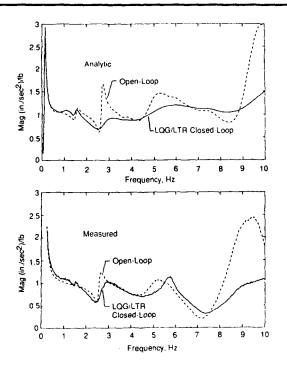


FIGURE 33

One remaining question was whether the discrepancies between predicted and measured performance of the modern algorithms was due to model errors, parameter identification errors, or some unknown problem in trying to couple modern control algorithms to heavily damped structures with high modal density. Figure 34 shows some of the discrepancies. The 1.5 Hz peak is due to an actuator, and the value of the FRF at the peak depends on the friction in the bearings. The discrepancy in open-loop magnitude at approximately 9.5 Hz is probably also due to actuator friction from the horizontal actuators interacting with a mode involving motion of the secondary mirror. Actuator friction is unpredictable, and these peaks varied from test to test.

Analytic/Measured FRFs

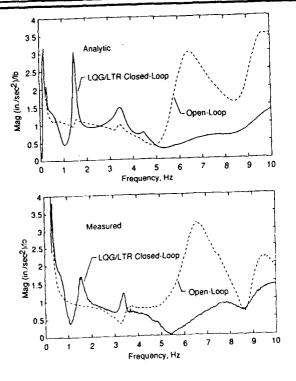


Figure 34

To investigate this issue, over 400 open-loop transfer function between actuator commands, sensor responses, disturbance points, and line of-sight variables were determined experimentally. Several closed-loop FRFs were then synthesized using the experimental transfer functions and the analytic control law to produce the synthesized closed-loop FRFs such as that shown in Figure 35.

As can be seen, the agreement between the measured and synthesized closed-loop FRFs, with the exception of those discrepancies due to actuator friction, is outstanding. Thus, it is apparent that good closed-loop predictions are possible if the plant is well-characterized.

Measured/Synthesized FRFs

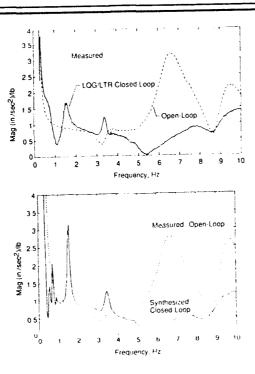


Figure 35

Nearly 200 accelerometer cables were required during the DTA model tests, and there was some concern that these cables were responsible for the discrepancies between the model and the measured test results which were so critical to control system performance. One disturbing fact was that the DTA rigid body modes were higher in frequency than predicted. It was postulated that even though the stiffness of each cable was very small, the collective effect might be sufficient to cause the apparent discrepancy.

Prior to test teardown, almost all the cables were removed and a few FRFs retaken. Figure 36 shows the FRFs with and without cables, and confirms the theory.

Rigid Body Modes

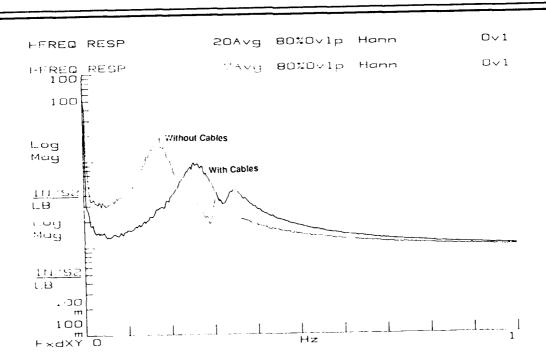
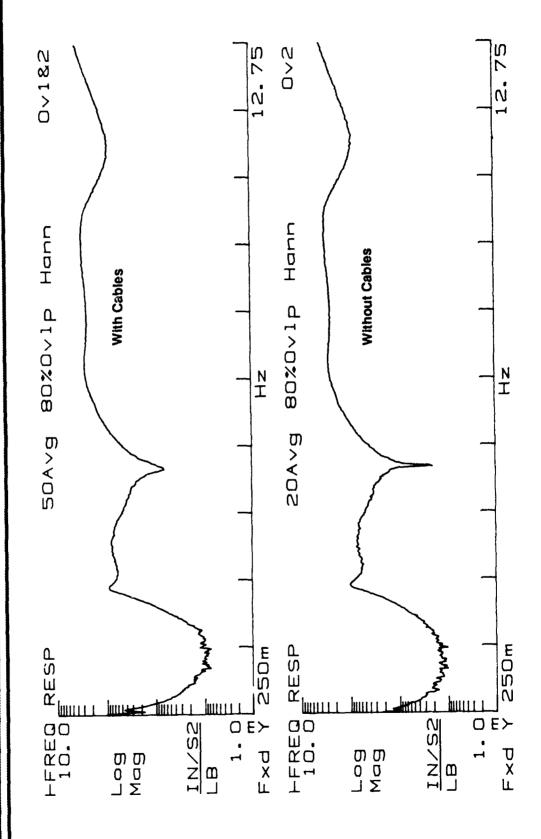


Figure 36

Figure 37 shows FRFs generated over the frequency range of interest with and without cables. As can be seen, the presence of the cables did not produce any appreciable effect in the frequency range of the flexible modes used in control design.

Typical Open-Loop FRF



Time does not permit a detailed discussion of the H-infinity design. A non-standard approach to H-infinity design was required to produce an open-loop stable compensator which did not attempt to do the pole-zero cancellations of lightly damped system modes that this algorithm typically does. By introducing additional modal uncertainties in the synthesis model, a stable compensator tolerant to some errors in specific modes was achieved and implemented, and was thus superior to the LQG/LTR system.

It must be remembered that the accuracy of the DTA finite element modal far exceeds that of a typical spacecraft. However, increases in control performance goals are accompanied by increases in sensitivity to model errors. In fact, even excellent accuracy in structural models may not be sufficient for aggressive designs which use non-collocated sensors in control systems for structures with closely spaced flexible modes.

Passive damping does allow the use of reduced order design models and compensators by increasing the stability robustness of the closed loop system, resulting in simpler, more reliable systems.

Modern Control Summary

- H_∞ Design More Tolerant of Model Errors
- DTA Model Accuracy Very High by Current Standards
- Model Accuracy Required for Aggressive Algorithms with Non-Collocated Sensors May Not Be Achievable by Purely Analytic Means
- Passive Damping Does Permit Use of Reduced Order Design Models and Compensators

FIGURE 38

In summary, since its inception, the PACOSS program has demonstrated that the best approach to structural vibration control requires a blend of passive and active vibration suppression. PACOSS has developed effective passive damping treatments, based on both viscoelastics and viscous fluids. PACOSS has also developed effective methods for determining a good if not optimal passive/active mix for generic systems. A highly effective active/passive control strategy for the neutral particle beam was developed. A similar study for Zenith Star demonstrated the effectiveness of the approach.

PACOSS technology is now available for use in the design of real flight systems.

Summary

- Best Approach Is Active/Passive Mix
- Effective, Predictable Passive Damping Treatments Developed and Demonstrated
- Methods To Determine Effective Mix Developed
- System Studies Show Effectiveness on Specific Systems
- Ready To Apply to Flight Hardware

FIGURE 39

RESEARCH STATUS OF THE DSMT **PROGRAM**

Paul E. McGowan NASA Langley Research Center

Lockheed Engineering and Sciences Co. **Mehzad Javeed**

Harold H. Edighoffer AS&M, Inc. Fourth NASA/DOD CSI Technology Conference Orlando, FL

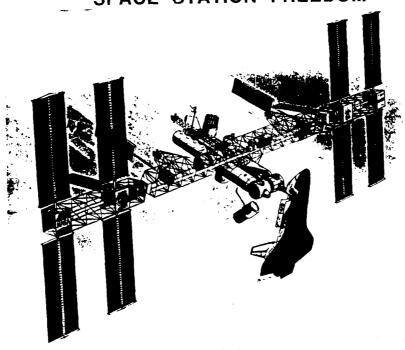
November 5-7, 1990

SPACE STATION FREEDOM

Verification of analytical models for spacecraft has historically been accomplished through ground tests of space hardware prior to flight. Due to the large size and flexibility of current space structure designs, ground tests of full-scale hardware may be limited to components and subassemblies. An example of such a structure is the proposed design for Space Station Freedom, which consists of an erectable truss structure interconnecting a number of flexible components, payloads and modules. When fully assembled the station has planform dimensions of approximately 200 ft. by 550 ft., weighs approximately 600,000 lbs, and its lowest natural vibration frequency is much lower than 1 Hz. No practical method exists for verifying through ground tests an integrated configuration of this structure. Thus, analysis models for structural dynamics predictions will be verified primarily through synthesis of component analysis models.

Ground tests of dynamically scaled models offer a potential to verify analysis methods for prediction of dynamic characteristics of large. flexible space structures. The use of scale models for structures such as space station is relatively new, but scale models do have a firm historical basis in the aircraft and space launch vehicle fields. Although the scale model may not replicate exactly the full-scale hardware, it can be used to examine sensitivity of the complete system response to modeling accuracy at the component level. By using the same analysis methods for predicting the scale model dynamics as those proposed for the full-scale system, the accuracy and viability of those methods can be evaluated.

SPACE STATION FREEDOM



DYNAMIC SCALE MODEL TECHNOLOGY

As part of the Control Structures Interaction (CSI) program at the NASA Langley Research Center (LaRC), the Dynamic Scale Model Technology (DSMT) project is developing scale model technology for large space structures. The objective of DSMT is to use scale models for verification of analytical methods for complex space structures which are too large to be ground tested. Space station was selected as the focus structure for DSMT since the station represents the first opportunity to obtain flight data on a complex, three-dimensional space structure. Under DSMT two laboratory models have been developed, namely, a generic simulated model and a hybrid-scale The scale model hardware consists of an erectable truss structure and includes many flexible components, modules and payloads which can be assembled to represent various stages of Space Station Freedom. Since the model is a good representation of space station it also provides a test-bed for examining some kev technical issues such as understanding interactions between flexible components and the global truss structural modes.

DYNAMIC SCALE MODEL TECHNOLOGY

PROGRAM OBJECTIVE:

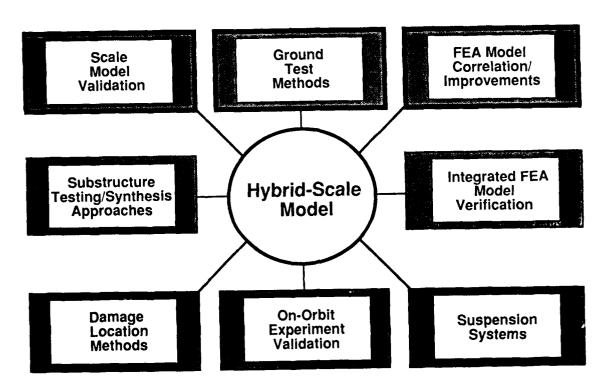
DEVELOP SCALE MODEL TECHNOLOGY TO VERIFY ANALYTICAL MODELS OF COMPLEX SPACE STRUCTURES TOO LARGE FOR GROUND TESTING.

- FOCUS STRUCTURE IS SPACE STATION FREEDOM
 - REAL STRUCTURE TYPICAL OF FUTURE SYSTEMS
 - OPPORTUNITY FOR ON-ORBIT DATA
- TWO MODELS:
 - 1) GENERIC SIMULATED MODEL (NOT-TO-SCALE)
 - 2) HYBRID-SCALE MODEL
- TEST-BED FOR USE IN EXAMINING KEY SPACE STATION FREEDOM DYNAMICS ISSUES.

DSMT RESEARCH AREAS

Depicted in the figure are the main research areas which are being studied using the hybrid-scale space station model. Since DSMT is a technology program these research areas are selected to address broad technical issues pertaining to other spacecraft structures as well. The eight major areas are interrelated and essentially involve validation of scaling laws, verification and improvement of analysis models through ground vibration tests, development of advanced suspension systems, validation of on-orbit experiment designs, substructure synthesis approaches, and development of damage location approaches. In this paper only the scaling, ground test and analysis approaches are addressed.

DSMT RESEARCH AREAS

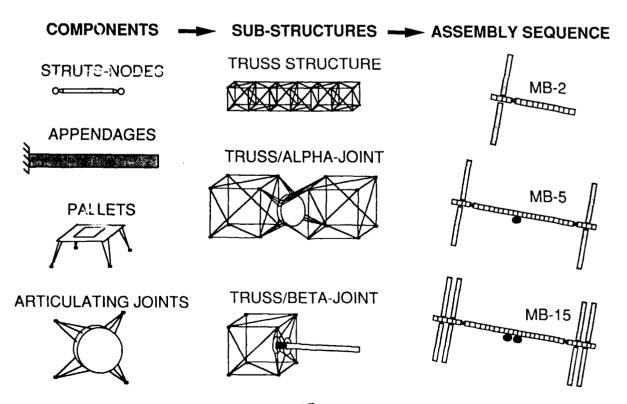


DSMT TEST/ANALYSIS VERIFICATION APPROACH

The approach adopted for verifying analytical models of the hybrid scale model consists of performing test/analysis updates at the component, substructure, and finally assembly sequence levels. As component models are refined that information is used to develop improved substructure analysis models which in turn lead to more accurate representations of the build assembly configurations. This approach parallels that of the full-scale space station program with the exception that DSMT can examine mated assembly configurations whereas space station cannot.

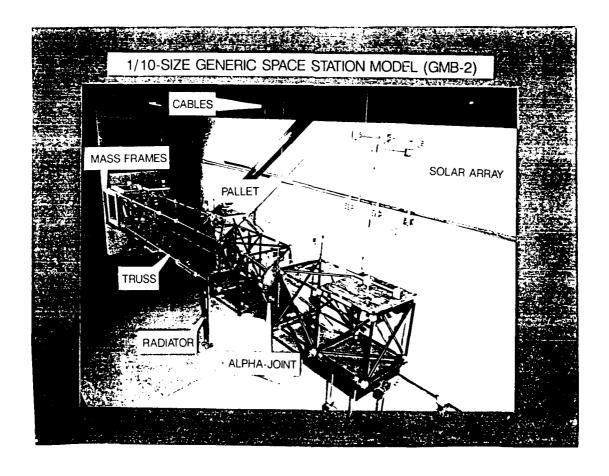
For the hybrid-scale HMB-2 model, the structure has been subdivided into twenty two components. These components are generally in one of four categories, namely, 1) truss structure, 2) appendages, 3) pallets, and 4) articulating joints. Each component will be individually tested and the corresponding analytical model will be updated to reflect the results of test data analysis. At the intermediate level substructures consisting of two or more components will be tested and analyzed to insure that the fidelity of the analytical model is preserved at all levels of complexity. Finally, the MB-2, MB-5, and MB-15 configurations will be studied to evaluate the primary object of this research program.

DSMT TEST/ANALYSIS VERIFICATION APPROACH



1/10-SIZE GENERIC SPACE STATION MODEL (GMB-2)

The Generic MB-2 configuration space station model (GMB-2) is a 1/10-size simulated model utilizing commercially available truss hardware known as MEROFORM. In the figure the GMB-2 model is shown suspended in the configuration used for dynamic testing. The model was designed to simulate the dynamics of the more complicated hybrid-scale model. Simulated appendages were fabricated to have characteristics resembling the hybrid model. The model was used to study and evaluate analytical modeling and analysis techniques as well as experimental testing methods prior to examining the hybrid model.



SUSPENDED GENERIC MODEL TEST/ANALYSIS COMPARISONS

The generic GMB-2 model suspended by six cables was analyzed MSC/NASTRAN finite element model and was compared An initial finite element model was developed with the test results. based on component test/analysis correlations. This initial model still produced some inaccurate predictions of higher modes. updated model which was in good agreement with test results was developed by performing additional model refinement especially at the main structural interfaces. Mode No. 4, the rigid body roll mode was improved because of the improved mass distribution of the components giving the correct roll mass moment of inertia. of the solar array and radiator modes dominated the equivalent system modes. Thus, the solar array and the radiator truss mounting plates were revised at the component level to correct the plate bending stiffness and match the static and dynamic response at the component level. These appendage modes matched the analysis at the component level and then correlated at the system level without additional adjustments.

SUSPENDED GENERIC MODEL Test/Analysis Comparisons

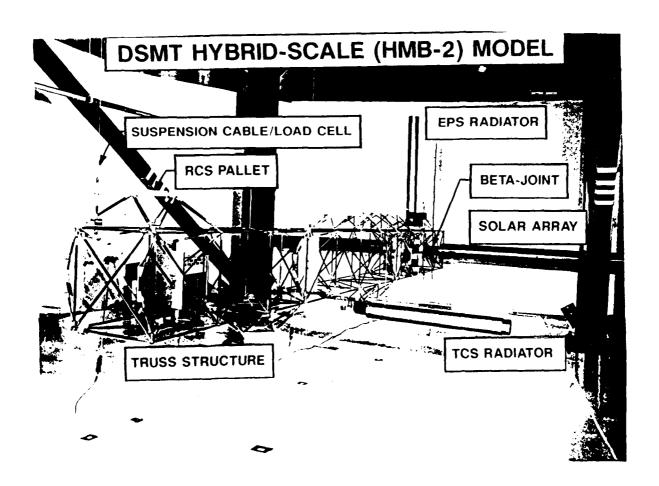
FREQUENCY (Hz)

| | ANALY | (SES | | |
|------------------|-----------|-------|-------|----------------------------------|
| MODE | INITIAL _ | FINAL | TEST | <u>DESCRIPTION</u> |
| | | | | |
| 1 | 0.085 | 0.088 | * | Yaw |
| 2 3 | 0.118 | 0.117 | • | Y Trans |
| 3 | 0.118 | 0.118 | * | X Trans |
| 4 | 1.89 | 1.65 | 1.60 | Rigid Roll |
| 4 5 6 7 | 2.40 | 1.94 | 2.07 | Rigid Pitch |
| 6 | 2.59 | 2.56 | 2.49 | SA OP B1 Sym |
| 7 | 3.54 | 2.65 | 2.78 | Z Trans + SA OP B1 Anti-Sym |
| 8 | 3.14 | 2.74 | 2.89 | SA OP B1 Anti-Sym |
| 8 9 | 3.27 | 3.25 | 3.05 | SA IP B1 Anti-Sym (Top SA IP B1) |
| 10 | 3.38 | 3.38 | 3.28 | SA IP B1 Sym (Bot SA IP B1) |
| 23 | 5.88 | 5.70 | 5.97 | Radiator OP B1 |
| 24 | 7.12 | 7.14 | 7.12 | SA T1 Sym (Top SA T1) |
| 25 | 7.16 | 7.21 | 7.34 | SA T1 Anti-Sym (Bot SA T1) |
| 32 | 12.95 | 9.10 | 8.17 | Truss X-Z B1 |
| 33 | - | 9.36 | | Twist of 2 Bay Section |
| 38 | 13.48 | 9.84 | 8.94 | Truss X-Y B1 |
| 55 | 17.54 | 17.47 | 19.91 | Radiator IP B1 |
| 56 | 17.63 | 17.75 | 17.76 | SA OP B2 Sym (Except Mid Pts) |
| 61 | 16.53 | 18.39 | 19.09 | SA OP B2 Anti-Sym |

SA: Solar Array, OP:Out-of-Plane, IP:In-Plane, B1:1st Bending, B2:2nd Bending, T1:1st Torsion Did not measure

DSMT HYBRID-SCALE MODEL

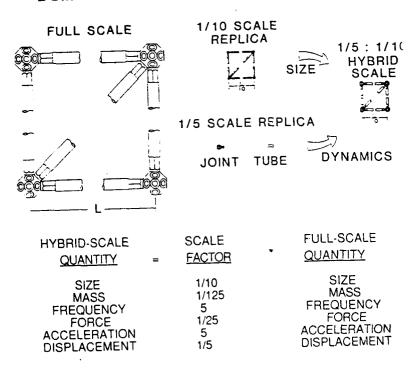
Shown in the figure is a hybrid-scale structural model of an early Space Station Freedom assembly configuration (MB-2). scaling refers to the 1/5:1/10 scale factor applied to the model design. Hybrid scaling technology was developed for this model to achieve a ground test article which existing test facilities can accommodate while employing realistically scaled hardware. truss planform dimensions have been scaled to 1/10-size of the fullscale station design. The truss nodal joints, mass and frequencies are This design provides a model which can be tested in existing facilities, yet has the low frequency dynamics characteristic of the station structure. The model was developed by the Lockheed Missiles and Space Company, Sunnyvale, CA. The MB-2 configuration consists of ten truss bays which are connected by an articulating rotary joint and on which a number of solar arrays, radiators and pallets are mounted. Ground tests of this model will be performed at LaRC to develop techniques for predicting the on-orbit dynamic response of such structures.



DSMT HYBRID-SCALE MODEL DYNAMICS

Hybrid scaling provides a dynamically scaled space station model such that a realistic test article can be obtained for developing test and suspension techniques required for verifying analytical models. Hybrid scaling employs classical distorted scaling techniques, which have historically been used extensively for wind tunnel models. When used for large space structures it permits the use of different scale factors for the truss structure components, appendages and payloads while sacrificing local dynamic behavior, but retaining overall global dynamics behavior. The hybrid-scale model truss structure bay size and truss joint components were selected to be This results in a model which is 1/10 and 1/5 scale, respectively. small enough (50' x 30' planform) to be assembled and tested in an existing LaRC facility. Furthermore, the 1/5-scale joints are essentially the minimum size at which erectable joints can be large manufacturing fabricated without incurring compromising joint performance. Properly distorting the truss component stiffnesses and masses yields a model which possesses the same global dynamic properties as would a fully 1/5-scale replica model. Some of the scale factors which apply to the hybrid model are listed in the figure.

DSMT HYBRID-SCALE MODEL DYNAMICS



DSMT HYBRID-SCALE MODEL FEATURES

The DSMT hybrid-scale model utilizes erectable joints and modular components such that any number of space station configurations can be assembled. This allows the model to be representative of each of the approximately 20 assembly flights required to reach the assembly complete station. Depicted in the figure are the three focus configurations selected for study. The MB-2, MB-5, MB-15 designations refer to space station mission build configuration numbers. As seen in the table these three structures span a wide range of structural parameters. Also, by varying mass properties of the payload components, the hybrid-scale model structure can be adjusted to reflect changes in the station design.

DSMT HYBRID-SCALE MODEL FEATURES

- ERECTABLE JOINTS AND STANDARDIZED COMPONENTS PERMIT TESTBED TO BE ASSEMBLED IN ANY CONFIGURATION
- MASS PROPERTIES OF MANY COMPONENTS CAN BE ADJUSTED VIA MODIFICATION OF LUMPED WEIGHTS





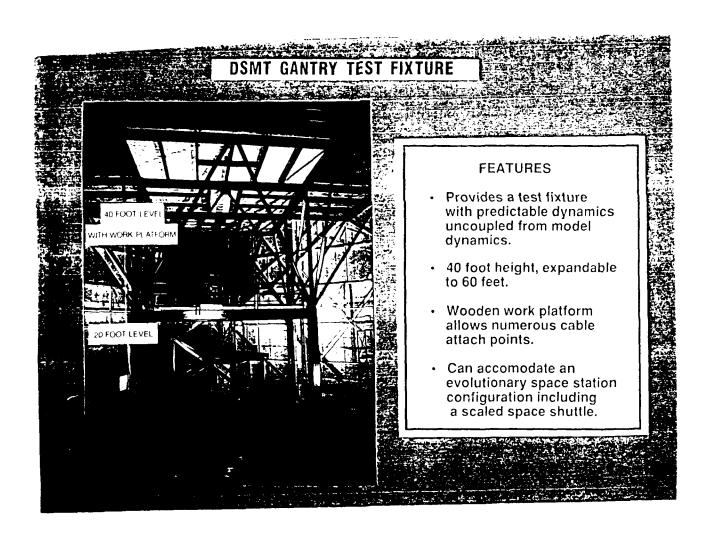
PSC 20/13 MB-15



| 1/5:1/10 Scale | HMB-2 | HMB-5 | HMB-15 |
|---------------------------------------|---------|---------|---------|
| Dimensions (ft) | 19 x 23 | 35 x 23 | 48 × 23 |
| Weight (lbs) | 363 | 1306 | 3621 |
| Freq Range (Hz) (1st 10 Sys Modes) | 5 - 37 | 2 - 8 | 1 - 7 |

DSMT GANTRY TEST FIXTURE

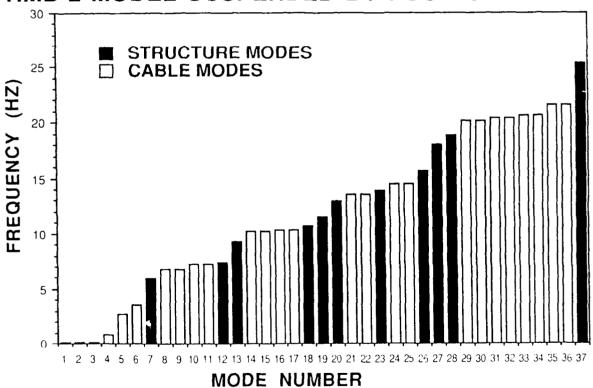
The gantry fixture is the support structure for the DSMT hardware. The fixture is capable of supporting various configurations of the DSMT space station model. There are currently two working platforms at 20 ft. and 40 ft., and the gantry can be expanded to 60 ft. These platforms allow for numerous support locations as well as various support mechanisms. The structural characteristics of the gantry are known and uncoupled from the current suspended models. Provisions were made to have the capability to remove some structural members from the gantry for positioning of large models.



VIBRATION FREQUENCIES FOR HYBRID-SCALE HMB-2 MODEL SUSPENDED BY FOUR CABLES

The hybrid-scale HMB-2 model suspended by four cables was evaluated using an MSC/NASTRAN finite element model. Depicted in the figure is the modal density for this structure in the suspended configuration. There are 37 modes in the frequency range of interest from (0-25 Hz), 11 of these modes are considered global structural modes. Analysis of this structure required that the cable forces needed to keep the model level due to gravity loading be determined using a static analysis. The second step was to perform a non-linear analysis imposing preload cable strains and gravity forces to arrive at the deformed level position with the correct cable forces. The final step was to perform the normal modes analysis using a combined stiffness matrix consisting of the elastic stiffness plus the differential stiffness due to the internal forces from the second step.

VIBRATION FREQUENCIES FOR HYBRID-SCALE HMB-2 MODEL SUSPENDED BY FOUR CABLES



DSMT COMPONENT TEST/ANALYSIS RESULTS

A number of components from the HMB-2 scale model have been examined to date. Listed in the figure are the test/analysis correlations for six components. The initial analysis models were based on preliminary design information and were developed prior to fabrication of the hardware. These models were updated based on the results obtained from the analysis of the test data associated with each component. In performing the analysis updates the geometry, mass distribution, and stiffness characteristics of components are examined and corrected as part of the verification process. In addition, design sensitivity analysis methods are used to examine the influence of various physical and material properties on the component structural characteristics. Information from the resulting component analysis models are now being included in a new analysis model of the assembled HMB-2 structure.

DSMT COMPONENT TEST/ANALYSIS RESULTS

HMB-2 MODEL WITH RIGID APPENDAGES

FUNDAMENTAL FREQUENCY (HZ)

| COMPONENT | INITIAL ANALYSIS | FINAL ANALYSIS | TEST |
|----------------|---------------------|-------------------|-------|
| EPS RADIATOR | 46.19 | 44.17 | 43.53 |
| SOLAR ARRAY | 21.29 | 19.83 | 18.87 |
| TCS RADIATOR | 26.36 | 23.45 | 23.10 |
| BETA-JOINT | 157.0 | 72.70 | 69.70 |
| TRUSS LONGERON | 22.09 | 19.74 | 19.75 |
| ONE TRUSS BAY | 92.17 | 77.80 | 77.90 |

POTENTIAL VERIFICATION MATRIX FOR ON-ORBIT STRUCTURAL DYNAMICS PREDICTION

For a structure as complex as the space station numerous programs are required to develop a verification matrix which will allow the accurate prediction of structural dynamics of the mated structure in zero-g. As shown in the table, DSMT is one important element in such a matrix, but it alone is not sufficient for complete analysis verification. DSMT does provide verification of analysis at both the component and mated levels, but in a 1-g environment. The MODE experiment provides a zero-g verification of similar hardware to DSMT, but only at the component level. In addition, there will be component level full-scale ground tests of space station hardware. Finally, the proposed MIE project will provide on-orbit data from components, which are instrumented on the station, and on the mated station for final analysis verification.

POTENTIAL VERIFICATION MATRIX FOR ON-ORBIT STRUCTURAL DYNAMICS PREDICTION

| | SUB-SCALE | | FULL-SCALE | |
|-----|--------------------|-----------------|-------------------------|-----------------|
| | COMPONENT | MATED | COMPONENT | MATED |
| 1-g | DSMT Program | DSMT Program | S.S. Freedom Project | |
| 0-g | MODE Experiment | | MIE Project | MIE Projecty |

DSMT=Dynamic Scale Model Technology (NASA LaRC)
MODE=Mid-deck On-orbit Dynamics Experiment (MIT/NASA LaRC)
MIE=Modal Identification Experiment (NASA LaRC)

Goal for On-orbit Structural Dynamics Predictions

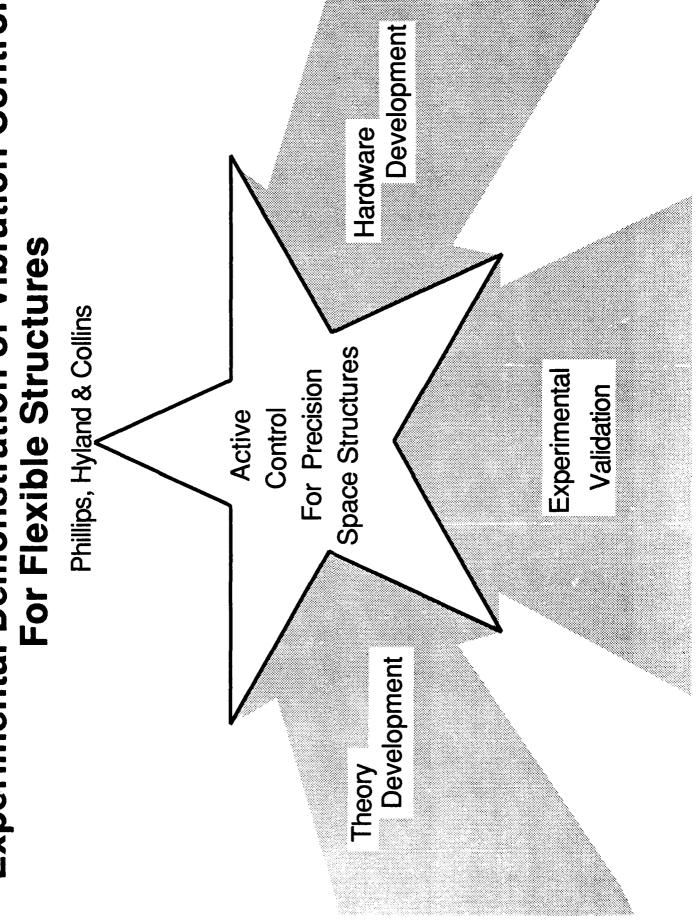
CONCLUDING REMARKS

DSMT is a technology program which has Space Station Freedom as a focus structure. The hybrid-scale model hardware is the nucleus of a broad based research effort which includes the development of ground tests and analysis methods for a large class of structure. Due to the resemblance of the scale model to space station, DSMT does provide a ground test-bed for examining key technical issues. Also, the approach for analysis verification does parallel that proposed for space station, with the added benefit of providing mated structure test/analysis correlation. Finally, the use of scale models should be considered an integral part of an overall verification plan for a complex space structure.

CONCLUDING REMARKS

- DSMT IS A TECHNOLOGY PROGRAM WITH SPACE STATION FREEDOM AS A FOCUS STRUCTURE.
- GROUND TEST/ANALYSIS OF MODEL HARDWARE PROGRESSING WELL.
- SCALE MODEL HARDWARE PROVIDES GROUND TEST-BED FOR EXAMINING SPACE STATION TECHNICAL ISSUES.
- APPROACH FOR ANALYSIS VERIFICATION EXPLOITS USE OF COMPONENT LEVEL TEST/ANALYSIS UPDATES.
- SCALE MODELS ARE AN INTEGRAL PART OF ON-ORBIT STRUCTURAL DYNAMICS ANALYSIS VERIFICATION.

Experimental Demonstration of Vibration Control



We believe that active control for Precision Space Structures (PSS) is (and should be) a <u>rising star</u>.

Three of the activities providing the propulsive forces for this rise are: Basic theory development for structural control (to execute basic design tradeoffs) and experimentation for two purposes...

... experimentation for validation of control design approaches (illustrated here by experiences on NASA test-beds) and experimentation for development and test of **new** hardware which makes the control problem easier (illustrated by testing on the Harris MHPE).

This presentation is an overview of progress in both experimental validations and hardware developments.

Two Aspects of Experimentation are Covered in this Presentation

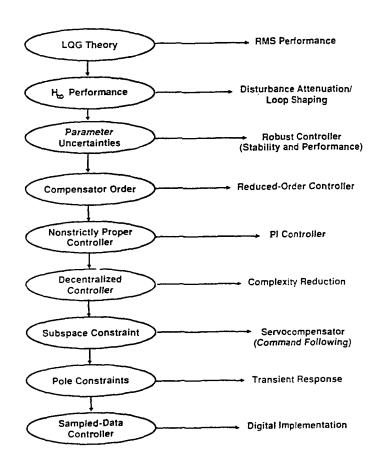
- Experimentation for control design theory validation
 - using NASA test-beds
- * Experimentation for development and test of new structural control hardware
 - using the Harris MHPE test-bed

First the starting point in our technology development is basic control design theory for PSS.

The product of this theoretical effort is:

Optimal Projection for Uncertain Systems (OPUS)

Opus is an optimization-based theory incorporating various design constraints (reduced-order, decentralization) and effects of uncertainty (structured/unstructured, parametric/nonparametric) to give a sufficiently comprehensive framework for design and performance evaluation.



OPUS systematically addresses numerous practical control-design criteria within a unified framework.

We discuss experimental validation of the OPUS design theory on NASA hardware as part of Harris activities on the NASA CSI GI Program. This chart summarizes the GI Program Plan, the NASA testbeds used and the composition of the Harris GI team.

The following contains a very brief overview of our results the details of which are given in Harris contractor reports to NASA.

NASA Controls-Structures Interaction (CSI) Guest Investigator (GI) Program

Administered by the CSI Office, NASA Langley Research Center

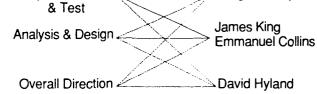
Purpose: Experimental evaluation of advanced techniques in active structural control, structural modelling, fault detection & fault-tolerant control

Plan: Two-year research grants for the period Jan. 30, 1989-Jan 30, 1991 were awarded to eight investigative groups. Each GI spends a year of research effort on each of two NASA facilities

Test-beds:

ACES (Advanced Control Evaluation for Structures)
Facility - at NASA/MSFC
Minimast Facility - at NASA/LaRC

Harris CSI GI Team Implementation Douglas Phillips



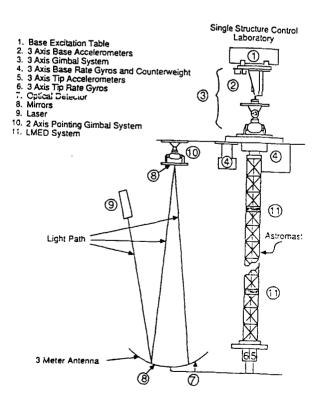
We were first assigned to the ACES facility at NASA/Marshall.

Described from the top down; the whole ACES test article is suspended from the Base Excitation Table (BET) (which provides disturbance inputs) and is pivoted via the Advanced Gimbal System (AGS) holding the base plate for the main structure. The structure consists of the following components:

- * two horizontal arms -one holding the Image Motion Compens.Gimbal (IMC)
- * a 45 ft. Astromast
- * two legs at the Astromast tip, one holding a 3 meter antenna structure

In the Line of Sight (LOS) monitoring system, light from a laser is reflected from a mirror on the antenna, up to a mirror on the IMC and then down to a detector array. For control, Harris used: IMC, AGS, LMEDs, Rate Gyros, Optical LOS detector, and the LMED accelerometers, for reduction of LOS errors as measured by LOS Optical Detector.

THE ACES CONFIGURATION



On ACES, the Harris GI team provided its own models for use in control design by using the Eigensystem Realization Algorithm (ERA).

Developed by Jer-Nan Juang, Richard Pappa et al at NASA/Langley, ERA has proven a most effective system identification tool.

As this comparison of ERA model frequency response versus FRF data shows, ERA produced an overall system model of excellent quality for control design.

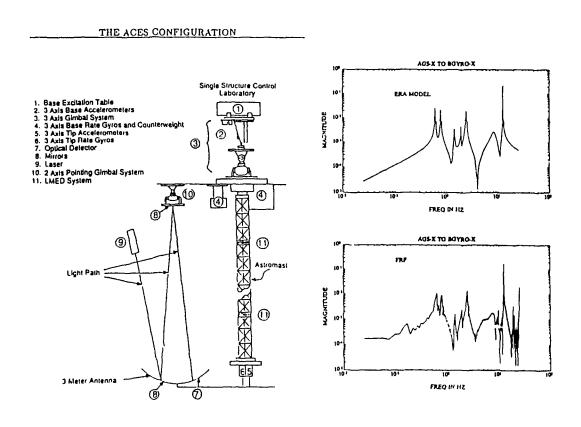
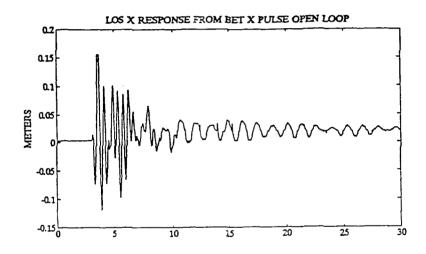


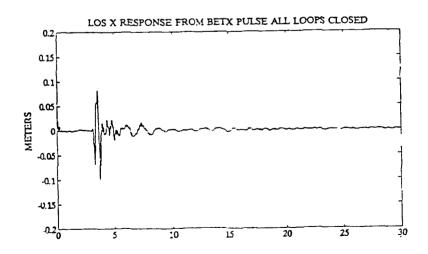
Figure 14. The NASA/MSFC ACES structure provides a case study for modeling in support of control design.

The OPUS design for ACES was decentralized with low-order sub-controllers. One feature of the design is that it is "connectively stable" i.e., subsets of hardware can fail and stability is maintained, with graceful performance degradation.

The full design was tested at MSFC on Jan. 15, 1990. This chart shows test data on open—vs. closed—loop LOS response to a BET impulse disturbance. LOS performance improvement is very satisfactory. The sizable open—loop bias error reduced by three orders of magnitude and the effective damping decay time is reduced by nearly a factor of ten.

NASA CSI PROGRAM



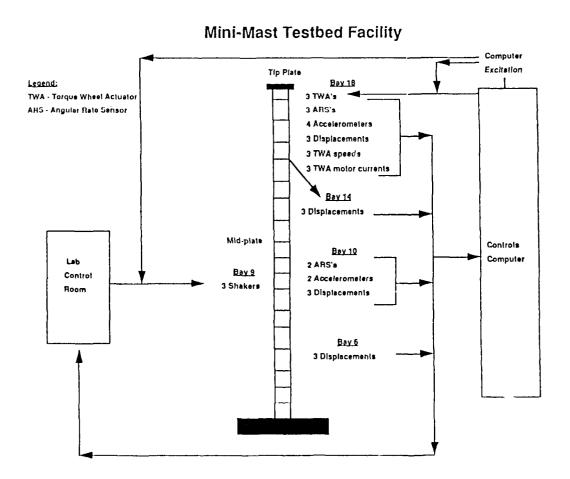


During the second year of our CSI GI Program, we were assigned to the NASA/Langley Minimast facility.

The Minimast comprises the following features:

- * A deployable/retractable truss beam, ~20 M high, cantilevered to the base (18 Bays)
- * 3 disturbance shakers at Bay 9
- * 2 instrumentation platforms at Bays 10 & 18 (Tip)

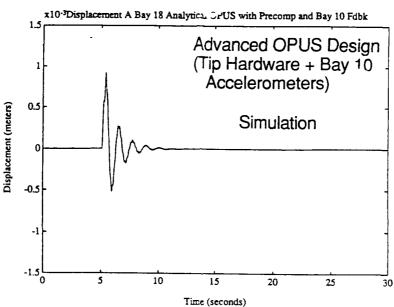
For control, we used the 3 torque-wheel actuators at the tip and accelerometers at Bays 10 and 18. The control goal was to suppress tip displacement and torsional rotation. For use as a design model we were provided an excellent FEM by LaRC and validated this model with open-loop test data comparisons with ERA.

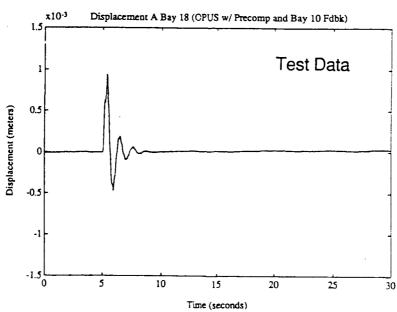


Several control approaches were tested, ranging from simple rate feedback to an OPUS design using Tip hardware and Bay 10 accelerometers. All designs were tested Aug. 29, 1990. Closed-loop results virtually replicated analytical predictions.

We illustrate this agreement here with a comparison of prediction vs. test of tip displacement response to a Bay 9 shaker impulse, for the OPUS design closed-loop case.

Minimast: Analytical Prediction vs. Test Data



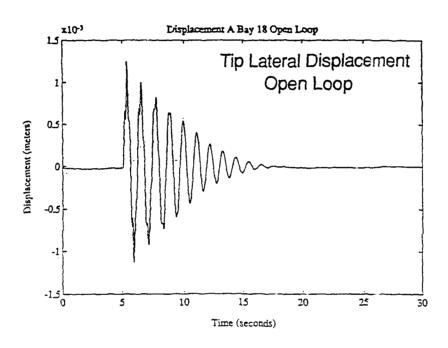


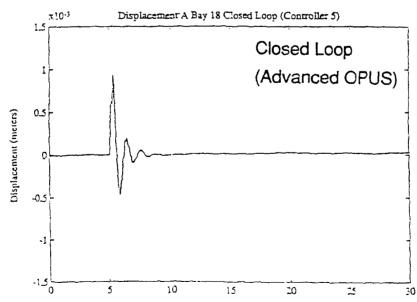
This chart gives test data showing performance of the OPUS design.

The chart includes open- vs. closed-loop results for tip displacement due to identical shaker impulses.

The closed-loop response exhibits striking performance improvement and requires only three oscillations to damp to imperceptible amplitude.

Minimast: Open-Loop vs. Closed-Loop Performance

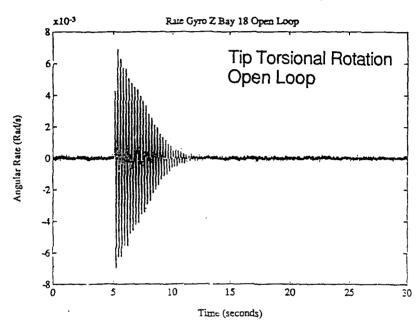


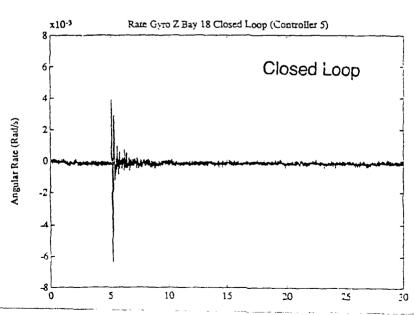


This chart gives open- vs. closed-loop comparison for tip torsion angular rate due to z-axis torque wheel input.

Closed-loop vibration damps out in $\sim\!2$ periods of the first torsion mode.

Minimast: Open-Loop vs. Closed-Loop Performance





The foregoing results indicate that the selected system ID and control design tools provide effective reliable means to obtain high performance control strategies for a given set of control hardware.

Now we switch gears in this presentation to consider experiments for the development and demonstration of **new** hardware offering intrinsically better capabilities for vibration control.

We illustrate by test activities on the Multi-Hex Prototype Experiment (MHPE).

- Experimentation for the purpose of theory validation (reliable methods for securing best performance with given hardware)
- Experimentation for improved hardware (enhanced hardware capability to facilitate implementation)



Illustrated by the Multi-Hex Prototype Experiment (MHPE) testing activities supporting LPACT actuator/sensor demonstration

MHPE

- fully instrumented and operational vibration-control test-bed (live demo.s of vibration control provided since Oct. 1988)
- focusses on vibration control problems of a distinct class of LSS of long-term interest

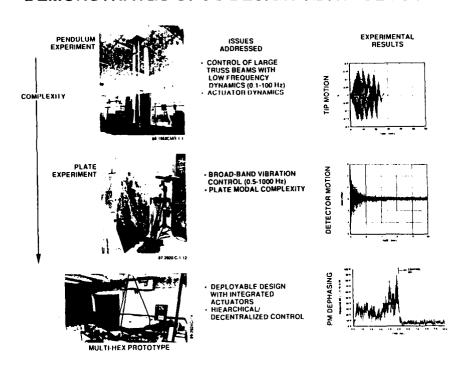
The MHPE is the third in a sequence of IR&D experiments ranging from the simple one- and two-dimensional structures to a complex built-up structure -i.e., MHPE.



GOVERNMENT AEROSPACE SYSTEMS DIVISION

Electronic Systems Sector

A SEQUENCE OF HARRIS CONTROLS EXPERIMENTS DEMONSTRATES OPUS DESIGN TECHNOLOGY



392-01 (M)

MHPE addresses the generic configuration shown here.

This generic concept consists of a secondary mirror and support platform and a secondary mirror support tower connected to the center of a segmented deployable primary reaction structure. The reaction structure supports a segmented primary mirror or reflector surface. The system might employ active mirror figure control devices which connect the facesheets to the reaction structure. A primary support truss connects the reflector to the spacecraft main body through an isolation subsystem - which is essentially equivalent to a low stiffness isolation mount.

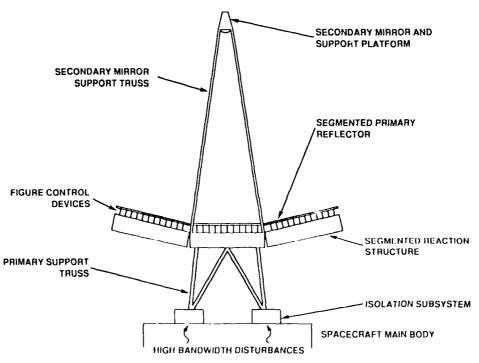
The system must maintain its alignment and geometric accuracy in the face of broadband vibrational disturbances propagating from the spacecraft main body.



Electronic Systems Sector

GOVERNMENT AEROSPACE SYSTEMS DIVISION I

GENERIC LSS CONFIGURATION MOTIVATING THE MHPE DESIGN

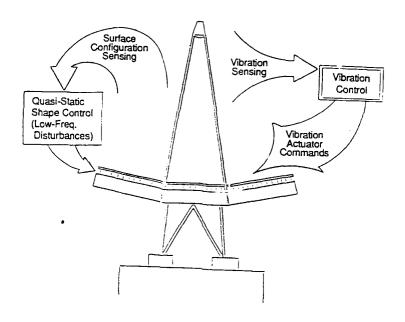


392-22 (M)

Control issues of such a system concept include:

- * Quasi-static adjustment of the PM surface & PM/SM alignments to correct errors due to low frequency (<1st mode frequency) distortions (e.g., thermal)
- * Vibration-induced alignment & surface errors (> 1st mode frequency)

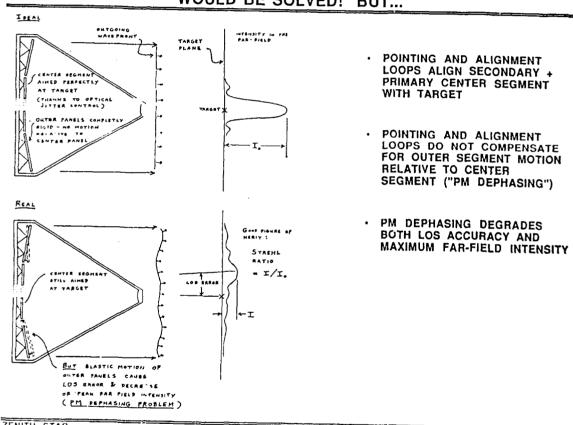
The Quasi Static errors are to be corrected by a separate (low bandwidth) sensing & control system. MHPE assumes such a quasi-static control is operating - and addresses mainly the vibration-induced errors (due to high bandwidth disturbances)



- * Regarding Control of Quasi-Static Errors (With Frequency Content <1st Mode Frequency), MHPE Assumes Either "Set & Forget" or Ideal Operation of a Quasi-Static Shape Controller.
- * MHPE Focusses on <u>Vibration Induced</u> Errors Due to Broad-Band Disturbances.

Vibration-induced errors include not only LOS jitter, but also "Primary Mirror dephasing". The PM dephasing issue illustrated here, arises because vibrational disturbances cause misalignments of the individual PM segments relative to one another. According to the laws of diffraction such "dephasing" of the PM segments can cause considerable reduction of the peak radiation intensity in the far field. Often, PM dephasing cannot be readily compensated by alignment elements in the system optical train and structural control of the PM assembly may be desired.

IF ONLY THE PRIMARY MIRROR WERE RIGID, OUR PROBLEMS WOULD BE SOLVED! BUT...



ZENITH STAR ACTIVE STRUCTURAL CONTROL

HARRIS CORPORATION

Motivated by these concerns, initial MHPE configuration was made operational in May '88. Live demos of vibration control have been given since October '88 (and continue).

The MHPE has been incrementally upgraded in Jan. '89, and in March '90 to reach its present configuration in May '90 .

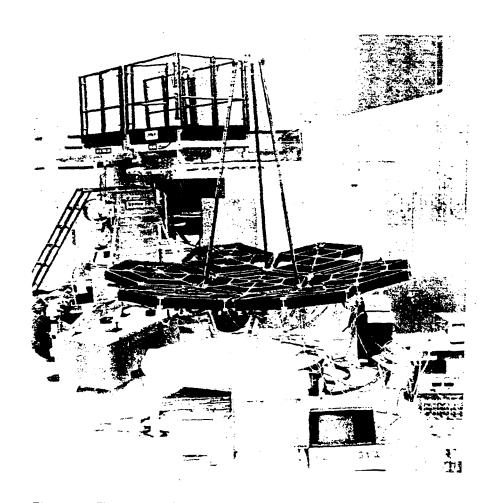


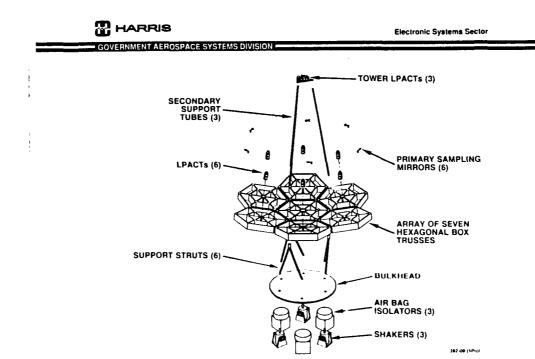
Figure 2.8. The present configuration of the MHPE testbed includes 3 LPACTs on the triangular plate at the top of the secondary tower and a small mirrors between the center and outer edge of each of 6 outer hexagonal panels. The mirrors are used in a laser-based optical system for visual representation of the line-of-sight performance. The Optical Precision Measurement System (OPMS) is located in the circular table underneath the hexagonal panels.

As this illustration indicates, MHPE emulates most features of the generic system, including the following features:

- * An all Gr/Ep structure
- * The secondary platform holds an active secondary mirror
- * The Primary Reaction Structure is a 4 M diameter array of 7 Gr/Ep Hex Panels
- * PM simulated by small mirrors distributed over the Hex array
- * Base-plate simulates S/C bulkhead where shakers used to input disturbances

Los jitter & dephasing are monitored by 3 complementary subsystems:

- 1. Accelerometer based "pseudo-dephasing" measurement system.
- 2. Optical Precision Measurement system (OPMS) using laser interferometry to measure panel to-panel misalignments.
- 3. LOS scoring system laser source, faceted secondary mirror and primary mirror sub-apertures on the hex array.



Besides addressing vibration control problems of a generic PSS concept, MHPE both stimulated the invention of & served as a test vehicle for a new actuator, the Linear Precision Actuator (LPACT). The patented LPACT device is a bearingless voice coil proof-mass actuator which uses a proof-mass-mounted accelerometer to close a force control loop which serves to override nonlinearities and temperature-dependent effects and shape the actuator frequency response.

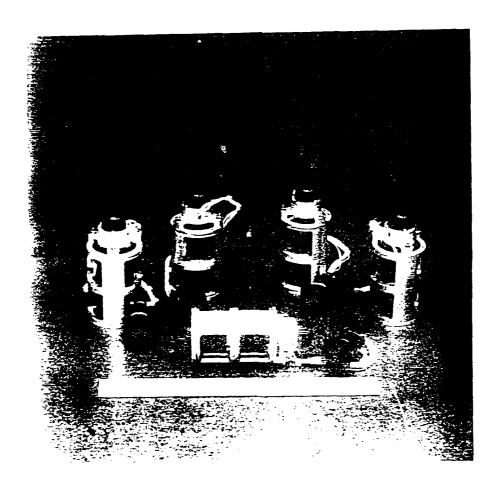


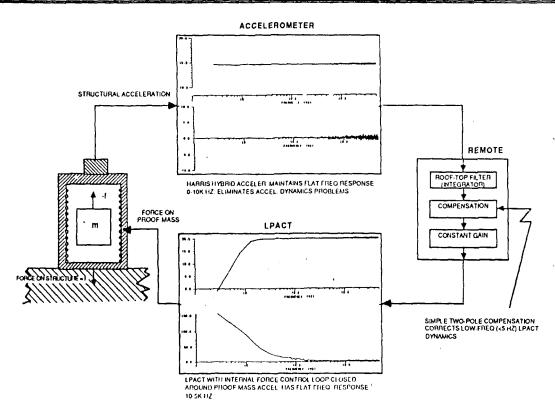
Figure 2.5. The firms a near Problem A value of PAV 1 as a proof mass actuator to conditions out to prove the second long of the PAV To such a leavest random function a such as a great condition response over the freeze and the PAV To such a leavest random function a such as a great condition response over the freeze and the PAV To such a leavest random function as such as a great condition of the page for the page of the

With its force compensation loop, the LPACT has flat frequency response from 3-10 Hz to >5 K Hz. Each LPACT has a casing-mounted accelerometer of a new design. The "Hybrid Accelerometer" has flat frequency response form DC. - >10 K Hz.

The diagram illustrates that: with the LPACT actuator and a colocated hybrid accelerometer, it is now possible to implement a simple colocated rate feedback controller to provide highly robust broad-band damping — and without fear of destabilizing even very high frequency modes due to phase shifts arising from actuator and sensor dynamics.

Thus, improved hardware simplifies control.

ACTIVE STRUCTURAL CONTROL DESIGN IS STRAIGHT FORWARD AND ROBUST



ZENITH STAR ACTIVE STRUCTURAL CONTROL

- 11 -

HARRIS CORPORATION 2/1/89-1

The MHPE is equipped with 9 LPACTS:

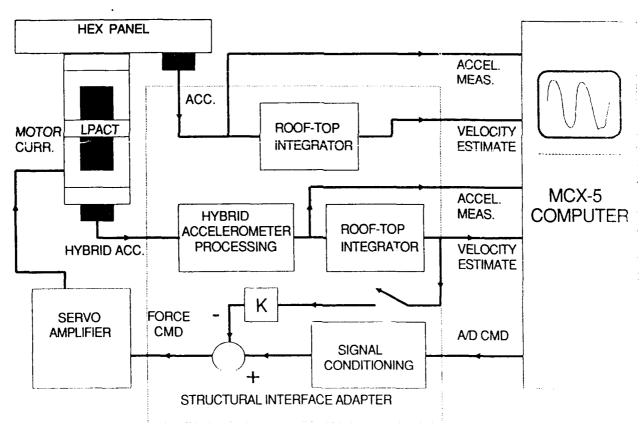
- * 3 on the secondary platform
- * 6 within outer hex panels

Data acquisition and on-line control are executed via the MCX-5 computer.

The facility is set up to implement centralized MIMO algorithms and/or the decentralized stand-alone LPACT loops.

Both have been included in live demonstrations for Harris visitors.

Here, we give a quick sketch of a decentralized design demo. - that best illustrates the capabilities of the actuators.

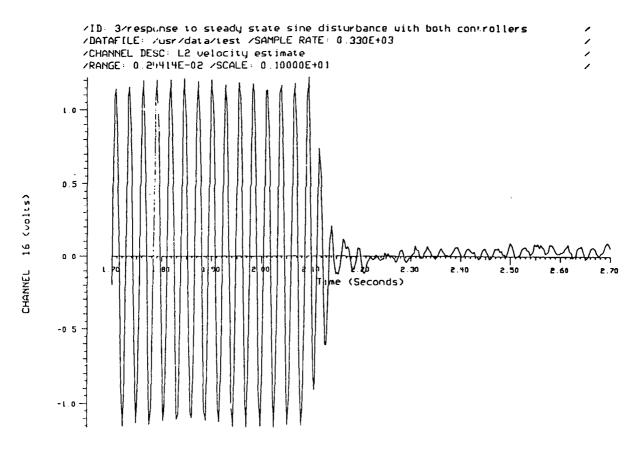


MHPE CONTROL SYSTEM HARDWARE

This design gives order-of-magnitude overall reduction of LOS jitter & dephasing.

To illustrate for visitors we show open-loop vs. closed-loop behaviors for a medley of modes - starting with lower frequency modes (that can be felt) and going up to higher frequency modes (that can be heard).

For example, this chart shows accelerometer response to continuous 35 Hz excitation of a "panel" mode. When the control is turned on at t=2.2 vibration amplitude drops by factor of approximately ten.



both controllers on t=2 2 secs

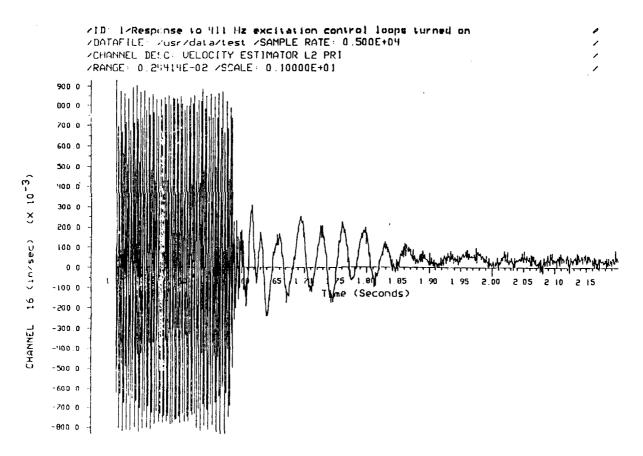
Fri Mar 9 10-43:22 1990

Similar results are obtained even for very high-frequency modes.

Here's an open-loop/closed-loop demonstration for a 411 Hz mode.

Switching on the control a t=1.58s results in quick amplitude reduction.

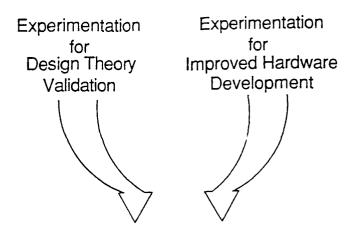
Overall there is sizable damping up to ~900 Hz (where control rolls off). Such results show that development of improved hardware makes even simple control approaches effective and generally increases the scope for even more performance improvement via centralized design.



controller turned on at t=1 58 secs

Sun Mar 18 11-13 15 1990

In closing, results for theory validation & hardware development demonstrate the capability of active structural control technology to provide **significant reliable** and **predictable** PSS performance improvement. The capability of the new technology allows system designers to trade-off structural mass for added system adaptability and "intelligence" attained via on-board active control devices and algorithms. Experimentally validated methodologies for system identification and control, such as ERA and OPUS provide reliable, predictable engineering **tools** with which to carry out this tradeoff. The resulting enhancement of space system capability with reduced weight and cost will help advance the Nation's future space activities.



- * Significant and predictable PSS performance improvement
- Capability to trade-off structural mass for added system "intelligence"

References

- 1. Controls-Structures Interaction Experiments for Large Space Structures Guest Investigator Program. NASA Research Announcement NRA 89-LaRC-3, June 6, 1989.
- 2. NASA Langley Research Center Controls-Structures Interaction Office Phase I Guest Investigator Program. Second-Year Mid-Year Review, July 9-10, 1990, Williamsburg, VA.
- 3. E. G. Collins, Jr., D. J. Phillips and D. C. Hyland, Design and Implementation of Robust Decentralized Control Laws for the ACES Structure at Marshall Space Flight Center, NASA Contractor Report 4310, July 1990.
- 4. D. J. Phillips and E. G. Colins. Jr., "Four Experimental Demonstrations of Active Vibration Control for Flexible Structures," Proc. AIAA Guid. Nav. Contr. Conf., pp. 1625-1633, Portland, OR, August 1990.
- A. W. Daubendiek, D. C. Hyland, and D. J. Phillips, "System Identification and Control Experiments on the Multi-Hex Prototype Test Bed," 2nd USAF/NASA Workshop on System Identification and Health Monitoring of Precision Space Structures, Pasadena, CA, March 1990.
- D. C. Hyland, "An Experimental Testbed for Validation of Control Methodologies in Large Space Optical Structures," in Structural Mechanics of Optical Systems II, pp. 146-155, A. E. Hatheway, Ed., Proceedings of SPIE, Vol. 748, Optoelectronics and Laser Applications Conference, Los Angeles, CA, January 1987.
- 7. D. C. Hyland and D. J. Phillips, "Development of the Linear Precision Actuator," 11th Annual AAS Guid. Contr. Conf., Keystone, CO, January 1988.
- 8. D. C. Hyland, "Experimental Investigations in Active Vibration Control for Application to Large Space Systems," in Space Structures, Power, and Power Conditioning, R. F. Askew, Ed., Proc. SPIE, Vol. 871, pp. 242-253, 1988.

The LaRC CSI Phase-0 Evolutionary Model Testbed: Design and Experimental Results

W. Keith Belvin Kenny E. Elliott NASA Langley Research Center Hampton, VA

and

Anne Bruner

Jeff Sulla

Jim Bailey

Lockheed Engineering & Sciences Company

Hampton, VA

Presented at the Fourth Annual NASA/DOD Conference on Control/Structures Interaction Technology.

November 5-7, 1990 Orlando Florida

Abstract

A testbed for the development of Controls-Structures Interaction (CSI) technology is described. The design philosophy, capabilities and early experimental results are presented to introduce the reader to some of the ongoing CSI research at the NASA Langley Research Center. The testbed, referred to as the Phase-0 version of the CSI evolutionary model (CEM), is the first stage of model complexity designed to show the benefits of CSI technology and to identify weaknesses in current capabilities. Early closed-loop test results have shown non-model based controllers can provide an order of magnitude increase in damping in the first few flexible vibration modes. Model-based controllers for higher performance will need to be robust to model uncertainty as verified by system identification tests. Data are presented that show finite element model predictions of frequency differ from those obtained from tests. Within the paper, the hardware implementation of CSI systems is emphasized. Plans are also presented for evolution of the CEM to study integrated controller and structure design as well as multiple-payload dynamics.

Introduction

The focused research being performed for the development of CSI technology consists of three complimentary stages: design, ground testing, and flight testing. Within each of these stages, further divisions can be made, e.g. micro-precision disturbance rejection, global line-of sight pointing control, multiple-payload isolation, multi-body robotic control, etc. Hence, it is important to establish the CSI technology to be addressed by the testbed described herein.

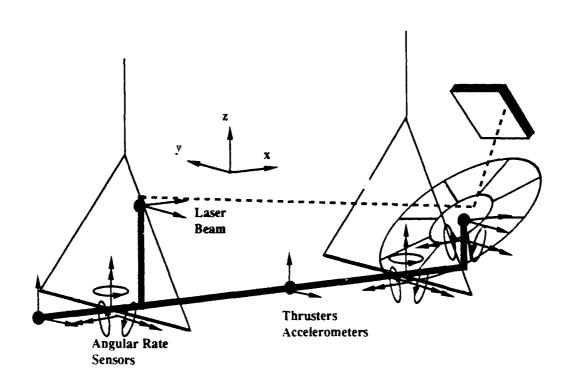
The CSI evolutionary model (CEM) is first and foremost a ground based testbed for validation of design methodology and hardware implementation. As such, the CEM has been designed to permit numerous hardware changes. There are three planned phases for the evolution of the hardware. Phases 0 and 1 are both linear time invariant systems; however, the design philosophy are different. Phase-0 is based on a classic design of uniform strut size in the truss, nominal placement of actuators and sensors, and subsequent controller design based on the fixed plant. Phase-1 will be fabricated based on an integrated controller and structure design, whereby both structure and controller design variables are sized simultaneously. Performance and stability comparisons between Phase-0 (uniform truss stiffness and mass) and Phase-1 (tailored truss stiffness and mass) will be made to establish the benefits of integrated design. Phase-2 will permit appendage articulation for the study of time variant dynamics typical of multiple payload platforms (MPP).

There are two major CSI technologies being addressed by the Langley Research Center using the CEM. In Phases 0 and 1, global line-of-sight (LOS) pointing is the primary objective. In Phase-2, MPP will be studied to develop multiple-payload isolation technology. For additional NASA related CSI research, the reader is referred to the Jet Propulsion Laboratory (JPL) for CSI technology developments aimed at optical systems, which require micro-precision control, and to the Marshall Space Flight Center for the development of CSI flight experiments. In addition, both Langley and JPL are developing analysis and design tools for CSI systems.

The remainder of this paper will focus on the design and early experimental results of the Phase-0 version of the CEM. Future plans for CEM-based focused research are also presented.

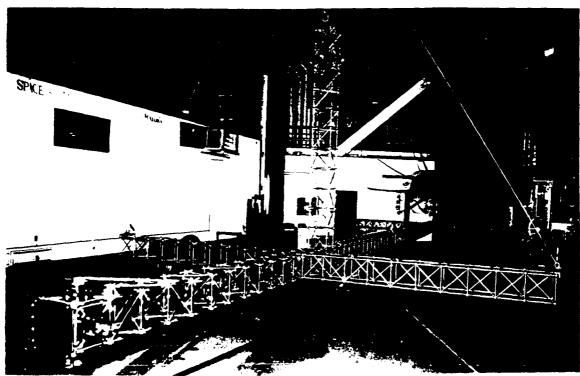
CSI Evolutionary Model

The CEM has been designed to possess dynamic properties typical of spacecraft platforms proposed for remote sensing and communications. As shown in the schematic below, the Phase-0 version of the CEM consists of a long truss-bus and several appendages with varying degrees of flexibility. To monitor the LOS pointing accuracy, a low powered laser has been mounted on the vertical tower such that the beam reflects upon a mirrored surface mounted on the reflector. The beam reflection is measured by a photo-diode array attached directly above the reflector. This laser-reflector-detector system enables the pointing accuracy of the CEM to be measured to a tolerance of 500 micro-radians when the photo-diode array is mounted on the laboratory ceiling (700 inches above the reflector). The CEM is suspended by two cables attached to the laboratory ceiling. By using springs in series with the cables, all 6 "rigid"body modes have a frequency below 1 Hz. The first flexible body frequency is at 1.5 Hz with a total of 31 modes below 10 Hz. The following pages describe the hardware in more detail.



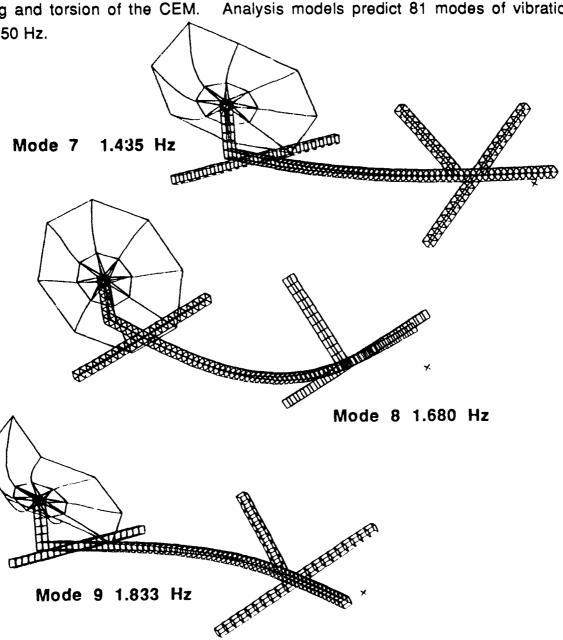
CEM Structural Hardware

The design of the CEM was driven by several conflicting criteria. A large model was desired such that actuators would need to be sized for large inertia properties typical of space platforms. The model was to be ground tested, hence, the design of the suspension system and truss strength must withstand gravity preload. Moreover, while a strong truss was desired to permit significant dynamic member loads during controls testing, only moderate truss stiffness was desired to enable visual indication of the effects of flexible body dynamics. These criteria were used to select a truss structure with a 10 inch cubical bay. The truss tubes are aluminum with special end fittings to permit assembly using node-ball joints. For analysis purposes, an effective area of the truss members has been used to model the stiffness from node-center to nodecenter as: longerons and battens = 0.12316 in^2 , diagonals = 0.1166 in^2 . There are 62 bays along the main bus, 11 bays on the laser tower, 4 bays on the reflector tower and four horizontal 10 bay appendages to which the suspension cables are attached. The reflector has eight 0.25-inch thick aluminum ribs which taper in width from 2 inches to 1 inch over their 96-inch length. One end of the ribs attaches to a hub, which is affixed to the truss reflector tower, while the other end of the ribs are connected to each other by a pretensioned cable. A honeycomb panel with a mirrored surface is affixed to the ribs and to the hub.



Typical CEM Vibration Modes

The cable suspended CEM has six "rigid" body modes of vibration. Three of the modes occur near 0.15 Hz and involve horizontal translation and rotation in the X-Y plane. Two modes occur at 0.72 and 0.74 Hz and involve vertical bouncing in the X-Z plane. The sixth "rigid" mode involves compound pendulum dynamics in the Y-Z plane at a frequency of 0.90 Hz. The first three flexible-body modes of vibration, shown below with the fintie element model (FEM) predicted frequency, involve bending and torsion of the CEM. Analysis models predict 81 modes of vibration below 50 Hz.

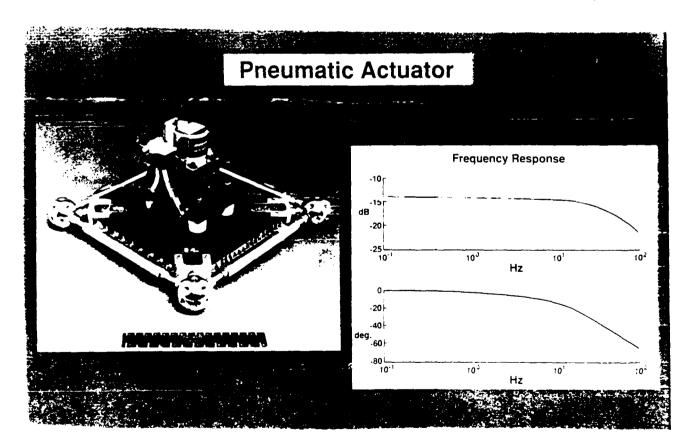


CEM Actuation Devices

Compressed air thrusters [1] are the primary control actuators on the CEM. The 16 thrusters are proportional bi-directional force actuators and produce up to 2.2 lbs of force. A local controller is implemented for each thruster to linearize the input/output response. As shown below, the thruster dynamics are easily described by the first order model

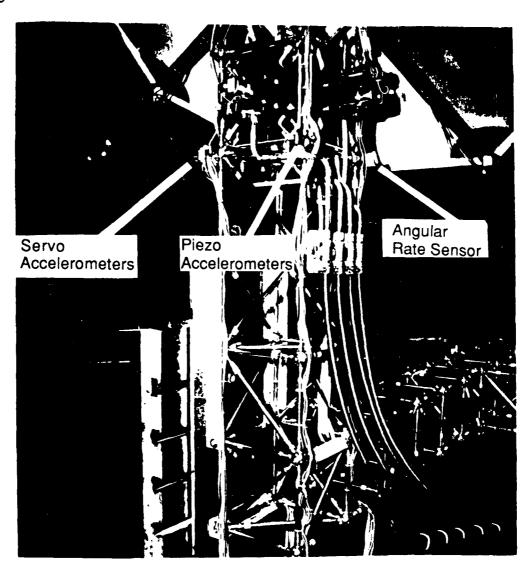
where s is the Laplace variable. This model, developed from aggregate bench tests of the thrusters, indicates 1 db magnitude attenuation and 12 degrees of phase lag at 10 Hz. The thrusters have been installed in four groups on the CEM. Each group has four thrusters acting in pairs to achieve pure translational forces.

In addition to the air thrusters, proof-mass, piezo-electric, piezo-ceramic, and visco-elastic actuation devices are planned for implementation during the CEM test period.



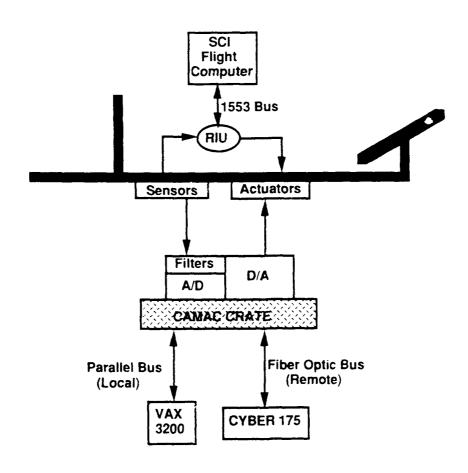
CEM Sensors and Filters

Currently, there exist two classes of sensors on the CEM: control sensors and system identification sensors. For control, servo accelerometers with 5 volts/g sensitivity and angular rate sensors with 3-10 volts/radian/second sensitivity are used. For ID, piezo film accelerometers with 1 volt/g sensitivities are used. There are a total of 28 servo accelerometers, 8 angular rate sensors, and 195 piezo film accelerometers on the CEM. Sensor dynamics for the servo accelerometers (primary control sensors) can be virtually ignored up to a bandwidth of 300 Hz unless the sensor data are preprocessed by available analog filters. Three-pole Bessel filters with 10, 20, 50 and 100 Hz cut off frequencies are available to pre-process the data. Typical sensor mountings on the CEM are shown below.



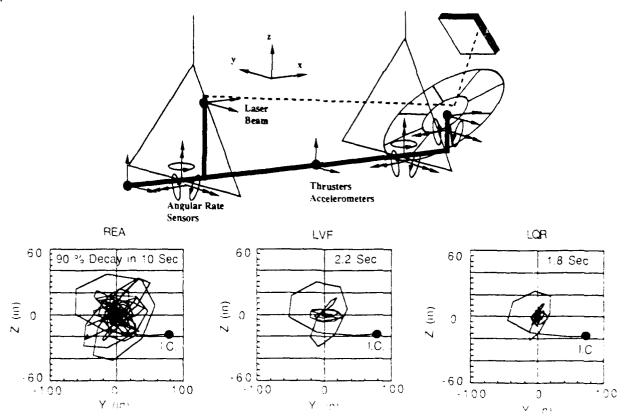
CEM Real-Time Digital Computers

There are three non-pc based computers used for real-time computing. As shown below, a VAX 3200 and a CYBER 175 [2] are interfaced to a CAMAC crate which provides a digital interface to a number of bus protocols. In addition to these computers, an SCI flight equivalent computer will be interfaced to the CEM via a Remote Interface Unit (RIU) which provides local digital processing, A/D and D/A conversion, and interfaces to the SCI computer over a 1553 digital bus. Each of these computers is capable of performing real time computations although the control updates rates have not been fully tested. Typical controllers (16 states, 8 input and 8 output signals) have been executed at a rate exceeding 150Hz using the CYBER and VAX computers. The CYBER computer is part of Langley's Advanced Real-Time Simulation (ARTS) system. The ARTS system is currently being upgraded to a 4-processor CONVEX computer which should permit considerably faster controller update rates. The SCI computer update rates are not yet tested.



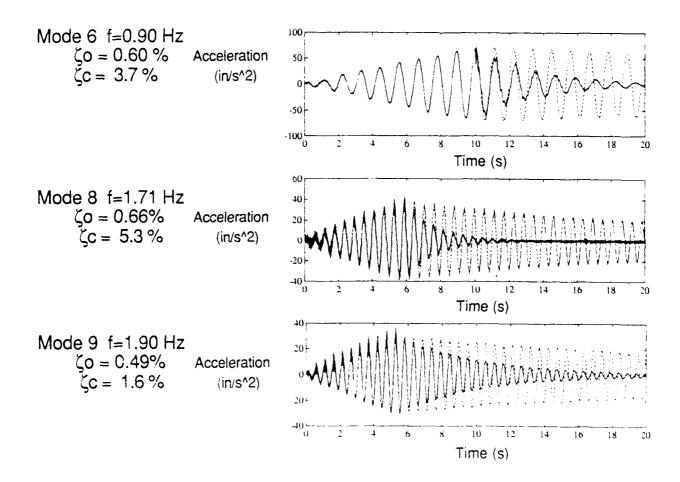
Line-Of-Sight Pointing Control

For the Phase-0 CEM, the LOS pointing accuracy is the performance measure of primary interest. Simulation studies [3] have shown that the amount of energy used to control LOS pointing varies greatly for different controllers. As the charts indicate below, linear quadratic regulator (LQR) controllers had better performance than local velocity feedback (LVF) or robust eigensystems assignment (REA) controllers. Since the LQR model-based controller provided the best performance, it is natural to select a model-based controller for high performance. However, model based controllers can lose stability margins due to model uncertainties. Thus, the approach taken by the Ground Test Methods team at Langley, is to concentrate first on a low authority controller (LAC) loop using non-model based controllers for stability robustness. High authority controller (HAC) loops will then be closed to optimize the CEM LOS pointing. To this end, the following pages describe early non-model based controller results. In addition, finite element modeling and preliminary system ID test results are presented to indicate the level of model uncertainty to be expected during the design of high performance controllers.



Virtual Passive Controller Results

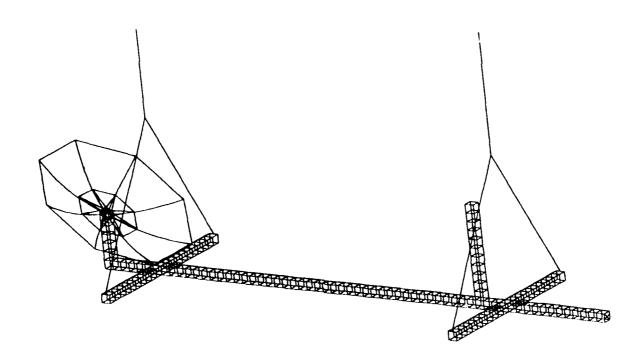
A recent paper [4] documents a controller design approach based upon a virtual passive design philosophy. In effect, a spring-mass-damper system is designed using local sensor and actuator feedback to "absorb" the energy of the system. Although the resulting controller could be implemented with only passive elements, practical considerations usually lead to an active implementation. In the results below, 8 Lacoupled second-order systems were designed using collocated sensor/actuator feedback. The three traces show typical levels of damping produced by this controller. With the damping increased by factors of 3 to 8 over the open-loop damping using this highly stable LAC loop, high performance controllers are now practical. The model to be used for the HAC loop will be based upon a finite element model (FEM) which is described next.



Finite Element Modeling of the CEM

The CEM was modeled with the NASTRAN program using beam, rod and plate elements. Since the CEM is cable suspended and gravity loaded, it was necessary to calculate the differential stiffness of the FEM elements to accurately predict the CEM dynamic behavior. The FEM, shown below without the truss diagonals for clarity, has all truss elements modeled from joint-to-joint with a single two-noded beam element. In addition, the reflector ribs and part of reflector-to-truss interface are modeled with beam elements. The mirrored panel and a portion of the reflector-to-truss interface was modeled with triangular plate elements.

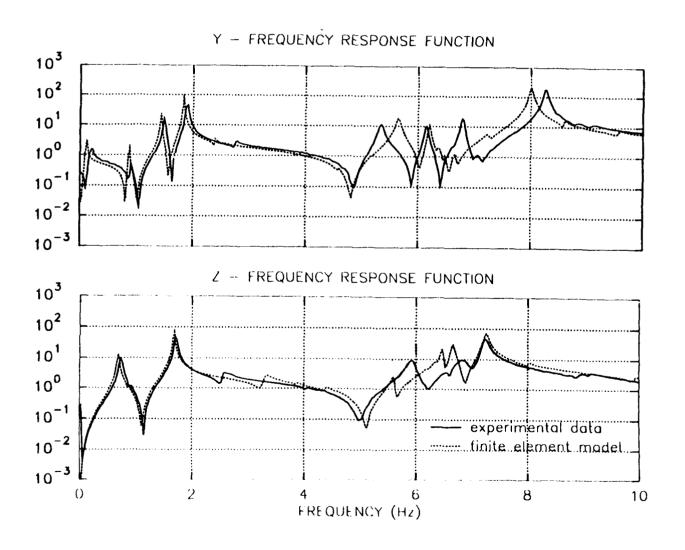
The suspension cables were modeled by rod elements and spring elements. There exist over 3000 degrees of freedom in the model. A number of lumped masses representing the inertia of the node balls, actuators, sensors, etc. were included in the model. With the origin defined at the end opposite the reflector as indicated in the figure, the center of gravity is located at x=346.03 in., y=0.09 in. and z=19.85 in. The total mass of the model is 1.92319 lb-s²/in. Rotational inertias in units of lb-in-s² are: Rxx=6915.94, Ryy=95197.13, Rzz=93558.3, Rxz=2288.47, Rxy=-17.74, Ryz=1.43.





CEM Structural System ID Tests

Modal vibration tests of the CEM have been performed using 24 servo and 195 piezo channels of accelerometer data. Multi-Input, multi-Output (MIMO) tests were performed to measure the frequency response functions (FRFs) between the acceleration output to force input. These FRFs are in process of being reduced to modal vibration parameters, namely frequencies, damping, and mode shapes over the frequency range of 0 to 10 Hz. The plots below show typical FRFs taken in the vertical and horizontal planes at the center of the main truss. Also shown on the FRFs is the predicted response using the NASTRAN model. These data show relatively good agreement for some of the dominant modes; however, additional FEM refinement appears necessary. The next chart compares, in more detail, the system ID test and analysis results.



System ID Test and Analysis Results

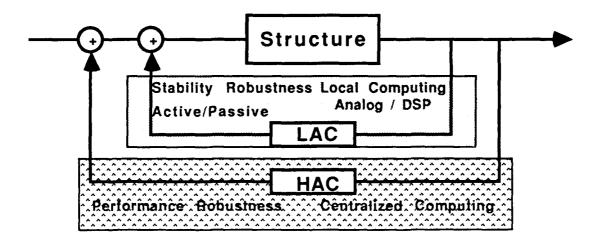
Preliminary results of the system ID testing described previously have been compared to the NASTRAN FEM in the table below. The data show the FEM model predicts the frequencies of the first three flexible body modes to an accuracy level of 5 percent or less. However, the first three "rigid" and several higher frequency modes are not predicted as well. Data reduction is continuing to identify all modes below 10 Hz. The open-loop damping data show the CEM to be lightly damped. This low inherent damping, typical of high quality truss structures, reinforces the need for augmenting the stability robustness by LAC loops. High modal density, low inherent damping, and model uncertainty make the CEM an ideal testbed for development of CSI technology. The following pages describe plans for the CEM testbed research and development.

| Mode | Test | Test | Analysis | Frequency |
|-------------|-----------|-----------|-----------|-----------|
| Number | Damping % | Frequency | Frequency | Error % |
| 1. | 4.7 | 0.145 | 0.112 | -22.8 |
| 2. | 7.0 | 0.149 | 0.113 | -24.2 |
| 3. | 7.0 | 0.148 | 0.118 | -20.7 |
| 4. | 1.5 | 0.718 | 0.665 | -7.4 |
| 5. | 1.2 | 0.740 | 0.691 | -7.1 |
| 6. | 0.60 | 0.900 | 0.872 | -3.1 |
| 7. | 0.41 | 1.50 | 1.435 | -4.3 |
| 8. | 0.66 | 1.71 | 1.680 | -1.8 |
| 9. | 0.49 | 1.90 | 1.833 | -3.5 |
| 10. | | | 2.388 | |
| 11. | | | 2.533 | |
| 12. | 2.1 | 2.57 | 3.304 | -22.2 |
| 13. | | | 3.447 | |
| 14. | | | 3.546 | |
| 15. | | | 3.867 | |
| 16. | 0.42 | 4.04 | 4.036 | -0.01 |
| 17. | 0.91 | 4.30 | 4.388 | 1.9 |
| 18. | | | 4.574 | |
| 19. | | | 4.648 | |
| 20. | | | 5.599 | |
| 21. | | | 5.609 | |
| 22. | 0.69 | 5.33 | 5.648 | 6.0 |
| | 1.1 | 5.92 | | |
| 23. | 0.30 | 6.14 | 6.200 | 1.0 |
| 24. | | | 6.351 | |
| 25 . | 0.30 | 6.65 | 6.473 | -2.7 |
| 26. | | | 6.660 | |
| | 0.22 | 6.79 | | |
| 27. | 0.56 | 7.24 | 7.253 | 0.2 |
| 28. | 0.31 | 8.26 | 8.004 | -3.1 |
| 29. | 0.21 | 9.11 | 8.598 | -5.6 |
| 30. | | | 9.566 | |
| | | | | |

Hardware Implementation of CSI Technology

The need for experimental verification of CSI technology is quickly realized when one tries to transform a paper design into hardware. "Real world" constraints, such as using accelerometers because inertial displacement and velocity measurements are either unavailable or extremely expensive, lead to controller modifications and sometimes new theoretical developments. The simplicity of single-Input, single-Output (SISO) control, particularly for LAC loops using collocated sensors and actuators, leads to distributed rather than centralized processing and perhaps passive instead of active methods.

The Langley Ground Test Methods team seeks to develop a solid experience base for implementation of CSI designs in hardware. This experience base will be built by ground testing various actuators and sensors, implementing both localized and centralized controllers, and developing ground test methodologies for verification of controlled structure designs. As indicated by the LAC/HAC schematic below, particular emphasis will be placed on the hardware implementation of LAC loops using analog, passive, and local digital computing (e.g. DSPs) to enhance stability robustness for high performance controllers.



Integrated Controller Structure Design

The Phase-0 version of the CEM is constructed from uniform truss members, which is typical of conventional spacecraft design. An exciting technology described in [5] and elsewhere is integrated structure and controller design. The Langley Analysis and Design Methods team is currently performing an integrated design for the CEM. The tailored truss resulting form this integrated design will be constructed and tested to assess the benefits of integrated structure and controller design. This new version of the CEM will be referred to as Phase-1.

Optimal Structure + ≠ Optimal System Optimal Controller

Simultaneous Design
of =
Structure and Controller

Better Performance Less Control Energy Lower System Weight

Planned Evolution of the CEM

The CEM will evolve from Phase-0 to Phase-1 in calendar year 1991 as indicated below. Phase-1 tests will verify the integrated design approach and will use the best implementation of hardware based on Phase-0 testing. Methodologies for on-line verification of stability and robustness will be studied to verify the design. Global LOS pointing will remain the primary performance criteria.

In calendar year 1992, the Phase-1 hardware will be modified by including gimbaled appendages. This new configuration, referred to as Phase-2, will continue to build upon Phase-0 and Phase-1 experience. However, the focus will be on multi-payload isolation. In addition, numerous advances in hardware and theory will be needed to design and simulate the time varying dynamic nature of Phase-2.

CY-90 CY-91 CY-92 CY-93

Phase-0

Uniform Truss

Phase-1

Integrated Structure and Control Design

Phase-2

Multi-Payload Gimbaled Appendages



Summary

The Phase-0 version of the CEM is operational and preliminary control and system ID results have been presented. Non-model based controllers using collocated sensors and actuators provide an order-of-magnitude increase in the open-loop damping and should enable good stability robustness for high performance controllers. Model based control design will not require extreme conservatism on model uncertainty since the system ID data and the FEM data show reasonable agreement. Of course, model based controllers will be affected by unmodeled dynamics and perhaps spillover since the CEM has high modal density.

Hardware implementation issues of controlled structure systems are being studied to enhance simplicity, cost-effectiveness, and reliability using the CEM testbed. Actuator/sensor tests, active/passive implementations, and centralized/distributed computing are being performed to build an experience base for future CSI systems. This experience base will be mandatory for developing verification methodologies of CSI designs.

The planned evolution of the CEM will provide a ground-based testbed to develop focused CSI technology for both linear time-invariant systems as well as multi-body dynamic systems. Periodic reporting of CEM test results will continue in this forum.

Acknowledgements

It is the authors' pleasure to present design and test results of the CEM in this paper. However, numerous persons are responsible for designing, testing, and maintaining the CEM. We wish to recognize Jerry Newsom of the CSI Office, Langley Research Center, for supporting this focused technology development activity. In addition, we recognize all those persons associated with the Ground Test Methods team at Langley for their day-to-day efforts which have made the CEM a viable testbed. Finally, we wish to acknowledge the test and analysis support of the Analysis and Design Methods team at Langley for their work with Phase-0 and their on-going design of Phase-1.

References

- 1. Jacot, A. D.; Bushnell, G. S.; and Anderson, T. M.: Bi-Directional Thruster Development and Test Report. NASA CR 182013, February, 1990.
- 2. Wood, D. V.; Geyer, D. W.; and Sulla, J.: Real-Time Control System for Mini-Mast Using the Advance Real-Time Simulation System at NASA Langley Research Center. 61st Shock and Vibration Symposium, Pasadena, CA, October, 1990.
- 3. Lim, K. B.; and Horta, L. G.: A Line-OF-Sight Performance Criterion For Controller Design Of A Proposed Laboratory Model. AIAA no. 90-1226, AIAA Dynamics Specialist Conference, Long Beach, CA, April, 1990.
- 4. Juang, J. N.; and Phan, M.: Robust Controller Design for Second-Order Dynamic Systems: A Virtual Passive Approach. NASA TM-102666, May 1990.
- 5. Maghami, P. G.; Joshi, S. M.; and Gupta, S.: Integrated Control-Structure Design for a Class of Flexible Spacecraft. Fourth NASA/DOD CSI Technology Conference, Orlando, FL, Nov. 5-7, 1990.

JPL CSI PHASE-0 EXPERIMENT RESULTS AND REAL TIME CONTROL COMPUTER

James L. Fanson Hugh C. Briggs Cheng-Chih Chu Boris J. Lurie Roy S. Smith Daniel B. Eldred Dankai Liu



Jet Propulsion Laboratory California Institute of Technology Pasadena, California 4th NASA/DoD Control/Structures Interaction Technology Conference Orlando, Florida November 5-7, 1990

The JPL CSI Phase-0 Experiment Results and Real-Time Control Computer

Initiative. Three NASA Centers participate in the CSI Program: Langley Research Center, Marshall Space Flight Center and the Jet Propulsion Laboratory. This multi-year program to develop and validate new design technologies is organized around five elements: program goal is to develop validated technology that will be needed to design, verify and operate interactive control/structure Systems and Concepts, Analysis and Design, Ground Test Methods, Flight Experiments and Guest Investigation Program. The CSI The NASA CSI Program is an element of the Control of Flexible Structures Task in the NASA Civilian Space Technology syste ns to meet the ultra-quiet structure requirements of 21st century NASA missions.

multi-disciplinary environment and develop additional tools such as simultaneous structure and control optimization methods and conceptual design tools for flexible spacecraft structure/control architectures. New CSI systems and concepts, such as active The CSI Program will integrate the advances made in other discipline technology programs to make a new spacecraft design methodology. Controls programs such as Computational Controls will develop a new generation of tools for multi-body simulation, multi-body component representation, and control analysis and synthesis. Structures technology programs such as Computational Mechanics are developing advanced finite element analysis codes. CSI will integrate these tools into a structure, will be developed and integrated into the focus mission design example.

ics and development of ground test methods for controlled flexible spacecraft structures. Microdynamics characterizations of to the submicron regimes required for future spacecraft. In addition, disturbance sources will be characterized at the microdynamic Other developments that will enable high-performance, flexible spacecraft design include an investigation of microdynamspacecraft components such as joints and struts will identify the linearity of typical elements when dynamic motions are restricted level to support analysis of ultra-quiet spacecraft systems.

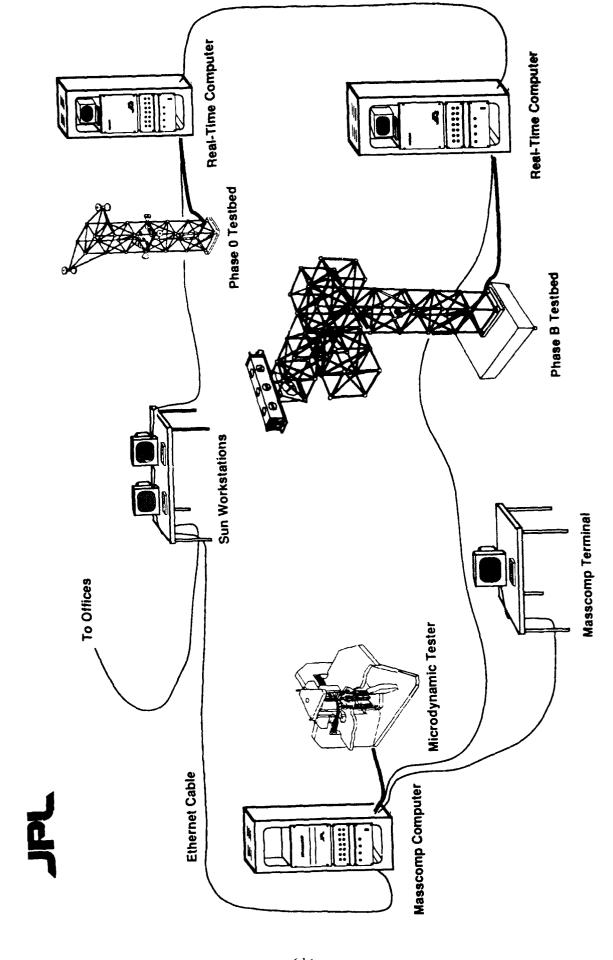
This paper describes recent advances in structural quieting technology as applied to active truss structures intended for high precision space-based optics applications, as well as the development of a real-time control computer network and environment for carrying out the digital control portion of this technology. The research described in this paper was carried out by the Jet Propulsion Laboratory, California Institute of Technology, under a contract with the National Aeronautics and Space Administration.

The CSI Laboratory

Greater detail about the design environment software and analytical tools are described in "The JPL Control/Structure Design The CSI design environment is an important element of the methodology and consists of several components. The first half of this paper addresses the computer systems, the laboratory testing facilities, and the results of validation testing to date. Methodology" by H.C. Briggs and W.E. Layman in the Proceedings of the 3rd Annual Conference on Aerospace Computational Control, Oxnard, CA, August 28-30, 1989. This chart emphasizes the laboratory segment of the environment. There are three test and evaluation facilities resident computers developed for the Phase 0 and Phase B facilities are described in more detail in following charts. Three computers reside permanently in the laboratory, including a Sun SparcStation, a Sun 386i, and a Masscomp data acquisition system made by in the lab: the Phase 0 Precision Truss Experiment, the Phase B Testbed, and the Microdynamics Tester. The real-time control Concurrent Computer Corp. The Suns are used to develop and compile code for the real-time controllers, to run experiments, and to analyze and display results. The Masscomp is used primarily as a data acquisition system for the Microdynamic Tester and will also serve as the experiment supervisory control computer for the Phase B Testbed.

it makes it easy for an analyst to access the laboratory computer resources from his own office. It is even easy for a guest All the laboratory computers including the real-time computers are intimately interconnected via an ethernet to form a local area network (LAN). This local LAN in turn is connected to the Jet Propulsion Laboratory main network, using the Sparc Station as a gateway between the two networks. The concept of networking is fundamental to the CSI environment, because investigator, for example, to run a control experiment from across the country, using the nationwide internet network to remotely log in to the real-time computers.

The CSI Laboratory

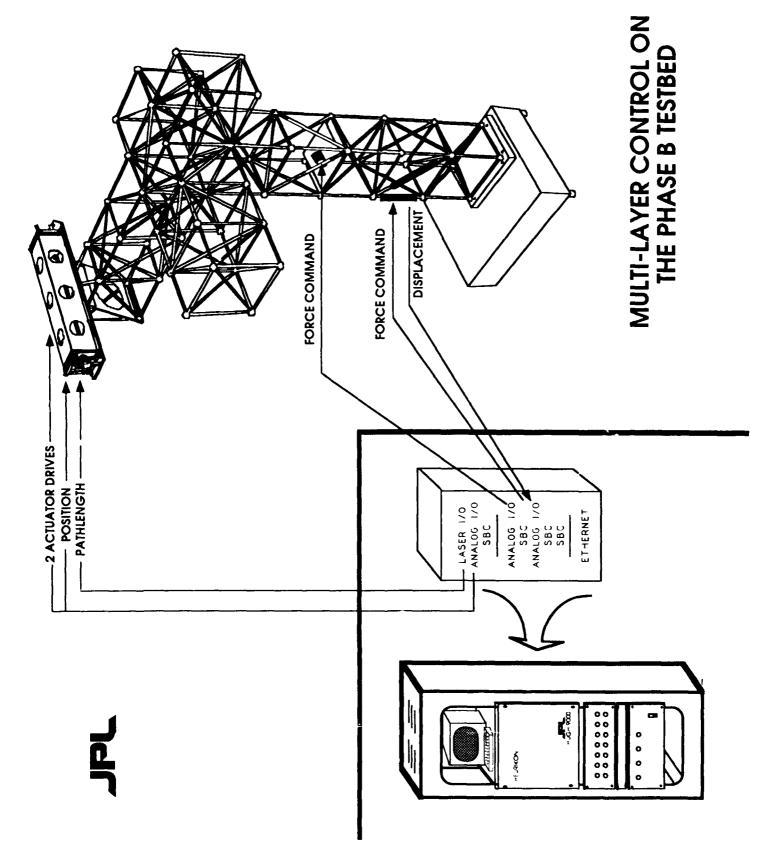


Multi-Layer Control on the Phase B Test Bed

to meet the stringent stability requirements. The extreme quieting required will be achieved with a layered architecture with each A new control system architecture was developed during the initial study of the JPL Focus Mission Interferometer (FMI) layer providing a factor of 10 to 100 reduction in disturbance. The Phase B Test Bed was designed to validate a simple three-level hierarchical control consisting of optical path length control, active structure control and disturbance isolation. This chart illustrates the real-time control computer organization to execute this architecture.

elements, and assorted amplifiers, patch panels and interfaces. The optical delay line is installed on top of one arm of the truss structure and contains a flexure-mounted delay line which is driven by an electro-dynamic motor and a fine path control piezoelectric actuator. The position of the delay line can be read by the computer through a A/D converter while the actuators are commanded through D/A converters and power amplifiers. The total path length error is measured by a laser metrology system with a chassis-mounted interface board. The computer can read the total fringe count from a register for as many as 12 metrology channels. The active elements for the active structure loop are commanded through D/A channels and their displacement The control computer is contained in a cabinet with a local terminal, a VME chassis containing the control computer and force are read through A/D channels.

The computer system is configured as three logical controllers, each having a CPU, D/A, A/D and array processor. All controllers reside in the VMEbus chassis in the electronics rack and are accessible over the laboratory LAN. The investigator can load the control software, execute an experiment, acquire performance data, and analyze the results from either a workstation in the lab or, Each layer of the architecture executes as a separate control loop on an individual real-time single board computer (SBC). with another engineer in the lab, from the workstation in his office.

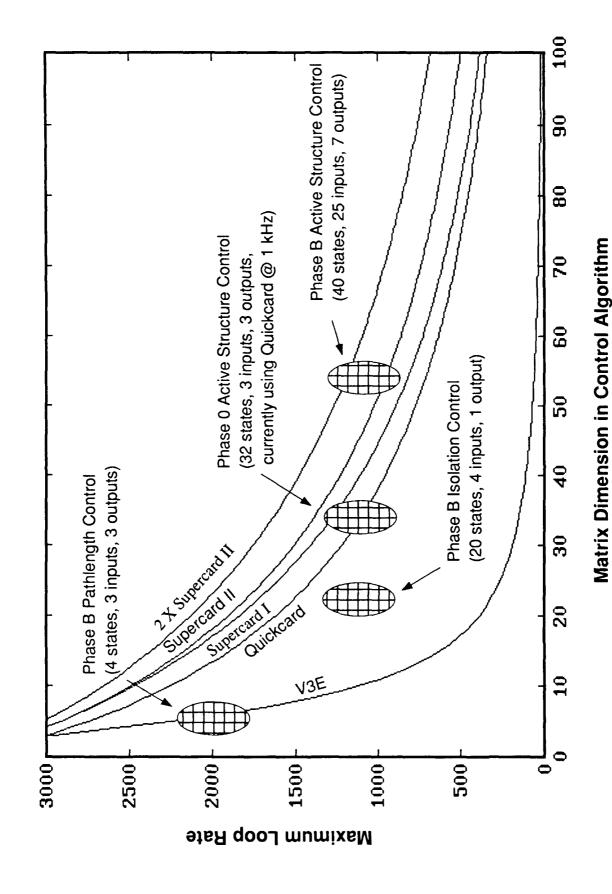


Requirements and Performance

The performance of the real-time controllers is shown on the facing page. The hardware listed includes a Heurikon V3E, which is based on a 25 mHz 68030 microprocessor, and three array processors from CSPI: a Quickcard, a Supercard I, and a Supercard II. These curves are computed from a combination of several timing measurements, including time for matrix-vector multiply, for analog input and output, and for overhead demanded by the real-time operating system kernel. The system timing was measured using a VMetro bus analyzer while the system executed problems of various sizes. The relationship between problem size and the resulting computation time was found empirically to closely fit a quadratic equation. The time required for an analog digital to analog conversion including the overhead of subroutine calls. For the curves plotted, it was assumed that the number of inputs and outputs were each 10% of the number of states, though the results are relatively insensitive to this ratio. Finally, the overhead per control loop iteration imposed by the real-time kernel and the array processor was determined to be about 300 microseconds, though this figure depends on many factors and can vary. The time required per iteration is converted to a loop rate input and output was found by measurement to be 7.5 microseconds per analog to digital conversion and 37 microseconds per to clearly show the capabilities of the hardware relative to the control system requirements.

estimating required sample rates for the control loops which would be implemented on the Phase 0 and the Phase B testbeds. It is The computational requirements for the real-time computers were determined by performing operation counts and assumed that the controllers can be implemented in the form of a matrix-vector multiply, which is possible for most for linear accurately positioning a mirror within the optical path. This mirror is driven by a two-stage actuator, the first being a large mechanical trolley which is driven by a voice-coil actuator, and the second being a piezoelectric stack, for high-bandwidth, fine motion control. Inputs to the path length control loop are provided by an interferometer, which measures optical path length; an Supercard II is marginal with respect to the Phase B structural control. If this were to be a problem, then it is possible to combine systems, and which makes implementation in an array processor possible. In the event that the matrix is not square, as would be the case if the number of inputs and outputs differed, the matrix dimension can be approximated as the square root of the number of elements in the matrix. A typical controller example is the path length control on the Phase B testbed, which is accomplished by motion control. The piezoelectric actuator in turn is a two-stage actuator which accepts separate inputs for coarse and find eddy current sensor, which provides the trolley displacement relative to the underlying structure; and an accelerometer mounted at the base of the trolley. Preliminary designs showed that approximately 4 internal states would be used in the path length control algorithm, and its loop rate would have to be about 2 kHz or higher. The controller for this problem can thus be implemented in terms of a 7 by 7 matrix multiplying a 7 element vector. According to the chart, the performance of the V3E alone for this application would be marginal, but any of the array processors would have ample power. Furthermore, the performance of the two array processors in a single control loop to roughly double the number of computations which can be performed at a given rate. It is anticipated that the performance of available computer hardware will continue to increase so that by the time extra capacity is needed it will be available.

Requirements and Performance



Control Routine Sequence Overview

completion of an experiment, writes the measured performance data to another Pro-Matlab data file. With this software, the investigator works in Pro-Matlab to design and evaluate controllers, leaving only to command the real-time computer during the law. All device interface routines are supplied. This software loads controller parameters from a Pro-Matlab data file and, upon The investigator is supplied with a standard control routine that executes a constant coefficient, linear update control

software from the file server. The controller is invoked by spawning a task from the shell with the highest priority in the real-time computer. This task loads the controller parameters from the Pro-Matlab file on the investigators workstation, sets up An investigator begins an experiment by logging in into the real-time controller VxWorks shell and down loading the control This chart illustrates the simple structure of the control software and the major elements of the control cycle timing. the appropriate data structures, and initializes devices such as the array processor.

The cycle logically begins with the acquisition of sensor data and continues with starting the array processor, posting the output commands and saving the controller data. In practice, the SBC activities are collected at the top of the loop, beginning with The control cycle has been optimized for parallel execution of the Single Board Computer (SBC) and the array processor. posting the prior cycle output commands. This frees the SBC for other tasks during the array processor computation time.

the remaining 600 µsecs involves a 50 by 50 matrix multiply. Notice that the SBC can execute the VxWorks shell and respond to The speed of the system is constrained by several components. At present, the components are nearly balanced in that there are no excess SBC cycles and no excess array processor capacity. The time line at the bottom of the chart breaks out the major components of a typical 1 KHz cycle. The period begins with the clock tick which is serviced by a routine that gives a semaphore. The control routine has suspended waiting for this semaphore and is in control of the CPU 185 µsecs later. This is the time required by the VxWorks Wind scheduler to identify the control task as the highest priority, ready-to-run task and perform a context switch. The control software requires approximately 135 usecs to post commands to the D/A, acquire sensor signals from the laser interface and A/D, and initiate the array processor. The largest problem the array processor can handle in user inquiries while the array processor is working.



Control Routine Sequence Overview

```
Controller ( )

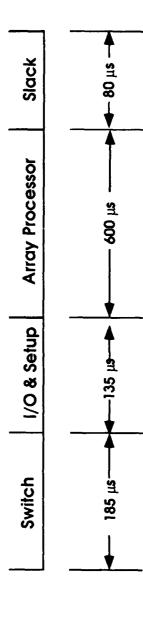
Load Control Parameters (Using Matlab Format)
Initialize Data Structures and Hardware

Do

{ Output Control Commands Input Sensors Load Array Processor Save History
}

Write History File (Using Matlab Format)
```

Computation Speed



CSI Experiment Integration

The electronic connection of the laboratory to the office has been quite successful utilizing off-the-shelf commercial computer equipment. This capability is the physical basis for the integration of the CSI Laboratory into the design environment. This chart addresses the logical integration which is based again upon the commercial capabilities of VxWorks and the workstation

The computer is loaded and the experiments are run from this window. The top right window contains the controller software computer. Several windows have been opened to support a multi-threaded interactive session of controller design, experiment, evaluate and modify. While the screen may appear to be cluttered, it is very effective once the organization of the virtual world it and is used to rebuild the control module. The lower two windows show Pro-Matlab and its graphic display window. All files reside on the investigator's workstation and are accessed over the network by the VxWorks shell, including the controller design The right side of the chart contains an actual image of a workstation screen during a session with the real-time control represents is mastered. The top left window communicates over the network with the VxWorks shell on the real-time computer. parameters and the measured performance data. The lower left section of the chart addresses the benefits of this environment that result from the integration of office and lab. The environment is simple enough that the principal investigator can be completely in charge of the experiment. The resulting interactive, investigative experimental style leads to better understanding of the interactions between the controller and the test article. A major advantage of this environment is the extremely quick turn around for controller design and evaluation which is on the order of a few minutes. It is now possible to spend more time deciding what to do than doing it.

experiments that the safety review board would find the ground test experiences supportive of a request for an interactive Shuttle-based experiment. The essential command, control and communications features associated with an experiment in the A design goal of the laboratory was to establish an environment sufficiently similar to that of in-space flight Shuttle bay which is controlled remotely from a Payload Operations Control Center have been replicated in the CSI Laboratory.

CSI Experiment Integration

Investigator Interface

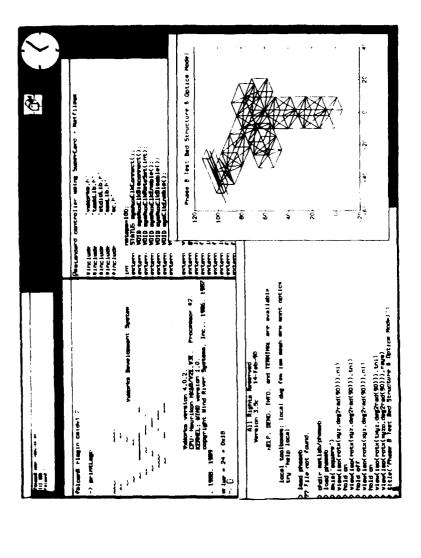
- Use Personal Workstations
- Remote Login From Office or Work in Laboratory
- Use Personal Files for Design, Analysis and Test

Multiple Presentation Threads

- Edit Controller Source Code
- Run Real-'1.me Controller
- Design Controller and Plot Results in Pro-Matlab

This Integrated Experiment Environment Promotes

- Direct Investigator Interaction with Experiment
- Interactive Investigation of Phenomena
- Growth in Experiment Complexity
- Short Controller Evaluation & Modification Cycle ~ Minutes
- Investigator Responsibility for Experiment Performance
- Working in Geographically Dispersed Environments
- Development of a Relevant History in Preparation for Flight Experiment Safety Review



UNCONTROLLED CONTROLLED = GLOBAL CONTROLLER OUTPUT ACCELERATION MEASURE Kg(s) GLOBAL STRUCTURAL CONTROL 7 9 10 11 FREQUENCY (Hz) INPUT DISTURBANCE FORCE CSI STRUCTURAL QUIETING TECHNOLOGY STUDIES . 5 OUTPUT ACCEL. /IMPUT FORCE 10-2 UNCONTROLLED CONTROLLED 7 LOCAL CONTROLLER OUTPUT ACCELERATION MEASURE 5 K₁(s) LOCAL CONTROL (ACTIVE DAMPING) 2 9 10 11 1 FREQUENCY (Hz) INPUT DISTURBANCE FORCE LOCAL 10-2 10-2 OUTPUT ACCEL. /INPUT FORCE <u>ق</u> 5 UNDAMPED = DAMPED OUTPUT ACCELERATION MEASURE ç PASSIVE DAMPING 2 9 10 11 FREQUENCY (Hz) INPUT DISTURBANCE FORCE PASSIVE VISCOUS DAMPER-10-2 10-1 . 6 102 5 9 OUTPUT ACCEL. / IMPUT FORCE

CSI Structural Quieting Technology Studies

The top level architecture for achieving submicron stability on a complex optical system involves a layering This paper describes recent advances in the structural quieting area. By structural quieting, we mean that the structural portion of the spacecraft is designed so as not to deform or vibrate at locations, in directions, or over requency ranges that adversely affect the overall performance of the spacecraft. Our approach to this objective involves the use of passive damping, active damping, and active structural stabilization. Passive and active damping have the effect of reducing vibration at all points of the structure by preventing structural resonances of technologies including active vibration isolation, structural quieting, and active optical compensation [2]. from building up to large amplitude.

all three modes would be heavily damped. The second figure illustrates the damping achieved with two active The first figure shows the level of damping achievable with a single D-strut viscous damper located in one member of the structure. The first and third (torsion) modes of the truss are very heavily damped. The second mode is not because it does not involve participation of that member of the structure. If two D-struts were used, members under collocated control for active damping. Two longeron active members were used in this case, The accompanying figure illustrates current levels of performance for the three components of quieting. damping the first two bending modes. Torsion did not involve the longerons and is not completely damped.

The third figure shows a noncollocated multivariable stabilization controller which uses acceleration measurements at the top of the structure and three active members at the bottom bays.

Local Controllers—Active Damping

Passive dampers, such as fluid dashpots, dissipate energy by causing the dual power quantities of force simulate a passive damping device over a specified frequency range. In this respect, all active members work independently of each other. The active member can be made to emulate the passive damper by appropriate and velocity to be in phase locally at the damper. Active damping is achieved by making each active member feedback of collocated force and velocity.

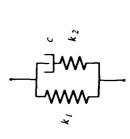
strut controller can be adjusted to a wide range of parameter values allowing for great flexibility. Because the reedback is collocated, the dial-a-strut implementation wide robustness margins. One additional benefit of the bridge feedback approach that is used in the implementation is that the impedance enforced by the feedback is optimal impedance match. The required impedance measurement is easily obtained by exciting the structure independent of the shape of the loop transmission function, so long as the gain is sufficiently high. This means Our implementation exactly parallels the mechanical scheme depicted in the figure. An analog bridge feedback circuit has been designed with three dials corresponding to c, k_1 , and k_2 , such that the engineer need only measure the input impedance of the structure and then adjust the dials to the desired setting for an using the active member and measuring the resulting ratio of force to velocity at the member. This dial-athat the loop shape can be designed to satisfy other objectives (for example, structural stabilization).

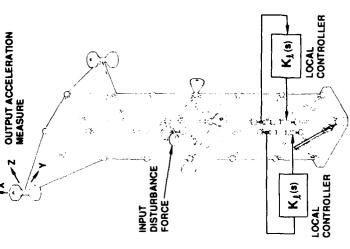
the active member regains its high open-loop static stiffness, a property that cannot be achieved with passive The feedback gain is made to decrease to zero at dc, so that at frequencies below the first structural mode, damping The figure shows an example of damping performance for one and two active members located in longerons of the testbed structure. The resonance peak at 11.5 Hz corresponds to a torsional mode that does not involve strong participation of the two longerons used in the test, which is why the damping in this mode is less than that for the two bending modes.

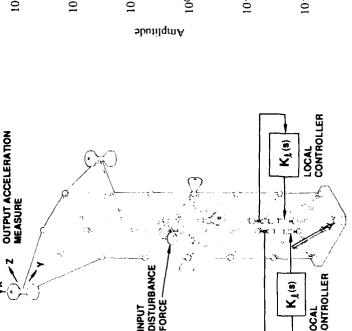


Local Controllers--Active Damping

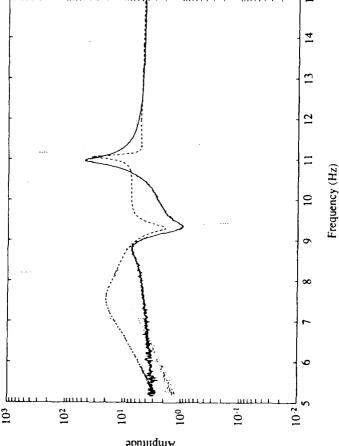
- Very Stiff at Low Frequency Emulates Passive Damper over Specified Frequency Range Parameters Tunable (Dial-a-Strut)







Local Feedback of Force and Velocity



Open Loop vs. Closed Loop for one and two Dial-a-Struts

Global Controllers—Stabilization

by damping alone. In these experiments however, the outer loops are designed without the damping loops controllers. In order to assess the effect of damping on the design process, a passive damper is placed in one The structural stabilization loop is intended to be closed around the local active damping loops to provide present. This leads to a lightly damped structure that presents a worst case plant for which to design robust additional stabilization to specific measures of performance—line of sight, for example—that cannot be achieved of the non-active members of the truss, which increases the damping in the lower three modes from about 0.1 percent of critical to about 1.0 percent of critical. Robust control methods (H_{∞} and μ -synthesis) have been developed to enable the design of multivariable controllers that will perform on systems that are uncertain [3]. Our experiments are designed to explore the applicability of these methods to the structural control problem, starting with lightly damped structures and progressing to the more heavily damped.

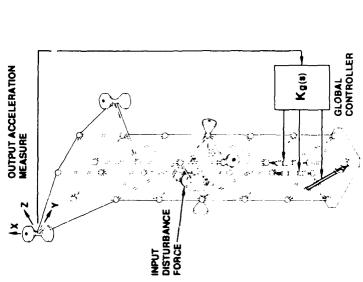
block perturbations Δ_a and Δ_m , additive and output multiplicative blocks, respectively. Different controller The block diagram used for control design is shown in the figure. The inputs and outputs are normalized by means of frequency domain weighting functions. The plant uncertainty is parameterized by means of two full designs are obtained by manipulating the weights. The controllers were designed to minimize the response in three directions of a point at the top of the structure, using measurements from three accelerometers at the top location, and using three active members at the base of the truss as shown in the figure. No collocated measurements were used. The modes of the structure are divided into two groups, the first group near 10 Hz, and the higher group starting at approximately 30 Hz. The higher modes involve significant bending of the truss members, and are therefore only marginally controllable from the location of the active members. Performance was requested for the lower modes only, the loop gain diminishing rapidly after 11 Hz. All algorithms were implemented on the HUGH 9000 real time control computer at an update rate of 1000 samples per second. The number of controller states varied from

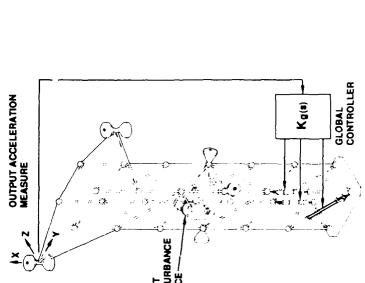
Interconnection Structure

Global Controllers--Stabilization

Wace

actuator penalty





disturbance

noise

Waser

×

Wans

۵,

delay

Wperf

Wadd

Wmule

accelerations weighted

4

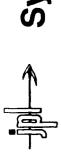
Noncollocated Acceleration

System Identification for Nominal Model

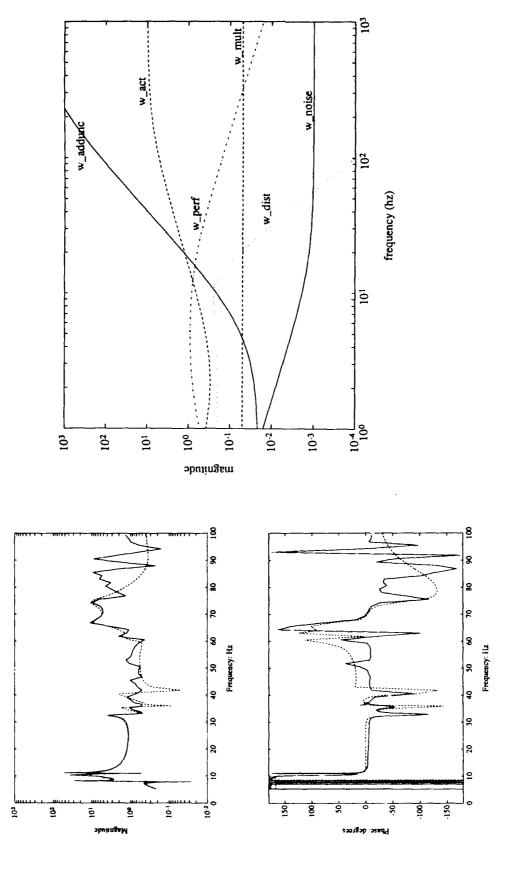
the state space model, and used measured values of modal frequency and damping. Even though the finite element model was considered well correlated from a structural engineering standpoint, our experience on this structure indicated that with damping on the order of 0.1 percent of critical, it was not possible to obtain a early experiments, we relied on a finite element model of the structure to provide the mode shapes used in sufficiently accurate plant model for control design [2]. We therefore began using models based on input/output The primary challenges in designing the outer loops are 1) to obtain an accurate mathematical model that relates inputs from the disturbances and actuators to the outputs from the sensors, and 2) to parameterize the uncertainty in the model in a way that is both pliysically meaningful and mathematically tractable. In measurements from the physical system.

single-input/multi-output transfer function measurements. The results have been mixed. Some of the elements We have developed an ad-hoc methodology for obtaining multi-input/output state space models from of the transfer function matrix are well modelled, some elements less well modelled. The figure shows an element on the undamped plant of intermediate quality, some elements are better than this one, some worse.

of ignorance about the higher modes. Notice also that less performance is requested at higher frequency in the An example set of weighting functions is shown in the figure. These correspond to the design K2. Notice that the additive uncertainty weight w_addunc increases rapidly with frequency corresponding to a higher level



System Identification for Nominal Model



Ad-hoc Multivariable Identification

Choice of Weighting Functions

Designs for Undamped Plant

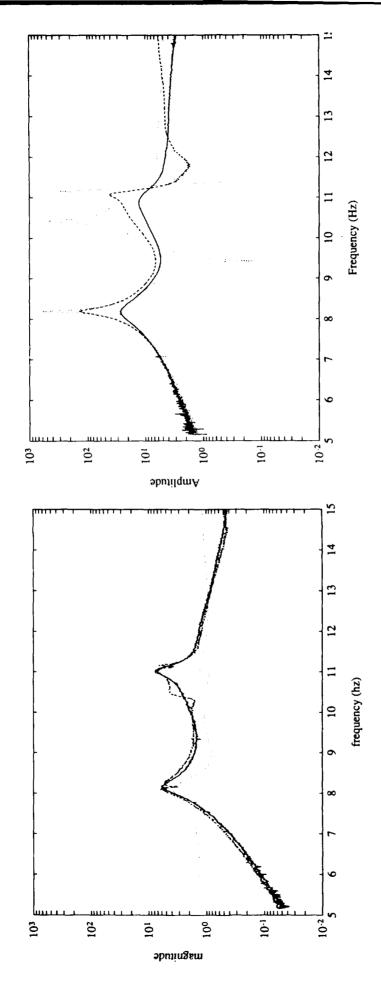
Two controllers were designed for the undamped structure. The first, K_1 , is a nonaggressive design that achieved gain stabilization in the higher modes, that is, the loop transmission function is less than one for the higher frequency modes. The second controller, K2, is a more aggressive design that resulted from significantly lowering the additive uncertainty weight associated with the higher frequency modes.

actual measured open loop plant transfer function, and based on the nominal plant model (uncertainty weights set to zero). The first observation is that the two predictions do not coincide, a result of the fact that the reduced order identified model is in error to some degree. In the case of the undamped structure, a local mode from the disturbance shaker was not included in the model with the result that the transfer functions from the and the z-accelerometer output for controller K₂. Overplotted are the closed loop predictions based on the second observation is that the prediction based on the measured open loop transfer function differs only slightly The left hand figure shows the actual closed loop performance measured between the disturbance input disturbance input were not well represented. This was corrected in the model of the damped structure. from the actual measured closed loop performance.

disturbance force input to z-accelerometer output are plotted for the open loop case and for both controllers The effect of feedback on performance is shown in right hand figure. Frequency response functions from K_1 and K_2 . As expected, design K_2 results in superior performance.



Designs for Undamped Plant



Predicted and Measured Closed Loop Performance for K2

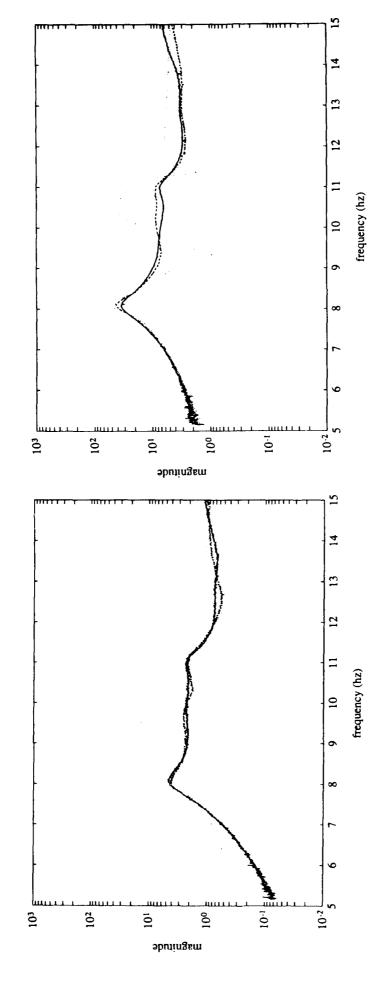
Open Loop and Closed Loop Performance for K1 &K2

Designs for Damped Plant

loop performance for design K₄. The predictions based on measured plant data and the nominal model agree To determine the effect of damping on the closed loop performance, a D-strut passive damper was installed in the truss to add a small amount of damping to the lower modes. The higher modes were largely unaffected. Controllers K₃ and K₄ were designed with similar weighting functions as the previous cases, but were both designed with gain stabilized higher modes. The left hand figure compares the measured and predicted closed much more closely in this case due to an improved identified model. The closed loop performance on the damped plant is somewhat better than on the undamped plant in the second and third modes, and somewhat poorer in the first mode. These differences are more likely the result of different choices of weighting functions than on the passive damping level. On balance, the passive damping does not appear to have contributed significantly to the closed loop performance on the nominal system.



Designs for Damped Plant



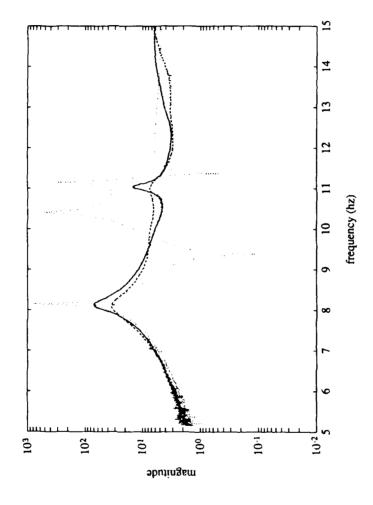
Predicted and Measured Closed Loop Performance for K4

Open Loop and Closed Loop Performance for K3 &K4

Robust Performance Test

As a test of the robust performance characteristics of controller K_4 (designed for the damped structure), it was closed on the undamped structure. The system remained stable, and the performance on both plants is compared in the figure. Performance dropped by approximately a factor of two in the first and third modes, with no change in the second mode, even though the damping in the plant dropped by an order of magnitude. The robustness of the controllers to other forms of plant perturbation remains to be tested.

Robust Performance Test









Conclusions and Future Work

- Collocated Feedback on Active Members is Very Effective for Active Damping
- Dial-a-Strut Controller Implementation is Versatile and Robust
- Improved System Identification Needed for Multivariable Damped Models
- Robust Design Approaches Produce Good Controllers, but More Work is Needed to Select Appropriate Weights, Uncertainty
- Further Tests of Robust Performance Planned
- Simultaneous Local/Global Controller Implementation Planned

Conclusions and Future Work

Our work has demonstrated that collocated control on active members is an effective means of achieving high levels of damping in truss structures. Minimal knowledge of the plant drive point inspedances is required to achieve good impedance matches even with relatively simple force feedback techniques. The dial-a-strut The noncollocated robust control approaches are complex to implement, but do produce controllers with good ad-hoc approach to the identification problem has given mixed results. There is a strong need for improved performance. It is very important to have an accurate multi-input/output model for this design paradigm. Our implementation of the bridge feedback method makes the impedance matching task particularly straightforward. identification methods, particularly for more heavily damped structures.

feel that scaling these weights to more physically motivated values will achieve improved performance. The We have found that added passive damping in the lower modes did not significantly improve closed loop performance. We expect that damping in the higher frequency modes will result in higher available loop gain that will in turn enable higher performance. This will be a topic of future research. Our single test of robust performance showed that a controller designed for a damped structure still performed well when the damping of the structure was reduced by a factor of ten. Further robustness tests involving modal frequencies are planned for future work. Finally, the selection of weights for the robust controllers has been somewhat arbitrary. We parameterization of uncertainty is also very crude in our designs, improved methods using modal parameters may lead to superior performance and is a good topic for future work.

References

- 1. Laskin, R. A., and M. San Martin, 1989. "Control/Structure System Design of a Spaceborne Optical Interferometer," Proceedings of the AAS/AIAA Astrodynamics Specialist Conference, Stowe VT.
- 2. Fanson, J. L., C-C. Chu, R. S. Smith, and E. H. Anderson, 1990. "Active Member Control of a Precision Structure with an H_{∞} Performance Objective," Proceedings of the AIAA Dynamics Specialists Conference, Long Beach, CA, pp. 322-333.
- 3. Morari, M., and E., Zafiriou, 1989. Robust Process Control, Englewood Cliffs: Prentice-Hall Inc.

NASA/DoD CSI Conference Nov 1990

The Multi-Loop Control/Structure Interaction Effect: experimental verification using the ASCIE test bed.

Jean-Noel Aubrun and Kenneth R. Lorell

Lockheed Palo Alto Research Laboratory 3251 Hanover St., Palo Alto, CA 94304

ABSTRACT

The Control/Structures Interaction phenomenon has its origin in the spillover of control energy into unmodelled vibration modes, a principle clearly established by M.Balas more than a decade ago. A second principle has been found that establishes a bandwidth limitation related to the number of closed-loops in the system. Essentially, each new loop that is being closed brings the system one step closer to instability.

This paper presents a theoretical derivation along with experimental results in support of this principle. The theory indicates that in the worst case, the bandwidth is inversely proportional to the number of loop closures. This effect has serious implications for the design of systems with a large number of actuators and sensors. This result is supported by experiments conducted on the Advanced Structures/Controls Integrated Experiment (ASCIE) which demonstrated the interaction of the segment alignment system with the structural modes. These experiments confirmed that, as the number of actuators being controlled is increased from one to the full eighteen required for six-segment control, the interaction increases and the achievable control bandwidth decreases. With a classical controller, the maximum bandwidth was found to be less than 1 Hz, while the first (destabilized) vibration mode was at about 16 Hz.

INTRODUCTION

In the late 1970's Marc Balas [1] brought quite a challenge to the controls community by discovering the unavoidability of the spillover problem and the subsequent performance limitations that large flexible systems will have to endure. This inherent bandwidth limitation due to interaction of the control system with unmodelled modes is the essence of the Control/Structures Interaction (CSI) phenomenon. This has been demonstrated experimentally in the past on simple beams structures (usually using only a few actuators and sensors), and very recently on a complex three-dimensional system known as ASCIE.

ASCIE, which stands for Advanced Structures/Controls Integrated Experiment, was developed at Lockheed Palo Alto Research Laboratory to conduct interdisciplinary studies including, in particular, the study of CSI in large segmented optical systems [4,5]. In these systems, many actively controlled elements (e.g., active mirrors) are required to achieve line-of-sight accuracy and image quality. For example, because of the prohibitive weight penalty incurred by stiff monolithic reflectors, the use of a segmented primary mirror is a major design concept for the new generation of large ground and space-based telescopes [2,3].

The problem is that the active elements produce dynamic forces on the structure supporting them, thereby inducing disturbances. This phenomenon is described as CSI and invariably leads to instability as the control gains are increased and thus seriously limits the performance of control systems for large structures.

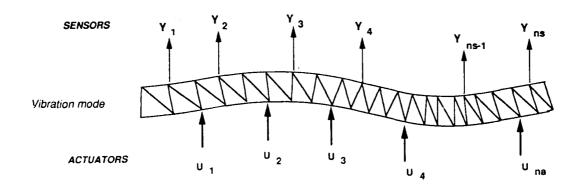
Designed to study these issues, the ASCIE test article emulates a Cassegrain telescope with an actively controlled segmented primary mirror. The primary mirror control system uses a classical integral control approach. It was modeled after the Keck Ten Meter Telescope [5,6] to serve as a baseline for evaluating various control schemes and their ability to deal with CSI.

In 1989 the complete ASCIE system became fully operational, with all six segments functioning at optical tolerance levels. For the first time, a full closed loop segment control system was operated in the presence of a flexible structure with the corresponding dynamical interaction between the structure and the control system.

One of major features of ASCIE is that it is truly a multi-input, multi-output system, with 18 actuators and 42 sensors which are not colocated. This brings a new dimension to the study of the CSI phenomenon. It is now possible to study the effects associated with the number of actuators and sensors with traceability to real systems. This paper addresses some fundamental bandwidth limitations associated with the number of loop closures.

FIGURE 1 BASIC ASSUMPTIONS

Consider the general case of a structure where n_s sensors measure the displacements y_i at n_s points, and n_a actuators are deforming the structure by applying displacements u_i at na points. The relationship between the y's and the u's is defined by the rectangular matrix A. Considering a particular vibration mode (critical mode) of modal amplitude q. the sensors are also affected by this vibration according to the mode shape vector Φ^{S} . The goal of the control system is to keep all the y_i 's at zero. Thus, in its simplest form, a control law will use integral control using the pseudo-inverse A of the matrix A. In essence, the sensor readings are converted into equivalent motions at the actuator locations through A^{\sim} . The transfer function (k/s) of the control compensation is the simplest form of practical alignment algorithms, and in fact is used for the Keck telescope. It is quasi-static in nature and does not take into account the existence of the critical mode. But this model is easy to understand and it represents generically the case of a control system that ignores vibration modes which will destabilize it due to spillover. The dynamics of the critical mode are represented in the last equation, showing the modal transfer function relating the modal amplitude q to the control input vector U through the mode shape vector Φ^{a} at the actuator locations.



Sensor output:

Y = A U + D q

Control law:

U = - (k/s) A Y

Structural dynamics:

 $q = (\Phi^{a}/D(s)) U$ $D(s) = s^{2} + 2\zeta \omega_{c} s + \omega_{c}^{2}$

FIGURE 2 MODAL SPILLOVER PATH IN A MULTI-LOOP SYSTEM

This block diagram describes the path of control and spillover signals in a system containing several actuators. Conceptually, the control system can be decomposed in separate controllers, each feeding one actuator. All controllers are fed by the sensor measurements. Consider the path taken by a single vibration mode. Usually, one particular mode goes unstable when the loop gain is too high, thus it is called a critical mode. Consider that mode and its modal amplitude q. This amplitude is picked up by the sensors and thus fed along the measurement Y to the controllers as shown in the first equation. The controllers in turn modify this signal and produce an extraneous control vector $\mathbf{U_q}$ according to the closed-loop equation shown next. Through the structural dynamics, this control $\mathbf{U_q}$ produces a modal amplitude given in the last equation. Thus it is seen that though this process, the vibration of the critical mode is fedback to itself. Since only this mode is of interest one can determine the stability characteristics of the system by just examining the "modal gain" as shown in the next figure.

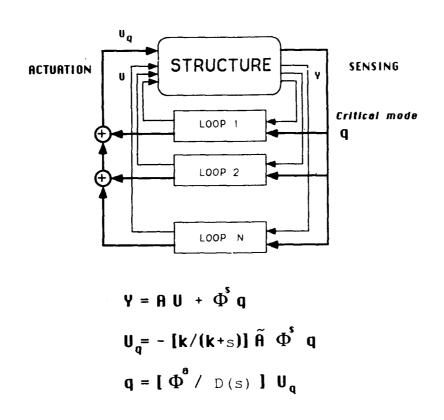
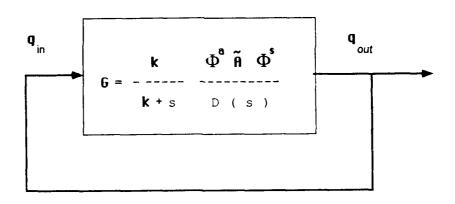


FIGURE 3: MODAL GAIN IN A MULTI-LOOP SYSTEM

By just looking at the path taken by the vibration around the closed-loop system, one may understand the concept of the modal gain representation of the system [8,9]. The modal amplitude q_{out} is generated by the structure/control system combination which itself is driven by the modal amplitude q_{in} . Of course q_{out} and q_{in} are one and the same modal amplitude q_{in} this representation makes it readily possible to determine the modal stability of the system. For instance one may look at the Nyquist plot and determine the value of the real part of the gain at the crossing of the real axis. This crossing, in the case studied here, will happen at a frequency close to the modal frequency ω_{c} of the critical mode, and a stability condition is obtained that involves the loop gain k, the mode shapes, the critical mode damping ratio ς , and frequency ω_{c} .



$$@ \omega = \omega_c : \text{Im}(G) = 0$$
, Re(G) = k[$\Phi^a \tilde{A} \Phi^s$] /(2 $\zeta \omega_c^3$)

STABILITY MEANS: Re(G) < 1

FIGURE 4 TRANSFORMING THE STABILITY CONDITION

This figure shows two important steps in transforming and interpreting the stability condition shown in the previous figure. First recognize that the gain k is nothing more than the bandwidth $\omega_{\rm b}$ of the alignment system. But more importantly, the meaning of A is that it transforms motions of the structure at the sensor location into equivalent motions at the actuator location. Thus the sensor mode shapes Φ^2 are transformed by the matrix A into the actuator mode shapes Φ^2 . (The fact that the transpose sign is used here reflects the fact that in the previous definitions, the actuator mode shapes were represented as row vectors, while the sensor mode shapes were column vectors). Thus the stability condition is now expressed entirely with actuator mode shapes.

Control system bandwidth : $\omega_b = k$

A transforms motions y into equivalent motion at actuators

Thus:
$$\vec{A} \Phi^s = [\Phi^a]^T$$

STABILITY CONDITION BECOMES:

$$\omega_{_{\boldsymbol{b}}} \ \boldsymbol{x} \quad \boldsymbol{\Phi^{\boldsymbol{a}}} \quad \boldsymbol{\Phi^{\boldsymbol{a}^{\boldsymbol{J}}}} \ < \ 2 \ \zeta \ \omega_{_{\boldsymbol{c}}}^{\boldsymbol{3}}$$

FIGURE 5 THE MULTI-LOOP THEOREM

The final transformation is in evaluating the the scalar product of the actuator mode shapes. It can be expressed as the sum of squares of each mode shape value at each actuator. At this point one may take the statistical view that there is little chance that the actuators are at node points and thus the value of the mode shape may be represented by a statistical average. Thus each new actuator brought to the system adds in an average contribution $<\phi^2>$ to the sum. Finally, the following result is obtained:

The product of the maximum control system bandwidth by the number of actuators on the structure is a constant.

Thus, for a given control algorithm, the more loops that are closed, the less bandwidth is achievable. Note that the bandwidth is limited by the natural structural damping, which is a well known fact, but also by the cube of the modal frequency. The other interesting feature in the stability condition is that it involves the inverse square of the mode shape, which, because of the usual mode shape normalization, represents the mass of the associated finite elements. This indicates that light structures are more difficult to control than heavy ones, an unpleasant situation, of course, for space applications.

$$\Phi^{a} \Phi^{a^{T}} = \sum_{i} (\Phi_{i}^{a})^{2} \cong N < \Phi^{2} >$$

Thus:

$$\omega_{\mathbf{b}} \times N < 2 \zeta \omega_{\mathbf{c}}^3 / \Phi^2$$

FIGURE 6 ASCIE SYSTEM DESCRIPTION

The ASCIE is built to replicate a large Cassegrain telescope with a segmented primary mirror. It consists of a 2-m, 7-segment, actively-controlled primary mirror supported by a lightweight, flexible truss structure. The truss has been specifically designed to emulate the structural dynamic properties of a large space structure.

The segmented primary mirror is made of seven hexagonal segments, six of which are actively controlled. The seventh central segment is passive and acts as the reference surface for the actively controlled segments. Each of the active segments are controlled in three degrees of freedom; two angular (tilts), and one translational (piston). The other three degrees of freedom are passively restrained by the flexure mounting system which attaches the segment to its positioning actuator.

The ASCIE segments are not real optical surfaces. They are fabricated from aluminum plates and have the correct mass, inertia, and stiffness characteristics of glass segments. Thus, instead of optical surfaces, ASCIE utilizes an optical calibration and scoring system (OCSS) that consists of a single laser beam reflected off small flats located on each of the six segments. The six returning laser beams are directed onto linear photodetectors which measure the angular displacements of the controlled segments. The OCSS eliminates the requirement for optical surfaces on the segments and provides for an independent control system performance measurement capability.

The ASCIE control system hardware involves a total of four computers (Harris- 800 superminicomputer, Floating Point Systems FPS 120B Array Processor, and two PC's), 59 sensors (24 segment edge sensors, 18 actuator position sensors, and three secondary mirror sensors), and 21 actuators (18 segment positioning and three secondary mirror control actuators). The full set of interface electronics contains four card racks holding nearly 60 electronic cards and communicates with the four computers and the ASCIE experiment using 36 separate cables.

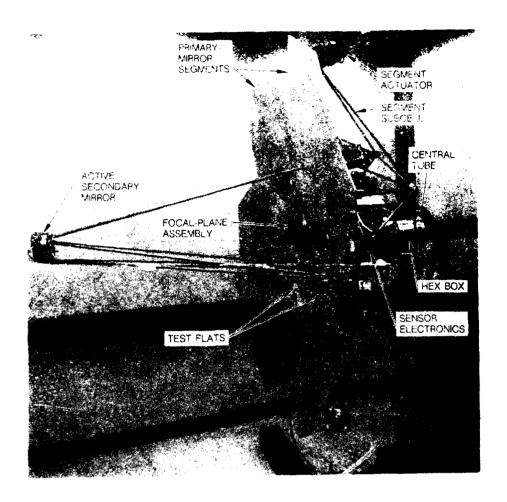


FIGURE 7 ASCIE PRIMARY MIRROR SEGMENT CONTROL SYSTEM

The ASCIE segments are controlled through the use of an array processor which processes the signals coming from the 24 edge sensors and computes the control signals for each of the 18 segment positioning actuators. This figure illustrates the concept of the ASCIE segment control system. The block marked control law indicates that the algorithm used to provide segment control is a separate, programmable portion of the array processor code. This architecture closely matches the conditions of the theory previously discussed and thus was appropriate to validate it experimentally. One powerful feature of the system is its capability to change gain matrices while the system is running in closed-loop. Thus stability margins can be measured directly and safely, and comparisons between various control designs can be made more easily.

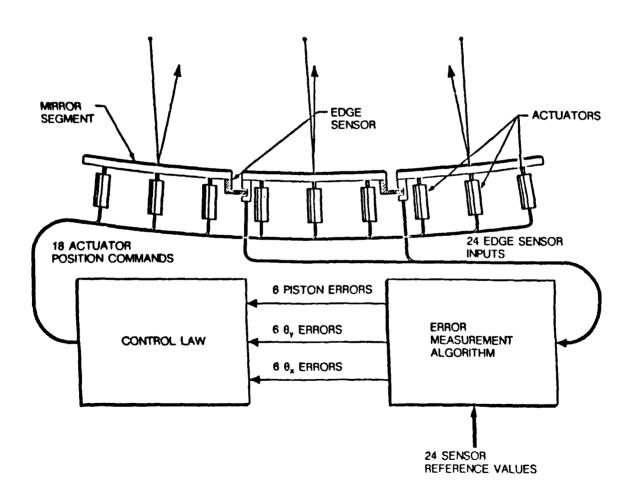


FIGURE 8 CONTROL ALGORITHM

The ASCIE baseline controller is identical to that used for the Keck Ten Meter Telescope. It is essentially quasi-static in nature and does not take into account the effects of structural dynamics. This algorithm is thus ideal to demonstrate the CSI phenomenon and provides a baseline design that can be used for comparison with more advanced algorithms. The array processor implementation of this controller can be simply described by the equations shown in the figure. The vector U contains the actuator commands, X contains the segment tilt and piston errors as calculated form the edge sensor measurement vector Y, and K is a scalar gain. Xo corresponds to the initial reading of the edge sensors after alignment has been achieved through the optical calibration system (Xo = A~ Yo). The 18x18 matrix B transforms tilt and piston errors into actuator position errors, the 24x18 matrix A transforms tilt and piston motions into edge sensor readings. The inverse transformation A needed for control is the least-square inverse of A. The structure of the gain matrix loaded in the array processor is shown as the next equation in the figure. The 24x1 vector X is not essential for control but is used for data acquisition and display purposes and the whole control equation can be rewritten as Eq. (3) of the figure. This is the discrete equivalent of integral control. The bandwidth $\boldsymbol{\omega}$ of such a system (for $K << T_s$) is then given by Eq. (4), where T_s is the sampling period.

(1)
$$U_{n+1} = U_n - k B X_n$$

 $X_n = \widetilde{A} Y_n - X_0$

CONTROL EQUATIONS

(2)
$$\begin{vmatrix} U \\ X \end{vmatrix} = \begin{vmatrix} -kB\widetilde{A} & I & kB \\ \widetilde{A} & 0 & -I \end{vmatrix} \begin{vmatrix} Y \\ U \\ X_0 \end{vmatrix}$$

ARRAY PROCESSOR

(3)
$$U_{n+1} = U_n + k B \tilde{A} (Y_0 - Y_n)$$

CONTROL LAW

(4)
$$\omega = k/T_s$$

Control Bandwidth

FIGURE 9 EXPERIMENTAL RESULTS - FOCAL PLANE DISPLAY

The ASCIE was successfully run with all six segments actively controlled and a gain K = 0.016 corresponding to a bandwidth of 0.7 Hz at a sampling period of 5 ms. Independent determinations were made of control system performance using both the calculated tilt and piston errors based on edge sensor measurements, and tilt-only errors based on OCSS measurements. Computed piston and tilt errors were found to be of the order of 250 nm and 700 nrad rms, respectively. This figure shows the output of the OCSS computer which displays a cumulative sampled ray trace from each of the six photodetectors at the ASCIE focal plane. Each sample is displayed as a dot on the screen, and the accumulation of dots over a 60 second sample time is displayed superposed on a set of calibration circles. All of the six photodetector outputs have been adjusted so that their origins are coincident with the origin of the calibration circles. If the segment control system were operating correctly, the pattern of dots from the six segments will be virtually a point at the origin. Because noise, vibration, and control system errors distort the image and degrade the optical system performance, the combined samples tend to generate a distributed image at the center of the calibration circles.

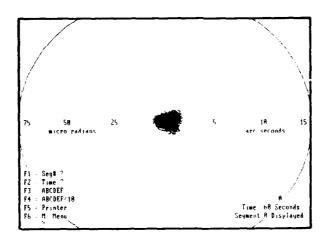


FIGURE 10 EXPERIMENTAL RESULTS - FOCAL PLANE DISPLAY OF CSI INSTABILITY

When the gain K of the segment control system is increased, the actuators have more authority to excite the vibration modes of the system. The vibration is sensed by the sensors, and for some modal frequencies, is positively fed back to the actuators. When the gain is high enough, the system becomes unstable and oscillations are induced by the control system into the backup structure which supports the segments. This oscillation is known as CSI. This figure is a plot of the OCSS output similar to the previous figure, except that the gain has been increased by a factor of 1.4. The star pattern is generated when the structural resonance caused by CSI moves the segments in an uncontrolled fashion. These motions are extremely small. Note that the angles range from 25 to 50 microradians.

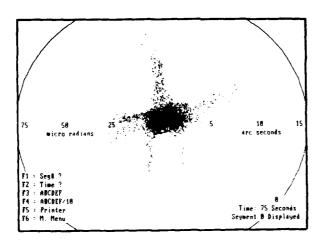


FIGURE 11 FREQUENCY SPECTRUM

The plot in this figure was generated by connecting a spectrum analyzer to the sensor signal from one of the segment actuators. The plot shows the magnitude of the frequency spectrum of the motion of the actuator. In plot (a), the gain is below the stability margin and the actuator response corresponds to the focussed focal plane display. Plot (b) shows the spectrum when the gain is increased beyond the stability margin. The peak occurs at a frequency of 16.2 Hz and represents the first mode to be driven unstable by the CSI phenomenon.

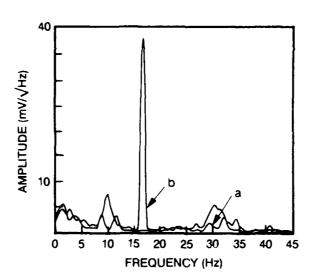
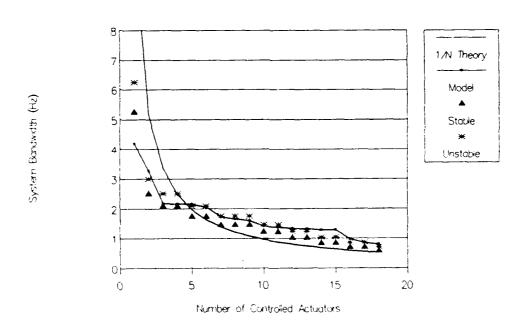


FIGURE 12 VERIFICATION OF THE MULTI-LOOP STABILITY THEOREM

To better understand the principle on which CSI operates, a series of tests were conducted in which the coupling of the control system to the structural dynamics was gradually increased. This was accomplished by increasing the number of loop closures until all loops were closed and all segments controlled. The same set of sensors was used in these tests, (the information about a particular segment was always derived from sensing all the edge sensors) while the loops were opened or closed at the actuator level. At each step, the gain was adjusted until the system became unstable. This plot shows the variation of the maximum control system bandwidth with the number of actuators being controlled. The theory predicts a decrease in bandwidth inversely proportional to the number of actuators. This law has also been plotted in this figure, the scale factor was adjusted for best fit. There is a general agreement with the measured behavior, but discrepancies are noticeable and indicative of the statistical nature of the theorem. However, the exact application of the formula (using the $\Phi\Phi^{i}$ expression) was performed using mode shape values obtained from the ASCIE finite element model. A damping of 1.2 percent was used and the corresponding curve ("model") is also shown in Fig. 12. The agreement is, of course, better in this case since variations in individual mode shapes were taken into account.

CSI EFFECT ON MAXIMUM BANDWIDTH



CONCLUSION

This paper has presented experimental evidence of the CSI phenomenon in a large flexible structure using the ASCIE testbed, and related the resulting stability margin to the amount of coupling between the control system and the structure. These results are in good agreement with the theory that indicates that CSI effects will decrease the system bandwidth as the number of closed loops is increased. This has serious implications for the design of future systems which must employ a very large number of actuators and sensors.

REFERENCES

- 1. Balas, M., "Active Control of Flexible Systems". J. Optimization Theory and Appl., 25 (1978), 415-436.
- 2. Swanson, P. N., S. Gulkis, T. B. Kuiper and M. Kiya (1983). Large deployable reflector (LDR): a concept for an orbiting submillimeter-infrared telescope for the 1990s. Optical Engineering, 22, 725-731.
- 3. Mast, T. S., and J. E. Nelson (1981). Figure Control for a Fully Segmented Telescope Mirror. Keck Observatory Report No. 77.
- 4. Aubrun, J-N., and Lorell, K. R.: The Development of an Integrated Experiment to Study the Controls/Structures Interaction Problem in Large Optical Systems, Proceedings of the XIth IFAC Symposium on Automatic Control in Aerospace, Tsukuba, Japan, July 17-21, 1989.
- 5. Lorell, K. R., Aubrun, J-N., Zacharie, D. F., and Perez, E. O.: A Control Technology Testbed for Large Segmented Reflectors, IEEE Control Systems, 9,6, October, 1989.
- 6. Gabor, G. (1981). The Mirror Control System for the U.C. Technical Demonstration Prototype. Keck Observatory Report No. 77.
- 7. Nelson, J. E., Mast, T. S., and Faber, S. M. (1985). The Design of the Keck Observatory and Telescope (Ten Meter Telescope). Keck Observatory Report No. 90.
- 8. Aubrun, J-N., Lorell, K. R., Mast, T. S., and Nelson, J. E. (1987). Dynamic analysis of the actively controlled segmented mirror of the W. M. Keck Ten Meter Telescope. IEEE Control System, 7, 6, 3-10.
- 9. Aubrun, J-N., Lorell, K. R., Havas, T. W., and Henninger, W. C. (1988). Performance analysis of the segment-alignment control system for the Ten Meter Telescope. Automatica, 24, 4, 437-453.



THE MODE FAMILY OF ON-ORBIT EXPERIMENTS:

THE MIDDECK ACTIVE CONTROL EXPERIMENT (MACE)

Prof. Edward F. Crawley

MIT Dr. David W. Miller

PSI LMSC MDESC

Dr. Andy Bicos

Mr. Mel Waldman

Dr. Javier de Luis

November 1990

ABSTRACT

Experiment (MODE) which investigates the nonlinear behavior of contained fluids and truss structures in zero gravity. The objective of Center (SERC) at the Massachusetts Institute of Technology is described. This is the second in a family of flight experiments being developed at M.I.T. The first is the Middeck 0-Gravity Dynamics the MACE program is to investigate and validate the modeling of the program, is necessary in order to fully understand both how flexibility of Experiment (MACE) I roposed by the Space Engineering Research dynamics of an actively controlled flexible, articulating, multibody the platform affects the pointing problem, as well as how gravity tests, and performance metrics of the test article, and defines the tests A flight experiment entitled the Middeck Active Control approach for the program are presented. The rationale shows that onorbit testing, coupled with ground testing and a strong analytical perturbs this structural flexibility causing deviations between 1- and 0gravity behavior. The experimental approach captures the essential physics of multibody platforms, by identifying the appropriate attributes; platform free floating in zero gravity. A rationale and experimental required to successfully validate the analytical framework

OUTLINE

MODE family of experiments

Overview of the Middeck Zero-Gravity Dynamics Experiment

The Middeck Active Control Experiment (MACE)

Objectives, rationale and focus mission Science development approach On-orbit tests

Summary

THE MODE FAMILY OF EXPERIMENTS

reusable facility is used to investigate the gravity dependent behavior in inexpensive dynamic and control experiments designed to exploit the interactive, shirt sleeve environment of the STS Middeck. The first behavior of fluids and truss structures in zero gravity. The second flight modifies the dynamics test facility to include the capability for performing closed-loop active control experiments. This modified, facility uses a reusable dynamic test facility to investigate the nonlinear The MODE family of experiments is a series of small, relatively the closed-loop performance of a flexible, multi-payload platform

THE MODE FAMILY OF EXPERIMENTS

Structural Test Article (STA)

Coupled Non-Linear
Dynamics of Fluids and
Structures in Zero
Gravity

Non-Linear Dynamics of Jointed Truss Structures in Zero Gravity

MACE Test Article

Influence of Gravity on the Active Control of a Multibody Platform

> Flight # 1: August 1991

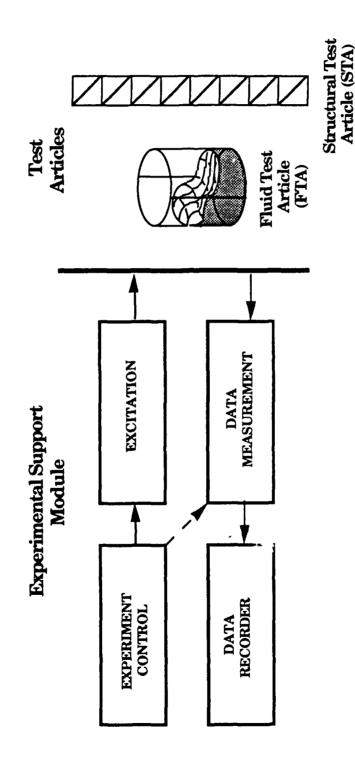
Flight #2: September 1993

experiments designed to advance technology of interest to NASA MACE is part of a logical sequence of cost-effective flight in the area of controlled structures.

THE MIDDECK 0-GRAVITY DYNAMICS EXPERIMENT (MODE)

(ESM) containing the equipment typical of a generic dynamic test the first flight of MODE, the test articles will consist of several fluid test MODE consists of two elements: the experiment support module facility and the two types of test articles. The ESM, which is contained in one Middeck locker, houses the experiment control computer, data acquisition and storage system and sensor and actuator electronics articles (FTA's) and several geometries of a structural test article (STA). which can be reconfigured to accommodate various test articles.

THE MIDDECK 0-GRAVITY DYNAMICS EXPERIMENT (MODE)



on the first flight to test two rather different types of test articles. MODE provides a reusable dynamics test facility which will be used

FTA OBJECTIVES, REQUIREMENTS AND APPROACH

A rationale justifying the performance of the FTA experiment on-orbit has been developed and is explained on this viewgraph.

FTA OBJECTIVES, REQUIREMENTS AND APPROACH

Engineering science objective is to characterize fundamental 0-g slosh behavior and obtain quantitative data on slosh force and spacecraft response for correlation of numerical model.

Requirements

Scaled tank

Properly modelled fluid

Simulation of coupled spacecraft mode

Harmonic excitation

Measurement of slosh force

Modelling approach

Find fluid flow potential and free surface motion solutions. Express kinetic and potential energies in terms of

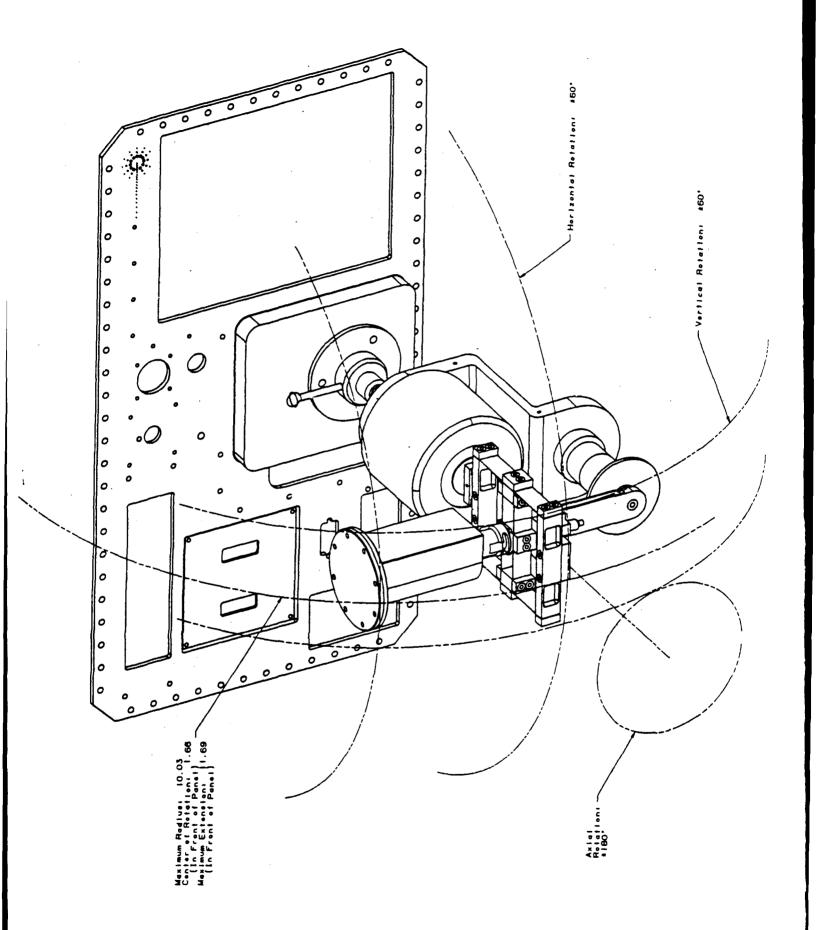
generalized coordinates.

Derive governing differential equations by applying Lagrange's Principle.

Verify predictions with MODE flight and ground test results. Solve nonlinear equations subject to harmonic excitation.

FTA CONFIGURATION

shaker to the ESM electronics. The shaker harmonically excites the and decreasing frequency sweep which encompasses the two The FTA assembly, which is stored in a separate locker for launch and landing, is attached to the front panel of the ESM. An umbilical, force balance, to which the FTA is attached, through both an increasing resonances associated with the slosh motion of the fluid coupled with an electronically synthesized spacecraft mode. This sweep is performed at which is not shown, connects the various FTA sensors and the linear three different forcing levels to reveal the nonlinear characteristics. Two geometries of FTA's are used: a flat bottom cylinder and a spherical bottom cylinder. Two different types of fluids will be tested: silicon oil and water. This requires that a total of four FTA's be flown.



STA OBJECTIVES, REQUIREMENTS AND APPROACH

A rationale justifying the performance of the FTA experiment on-orbit has been developed and is explained on this viewgraph.

STA OBJECTIVES, REQUIREMENTS & APPROACH

gravity on joints, to quantify the changes due to the absence of fundamental changes in dynamics in 0-g due to absence of suspension and gravity load on members, and to obtain quantitative data for correlation with numerical models. Engineering science objectives are to characterize the

Requirements

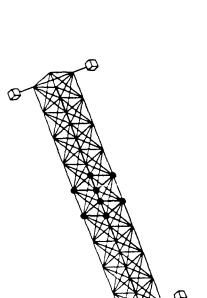
Truss structure containing elements of future space structures. Reconfigurable truss with deployable and erectable bays. Nonlinear joints with variable pre-load to test nonlinear behavior in several gravity/joint pre-load conditions.

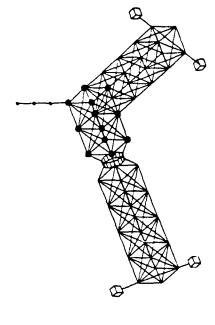
Modelling approach

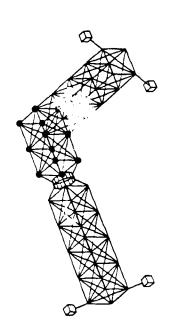
Verify predictions with MODE flight and ground test results. Develop global linear model using FEM and modal test data. Insert describing functions into global model and solve for Develop Force-State Map of non-linear sub-components. Develop describing functions from Force-State Map. forced response using Harmonic Balance Method

STA CONFIGURATIONS

The STA consists of five types of elements: two four bay deployable tension cables. The tension in the cables on one of the deployable bays is adjustable. Testing will involve frequency sweeps at three different truss assemblies; two erectable truss bays; an alpha joint assembly; rigid end masses and a flexible appendage. This viewgraph shows the four different configurations in which the STA will be tested. The ring in three of the four configurations is an alpha joint and the large black dots indicate the nodes of the erectable bays. All deployable bays have preload forcing levels to identify the nonlinear characteristics of the STA's forced behavior.



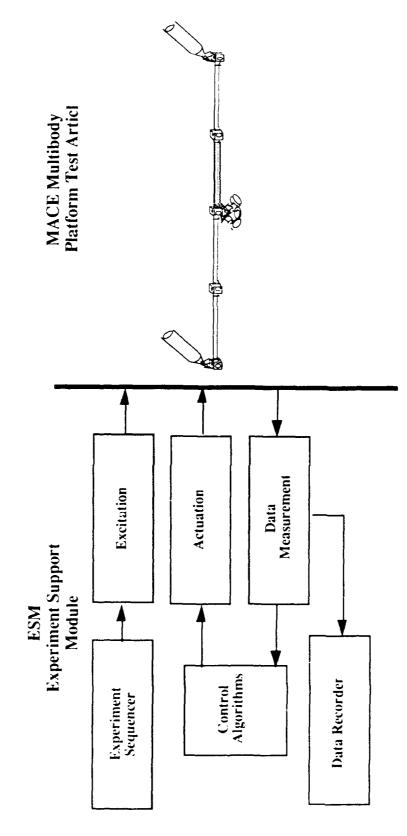




THE MIDDECK ACTIVE CONTROL EXPERIMENT (MACE)

test a multibody platform representative of high mass fraction, multiple payload platforms. The shaded boxes in the ESM are components which MACE employs the same concept as MODE. An ESM is used to also exist in the MODE ESM. The unshaded boxes are components which are unique to the MACE ESM: the realtime feedback control computer and the control actuator drive electronics.

THE MIDDECK ACTIVE CONTROL EXPERIMENT (MACE)



- Substantial commonality of ESM hardware/software
- Significant savings in integration/certification process.

OBJECTIVES AND RATIONALE

the accuracy with which the on-orbit closed-loop behavior can be orbit, open-loop behavior can be predicted. The fundamental difference between the two is that no measure of open-loop roodel accuracy is sufficient to guarantee accurate prediction of closed-loop behavior at MACE differs from MODE in the sense that MACE investigates predicted whereas MODE investigates the accuracy with which onarbitrarily large levels of control authority.

OBJECTIVES AND RATIONALE

sufficient versatility in the design to allow identification and tuning of designers to either be able to predict on-orbit behavior or allow Objective: to develop a well verified set of tools that will allow the structure on orbit.

- Since the model fidelity required for stability and performance robustness is intimately related to the level of applied control authority, closed-loop testing is required.
- Vehicle qualification testing will most likely occur on the ground where suspension and direct gravity effects will cause the 1-g and 0-g dynamics to differ.
- Differences between the ground and on-orbit environment cause perturbations which can substantially alter closed-loop behavior.
- for comparison with ground testing and analytical predictions to Therefore it is essential to perform on-orbit closed-loop testing develop these tools.

CAPTURING THE ESSENTIAL PHYSICS: TEST ARTICLE REQUIREMENTS

Several types of proposed mission vehicles were reviewed. These multiple payload platforms and robotic devices. Multiple payload platforms were selected as the mission focus for the MACE test article because large angle scanning of multiple payloads presented about the most difficult to test on the ground and therefore accurately predict on orbit. This viewgraph lists some of the essential characteristics of a test included interferometric telescopes, deformable optical surfaces, article representative of a multiple payload platform.

CAPTURING THE ESSENTIAL PHYSICS: TEST ARTICLE REQUIREMENTS

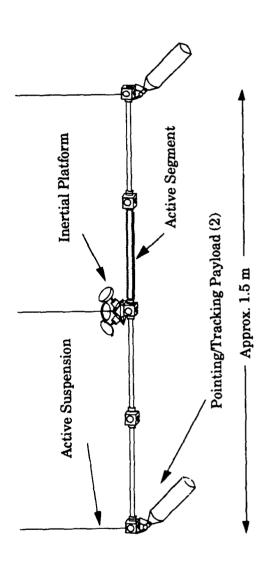
appendages with pointing and positioning requirements, necessitates The simulation of a vehicle with payloads and articulating a test article with the following attributes:

- appropriately scaled to fit in the middeck while preserving the essential performance requirements.
- two gimballing payloads to enable implementation of multiple interacting control systems with independent objectives.
- two rigid payloads and a flexible appendage, representative of compact high mass fraction devices and a robotic servicer.
- flexible bus with resonances within the controller bandwidth and to exhibit suspension coupling, gravity stiffening and droop.
- undergoes full 3-D kinematic and coupled flexible motion. sufficiently complex geometry such that the test article

GROUND BASED ENGINEERING MODEL TESTBED

which is the structural interconnect between the payloads and the assembly is completed and the first of two two-axis gimbals is being tested. Fabrication and assembly of the EM should be complete by the The purpose of the Engineering Model (EM) is to develop science. The EM is presently being fabricated at M.I.T. The segmented bus, inertial platform, is being dynamically tested. The three torque wheel beginning of 1991

GROUND BASED ENGINEERING MODEL TESTBED



- Three zero spring rate pneumatic/electric suspension devices from CSA engineering with maximum stroke of 63.5 mm.
- AC100 real time control computer from Integrated Systems, Inc.

MACE SCIENCE DEVELOPMENT APPROACH

Six different avenues are being pursued in the development of the MACE science. At first glance, these avenues infer a vast analysis and test matrix. In reality, only a subset will be pursued for the first flight.

- 1) Control objectives refer to studying various combinations of single and multiple payload pointing and scanning.
- Control topologies refers to the feedback paths which are allowed to exist due to different systems integration constraints. Hardware suites refers to exploring the performance and robustness improvement obtained as additional suites of hardware become available.
- 3) Control approach refers to the method by which the control algorithms will be derived.
- words, the lowest fidelity model provides fundamental insight while the 4) Model complexity refers to the accuracy and complexity of the models on which these control formulations will be exercised. In other highest fidelity model is used to derive algorithms for implementation.
- 5) More complex test article geometries can be used to further challenge ground testing.
- 6) Fundamental to the flight experiment is the understanding or gravity influences on the problem.

MACE SCIENCE DEVELOPMENT APPROACH

The MACE program will pursue six different avenues in developing controllers for multiple payloads on a flexible bus structure.

- 1) Control objectives
- Control topologies and sensor/actuator suites. 6
- Control approach to the pointing and scanning problems. $\widehat{\mathfrak{S}}$
- 4) Evolution of structural model fidelity.
- Evolution of structural configuration to more complex $\widehat{\Omega}$
- Influence of gravity on closed-loop behavior. (9

SCIENCE DEVELOPMENT APPROACH: CONTROL OBJECTIVES

Viewgraph is self-explanatory.

SCIENCE DEVELOPMENT APPROACH: CONTROL OBJECTIVES

Control Objectives:

- Pointing performance of single and multiple payloads.
- Scanning performance of single and multiple payloads.

Performance Metrics:

- Stability--RMS 2-axis angular position about pointing line of sight or scanning reference profile.
- Jitter--RMS 2-axis angular rate about pointing line of sight or scanning reference profile.
- Slew response time-time required to complete maneuver.
- performance associated with addition of an interacting, Percent degradation-reduction from single payload controlled payload.

SCIENCE DEVELOPMENT APPROACH: TOPOLOGIES AND HARDWARE SUITES

Four topologies will be investigated. The first called central has the the attitude of the assembly. The closed-loop poles are in a Butterworth This "central" topology is used as the low gain baseline against which payloads clamped to the bus and the torque wheels are used to control pattern with a bandwidth equal to one-tenth of the first flexible mode. other designs are compared. The localized topology assumes that payload control design is independent of bus design. Therefore, all payload feedback loops are closed locally and the inertial attitude of the payload is measured locally.

attitude from a measurement of the inertial attitude at the center of the The centralized topology requires that the payload infer its inertial bus and other available sensors.

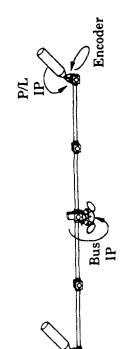
loops and provides inertial attitude measurements on the bus and on the payload. This topology is used as the high performance scenario for The global topology places no constraints on the allowable feedback comparison purposes.

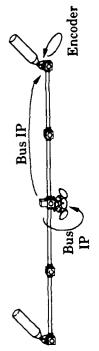
flexibility are added. The purpose of this progression is to investigate the First, the control hardware is limited to existing pointing and angle encoders. Then, sensors whose sole function is to measure the flexibility in the bus become available. Finally, actuators used to control scanning hardware such as torque wheels, gimbals, rate gyros and cost/benefit of each additional suite.

SCIENCE DEVELOPMENT APPROACH: TOPOLOGIES AND HARDWARE SUITES

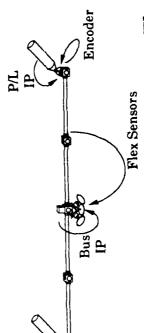
Localized

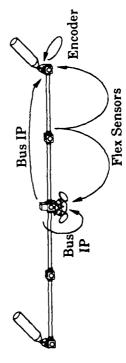
Centralized



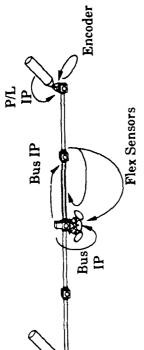


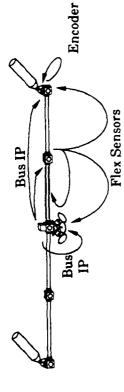
Existing Hardware





Flexibility Sensors





Flexibility Actuators

SCIENCE DEVELOPMENT APPROACH: CONTROL APPROACH

Depending on the amount of motion and deformation, the scanning There are basically two control objectives: pointing and scanning. The pointing problem falls more directly under linear control. problem may have to be handled with nonlinear techniques

properties inherent to the system. Such decoupling properties include closure, Nyquist Array, Inverse Nyquist Array and perturbation techniques rely on these decoupling assumptions. Direct optimization is another way to approach the problem. It relies less on understanding the properties of the system and is easier to derive for more complex algorithms with simplified structure. Most of these rely on decoupling weak subsystem coupling or time scale separation. Successive loop There already exists some techniques to generate linear control systems with stronger coupling. The scanning objective is a classic example of a servomechanism problem. The linear techniques used in the pointing problem may be applicable to this problem. However, the important transformation in the dynamics due to large slews of significant fractions of the spacecraft may render a linear approach inadequate. Therefore, nonlinear control design methods may be required such as gain scheduling, sliding mode control or more generic adaptive control schemes.

SCIENCE DEVELOPMENT APPROACH: CONTROL APPROACH

Pointing

Successive loop closure

Nyquist Array, Inverse Nyquist Array methods

Perturbation techniques (weak coupling, connective stability) Constrained architecture LQG and other direct optimization techniques

Scanning

Linear servomechanism methods (similar to above)

Nonlinear methods if necessary

Gain scheduling (slow scanning, wide range)

Sliding mode control (require numerous, high quality sensors)

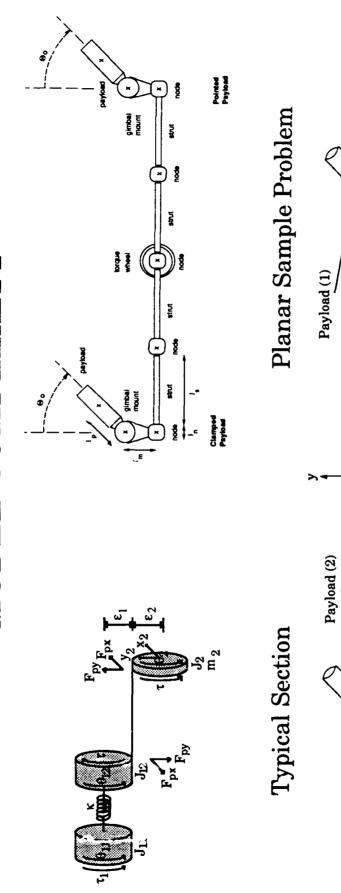
Adaptive control

SCIENCE DEVELOPMENT APPROACH: MODEL COMPLEXITY

payload attached to a flexible bus. This is a lumped-inertia model of the The typical section model is used to study the fundamental problem of pointing and scanning a non-center of mass mounted

model allowing easier interpretation of the effectiveness of a particular by the model's geometry. This greatly simplifies the complexity of the control architecture. This planar sample problem is available as a The planar sample problem is more representative of the actual test article. However, motion is restricted to lie within the plane defined document to enable interested researchers to submit control designs. The nonlinear three-dimensional model is a detailed model of the actual EM which has been verified experimentally. This model is used to formulate the control algorithms that are actually implemented on

SCIENCE DEVELOPMENT APPROACH MODEL COMPLEXITY



Active Segment

Color Co

Nonlinear Three-Dimensional Model

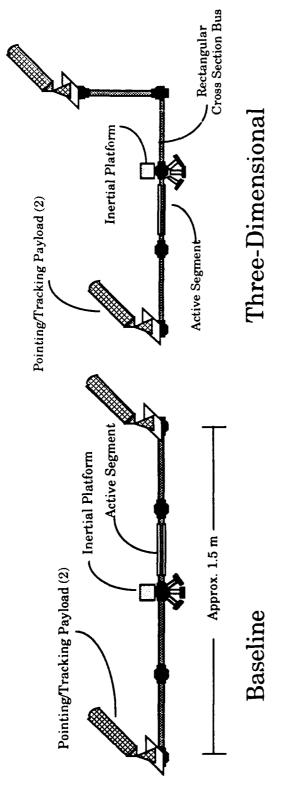
SCIENCE DEVELOPMENT APPROACH: EVOLUTIONARY CONFIGURATIONS

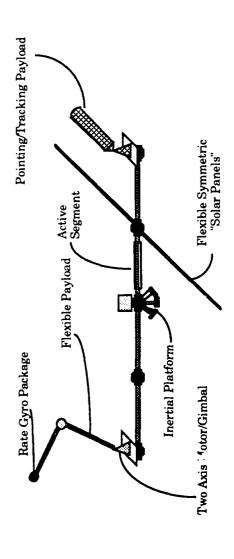
The EM bus is composed of removable struts and nodes. This enables assembly of the EM in various geometries. More complex geometries are harder to test on the ground because they couple more with the suspension and gravity effects.

The baseline configuration is the one that will be studied.

The three-dimensional configuration has an 'L' and a rectangular cross-section strut designed to cause bending/torsion coupling and both in- and out-of-plane bending. The flexible appendage configuration includes a flexible. articulating payload, representative of a robotic servicer, and two flexible appendages, representative of the roll/bending coupling caused by solar panels.

SCIENCE DEVELOPMENT APPROACH: EVOLUTIONARY CONFIGURATIONS





Flexible Appendage

Viewgraph is self-explanatory.

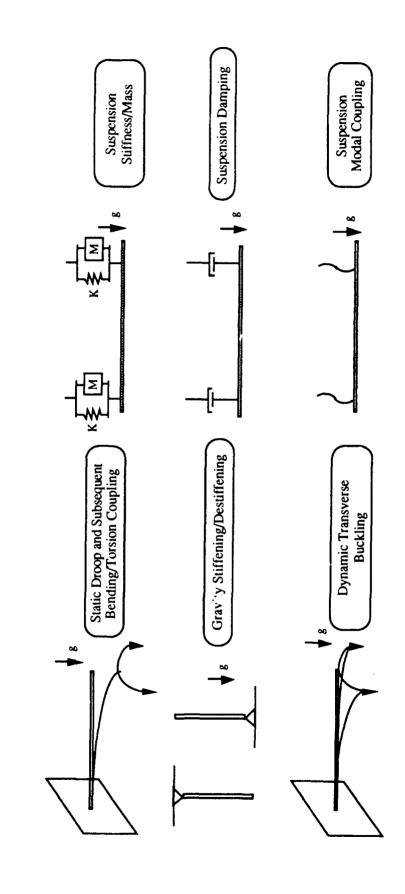
Objective:

effects of a gravity field and a suspension system on the Identify and quantify the magnitude of the perturbation dynamics of the MACE test article.

Approach:

- Identify the distinct types of gravity/suspension perturbations.
- perform a parametric analysis of the effect on the system influence parameter for each important effect and Identify a non-dimensional gravity or suspension dynamics.
- Compare analytical results with finite element results.
- Rank the effect types in order of impact on the structural dynamics based on the non-dimensional system parameters.

the left column and are characterized by the application of distributed as suspension loads on the structure. These are indirect because the suspension system, which is the influencing factor, is essential in the effect or an indirect gravity effect. Direct gravity effects are shown in body forces on the structure. Indirect gravity effects are characterized A gravity effect can be characterized as either a direct gravity testing of structures in the one-gravity environment.



THREE CLASSES OF CONTROL ALGORITHMS WILL BE IMPLEMENTED ON ORBIT

significant will be determined. Second, the ability to predict on-orbit objectives. First, the gravity effects which most influence the problem will be identified and the level of control authority where they become closed-loop behavior will be determined. Third, the ability to tune the The on-orbit tests are designed to achieve the three MACE test article on orbit will be tested.

THREE CLASSES OF CONTROL ALGORITHMS WILL BE IMPLEMENTED ON ORBIT

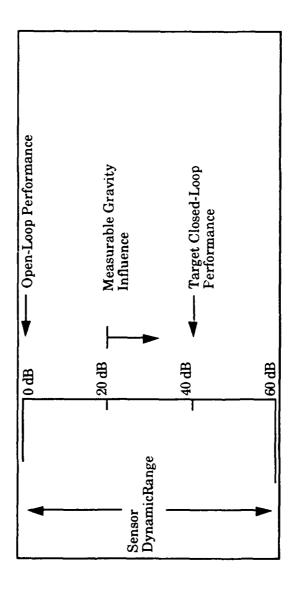
- 1) Implement same algorithms as implemented on the ground
- Algorithms based on model which includes gravity and suspension effects.
- important and when (what gain) they become important. These tests help identify what gravity perturbations are
- Implement algorithms based on model of predicted 0-g behavior.
- The gravity parameter in the 1-g model is set to zero and the control algorithms are rederived.
- These tests determine the accuracy to which 0-g closedloop performance can be predicted.
- Implement algorithms based upon on-orbit identified model.
- First test is an open-loop ID of the structural dynamics.
- Uplink/downlink capability is being developed to enable downlink of open-loop identification and uplink of associated control algorithms.
- These tests identify the ability to which the test article's control algorithm can be tuned on orbit.

VALIDATION OF THE ANALYTICAL FRAMEWORK

Three different control algorithms will be implemented on orbit is one that is based upon on-orbit identification of the test article based upon three different models of the test article. The first model is algorithms based upon this model identify the types of gravity effects which are important and at what level of control authority they become dynamics. Control algorithms based upon this model reveal the ability the model of the test article with gravity and suspension effects. Control important. The second type of model uses the one-gravity model with identify the ability to predict on-orbit behavior. The third type of model gravity terms set to zero. Control algorithms based upon this model to tune the test article on orbit.

VALIDATION OF THE ANALYTICAL FRAMEWORK

- Ground testing will include suspension and gravity effects, typical of preflight qualification testing.
- Realistic goal is to improve pointing/scanning performance by 40 dB over open-loop value.



- Independent of absolute performance level, this demonstrates CST effectiveness.
- Sensor dynamic range of 60 dB is typical.

SUMMARY

Viewgraph is self-explanatory.

SUMMARY

- The MODE family of flight experiments is designed to verify analytical tools developed to predict the gravity dependent behavior of proposed space structures.
- The MODE family of flight experiments uses reusable dynamic and control tests facilities and exploits the unique environment on the STS middeck.
- MACE investigates gravity dependent phenomena pertinent to the closed-loop dynamics of proposed space structures.
- perturbations in the dynamics due to the change from 1 to By comparing performance as a function of control authority between ground and on-orbit testing, 0-g will be identified.
- performance deviations occur, either analytical predictive capabilities or on-orbit identification procedures can be By noting the level of control authority where these

INSTRUMENTATION FOR A LARGE SPACE STRUCTURE SPACE STATION FREEDOM: DYNAMIC

Visiting Professor of Mechanical Engineering Old Dominion University John P. Raney Norfolk, VA

James W. Johnson
NASA Langley Research Center
Hampton, VA

4th NASA/DOD CSI Conference Orlando, Florida November 5-7, 1990

INTRODUCTION

The purpose of this paper is to discuss a proposed approach called Modal Identification Experiment (MIE) for obtaining on-orbit dynamic response measurements on Space Station Freedom, the first of a family of large, flexible space structures.

conceptual design study which provides a conceptual design of a proposed measurement system and an experimental protocol for inobstrusively collecting dynamic response data NASA's Office of Aeronautics, Exploration, and Technology (OAET) has supported a Phase A feasibility study completed in March 1989 and a recently concluded Phase B critical to characterizing important vibration modes of Space Station Freedom. The objectives in collecting on-orbit dynamic data are fourfold. First, there a need to to model large space structures. Utilizing on-orbit data, structural engineers can evaluate and devise improved methods for modelling the complex structures that constitute a response behavior of Space Station Freedom which can be used to validate prelaunch develop and demonstrate the technology to perform on-orbit structural testing of large space structures. Second, modal realization or system identification methodology must on-orbit structural characterization. Third, there is a need to improve upon our capability significant portion of NASA's future missions. Finally, the proposed measurements will provide an invaluable characterization of the on-orbit dynamic environment and be developed, improved, and validated adequate to the stringent requirements imposed by loads calculations.

OBJECTIVES RESEARCH MIE BASIC

- O DEVELOPMENT OF IN-SPACE MODAL TEST TECHNIQUES FOR LARGE SPACE STRUCTURES.
- VALIDATION OF MODAL REALIZATION TECHNIQUES FOR LARGE SPACE STRUCTURES.
- DEVELOPMENT OF VALIDATION/MODIFICATION TECHNIQUES FOR ANALYTICAL DYNAMIC MODELS SPACE STRUCTURES. 0

ENGINEERING OBJECTIVE

STATION CREATION OF AN ENGINEERING DATABASE DEFINING THE DYNAMIC ENVIRONMENT OF THE SPACE STATIC FOR PAYLOAD APPLICATIONS. 0

pac 10/18/90

RESEARCH REQUIREMENT MIE

THE EXPERIMENT REQUIREMENT IS:

TO OBTAIN A SUFFICIENT QUALITY AND QUANTITY OF ON-MEASURABLE ACCELERATIONS TAKEN OVER SUFFICIENT 9 F TIME AND ADEQUATELY DISTRIBUTED SPATIALLY TO INTERMEDIATE AND FINAL BUILD CONFIGURATIONS REALIZE IMPORTANT MODES FOR A SEQUENCE OF ORBIT, TIME-DOMAIN TEST DATA COMPOSED OF SPACE STATION FREEDOM.

WHY SPACE STATION FREEDOM?

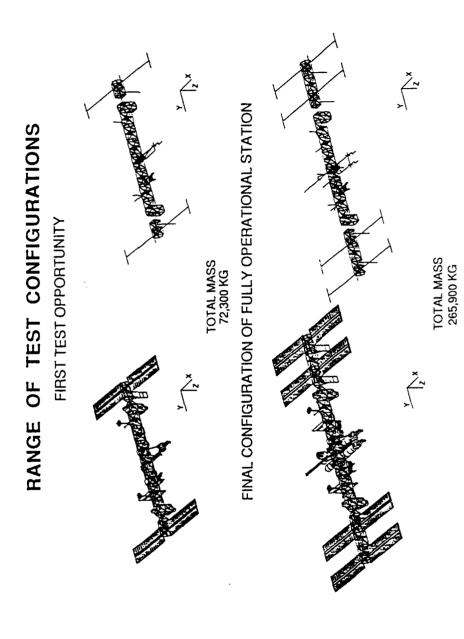
As the world's first large flexible space vehicle, Space Station Freedom presents a unique opportunity to commence the timely development of on-orbit structural characterization technology. In addition, the planned station build sequence presents the opportunity to complete (AC). For example, assessment of the dynamic behavior of the photovoltaic power system structures should be greatly enhanced by data from several configurations acquire dynamic response data from the early unmanned structures up through assembly of which it is an integral part.

SPACE STATION PROVIDES ON-ORBIT TEST **OPPORTUNITY**

- RESONANT FREQUENCIES WITH HIGH MODAL DENSITY CHARACTERISTIC OF LARGE SPACE STRUCTURES (BELOW ONE HZ). 0
- CONTROLLED AND MEASURABLE EXCITATIONS AVAILABLE. 0
- DATA HANDLING OF DISTRIBUTED SIGNALS PROVIDED. 0
- ORDERLY INCREASE IN COMPLEXITY OCCURS WITH BUILD-SEQUENCE CONFIGURATIONS. 0
- REFINED INTEGRATED MATH MODEL AVAILABLE FOR EACH BUILD CONFIGURATION. 0
- COMPONENT TEST RESULTS AVAILABLE TO STUDY COMPONENT MODE SYNTHESIS TECHNIQUES. 0

Range of Test Configurations

Several test configurations will be available between the first opportunity and the fully operational or assembly complete obtained during station assembly become critical to the thorough assessment of station dynamic behavior in the light of station. Data obtained from these intermediate configurations will allow improved insight into the individual effects of incremental additions of structural and systems components on overall station dynamic characteristics. These data the extreme complexity of the assembly complete station as currently baselined.



csi9

Uniqueness of On-Orbit Modal Testing

transients and wide temperature swings from -80° C to +75° C as the orbital environment changes from night to for on-orbit modal testing is hostile to the test engineer in several respects. The test engineer must contend with attitude changes. The thermal environment is uncontrolled and continuously varying causing thermal gradients The identification of the dynamics of spacecraft in the past has been accomplished through ground testing since lested on earth without having the test environment adversely affect the results of the test. The test environment consequences of unbalanced test excitation forces must be considered and countered to prevent uncontrolled systems were typically designed to tolerate ascent loads and were thus usually stiff and strong enough to be due to shadowing of one component of the system by another. The test structure also experiences thermal the absence of gravity and must test in a vacuum. The test article is in a true free-free condition and the day and back again every 90 minutes.

to the truss, high modal densities are expected and will be difficult to separate. Since the station attitude must be nonlinearities. Because of the configuration of the station with multiple components (PV and radiators) attached structure often exhibits nonlinear behavior. Because of the size and low frequency character of the station, long filtered from the modal test data if possible. The station has lineal dimensions on the order of 100 meters in the maintained at all times, an attitude control system will be active and the dynamics of the control system must be structure which means that the station behavior should be similar to joint dominated structure. Joint dominated during the construction phase so that test procedures must be able to adapt to the large range of frequencies, The space station as a test article is highly complex. The station will offer several distinct test configurations response levels and excitation requirements. The major load transfer components of the station are truss later build configurations and the limited number of sensors available will restrict the amount of spatial test times will be required to obtain reasonable test information especially if the response has some information available to reconstruct the modes.

MODAL UNIQUENESS OF ON-ORBIT TESTING

ENVIRONMENT HOSTILE

TO TEST ENGINEER - MINIMAL GRAVITY, VACUUM

TO TEST ARTICLE.

TRUE FREE-FREE CONDITIONS

TEMPERATURE GRADIENTS - SHADOWING, THERMAL TRANSIENTS

WIDE TEMPERATURE RANGE

SPACE STATION STRUCTURE HIGHLY COMPLEX

MULTIPLE TEST CONFIGURATIONS - ADAPTIVE TESTING PROCEDURES

JOINT DOMINATED STRUCTURE - POSSIBLE NONLINEARITIES

LOW FREQUENCIES REQUIRE LONG TEST TIMES

HIGH MODAL DENSITIES

ATTITUDE CONTROLLERS ACTIVE DURING TEST

LARGE DIMENSIONS

Uniqueness of On-Orbit Modal Testing (Cont.) Test Parameters

Normal considerations associated with laboratory and field test parameters sometimes differ considerably for onand connections were made. Since there will be large variations in temperature, compensation will be required nstalled on structural components on earth and then be connected to signal transmission systems on-orbit after rigors of ascent and then be used for several years without recalibration. The sensors, where possible, must be be subject to continual thermal cycling, transducers could fail and replacement of these sensors would be most compensation in the accelerometers. Since the tests will occur over a several year period and the sensors will the components are assumbled. Installation procedures must be validated on-orbit to assure proper direction installed cannot in general be easily moved. The sensors must be calibrated before installation, undergo the either by measurements of nearby transducers which doubles the number of sensors required or by internal orbit testing. For instrumentation, the number of sensors which can be used is severely reduced and once difficult or impossible so that redundant sensor placements in important locations would be prudent.

be unknown until the tests are performed signal conditioning and management systems must have variable gain Since excitation and response levels will vary from configuration to configuration and system damping levels will amplifiers. The amount of information stored on-orbit will be limited by the storage capacity of the on board equipment and by the amount of information which must be managed during normal operations.

consistent with safety, to excite modes of interest. Modes with node points near excitation locations will be The location and force levels of the excitation will be fixed and only the force-time history can be varied difficult to recover.

equipment are added to the station. The test engineer will not be able to increase the excitation level to improve Noise levels will be uncontrollable and will vary from one configuration to another as operational payloads and the signal resolution.

measurements of the applied excitation level available to compute frequency response functions. The station will have attitude and pointing control systems active and the station configuration might be continuously changing Test procedures will differ in that test times will be severely limited and there will most likely not be direct during acquisition of test information so that the station dynamics will be non-stationary.

UNIQUENESS TESTING (CONT) OF ON-ORBIT MODAL

TEST PARAMETERS

INSTRUMENTATION

NUMBER AND LOCATION LIMITED AND FIXED INSTALLATION AND CALIBRATION DIFFICULT COMPENSATION REQUIRED FOR TEMPERATUR NO REPLACEMENT OF FAILED TRANSDUCERS **TEMPERATURE** VARIATION

SIGNAL CONDITIONING AND MANAGEMENT

ADJUSTABLE NUMBER OF GAIN AMPLIFIERS REQUIRED TO CHANNELS AND DATA STORAGE LIMITED IMPROVE RESOLUTION

EXCITATION

TYPE, LOCATION AND AMPLITUDE FIXED

NOISE

WILL WILL CHANGE FOR EACH TEST CONFIGURATION CAN'T INCREASE FORCE LEVEL TO INCREASE S/N RATIO LEVEL UNCONTROLLABLE

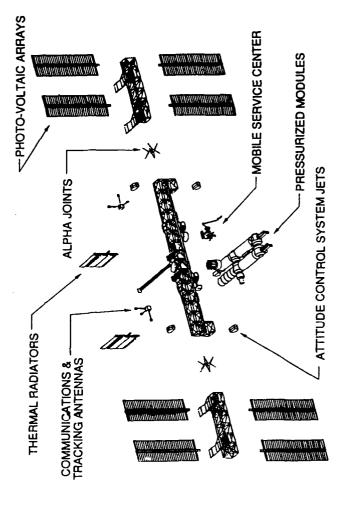
PROCEDURAL DIFFICULTIES

NON-STATIONARY TEST TEST MUST BE NON-INT TEST TIME ABILITY TO SEVERELY MEASURE NON-INTRUSIVE LIMITED EXCITATION ARTICLE TO STATION OPERATIONS FORCES IN DOUBT

Space Station Freedom Assembly Complete Configuration

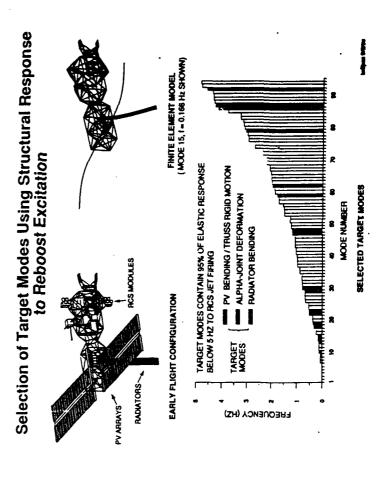
wall graphite-epoxy composite tubes with protective aluminum coating. The major component of the station is the pressurized module cluster which contains five modules of which one is a habitation module, three are laboratory modules and the fifth is a smaller supply module replaced after each Shuttle rendezvous. The station is powered excess heat generated by the solar energy systems and the second type is located at two places on the inboard momentum management and attitude controi system which uses control moment gyros, gravity gradient torques make up the station are installed on a truss structure with longerons, battens, and diagonals composed of thinby eight photo-voltaic arrays which track the sun. The tracking is supplied by alpha joints which use motors to and torques caused by drag forces to maintain the attitude. Four reaction control modules are installed on the higher altitudes. There are two types of thermal radiators installed, one near the arrays which is used to reject The assembly complete configuration is the final construction configuration for which a modal test is planned The various components which main inboard truss to provide both forces and torques for major maneuvers such as reboost of the station to rotate the outboard sections of the truss and the arrays with respect to the inboard section of the truss. The inboard truss and module cluster is held at a constant attitude with respect to the earth radius vector by a under the MIÉ research program. This configuration has 267,400 kg mass. truss and used to reject excess heat generated in the pressurized modules.

SPACE STATION FREEDOM ASSEMBLY COMPLETE CONFIGURATION



Selection of Target Modes Using Structural Response to Reboost Excitation

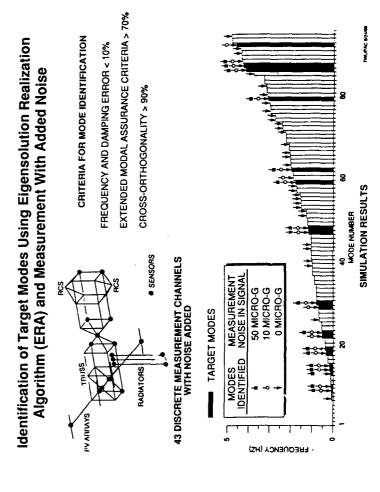
A complete end-to-end on-orbit modal test simulation of an early flight configuration was performed to assess the jets located at the Reaction Control System (RCS) module firing in a manner consistent with a reboost maneuver and results were used to define a set of target modes for modal testing. Of the 88 undamped modes below 5 Hz, undampéd elastic modes below 5 Hz were identified. The dynamic response was computed of the spacecraft to feasibility of the MIE experiment. A finite element model of an early flight configuration was developed and the the 19 modes which accounted for 95% of the global acceleration response of the structure were selected as target modes. The lower frequency target modes were complex modes coupling truss rigid body motion with motion of the photovoltaic (PV) arrays and modes with deformation in the alpha joint region. The higher frequency target modes were, in general, radiator bending modes.



Identification of Target Modes Using Eigensolution Realization Algorithm and Measurement With Added Noise

A set of 43 accelerometer response measurements were taken at the sensor locations shown. The Eigensolution as an excitation device and accelerometers as sensors should be successful in identifying the target modes with noise in the measurement. Without noise, 52 modes including all 19 target modes were identified. When white noise levels of 10 microG (0.56 % S/N) and 50 microG (2.8% S/N) were added to the measurements, 20 and 17 Realization Algorithm (ERA), was used to identify the modes from computed response measurements corrupted assurance criteria was greater than 70%, and that the cross-orthogonality between the measured mode and the actual mode was greater than 90%. The simulation results indicated that on-orbit modal testing using RCS jets modes were recovered respectively. Only one target mode could not be recovered with 10 nicroG noise and particular mode is that the measured frequency and damping errors were less than 10%, that the modal with various levels of white noise. The criteria for accepting that the procedure has accurately identified three target modes could not be identified with 50 microG noise in the measurement signal

This in-house study helped to establish the confidence required to proceed with the MIE phase B conceptual design study, the results of which are summarized below.



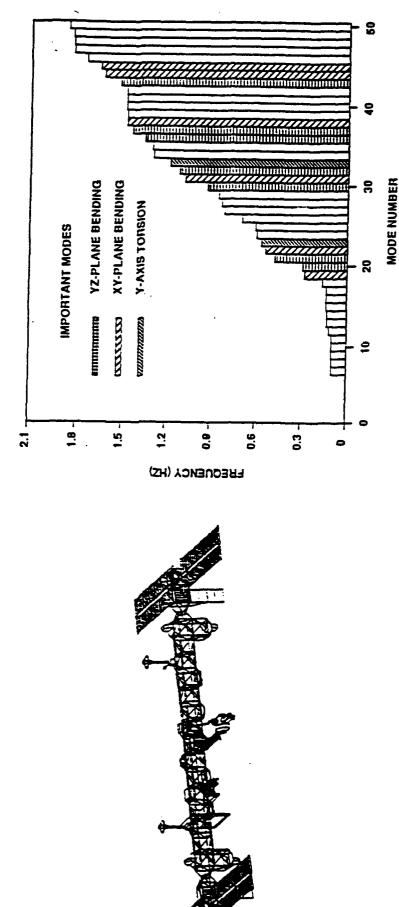
Selected Configurations and their Important Modes

System (TDRSS) antennas, and mass distribution consistent with the assembly sequence. The FEMs have the PV arrays in the vertical or YZ-plane. The modes of the three configurations with frequencies in the zero to five Hertz range were determined. For this frequency range, the MB6 model has 87 modes, the PMC model has 100 modes, and the AC Although it is the intention of MIE to conduct modal identification on as many assembly configurations as possible, three Sequence Baseline Manifest, dated 15 November 1989, and developed by the Space Station Engineering Integration Contractor (SSEIC). The models include the most recent changes, such as the Warren truss, the lower propulsion configurations were selected as the study configurations because of the availability of FEMs and SSF resources, such as power, EVA time, propellant, and DMS capability. The FEMs were based on the Level II Reference Assembly modules located one bay below the truss, the hydrazine propulsion system, two Tracking and Data Relay Satellite configurations were selected for use during the Phase B Concept Definition Study. The MB6, PlAC, and AC model has 169 modes.

the first test configuration. The PMČ model is the MB10 assembly configuration structure with mass added to represent the outfitting flights. The PMC model has almost twice the mass, 364737 pounds, as the MB6 model, 159407 pounds, Earlier configurations do not appear to have the resources available to support the experiment. If the assembly sequence changes and an earlier flight has the resources to support MIE, then that configuration shall be selected as The earliest configuration that is likely to be considered as a test configuration is the MB6 assembly configuration. and half the mass of the AC model, 586106 pounds. The selection of important modes was limited to the first fifteen to twenty global structural modes with frequencies below five Hertz. These modes include the first and second truss bending modes in the XY- and YZ-planes and the first truss structure, and mode shape plots were used to select the important modes. For the MB6 model, the frequency range of the fifteen important modes is 0.286 to 1.654 Hertz. The frequency range of the fifteen important modes for the PMC model is 0.228 to 1.448 Hertz. Twenty important modes were selected for the other configurations. The frequency torsional mode. Kinetic energy, the ration of the maximum truss deflection to the maximum deflection of the entire range of the important modes for the AC model is 0.115 to 1.164 Hertz.

MIE CONFIGURATIONS AND THEIR IMPORTANT MODES MB6 CONFIGURATION SELECTED

FREQUENCY DISTRIBUTION

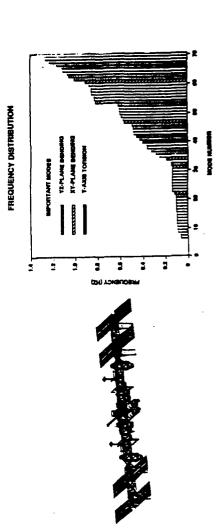


Assembly Complete Frequency Density

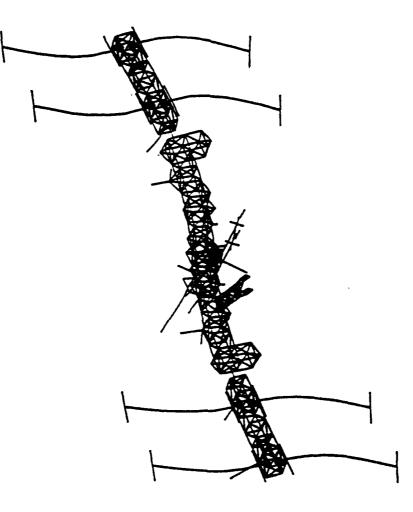
range of interest in the experiment so that the modules are represented as beam elements with appropriate mass distributions occur in the range of interest of the experiment but will most likely be equilibrated locally and should not contribute to the overall dynamic response of the station to major loads. The array mast and the radiators are modelled using an equivalent beam representation where the beam is sized to give the same first four beam bending and torsion modes and aimilar mass configuration has over 3800 degrees of freedom but contains no detailed representation of the photovoltaic blankets or the distributions as the actual components. The pressurized modules have fundamental frequencies well above the trequency array mast structure. Low frequency modes associated with blanket motion are not modelled. These blanket modes do The finite-element model used to represent the low frequency dynamic characteristics of the assembly complete station and truss attachment points to simulate the rigid body dynamic character of the module cluster.

The model has 169 modes under five Hz. The lowest mode with considerable modal strain energy in the truss structure occurred at 0.115 Hz and is characterized by truss bending, coupled with PV array motion.

SELECTED MIE CONFIGURATIONS AND THEIR IMPORTANT MODES
ASSEMBLY COMPLETE CONFIGURATION



SELECTED MIE CONFIGURATIONS AND THEIR IMPORTANT MODES TYPICAL ASSEMBLY COMPLETE CONFIGURATION MODE SHAPE



csi6

MIE Definition Studies

Disturbance events from orbiter docking, module berthing, reboost, CMG's, and crew activities were evaluated. A wide variety of measurement devices, including optical sensors to measure displacement, fiber optic sensors, laser doppler various methods for exciting the Space Station structure, measuring its response, and recovering the vibration modes. A Phase A study was conducted in 1988 to begin experiment definition for MIE. The study objective was to evaluate velocimeters, and geometric position sensors were considered.

servo accelerometers to measure the responses, and free decay time domain modal identification in order to minimize It was determined that the experiment was feasible using RCS thruster firings during reboost as the excitation. Linear the excitation time required

the MB-6, PMC, and Assembly Complete configurations, end-to-end simulations were conducted to estimate experiment A Phase B study, which provided a baseline experiment design, was completed in August 1990. This design includes baseline design is derived from trade studies and sensitivity analyses conducted by numerically simulating modal test using finite element models of selected Space Station assembly configurations. After choosing a baseline design for points on the station at assembly complete, and a minimum 100 second free decay period for modal recovery. The experiment-unique forcing functions for thruster firings, 189 single axis acceleration measurements located at 107 performance for each case.

MIE Definition Studies

Phase A Study Established Feasibility, December 1988

Excitation

Reboost Transients

Acceleration

Response Measurements

Modal Identification

Free Decay

Phase B Study Povided Baseline Design Concept, August 1990

Excitation

Random RCS Thruster Firing

- Response Measurements

189 Accelerations

- Modal Identification

Free Decay

LaRC SSFO __

MIE Baseline Experiment Design

Simulation of a Typical On-Orbit Test

the selected measurement points, and recovery of the system modes from the response set using standard time domain Numerical simulations of on-orbit modal tests were used during Phase B in trade studies, sensitivity analyses and endexcitation, selection of a set of measurement points on the system, computation of the forced response of the system at requirements. These target modes were then used in the design process and in assessing performance. The end-towere first identified using MSC/NASTRAN normal mode analysis and selection criteria derived from the MIE research to-end performance analyses. For design studies on any given Space Station assembly configuration, target modes end simulation of a modal test included selection of a set of forcing functions for the various RCS thrusters used for free decay identification techniques.

pulse excitation functions that were baselined for the experiment. Both random pulsing and reboost were evaluated as The station design includes RCS thrusters located on both the port and starboard sides of the module cluster and both above and below the transverse boom. There are four individual thrusters in each of the X and Z directions at each direction. There are also reboost thrusters at each location. The attitude control thrusters are used for the random location for attitude control. For example, there are two 25 pound thrusters for the +X direction and two for the -X excitations during Phase B.

Simulations were run with measurements located on the truss, PV arrays, thermal radiators, and in the module cluster. Measurement sets ranging from greater than 200 single axis accelerations to sets with less than 50 were considered. Additive noise and measurement system errors were included in the simulated measurement time histories. Both the Eigensystem Realization Algorithm, ERA, and Time Domain Polyreference were used to recovery modes from the response time histories. In applying these algorithms, emphasis was placed on recovering Target Modes.

csi5

csi3

MIE Baseline Experiment Design

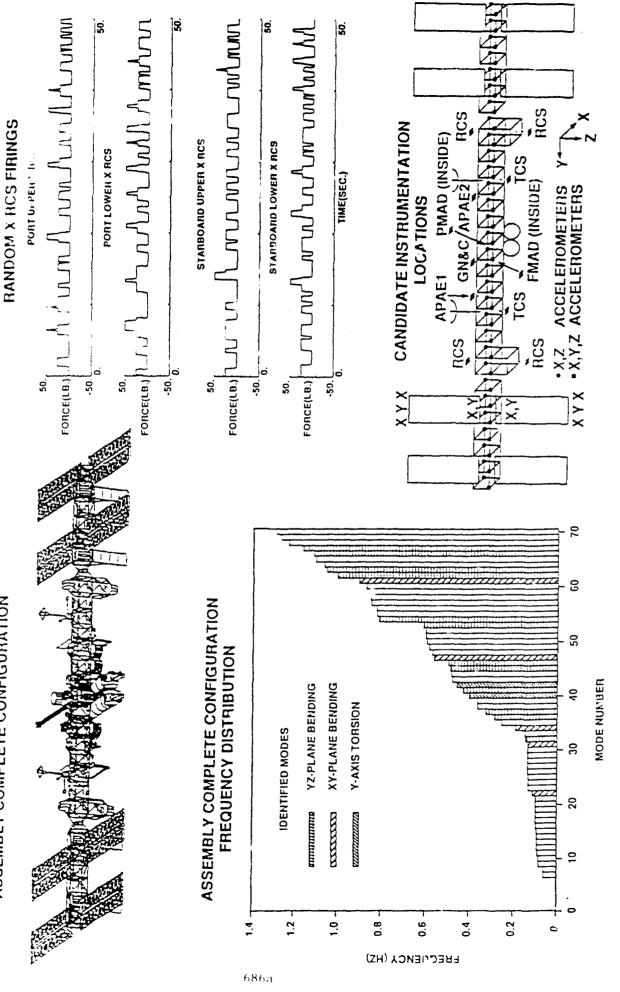
Forcing Functions

increased by pulsing the thrusters. Even though there is coupling between many modes with motions in the XY and YZ planes, some modes cannot be adequately excited without using Z thrusters. The forcing functions are designed to excite each important mode but not exceed any of the SSF safety limits. Multiple linearly independent forcing functions identified as the best operational excitation for conducting MIE. However, response levels of the important modes are are necessary for identifying closely spaced modes and assessing nonlinearities. The forcing functions are also Several potential excitation sources for MIE were evaluated during the Phase B Definition Study. Reboost was designed to permit modal identification by other methods.

attitude rates are minimize by balancing the moments from the thruster finings. The +Z and -Z thrusters on the same side cycles of the lowest frequency important mode with a minimum of twenty seconds, so that there is sufficient excitation for the lowest frequency imortant modes to reach measureable resonse levels. The thruster on/off times are rounded to the of SSF are not allowed to fire at the same time. Each free decay period is at least fifteen cycles of the lowest frequency acceleration or load limits but excite important modes to measurable levels. The length of an excitation is at least five nearest minimum thruster pulse time, which is currently 0.2 seconds. The effects of the thruster firing on attitude and The pulsed thruster firings can be designed to maintain attitude and attitude rates within their limits and not exceed important mode with a minimum of 100 seconds.

MIE BASELINE EXPERIMENT DESIGN SIMULATION OF A TYPICAL ON-ORBIT TEST

ASSEMBLY COMPLETE CONFIGURATION



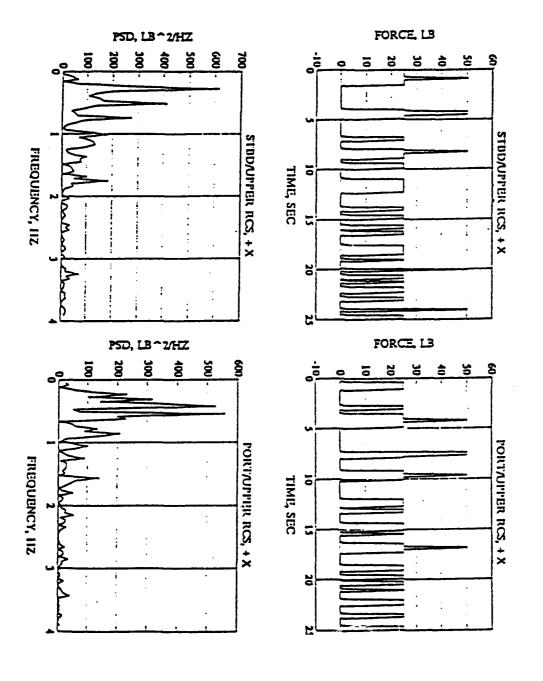
csi2

MIE Baseline Experiment Design

Measurement Locations

The frequency and damping factor of the important modes may be determined with only one accelerometer. Describing the mode shape requires more accelerometers. Modal assurance criterion and spatial distribution were used to select a torsion modes, separating closely spaces modes, and integrating math models. Separation of closely spaced modes is shapes. The maximum truss motion generally occurs at the truss tip, so instrumentation will be located there whenever aid in determining local dynamics and math model verification. The module cluster is instrumented to provide data for also the reason for the instrumentation on the TCS radiators. Data from the instrumentation on the various pallets will instrumented as they are anticipated to be a source of nonlinear structural behavior because of the utility tray to truss possible. Accelerometers are located at the PV array tips and bases to provide data for identifying PV bending and verifying the math models of the module attachments and the dynamic motion of the modules. The utility trays are changes in configurations. Spatial coverage is also necessary for determining the global characteristics of mode measurement set. The accuracy required in describing mode shapes determines the number of accelerometers. During the Phase B study, good spatial coverage of the SSF was found to be desirable to minimize the effects of attachment. Instrumentation on the utility trays will also provide data for describing the global mode shapes.

MIE BASELINE EXPERIMENT DESIGN RANDOM EXCITATION DESIGN TYPICAL FORCING FUNCTIONS AND PSDs



MIE Baseline Experiment Design

Simulation Results

functions were designed to excite each configuration's important modes to more measurable levels. The measurement for ten seconds with fifty pounds of force followed by 100 seconds of free decay. Also, four linearly independent forcing identification capability on data with noise and errors. A short reboost was simulated by two diagonal X thrusters firing simulations were made with the structural responses corrupted with data acquisition system errors to determine modal locations used in the simulations were the 189 accelerometers distributed throughout the SSF truss, pallets, modules, acquisition system errors were included in the responses at each measurement location. ERA was used to determine The on-orbit MIE was numerically simulated to assess the performance of the baseline experiment design. The PV arrays, and TCS radiators. The thirty utility tray measurement locations are not included in the FEMs. Data the effects of the corrupted response and damping on modal identification capability.

Although all of the important modes were identified for the PMC 2% damping factor cases, additional filtering within ERA All of the important modes were identified from the random forcing function responses, regardless of damping. Except responses. Large damping factors significantly reduce the number of modes identified from the reboost responses. for the PMC 1% damping factor case, only about one third of the important modes were identified from the reboost was required.

MIE BASELINE EXPERIMENT DESIGN SIMULATION RESULTS

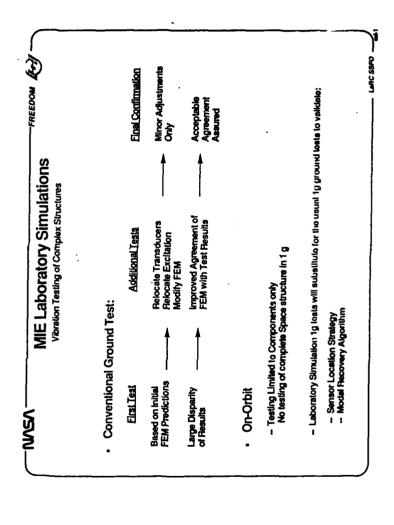
| CONFIG | FORCING FUNCTION | DAMP, | NO OF IDENTIFIED IMP MODES | NO OF TOTAL ID MODES |
|--------|---------------------|-------|----------------------------------|----------------------------|
| MB6 | HANDOM | 1.0 | 15 | 18 |
| | REBOOST | 1.0 | S | 9 |
| | RANDOM | 1.0 | 15 | 16 |
| PMC | | 2.0 | 15 | 91 |
| | REBOOST | 1.0 | 12 | 13 |
| | | 2.0 | þ | 4 |
| AC | RANDOM | 1.0 | 20 | Z |
| | REBOOST | 1.0 | 4 | • |

PA1 PA2 PA3 PA4 PA5 PA6 **MIE BASELINE EXPERIMENT DESIGN** PROP MOD PROP MOD **PORT** PBLL7 SB7 SB6 SB5 SB4 SB3 SB2 SB1 PB1 PB2 PB4 PB5 PB6 PB7 ⋖ **MEASUREMENT LOCATIONS** TCS PAL & RAD • APAE2 C&T Antenna & Boom - PORT -IUD (INSIDE) **ESA** GN&C -STBD IFS (INSIDE) C&T Antenna & Boom TCS PAL & RAD APAE1 PROP MOD PROP MOD STBD-4 SBLL8 . 888 ıL < SA3 SA2 SA1 ■ X,Y,Z ACCELEROMETERS ■ X,Y,Z ACCELLEROMETERS ■ X ACCELLEROMETERS ACCELEROMETERS SA6 SA4 L ower face U pper face Front face A ft face ⋖ \supset ıL

MIE Laboratory Simulations

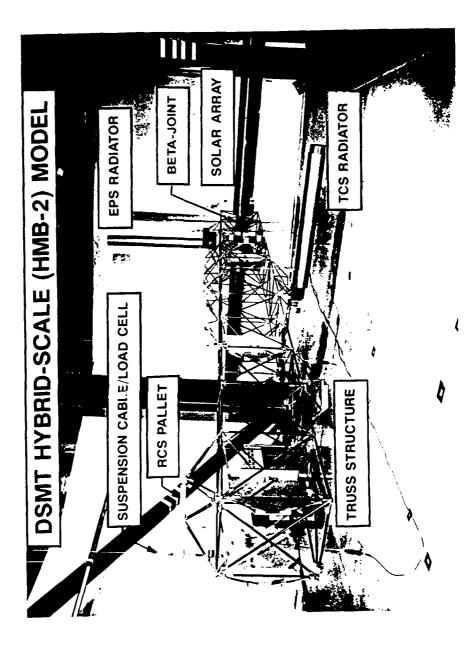
As previously observed, on-orbit testing of a structure which cannot be tested fully assembled in a 1 g environment presents a unique set of challenges. For example, the opportunity to conduct a series of tests (possibly relocating sensors and excitation sources until satisfactory results are obtained) is not available to the on-orbit test engineer. Use of a dynamically scaled model such as the Langley DSMT can partially compensate for some of the uncertainties encountered.

The DSMT will be utilzed in the evaluation of sensor placement strategy, forcing function design, and evaluation of robustness of proposed modal recovery algorithms.



Utilizing the DSMT Hybrid Scale Model

Dynamic Scale Model Technology program will be used to conduct the MIE Laboratory Simulations. These simulations will, however, be unique since the objective is to simulate the MIE on-orbit modal test rather than conduct a traditional ground vibration test. For example, the excitation, data records, and modal recovery methods applied will duplicate those planned for MIE. The Langley hybrid scale model of the Space Station and its suspension system and data acquisition in use in the



MIE Engineering Model

used include an early configuration, an intermediate configuration, and the Assembly Complete configuration. The truss configurations for testing. Excitation forces scale as 1/25 and modal frequencies scale as 1/10. The three models to be The DSMT hybrid scale model hardware consists of a set of erectable joints, struts and standardized components so length will vary by more than a factor of 2 and the weight by a factor of 10 between the early configuration and the that many different configurations of the Space Station may be assembled. The plan is to use three assembly Assembly Complete.

MIE ENGINEERING MODEL

- ERECTABLE JOINTS AND STANDARDIZED COMPONENTS PERMIT TESTBED TO BE ASSEMBLED IN ANY CONFIGURATION
- MASS PROPERTIES OF MANY COMPONENTS CAN BE ADJUSTED VIA MODIFICATION OF LUMPED WEIGHTS







| 1/5:1/10 Scale | HMB-2 | 2 0 M | HMB-2 HMB-5 HMB-15 |
|-----------------|---------|---------|--------------------|
| Dimensions (ft) | 19 x 23 | 35 x 23 | 48 x 23 |
| Weight (lbs) | 363 | 1306 | 3621 |
| Freq Range (Hz) | 9 - 37 | 2 . 8 | 1.7 |

Concluding Remarks

The MIE is a well defined experiment which, if implemented, will return invaluable scientific and engineering dynamic response data leading to validation of on-orbit modal recovery procedures in addition to dynamic characterization of Space Station Freedom and its dynamic environment. It is supported by the structural dynamics community and its importance is generally recognized within the Space Station Freedom Project activity.

Concluding Remarks

- Structure The OAET-sponsored Modal Identification Experiment could Provide Critical On-Orbit Dynamic Data for the World's First Large Space
- and is Supported by the Structural Dynamics Community The Experiment is Feasible, Relatively low cost and Schedule Risk,

References

- Cooper, Paul A. and Johnson, James W.: Space Station Freedom On-Orbit Modal Identification Experiment An Update, 2nd USAF/NASA Workshop on Systems Identification and Health Monitoring of Precision Space Structures, Pasadena, CA, March 29, 1990.
- Kaszubowski, Martin J.; Martinovic, Zoran N.; and Cooper, Paul N.: Structural Dynamic Characteristics of a Space Station Freedom First Assembly Flight Concept, AIAA Paper No 90-06748, AIAA 28th Aerospace Sciences Meeting, Reno, NV, January 8-11, 1990. તાં
- Lim, Tae W. and Cooper, Paul A.: Control/Structure Interaction Study of a Space Station Freedom First Flight Concept During Reboost, AIAA Paper No. 90-0747, AIAA 28th Aerospace Sciences Meeting, Reno, NV, January က
- McDonnell Douglas, GE, Honeywell, IBM, Lockheed: Space Station Freedom Modal Identification Experiment, Contract NAS9-18200, Task Order C90KC048, Final Review of Phase B Concept Definition Study, August 14, 1990. 4
- Pappa, Richard S.: Identification Challenges of Large Space Structures, Sounds and Vibration, IES Show Issue, Ś
- Blelloch, Paul; Engelhardt, Charlie; Hunt, David L. Simulation of On-Orbit Modal Tests of Large Space Structures, 8th International Modal Analysis Conference, Kissimmee, FL, January 29-Feburary 1, 1990. 6
- McGowan, Paul E.; Edighoffer, Harold.; Wallace, John W.: Development of an Experimental Space Station Model for Structural Dynamics Research: 60th Shock and Vibration Symposium, Virginia Beach, VA, November 7.
- Gronet, Marc and Davis, Darby: A Plan for Utilization of an Engineering Model for MIE, Supporting Studies, MIE Phase B Final Review, August 15, 1989. ထ
- Schenk, Axel: Simulation of On-Orbit Modal Identification, 41st Congress of the International Astronautical Federation, Dresden, Germany, October 6-12, 1990. ത്
- Doiron, Harold H.: Structural Technology Challenges for Evolutionary Growth For Space Station Freedom. 9



12-METER TRUSS ZERO-G FLIGHT TEST

W. Yuen, A. Swanson, and R. Mackaman

Flight Dynamics Laboratory
Wright Research and Development Center
Wright-Patterson AFB, OH

INTRODUCTION

The 12-meter truss zero-g flight test experiment was conducted by the Structural Dynamics Branch of the Air Force Flight Dynamics Laboratory under an in-house Large Space Structure Technology Program. The goals of this program are to investigate flexible structure dynamics, ground test methods, and passive and active damping. The Structural Dynamics Branch (FIBG) conducted both the ground and flight tests of the 12-meter truss. Three FIBG engineers performed the flight tests on 1 and 2 February 1990 aboard NASA's KC-135 aircraft which flew parabolic maneuvers to achieve the micro-gravity environment.

BACKGROUND

Space system missions using large radar and optical devices are leading towards larger spacecraft with more stringent requirements for line-of-sight and figure control, and settling times. The high cost of transporting material into orbit causes large space structures to be lightweight, flexible, and lightly damped. The structural vibration control problem thus becomes a critical challenge. For active control of these structures, system modeling and modal parameter identification are very important, and error reduction is critical. The earth's gravity environment poses an additional problem to the control system designer by thwarting his attempts at pre-flight system validation tests. All methods of supporting or suspending a space structure for ground test alter its dynamic behavior to some degree.

The Flight Dynamics Laboratory's in-house Large Space Structures Technology Program is currently investigating methods for ground test and analysis of large space structures to predict on-orbit dynamic behavior. The Air Force fabricated two 12-meter truss structures for analysis, modal characterization, and controls studies. Uncertainty remains of how much a suspension system contributes to a flexible structure's dynamics. To resolve this uncertainty, a reduced gravity flight test program was initiated with NASA Johnson Space Center to use their reduce gravity aircraft for testing a 12-meter truss in zero gravity.



12-METER TRUSS ZERO-G FLIGHT TEST

BACKGROUND

- LARGE SPACE STRUCTURE (LSS) REQUIREMENTS
 - POINTING CONTROL
 - STRUCTURAL STABILITY & SHAPE CONTROL
 - SETTLING TIMES
- LSS TECHNICAL CHAILENGES
 - LOW FREQUENCY & MINIMAL DAMPING
 - ACCURALE SYSTEM MODELING
 - STRUCTURAL PARAMETER IDENTIFICATION IN ONE-G **ENVIRONMENT**
- MEETING & ADDRESSING THESE CHALLENGES
 - STUDY LSS DYNAMICS USING 12-METER TRUSS
 - GROUND TEST AND SUSPENSION SYSTEM METHODS
 - ACTIVE AND PASSIVE CONTROL METHODS

OBJECTIVES

The primary aim of the test is to determine the effects the LSSTP ground suspension system has on this structure. A secondary objective is to evaluate NASA's aircraft for the testing of other large space structures.



12-METER TRUSS ZERO-G FLIGHT TEST

OBJECTIVES

- DETERMINE EFFECTS OF LSSTP GROUND SUSPENSION SYSTEM ON TEST STRUCTURE.
- EVALUATE MICRO-GRAVITY AIRCRAFT FOR TESTING LARGE SPACE STRUCTURES

APPROACH

To determine the effects of the suspension system on truss dynamics, two modal tests were performed; ground and flight test. An impulse force was used to excite the truss modes. Measured truss responses were then compared. Identical hardware, data acquisition, and analyses were used in both tests.

The short float times experienced on a preliminary flight with a 2-meter truss were initially of great concern as FIBG was preparing for the 12-meter truss flight test. The frequency-domain data analysis techniques in use give better frequency resolution for longer record lengths. The Eigensystem Realization Algorithm (ERA) time domain technique, on the other hand, produces frequency resolution independent of data record length. The record length requirement was just two complete cycles at the lowest structural frequency. Since the first mode of the truss is near 10 Hz, 0.2 seconds of free-float duration would be required and should be easily achieved. Using ERA eliminates the possible need to use suspension systems or other techniques to increase float duration on the flights.

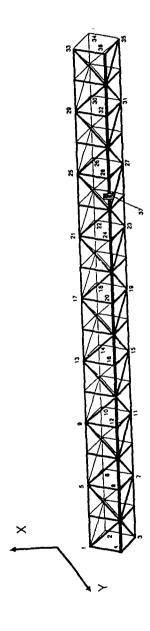


12-METER TRUSS ZERO-G FLIGHT TEST

APPROACH

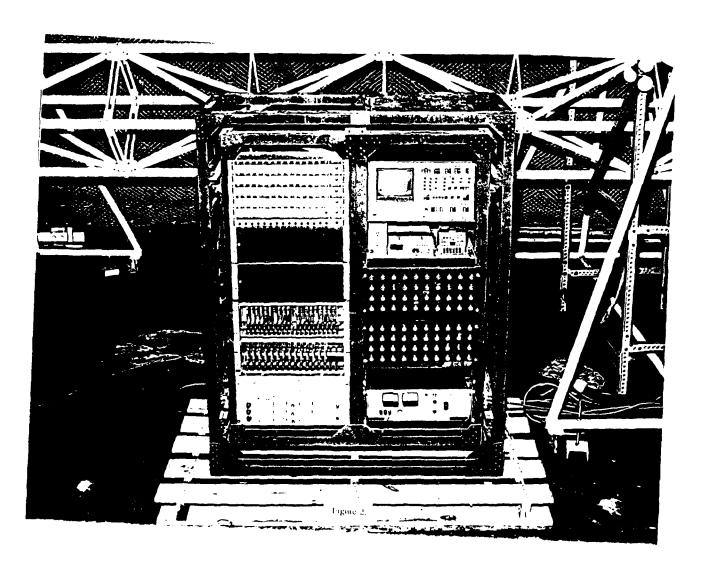
- PERFORM GROUND AND FLIGHT TESTS
 - SAME PROCEDURES AND HARDWARE
 - SAME ANALYSIS PROGRAM
- USE LOW RESTRAINT SUSPENSION SYSTEM FOR GROUND TEST
- USE KC-135 AIRCRAFT FOR FLIGHT TEST
 - PARABOLIC FLIGHT TO ACHIEVE REDUCED GRAVITY
 - EXCITE AND MEASURE TRUSS RESPONSE DURING ZERO-G PORTION OF FLIGHT

The 12-meter truss resonant frequencies and mode shapes were measured using 72 piezoresistive accelerometers distributed over the entire truss, with one attached to the impulse site to measure force input. Two accelerometers configured to measure x and y direction motion were hot-glued to aluminum blocks that were glued to the truss at each measurement location. Figure 1 shows the accelerometer locations. Nine capacitive type accelerometers were used to measure low frequency (below 1 Hz) accelerations and aircraft interior noise. Three were mounted on the truss CG, and 6 were attached to the aircraft floor.



rgure 1.

Figure 2 shows the instrumentation rack used on both the ground and flight tests. The accelerometer signals were filtered (100 Hz lowpass), multiplexed, and recorded on a Honeywell 101 FM tape recorder at a tape speed of thirty inches per second. A patch panel was configured to allow signal monitoring before final recording.



The force input mechanism used to excite the truss was a solenoid powered impact device shown in Figure 3. With a 2 lb weight attached to the solenoid shaft, the device generated a 20 lb force. This device was bolted onto the truss at a location where both bending and torsion modes would be optimally excited. A manually operated switch with a 40 volt power supply activated the solenoid.

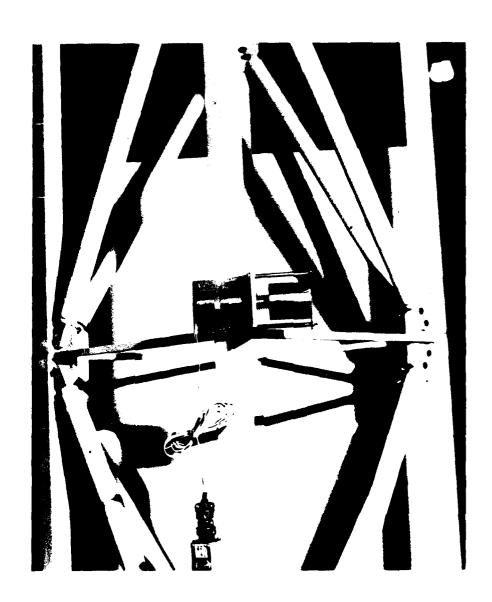
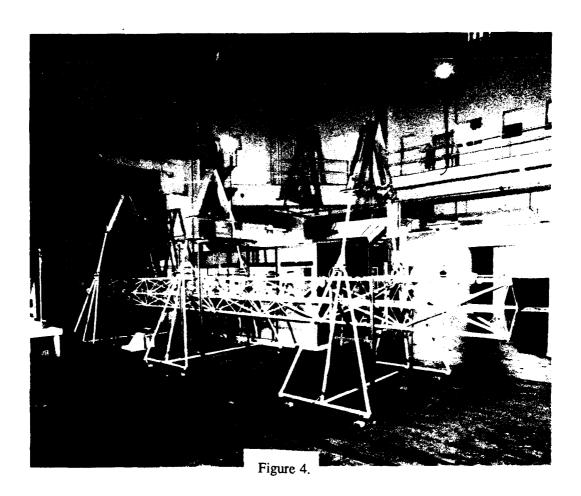
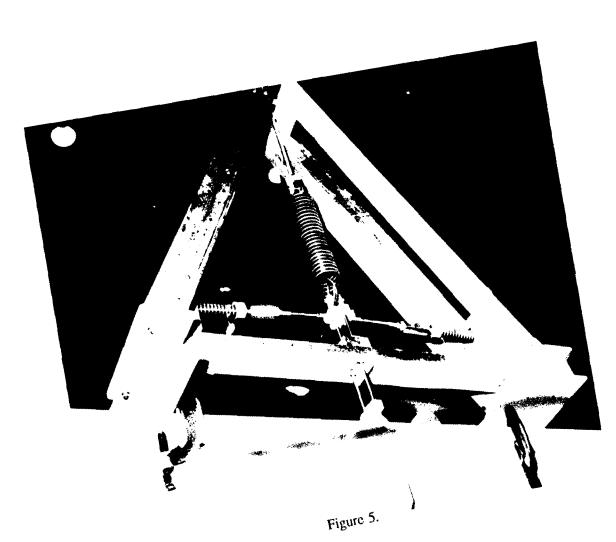


Figure 3.

The ground vibration test was performed before the flight test to check out the flight test equipment and to record truss response in a ground test using soft suspension to simulate the free-free boundary condition. The truss modes were excited and measured using impulse response the technique and analyzed with ERA. Three zero-spring rate mechanisms (ZSRM) were used to suspend the 12-meter truss as shown in Figure 4.



The zero-spring rate mechanism was designed to provide low restraint spring forces without the large displacements associated with normal springs that have low stiffness. Figure 5 shows that each ZSRM consists the displacements associated with normal springs that have low stiffness. Figure 5 shows that each ZSRM consists displacements associated with normal springs that have low stiffness. Figure 5 shows that each ZSRM consists which reduce the vertical springs which reduce the vertical spring which supports the test article weight and two side horizontal spring when displaced of one vertical spring which supports the test article weight and two side horizontal spring when displaced springs are in compression acts against the vertical spring when displaced springs are in compression acts against the vertical spring when displaced springs are in compression acts against the vertical spring when displaced springs are in compression acts against the vertical spring when displaced springs are in compression acts against the vertical spring when displaced springs are in compression acts against the vertical spring when displaced springs are in compression acts against the vertical spring when displaced springs are in compression acts against the vertical spring when displaced springs are in compression acts against the vertical spring when displaced springs are in compression acts against the vertical spring when displaced springs are in compression acts against the vertical spring when displaced springs are in compression acts against the vertical spring when displaced springs are in compression acts against the vertical spring when displaced springs are in compression acts against the vertical springs



As with the ground test, the same test hardware and instrumentation were used on the flight test. However, the free-free boundary condition or zero-gravity environment was simulated in NASA's KC-135 reduced gravity aircraft while it performed parabolic flight profiles.

The Reduced Gravity Office (RGO) of the Lyndon B. Johnson Space Center operates a modified KC-135A turbojet transport to provide a reduced gravity environment for research projects. The aircraft (Figure 6) achieves micro-gravity by flying through a parabolic flight trajectory so that its downward acceleration is equal to the gravitational acceleration. Figure 7, a photograph of the nose of the KC-135, illustrates the trajectory. Each flight provides up to forty 25-second intervals of zero gravity. The aircraft offers a $60 \times 6 \times 10$ foot test section, ample room for the truss and support equipment. The aircraft provides up to forty 25 second intervals of zero gravity per flight by repeatedly flying the parabolic arcs.

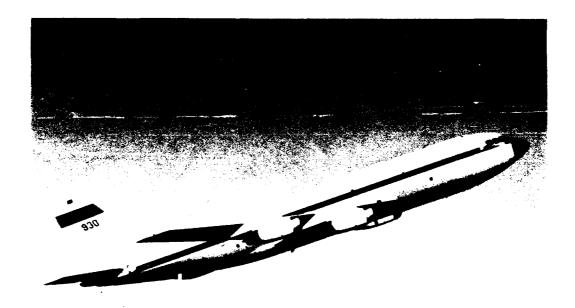
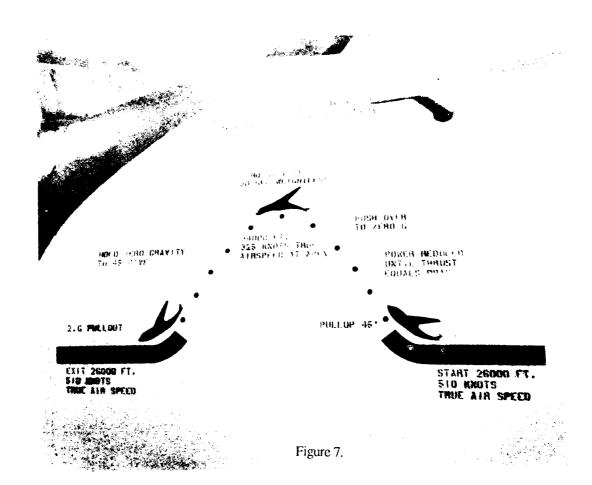
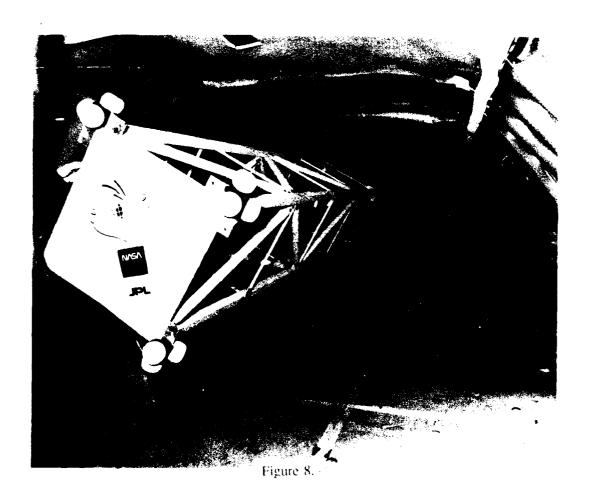


Figure 6.



Before the onset of micro-gravity for each parabola, the data recorder was turned on. The excitation device was turned on about a second after manual truss release during each zero-g period. NASA's aircraft flew twenty parabolas on the first day and forty on the second day. Figure 8 shows the truss in micro-gravity during one of the parabolic maneuvers. FIBG dedicated one half of the second flight to testing the JPL active member control system. The tests required replacing two diagonals from two bays in the center of the truss with their actuators and turning on a controller before each parabola.

During the first three to five parabolas of each flight, the pilot and test director practiced optimizing the duration of micro-gravity through intercom communications. The test director floated a pen in the test section and relayed its motion to the pilot who would correct the flight trajectory to minimize pen drift. The truss remained secured to the floor during these maneuvers.



RESULTS

The truss achieved unimpeded float times often greater than six seconds. All the instrumentation operated during the flight as planned. However, at the completion of the flight tests, two bolts on one end of a truss diagonal member were found to be loose. The effects from this was not known until the 12-meter truss finite element model was modified by removing the corresponding diagonal to match the flight test condition. The results showed coupling between the bending and torsion modes. Data from the flight test were analyzed and showed the same effects. The mode shapes from the updated model and the flight test corresponded better, indicating a significant effect of the loose diagonal on the truss's dynamics. Since the flight test results with the loose diagonal could not be correlated with the ground test, a second ground test was performed with the same diagonal member loose. Frequencies and mode shapes between the new ground test and flight test were compared.



12-METER TRUSS ZERO-G FLIGHT TEST

RESULTS

- DISCOVERED LOOSE DIAGONAL MEMBER
 - COUPLED BENDING AND TORSION MODES
 - REPEAT GROUND TEST WITH DIAGONAL LOOSE
- COMPARED FREQUENCIES AND MODE SHAPES
 - FIRST GROUND TEST, FLIGHT TEST, SECOND GROUND TEST
- SUSPENSION SYSTEM TRANSFER ENERGY INTO TRUSS FRAME MODES
- FUNDAMENTAL BENDING AND TORSION MODES CORRESPOND WELL

The ground and flight test structural modes identified using ERA are shown on Table 1. Bending and torsion modes compared well between the two tests with resonant frequencies varying less than 0.5 Hz between tests. All modes except for the first x-direction bending mode correlated better than 80%. The frame modes did not correlate well and several of the ground frame modes appeared to be coupled. Frame modes are truss cross-sectional distortions in which the cross-section expands in one diagonal direction and contracts in the other.

TABLE 1.

| Mode Description | GROUND TEST Freq. (Hz) | FLIGHT TEST Freq. (Hz) |
|---------------------------------------|---------------------------|---------------------------|
| Mode Description | 1164. (112) | 7704. (112) |
| First Y-bending + 1st Torsion | 11.7 | 11.8 |
| First X-bending + 1st Torsion | 12.2 | 12.3 |
| First Torsion | 12.7 | 12.9 |
| Second Bending - Off diagonal | * | 22.4 |
| Frame Mode - Asymmetrical | 22.5 | * |
| Frame Mode - One end | 23.3 | * |
| Second Bending - Off diagonal + Frame | 23.3 | * |
| Second X-bending + Frame | 24.6 | 24.2 |
| Frame Mode | * | 25.2 |
| Frame Mode + 2nd Torsion - One end | 27.4 | • |
| Frame Mode + 3rd Bending + Torsion | 31.3 | * |
| Third Bending - Off diagonal | * | 32.3 |
| Third Bending - Off diagonal | 36.2 | 36.5 |
| Third Torsion | * | 39.2 |
| Third Torsion + Frame | 39.6 | • |
| | | |

A frequency response plot (Figure 9) shows the various truss modes as measured by the accelerometer located at position 1y for the ground and flight tests. The peaks correspond to the bending, torsion, and frame modes listed in Table 1. The friction in the ground suspension system also reduced response amplitudes as compared to flight test levels.

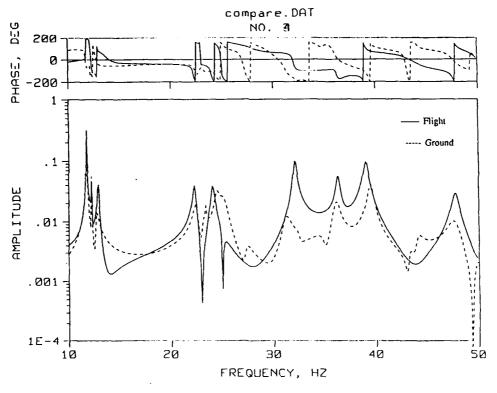


Figure 9.

Correlation between frame, bending and torsion modes for ground and flight tests was measured using modal assurance criteria (calculated with ERA). Criteria values ranges from 0 to 100, with 100 implying a perfect correlation between two modes. The following two tables list values for several bending, torsion, and frame modes.

Earlier tests showed that truss frame modes were excited when vibration amplitudes were too low to overcome stiction in the shafts and bearings. With the vertical motion constrained, the suspension cable stiffness becomes a boundary condition which affects truss dynamics. This transfers energy into the frame modes. As a result, there were more frame modes and coupling of frame modes measured in the ground test than in the flight test. This also explains the lower correlation between ground and flight test frame modes.

| PERCENT CORRELATION OF FRAME MODES FOR GROUND AND FLIGHT TESTS | | | | | |
|--|------|--------------------|----|------------------|--|
| | 22.5 | Flig 22.4 86 | | des (Hz) 32.3 0 | |
| Ground | 23.2 | • | 45 | 0 | |
| Modes | 23.3 | 14 | 31 | 0 | |
| (Hz) | 25.2 | 4 | 44 | 1 | |
| | 31.3 | 0 | 0 | 54 | |
| | 32.7 | 2 | 25 | 6 | |
| | 35.1 | 0 | 2 | 23 | |
| | | | | | |

| PERCEN' MC | T CORR | | | | | | SION |
|---------------|-------------------|------|------|------|------|-------|------|
| | Flight Modes (Hz) | | | | | | |
| | | 11.8 | 12.3 | 12.9 | 24.2 | _36.5 | 39.2 |
| | 11.7 | 80 | 6 | 2 | 0 | 1 | 0 |
| Ground | 12.2 | 4 | 60 | 8 | U | 1 | 0 |
| Modes | 12.7 | 0 | 0 | 88 | 1 | 0 | 0 |
| (Hz) | 24.6 | 0 | 0 | 1 | 82 | 0 | 0 |
| | 36.2 | 2 | 1 | 0 | 0 | 85 | 1 |
| | 39.6 | 0 | 0 | 0 | 0 | 0 | 85 |

Figure 10 to 13 compare mode shape: 'extween the second ground test and the flight test data. Figure 10 is a plot comparing the first x-direction bending mode coupled with the first torsion mode. Figure 11 shows the first y-direction bending mode coupled with the first torsion mode. Figure 12 shows the second x-direction bending mode coupled with a frame mode. Figure 13 shows a dominant frame mode from the flight test and a dominant second y-direction bending mode from the ground test.

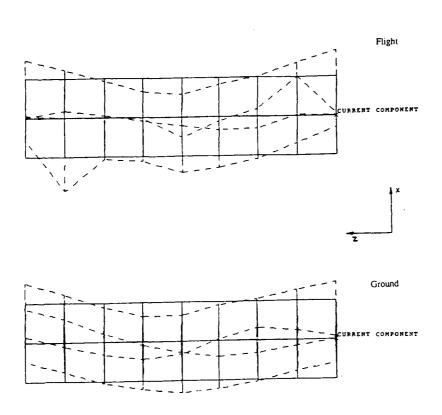


Figure 10

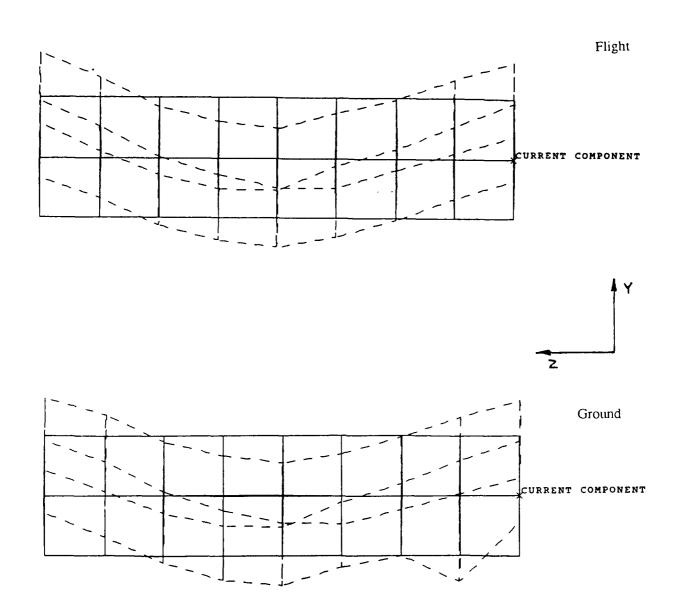


Figure 11.

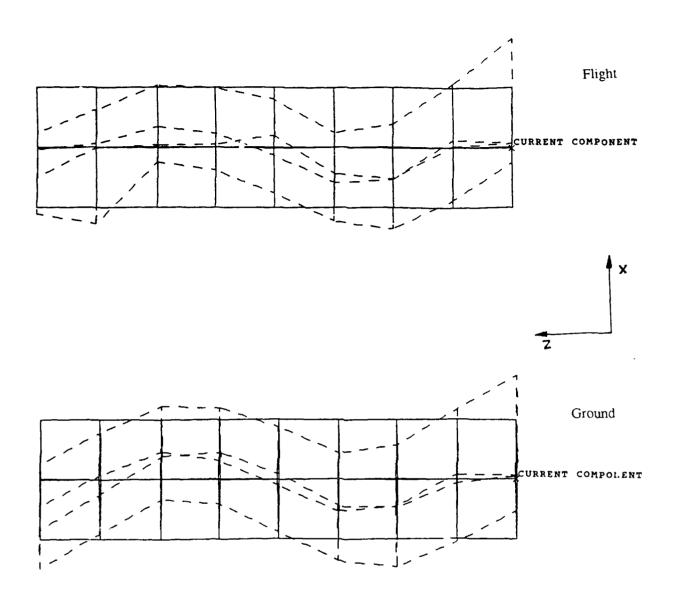


Figure 12

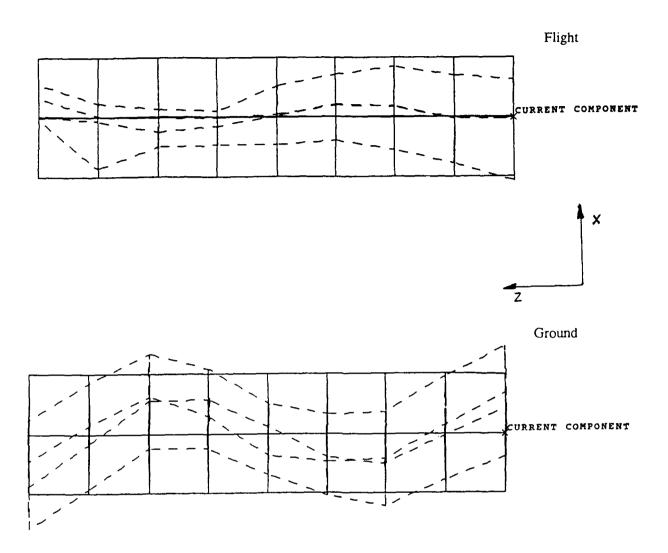
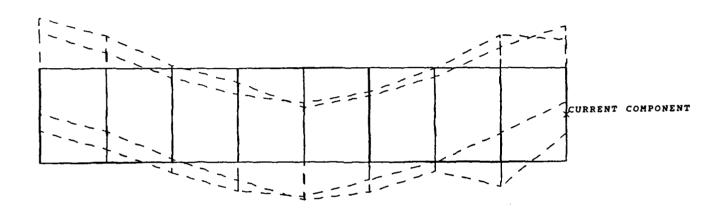


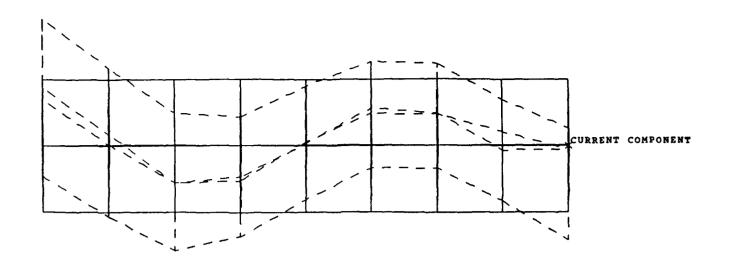
Figure 13.

To illustrate the effects of the loose diagonal members on truss dynamics, corresponding mode shapes were computed from ground tests with diagonals tightened and plotted in Figures 14, 15, and 16. Figure 14 is an off-diagonal bending mode that separated into the first two x-direction bending modes described in Figures 10 and 11. Figure 15 shows the second x-bending mode. Figure 16 shows an unsymmetric frame mode. With the tightened diagonal member, resonant frequencies were higher than the corresponding flight/ground test modes and bending modes were no longer coupled with torsion modes.



z_{Y

Figure 14.



z_\x

Figure 15.

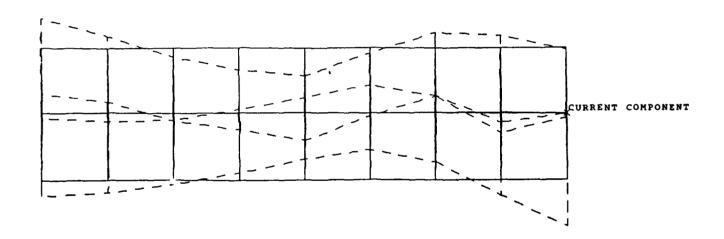
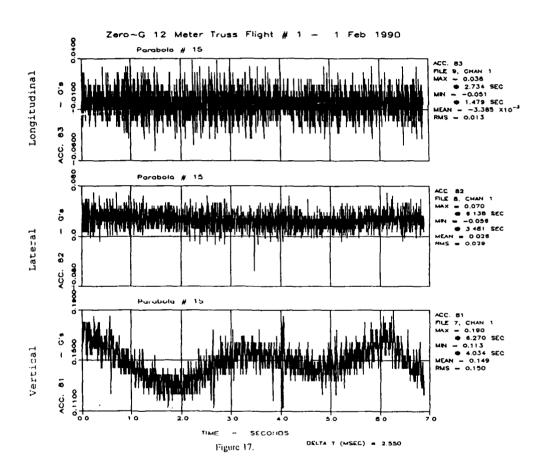
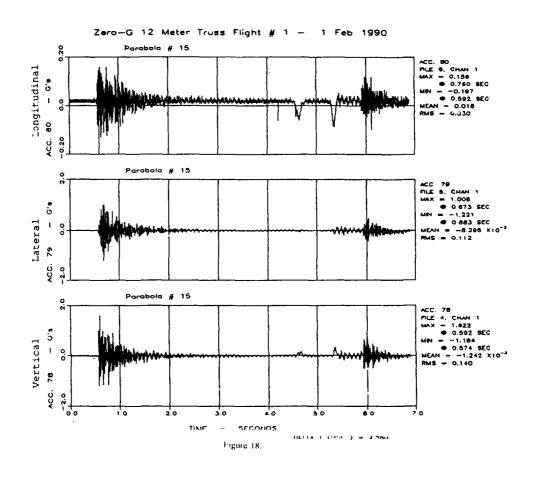


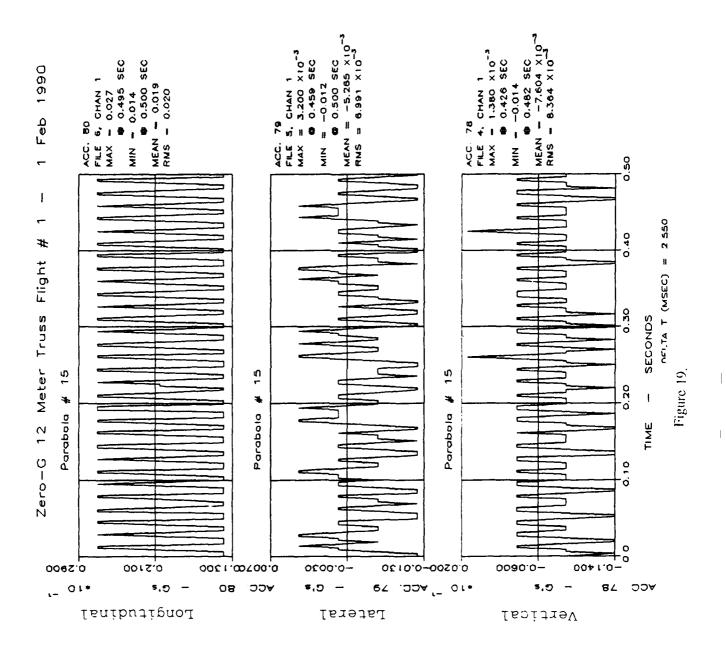
Figure 16.

Another objective of the flight test was to evaluate the zero-gravity environment provided by the aircraft. Figures 17 through 19 show acceleration response data from accelerometers mounted on the aircraft floor and on the truss. Figure 17 shows acceleration levels for a triax block (3 orthogonal accelerometers) mounted on the aircraft floor.



Accelerometer 81 was positioned vertically, 82 was horizontal, and 83 was along the longitudinal axis of the aircraft. The rms accelerations in these directions are .15, .029, and .013 g's respectively. Besides the high frequency noise present, accelerometer 81 shows the low frequency errors in the flight trajectory. Figure 18 shows the response of the accelerometers mounted near the center of the truss. Each curve shows the solenoid impact at .6 seconds and the truss impact with the aircraft 5.5 seconds later. Magnifying .5 seconds of data preceding the initial impact (Figure 19) reveals the noise level of the floating truss. Root-mean-square accelerations are .008, .007, and .02 g's for the vertical, latitudinal, and longitudinal directions respectively.





CONCLUSIONS AND RECOMMENDATIONS

The objective, to evaluate ground testing techniques, was met successfully. Good correlation between ground and flight test results was achieved confirming that laboratory zero-g simulations are valid techniques. Discrepancies and inaccuracies encountered in measured structural parameters can be avoided or accounted for with careful engineering and analysis procedures. Suspension system friction, inertial mass effects, and dynamics are the main sources of ground test inaccuracies. The good correlation between the first two bending and torsion modes from the flight and those from the ground tests indicates the suspension system had minimal effects on these modes. However, the stiction and friction in the suspension system resulted in a stiff suspension when the bearing and shafts binded, transferring impulse energy to the frame modes. If suspension system dynamics can be quantified for a particular free-free simulation system, good results can be obtained.

The NASA KC-135A provided a very good reduced gravity environment for the 12-meter truss dynamic tests. Experiments that require more than 5 to 10 seconds of free float time, however, may require a light suspension system to keep the test article away from the fuselage. In any case, test procedures should remain simple as the fast pace and the physiological effects on the experimenters make complex tasks difficult. These difficulties became apparent for the flight test engineer in charge of the instrumentation on the 12-meter truss test. During each period of zero-g, the recorder needed to be turned on; voice annotation made of the parabola number, tape footage, and truss status; and the exciter activated. The flight engineer had to operate the recorder while fighting to maintain an upright attitude close to the equipment and while closely watching the truss's motion.

A solution to achieving better frame mode correlation is to suspend the truss in a vertical position, which puts the frame mode displacement axis perpendicular to the suspension system bearing's line of action. This configuration requires a tall facility to suspend the 12-meter truss on a cable from one end. Alternatively, a second generation suspension system has already been developed and is being used in space structure experiments. The design is a pneumatic system that uses air pressure and pistons to support loads. These units achieved low friction and stiffness, making them potential replacements for the existing mechanical systems.



12-METER TRUSS ZERO-G FLIGHT TEST

CONCLUSIONS AND RECOMMENDATIONS

- ZERO SPRING RATE MECHANISMS PROVIDE ACCURATE SIMULATION OF FREE-FREE BOUNDARY CONDITION
- MICRO-GRAVITY ENVIRONMENT ON AIRCRAFT OPTIMAL FOR TEST ARTICLES
- EFFECTS FROM SUSPENSION SYSTEM NEED TO BE QUANTIFIED OR ELIMINATED FOR MORE ACCURATE RESULTS
- VERTICAL TRUSS SUSPENSION OR PNEUMATIC SYSTEM WOULD ELIMINATE FRICTION AND SUSPENSION STIFFNESS EFFECTS

SHUTTLE REMOTE MANIPULATOR SYSTEM (RMS) - BASED CONTROLS - STRUCTURES INTERACTION FLIGHT EXPERIMENT

Martha E. Demeo
The Charles Stark Draper Laboratory
Cambridge, MA

Anthony Fontana
NASA Langley Research Center
Hampton, VA

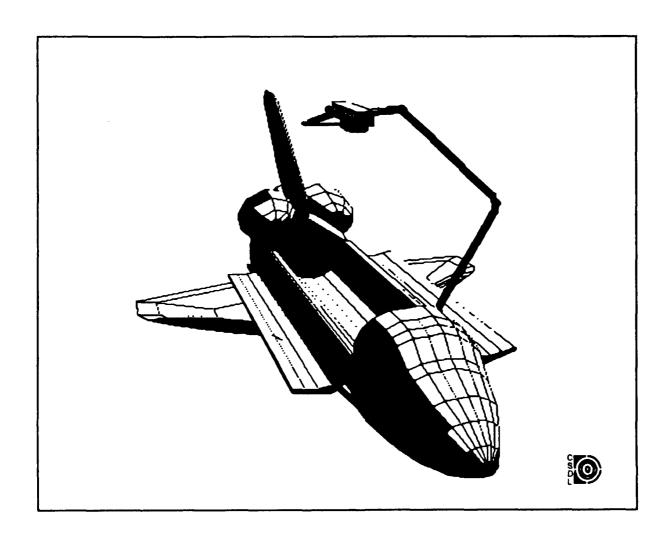
Dr. Elizabeth M. Bains NASA Johnson Space Center Houston, TX

Fourth Annual NASA / DOD Conference on Controls - Structures Interaction Technology 5-7 November 1990 Orlando, FL

Shuttle RMS-Based CSI Flight Experiment

Future large space structures are expected to be highly flexible, due to increased size and mass component distribution, and to operate under stringent performance requirements, such as precision pointing, shape control, and vibration suppression. In order to avoid flexible structure and control interaction, the control system strategy must take into account the flexible body responses as well as the rigid body dynamics. The approach for accomplishing this control strategy is commonly referred to as the flexible-body approach or the CSI approach.

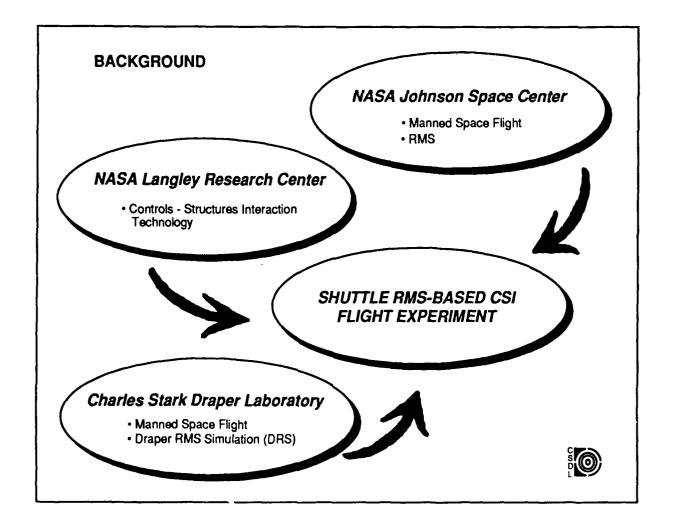
Although there has been significant theoretical and ground test development in this field over the past fifteen years [1], there is almost a complete absence of on-orbit validation of the technology. The purpose of this study is to investigate the feasibility of an experiment which would demonstrate the on-orbit characterization and flexible-body control of large space structure dynamics using the Shuttle RMS with an attached payload as a test article.



NASA has recognized the need for a proven CSI technology and has undertaken to advance CSI technology to a point where it can be used in spacecraft design for future missions. As part of the NASA CSI Program's In-Space Flight Experiment area, the conceptual definition of a CSI experiment using the Shuttle RMS was pursued by the Charles Stark Draper Laboratory.

The experiment concept reflects a collaborative effort between the NASA Langley Research Center, the NASA Johnson Space Center, and the Charles Stark Draper Laboratory.

The work presented herein was supported by funds provided by the National Aeronautics and Space Administration Langley Research Center and administered under contracts NAS9-17560 and NAS9-18147. The details of this study were published in NASA-CR-181952 [2].



The RMS is a flexible structure which can be configured to represent a typical large space structure. In addition, the structural dynamics of the RMS which include dynamically coupled and closely spaced modes are difficult to characterize using ground tests. The RMS-based experiment covers the full range of control technology from vibration suppression to multibody, large-angle maneuvers. Also, if the performance is improved, several structural modes will fall within the control system bandwidth. And finally, a successful experiment would validate analytical predictions and ground tests results.

The RMS is a flight qualified system. The Canadian government and its prime contractor, SPAR Aerospace Limited, did an excellent job in the design, development, manufacture and qualification of a very versatile and reliable device in the RMS. The RMS has well established and flight proven safety strategies. In addition, although a specially designed test structure could be better instrumented and less complicated than the RMS, an RMS-based experiment would be significantly less costly to implement. As will be discussed later, the additional hardware required for the experiment has design maturity and flight proven operational and safety strategies (e.g. the SPAS payload has a flight proven release/recapture system and a standard Hitchhiker carrier is used to support the experiment computers in the Shuttle cargo bay).

WHY IS RMS - BASED EXPERIMENT ATTRACTIVE?

TECHNOLOGY VIEWPOINT

- RMS dynamics are difficult to characterize using ground tests
- RMS has desired flexible-body dynamics (dynamic modal coupling, etc.)
- Covers range of CSI technology challenges
 - Vibration suppression with fixed RMS geometry
 - · Large angle flexible body maneuvers
- · Controller bandwidth can include several structural modes
- · Highly visible test article for validation of CSI technology

PRACTICAL VIEWPOINT

- Flight qualified structures/systems exist
- Flight proven safety strategy
- Cost Effective
- Improved RMS operational capability ...



A successful experiment would not only validate CSI technology but also demonstrate potential operational benefits for both the Shuttle RMS (SRMS) and the Space Station RMS (SSRMS). Areas of possible improvement include the following:

- Improved handling of heavier payloads. As evidenced by previous missions, the dynamics of the RMS are apparent to the astronauts and become more pronounced with heavier payloads. [3]
- Improved flexible payload handling. The integrated approach of CSI technology would accommodate the dynamics of a flexible payload on the RMS.
- The authority of the on-orbit Flight Control System (FCS) can be improved by suppressing the low frequency structural dynamics of the RMS. [4]
- Reduced cost of space station assembly. The experiment controller will suppress the oscillations of the RMS / payload system which add time to payload deployment, retrieval and maneuvering. [3]

POTENTIAL FOR IMPROVED OPERATIONAL CAPABILITY OF THE RMS

HEAVY PAYLOAD HANDLING

RMS dynamics are apparent to astronauts and become more pronounced with heavier payloads. (Hef: NASA/JSC/MOD, "RMS Mission Histories")

FLEXIBLE PAYLOAD HANDLING

CSI tounnology would accommodate the dynamics of a flexible payload on the RMS.

FLIGHT CONTROL SYSTEM (FCS) STABILITY AND PERFORMANCE

FCS improved by suppressing the low frequency structural dynamics of the RMS which "can feed back through the orbiter based FCS sensors and adversely affect the FCS performance and stability" (Ref: Sargent, D.G., "The Impact of the Remote Manipulator Structural Dynamics on the Shuttle On-Orbit Flight Control System", AIAA-84-1963).

SPACE STATION ASSEMBLY

The oscillations of the RMS/payload system add time to payload deployment, retrieval and maneuvering. On STS-8, maneuvering the 7460 lb. Payload Flight Test Article (PFTA) on the RMS it was noted that "Their (the oscillations) prime impact was on time, in that the crew would have to wait for the oscillations to damp sufficiently to determine the results of the last input and to insure that the next input would not be phased improperly so as to constructively enhance the oscillation."

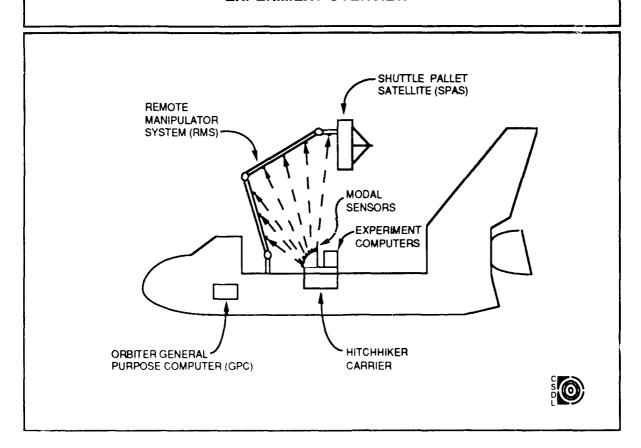
(Ref: NASA/JSC/MOD, "RMS Mission Histories")

A cartoon of the experiment depicts the Orbiter with the Shuttle Pallet Satellite (SPAS) payload deployed on the end of the RMS. The Hitchhiker carrier which supports the modal sensor processors and the experiment computers is also shown mounted in the cargo bay.

The SPAS is equipped with accelerometers and rate gyros and the RMS is instrumented with joint encoders and tachometers. In addition to these sensors, the use of optical sensors is depicted in order to convey the need for additional sensors to measure the modal displacement of the RMS/SPAS system. In actuality, these modal sensors will probably be accelerometers or strain gauges rather than optical sensors which rely on line-or-sight.

The control algorithms reside in redundant experiment computers mounted on the Hitchhiker. Control of the RMS joints is via the Orbiter General Purpose Computer (GPC).

EXPERIMENT OVERVIEW



1 76.

The experiment will require two Shuttle flights. On the first flight, the RMS will be used to grapple and deploy the 4000 lb. SPAS payload into various arm configurations. The RMS/SPAS system will then be excited by use of the RMS joint servos for the purpose of system identification. The characterization data collected from the RMS, SPAS and modal sensors will be recorded and downlinked for ground processing. Between Shuttle flights, the system models will be updated and the initial control gains will be derived. On the second flight, selected characterization tests will be repeated and the data downlinked for overnight processing. The control parameters will be updated and then uplinked to the experiment computers. The control experiments will then be conducted in a conservative order starting with vibration suppression with a static RMS configuration (mass properties fixed) and ending with vibration suppression during large angle articulation of flexible members where variable mass properties cause continuous change in mode shape and frequency.

ON-ORBIT TEST STRATEGY AND SEQUENCE

◊ Flight One [CHARACTERIZATION]

 Excite and characterize flexible modes below 1.5 Hz in several geometric configurations of RMS using joint motors

(post-flight) • Analyze modal data and update RMS simulation(s)

(post-flight) • Make predictions of controller performance during experiments and update performance monitoring algorithms in experiment computers

♦ Flight Two (6 months later) [CHARACTERIZATION & CONTROL]

- · Repeat selected characterization tests to define any changes from Flight One
- · Process modal data overnight and update controller parameters as required
- · Conduct control experiments in a conservative order :
 - Perform vibration suppression experiment at 3 fixed configurations
 - Perform single-axis, single-member articulation experiments with vibration suppression
 - Perform multi-axis, multi-member articulation experiments with vibration suppression



The candidates considered to provide an adequate inertial load on the RMS and to produce RMS/payload system frequencies on the order of 0.1 Hz were the (1) Get Away Special Canister (GAS CAN), (2) SPARTAN, (3) EUropean REtrievable CArrier (EURECA), and (4) Shuttle Pallet Satellite (SPAS).

The payload selected to meet the objectives of the RMS-Based CSI Flight Experiment was the veteran SPAS payload. The mass of the SPAS, 4000 lb., exerts a suitable inertial load on the RMS. Another attractive feature is that the SPAS's attitude control system package contains linear accelerometers and rate gyros which could be used to sense tip oscillations of the RMS/SPAS system. The operating range and accuracy of these sensors are 10^{-1} g to 10^{-4} g and \pm .005 °/sec, respectively. In addition, the SPAS has suitable communication interfaces while stowed (via hard wire umbilical) and while deployed on the RMS (via RF link). The SPAS also possesses internal power and on-board data storage capabilities. Furthermore, the SPAS is flight qualified (STS-7 and STS-11). The Strategic Defense Initiative Office (SDIO) owns SPAS and has agreed to the concept of time sharing with NASA on a future flight. [5]

RMS DEPLOYABLE PAYLOAD

SHUTTLE PALLET SATELLITE (SPAS)

- •SPAS has sufficient mass to provide 8 to 10 modes below 1.5 Hz for compatibility with 12.5 Hz GPC sample rate.
- Attitude control system package contains linear accelerometers and rate gyros to formulate end-point inertial navigator
- RF data link to Orbiter
- •Flight qualified (STS-7 and STS-11)
- · SDIO owns SPAS and is willing to time share with NASA

The original concept for the RMS-Based CSI Flight Experiment considered SPAS mounted actuators. The reasons for this were to provide excitation for dynamic characterization of the RMS, to provide actuators external to RMS for use in simple control experiments and to provide an additional control point for flexible body control experiments. The simple control experiment would use a single control point located at the tip of the RMS. However, from a technology standpoint, the simple experiment is not very attractive since a limited number of modes are controllable from a single location (possibly only one mode) and for certain geometric configurations of the RMS these controllable modes might not include the most troublesome mode. In addition, from an operational standpoint, JSC would probably have little interest in using a live load to improve RMS performance.

If payload mounted actuators were not employed, the cost of developing proof-mass actuators, modifying (and possibly flight qualifying) proportional thrusters or modifying CMG designs would be avoided and the cost of modifying the SPAS to accommodate the actuators (mechanical mounting and integration) would be avoided. In addition, safety analyses would be less extensive since it would not be necessary to prove that failures in the actuator control loops could not overload or dynamically fail the RMS structure. Thus, it became apparent that technical risk and cost could be minimized if the SPAS actuators could be eliminated. Therefore, it was decided midstream to discontinue the SPAS actuator analysis and to pursue using the RMS joint motors for excitation and control.

ACTUATORS

- ♦ Actuators required for the characterization and control of the RMS/SPAS
- ◊ Options
 - · Use existing RMS joint motors
 - Use SPAS mounted actuators
 - · Proof-mass actuators
 - Control moment gyros
 - Proportional thrusters
- ◊ Decision
- Use existing RMS joint motors
- Rationale
 - Actuators & SPAS modification very costly
 - Use existing safety strategy
 - RMS motors adequate



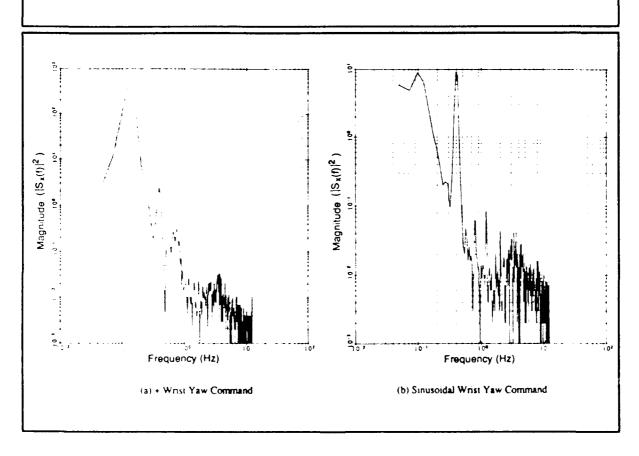
Based upon the desire to eliminate the option of SPAS mounted actuators, the feasibility of using the RMS joint motors for excitation and control was investigated. The Draper RMS Simulation (DRS) was employed to obtain predictions of the number and frequency location of modes which may be excited by an RMS maneuver or the Orbiter Primary Reaction Control System (PRCS) jets. The simulation results were analyzed for frequency content by taking a Fast Fourier Transform (FFT) of the largest resulting payload deflection.

The dominant first bending mode of the RMS/SPAS system was demonstrated to be on the order of 0.1 Hz for several different arm configurations and excitations. An example is shown in Figure (a).

Further, given the objectives of the RMS-based CSI experiment to control at least 5 modes (2 in-plane, 2 cross-axis and 1 torsional) for each arm configuration, an effort was undertaken to determine if the higher modes may be selectively excited by the RMS joint maneuvers. The ability to selectively excite the higher modes of the RMS/SPAS system would be particularly useful for system identification.

Selective excitation of a higher mode of the RMS/SPAS system is depicted in Figure (b). In this case, a modified version of DRS was used to drive the RMS with a sinusoidal rate command to the Wrist Yaw (WRY) joint. The driving frequency of this sinusoid, f = 0.4 Hz, was selected from the previous simulation of a nominal +WRY command to the RMS/SPAS system in the same configuration, Figure (a). The amplitude of the sinusoid servo rate command was selected to produce WRY joint rates below the limit specified by the Level-C data for the SPAS payload (< 0.6°/sec).

FREQUENCY RESPONSE OF RMS/SPAS SYSTEM



The high fidelity system identification required for the CSI problem will exceed the capability of existing RMS and SPAS instrumentation. This instrumentation was primarily intended to support the systems' operational capabilities. The specific sensors and actuators were not chosen or located on the arm or paylo. I for the purposes of facilitating system identification [6]. As a result, these sensors will be supplemented by modal displacement sensors distributed along the RMS.

In terms of technical preference, the most appealing instrumentation candidates (to augment the existing RMS and SPAS payload sensors) are the fiber optics strain sensor and the accelerometer. Both choices solve the field-of-view or line-of-sight problems which are inherent in optical sensors. In terms of implementation, both of these candidates would also require removal of the RMS thermal blanket for installation of wiring harnesses or optical cables. However, given the ease of implementation and lack of development required, accelerometers were selected as the sensor of choice to measure the modal characteristics of the RMS/SPAS system.

SENSORS

- The RMS/CSI flight experiment requires sensors to measure the mode shape, frequency and damping of the RMS/SPAS system
- The identification of mode shapes would require more sensors than are currently supported by the RMS and SPAS
- Accelerometers selected
 - Adequate sensitivity
 - Flight qualified
 - No field-of-view, line of sight problems (as with optical sensors)

BUT...

Requires installation of sensors and wiring under RMS thermal blanket (RMS modification by SPAR)



In order to estimate the size of the control algorithms and calculate the required experiment computer speed, the following experiment objectives were derived from the initial requirements for the feasibility study:

- ♦ At least 10 flexible modes of the experiment shall be characterized by ground-based system identification techniques applied to data taken during orbital flight. The state estimator in the on-orbit experiment shall also track 10 flexible modes. This will allow control of approximately 5 flexible modes.
- ♦ The experiment sample data rate will be fixed at the GPC cycle rate of 12.5 Hz since the GPC will be part of the closed-loop controller.
 - ♦ Number of States = 44
 - 16 modes estimated x 2 states/mode = 32
 - 6 RMS joint motors x 2 states/actuator = 12
 - \Diamond Number of Actuators = 6
 - RMS joint motors = 6
 - \Diamond Number of Sensors = 30
 - 6 modal sensors each plane x 2 planes = 12
 - 6 RMS joint motors x 2 sensors/ motor = 12
 - 6 SPAS sensors = 6

PRELIMINARY EXPERIMENT GOALS AND BASELINE FEATURES

- ♦ Characterize flexible modes below 1.5 Hz (probably 10 modes)
- ♦ Control flexible modes within bandwidth = 0.5 to 1.0 Hz (probably 5 modes)
- ♦ Sample Data Rate = 12.5 Hz (same as Orbiter GPC)
- ♦ 44 States (10 flex modes, 6 rigid modes, 6 RMS joints)
- ♦ 6 Actuators (RMS joint motors)
- ♦ 30 Sensors (12 accelerometers, 12 RMS joint, 6 SPAS)

USED TO SIZE CONTROL ALGORITHMS AND CALCULATE REQUIRED EXPERIMENT COMPUTER SPEED



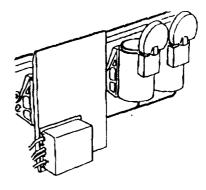
Two options were considered for the location of the experiment algorithms: in dedicated experiment computers located in the Orbiter cargo bay or in the Orbiter SM GPC. The choice between the two options was primarily dependent on the availability of the SM GPC resources and the speed of the Orbiter GPC.

An estimation of experiment computer speed requirements was made in order to determine whether the Orbiter GPC is fast enough to do all of the experiment computations. The estimation was based upon an estimated number of states, actuators, and sensors. The results indicated that the experiment algorithms will require from 290k to 1.2M AFLOPS (Arithmetic Floating Point Operations Per Sec).

The time expended by a single precision multiply and a single precision add of the new Orbiter GPC were obtained. Assuming that there was roughly one add associated with each multiply for the multiplication of large matrices (ignoring associated indexing and storage reference operations), the number of AFLOPS accommodated by the GPC was then estimated by adding the number of adds and multiplies. Further, estimating that the SM GPC overhead functions, such as Orbiter fault detection and annunciation and waste water dumps, comprise 25% of the GPC CPU, the available GPC speed was reduced to 86k AFLOPS. After comparing this estimate to the experiment computer speed estimate of 1.2M AFLOPS, it was determined that the experiment computations be performed in experiment computers mounted in the Shuttle cargo bay.

EXPERIMENT COMPUTATIONS

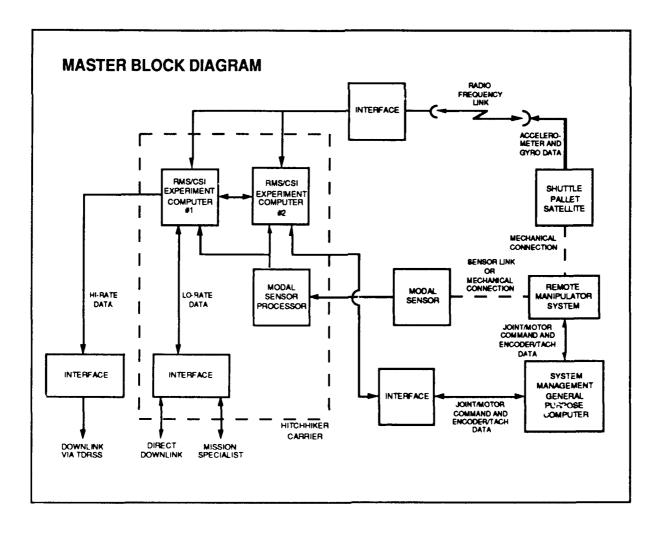
- ♦ Orbiter GPC's have insufficient speed for multi-mode CSI experiment
- Critical algorithms performed in redundant experiment computers with independent software development
- Experiment computer executes:
 - Excitation algorithms
 - Control algorithms
 - Experiment data handling
 - Experiment performance monitoring
- ◊ Electronics mount on HITCHHIKER-G carrier
 - Redundant SCI-MAST computers (currently being flight qualified)
 - Redundant FMDM's for direct GPC interface





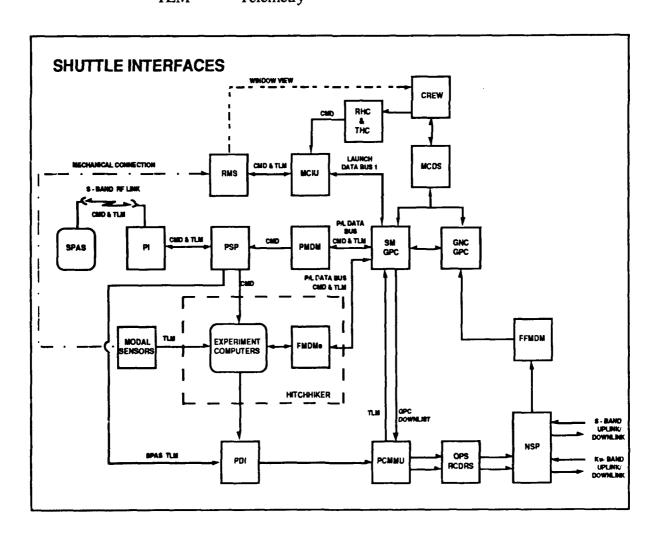
The general interface requirements for the RMS-Based CSI Flight Experiment are summarized in the Figure below. This block diagram depicts the main components of the experiment, namely the SPAS, RMS, SM GPC, modal sensor, and the redundant experiment computers. The carrier mounted experiment computers acquire accelerometer and gyro data from the SPAS, modal sensor data from the RMS mounted modal sensors, joint encoder and tachometer data from the RMS by way of the GPC, housekeeping data and uplinked experiment control parameters. In turn, the experiment computers send joint motor commands to the RMS via the GPC and send selected sensor data, status discretes, housekeeping, estimator states, and modal sensor data to recorders for subsequent downlink and/or mission specialist.

In order to accommodate these communication requirements, the experiment will employ interfaces between (1) the GPC and the RMS (command and telemetry), (2) the SPAS and the GPC (command and telemetry), (3) the SPAS and the experiment computers (telemetry), (4) the GPC and experiment computers (command and telemetry), (5) the recorders and/or mission specialist and the experiment computers and (6) the RMS mounted modal sensors and the carrier mounted experiment computers.



ACRONYM DEFINITIONS

CMD Commands Flight Forward Multiplexer-Demultiplexer Flexible Multiplexer-Demultiplexer **FFMDM FMDM** GNC GPC Guidance Navigation and Control General Purpose Computer
Multi-Function CRT Display System **MCDS MCIU** Manipulator Control Interface Unit Master Memory Unit Mission Station Distribution Panel Network Signal Processor **MMU** MSDP NSP OPS Operational **PCM** Pulse Code Modulator **PCMMU** Pulse Code Modulation Master Unit PDI Payload Data Interleaver PΙ Payload Interrogator P/L Payload PSP PMDM Payload Signal Processor Payload Multiplexer-Demultiplexer **RCDRS** Recorders RF RHC Radio Frequency Rotational Hand Controller **RMS** Remote Manipulator System Serial Input/Output
System Management
Shuttle Pallet Satellite
Translational Hand Controller SIO SM **SPAS** THCTLM Telemetry



With consideration to the objectives of the experiment, the following fundamental safety strategies were established. By adhering to these strategies, it is anticipated that the RMS/CSI experiment will not add any CRIT 1 or CRIT 2 failures.

- (1) Absence of dynamic interaction between active DAP and dormant payload of SPAS weight class established by Volume XIV Generic DAP Stability Envelope and by previous flights of the RMS/SPAS.
- (2) The Orbiter shall be in free drift during active experiment periods to eliminate the possibility of dynamic interaction between the DAP and experiment control systems.
- (3) RMS operating boundaries are restricted to those validated by analyses and previous missions to insure safe dynamic loads.
- (4) The crew visually monitors the RMS during experiment periods and may halt undesired motion of the arm by terminating the experiment and applying the brakes.
- (5) The RMS structure and joint motors were designed to protect the structural integrity of the arm. The torque output of the RMS joint motors is limited by a circuit in the servo electronics so as to prevent overloading the RMS structure.

SAFETY STRATEGY

GENERAL ITEMS:

- Absence of dynamic interaction between active orbiter DAP and dormant payload of SPAS weight class
- Orbiter in free drift during active experiment periods to eliminate the possibility of dynamic interaction between the two control systems (DAP and experiment)
- RMS operating boundaries restricted to those validated by analyses and previous missions to insure safe dynamic loads
- Crew visually monitors RMS during experiment periods
 - · Operator can stop undesired motion by applying brakes
- Structural integrity of RMS protected by original design of structure and joint motor sizing



Existing safety strategies, procedures, and algorithms will be augmented to avoid introducing potential CRIT 1 or CRIT 2 failures. Three tiers of safety, experiment performance monitoring, GPC safety algorithms and crew (manual) shut-off, are used to detect anomalous controller performance, prevent RMS structural overloads, avoid collisions, and detect hardware failures.

FIRST: Experiment Computer Performance Monitoring. These algorithms will be executed in identical, redundant experiment computers. The software, developed by two independent contractors, will use redundant sensor data to check for differences between actual and predicted dynamic performance during the experiment. If either computer detects an out-of-limit condition, the experiment will be automatically shut-down. The performance limits will be set well inside safety limits. Further, the performance monitoring algorithms in the experiment computer will determine the validity of joint rate commands forwarded (via the GPC) to the RMS.

SECOND: SM GPC's Rate Limits. The RMS software will prevent the arm from commanding rates which exceed the payload/joint dependent limits.

THIRD: Crew Monitoring. The crew will have the ability to manually shut-down the experiment, apply brakes, and allow the RMS to damp naturally.

SAFETY STRATEGY cont'd

1st Tier: EXPERIMENT COMPUTER PERFORMANCE MONITORING

- Executed in identical, redundant experiment computers with independent S/W
- Detect differences between predicted and actual dynamic response

2nd Tier: ORBITER SM GPC

- RMS software prevents arm from commanding rates which exceed the payload/joint dependent rate limits
- Rate Envelope Consistency Check compares the instantaneous actual rates against a rate boundary envelope based on correlated joint rate commands

3rd Tier: MANUAL (CREW) POWER SHUT-OFF OF EXPERIMENT

- Independent of experiment computers
- RMS damps naturally with brakes on



The cost estimate was based upon the level of effort required to support the subschedules identified in the Table below. Standard transportation costs, e.g. launch, payload deployment, etc., for flying the SPAS and Hitchhiker payloads are not included. Further, it is assumed that the rental costs for both the SPAS and the Hitchhiker by a NASA agency are absorbed in these standard transportation costs. The cost estimates are for a two flight scenario and are in 1989 dollars unless otherwise indicated. The Modal Sensor Subschedule hardware costs were based upon the use of accelerometers as the baseline RMS mounted modal sensors.

The total cost of the two flight experiment is estimated at \$27.8 M. The highest price tag is attached to the experiment computer subschedule at \$10.8 M which is 39.1% of the total cost and 42.6% of the total engineering cost. This is a result of the substantial cost incurred in software development, testing, and documentation. The second highest total cost is associated with the mounting of accelerometers on the RMS at \$5 M. The third highest total cost belongs to the Hitchhiker subschedule. The experiment hardware included in this subschedule consists of two flight qualified FMDMs, two functional equivalent FMDMs, Hitchhiker avionics and ground support equipment. The estimated cost of this hardware is \$3.7 M which is 50.7% of the total cost of experiment unique hardware.

COST SUMMARY (MILLIONS)

| | SUBSCHEDULE | ENGINEERING | EXP UNIQUE HARDWARE | TOTAL COST | COMMENTS |
|---|--------------------------------------|-------------|------------------------|------------|--|
| | ALGORITHM DESIGN | 1.0 | 0.0 | 1.0 | |
| | MODAL SENSOR | 0.4 | * 0. i | 0.5 | * Accelerometers |
| | HITCHHIKER | 1.0 | *3.6 | 4.6 | * Functional equiv HH * Redundant FMDM's |
| | GPC SOFTWARE MODIFICATION * | 1.2 | 0.0 | 1.2 | * IBM |
| | RMS MODIFICATION * | 5.3 | 0.0 | 5.3 | *SPAR |
| | EXPERIMENT COMPUTER | * 8.7 | " 2.1 | 10.8 | * S/W dev ** FL & FE computers |
| | MISSION OPERATIONS DEVELOPMENT | 0.4 | 0.0 | 0.4 | |
| | VERIFICATION | 0.9 | * 1.0 | 1.9 | * SAIL |
| | SECOND FLIGHT | 2.0 | 0.0 | 2.0 | ٩ |
| • | TOTAL | 21.0 | 6.8 | 27.8 | |

There are several factors which tend to minimize the cost of this on-orbit CSI experiment:

- (1) A flight qualified flexible test article exists (RMS) which has a flight proven operational capability and safety strategy. Further, procedures for RMS modification exist via the SPAR support contract with NASA/JSC.
- (2) A flight qualified payload which possesses flight proven safety strategies, release/recapture mechanisms, RF data link and sensors (to form inertial navigator for end position control and safety strategy) exists (SPAS). In addition, SDIO owns a SPAS and is willing to share it with NASA on a future flight.
- (3) The GSFC supports standard integration and testing of the Hitchhiker carrier at no cost to a NASA organization.
- (4) Procedures for GPC software modification, i.e. a software Change Request (CR), are well established via an IBM support contract to NASA/JSC.
- (5) The facility for system-level integration and testing of the experiment hardware, software, and interfaces exist (JSC/SAIL).
- (6) The experiment computers will be flight qualified in early 1990 as a fallout of LaRC's COFS program. Flight units and functional equivalent units can then be purchased from SCI Technology, Inc. at reasonable prices.

FACTORS THAT TEND TO REDUCE COST

- ♦ Flight qualified flexible article exists (RMS)
- ♦ Flight qualified grappled payload exists (SPAS)
- Flight qualified carrier for payload bay electronics
- Procedures for GPC software modifications in place
- ♦ Experiment computer will be flight qualified in early 1990
- ♦ Facility for system-level integration and verification testing exists (JSC/SAIL)



The RMS-Based CSI Flight Experiment will enable the advancement of CSI technology through the demonstration of on-orbit characterization and flexible-body control of large space structure dynamics. The Shuttle RMS with an attached payload is a viable test article because it is capable of large angle articulation of flexible members which are difficult to characterize using ground test techniques.

In addition, by utilizing existing hardware, the experiment minimizes the costs and risk of implementing a flight experiment. The RMS, SPAS, and Hitchhiker are flight qualified systems which have well established integration, operation, and safety strategies. Further, although specially designed test structures could be better instrumented and less complicated than the RMS, an RMS-based experiment would be less costly to implement.

The experiment also offers the promise of spin-off enhancement to the Shuttle RMS and Space Station RMS. The potential for improvement exists in the handling of heavy and/or flexible payloads, Orbiter DAP performance and space station assembly. With respect to the Orbiter DAP, it is anticipated that suppressed modal vibrations will reduce dynamic coupling with the DAP and will increase stability margins. With respect to space station assembly, it is anticipated that the experiment controller would suppress the oscillations of the RMS/payload system and thus shorten the assembly timeline.

CONCLUSION

- ♦ Experiment will advance CSI technology
- Use of existing hardware reduces cost and risk
- Experiment offers promise of spin-off enhancement to Shuttle RMS and Space Station Assembly



REFERENCES:

- [1] "NASA/DOD Controls-Structures Interaction Technology 1989," NASA-CP-3041, Conference Proceedings, San Diego, CA, 29 January 2 February 1989.
- [2] Demeo, M.E., "Remote Manipulator System (RMS) Based Controls-Structures Interaction (CSI) Flight Experiment Feasibility Study," NASA-CR-181952, January 1990.
- [3] Bole, Catherine D. and Rhonda R. Foale, "RMS Mission Histories," NASA JSC-23504, March/April 1989, p. 13 and p. 16.
- [4] Sargent, Darryl G., "Impact of Remote Manipulator Structural Dynamics on Shuttle On-Orbit Flight Control," AIAA-84-1963, AIAA Guidance and Control Conference, Seattle, Washington, 20-22 August 1984.
- [5] "Space Shuttle System Payload Accommodations," NSTS-007700, NASA/JSC, Volume XIV, Revision J, 27 January 1988.
- [6] Lepanto, Janet A., "Remote Manipulator System/Large Space Structure RTOP, Final Report," CSDL-R-1755, 18 December 1984.

ACTIVE DAMPING APPLICATION TO THE SHUTTLE RMS

by

Michael G. Gilbert Michael A. Scott Sean P. Kenny

NASA Langley Research Center Hampton, VA. 23665

Fourth NASA/DOD CSI Conference Orlando, FL November 5-7, 1990

ABSTRACT

Control-Structure Interaction (CSI) is a relatively new technology developed over the last 10 to 15 years for application to large flexible space vehicles. The central issue is recognition that high performance control systems necessary for good spacecraft performance may adversely interact with the dynamics of the spacecraft structure, a problem increasingly aggravated by the large size and reduced stiffness of modern spacecraft structural designs. CSI analysis and design methods have been developed to avoid interactions while maintaining spacecraft performance without exceeding structural capabilities, but they remain largely unvalidated by hardware experiments or demonstrations, particularly in-space flight demonstrations. One recent proposal for a low cost flight validation of CSI technology is to demonstrate active damping augmentation of the Space Shuttle Remote Manipulator System (RMS). This paper describes an analytical effort to define the potential for such an active damping augmentation demonstration to improve the structural dynamic response of the RMS following payload maneuvers. It is hoped that this study will lead to an actual inflight CSI test with the RMS using existing Shuttle hardware to the maximum extent possible. By using the existing hardware, the flight demonstration results may eventually be of direct benefit to actual Space Shuttle RMS operations, especially during the construction of Space Station Freedom.

A summary of the motivation for the proposed flight test is given along with the task relationships between NASA Langley Research Center, NASA Johnson Space Center, and Charles Stark Draper Laboratories. The current approach to the active damping augmentation feasibility study tasks are summarized, and results from the initial linear analyses are presented. The results form the basis of the preliminary conclusions that the RMS could be used for an in-flight active damping demonstration using the SPAS payload, and that the only additional hardware needed on the RMS would be a small number of feedback accelerometers. Plans for continued analyses and verification of results using a nonlinear simulation of the RMS, which includes nonlinear joint gearboxes and Space Shuttle computer hardware and software models, are given.

ACTIVELY AUGMENT RMS DAMPING

The Control-Structures Interaction (CSI) program at NASA Langley Research Center (LaRC) is dedicated to the development, application, and validation of new technologies for the control of large spacecraft systems which have significant structural flexibility. An important goal of this program is in-space flight tests to demonstrate quantitatively the benefits of CSI technology. One such proposed inflight demonstration is to actively augment the structural dynamic damping of the Space Shuttle Remote Manipulator System (RMS) arm, which currently exhibits low damping and long periods of oscillatory motion following routine operational maneuvers. This demonstration would provide a direct quantitative measure of the benefit of CSI technology as a part of the CSI program, while also measuring potential performance improvements in the current RMS which could ultimately have a significant impact on the assembly of Space Station Freedom (SSF).

This paper will describe an ongoing analysis effort at LaRC to determine the feasibility of providing active damping augmentation of the RMS following normal payload handling operations. The flight demonstration effort is motivated by a study completed by Charles Stark Draper Laboratory (CSDL) [1-2], which proposed using the Shuttle RMS for a CSI flight experiment. The flight experiment study proposed adding additional sensors to the arm, the installation of a flight experiment computer and hardware in the Shuttle cargo bay, and the use of an instrumented payload at the end of the arm to measure performance. However, the current flight demonstration feasibility study is restricted to the use of existing RMS hardware only if possible, and the minimal addition of new sensor hardware only if necessary. The use of an instrumented payload would be retained, but the flight experiment computer and hardware would be eliminated in favor of using the existing Shuttle General Purpose Computers (GPC's) for control law implementation. The demonstration feasibility study is considering active damping control laws for use in the time period following the end of arm-move commands and the beginning of the normal arm position-hold function, although active damping of arm motion following Shuttle thruster firings is also a possibility.

ACTIVELY AUGMENT RMS DAMPING

Proposed inflight demonstration of CSI technology:

- Quantitative measurement of CSI technology benefits
- Improve current RMS operations
- Potential benefits for SSF assembly

Scaled-down version of CSDL experiment definition

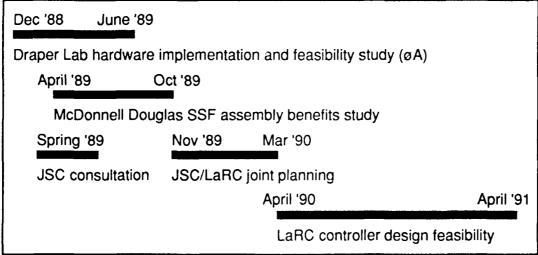
- Use existing hardware if possible, minimal additional hardware if necessary
- Actively damp between move command and position-hold functions, possibly after STS thruster firings
- Cast as development test to improve existing Shuttle hardware

RMS-BASED CSI FLIGHT DEMONSTRATION

The chart below summarizes the history of the proposed RMS CSI flight demonstration efforts. The original CSDL study [1-2] was completed in the period of December 1988 to June 1989. A study of CSI technology benefits for the assembly of Space Station Freedom was conducted by McDonnell Douglas Space Systems Co. from April to October 1989 [3]. This study determined that approximately 10 hours of cumulative time would be spent over 15 SSF-assembly Shuttle flights waiting for arm motions to damp down to ± 1 inch amplitudes following maneuvers with SSF components. The study also showed that a simple increase of two in the inherently small level of damping of the arm could reduce the cumulative settling time to 4 hours, a reduction in time approximately equal to the programed arm-operation time on a single assembly flight. This study became a prime motivator for the proposed flight demonstration. Also during 1989, LaRC consulted with the NASA Johnson Space Center (JSC) about a potential RMS-based flight demonstration, and following the McDonnell Douglas study results, a joint LaRC/JSC planning effort led to the current effort. The feasibility study has been ongoing since April 1990 and is scheduled to last until April 1991, at which time a decision to proceed to an actual flight test will be made.

RMS-BASED CSI FLIGHT DEMONSTRATION

History



LaRC / JSC BRIDGING PROGRAM

The joint LaRC-JSC RMS flight demonstration effort, referred to as a "bridging program" is divided into four tasks as shown below. The first two tasks, determination of feasibility using existing hardware and, if not feasible, the definition of the minimal set of additional needed hardware, is an LaRC activity. The third and fourth tasks, ground-based evaluations and the actual flight test, are JSC responsibilities. The decision to proceed with the flight demonstration will be made jointly. The Charles Stark Draper Laboratory, under contract to JSC, is and will be assisting with all tasks in the program.

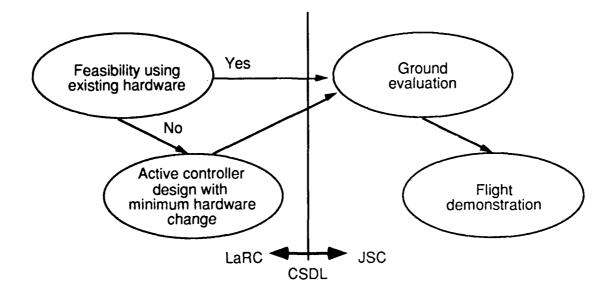
Larc / JSC Bridging Program

TASK 1: Determine active damping control feasibility using EXISTING hardware

TASK 2: Active damping controller design with MINIMUM hardware changes

TASK 3: Ground evaluation of active damping control

TASK 4: On-Orbit Demonstration



FEASIBILITY STUDY APPROACH

Under the LaRC-JSC bridge program, the feasibility of actively augmenting the damping of the RMS arm will be determined by LaRC. The approach to this feasibility study is shown below. The first activity is to define payload and arm configuration combinations of interest which are consistent with the types of payloads expected during Space Station Freedom assembly. The second step is to examine RMS dynamics and operational characteristics using the Draper RMS Simulation (DRS) nonlinear simulation code [4]. This code was obtained for this study from CSDL through JSC and is used routinely for predicting arm dynamic motions in on-orbit RMS operations. The simulation includes models of the RMS structural dynamics, joint servos, motors, and gearboxes, and the software modules loaded in the Shuttle GPC for RMS control. The key activities for determining active damping augmentation feasibility involves the design and simulation of active damping control laws. For this purpose, two approaches to linear control design model development have been undertaken. One of these approaches is to use system identification methods on output data from the DRS to identify linear state-space models which closely match the DRS response for specific commanded arm movements. The other approach is to use a NASTRAN finite element model representation of the arm and calculate linear vibration modes for particular configurations and payloads. The mode frequencies and mode shapes are then used to obtain a linear state-space model for control design purposes. With a linear control design model, various active control law design concepts can be evaluated, as can the requirements for feedback sensors to measure arm motions. The final step is to simulate the active damping control laws in a modified version of the DRS to determine the effects of system nonlinearities and computer time delays.

FEASIBILITY STUDY APPROACH

Define payload/arm configurations of interest

Examine existing RMS capabilities and dynamic response

Using nonlinear CSDL RMS simulation code (DRS)

Develop linear dynamic models for control design

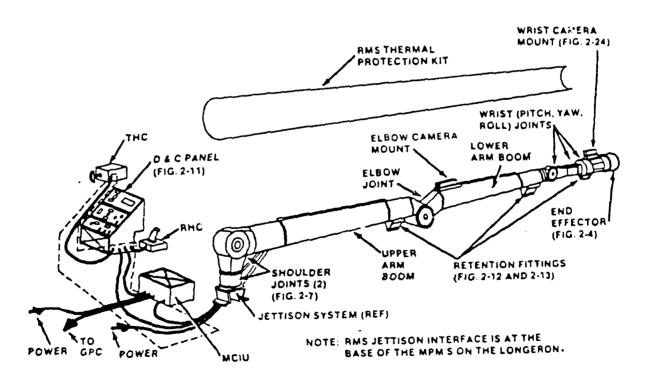
Synthesize active damping augmentation controller

Evaluate controller performance using DRS

REMOTE MANIPULATOR SYSTEM

The figure belows summarizes some of the design characteristics of the Space Shuttle Remote Manipulator System (RMS) arm [5]. The system is a six-joint telerobotic system controlled from a panel located on the aft flight deck of the Space Shuttle. These six joints are directly analogous to the joints and freedoms of a human arm, defined as shoulder yaw and pitch, elbow pitch, and wrist pitch, yaw, and roll. An end effector for grappling payloads is mounted at the free end of the arm. From the control panel and translational and rotational hand controllers, commands to move the arm are processed by the Manipulator Control Interface Unit (MCIU) and the Shuttle GPC to provide electrical signals to drive the joint servo motors. Data in the form of angle position and motor shaft rate from an encoder and tachometer at each joint are returned to the MCIU and GPC for control purposes.

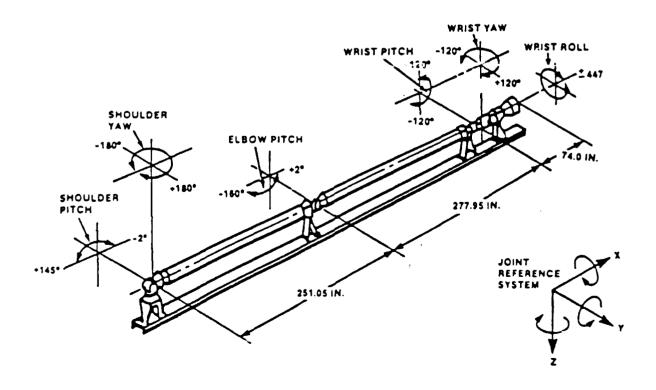
REMOTE MANIPULATOR SYSTEM



RMS DIMENSIONS AND IOINT LIMITS

The figure below defines the joint movement limits and dimensions of the RMS arm [5]. The arm is shown mounted in the Manipulator Positioning Mechanism (MPM), which is mounted via a swingout joint to the side wall of the Shuttle payload bay. The MPM is used to secure the RMS during launch and reentry of the Shuttle, and is positioned at an angle of 19.4° relative to the stowed condition during arm on-orbit operations. Also shown is the joint reference coordinate system.

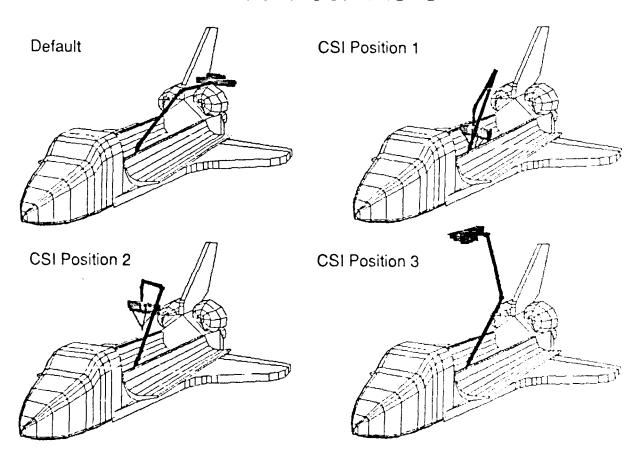
RMS DIMENSIONS AND JOINT LIMITS



RMS CONFIGURATIONS

Four standard RMS configurations have been adopted for the current feasibility study. This configurations are shown below with the SPAS free-flyer spacecraft as an attached payload. The first configuration is the default configuration of the DRS in the absence of any other specified configuration. The other 3 configurations are actual configurations used during the deployment of the SPAS satellite on a previous Shuttle mission. The first of these, configuration 2, is the position of the arm and payload just after release from the cargo bay attachments. Configuration 3 is the position of the arm and payload after being lifted from configuration 2 to a point which completely clears the sides of the cargo bay. Configuration 4 is the actual deployment positioning at the time of the SPAS deployment. In the current study, these four configurations have been analyzed with several other payloads in addition to the SPAS.

RMS CONFIGURATIONS



DYNAMIC RESPONSE ANALYSIS CASES

The table below summarizes, by operating mode, payload, and position, the dynamic response analysis cases which have been considered to date. The responses of the RMS to commanded movements in single joint operating mode and the four manual operating modes have been computed with the DRS using the various combinations of payloads and configurations as shown. Data from the single joint mode cases with the SPAS payload have been used extensively for single-input, single-output, linear system model identification purposes as will be discussed shortly. Data from the other cases have been used primarily for dynamic response characterization purposes, although it will also be used for multi-input, multi-output, linear system identification purposes as the study progresses.

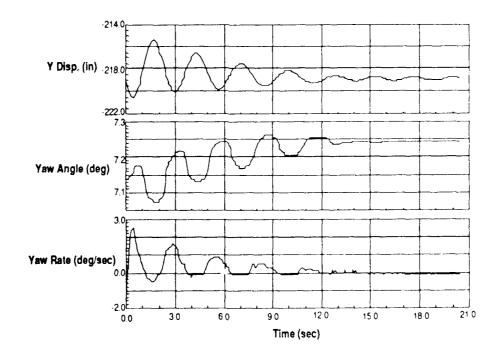
DYNAMIC RESPONSE ANALYSIS CASES

| Operating Mode | | Payload | | | Position | | | |
|----------------|----------|---------|------|---------------|----------|---|---|---|
| | | None | Spas | LDEF Class | Def. | 1 | 2 | 3 |
| Manual | Unloaded | X | | | | | | × |
| | Loaded | | Х | | X | X | x | х |
| | End Eff. | | Х | | | | | X |
| | Payload | | Х | | | | | × |
| Single Joint | | | х | Х | × | Х | × | х |

TYPICAL RESPONSE AND SENSOR OUTPUTS

The time response data shown below are typical of the kind of RMS motions encountered during normal arm maneuvers. The data are the free responses following a 10-second rotation command to the shoulder yaw joint in single joint mode, with no payload and the other joints held approximately fixed by the RMS position-hold function. Shown are the lateral displacement of the free end of the arm, the shoulder yaw-joint angle encoder response, and the shoulder yaw-joint rate derived from the motor shaft tachometer. The peak-to-peak free oscillation of the arm after the command is about 5 inches, while the actual measured angle change during the same time is on the order of 0.1 degree. The discrete stepping of the encoder response is due to word length limitations in the Shuttle GPC, indicating that the signal is at the limit of useful resolution. The yaw-joint rate is on the order of 3.0 degrees/ second, and again has discrete stepping characteristics which is limiting the useful resolution of these data. These types of responses are typical for all configurations and payloads analyzed to date, and are an indication that the existing RMS sensors may not be completely adequate for active damping augmentation purposes.

TYPICAL RESPONSE AND SENSOR OUTPUTS



LINEAR FLEXIBLE MODEL DEVELOPMENT

A NASTRAN finite element model developed by CSDL [6] has been adopted and subsequently modified for the purposes of linear control system design and dynamic simulation. The RMS is modeled in a spatially fixed arm configuration with the brakes on (i.e., the joints are locked). Preliminary studies will be conducted assuming the orbiter is fixed.

The model consists of 26 prismatic beam elements. Elements used in this model have been developed to represent extensional and torsional stiffness, as well as bending stiffness and transverse shear flexibility in two perpendicular directions. The joint housings, gear trains, and Shuttle and payload attach points are modeled by a total of 16 beam elements. Each joint assembly is represented by a pair of inboard and outboard beams. A total of seven joints, including the shoulder swing out, have been modeled. The upper and lower arm booms are discretized into 4 elements each. Longeron and payload grapple point stiffnesses are also modeled. At each joint, both cylindrical and rectangular coordinate systems are defined. This dual coordinate system scheme permits RMS configurations to be varied without explicitly calculating global frame nodal coordinates. New arm configurations may be defined by specifying only the appropriate joint angles, all nodal coordinate transformations are calculated internal to NASTRAN.

LINEAR FLEXIBLE MODEL DEVELOPMENT

Wrist Pitch

Payload C.G.

Wrist Roll

2 Element Joint

Boom

Attachments

Rigid Offset

Wrist Yaw

NASTRAN finite element model of RMS

- 14 elements for joint/housing stiffness
- 8 elements for graphite epoxy booms (arms)
- 2 elements for shoulder and grapple attachments

2 rigid elements for Shuttle and payload c.g. offsets

Linear vibration analysis about each configuration of interest

- 10 normal mode frequencies and mode shapes
- Apply relative inter-body torque across joint for transient analysis

Shoulder Pitch Elbow Pitch Shuttle C.G. Shoulder Yaw **Swingout**

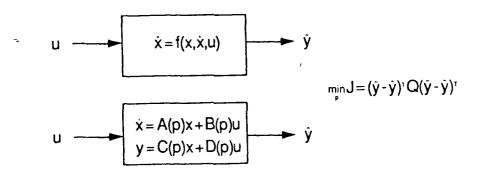
LINEAR SYSTEM IDENTIFICATION APPROACH

For the purpose of evaluating active damping-augmentation controller feasibility, linear, single-input, single-output, state-space control law design models of the RMS have been derived from DRS response data using linear system identification methods. The data have been obtained for single joint mode cases with the SPAS payload using the desired joint rate command as the input signal, and either the joint tachometer or a linear acceleration measurement at the tip of the arm as the output signal. For a given model order, usually 6 to 10 states corresponding to 3 to 5 vibration modes, frequency and damping parameters were selected to make the model best match the DRS response data in a least-squares sense. Following the least-squares parameter selection, an iterative Maximum Likelihood method was used to further refine the model parameters. These models are then used to evaluate the effects on RMS damping arising from feedback of the tachometer or acceleration signals through simple gain loop-closures. In all cases, the system identification process has been greatly complicated by the highly nonlinear characteristics of the actual joint hardware. System identification methods for multi-input, multi-output models, which correspond to the manual mode operations of the arm, are currently being evaluated, with the Eigenvalue Realization Algorithm (ERA) [7] showing potential for this class of problem.

LINEAR SYSTEM IDENTIFICATION APPROACH

Linear system identification approach:

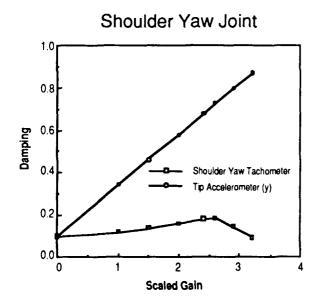
- Single-input, single-output, state-space models
- Using Least-Squares and Maximum Likelihood methods
- 3-5 structural modes
- Joint rate command inputs, joint tachometer or tip acceleration output
- Complicated by highly nonlinear joint dynamics
- ERA method for multi-input, multi-output

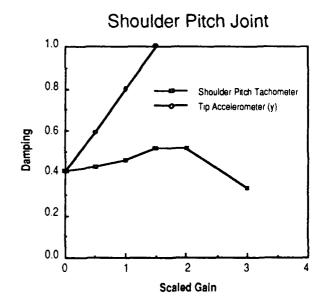


SISO ACTIVE DAMPING AUGMENTATION RESULTS

Using the single-input, single-output (SISO), linear state-space models derived from system identification, simple gain feedbacks of tachometer or acceleration signals to the joint rate command for single joint mode cases have been completed. Results are shown in terms of RMS damping improvement as a function of a scaled gain parameter, which normalizes the actual feedback gain by the overall loop gain. For CSI Position 1 with the SPAS payload, results are shown below for the shoulder-yaw and shoulder-pitch joints. The initial damping values for zero gain for the two joints are different because the joints excite and are able to control different structural modes. For both joints, feedback of the tachometer signal initially resulted in a small increase in RMS damping. Feedback of the acceleration signal in both cases showed larger achievable increases in damping. While the trends for the two joints are the same, the differences of the results in terms of which mode is being influenced illustrate the high configurational dependence of RMS dynamics.

SISO ACTIVE DAMPING AUGMENTATION RESULTS Position 1



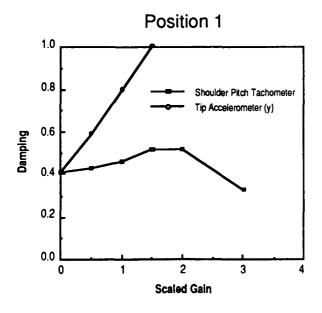


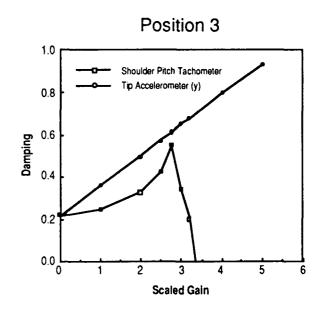
SISO ACTIVE DAMPING AUGMENTATION RESULTS

Results similar to the previous page further illustrate the configurational dependence of RMS dynamics. The result on the left, which is the same as previously shown for shoulder pitch in CSI Position 1, is now compared the shoulder pitch result in CSI Position 3. Note the differences in open loop damping and the effect of tachometer feedback for the two configurations. Feedback of tip acceleration is less affected by the configuration change, and appears to be more desirable than tachometer feedback for active damping augmentation.

SISO ACTIVE DAMPING AUGMENTATION RESULTS

Shoulder Pitch Joint

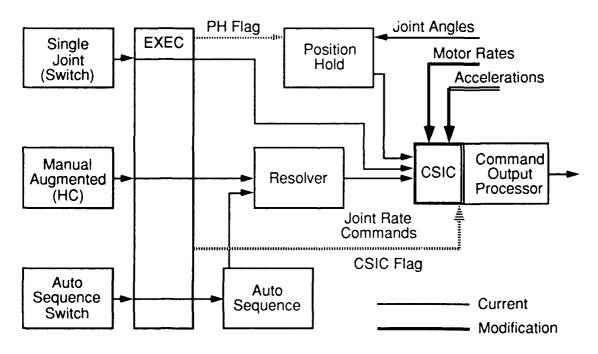




CSI CONTROLLER IMPLEMENTATION IN GPC SOFTWARE

Based on the recommendations of CSDL, a potential means of implementing an active damping augmentation controller in Shuttle GPC software has been identified. This implementation would allow the use of all existing RMS health and safety monitoring functions, greatly simplifying flight experiment requirements. The Control-Structure Interaction Controller (CSIC), as it is called, would be a software module which acts as a preprocessor to the existing Command Output Processor (COP). It would be controlled by the executive function of the existing software by a flag which would activate the CSIC when joint movement commands are zeroed. Using motor rate and acceleration feedback signals, the CSIC would damp the free response of the arm to some level, at which time the normal position-hold function of the arm would be activated. With this implementation, the damping function of the CSIC could be expanded to damp RMS motions following Shuttle thruster firings as well, since the GPC software knows when thruster firings have occured.

CSI CONTROLLER IMPLEMENTATION IN GPC SOFTWARE



CSDL currently modifying DRS for evaluation of CSIC concepts

CONCLUSIONS AND FUTURE PLANS

This paper has summarized an ongoing analytical study to determine the feasibility of actively augmenting the damping of the Shuttle RMS as a proposed CSI flight demonstration. Based on initial results, such an experiment appears feasible using the existing joint hardware and Shuttle computers and software. However some additional feedback sensors in the form of accelerometers located at the tip of the arm will be required. Because of the high dependence of the arm dynamics on configuration, the actual flight demonstration would likely be restricted to a few known configurations. The current feasibility study is continuing, with the assessment of controller performance using a modified version of the DRS, which includes the CSIC controller implementation, to begin shortly. The multi-input, multi-output system identification efforts and linear flexible model development efforts will continue, as will studies to define the minimum set of new feedback sensors.

CONCLUSIONS AND FUTURE PLANS

Active damping demonstration using RMS appears feasible

- GPC software implementation using existing joint motors
- Linear single-input, single-output studies indicate acceleration feedback necessary
- Flight tests would be limited to known configurations
- Technology could be applied for general RMS use

Feasibility study is continuing

- Plan to evaluate gain closures using DRS
- Define minimal additional sensors (accelerations)
- System ID and control designs for manual mode operations
- Linear flexible models for control concept evaluation

REFERENCES

- [1] Demeo, M. E.: Remote Manipulator System (RMS) Based Controls Structures Interaction (CSI) Flight Experiment Feasibility Study. NASA CR 181952, January 1990.
- [2] Demeo, M. E.; Fontana, A.; and Bains, E. M.: Shuttle Remote Manipulator System (RMS) Based Controls Structures Interaction Flight Experiment. Fourth NASA / DOD Conference on Controls Structures Interaction Technology, Orlando, Florida, November 5-7, 1990.
- [3] Lamb, B. A.; and Nowlan, D. R.: Benefits of Control Structure Interaction (CSI) Technology to Space Station Assembly by Flexible Rebotic Systems (RS). CRAD NAS1-18763, November 1989.
- [4] Gray, C.; et. al.: Validation of the Draper RMS Simulation (DRS) Against Flight Data. CSDL-R-1755, Volumes 1-2, April 1985.
- [5] NSTS 07700, Volume XIV, Appendix 8, System Description and Design Data Payload Deployment and Retrieval System, Revision J, May 1988.
- [6] Abelow, A. V.: Comparisons of Remote Manipulator System Finite Element Models. Charles Stark Draper Laboratory Report R-1210, November 1978.
- [7] Juang, J.-N.; and Pappa, R. S.: An Eigensystem Realization Algorithm for Modal Parameter Identification and Model Reduction. Journal of Guidance, Control, and Dynamics, Vol. 8, No. 5, September-October 1985, pg. 620-627.

^{*} U.S. GOVERNMENT PRINTING OFFICE: 1991/548-076/44256/176